Sedimentology and tectono-stratigraphic development of the syn- to post-rift transition in Southern Neuquén Basin (Argentina) and controls on early post-rift submarine lobes of the Los Molles Formation

Aurélia Marie-Luce Jenny Privat

Submitted in agreement with the requirements for the degree of Doctor of Philosophy (Ph.D.) in Geosciences

School of Earth and Environment

The University of Leeds

United Kingdom

June 2019

The candidate confirms that the work submitted is her own, except where work which has formed part of jointly authored publications has been included. The contribution of the candidate and the other authors to this work has been explicitly indicated below. The candidate confirms that appropriate credit has been given within the thesis where reference has been made to the work of others.

Chapter 4 is based on a manuscript "*Evolution from syn-rift carbonates to early post-rift deep-marine intraslope lobes: the role of rift basin physiography on sedimentation patterns*" that is founded on a detailed case study conducted in the Chachil basin, which is in re-review at *Sedimentology*. Authors contributions:

Privat, A. M-L J. – Main author. Responsible for data collection, processing, interpretation and writing of the manuscript. Assistance in the field for data collection was mainly provided by Louis Thoreau and Andy Emery.

Hodgson, D. M. – Discussion and detailed manuscript review.

Jackson, C. A-L. – Discussion and detailed manuscript review.

Schwarz, E. – Discussion and detailed manuscript review.

Peakall, J. – Discussion and detailed manuscript review.

Submitted: 29th October 2018

Resubmitted: 1st May 2019

Acknowledgements

I would like to thank my supervisors, Dave Hodgson, Chris Jackson, Ernesto Schwarz and Jeff Peakall, for their support and stimulating scientific discussions during these four last years and I am grateful for the financial support from the sponsors of the LOBE2 project. I would also like to thank my examiners Richard Collier and Matthew Watkinson for accepting to judge my thesis. A special thank to Dave for giving me this opportunity to work in the Neuquén Basin and welcoming me in UK. You have always been understanding and present whenever I asked you and I am very grateful for the support, trust and freedom that you gave me in that project. A huge thank to Chris and Jeff for coming out in the field and for always being positive, supportive and present to discuss ideas. Last but not least, Ernesto thank you for your constant guidance in and out of the field despite the long distance, with all the time and energy you took to share your knowledge, understanding and criticizing my work, always to push me to reflexion and improvement. You are all incredible teachers and amazing personalities. I should also thank my former supervisors Julien Bailleul and Sebastien Migeon for their support, and for encouraging me to get that thesis and leave for UK despite my concerns about weather issues.

Thanks to Yvonne, Andy and Lucho for your precious help in the field in Argentina, despite the rude conditions (snow, storms, >100 km/h gravelly wind or heat) you have all been warriors and I really enjoyed the time spent together. I also loved fieldwork in South Africa with you Yvonne, whatever scorpio, bees, rockfalls or chickenpocks it was all fun! Special thanks to my bro, Luch, despite your crush on ammonias, you made it from Chos Malal to Zapala for the longest and hardest fieldseason. The basic idea was just to get a criminal case in order to be locked more than 2 months in the field and collect the best dataset of this thesis, fitting our classic “take it easy mind” in the worst expectable situation. You are an amazing geologist and friend, and I could never make it without you. Big up to the “old” StratGroup family who welcomed me in UK with all the fun and warmth needed: Luz Gomis-Cartesio, Andrea Ortiz-Karpf, Yvonne Spychala, Miquel Poyatos-Moré, Marcello Gugliotta, Kevin Boulesteix, Menno Hofstra, Hannah Brooks, Sarah Cobain, Jannet Richardson, Catherine Russel, Chris Stevenson, Dan Bell, Bonita Barrett-Crosdil, Grace Cosgrove…and I forget many. Grazie mille to Riccardo Teloni, I would end mad without that routine

drifting from the office to nightclubs, but also without your support camel. Merci to my sedi french bae Pauline Cornard, wouldn't be the same fun without our regular teaming for the worst and the best mess. Muchas gracias to Marina Coronel, Gastón Álvarez-Trentini, Manuel Isla, Marian Ramírez, Augustín Argüello, Ernesto Schwarz and Gonzalo Veiga for the warm welcoming in La Plata, from the office to asados. Thanks to Jonatan Arnol for all the help and work for U-Pb age dating at the CIG of La Plata. Thanks also to my friends Marcos and Carlos Retamal for welcoming and helping us in Zapala, and for all the good time spent together.

Thanks to my best friends, Blandine for your unconditional understanding and support despite the distance, Fred and Mathilde (La bonde!) for your love-sur-porc lkl, but mostly for bringing me the fundamental dose of weirdness and craziness each time that we see. Thanks for my 074 friend family: Ln, Marion, Marie, Lise, Mandoue, Lucho, Simon, Pepit, Got, Charlie…almost 10 years that love is in the air and things remain the same whatever the country. I am also thankful to my Villefranche sedimentologist and mermaid team, Flore Mary, Virginie Hassoun Maelle Kelner and Cecile Joubert for all the fun and support since the master. Flore, thanks for "trying to" relax me/you during this last stressful year! Yes, we'll just settle our clastic lab there forever, looking at sand or chasing urchins, and make it to Monaco by night, no problem. Finally, I am so grateful to Adrien for the trust, help, patience and all the love you gave to me during all these years. I have been very lucky to get myself a servietsky on my side working out the confusing mechanics of my "coconut" brain, plus making all concessions to accommodate my sea and sand addictions.

I am incredibly grateful to my family, especially my wonderful parents and amazing sister for always giving me the best, protecting me, managing with all the health issues and believing in me all the way whatever the difficulties, enough to encourage me to leave our remote New-Caledonia island to go study on the other side of earth. Neurotransmitter deficiencies made my life complicated, impulsive and delusional, but each day reminds me to put into perspective the recipe of unconditional happiness. I dedicate this tesis to my special great grandma for giving me that hereditary neurodivergence mess, and to all the people trying to tame that health and mental condition and their difference to try to be "normal", as this is the best challenge I am/have learned from.

Abstract

Marine rift basin-fills record the interplay between sediment supply and accommodation, which controls the organization and evolution of depositional environments in time and space. This study documents the tectono-stratigraphic architecture of multiple exhumed Early Jurassic marine rift depocentres of the southwestern Neuquén Basin, Argentina. Petrographic analyses of sandstone and new U-Pb ages are used to revise the current chronostratigraphic framework framework and to reassess sediment sources. This provides new insights in the timing of depocentre linkages, contrasting syn- to post-rift transition signatures, and diachroneity of early post-rift lobes in adjacent rift basins. The development of intraslope lobes in the Los Molles Fm. is documented from the late Early Toarcian, while the true basin-floor of the Neuquén Basin remained sand-starved during the Early Jurassic.

At basin margin-scale, the late syn-rift is characterized by transverse systems, with mixed contribution of intrabasinal siliciclastic intrarift or volcanic arc-derived sediment supply and extrabasinal cratonic sediment supply from the southeastern basin margin. The early post-rift is characterized by the development of extrabasinal volcanic arc-derived intraslope fans, with axial sediment routeing across a low- to moderate-gradient ramp-type system flanking the volcanic island arc basin margin. At a regional-scale, inherited topography results in initial trapping of sands in depocentres proximal to the source, until healing of intrabasinal relief enables overspill, bypass and progradation of intraslope fans into more distal sand-starved depocentres. At the scale of individual depocentres, this study demonstrates the interactions of sediment gravity flows with subtle inherited rift and compaction-enhanced topography, and their impact on the characteristics of early post-rift lobes.

This study extends established tectono-stratigraphic models of marine rift basin-fills during the syn- to post-rift transition to backarc settings, and provides new outcrop-based models for different types of low aspect ratio early post-rift lobes.

Table of content

Acknowledgements iii

Abstract v

Table of content vii

List of figures xv

List of tables xxix

Chapter 1 Introduction 1

1.2. Background 1

1.2. Thesis rationale and relevance to current research 4

1.3 Objectives and research questions 8

1.3 Methodology 10

1.3.1 Outcrop data 10

1.3.2 Geochronological data 12

1.3.3 Thin section data 13

1.4 Thesis outline 14

Chapter 2 Scientific background 19

2.1 Models and nomenclature for the genesis and evolution of rift basins 19

2.1.1 Diversity of rift architecture 19

2.1.2 Kinematic rift models 23

2.1.3 Stratigraphy of rift basins 25

2.1.4 Surface processes 29

2.1.4.1 Fault growth and structural heritage 29

2.1.4.2 Sedimentation and subsidence 31

2.1.5 Back-arc basins 33

2.2 Sedimentation patterns during the syn- to post-rift transition 35

2.2.1 Early rift 38

2.2.2 Rift climax 41

2.2.3 Late Rift 43

2.2.4 Early post-rift 44

2.2.5 Late post-rift 49

2.3 Submarine fans in topographically complex settings 50

2.3.1 Intraslope lobes 51

2.3.2 Early post-rift lobes 56

2.3.3 Interactions of sediment gravity flows with seabed topography ... 61

Chapter 3 Introduction to the Neuquén Basin 67

3.1 Introduction 67

3.2 Orogen to rift evolution: Palaeozoic to Early Jurassic 71

3.2.1 Pre-Andean to Pangea breakup evolution 71

3.2.2 Pre- and syn-rift sedimentation 73

3.2.3 Rifting mechanism in the Neuquén Basin 75

3.2.3 Structural style and deformation of the Neuquén Basin 77

3.3 Back-arc to foreland evolution: Jurassic to Cenozoic 81

3.3.1 Syn- to post-rift post-rift back-arc evolution 81

3.3.1.1 Onset of subduction and Early Andean volcanic island arc 81

3.3.1.2 Marine flooding of the Andean Basin and syn-to-post-rift transition 83

3.3.1.3 Early Jurassic palaeogeographic changes 86

3.3.2 Late post-rift sag to Andean foreland evolution 87

3.4 Syn- to post-rift stratigraphy 90

3.4.1 Lower Cuyo Group 90

3.4.2 Upper Cuyo Group 95

3.4.3 Early Jurassic stratigraphic scheme of this study 95

3.5 Los Molles Fm. 99

3.5.1 Early Jurassic Lower Los Molles Fm. 99

3.5.2 Middle Jurassic Middle and Upper Los Molles 101

Chapter 4 Evolution from syn-rift carbonates to early post-rift deep-marine intraslope lobes: the role of rift basin physiography on sedimentation patterns 105

4.2 Introduction 105
4.3 Geological setting and stratigraphy 107
4.4 Study area and data 108
Chachil Graben 108
Data and methodology 110
4.5 Stratigraphy and facies associations 115
FA1: Carbonate platform 120
FA2: Proximal periplatform 124
FA3: Distal periplatform 125
FA4: Siliciclastic-starved lower slope 127
FA5.1: Intraslope lobes- Distal lobe fringe 128
FA5.2: Intraslope lobes- Frontal lobe fringe 135
FA5.3: Intraslope lobes- Lobe axis 139
4.6 Synthesis of depositional systems and architecture of tectono-sedimentary units 141
Unit 1 141
Unit 2 144
Unit 3 146
Unit 4 147
4.7 Discussion 150
4.7.1 Early post-rift inherited topography 150
Unit 3 150
Unit 4 152
4.7.2 Controls on sedimentation during the syn- to post-rift transition 155
Late syn-rift 155
Early post-rift 156
4.7.3 Implications for characteristics of early post-rift lobe complexes 158
4.8 Conclusion 160

Chapter 5 Deciphering the stratigraphic variability of syn- to post-rift transition successions and physiographic evolution across several basins of the southern Neuquén Basin based on new U-Pb ages in the Los Molles Fm. 165

5.1. Introduction 165

5.2. Geological setting 167

5.3. Study area and structural framework 171

5.3.1. Structural framework 171

5.3.2. Stratigraphy of the study area 175

5.4. Methods 176

5.4.1. Fieldwork 176

5.4.2. Geochronology 182

5.4.2.1. Analytical method 182

5.4.2.2. Results 184

5.5. Facies associations 187

5.5.1. Unit 1 196

5.5.1.1. Description 196

FA1.1 196

FA1.2 196

5.5.1.2. Interpretation 199

FA1.1: Alluvial fans 199

FA1.2: Slope aprons 199

5.5.2. Unit 2 200

5.5.2.1. Description 200

FA2.1 200

FA2.2 203

FA2.3 204

FA2.4 206

FA2.5 206

5.5.2.2. Interpretation 208

FA2.1: Lower shoreface 208

FA2.2: Shoreface-offshore transition 209

FA2.3: Offshore 210

FA2.4: Prodelta 211

FA2.5: Delta-front....211
5.5.3. Unit 3....213
5.5.3.1. Description....213
FA3....213
5.5.3.2. Interpretation....215
FA3: Siliciclastic-starved basin....215
5.5.4. Unit 4....216
5.5.4.1. Description....216
FA4.1....216
FA4.2....218
FA4.3....219
5.5.4.2. Interpretation....221
FA4.1: Distal ramp lobes....221
FA4.2: Proximal ramp lobes....222
FA4.3: Sand-starved slope....224
5.6. Synthesis of depositional systems....224
Unit 1....224
Unit 2....227
Unit 2A....227
Unit 2B....233
Unit 3....235
Unit 4....235
5.7. Stratigraphic architecture....242
5.7.1. J1.1 sequence....242
5.7.2. J1.2 sequence....246
5.7.3. Summary and implications for the syn- to post-rift transition....247
5.8. Discussion....249
5.8.1. Chronostratigraphy: Revision of the stratigraphic framework at the light of new U-Pb ages....249
5.8.2. Evolution of syn- to post-rift sedimentation at a regional-scale 257
5.8.2.1. Late syn-rift sedimentation (Early-Late Pliensbachian)....257
5.8.2.2. Early post-rift sedimentation (Early Toarcian-Aalenian)....265

5.8.3. Effects of inherited rift topography during the syn- to post-rift transition 273
5.8.4. Early post-rift depositional system 275
5.8.5. Early post-rift sediment supply 276
5.9. Conclusion 279
Chapter 6 Textural and compositional analysis of sandstone in the Early Jurassic Los Molles Formation 283
6.1. Introduction 283
6.2. Geological setting 284
6.3. Methods 289
6.4. Stratigraphic units 293
6.4.1. Characteristics of sandstone lobe complexes 293
J1.1 sequence Delta-front lobes 293
Description 293
Interpretation 294
J1.2 sequence Intraslope fan lobes 295
Description: Lower J1.2 lobes 295
Interpretation Lower J1.2 lobes 296
Description Upper J1.2 lobes 296
Interpretation Upper J1.2 lobes 297
J2.1 sequence Intraslope fan lobes 298
Description J2.1 lobes 298
Interpretation J2.1 lobes 299
6.4.2. Delta-front and intraslope fan sandstone petrofacies and textural characteristics 301
6.4.3. Sandstone composition 312
Grains 312
Matrix and cement 320
6.5. Analysis of compositional stratigraphic trends 320
6.6. Discussion 328
6.6.1. Source provenance 328

6.6.2. Implications for sediment supply from the Early Andean volcanic island arc margin 332

6.6.3. Stratigraphic architecture of intraslope fans of the Los Molles Formation.....334

6.6.4. Change recorded within an intraslope fan sequence (J1.2) ...334

6.6.5. Change recorded across intraslope fan sequences (J1.2-J2.1) 336

Conclusion.....338

Chapter 7 Discussions and conclusions 343

7.1 What factors controlled the temporal and spatial variability of the syn- to post-rift transition sedimentation?.....343

7.1.1 Intrabasinal topography.....343

7.1.2 Sediment supply.....347

7.2 What are the characteristics of the syn-to post-rift transition signature?.....349

7.2.1 Depocentre-scale perspective.....349

7.2.2 Basin-scale perspective 350

7.3 What were the timing and source for early post-rift sand supply, and their implications for palaeogeographic evolution of the Southern Neuquén Basin margin?..... 353

7.3.1 Revised timing of sand supply in the Early Jurassic Los Molles Formation.....353

7.3.2 Insights from the palaeogeographic evolution of the Southern Neuquén Basin margin 354

7.3.3 Implications of sandstone source type for hydrocarbon reservoirs distribution along the Southern Neuquén Basin margin.....362

7.4 What are the characteristics of early post-rift intraslope fan deposits of the Early Jurassic Los Molles Formation and how do they compare to other deep-marine sandy systems?.....366

7.4.1 Facies characteristics of lobes in the Early Jurassic Los Molles Formation.....366

7.4.2 Comparison of intraslope lobe complex dimensions, stacking patterns and termination style of the Early Jurassic Los Molles Formation with other basin-floor and intraslope systems 372

7.4.3 Controls on confinement and development of bed-scale heterogeneity in intraslope lobe complexes of the Early Jurassic Los Molles Formation 377

Chapter 8 Conclusions 381

References 389

Appendices 433

List of figures

Figure 2.1: Scheme (Gartrell et al., 2001) showing the three end member modes of lithospheric extension depending on thermal state of the lithosphere and crustal thickness. Hot and weak lithosphere promotes ductile deformation with strong decoupling between brittle crustal and mantle. This can promote a metamorphic core complex mode in the case of thick and high heat flow conditions (A),or wide rift mode in the case of intermediate crustal thickness (B). Cooler and stronger, thin crust leads to preferential coupling between crust and mantle and brittle deformation results in narrow rifts. Plots show yield strength with depth for hypothetical geothermal gradients and crustal thickness (modified after Buck, 1991). _____ *21*

Figure 2.2: Schematic cross sections and seismic examples (Franke, 2013) showing pre-rift, syn-rift and breakup rift evolution of rifts, with formation of a rift onset unconformity (ROU) with top-lap truncations of seismic reflectors from below, which is overlain by wedge-shaped syn-rift successions. Continental breakup leads to formation of the breakup unconformity truncating the syn-rift sediments then onlapped by post-rift successions, and amalgamated with the rift-onset unconformity at basin margins. _____ *25*

*Figure 2.3: Ideal syn- to post-rift transition record after Prosser (1993).*_____ *26*

*Figure 2.4: Conceptual model showing the differences with rift development without influence of pre-existing structures or with reactivation of pre-existing structures during rifting modified after Whipp et al. (2013) and modified after Gawthorpe and Leeder (2000). (a) Fault initiation stage record low displacement faults and extensional folds. (b) Fault linkage and strain localization onto larger faults whereas faults in strain shadow zones are abandoned. (c) Through-going fault phase with localized deformation onto few major fault systems. (d) Structural framework during the rift phase with oblique extensional reactivation of inherited rift structures which rapidly reach their full-length prior accumulating significant displacement, whereas newly formed structures develop perpendicular to inherited reactivate drift structures. (e) During rift climax these newly formed structures are rapidly abandoned with strain localization onto larger and older inherited faults.*_____ *30*

*Figure 2.5: Diagram showing the different classes of sedimentary basins and their respective lifetime, basement type and deformation style, with estimated heatflow compiled from Blum and Hattier-Womack (2009).*_____ *35*

Figure 2.6: Conceptual tectono-sedimentary model for marine rift basins (Duffy et al., 2015, after Gawthorpe and Leeder, 2000) showing the effects of topography and fault geometry on base-level and sedimentation in marine rift basins. _____ *36*

Figure 2.7: Conceptual internal architecture of an ideal rift sequence (Martins-Neto and Catuneanu, 2009) with coarsening-upward vertical stacking pattern, and shift from underfilled to filled and overfilled conditions and correlation with gamma-ray log. _____ *37*

Figure 2.8: Example of (A) fault growth folding above blind propagating normal fault with thinning an donlapping towards the blind fault and (B) surface breaking fault with wedging and thickening towards the fault. (Gawthorpe et al., 1997) _____ *39*

Figure 2.9: Model for rift climax deep-marine sedimentation, showing the development of coarse-grained slope aprons associated with fault-scarp degradation and restricted catchments and submarine fan fed by a larger point source enabling high sediment supply. (Leppard and Gawthorpe, 2006) _____ *42*

Figure 2.10: Conceptual model for the evolution of sedimentation during rifting from shallow- to deep-marine setting (Henstra et al., 2018; modified after Gawthorpe and Leeder (2000) and Ravnås and Steel (1998). (a) Rift initiation with distributed strain across multiple isolated fault segments. (b) Rift climax and through-going fault phase promoting the development of transverse sedimentary systems. (c) Fault abandonment and development of axial sedimentary systems. _____ *45*

Figure 2.11: Examples of small-scale early post-rift faults in the Pattani and North Malay basins (Morley, 2015) which can be nucleated in the post-rift deposits or which can have relationship with syn-rift faults (A2 and B2)or nucleated above basement highs (C2). _____ *46*

Figure 2.12: Example of early post-rift onlap and compaction-related synclines in a half-graben (Faerseth and Lien, 2002). _____ *48*

Figure 2.13: Classification of lobes, lobe elements and lobe complexes by Prélat et al. (2009) and Deptuck et al. (2008) used to characterize submarine fan systems (modified after Cullis et al., 2018). _____ *50*

Figure 2.14: Perspective of perched and ponded aprons of the Brazos-Trinity intraslope basin in the Gulf of Mexico (Prather et al., 2017). _____ *52*

Figure 2.15: Conceptual model for the depositional evolution of a stepped slope profile describing the depositional and erosional response of sediment gravity flows to slope build-up and reduction of accommodation (Hay, 2012). _____ *54*

Figure 2.16: Interpretative sketch showing the architecture of the Ogooue along ramp and step slope (a) and bathymetric profile showing the subtle changes of slope gradient (<2) (b) which control changes in sedimentary processes and sand distribution in intraslope basins. _____ *55*

Figure 2.17: Seismic line along-strike the Late Cretaceous Kyrre slope fan across the Måløy Slope and reflection strength amplitude map of depositional systems showing the effect of compaction-related topography onto development of early post-rift sand distribution across the slope (Jackson et al., 2008). _____ *57*

Figure 2.18: Example of lateral onlap of intraslope fan offshore West Africa showing three-dimensional seismic root-mean-square map of stratigraphic traps on a semiconfined basin slope and interpretation sketch showing two sandstone-prone units with different termination styles (Bakke et al., 2013). ____ *58*

Figure 2.19: Diagram showing the different sandy versus heterolithic pinchout styles (Bakke et al., 2013). _____ *58*

Figure 2.20: Example of early post-rift slope apron type lobes developed in the Sea Lion Fan showing the geometry and distribution of facies associations at the scale of lobes developed in a lacustrine setting (Dodd et al., 2019). _____ *60*

Figure 2.21: Diagram showing the variable interaction of a range of sediment gravity flows with seabed topography, depending on their laminar (L) or turbulent (T) behaviour and co-genetic turbulent-laminar or transitional behaviour, with flow classification after Haughton et al. (2009) (Bakke et al., 2013). __ *62*

Figure 2.22: Model illustrating the change in porosity, permeability and quartz cementation in High Density Turbidites (HDT), Hybrid Event Beds (HEB) and Low Density Turbidites (LDT). Dashed lines represent previously published depth trends for reservoir sandstones of the Norwegian continental shelf (see Porten et al., 2016). The variability in evolution of reservoir properties with burial is controlled by original sediment composition (grain-size, sorting, detrital clay content and ductile grains) and quartz cementation._____ 63

Figure 3.1: Map of the Neuquén Basin. _____ 68

Figure 3.2: Bloc diagrams showing the main stages of basin evolution from Late Triassic to Cenozoic (Howell et al., 2005). (A) Late Triassic-Early Jurassic time with opening of rift basins. (B)Jurassic-Early Cretaceous evolution in a back-arc setting with subduction along the western Gondwana margin. (C) Late Cretaceous Andean uplift and foreland evolution with fold and thrust belt development._____ 69

Figure 3.3: Chronostratigraphic chart of the Neuquén Basin (Howell et al., 2005). _____ 70

Figure 3.4: Schematic cross section showing the Late Palaeozoic to Middle Jurassic geodynamic evolution of the southwestern Gondwana margin and the Neuquén Basin (Franzese and Spaletti, 2001)._____ 73

Figure 3.5: Map of the Neuquén Basin showing the distribution of syn-rift depocentres modified after (Bechis et al., 2014)._____ 79

Figure 3.6: Schematic cross sections showing the change from (a) Early Jurassic-Cretaceous intra-arc extension, (b) stationary stage during the Aptian-Albian and (c) Late Cretaceous to present Andean compression (Ramos, 2010.) _____ 82

Figure 3.7: Palaeogeographic evolution of the Neuquén Basin with marine flooding during the Early Jurassic (Damborenea et al., 2013). (a) Palaeogeographic reconstruction of the Neuquén Basin as part of the southwestern Gondwana. (b) Representation of the the Early Jurassic palaeoseaway of marine flooding from Peru to the Chubut Basin to the south. (c) Map showing the distribution of depositional environments in the Neuquén Embayment. _____ 84

Figure 3.8: Cross sections showing the change of subduction regime and foreland evolution evolution of the Neuquén Basin (Horton et al., 2016). _____ 88

Figure 3.9: SW-NE seismic line in the Portezuelo Grande area modified after Pángaro et al. (2002). Seismic lines show the impact of the distribution of the Precuyano deposits on the sedimentation of the Lower Cuyo Group. Note the stratovolcano (1500 m high) that formed syn-rift relief, which influenced the sedimentation up to Lower Toarcian and produced thickness variations in the Pliensbachian Lower Cuyo Group. The base of the Lower Cuyo Group (Sinemurian-Pliensbachian to Lower Toarcian) is interpreted as a late syn-rift succession that deposited (i) unconformably onlapping onto the erosional angular intra-Liasic discordance at the top of the Precuyano strata; or (ii) conformably where the Precuyo deposits lack due to non-deposition or were not eroded (Pángaro et al., 2009). _____ 91

Figure 3.10: (1) W-E seismic line in the Piedra Chenque area and (2) WSW-ENE seismic line in the Aguada Toledo area modified after Pángaro et al. (2006). Seismic lines flattened at the top of Lower Toarcian, and interpreted as sharp rift-sag transition. Line 1 shows along-strike effects of structural palaeohighs (Divisadero Fault anticline) and tectonic subsidence related to rift faults accommodated from Pliensbachian to Upper Toarcian by thickness variations and onlap/toplap in the Lower Cuyo Group. The

seismic line (2) shows the hiatus of the Pliensbachian-Early Toarcian Lower Precuyo deposits, interpreted to be the result of short duration rifting in this sector. The Lower Toarcian strata onlap Precuyo deposits and sedimentation could interact up to the Upper Toarcian with palaeoreliefs formed by rotated blocks (Pángaro et al., 2006). 92

Figure 3.11: SW-NE seismic line in the Entre Lomas SW-NE seismic line in the Entre Lomas area modified after Cristallini et al. (2009). Interpreted and uninterpreted lines evidence normal faulting localized above basement highs and affecting in the Lower Cuyo Group deposits, Faults propagated parallel to NW-oriented Precuyo faults or propagated "en-échelon" above W-NW Precuyo faults. The normal faulting in the Lower Cuyo Group is interpreted as a result of differential compaction produced by abrupt thickness variations of the Precuyano Cycle syn-rift deposits (up to 2000m thickness change across 10 km distance; Entre Lomas-Estancia Vieja). 93

Figure 3.12: Stratigraphic scheme of the Cuyo Group. The Lower Cuyo Group is detailed based on results presented in this study showing the different formations names, their respective units and their stratigraphic architecture across the study area. Age constrains from this study and the literature are shown, together with other stratigraphic schemes existing from the subsurface and outcrop studies. Note the long-lived effects of the inherited rift topography recorded in the Los Molles Formation and the different hypothesis for Late Toarcian-Aalenian onset of sand supply which cannot explain the deposition of sandstone since the late Early Toarcian in the study area. 97

Figure 4.1: A- Map of the Neuquén Basin showing the location of the Chachil Graben detailed in fig. 4.1-B and the Pliensbachian-Toarcian palaeogeographic setting (subsurface palaeoshelf southern border of the Neuquén Basin and depocentres after Gómez Omil et al., 2002 and García Morabito et al., 2011). B- Map of the Chachil and Catán-Lil Graben (including structures after Leanza, 1990; Franzese et al., 2006; Muravchik et al., 2014) showing location of the panorama in fig. 4.1-C and detailed geological map of the study area in fig. 4.2-A. C- Panorama from the horst border to the adjacent hangingwall of the Chachil Graben showing structures and spatial distribution of the Lapa, Chachil and Los Molles formations. 106

Figure 4.2: Synthetic stratigraphic column representing thickness of lithostratigraphic units, changes in sediment composition and biota, source contribution and interpretations for tectonic stages. Numerical Early Jurassic ages from Ogg et al. (2016); (NC) nannofossil chronozones (Ballent et al., 2011); Standard European Ammonite Biozone (EAB) and Andean Ammonite Biozone (AAB) numbers (Riccardi, 2008); age at base of the Chachil Fm. (186.3 ± 0.4 Ma from Leanza et al., 2013 and modified after Armella et al., 2016); negative δ13C excursion and TOAE from Al-Suwaidi et al. (2016) in the Tenuicostatum-Dactylioceras hoelderi zones (AAB 15-16) equivalent to the Tenuicostatum-Spinatum EAB and constrained in NJ6 nannofossil chronozone from Angelozzi and Pérez Panera (2016); climate from Volkheimer et al. (2008); coastal onlap curve (Legarreta and Uliana, 1996); eustatic sea-level (Haq, 2018). 110

Figure 4.3: A- Detailed map of the Chachil Graben showing the relationship between structures and tectono-sedimentary units of the Chachil and Los Molles formations. B- Cross sections (not restored) indicated on the map with location of structures and locality names. 111

Figure 4.4: Table of the calculated average structural dip and dip direction of mean bedding planes for each tectono-sedimentary unit in each zone realized with Stereonet software. Zone SW includes sections 1-2-3-4, Zone Central includes sections 5-6-7 and Zone NE includes sections 8-9-10. Stereonet diagrams show the mean bedding values for each unit (colours in stereoplots correspond to colours of units in the table), the associated average dip direction vector (bold circle), and all the other dip direction vectors measured (circles). _____ *112*

Figure 4.5: Correlation panel (~10 km long transect indicated in fig. 4.3-A), showing relationships between units along the main hangingwall of the graben-horst border, average discordance angles (see fig. 4.4) and palaeocurrent measurements. Each rose diagram presents the detail of sole marks, ripples and dune-scale cross bedding current directions, each corresponding to a different colour indicated in the key. Note that the detailed architecture of the Lapa Fm. is not represented and that vertical offset on faults are approximate. Orientation of sections is located on map fig. 4.3. _____ *113*

Figure 4.6: Representative photographs of facies associations. A- FA1: Thin- to medium-bedded silicicified carbonate platform successions. B- FA3: Thin- to medium-bedded mud-rich mixed carbonate-clastic successions of distal periplatform. C- FA2: Medium-bedded mixed carbonate-clastic successions of proximal periplatform. D- Transition from FA4 to FA5.1. FA4: Very thin- to thin-bedded calcareous mudstone-dominated successions of siliciclastic-starved basin. E- FA5.1: Thin-bedded muddy heterolithic successions of distal lobe fringe with significant scouring. F- FA5.2: Thin- to medium-bedded sandy heterolithic successions of proximal lobe fringe. G- FA5.3: Medium- to thick-bedded sandstone-dominated successions of dirty lobe axis. H-FA5.3: Medium- to thick-bedded sandstone-dominated successions of cleaner lobe axis. _____ *116*

Figure 4.7: Detailed correlation panel showing the internal architecture and spatial facies relationships within Units 1 and 2 (Chachil Fm.); facies are detailed in Table 4.1. _____ *121*

*Figure 4.8: Representative photographs of facies. A- Fossiliferous packstone (F1b) bearing reworked volcaniclastic coarse sand-sized grains (K-feldspar) and abundant large broken bivalve shell fragments scattered throughout beds. B- Calciturbidite (F2b) characterized by their crude normal grading and a high proportion of bioclasts (crinoids (Cri), bryozoans (Bry), thick-walled disarticulated shells) with a few reworked volcaniclastic subrounded pebbles. C- Bioclastic packstone (F3a) with reworked volcaniclastic fine to medium sand-sized grains (quartz, K-feldspar) and small disarticulated to broken shells of bivalve and brachiopod concentrated in wavy normally graded grain-rich layers. D- Massive calcareous mudstone (F4a) bearing thin tuff layers, early diagenetic carbonate and pyrite concretions. E- Calcareous bioclastic sandstone (F4c) normally graded with bioclastic base. F- Silty mudstone (F5.1a) interbedded with sandy siltstone current-ripples (F5.1b) locally presenting an opposing palaeocurrent direction.*__ *123*

Figure 4.9: Detailed correlation panel showing the internal architecture and spatial facies relationships within Unit 4 (Lower Los Molles Fm.). _____ *131*

Figure 4.10: Panoramic view from UAV photograph (cars on the road for scale) showing the onlap limit of the Lower Los Molles Fm. (Unit 3) onto the Chachil Fm. (Units 1 and 2), the inferred location of the compaction hinge and distribution of lobe and injectites within Unit 4. Respective lateral and frontal pinchouts are indicated. A- View of slumped mudstone and sandstone interval (1.6 m thick and

kilometre-scale). B- View of the stepped sills injectited across the compaction hinge that pinchout across <2 km. Colours for lobes and facies distribution are detailed in fig. 4.9. _____ *132*

Figure 4.11: Representative photographs of facies associations. A- Injected sandstone (F5.1e) showing a single injected sill body cutting through mudstone. B- Chaotic muddy sandstone (F5.2e) bearing deformed mudstone and sandstone clasts and heterolithic rafts distributed in a patchy medium- to fine-grained matrix enriched in mud and clast-depleted at top. Bed is scouring and rafting into a pinch and swell, massive, mud-poor sandstone with locally low amplitude dune-scale bedforms developed at top (F5.2a). C- Chaotic sandy mudstone (F5.2f) characterized by a starry night-like matrix with plant material, bearing floating large mudstone, siltstone and sandstone clasts with well-preserved shallow-marine pecten and ostreid shells. D- Massive mud- and clast-poor sandstone division (F5.2a) scoured (0.4 m deep and 3 m wide) and filled by homogeneous massive silty mudstone (F5.2d). E- Massive sandstone (F5.3a) stacked into cross-bedded set of scour fill (up to 5 m long and 1.5-2 m thick). F- Medium-grained sandstone with anisotropic hummock-like bedform showing an asymmetric rounded ripple with low-angle foresets (<5°) draped by sinusoidal parallel laminae sets (F5.3c). G- Amalgamated granular sandstone (F5.3b) grading upwards into medium-grained sandstone with undulose laminations (F5.3c). Armoured mudstone clast with quartz pebbles and surrounding broken bioclasts locally found in granular sandstone (F5.3b) is shown in the frame to the left. _____ *134*

Figure 4.12: Different HEB bed types identified in the intraslope lobes, with some examples in photos. The facies in brackets are only locally present. HEB type 1 comprises a basal massive mud-poor sandstone with low amplitude dune-scale mud-rich bedforms at top (F5.2a) and pinch and swell geometry, sharply overlain and locally scoured by a chaotic muddy sandstone (F5.2e) or sandy mudstone (F5.2f). This is in turn overlain by a clast-rich muddy sandstone (F5.2c) with sheared basal contact, or just draped by structured fine-grained sandstone with planar wavy laminations and current ripples (F5.1d). HEB type 2 comprises a basal massive to laminated mud-poor sandstone (F5.2a), grading into banded muddy sandstone (F5.2b) (that can be absent) and/or a clast-rich muddy sandstone (F5.2c) capped by massive silty mudstone (F5.2d). HEB type 3 comprises a massive mud-poor sandstone (F5.2a) grading into a well-developed banded muddy sandstone (F5.2b) capped by massive silty mudstone (F5.2d). _____ *136*

Figure 4.13: Palaeogeographic evolution of the Chachil Graben illustrated in schematic cross sections (not restored) showing changes of depositional setting, facies distribution and inferred fault-block motion during deposition of the units (see the precise timing, fig. 4.2). Section numbers refer to spatial location on the map shown in fig. 4.3-A. _____ *143*

Figure 4.14: Block diagram showing the evolution of sedimentation patterns and interactions with topography in the Chachil Graben from an underfilled to a sediment-balanced depocentre during the syn- to post-rift transition, detailing relationships between facies distribution and structures. Detailed logs in lobes show typical facies association of cleaner lobes rich in HEB type 1 and dirty lobes rich in HEB type 2 and 3, and distal lobe fringe deposits. _____ *153*

Figure 5.1: General map of the Neuquén Basin showing the distribution of syn-rift volcanic depocentres, basement and structures (after Gómez Omil et al. (2002), Silvestro and Zubiri (2008), Yagupsky (2009), Cristallini et al. (2009),Pángaro et al. (2009), García Morabito et al. (2011), Sigismondi and Ramos

(2011), Bechis et al. (2014); location of the Early Andean magmatic arc is after Suárez and Marquez (2007) and volcanic arc depocentres after De la Cruz and Suárez (1997)). _____ *169*

Figure 5.2: Map of the Southern Neuquén Basin showing the structural configuration and distribution of syn-rift volcanic depocentres, basement and structures (after Gómez Omil et al. (2002), Silvestro and Zubiri (2008), Yagupsky (2009), Cristallini et al. (2009),Pángaro et al. (2009), García Morabito et al. (2011), Sigismondi and Ramos (2011), Bechis et al. (2014).) _____ *170*

*Figure 5.3: Regional geological map of the study area showing the location of the studied depocentres (Chacaico, Eastern and Western Catán-Lil, Chachil, La Jardinera), the location of the large-scale stratigraphic sections collected and U-Pb age data used in the stratigraphic chart of fig. 5.3 and 5.25. The map includes informations after Leanza and Blasco (1990), Gulisano and Gutiérrez-Pleimling (1995), Cucchi et al. (2005), Franzese et al. (2006, 2007), García Morabito et al. (2011) and Muravchik et al. (2014).*_____ *173*

Figure 5.4: Detailed map of the two investigated Eastern Catán-Lil and Chacaico depocentres showing the location of logs collected, spatial distribution of tectono-stratigraphic units presented in this study, and palaeocurrents collected in each of these units. _____ *177*

Figure 5.5: Correlation panel showing the spatial distribution of facies associations and relationships between late syn-rift and early post-rift units across structures in each basins (location of logs are shown in the map fig. 5.4), with palaeocurrents and location of the tuff 1 sample. Note that the main datum used to correlated unit is indicated in black dotted line. _____ *178*

Figure 5.6: Stratigraphic scheme for the Chacaico and Eastern Catán-Lil basins, (see section location fig. 5.3) integrated with available constrains of thickness and fossil data from the literature (Volkheimer, 1973; Gulisano and Gutiérrez-Pleimling, 1995; Franzese et al., 2006, 2007; Paim et al. 2008) and U-Pb zircon ages (186.3 ± 0.4 Ma in the Chachil Graben, Armella et al., 2016 modified from Leanza et al., 2013; 182.4 ± 2.3 Ma in the Chacaico Basin, Naipauer et al., 2018), as well as new U-Pb zircon data provided in this contribution (red stars).Nannofossil chronozones follow Ballent et al. (2011), standard European (EAB) and Andean (AAB) Ammonite biozone numbers follow Riccardi (2008) and bivalve biozones follow Riccardi et al. (2011). The TOAE is placed in the late Tenuicostatum-early Dactylioceras Hoelderi AAB after Al-Suwaidi et al. (2016) and in the NJ6 nannofossil chronozone after Angelozzi and Pérez Panera (2016). Note that the stratigraphic names for intraslope fans follow Paim et al. (2008). *181*

Figure 5.7: Sections located in the Chachil (see location of log in fig. 4.5) and Catán-Lil basins (see location of log in fig. 5.5) indicating the position of the tuff samples analysed in this study, at the base and top of Unit 3 which corresponds to the Lower Los Molles Fm. _____ *183*

Figure 5.8: U-Pb geochronology results. A- Mount map of the tuff 1 sample zircons analysed and Temora-2 standard zircons. B- Concordia diagram for the tuff 1, with ellipses at 68.3% confidence level (1σ) and concordia diagram for the tuff 3, with ellipses at 95% confidence level (2σ). Blue ellipse represents the centre of the obtained concordia age provided with 95% confidence level. N is the number of zircon grains recovered, n is the number of accepted zircon grains after excluding anomalous grains. MSWD is the Mean Square of Weighted Deviates. C-Diagram showing the frequency of ages and mean age

obtained in each samples and diagram showing the distribution of zircon spots realized for each sample. _____ *185*

Figure 5.9: A- Medium- to thick-bedded planar- to cross-stratified pebbly sandstone, very poorly sorted, coarse- to medium-grained and bearing normal coarse-tail graded, subangular volcanic, carbonate, metamorphic and granitic pebbles and rare cobbles (FA1.1). B- Siliceous carbonates containing wood fragments and well-preserved Araucariaceae plant stems found in the intervening fine-grained tuffaceous sandstone (FA1.1). D- Very thick-bedded sandstone with a very poorly sorted, ungraded, slightly muddy medium-grained sandstone matrix supporting subrounded volcanic and siliciclastic cobbles and boulders (FA1.2). C- Medium- to thick-bedded, poorly sorted and normally graded coarse- to fine-grained sandstone (FA1.2). _____ *198*

Figure 5.10: A- Succession of highly bioturbated sandy siltstone interbedded with thin to medium beds of fine- to medium-grained structured sandstone and skeletal grainstone (FA2.1). B- Example of anisotropic hummocky cross-stratification in sandstone (FA2.1). C- Thallasinoides bioturbations in sandstone. D- Very poorly sorted, crudely normally graded (with local basal inverse grading), coarse- to fine-grained polymictic gravelly sandstone, bearing subrounded to subangular siliciclastic, volcanic and metamorphic pebbles and cobbles with normal coarse-tail grading in their lower part. E- Moderately bioturbated silty mudstone and muddy siltstone successions (FA2.2). _____ *202*

Figure 5.11: A- Thickening and coarsening-upward succession including basal thin-bedded mudstone and silty mudstone (FA2.3) grading upwards into silty mudstone to muddy siltstone packages with uncommon thin to medium sandstone and breccias beds (FA2.4). B-Skeletal packstone-floatstone with normally graded bioclastic material including broken or disarticulated shells, crinoid ossicles and sponge spicules in a silty-marly matrix (FA2.2). C- Very poorly sorted, coarse- to fine-grained polymictic sandstone planar laminated (2-3 cm thick) with inverse or normal coarse-tail grading of sand- to granule-sized grains (FA2.2). D- Very fine- to fine-grained massive bioturbated sandstone including planolites, curvolithus and chondrite (FA2.2). E- Pyroclastic breccia with juvenile pumice lapillis (5 cm long) showing ragged margins floating in a tuffaceous clayey matrix (FA2.2-FA2.3). F- Thin-bedded siliciclastic mudstone to silty mudstone, with scarce fine-grained sandstone, tuff layers and breccias (FA2.3). G- Fine-grained sandstone with planar parallel and current ripple-cross-laminations (FA2.3). H-Fine-grained sandstone with convolute laminations (FA2.3). _____ *205*

Figure 5.12: A-Thickening- and coarsening-upward succession including medium- to thin-bedded massive mudstone and planar laminated silty mudstone with intervening fine-grained sandstone beds (FA2.4) grading upwards into medium- to thick-bedded sandstone-prone packages (FA2.5). Inset shows bioturbation (Ophiomorpha) at thick sandstone bed top). B- Fine-grained sandstone beds interbedded with planar laminated silty mudstone, showing undulatory to planar parallel laminations with soft sediment deformation (FA2.4). C- Medium- to fine-grained bioclastic sandstone lenses isolated within massive mudstone showing normal grading of granule- to pebble-size comminute shell debris and complete shells and siltstone pebbles (FA2.5). D- Moderately to well sorted, medium- to fine-grained normally graded sandstone, with planar and low-angle cross-laminations and siltstone pebbles (FA2.5). Inset shows carbonaceous-rich siltstone of sandy heterolithics. E-F Example of medium- to fine-grained

sandstone found in sandy heterolithic packages with quasi-planar to undulatory laminations associated with large anisotropic hummocks and asymmetrical rounded ripples with tangential to sigmoidal foresets (E) and symmetrical ripples with rounded crests (F). _____ 207

Figure 5.13: A-Thin- to very thin-bedded calcareous organic-rich mudstone found A- in the Catán-Lil Basin, with darker color, concretions and rare tuff beds and B- in the Chacaico basin, with a lighter color as more calcareous and bearing large ammonites deposited parallel to bedding._____ 214

Figure 5.14: A- Thick-bedded, poorly sorted, matrix-rich, medium- to fine-grained sandstone with a tabular geometry, internally massive to crudely normally graded, locally with faint planar laminations, bearing few mudstone clasts in the lower part of beds. B- Medium- to thick-bedded, poorly sorted, matrix-rich, medium- to fine-grained sandstone interbedded with massive silty mudstone and mudstone. Sandstone bear deformed mudstone pebbles distributed through the beds or near bed top, and with sharp base and deformed top. C-Thin- to medium-bedded mufstone-dominated heterolithics including including silty mudstone, mudstone and fine-grained sandstone that can be normally graded with planar laminations or massive with small subrounded deformed mudstone pebbles. _____ 217

Figure 5.15: A- Medium- to thick-bedded, poorly sorted, matrix-poor, coarse- to medium-grained sandstone with a tabular to mounded geometry, internally massive with outsized (very coarse) lithic grains, siltstone and/or mudstone pebbles and bioclasts near irregular erosive bed base and with sharp top. B-Coarse to medium-grained crudely normally graded sandstone bed, with a massive clast-bearing lower part and a finer-grained muddier upper part with parallel planar lamination enriched in carbonaceous material. Note the sharp grain-size break between the lower and upper bed part and the amalgamated bed top highlighted with white dot line. C- Example of finer-grained structured upper part of beds with carbonaceous-rich parallel planar and climbing ripple laminations. D-Example of finer-grained structured upper part of beds parallel planar to undulatory laminations. Note the darker carbonaceous material. E- Chaotic argillaceous and clast-rich sheared basal interval which marks the concave-up scoured base of a thick sandstone bed. F- Thin- to medium-bedded sandstone-dominated heterolithic packages consist of interbedded medium- to fine-grained sandstone internally planar laminated and with sharp planar base and top, massive siltstone and carbonaceous-rich mudstone. _ 220

Figure 5.16: Outcrop in the Tutavel sector (left) showing stratal relationships between units with onlap of the fine-grained strata of Unit 2A showing internal angular discordances onto alluvial fan deposits of Unit 1 unconformably overlying the granitic basement and Precuyano Cycle volcanic syn-rift deposits. Stratal dip angle decreases in overlying mudstone and sandstone of Unit 3 and 4. Note that distal ramp lobes of Unit 4 thin and pinchout towards the basin fault border northwestwards. Logs 8 and 7 shown in the correlation panel of figure 4 show thinning of proximal and distal ramp lobes from the Espinazo del Zorro to Tutavel sector. Location of the tuff 1 is also indicated.Location of the two outcrops A and B is shown on inset map (cf. fig. 5.4)._____ 226

Figure 5.17: Detailed spatial relationships between FA1.1, FA2.1 and FA2.2 in the Chacaico Basin. ___ 228

Figure 5.18: Outcrop in the Lapa sector showing successions which pass upwards from shoreface-offshore transition to fan-deltaic bottomsets in lower shoreface deposits (Unit 2A), with thickening of shoreface-offshore transition deposits and fan-deltaic deposits onlapping towards the flank of a NE-SW

trending blind fault growth fold in the Precuyano Cycle volcanic deposits. Note channelforms (red dotted lines) stacked towards the SE, away from the growth fold and local offset by syn-depositional antithetic and synthetic small-scale normal faults and the stratal decrease of dip angles southeastwards in overlying deltaic (Unit 2B) and deep-marine siliciclastic-starved basinal mudstone (Unit 3) and sand-starved slope mudstone deposits (Unit 4). _____ *229*

Figure 5.19: Detailed spatial relationships between FA1.2, FA2.2, FA2.3 and FA3 in the Chacaico Basin. _____ *232*

Figure 5.20: Detailed spatial relationships between FA2.4, FA2.5 and FA3 in the Chacaico Basin. ____ *234*

Figure 5.21: Detailed sections of the J1.2 distal ramp lobe complexes of Unit 4. _____ *239*

Figure 5.22: Outcrop view of onlapping proximal ramp lobe complexes (shown in fig. 5.23) towards the lateral basin margin. Location of the outcrop is shown on inset map (cf. fig. 5.4). _____ *240*

Figure 5.23: Detailed correlations showing the distribution of axis, off-axis and fringe facies associations in proximal ramp lobe complexes including the amalgamation rate in percentages and thicknesses. Quantitative diagrams in both distal and proximal ramp lobe deposits show the differences in the total proportions of facies association measured in the two types of lobe complexes, with a dominant occurrence of fringe and off-axis deposits in distal ramp lobes compared with proximal ramp lobes which are dominated by lobe axis and off-axis deposits. Note that lobe complexes with high amalgamation ratio include scours and channelforms in comparison with lobes having a lower amalgamation ratio and common finer-grained interbeds. _____ *241*

*Figure 5.24: Stratigraphic scheme showing the interpreted parasequences (PS), parasequence sets (PSS) bounded by Flooding Surfaces (FS) and the main sequences J1.1 and J1.2. The early post-rift is recorded by Unit 3 which represents a Maximum Flooding Zone (MFZ) recorded both across the Chacaico and Eastern Catán-Lil basins. Distribution of facies associations with their respective percentage are indicated for each parasequence. Compacted sedimentation rates (calculated from Table 5.1) are also shown for each parasequence.*_____ *243*

Figure 5.25: Stratigraphic scheme for the five main basins in the study area, integrated with available constrains of thickness and fossil data from the literature (Volkheimer, 1973; Gulisano and Gutiérrez-Pleimling, 1995; Franzese et al., 2006, 2007; Paim et al. 2008) and U-Pb zircon ages (186.3 ± 0.4 Ma in the Chachil Graben, Armella et al., 2016 modified from Leanza et al., 2013; 182.4 ± 2.3 Ma in the Chacaico Basin, Naipauer et al., 2018), as well as new U-Pb zircon data provided in this contribution (red stars).Nannofossil chronozones follow Ballent et al. (2011), standard European (EAB) and Andean (AAB) Ammonite biozone numbers follow Riccardi (2008) and bivalve biozones follow Riccardi et al. (2011). The TOAE is placed in the late Tenuicostatum-early Dactylioceras Hoelderi AAB after Al-Suwaidi et al. (2016) and in the NJ6 nannofossil chronozone after Angelozzi and Pérez Panera (2016). Note that the stratigraphic names for intraslope fans follows Paim et al. (2008). See location of sections on map fig. 5.3. _____ *254*

Figure 5.26: Correlation of lithostratigraphic units across the five depocentres of the study area showing the different sedimentary systems developed across depocentres, with indication of units thickness, basin-fill trends, sequences and nomenclature with formations. Constrains of volcanic syn-rift thickness

data from the literature (Gulisano and Gutiérrez-Pleimling, 1995; Franzese et al., 2006, 2007) and J2.1 sequence thickness after Paim et al. 2008 with J1.1 and J1.2 sequences thickness measured from the present study) and U-Pb zircon ages (186.3 ± 0.4 Ma in the Chachil Graben, Armella et al., 2016 modified from Leanza et al., 2013; 182.4 ± 2.3 Ma in the Chacaico Basin, Naipauer et al., 2018), as well as new U-Pb zircon data provided in this contribution (red stars).Note the maximum thickness are indicated (see range of thickness in fig. 5.25). _____ 255

Figure 5.27:Palaeogeographic block diagram of the studied depocentres of the southwestern Neuquén Basin representing the Early Pliensbachian configuration during late syn-rift deposition of the Unit 1 with first transgression. _____ 261

Figure 5.28: Palaeogeographic block diagram of the studied depocentres of the southwestern Neuquén Basin representing the Early-Middle Pliensbachian configuration during late syn-rift deposition of the Unit 2A with transgression and formation of fault-block ilsands. _____ 262

Figure 5.29: Palaeogeographic block diagram of the studied depocentres of the southwestern Neuquén Basin representing the Middle-Late Pliensbachian configuration during late syn-rift deposition of the Unit 2B with generalized flooding of fault-block islands. _____ 263

Figure 5.30: Palaeogeographic block diagram of the studied depocentres of the southwestern Neuquén Basin representing the Late-Early Toarcian configuration during onset of the early post-rift associated with maximum marine flooding at regional-scale and deposition of the Unit 3._____ 269

Figure 5.31: Palaeogeographic block diagram of the studied depocentres of the southwestern Neuquén Basin representing the late Early Toarcian configuration during the early post-rift deposition of the low-gradient distal ramp lobe complexes recording initiation of the J1.2 intraslope fan of Unit 4. _____ 270

Figure 5.32: Palaeogeographic block diagram of the studied depocentres of the southwestern Neuquén Basin representing the early Late Toarcian configuration during the early post-rift deposition of the low-gradient proximal ramp lobe complexes recording basinwards progradation of the J1.2 intraslope fan of Unit 4. _____ 271

Figure 5.33: Palaeogeographic block diagram of the studied depocentres of the southwestern Neuquén Basin representing the Late Toarcian configuration during the early post-rift deposition of the higher-gradient proximal ramp lobe complexes recording basinwards progradation of the J2.1 intraslope fan of Unit 4 _____ 272

Figure 6.1: Map of the Neuquén Basin showing the location of the study area (A) and the regional geological setting with location of the correlation panel across the Chacaico, Eastern Catán-Lil and Chachil basins (dark line AB).._____ 286

Figure 6.2: Cross section showing the stratigraphic architecture across the three studied depocentres (see Chatper 4 and 5 for descritpions of units) which is detailed in fig. 6.3. _____ 287

Figure 6.3: Correlation panel showing the stratigraphic framework across the three studied basins and the location of the sandstone sampled in lobe complexes which belong to J1.1, J1.2 and J2.1 sequences See detailed location of logs in Chapter 4 and 5.. _____ 288

Figure 6.4: J1.1 delta-front lobes in the Chacaico Basin and inset showing massive to planar laminated sandstone with enrichment in carbonaceous fragments near bed top (inset). _____ 294

Figure 6.5: J1.2 lower lobes, corresponding to medium- to fine-grained massive to planar laminated sandstone locally bearing deformed mudstone clasts. _____ *295*

*Figure 6.6: J1.2 upper lobes, corresponding to coarse- to fine-grained, normally graded sandstone with erosional base.*_____ *298*

*Figure 6.7: J2.1 lobes, corresponding to coarse or very coarse-grained sandstone, massive or crudely graded, with abundant mudstone clasts.*_____ *299*

*Figure 6.8: Samples distribution in standard diagram QtFL (Heller and Dickinson, 1985) and QmFLt diagrams (Folk et al., 1980) to emphasise sandstone compositional maturity based on the relative abundances of quartz, feldspar and lithic grains. Diagrams showing the proportions of different lithics including volcanic, metamorphic and sedimentary grains (LvLmLs), polycrystalline quartz, volcanic lithics and sedimentary and metamorphic lithics (Qp, Lv, Lsm) and the proportions of different types of volcanic lithics including felsitic, microlitic and vitric grains.*_____ *302*

Figure 6.9: Diagram showing the relationships between grain-size and matrix content of sandstones. The sampled sandstone of the Los Molles Formation have relatively high matrix content in comparison to other "matrix-rich" examples from the literature, and are above the 15% matrix threshold of Dott (1964) separating sandstones from wackes. Note that samples in the upper part of beds are not included. _ *303*

Figure 6.10: Thin section with localisation of the sample in sandstone beds of the J1.1 delta-front lobes in the Chacaico Basin, and photomosaic slices. Location of the imaged slice is shown on the thin section.305

Figure 6.11: Thin section with localisation of the sample in sandstone beds of the J1.2 lower and upper lobes in the Eastern Catán-Lil Basin, and photomosaic slices. Location of the imaged slice is shown on the thin section. _____ *306*

*Figure 6.12: Thin section with localisation of the sample in sandstone beds of the J1.2 upper lobes in the Eastern Catán-Lil Basin, and photomosaic slices. Location of the imaged slice is shown on the thin section.*_____ *307*

*Figure 6.13: Thin section with localisation of the sample in sandstone beds of the J1.2 upper lobes in the distal part of the system in the Eastern Catán-Lil Basin, and photomosaic slices. Location of the imaged slice is shown on the thin section.*_____ *308*

*Figure 6.14: Thin section with localisation of the sample in sandstone beds of the J2.1 lobes in the Eastern Catán-Lil Basin, and photomosaic slices. Location of the imaged slice is shown on the thin section.*_____ *309*

Figure 6.15: Thin section with localisation of the sample in sandstone beds of the J2.1 lobes in the Chachil Basin, and photomosaic slices. Location of the imaged slice is shown on the thin section. _____ *310*

Figure 6.16: Thin section with localisation of the sample in sandstone beds of the J2.1 lobes in the Chachil Basin, and photomosaic slices. Location of the imaged slice is shown on the thin section. _____ *311*

*Figure 6.17: Compositional pie charts showing the distribution of the main component grain classes in samples of the J1.1, J1.2 and J2.1 sequences (see percentages in Appendix 6-7-8).*_____ *312*

Figure 6.18: A-Example of MaS2 thin section showing quartz grains including monocrystalline non undulose (QmnU) and spherulitic (QSph) quartz with resorption embayments characteristic of volcanic rocks, muscovite (MS), feldspar with pertithe (KOp), plagioclase feldspar with polysynthetic twinning (Pg)

and microlitic volcanic lithics with pilotaxitic texture (Lvmpi), felsitic volcanic lithics with granular texture (Lvfgr) and recrystallized devitrified pumice grains (Lvpu) with remnant shard walls. Note the cryptocrystalline cement and pseudomatrix around grains. B-Example of PS1 thin section showing quartz grains monocrystalline non-undulose (Qmnu) and undulose (QmU) and polycrystalline (Qp) with sutured internal boundaries, muscovite (Ms), zircon crystal (Zr), metamorphic lithic (Lmg), plagioclase feldspar (Pg) locally with sericitized margins (Pgse), microlitic volcanic lithics including pilotaxitic texture (Lvmpi) and vitric fragment (Lvvgl), amorphous organic matter (Moam) and calcite crystals (CaC). Note the drusy calcite cement and dissolution replacement of feldspars with calcite. C- Example of MaS3 thin section showing quartz grains monocrystalline non-undulose (Qmnu) and polycrystalline (Qpf), plagioclase feldspar (Pg), muscovite (Ms), felsitic volcanic lithic with microcrystalline texture (Lvfmi) and extensive calcite cement. _____ 316

Figure 6.19:A-Example of MaS3 thin section showing a fragment of pumice (Lvpu) with spherulitic devitrification preserving tube vesicles and recrystallized cryptocrystalline texture. Note the pseudomatrix. B-Example of MaS4 thin section showing a glassy volcanic lithic (Lvvgl) with typical ragged margins and felsitic fragment with granular texture (Lvfgr).C-Example of MaS4 thin section showing microlitic volcanic lithic with trachytic texture (Lvmtr) and devitrification texture of glassy fragment (Lvvgl).Note the drusy calcite cement.D-Example of MaS4 thin section showing microlitic volcanic lithic with lathwork (Lvml) and trachytic texture (Lvmtr) and felsitic volcanic lithic with recrystallized microcrystalline texture (Lvfmi). _____ 317

Figure 6.20:A-Example of S5bisB2 thin section showing a fragment of structured organic matter. Note associated iron oxydes. B-Example of TutS1 thin section showing a fragment of pumice (Lvpu) with spherical devitrification with preserved tubes.C-Example of MaS2 thin section showing microlitic volcanic lithics with pilotaxitic texture (Lvmpi) including polycrystalline quartz (Qp) and euhedral feldspar phenocryst with a sieve texture with glass inclusions (Pgs), plagioclase crystal (Pg) and metamorphic lithic (Lmg). _____ 318

Figure 6.21:A-Example of MaS1 thin section showing sedimentary lithic shale (Lsh), volcanic lithics with vitric (Lvv) and felsitic granular texture (Lvfgr), zircon (Zr), amorphous organic matter fragment (Moam) and extensive drusy calcite cement.B-Example of ChaS2 thin section showing subhedral plagioclase crystal fragment (Pg), quartz grain monocrystalline non-undulose (Qmnu), bioclast calcilith (Ca Bio), volcanic lithic with felsitic granular texture (Lvfgr), vitric amygdule (Lvv) and spherulitic vitroclastic texture of glassy volcanic fragment (Lvvgl). Note the extensive intergranular siliceous recrystallization and paucity of calcite cement.C-Example of MaS1 thin section showing myrmekite vermicular texture of plagioclase feldspar characteristic of plutonic rocks and dissolution replacement calcite.D-Example of PS1 thin section showing microcline potassium feldspar with tartan twinning present as oversized grains.E-Example of PS1 thin section showing quartz grain monocrystalline non undulose (QmnU), polycrystalline (Qpf), microlitic volcanic lithic with trachytic texture (Lvmtr), calcite crystals (CaC), muscovite (Ms), plagioclase feldspar (Pg). Note the clay rim type coating and dissolution features (arrows). _____ 319

Figure 6.22: Standard provenance diagrams of QtFL and QmFLt to emphasise provenance (Dickinson, 1983). _____ *321*

Figure 6.23: Histogram showing the distribution of average percentages of component grain classes (see Appendix 6-7-8) for each sequence highlighting the compositional variability. _____ *323*

Figure 6.24: Composition curves of specific types of grains of component grain classes. _____ *324*

Figure 6.25: Palaeogeographic evolution maps showing the development of the J1.1 deltaic system and of the J1.2 and 2.1 intraslope fan system with their respective sediment sources and petrographic characteristics. _____ *331*

Figure 7.1: Comparison of different syn- to post-rift transition characteristics with changing conditions of intrabasinal-extrabasinal sediment supply, position (proximal versus distal) with respect to basin margin and early post-rift subsidence. _____ *346*

Figure 7.2: Late Pliensbachian-Early Toarcian palaeogeographic map of the Southern Neuquén Basin margin after Gómez Omil et al. (2002) and Brinkworth et al. (2018). Note the seismic-scale cross sections indicated correspond to fig. 7.4. _____ *357*

Figure 7.3: Early-Late Toarcian palaeogeographic map of the Southern Neuquén Basin margin after Gómez Omil et al. (2002) and Brinkworth et al. (2018). Note the seismic-scale cross sections indicated correspond to fig. 7.4. _____ *358*

Figure 7.4: Comparative sections seismic neuquen southern margin _____ *359*

Figure 7.5: Bloc diagrams showing the evolution of lobe complexes with healing of inherited rift topography by J1.2 to J2.1 intraslope fans, and summarizing their main characteristics. Termination pinchout styles shown in fig. 7.6 are indicated. _____ *369*

Figure 7.6: Schematic cross sections of termination pinchout styles indicated in fig. 7.5. Abrupt pinchout of matrix-rich sandstone associated with post-depositional remobilization and injection is recorded from depocentre (A) to lateral and frontal margins (B) of J1.2 distal ramp lobe complexes. J1.2 proximal ramp lobe complexes show lateral convergent onlap near depocentre horst border (C) and frontal pinchout with transition from matrix-poor to matrix-rich sandstone and increase in bed-scale heterogeneity (D). J2.1 proximal ramp lobe complexes record lateral pinchout with erosion, scouring and HEB development (E) and frontal termination with abrupt pinchout of thick HEBs offset by thin-bedded matrix-rich sandstone. Vertical scale is 5 metres. _____ *370*

Figure 7.7: Synthetic bloc diagram showing a range of intraslope, slope apron and basin-floor lobe complexes to compare dimensions, depositional setting and grain-sizes, with characteristics of the ramp-type lobe complexes of the Los Molles Formation. _____ *375*

Figure 7.8: Diagram comparing the dimensions of a range of intraslope lobe complexes with lobe complexes of the Los Molles Formation. _____ *376*

List of tables

Table 4.1: Descriptive facies table providing interpretation for depositional processes. Note abbreviations: Cobble (Co), Pebble (Pb), Granule (Gr), Very coarse (VCs) Coarse (Cs) Medium (Ms) Fine (Fs) very fine (VFs) sandstone, Mudstone (Mds), very poorly sorted (VPS), Poorly sorted (PS), Moderately sorted (MS). Volcanics (vg), quartz (qutz), K-feldspar (K-Fd).....117

Table 5.1: Summary of units thickness and relative ages used in the stratigraphic chart and to estimate compacted sedimentation rates.....181

Table 5.2: Summary of SHRIMP-II U-Pb results for zircons from tuff 1 and 3. 186

Table 5.3: Facies association table with bioturbation index (BI) following Taylor and Goldring (1993). RXL: Current ripple-cross-lamination; CRXL: Climbing ripple-cross-lamination; DXS: Dune-scale cross-stratification; PL: Planar lamination; UnL: Undulatory lamination; QPL: Quasi-planar laminations; SiL: Sinusoidal laminations; WR: Wave ripple; HCS: Hummocky cross-stratification; Cc-rich: Carbonacoeus-rich.....188

Table 6.1: Table showing the different textural characteristics of sandstone samples and their petrofacies.....291

Table 6.2: Table showing the recalculated parameters for ternary diagrams. 292

xxx

Chapter 1 Introduction

1.2. Background

This thesis entitled "*Sedimentology and tectono-stratigraphic development of the syn- to post-rift transition in Southern Neuquén Basin (Argentina) and controls on early post-rift submarine lobes of the Los Molles Formation*" has been submitted to the School of Earth and Environment at the University of Leeds in agreement with the requirements for the degree of Doctor of Philosophy (Ph.D.). The results of the present thesis were obtained in the frame of a Joint Industry project, Lobe 2 funded by a consortium of 16 companies (Equinor, Maersk Oil, Woodside, Total, Neptune Energy, Petrobras, Shell, Anadarko, BP, Chevron, Bayern Gas, VNG Norge, BHP Billiton, DONG Energy, Marathon Oil, and Premier Oil). This thesis extends investigations and insights developed during the earlier Lobe 1 and 2 joint industry programmes conducted in the Karoo Basin, South Africa, to the Neuquén Basin, Argentina, in the frame of an international collaboration between the University of Leeds, Imperial College London, and the Geological Survey Center (CIG) of the University of La Plata (UNLP-CONICET), Argentina. The objectives are to document the syn- to post-rift evolution of marine sedimentation in multiple rift depocentres, and analyse early post-rift lobes hosted in the Los Molles Fm. This research is driven by growing need for stratigraphic detail on shallow- to deep-water sedimentary systems evolution during the syn- to post-rift transition and associated post-rift prospectivity intimately related to the development of sandy lobes across complex intrabasinal topography, for which reservoir potential is difficult to assess due to multiple sources for sands and scattered distribution. Previously, these research topics have been poorly addressed at outcrop given the paucity of exhumed examples of marine rift basins that permit both regional-scale and fine-scale stratigraphic resolution, which is available in the Neuquén Basin. Another advantage to work in the Neuquén Basin is the potential to produce predictive models for deep-water reservoirs in a tectonically more complex setting, and with a coarser grain-size range, than base-of-slope and basin-floor fans of the Karoo Basin systems characterized by a maximum upper fine sand grain-size.

The Neuquén Basin is an ideal candidate to gain insights from both outcrop and subsurface given the excellent exposure of exhumed rift

depocentres, which have been uplifted in the eastern foothills of the Andes that form the western part of the Neuquén Basin. The outcrop work can be supported by the availability of subsurface datasets that image analogue quasi-contemporaneous rift depocentres in the eastern part of the Neuquén Basin. In addition, the study of Jurassic rift depocentres developed during greenhouse times permits better insights into tectonically induced accommodation given that rates of sea-level change had a lower rate (1 m/kyr) than more recent rift systems with high frequency glacio-eustatic rates of sea-level change (10 m/kyr) (cf. Leeder, 1995; Ravnås and Steel, 1998). Furthermore, the evolution of the Neuquén Basin in a volcanic back-arc setting with growth of the Early Andean magmatic arc contemporaneous with the syn- to post-rift transition means ash fall and tuff beds permit high temporal resolution dating of the Early Jurassic stratigraphy. Therefore, chronostratigraphy is constrained with relatively high temporal resolution (<1 Myr timescale) using new geochronology (U-Pb SHRIMP volcanic zircon dating) and ammonite and bivalve biostratigraphy. Exceptionally well-exposed outcrops of exhumed syn- and post-rift depocentres in the Catán-Lil department (39°S 70°W) located to the SW of the city of Zapala, in the southwestern part of the Neuquén Basin, were chosen to investigate multiple spatial and temporal scales of controls on the syn- to post-rift transition record and characteristics of associated early post-rift lobes of the Los Molles Fm. Our dataset includes seismic-scale correlation panels both of along-strike and downdip systems (>10 km long, 100 to 500 m thick), and results of detailed mapping to resolve the large-scale architecture and stacking patterns for various depositional systems making up the Early Jurassic stratigraphy. U-Pb geochronology on volcanic zircons of sampled tuff layers in the Los Molles Fm. permit refinement of the chronostratigraphy and establishment of spatio-temporal relationships between the investigated depocentres, integrated with microscopic scale analyses of thin sections of sampled sandstone to test source provenance.

From an applied perspective, the Neuquén Basin is one of the main oil and gas producing basins of Argentina and offers a range of hydrocarbon plays, which are concentrated within the Vaca Muerta and Los Molles Formations representing the two main source rocks of the basin. Stratigraphic or combined structural traps have been widely investigated in the southern part of the basin, associated with the Huincul High, a major ENE-WSW trending structure 250 km long and 120 to 60 km wide, which hosts a series of inverted rift depocentres attractive for

hydrocarbon exploration and exploitation. The Huincul High lies in the subsurface to the southeast and is exhumed to the southwest of the Neuquén Basin, which is the focus of the present field-based study. The very fine-grained successions of the Los Molles Fm. are known for their source rock potential (subsurface 2-11 % TOC, kerogen type II-III) and shale gas plays (Cruz et al., 2002; Gómez Omil et al., 2002; Veiga et al., 2002; Stinco and Mosquera, 2005; Villar et al., 2005; Pángaro et al., 2006; Ostera et al., 2016). Subseismic scale sandbodies recognized at outcrop within the Lower Los Molles Fm. were deposited in early post-rift setting with variable confinement and record the effects of interactions between sediment gravity flows with a range of intrabasinal relief. The resultant different lobe complex termination styles and intralobe facies distribution with development of bed-scale heterogeneity have implications for the types of traps and reservoir quality. Despite their development in a context suitable to hydrocarbon generation, short migration pathways and trapping, targeting such types of reservoirs remains challenging mostly due to the difficulty for seismic imaging beneath thick shales, lack of or very low acoustic impedance contrast and uncertainty of reservoir quality and geometry due to low vertical seismic resolution and sparse wells. Outcomes of the present study will help to improve strategies for the definition and assessment of stratigraphic and combined structural traps, and reduce uncertainties related to exploration and development of deeply buried analogue early post-rift plays in underexplored basins (Dampier Subbasin, NW shelf of Australia, Karner and Driscoll, 1999; North Viking Graben, Norwegian North Sea, Zachariah et al., 2009; Halten Terrace, Norwegian Sea, Moscardelli et al., 2013; Taranaki Basin, New Zealand, Strogen et al., 2014; Danish Central Graben, North Sea, Nielsen et al., 2015; Pelotas Basin, offshore Uruguay, Conti et al., 2017; Hammerfest Basin, Barents Sea, Sattar et al., 2017; North Falkland Basin, Dodd et al., 2019).

1.2. Thesis rationale and relevance to current research

Active deep-water rift basins are present around the world, and include the Gulf of Aden Rift, Red Sea Rift, Gulf of California Rift, Gulf of Corinth Rift, Terceira Rift, African Great Lakes of the East, West and Central Africa Rift. Their stratigraphic record enables semi-quantitative source-to-sink relationships to be established, and decoupling of tectonic, global sea-level change and short-term allogenic signals (climate, volcanism, oceanic circulation patterns). The syn- to post-rift transition is a critical stage of basin evolution, which is recognized in ancient rift basin-fills as a hiatal or angular unconformity, with strata onlapping onto fault-block highs that are laterally equivalent to a disconformable or a conformable transitional sequence in the deepest part of the basins, due to the diachroneity and polyphased nature of this event (Suez Rift, Bosence, 1998; NW Australian margin, Karner and Driscoll, 1999; Northern North Sea, Kyrkjebø et al., 2004; West Iberia-Newfoundland margins, Soares et al., 2012; Taranaki Basin, New Zealand, Strogen et al., 2014; North Falkland Basin, Lohr and Underhill, 2015; Pannonian Basin, Balázs et al., 2016; Fairway Basin, Northern Zealandia, Rouillard et al., 2017). Seismic reflection data has excellent lateral resolution, which permits the analysis of key regional stratigraphic markers. However, outcrop-based studies of ancient rift basins have highlighted the subseismic variability and complexity of the tectono-stratigraphic signature associated with the syn- to post-rift transition, both at depocentre-scale, and less commonly across multiple depocentres (Bahia Concepcion, Baja California, Ledesma-Vásquez and Hohnson, 2001; Niigata-Shin'etsu Basin, Central Japan, Takano, 2002; Lusitanian Basin, West Iberia, Alves et al., 2003; Pucara Basin, Central Peru, Rosas et al., 2007; Wollaston Forland, East Greenland, Surlyk et al., 2013; Taiwan, Yu et al., 2013; Sverdrup Basin, Canadian Arctic, Hadlari et al., 2016). Outcrop analogues are key to resolving the subseismic scale changes of stratigraphic architecture across the syn- to post-rift transition. Tycially, however, these studies lack detailed documentation of stacking patterns, depositional geometry and connectivity of sandbodies, facies distribution, and characterization of sedimentary processes, which make up shallow- and deep-water sedimentary systems.

The rapid temporal and spatial changes of accommodation, and external or internal sediment supply, are closely related to the variability of depositional

systems across rift depocentres and depocentre migration. In addition, patterns of depocentre linkage provide insights into basin configuration and controls during the final rifting. Models for rift basin evolution provide a basis for the analysis of syn-rift basin stratigraphy based on genetically- and temporally-linked depositional systems or parasequences (Gawthorpe et al., 1994; Howell and Flint, 1996; Dorsey and Umhoefer, 2000; Martins-Neto and Catuneanu, 2010), nomenclature for rift evolution based on basin-fill patterns (underfilled, filled or balanced and overfilled) (Prosser, 1993; Caroll and Bohacs, 1999; Ravnås and Steel, 1998), and fault evolution patterns (Gawthorpe and Leeder, 2000). However, controls such as inherited rift physiography, accommodation patterns, change in sediment source (intrabasinal versus extrabasinal), and strain evolution during the syn- to post-rift transition are poorly emphasised aspects of current conceptual rift basin models.

Typically, the margins of young rift basins are characterized by steep and/or topographically complex slopes outboard of narrow structural shelves with a fixed shelf edge position (*sensu* Helland-Hansen et al., 2012). This means that sediment dispersal patterns are complicated and evolve through time to make prediction of genetically connected and spatially disconnected sandstone-rich depocentres challenging. This basin configuration can promote sediment bypass across sediment-starved out-of-grade slopes and/or trapping across above-grade slopes with ponded or healed accommodation (*sensu* Prather et al., 2003), with significant implications for sediment storage or transfer downslope (Leeder et al., 2002; Ford et al., 2007; Strachan et al., 2013; Weiß et al., 2016). Such transient sediment storage across complex slope and basin-floor morphology affects sediment transfer to the deeper basin, which impacts the propagation of terrestrial climatic forcing signals to deep-water sedimentation with time lags up to Myrs in the sedimentary record (e.g Castelltort et al., 2004; Allen, 2008; Ducassou et al., 2009; Covault and Graham, 2010). The effects of seabed topography on sediment partitioning (*sensu* Prather et al., 2012) and evolution of fan architecture and stacking patterns in response to filling of slope accommodation have been observed in a range of physiographically complex settings (ponded, healed or stepped slopes, tortuous corridors, intrabasinal counterslope or lateral oblique slope) (Satur et al., 2000; Sinclair and Tomasso, 2002; Hooper et al., 2002; Booth et al., 2003; Prather et al., 2003; Hodgson and Haughton, 2004; Adeogba et al., 2005; Pyles et al., 2008; Romans et al., 2009; Cross et al., 2009; Kane et al.,

2010; Hay, 2012; Marini et al., 2015; Spychala et al., 2015; Jobe et al., 2017; Pinter et al., 2017; Bell et al., 2018).

Similar insights on the distribution and morphology of early post-rift sand fairways and sand-rich fans accumulated across inherited rift structures have been gained from subsurface systems (Argent et al., 2000; Modica and Brush, 2004; Martinsen et al., 2005; Fjellanger et al., 2005; Gjelbeg et al., 2005; Fugelli and Olsen, 2007; Jackson et al., 2008; Lohr and Underhill, 2015). Few subsurface studies document the architecture, facies distribution and bed-scale heterogeneity in early post-rift systems (Haughton et al., 2003; Southern et al., 2017; Dodd et al., 2019). This is despite the range of potential plays in underexplored post-rift successions and the associated risk for reduced reservoir properties (Lien et al., 2006; Amy et al., 2009; Porten et al., 2016). Subsurface datasets remain limited by their poor spatial and temporal resolution, with sparse wells, and a seismic-scale resolution with low impedance contrast posing problems for imaging isolated “thin” sandstone successions (<30 m). This are commonly overlooked in organic-rich fine-grained early post-rift successions, mostly regarded for their source rock and seal potential (Garret et al., 2000; Moscardelli et al., 2013).

Likewise, the confined offshore (>100 m depth) physiography of modern rift basins (e.g. Gulf of Aden Rift, Red Sea Rift, Gulf of California Rift, Gulf of Corinth Rift, Terceira Rift) and associated sandy systems remains poorly documented. However, modern systems permit direct high-resolution observation of variations in slope morphology and the resultant influence on sedimentary processes. Sediment gravity flow behaviour, sediment partitioning (bypass, erosion and/or deposition), and flow transformation across complex submarine slopes with structural or depositional reliefs have been poorly demonstrated in rift basin-fills. Few studies have reported changes in the distribution, thickness and nature of sediment gravity flow deposits across fault-related topography from exhumed systems (Ferentinos et al., 1988; Hodgson and Haughton, 2004; Pochat et al., 2007; Kane et al., 2010; Weiß et al., 2016; Henstra et al., 2016) or experimental modelling (Alexander and Morris, 1994; Gee et al., 2002; Ge et al., 2017). Difficulties for flow monitoring in such seismically active environments have limited our understanding of source-to-sink and deep-water sedimentation dynamics in rift basins and have contributed to making early post-rift fans one of the least explored types of deep-water clastic systems.

Rift basin topography can induce abrupt changes in confinement and gradient, which leads to flow transformation and waning-waxing behaviour. This complicates the location of erosion, bypass and depositional processes through time. The resultant distribution of sand-rich versus mud-rich deposits across topography, and the development of bed-scale heterogeneity in potential sand-rich accumulations, can form flow baffles within reservoirs (Amy et al., 2009) and reduce the porosity and permeability of reservoirs (Porten et al., 2016). This issue is important for petroleum prospectivity and characterization of reservoirs involved in stratigraphic and combined structural traps (hangingwall closures, compactional drapes, four way dip closure over buried topography) and assessment for the risks of leakage and post-depositional remobilization (Argent et al., 2000; Modica and Brush, 2004; Martinsen et al., 2005; Milton-Worssel et al., 2006; Jackson et al., 2008; López-Gamundí and Barragan, 2012). Therefore, improved understanding of sediment gravity flow interactions with complex seabed topography in rift basins could reduce uncertainty in predictions of reservoir and seal distributions, and reservoir quality distributions at the pinchout of sand-rich fans.

The stratigraphic archives of rift basin-fills provide the opportunity to constrain responses to the interplay of intrabasinal or extrabasinal controls, which can help to inform past palaeoenvironmental changes, and better forecast natural hazard prediction and related anthropogenic risks (Gulf of Corinth, Collier et al., 2000; Leeder et al., 2002; Red Sea and Gulf of Aden, Garzanti et al., 2001; Inner Moray Firth North Sea, McArthur et al., 2013; Southern Mexico, Martini and Ortega-Gutiérrez, 2016; East African rift, Schneider et al., 2016). Understanding mechanisms of rifting and sedimentation patterns in different source-to-sink configurations enable improved palaeogeographic reconstructions and provide insights into palaeoclimate, palaeooceanography, and palaeoenvironmental evolution. Such observations in ancient rift basins can help to explain the distribution of fauna and flora, speciation and diversification processes at a continental scale, as shown with the syn- to post-rift evolution of Zealandia in a back-arc setting (Pelletier, 2006; Rouillard et al., 2017). In the case of the Gulf of California, understanding the interactions between rift basin physiography and oceanic circulation, with seasonal upwelling variations causing fluctuations of nutrients, helps correlation of trophic level fluctuations and distribution of carbonate production along the rift, which has ecological implications for the

management of these sensitive biotopes (Halfar et al., 2004). Fine-scale observation of modern rift basin-fills, such as the Gulf of Corinth, have also helped to forecast short-term (10s to 100s kyrs) climate changes over the last ice ages, and the effects on onshore to offshore sediment transfer rate (Collier et al., 2000). This can be key for geohazard assessment as the physiography promotes mass movement, and flow transformation from slumps to debris-flows or turbidity currents, and considerable risk for cable breakage and landslide-generated tsunamis in areas of high coastal population density (Gulf of Corinth, Papatheodorou and Ferentinos, 1997; Lykousis et al., 2007). Other natural hazards characteristic of rift basins (e.g. Brune, 2016) along with earthquakes, includes volcanic eruptions with catastrophic degassing events and release of high-concentration of dissolved carbon dioxide and methane gas (Great Lakes of the East African Rift, Schmid et al., 2003), lava flows (Mount Nyiragongo, East African Rift, Favalli et al., 2009; Nabro volcano, Afar Rift, Hamlyn et al., 2014), ash or pumice falls, debris avalanches/mudflows, hydrothermal explosions and acid rains. These types of volcanic hazards involve days to decades timescales, long environmental recovery and cause a number of fatalities and migration of entire populations.

1.3 Objectives and research questions

The present study addresses a multiscale outcrop-based analysis of the evolution of sedimentation with changes in sediment supply and accommodation induced by the interplay of tectonism, eustasy and thermal subsidence in multiple marine rift depocentres (cf. Chapters 4-5-6). This contribution aims to refine and extend established models of sedimentation in marine rift basin-fills and factors of control during the syn- to post-rift transition, and to provide outcrop-based models for early post-rift lobes. The concepts and data can be used to improve prediction of reservoir potential in underexplored marine rift basin-fills that remain high-risk prospects for the hydrocarbon industry. The following research questions are addressed in the discussion (cf. Chapter 7).

Temporal and spatial variability of sedimentation, evolution of depositional systems, stacking and basin-fill patterns across single depocentres or at a

regional-scale, and the factors of control intervening during the syn- to post-rift transition are not resolved by current conceptual models for rift basin evolution

- **What factors controlled the temporal and spatial variability of the syn- to post-rift transition sedimentation?**
- **What are the characteristics of the syn- to post-rift transition signature?**

Studies of intraslope basins have demonstrated the importance of slope morphology on submarine fan development however the effects of inherited rift topography on siliciclastic systems have been poorly explored. The early post-rift setting remains a poorly investigated basin configuration for the factors of control onto the development of lobes and their characteristics in general, which needs to be better defined.

- **What were the timing and source for early post-rift sand supply, and their implications for palaeogeographic evolution of the Southern Neuquén Basin margin?**
- **What are the characteristics of early post-rift intraslope fan deposits of the Early Jurassic Los Molles Formation and how do they compare to other deep-marine sandy systems?**

1.3 Methodology

1.3.1 Outcrop data

The study area is located in the eastern foothills of the Andes, in the Catán-Lil department (39°S 70°W) located to the SW of the city of Zapala, in the southwestern Neuquén Basin, Argentina. Mezozoic sedimentary sequences, and specifically the Late Triassic to Early Jurassic deposits, were uplifted along basement-involved faults of the main exhumed rift basins. This configuration provides outcrops enabling two- and locally three-dimensional control for tracing structures and strike and dip sections of syn- and post-rift deposits. Mean bedding orientations were calculated for each unit from all measurements taken (Appendix 1 and 2) to constrain an average tectonic dip and dip direction to help identify dip discordances and subtle unconformities.

Stratigraphic vertical sections, measured at 1:25 scale with regular HCl test for change in the rocks carbonate content, document grain-size, sedimentary structures and palaeocurrents, types of bed contacts (amalgamated, erosional, sharp, loaded, deformed), body and trace fossils. A total of 399 palaeocurrent measurements collected from ripple, dune-scale cross-stratification and parting laminations, cross-stratification, flutes and grooves were plotted in rose diagrams to reconstruct the palaeoflow pathways with bedding restored using Stereonet software (Appendix 3). A total of 25 logged vertical sections with cumulative thickness of 5.9 km (Appendix 4) were used to identify facies and facies associations, and to interpret related sedimentary processes and depositional environments. Analysis of sedimentary facies, palaeocurrents, stratal geometries and thickness, onlap/truncation patterns and local deformation in relation to structures (faults and folds) were used to determine the influence of tectonism (locus and timing of fault/fold activity and reconstructed structure length) and inherited palaeotopography on sedimentation. Changes in facies associations, and deformation and evolution of sedimentary systems, permitted tectono-sedimentary units bounded by stratigraphic surfaces to be recognized, which mark major sedimentary changes across depocentres.

Marker beds and units chosen for log correlation mostly correspond to sandstone packages of the Los Molles, which permit physical correlation between logs as they could be walked out for several kilometres and constrained with

Unmanned Aerial Vehicle (UAV) photo panels. Detailed mapping and regular record of bedding strike dip information was conducted with Garmin GPS referencing, Digital Terrain Model (DTM) and UAV surveys and were integrated with previous structural and geological mapping studies (Leanza and Blasco, 1990; Gulisano and Gutiérrez Pleimling, 1995; Cucchi et al., 2005; Franzese et al., 2006; García Morabito et al., 2011; Muravchik et al., 2014). The presented maps and cross sections are shown across the actual structural and topographic configuration, given that structural restoration and backstripping would need more constraints on isopach distribution, burial depth, crustal parameters and palaeogeographic changes including bathymetry beyond the scope of the present study.

The palaeogeographic evolution of rift basins is based on spatial variations of facies associations (Table 4.1 and 5.3) and thickness, deformation and onlap/truncation patterns. These observations and data enable the description of the evolution of depositional systems across rift structures, and the definition of four tectono-sedimentary units (Unit 1, 2, 3 and 4) and three main sequences (J1.1, J1.2 and J2.1) bounded by stratigraphic surfaces which mark major sedimentary changes across depocentres. Spatio-temporal relationships between the four tectono-sedimentary units of the Early Jurassic Lower Cuyo Group were based on pre-existing geochronologic and biostratigraphic markers (Nannofossil chronozones, Ballent et al., 2011; Standard European (EAB) and Andean (AAB) Ammonite biozone numbers, Riccardi, 2008; Early Jurassic ammonite, bivalve and brachiopod biozones, Volkheimer, 1973; Gulisano and Gutiérrez Pleimling, 1995; Quattrocchio et al., 2007; TOAE in the late *Tenuicostatum*-early *Dactylioceras Hoelderi*, Al-Suwaidi et al. 2016 and TOAE in biozones 14-15, Angelozzi and Pérez Panera. 2016; U-Pb LA-ICPMS zircon age 186.3 ± 0.4 Myr at base of the Chachil Fm. in the Chachil Graben, Armella et al., 2016 modified from Leanza et al., 2013; U-Pb LA-ICPMS zircon age 182.4 ± 2.3 Myr in the Los Molles Fm. in the Chacaico Basin. Naipauer et al., 2018) and integrated with new U-Pb ages in the Lower Los Molles Fm. obtained in this study. This refined temporal and stratigraphic framework permitted estimation of sedimentation rates (Table 5.1).

1.3.2 Geochronological data

Two tuff samples were collected in the Lower Los Molles Fm. (i) Tuff 1 at the top of Unit 3 in the Catán-Lil basin (39° 15.427'S 70° 34.959'W) and (ii) Tuff 3 at the base of Unit 3 in the Chachil basin (39° 10.554'S 70° 31.447'W) (cf. Chapter 5). Tuff samples of 2 kg each were crushed and grinded to recover zircons at the CIG (Centro de Investigaciones Geológicas) and Museum of La Plata-UNLP. The first step for zircon separation is to use a 140 microns mesh for sieving, washing, and concentration of heavy minerals in the bottom and grooves of the tray, while the light minerals were discarded by its edge. The heavy mineral preconcentrate was washed with ethyl alcohol, recovered by filter paper, and oven-dried. Manual handpicking of 50 zircon grains was carried out under a binocular magnifying glass and stored inside an eppendorf tube to be sent for U-Pb geochronology at Research School of Earth Sciences (RSES) of the Australian National University (ANU). U-Pb dating was carried out using sensitive high-resolution ion microprobe (SHRIMP-II) following analytical procedures of Williams (1998) and Ireland and Williams (2003). Hand-picked grains (31 grains for Tuff1 and 29 grains for Tuff2) were mounted with standard zircon (Temora-2) in an epoxy disc, ground and polished to expose grain surface for laser ablation. Cathodoluminescence imaging was conducted using SEM-EDS (Scanning Electron Microscope with Energy Dispersive Spectroscopy) to characterize idiomorphic zircon crystals (internal texture with oscillatory zoning indicative of igneous origin) inherent to their volcanic provenance, to ensure the absence of inherited cores and define laser ablation spots within well-zoned rims of euhedral grains.

Analytical data were processed using SQUID (Ludwig, 2001a) and ISOPLOT/EX (Ludwig, 2001b), tabulated with isotopic data (Table 5.2). Uranium and thorium abundances have been calculated with reference to SL13 (238 ppm U) and the $^{206}Pb/^{238}U$ ratios have been normalized relative to a value of 0.0668 for the $^{206}Pb/^{238}U$ ratio of the standard zircon Temora-2 of 417 Ma (Black et al. 2004).

1.3.3 Thin section data

A total of 28 hand samples were collected (Appendix 5 in the three distinct stratigraphic units (J1.1, J1.2 and J2.1) and 15 samples were chosen for extraction of petrographic thin sections (cf. Chapter 6) (Table 6.1 and 6.2). Thin sections were analysed at the Centre of Geological Investigations Laboratory (CIG) of the National University of La Plata, Argentina and at the University of Leeds, UK. Digital images were taken at high magnification (4x) in plane (PPL) and cross polarized (XPL) transmitted light using a digital-camera equipped microscope, and stitched with the Photoshop software into high-resolution PPL and XPL photomosaic slices. The JMicrovision V1.27 software Java™ (Roduit, 2008) was used to proceed to semi-automatic digital point counting. Percentage abundance of component grains were defined with 600 modal point counts per thin section, stochastically distributed across an aleatory grid with a minimum interpoint distance larger than the maximum grain size fraction (Appendix 6-7-8).

1.4 Thesis outline

This thesis comprises 8 chapters and includes one manuscript submitted for publication in international peer-reviewed journal.

Chapter 2, "*Scientific background",* synthetises several aspects of the current knowledge which are relevant to understand key questions and objectives of the conducted research. This includes models and nomenclature for the genesis and evolution of rift basins, sedimentation patterns during the syn- to post-rift transition, and the development of submarine fans in topographically complex settings.

Chapter 3, "*Introduction to the Neuquén Basin*", provides the geological setting with a focus on the syn-rift and post-rift evolution, structural and sedimentological framework of the study area, with detailed literature review of the Early Jurassic stratigraphy in the southern Neuquén Basin.

Chapter 4 is based on a manuscript "*Evolution from syn-rift carbonates to early post-rift deep-marine intraslope lobes: the role of rift basin physiography on sedimentation patterns*" that is founded on a detailed case study conducted in the Chachil basin, which is in re-review at *Sedimentology*. This chapter provides a refined sedimentological analysis and addresses the evolution of, and controls on, the development of carbonate to siliciclastic systems during the syn- to post-rift transition. It highlights the role of inherited rift topography on sedimentation patterns during the syn- to post-rift transition, differential compaction controlling post-rift sedimentation patterns, and documents argillaceous intraslope lobes trapped in complex topographic setting. The chapter provides an outcrop-based model for the depositional architecture, termination style, distribution and types of hybrid event beds present in early post-rift intraslope lobes. Results have significant implications for predicting the location of clastic injectites and bed-scale heterogeneity within intraslope lobes departing from classic models.

Chapter 5 forms the basis for a manuscript on a larger-scale analysis of the contrasting signature of the syn- to post-rift transition across multiple depocentres, based on a refined Early Jurassic chronostratigraphic framework

constrained with new geochronological ages obtained in the Los Molles Formation. The aim is to address the evolution and control on the variability of late syn-rift and early post-rift depositional systems, and implications for analog rift basins. The effects of pre-rift inheritance and volcanism on stratigraphic architecture of the syn- to post-rift transition, individual basin-fill patterns, changes in the mode of sediment supply (intrabasinal versus extrabasinal) and sediment dispersal (transverse versus axial) and successive depocentre migration, are assessed from local (Chacaico and Eastern Catán-Lil basins) to regional-scale. The chapter provides an outcrop-based seismic-scale analog to assess the stratigraphic architecture and facies variability of the syn- to post-rift transition with outcomes for the spatial distribution and characteristics (dimensions, termination style, stacking patterns, facies) of early post-rift lobe complexes developed diachronously across basins with variable topographic confinement.

Chapter 6 is based on a manuscript that focuses on the stratigraphic evolution of compositional and textural characteristics of Early Jurassic sandstones of the Chacaico and Los Molles Fm. The aim is to investigate changes in sediment source areas during the syn- to post-rift transition with implications for temporal and spatial changes in the quality of reservoir sandstones. Two early post-rift intraslope fans of the Los Molles Fm. are used to compare petrofacies in relation to characteristics of lobe complexes and related depositional processes. This chapter highlights stratigraphic change in reservoir quality of sandstone depending on source, and within intraslope fans depending on effects of inherited topography, which can be used as analogues for early post-rift sandy systems developed across above-grade slopes.

Chapter 7 adresses the research questions and discusses results and implications in the frame of the initial objectives.

Chapter 8 synthetises the main findings of the present study and potential perspectives for further investigations to be conducted in the study area.

Bibliographic references are provided at the end.

Chapter 2 Scientific background

2.1 Models and nomenclature for the genesis and evolution of rift basins

Tectonically active rift basins, back-arc basins and passive margins form a group of genetically related extensional basins (Doglioni et al., 1998; Ziegler and Cloetingh, 2004; Cloetingh and Willett, 2013; Franke, 2013; Buck, 2015; Brune, 2016). Continental extension arises in a range of tectonic settings characterized by normal and strike-slip faulting, lithospheric thinning, variable magmatism with high heat flow near magmatic centres and magmatic underplating (post-orogenic gravitational collapse, back-arc extension behind island arc, pull-apart extension-transtension strike-slip) (Allen and Allen, 2013).

2.1.1 Diversity of rift architecture

The tectonic development of rifts (extension, uplift and subsidence) is mainly controlled by the lithospheric strength strongly dependent on its thermal structure (with a typical heat flow of 40-50 mW $^{m-2}$), initial crustal rheology, thickness and pre-existing structures, mode of extension (i.e. orthogonal or oblique), volcanism, and the rate, magnitude and width over which extensional strain is distributed (narrow versus wide rifts) (McKenzie, 1978; Ruppel, 1995; Ziegler and Cloetingh, 2004; Buck, 1991, 2004; Cloetingh and Willett, 2013). Rift-related magmatism, with lithospheric weakening and intrusive heating below the rift axis accommodate extension, playing a fundamental role in the breakup of strong thickened continental lithosphere and onto the evolution of rift, including changes in strain localization, volcano-tectonic subsidence, uplift and thermal subsidence patterns *(*Buck, 2004; Ziegler and Cloetingh, 2004*).* The development of large offset normal faults and significant rift topography, which is characteristic of brittle crustal thinning in non-magmatic rift settings, is hampered in magmatic rift settings by the lower differential stress required to accommodate extensional strain. In magmatic rift settings, strain is largely accommodated by intrusions, with little tectonic subsidence and preservation of crustal thickness, and volcanic heating and loading of the upper crust that tend to focus extension. This in turn increases eruption events of greater volumes of magmas, and can promote

anomalously large-magnitude thermal subsidence (Ethiopian Rift, Ebinger and Casey, 2001; Red Sea, Wolfenden et al., 2005; Great Rift Idaho, Holmes et al., 2008; Tongariro Graben, New Zealand, Gómez-Vasconcelos et al., 2017). The obliquity of rifting seem to have an important control on the distribution of volcanic activity focused where pure shear at the curved tips of oblique faults locally increases rates of extrusion (Ethiopian Rift, Korme et al., 1997; TVZ, New Zealand, Acocella et al., 2003).

Rift architecture depends of the degree of coupling between the brittle upper crust and ductile lower crust and mantle, which increases with the heat flow, producing a range of deformation styles between narrow (thin crust, low heat flow, brittle deformation), wide (intermediate crustal thickness and heat flow, ductile deformation) and core complex (thickened crust, high heat flow) modes of lithospheric stretching (Brun, 1999; Buck, 2015; Fig. 2.1.).

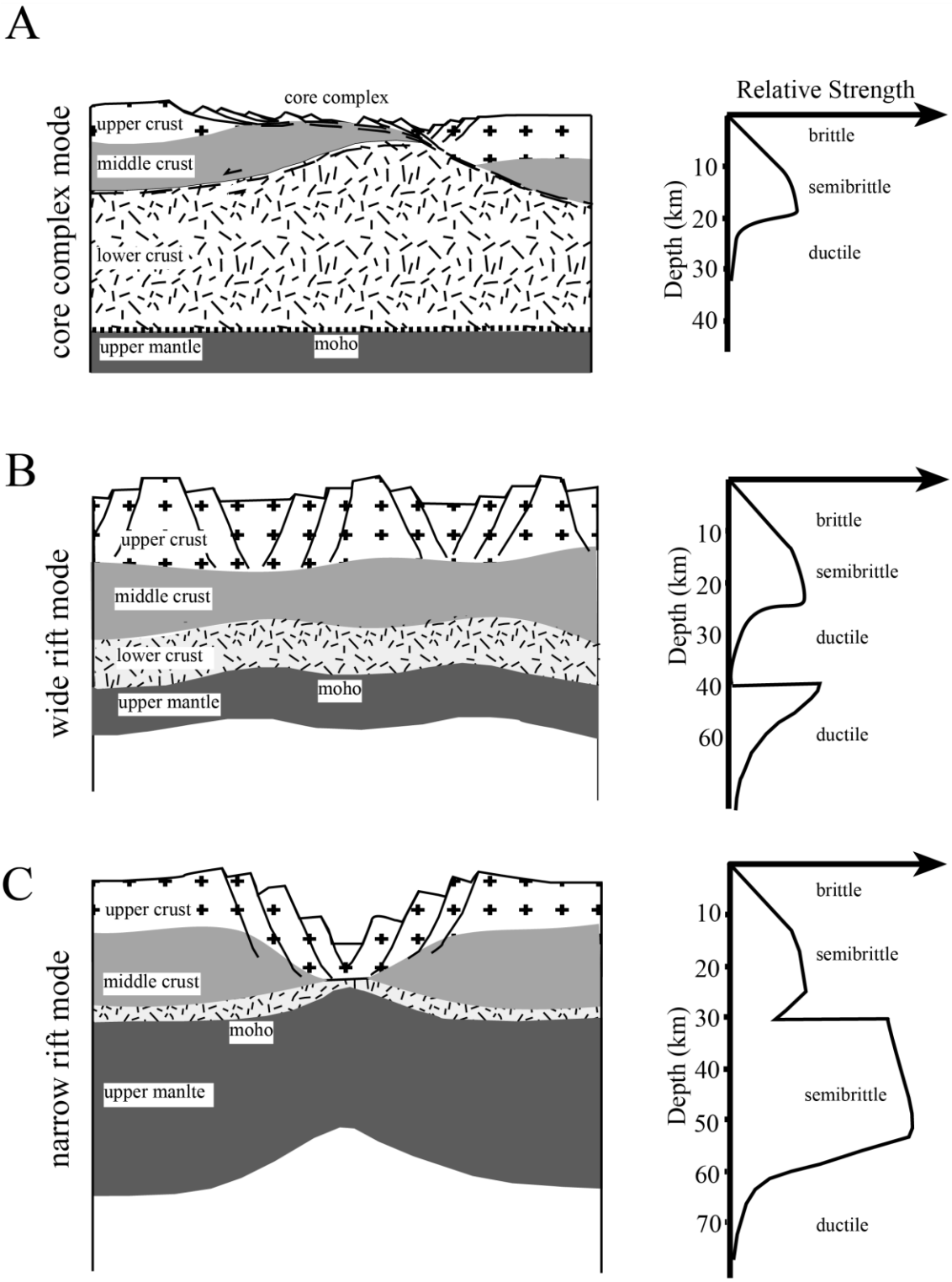

Figure 2.1: Scheme (Gartrell et al., 2001) showing the three end member modes of lithospheric extension depending on thermal state of the lithosphere and crustal thickness. Hot and weak lithosphere promotes ductile deformation with strong decoupling between brittle crustal and mantle. This can promote a metamorphic core complex mode in the case of thick and high heat flow conditions (A),or wide rift mode in the case of intermediate crustal thickness (B). Cooler and stronger, thin crust leads to preferential coupling between crust and mantle and brittle deformation results in narrow rifts. Plots show yield strength with depth for hypothetical geothermal gradients and crustal thickness (modified after Buck, 1991).

The metamorphic core complex mode of extension accommodates stretching with little subsidence and requires specific conditions to occur. This includes a marked decoupling between the crust and upper mantle and low sedimentation rates and/or low density sediments that promote low overburden pressures. These factors together with the presence of a basal shear zone at shallow depths in a relatively thin middle crust can lead to the development of low-angle detachments (Gartrell, 2001). In contrast, the strong crust-mantle coupling in the case of narrow rift and higher sedimentation and subsidence rates, enhanced by high overburden pressure, will prevent low-angle detachment and the basal shear zone to be sited at greater depth in a thicker middle crust involving high vertical loading, and the formation of steeply dipping master faults (Gartrell, 2001).

Narrow rifts (<100 km wide) form deep isolated basins with small amount of extension associated with cold and high strength lithosphere, accommodating extension with localized strain on a small number of high-angle faults accommodating large displacements (Gulf of Suez-Aden Rift, Bosence, 1998; New Zealand, Taupo Volcanic Zone, Acocella et al., 2003; Rhine graben, Hinsken et al., 2007; EAR and Main Ethiopian Rift, Ring, 2014).

Wide rifts (>100s to 1000 km wide) form multiple basins with horst and grabens or tilted blocks. These systems are associated with weak and hot lithosphere, accommodating extension with distributed strain over a broad area. A large number of small offset high-angle faults result from strain delocalization related to lithospheric strength on temperature. High strain zones on rift border faults accommodate large displacement related to deeply rooted upper-middle crust detachments (BRP, Braun and Beaumont, 1989; Aegean Sea and Central Greece, Goldsworthy et al., 2002; North American Rift system, Withjack et al., 2013; Zhejiang Province, eastern South China, Li et al., 2014).

2.1.2 Kinematic rift models

Passive rifting is controlled by stretching and thinning of cold dense lithosphere driven by far-field plate boundary forces (McKenzie, 1978) and may occur with limited or without volcanism after the onset of extension, with upwelling of hot asthenosphere due to adiabatic decompressional melting in response to rifting (Sengor and Burke, 1978). In the case of active rifting, crustal uplift and thinning occurs with thermal upwelling of the hot asthenosphere with decompression and partial melting at the base of the lithosphere, and volcanism peaking prior to, and during, large-scale extensional collapse with ascending mantle-derived magmas driven by sublithospheric mantle dynamics (Sengor and Burke, 1978; White and McKenzie, 1988).

Mechanical stretching models for passive rifting explain partitioning of extensional strain through the lithosphere and syn- rift and post-rift subsidence patterns, and include pure shear (McKenzie, 1978), depth dependent extension (Royden and Keen, 1980) and simple shear (Wernicke, 1985) models.

The pure shear model (McKenzie, 1978) assumes the crust and lithosphere undergoes uniform lithospheric stretching, with symmetric rifting driven by faulting of the brittle upper crust. Elevation of the geotherm with ductile thinning of the lower crust and subsidence or uplift result from isostatic adjustments to rising asthenosphere depending upon the ratio of crustal to lithospheric thickness. In the simple shear or non-uniform stretching model (Wernicke, 1985) crustal extension is accommodated by a large-scale, low-angle detachment with variable crustal versus lithospheric thinning, and no significant thinning of the mantle lithosphere. It forms an asymmetrical rift basin offset from the locus of rising asthenosphere with fault-block rotation, and limited subsidence of the brittle crust and uplift of basin margins during stretching. The depth-dependent stretching model (Royden and Keen, 1980; Kusznir and Karner, 2007; Huisman and Beaumont, 2014) assumes greater stretching of the lower crust and mantle lithosphere than the upper crust producing different subsidence patterns during extension as the crust may act as a detachment horizon. This model explains limited brittle syn-rift deformation and greater thermal subsidence and uplift of basin margins during stretching than the uniform stretching model.

All the three mechanical stretching models involve syn-rift brittle fracture of the upper crust that is controlled by the ratio of crustal to total lithosphere thickness and the amount of extension in the crust and lithosphere. Subsequent post-rift subsidence is driven by isostatic adjustment to lithospheric thermal re-equilibration and cooling of the thinned mantle lithosphere with thickening and increasing density. Uplift of rift basin margins with flexural rebound to accommodate extension rapidly ceases after rifting, with sediment loading and post-rift thermal re-equilibrium of the lithosphere (Roberts and Yielding, 1991; White and McKenzie, 1988; Japsen et al., 2012). Thermal subsidence and downwarping of the lithosphere is expected to produce a broad subsiding sag depocentre postdating extension-driven normal fault activity and overstepping of the rift zone. The thickness of post-rift sediment accumulated is a function of crustal density, water-depth and sediment load. The cumulative sediment thickness is nearly equal to the thickness of sediment accumulated during the syn-rift (McKenzie, 1978; Ziegler and Cloetingh, 2004).

In the case of pure shear in the uniform stretching model, the syn- to post-rift unconformity will normally affect the entire area of extended upper crust. The resulting basin architecture is a symmetric steer’s head form, where syn-rift and post-rift depocentres stack, with the post-rift thermal sag basin overstepping previous the rift depocentre and basin flanks (North Sea Rift, Roberts and Yielding, 1991). For areas undergoing simple shear in non-uniform stretching models or heterogeneous shear in depth-dependant stretching model, thermal uplift and subsequent syn- to post-rift unconformity development may be asymmetric to the rift structure. This is due to structurally linked rift basins subsiding diachronously with migration of extension, and limited geographic correspondence between the locus of extension and thermal subsidence. This produces a lateral offset between the axis of the syn- and post-rift depocentres in the case of simple shear model (Tucano and Sergipe–Alagoas Basin, NE Brazil, Karner et al., 1992), or in the case of depth-dependant model where anomalous post-rift subsidence is difficult to reconcile with the limited brittle deformation of the upper crust (NW Australian margin, Karner and Driscoll, 1999).

2.1.3 Stratigraphy of rift basins

Rift velocity is an important concept for continental breakup and the opening of new oceanic basins. A natural distinction can be made between rifts that evolved to continental breakup with ocean seafloor spreading and the development of passive or conjugate margins, and intracontinental or failed rifts that evolved to into thermal sag basins. Rift-related basins and passive margins have stratigraphic successions that can be subdivided into pre-, syn-, and post-rift sequences separated by two key unconformity surfaces that develop owing to onset of rifting (ROU) and onset of post-rift (BU or PRU) (McKenzie, 1978; Williams, 1993; Withjack et al., 2002). The rift onset unconformity (ROU) separates pre- and syn-rift strata and marks erosion and tilting of pre-rift fault-blocks. The transition from the syn- to post-rift strata is labeled “BU: breakup unconformity” in the case of oceanic accretion (Falvey, 1974; Braun and Beaumont, 1989), or the “PRU: post-rift unconformity” (Bosence, 1998), or “syn-rift unconformity” (Nøttvedt et al., 1995) in a failed rift setting (Fig. 2.2.).

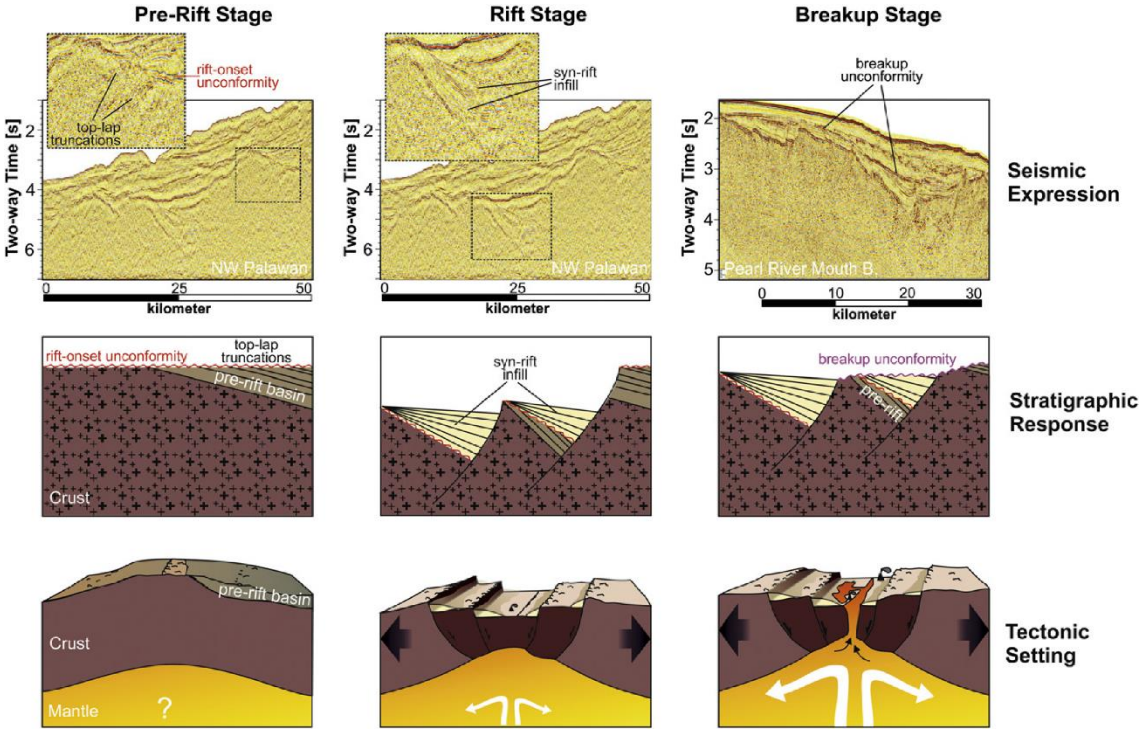

Figure 2.2: Schematic cross sections and seismic examples (Franke, 2013) showing pre-rift, syn-rift and breakup rift evolution of rifts, with formation of a rift onset unconformity (ROU) with top-lap truncations of seismic reflectors from below, which is overlain by wedge-shaped syn-rift successions. Continental breakup leads to formation of the breakup unconformity truncating the syn-rift sediments then onlapped by post-rift successions, and amalgamated with the rift-onset unconformity at basin margins.

The syn- to post-rift transition physically refers to a basin-wide diachronous time-line, which records a change from fault-controlled subsidence with lithospheric stretching and heating, to thermal subsidence with lithospheric cooling. In the subsurface this is expressed as an angular unconformity with onlaps on tilted fault blocks, depositional or erosional hiatus on rift shoulders, and in the deepest parts of rift basins a conformable transitional succession, which marks a change from divergent to parallel reflections and/or subtle facies variation (Main Porcupine Basin, Moore, 1992; NW Australian margin, Karner and Driscoll, 1999; Northern North Sea, Kyrkjebø et al., 2004; Norwegian Sea, Lien, 2005; West Iberia-Newfoundland margins, Soares et al., 2012; Taranaki Basin, New Zealand, Strogen et al., 2014; North Falkland Basin, Lohr and Underhill, 2015; Pannonian Basin, Balázs et al., 2016; Suez Rift, Bosence, 1998; Rohais et al., 2016; Hammerfest Basin, SW Barents Sea, Marin et al., 2017; Fairway Basin, Northern Zealandia, Rouillard et al., 2017; Fig. 2.3.).

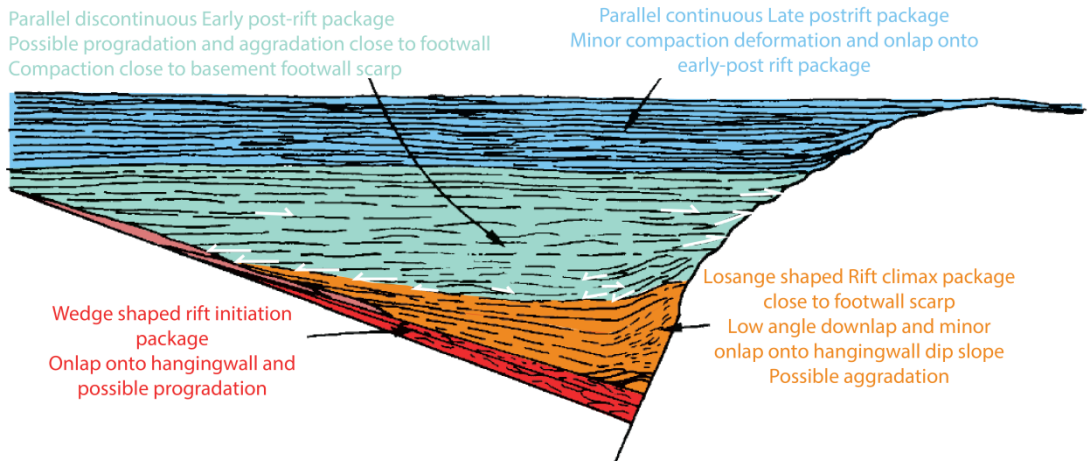

Figure 2.3: Ideal syn- to post-rift transition record after Prosser (1993).

The diachroneity of the syn- to post-rift transition at basin-scale means care must be taken as decreasing subsidence rates may indicate waning rate of extension, or result from strain localization to a narrower zone of deformation (strain softening, Kusznir and Park, 1987). The syn- to post-rift transition records deposition during the decay of active extension to complete thermal relaxation, and therefore should be regarded as part of the late syn-rift sequence, as they are not attributable to the end of rifting *sensu stricto* (cf. Soares et al., 2012).

The magnitude of post-rift subsidence of passive rifted margins in breakup is similar to intracontinental basins of 10s to 100s kilometres wide, is generally long-lived, and in the order of <10 m/Myr (Xie and Heller, 2009; Armitage and Allen, 2010). This is slower than syn-rift subsidence rates in the order of 1-10 km/Myr (250-400 m/Myr, Suez Rift, Moretti and Colletta, 1987; 1.5-8 m/kyr, Loreto basin, Baja California, Dorsey and Umhoefer, 2000; 10 m/kyr, Pattani and Malay basins, Southeast Asia, Morley and Westaway, 2006; 3.6 m/kyr, Gulf of Corinth, Moretti et al., 2004). The McKenzie (1978) lithospheric extension model assumes that thermal subsidence reaches its highest rate (at scale of 10s million years) and follows an asymptotic decrease. This reflects exponential subsidence decay with cooling of the rift thermal anomaly introduced by lithospheric stretching on a timescale of ~100 Myr. However, many rift basins present significant deviations from theoretical evolution of tectonic subsidence predicted by classic lithosphere stretching models.

Post-rift subsidence can be delayed with isostatic imbalance and may argue for support from the hot asthenospheric mantle at the end of rifting, promoting long-lived shallow-marine conditions and subsidence deficit observed for the Northwest Australian margin (Karner and Driscoll, 1999), the Iberia-Newfoundland margin (Péron-Pinvidic and Manatschal, 2008; Franke, 2013) or Angolan and Brazilian conjugated margins (Contreras et al., 2010). Thick sediment accumulations (2-8 km) can also have a thermal blanketing effect delaying the post-rift thermal subsidence of 10-20 Myr by preventing thermal dissipation of heat from the mantle that increase thermal gradients of the weakened lithosphere and enhance lithospheric flexural strength (Karner, 1991; Burov and Poliakov, 2001). In contrast, anomalous heating and high magnitude thermal subsidence associated with overestimated stretching factors in predictive thermal relaxation models are observed in many extensional back-arc basins which evolve with significant post-rift subsidence in the order of 100-600 m/Myr (Doglioni, 1995). Such high post-rift subsidence rates can be interpreted as the result of lithospheric and deep mantle perturbations associated with dynamic topography (>150 m/My) (Burgess et al., 1997; Burgess and Moresi, 1999), lithospheric-related processes including mantle delamination and asthenospheric upwelling (100 m/My) (New Caledonian Trough and Taranaki Basin, Baur et al., 2014), or ductile lower crustal flow process related to sediment-load driven crustal

thinning (up to 500 m/My) (Pattani and Malay Basins, Southeast Asia, Morley and Westaway, 2006; South China Sea, Clift et al., 2015).

2.1.4 Surface processes

2.1.4.1 Fault growth and structural heritage

Sedimentation patterns and depocentre migration can provide indications on the geometry, subsidence and strain evolution across rift faults, which develop on Myr timescales, with fault tip growth and fault segment linkage. Faults can grow with simple lateral fault tip propagation (‘isolated fault growth’, Walsh and Watterson, 1988), or with propagation of independent fault segments that link up along-strike and coalesce downdip to form large fault zones that accommodate much of the extensional strain (‘segment growth and linkage’, *sensu* Trudgill and Cartwright, 1994). Alternatively, rapid establishment of full fault length of large fault systems can arise with increasing cumulative displacement, accruing without significant additional lateral tip propagation and therefore preserving a constant length for much of its lifetime (coherent or constant length fault growth *sensu* Walsh et al., 2003; Whipp et al., 2014; Rotevatn et al., 2018; Fig. 2.4.).

Fault linkage has significant implications for the development and distribution of rift depocentres and produces specific onlap/truncation, stratal thickness patterns and facies variations depending on its timing in the rift evolution. Fault linkage can occur with different displacement rate and on different timescale and length scale in rift basins. The early fault linkage in the rift evolution is associated with weak subsidence and rapid merging of isolated depocentres into a larger one controlled by linked fault border with strain localization onto higher-displacement fault systems (1 Myr, Whakatane Graben, New Zealand, Taylor et al., 2004; 2.4 Myr Suez Rift, Jackson et al., 2002). The late fault linkage in the rift evolution is associated with formation of larger isolated thick depocentres (10-14 Myr, Statfjord East Field North Sea, Dawers and Underhill, 2000; Usuanga flats EAR, Morley, 2002; 1 Myr, Gulf of Corinth Rift, Bell et al., 2009). Fault linkage can also occur before major rift deformation with rapid establishment of a fixed length fault (i.e. no gradual lateral propagation), and results in direct formation of large depocentres bounded by a fixed basin margin (Morley, 1999). This contrasts to the fault propagation model, where pre-rift basement is progressively onlapped by syn-rift deposits with depocentre broadening (Schlische, 1995). Therefore, care must be taken when analysing the final structural rift configuration given that the thickest syn-rift depocentres are not

bounded by the faults that accumulated the highest displacement rates through rift evolution, nor were major surface breaking faults during the rift initiation and therefore may not reveal subsidence patterns throughout rift development (Gawthorpe et al., 2003; Finch and Gawthorpe, 2017).

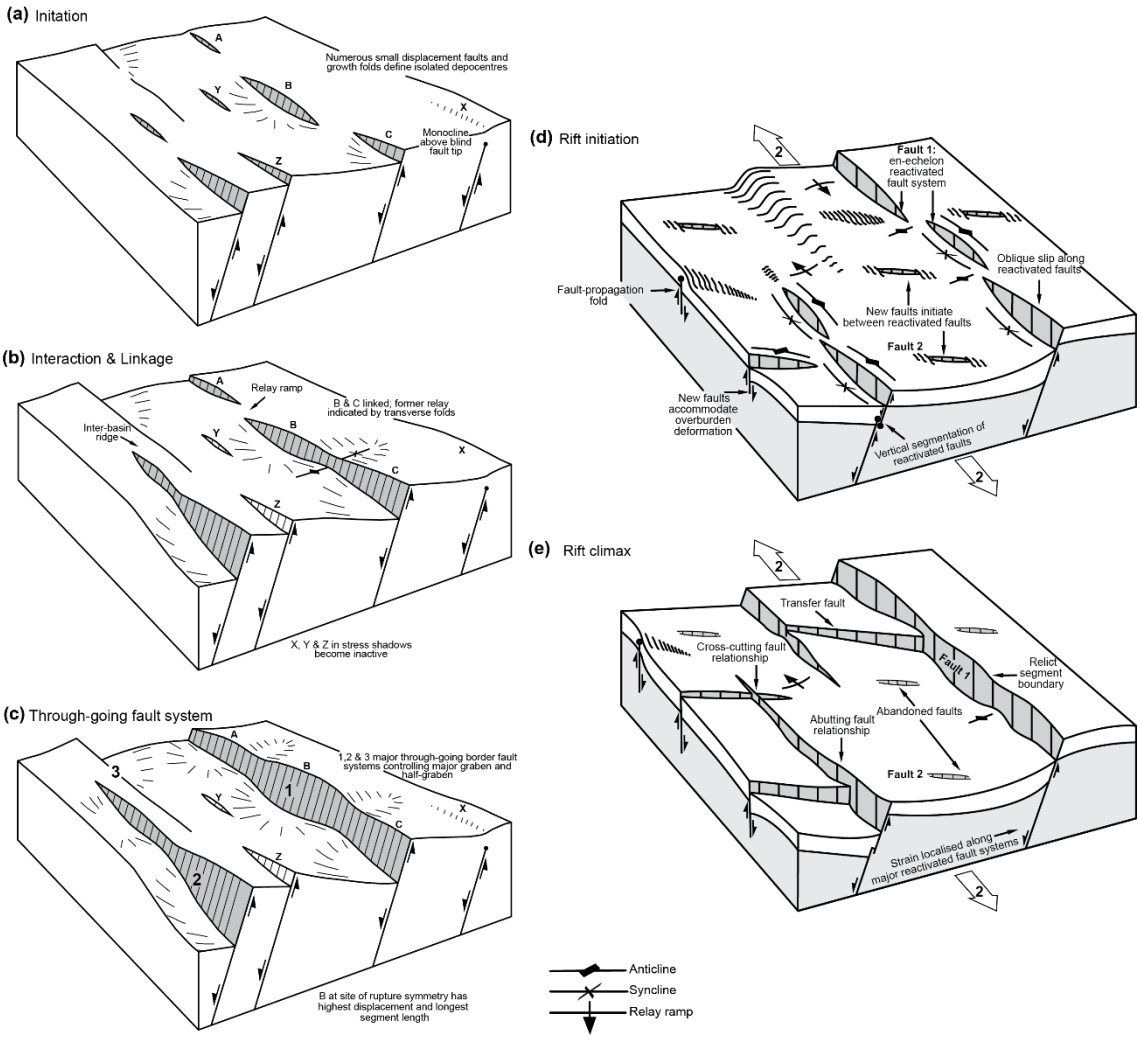

Figure 2.4: Conceptual model showing the differences with rift development without influence of pre-existing structures or with reactivation of pre-existing structures during rifting modified after Whipp et al. (2013) and modified after Gawthorpe and Leeder (2000). (a) Fault initiation stage record low displacement faults and extensional folds. (b) Fault linkage and strain localization onto larger faults whereas faults in strain shadow zones are abandoned. (c) Through-going fault phase with localized deformation onto few major fault systems. (d) Structural framework during the rift phase with oblique extensional reactivation of inherited rift structures which rapidly reach their full-length prior accumulating significant displacement, whereas newly formed structures develop perpendicular to inherited reactivate drift structures. (e) During rift climax these newly formed structures are rapidly abandoned with strain localization onto larger and older inherited faults.

The situation may be complicated by pre-existing fabrics. In the case of multiphase rifts and/or rifts developed with reactivation of inherited structures, the increased strain rate and strain localization onto larger fault zones (mostly

inherited) promote constant length fault growth (Corti et al., 2007; Fossen and Rotevatn, 2016; Jackson et al., 2017; Finch and Gawthorpe, 2017; Rotevatn et al., 2018). In the Suez Rift, the characteristic zigzag fault pattern is inferred as a result of reactivation of pre-existing fabrics from the Hercynian orogeny and Syrian Arc inverted Jurassic rift deep structures which formed major accommodation zones for Oligo-Miocene rifting and controlled changes of half-grabens polarity along-strike the rift (Patton, 1994; Montenat et al., 1998). Similarly, in the Tanganyika and Malawi rift the multiple reversals in the sense of asymmetry or polarity of half-grabens along-strike is intimately related to intervening transfer zones oblique to the main border faults, which accommodate deformation with strike slip and mostly represent inherited pre-rift structures (Morley et al., 1990). These complex changes of polarity and marked shifts in fault locus through time commonly reported in rifts developed with pre-existing tectonic fabrics, are also observed in modern rifts which lack strong influence of pre-existing tectonic fabrics (Whakatane Graben, New-Zealand, Taylor et al., 2004; Gulf of Corinth Rift, Bell et al., 2009). Therefore, the variability of rift architecture is a result of complex interactions between the mechanical behaviour of both pre- and syn-rift sediments and the way deformation is accommodated by fault growth, the obliquity of the extensional strain vector with respect to the inherited structural template which can induce local stress perturbation (Thailand Rift, Morley et al., 2004; Taupo Volcanic Zone, New-Zealand, Acocella et al., 2003; Gulf of Aden, Bellahsen et al., 2006; East African Rift, Corti et al., 2007, Morley et al., 2011; Norwegian North Sea Rift, Whipp et al., 2014; East Greenland Rift, Rotevatn et al., 2018).

2.1.4.2 Sedimentation and subsidence

Sedimentation rates are similar or faster to tectonic uplift and subsidence rates across normal faults, and sedimentary loading is comparable to tectonic loading. This exerts a strong control on the evolution of deformation, sustaining slip of large offset normal faults and affecting the isostatic balance of rift basins. Subsidence in rift basins is controlled by thermal and/or mechanical crustal thinning and sediment loading or unloading of the crust, which can have the potential to increase geothermal gradients. Surface processes exert a strong

control on the isostatic balance of rift basins, as erosional unloading and flexural rebound occur with tectonic uplift and subsidence rate (1-10 km/ Myr), similar to sedimentation rates and sedimentary loading comparable to tectonic loading (50-500 MPa) (Burov and Poliakov, 2001, 2003; Ziegler and Cloetingh, 2004; Armitage and Allen, 2010; Cloetingh and Willett, 2013). Sedimentation rates are on the order of (0.7-3 m/kyr, Gulf of Aden, Audin et al., 2001; 0.78 m/kyr Gulf Corinth Rift, Collier et al., 2000; 1.8 m/kyr, Gulf Corinth Rift, Moretti et al., 2004; 0.4-1 m/kyr, Whakatane Graben, New Zealand, Taylor et al., 2004; 0.64 m/kyr, Inner Moray Firth Basin, Scotland, McArthur et al., 2013). Erosional and depositional processes act at a similar time scale, or even faster than tectonism, and very high erosion and deposition rates (1.5 m/kyr) can sustain slip of large-offset normal faults that would be abandoned after a few kilometres of offset for lower erosion rates (0.15 m/kyr) (Olive et al., 2014). High sedimentation rates and thick sediment accumulations (several kilometres thick) can have a thermal blanketing effect. This promotes strain localization, narrow versus wide rift geometry, inhibits thermal heat dissipation, increase thermal gradients at depth, and enhances post-rift flexural strength of the lithosphere, thus delaying thermal subsidence (Karner, 1991; Burov and Poliakov, 2001).

In the northern part of the Gulf of Suez, sediment loading induced significant subsidence with rift narrowing and bathymetric deepening (Moretti and Colletta, 1987). A similar response is observed in the Gulf of California, where high sedimentation rates promote strain localization and switching from a wide to narrow rift geometry (Lizarralde et al., 2007). Here, sediment loading depresses crustal isotherms (i.e. thermal weakening) and enhances partial melting that counterbalance changes of gravitational forces associated with thinning. The hotter the thermal state of the crust, the higher the sediment rate must be to reduce crustal buoyancy forces (Lizarralde et al., 2007; Bialas and Buck, 2009). In the Gulf of Corinth, erosion and uplift (1.5 m/kyr) of footwall fault-blocks bounding the southern margin of the gulf created the modern high-relief associated with accumulation of ~1 km of sediments in the gulf interior. Sediment loading and lower crustal flow from beneath the depocentre towards rift borders induced 900 m of relative sea-level rise with subsidence, sustained uplift and growth of steeply dipping faults (Westaway, 2002). Similar onshore erosion and high rates of offshore sedimentation (0.3-0.5 m/kyr) induced flow of the ductile lower crust away from the basin centre and anomalously high thermal subsidence

rates during the post-rift development of the Malay and Pattani Basins of Southeast Asia (Morley and Westaway, 2006). When sedimentation rates are low and/or outpaced by the extension rate, lower crustal flowing towards the rift centre will be favoured and will promote low-angle dipping faults, such as in the Basin and Range Province or Aegean region (Westaway, 1998). In this scenario, the crustal thickness may be relatively uniform across weakly and highly extended domains. Necking of the more competent upper and middle crust is compensated by lower crustal flow that can be controlled by lateral lithostatic pressure variations induced by sediment loading and unloading, and regional-scale changes of the geothermal gradient (Westaway, 1998). Therefore, the effects of sediment load-driven subsidence can trigger substantial lateral crustal flow and strain accommodation by a thickened (~ 30 km) and thermo-mechanically weakened crust involving high geothermal gradient >400-500° (McKenzie et al., 2000). These effects are not expected in “cool” rifts, like the Atlantic margins, but are a common feature of high heat flow rift basins associated with subduction settings involving more complex processes than accounting by conventional stretching models (Westaway, 1998; Hall and Morley, 2004; Morley and Westaway, 2006; Clift et al., 2015).

2.1.5 Back-arc basins

Back-arc rift basins are commonly short-lived (3–15 Myr for rifted back-arc, Woodcock, 2004) as they are prone to destruction by compression, and can form large extensional regions that progress to crustal separation and opening of oceanic basins (e.g. Southwestern Japan Sea, South China Sea, Black Sea). Interaction between the two plates involved in subduction induces extensional and transtensional stresses in the back-arc, with more dynamic shifting of extensional locus and stress field through time than commonly observed in intracratonic or failed rifts (East African Rift, North Sea Rift, Suez Rift; Fig. 2.5.). Driving mechanisms for back-arc extension include a combination of surface kinematics, slab dynamics and interactions with mantle flow. Accommodation of back-arc strain involving tectono-magmatic processes, including volcanism and hydrothermalism, is promoted by thermomechanical weakening of lithosphere,

high mantle heat flow and slab fluid flow (Whittaker et al., 1992; Doglioni, 1995; Scholz and Campos, 1995; Doglioni et al., 1998; Sdrolias and Müller, 2006).

Back-arc rifts are associated with effects of slab pull, rollback or break-off, change in strike of the subducting plate, and mantle flow, in the Mediterranean region, Western Pacific region (Schellart et al., 2006) or Southeast Asia region (Morley, 2001). Slab retreat alone associated with uniform thickness and temperature of the lithosphere results in minor back-arc extension and subsidence. However, when stretching a lithosphere of uniform thickness but with temperature anomalies, extension and subsidence can be significantly enhanced. Large anomalies can occur with delamination processes related to post-orogenic lithospheric removal prior to, or during, slab rollback, which form high temperature zones that promote back-arc rifting and subsidence (Göğüş, 2015). Back-arc basins developed with initial orogen collapse of a thickened and thermo-mechanically weakened crust and extension with subduction slab dynamics, and/or mantle flow or lithosphere delamination processes show complex tectonic stress fields interacting with inherited structures (Aegean Sea and Central Greece, Goldsworthy et al., 2002; Zhejiang Province, eastern South China, Li et al., 2014; Alboran Basin, Do Couto et al., 2016; Pannonian Basin, Balázs et al., 2016).

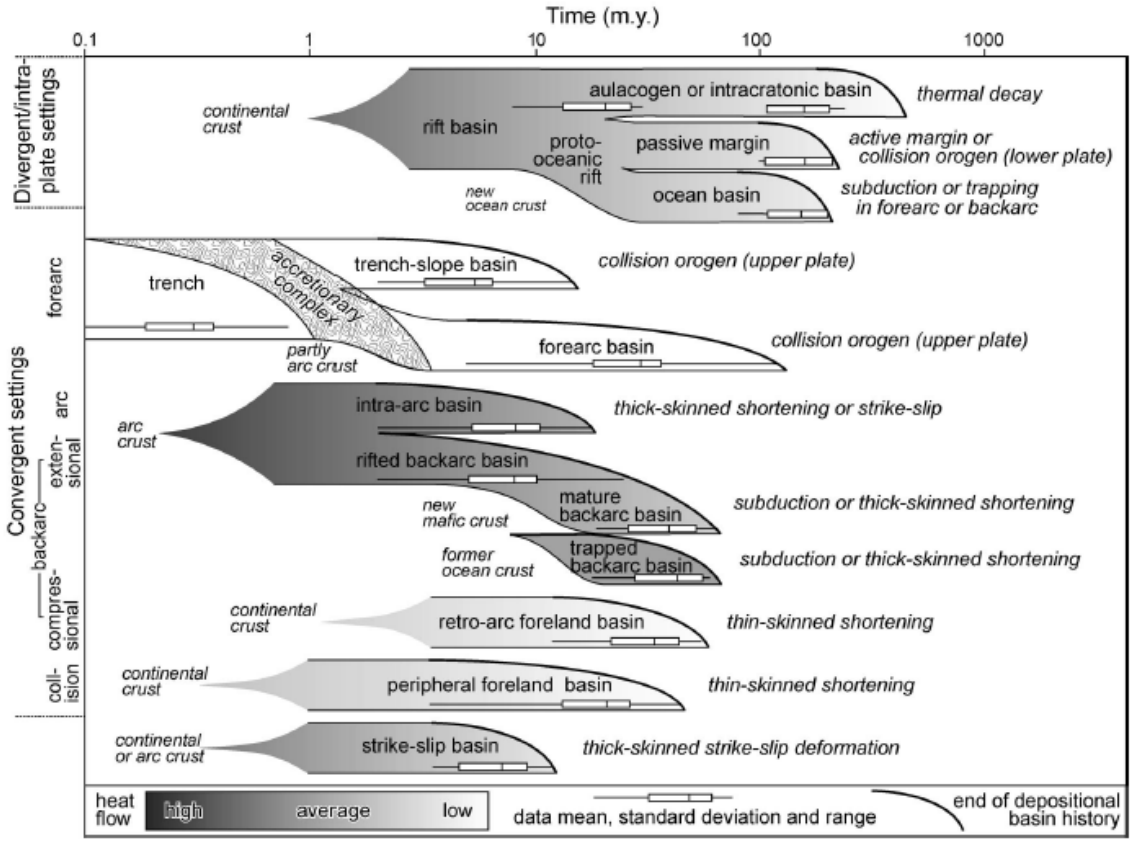

Figure 2.5: Diagram showing the different classes of sedimentary basins and their respective lifetime, basement type and deformation style, with estimated heatflow compiled from Blum and Hattier-Womack (2009).

2.2 Sedimentation patterns during the syn- to post-rift transition

The analysis of the interplay between tectonics, eustasy, climate, sediment source and supply rate in rift basin-fill, requires the identification of genetically linked depositional systems developed during distinct tectonic stages (Gawthorpe et al., 1994; Howell and Flint, 1996; Dorsey and Umhoefer, 2000; Martins-Neto and Catuneanu, 2010). Sediment supply rate in a depocentre depends upon the distance of rift basins from hinterland sources (proximal versus distal), and sediment yield from intrabasinal sources. The balance of sedimentation and accommodation can result in overfilled, balanced, underfilled, and starved basin-fill, and reflects the variability of documented early rift, rift climax, late rift and early post-rift stratigraphic signatures in marine rift basins (Prosser, 1993; Caroll and Bohacs, 1999; Ravnås and Steel, 1998; Figs 2.6-2.7.).

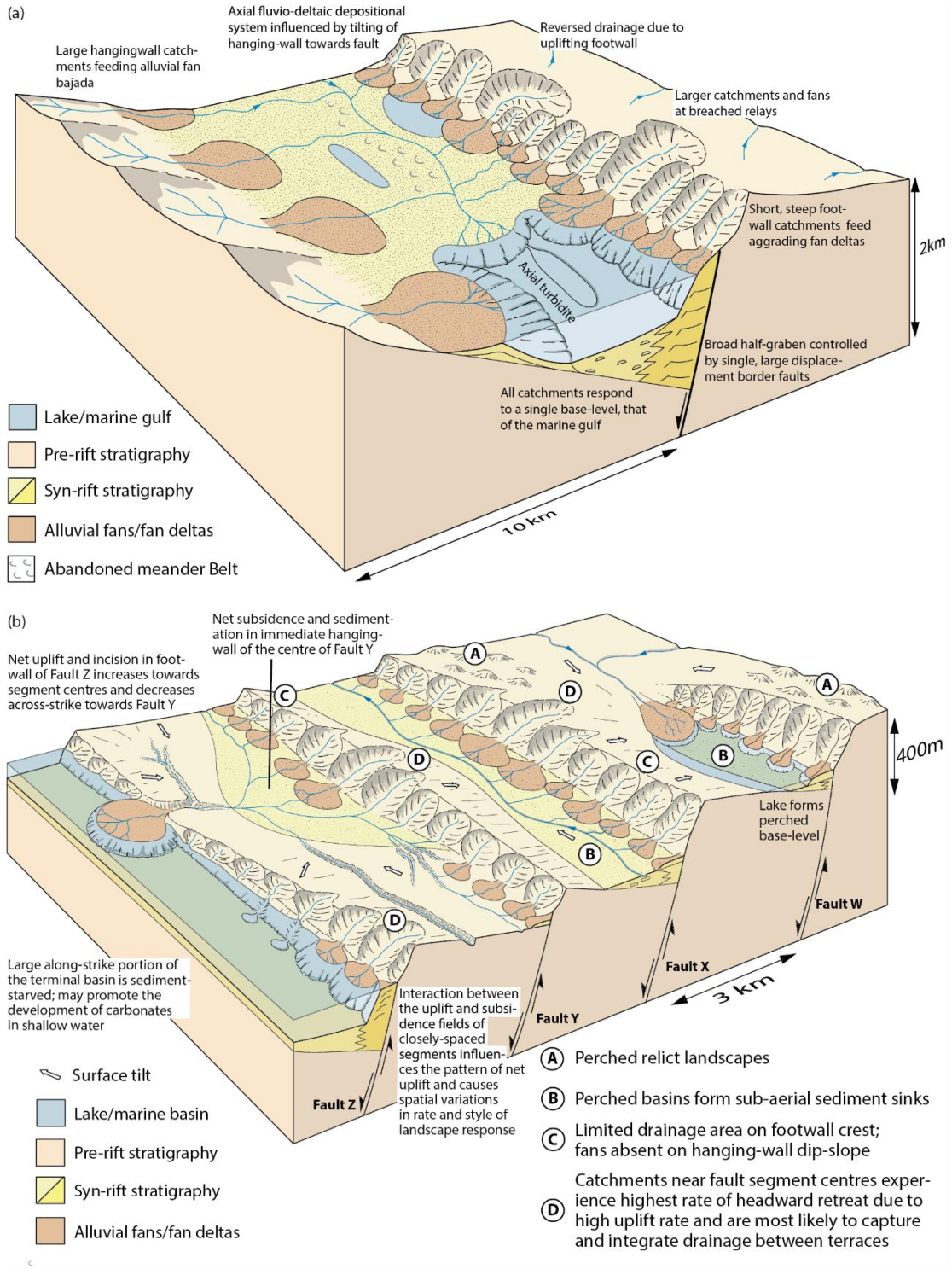

Figure 2.6: Conceptual tectono-sedimentary model for marine rift basins (Duffy et al., 2015, after Gawthorpe and Leeder, 2000) showing the effects of topography and fault geometry on base-level and sedimentation in marine rift basins.

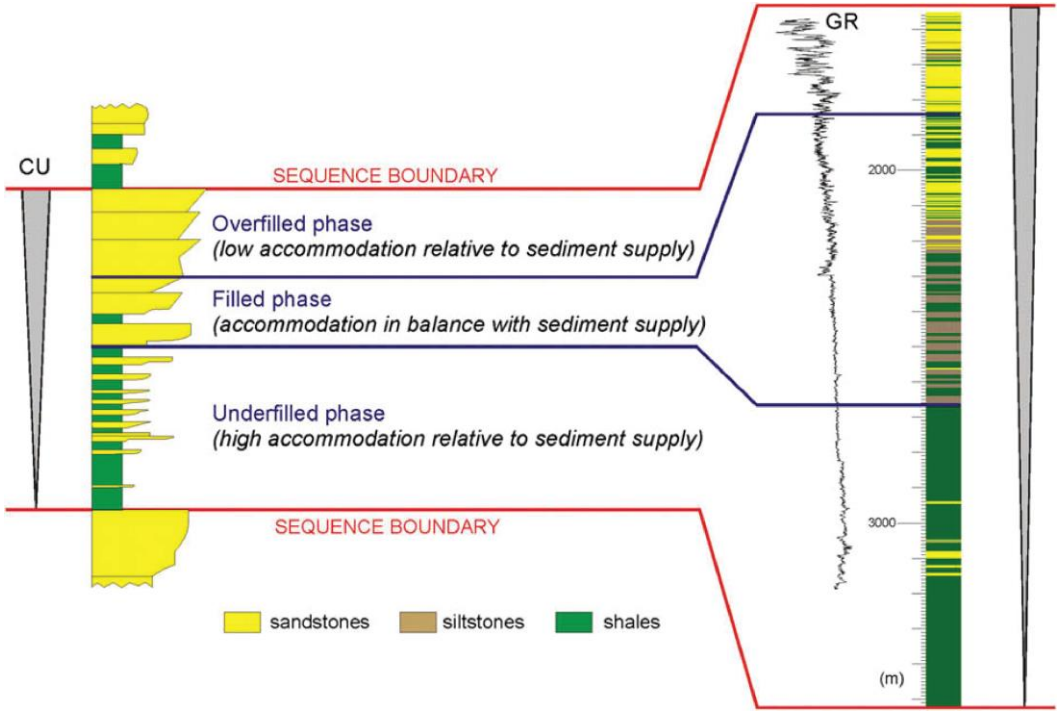

Figure 2.7: Conceptual internal architecture of an ideal rift sequence (Martins-Neto and Catuneanu, 2009) with coarsening-upward vertical stacking pattern, and shift from underfilled to filled and overfilled conditions and correlation with gamma-ray log.

Typically, a rift basin-fill records an evolution from underfilled to overfilled conditions. Initially the fill comprises transgressive deposits during tectonically-driven retrogradation with high subsidence rates and rapid relative sea-level rise. A subsequent regressive pattern, overlying a maximum marine flooding surface, corresponds to a progradational sequence developed with tectonic waning and subsidence decay (Martins-Neto and Catuneanu, 2010). A major weakness of rift basin-fill models is that they do not include syn-rift volcanism despite its implications for tectono-stratigraphic development of rift basins due to feedbacks between surface volcanism, tectonism and sedimentation. Lava flows can create dams raising basin margins, caldera collapse induces abrupt volcano-tectonic subsidence, cooling and loading of large volumes of dense igneous deposits increase hangingwall subsidence, magma retreat from magmatic chambers increases local crustal subsidence, hydrothermalism and volcanic activity induces modifications of surface morphology (vegetation type, slope gradient) with complex catchments reorganization (Orton, 2002; Ziegler and Cloetingh, 2004; Buck, 2004; Wooller et al., 2009; Rowland et al., 2010; Muravchik et al., 2011; D'Elia et al., 2018). These processes in volcanic rift basins where subsidence patterns are controlled by both tectonism and volcanism (magma

composition, supply rate and eruptive style) mean that the distribution of sedimentary environments are more complicated that non-volcanic rift basins.

Most rift basin models propose the recognition of system tracts associated with successive tectonic stages of rift evolution, with little to no emphasise on the post-rift evolution. The basic scheme of Gabrielsen et al. (1995), who define active stretching and thermal subsidence stages, is similar to the syn-rift and post-rift differentiation of Bosence (1998). Prosser (1993), Nøttvedt et al. (1995) and Ravnås and Steel (1998) provided a more detailed nomenclature and distinguish rift initiation, rift Climax (early, mid and late), and immediate or early post-rift and late post-rift. Gawthorpe and Leeder (2000) focused on fault evolution, considering fault initiation, fault interaction and linkage, through-going fault zone stages and fault death stages. A generic description of fault, sedimentation and stacking patterns is provided, with a non-exhaustive list of controls and processes during the different stages of rift basin evolution, as depicted by most of the previously cited rift basin models.

2.2.1 Early rift

Rift initiation is usually depicted starting with distributed and low strain, which may produce isolated discrete extension-related fold structures across blind faults and low fault displacement rates at surface breaks controlling the formation of slowly subsiding local depressions (Gupta et al., 1999; Gawthorpe and Leeder, 2000; Dawers and Underhill, 2000; Young et al., 2003; Jackson et al., 2002; Bell et al., 2009). Syn-rift strata can develop as divergent wedges towards the footwall of surface breaking faults with eventual decrease of stratal dips upwards with fault-block rotation or thinning and onlapping across blind faults and dipping into the hangingwall (Schlische, 1993, 1995; Gawthorpe et al., 1997; Sharp et al., 2000; Khalil and McClay, 2018; Fig., 2.8.). In the last case, deformation is accommodated by a range of fault-parallel longitudinal folds (fault-bend folds with rollover folds or drag folds, fault propagation or “forced” folds) and fault transverse folds. Transfer zones play a key role in the rift evolution as they connect adjacent extensional basins and constitute routing pathways for sediment supply. These structures are often localized as an effect of rift segmentation by basement fabrics and form between closely overlapping fault

segments that may or not dip in opposing directions (e.g. synthetic or conjugate transfer zones). They form either with soft fault linkage, corresponding to relay ramps or troughs, or with hard fault linkage, corresponding to transfer faults that accommodate displacement via subvertical strike-slip and oblique-slip (Morley et al., 1990; Gawthorpe and Hurst, 1993; Athmer et al., 2011; Mortimer et al., 2016; Moustafa and Khalil, 2017).

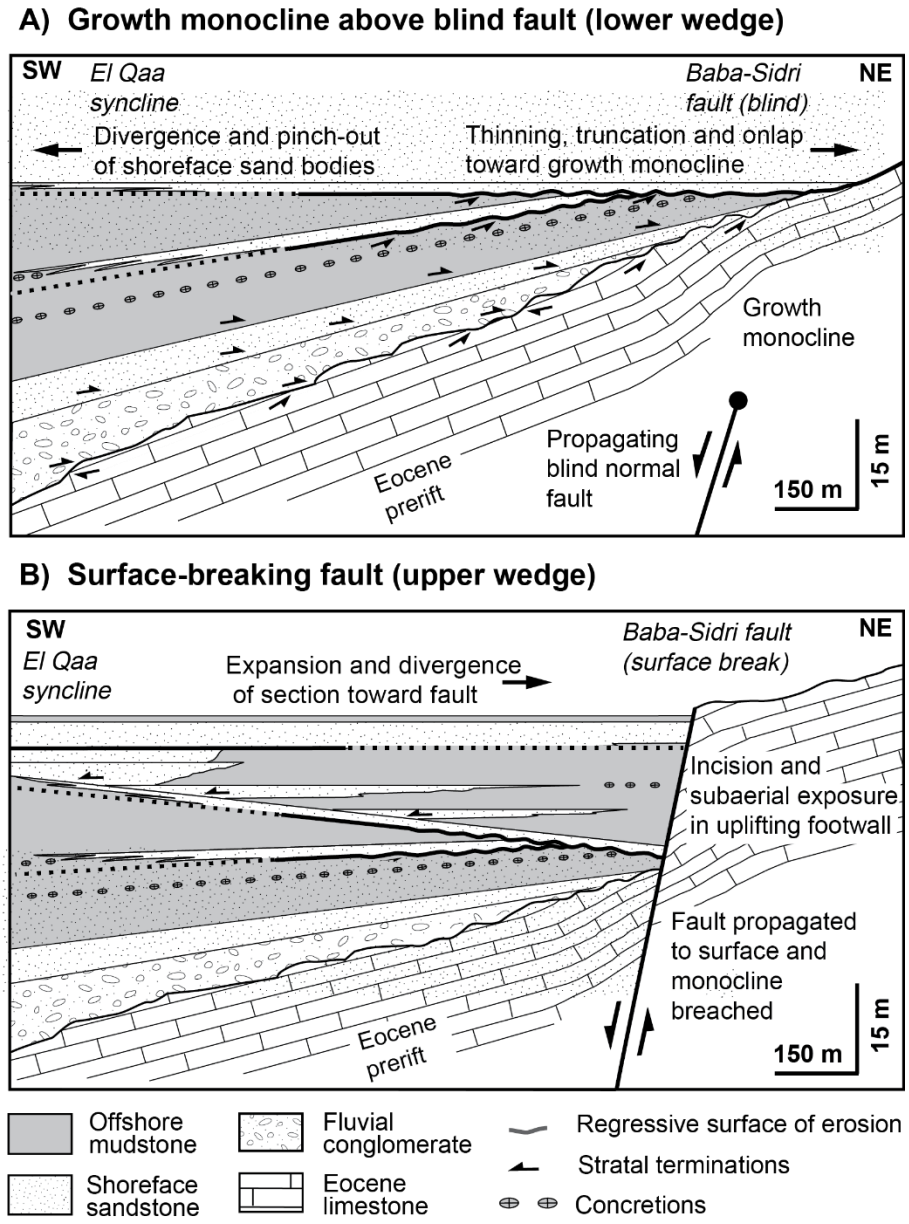

Figure 2.8: Example of (A) fault growth folding above blind propagating normal fault with thinning an donlapping towards the blind fault and (B) surface breaking fault with wedging and thickening towards the fault. (Gawthorpe et al., 1997)

Intracontinental rift basins are dominated by terrestrial depositional systems during the early post-rift. A transition to marine conditions tends to occur late

during the rift climax or late rift, depending on stretching, subsidence and proximity to any adjacent ocean for marine incursion. Extensional faulting promotes clastic sediment supply from pre-existing drainage basins that can exceed the capacity of isolated shallow basins bounded by small faults. This leads to the development of mainly transverse siliciclastic alluvial and fluvio-lacustrine or fluvio-deltaic systems with aggradational to progradational patterns (Prosser, 1993; Schlische and Anders, 1996; Gupta et al., 1999; Gawthorpe and Leeder, 2000; Lewis et al., 2015). Sedimentation patterns can vary markedly across 10s km in relation to the rift architecture and relative base level change. This results in contemporaneous development of extensive fault-transverse systems adjacent to large faults, feeding axial turbidites to the hangingwall, and minor development of transverse talus cones adjacent to low-relief faults with starvation of the hangingwall (Leeder et al., 2002; Duffy et al., 2015; Elliott et al., 2015).

Clastic systems and carbonate platforms or reefs systems can develop together with fan deltas and deltas along rift basin margins, if hinterland sediment supply doesn’t produce deleterious conditions for shallow carbonate factories. Also, fault-block highs and large horsts detached from the rift basin margin and remaining at shallow-water depths, isolated from clastic supply routes, form ideal offshore sites for fault-block carbonate accumulation (Lusitanian Basin, Leinfelder et al., 1998; Suez Rift-Red Sea-Gulf of Aden, Cross and Bosence, 2008). Carbonate sedimentation in rift basins is governed by the structural grain. This imparts significant changes in facies distribution and stratal architecture, and influences oceanic circulation and wind direction patterns to redistribute water and nutrients, which control trophic levels that determine the distribution of carbonate producers along the rift (Halfar et al., 2004; Dorobek, 2008; Purkis et al., 2012). The arid versus humid climate is an important factor as it controls suspended sediments and nutrient delivery by rivers and controls water turbidity, and temperature and salinity, which directly impact onto carbonate systems and determines whether or not clastic and carbonate systems can be coeval (Leeder and Gawthorpe, 1987; Collier and Thompson, 1991; Santantonio, 1994; Cross et al., 1998; Bosence, 1998; Cross and Bosence, 2008). Carbonate facies distribution is both depth and slope dependant. They tend to form ramps in the hangingwall dip slope passing basinward into siliciclastics, whereas they form rimmed shelves on footwalls, and their progradation is limited by the steepness

of bounding fault scarps (Cross and Bosence, 2008; Dorobek, 2008). On footwalls, reefs and microbial encrustations have the potential to develop onto slope gradients up to 10s degrees, which are prone to reworking and accumulation of carbonate talus fans into the hangingwall (Leeder and Gawthorpe, 1987).

2.2.2 Rift climax

During the rift climax, fault linkage and localization of displacement on major border fault systems produces significant topography and accommodation with high mechanical subsidence rates. This period is also marked by coeval abandonment of smaller intra-block faults, and/or faults in strain shadow zones, and merging of smaller depocentres into a broader depocentre that migrates towards the centre of the hard-linked fault (Gupta et al., 1999; Gawthorpe and Leeder, 2000; Young et al., 2002; Jackson et al., 2002; Gawthorpe et al., 2003; Cowie et al., 2005). This evolution is associated with rapid increase in water depths, depending on the relative sea-level position at the start of rifting, and tectonic accommodation outpacing sediment supply rate. The result is underfilled rift basins, with development of a range of shallow- to deep-marine or lacustrine relatively fine-grained clastic systems with aggradational to retrogradational stacking (Prosser, 1993; Ravnås and Steel, 1998). High strain accumulation and increasing subsidence rate during the rift climax commonly outpace accumulation rates of carbonate systems, which become drowned, and favour an increase of intrabasinal clastic supply with fault-block uplift (Leinfelder et al., 1998; Gupta et al., 1999; Cross and Bosence, 2008; Dorobek, 2008; Lachkar et al., 2009). Divergent and onlap stratal growth geometries, with seismically triggered soft sediment deformation structures and slumping develop in the starved centre of rift basins. The basin margins are associated with high-relief footwall scarp degradation-related coarse-grained clastic detritus adjacent to large linked fault border systems. Footwall catchments can develop with fault-block collapse that supply large and coarse-grained fan deltas, slope aprons and fault scarp degradation complexes (debris and breccias) into immediate hangingwalls (Ravnås and Steel, 1997; Leppard and Gawthorpe, 2006; McArthur et al., 2016; Rohais et al., 2016; Fig. 2.9). Discrete shallow-marine fringing shoreface and

small clastic fans systems may persist in overlap zones between unlinked faults or along the hangingwall dip slope (Ravnås and Bondevik, 1997; Dawers and Underhill, 2000; Muravchik et al., 2015).

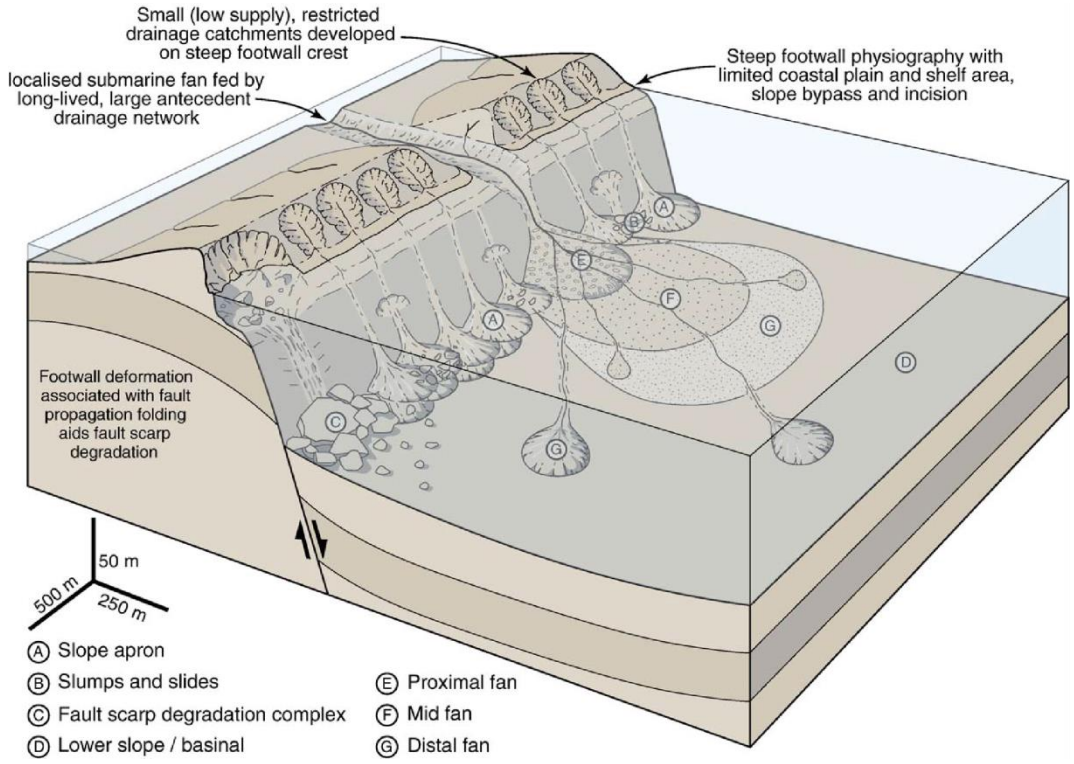

Figure 2.9: Model for rift climax deep-marine sedimentation, showing the development of coarse-grained slope aprons associated with fault-scarp degradation and restricted catchments and submarine fan fed by a larger point source enabling high sediment supply. (Leppard and Gawthorpe, 2006)

In a lacustrine basin, the increase of mechanical subsidence does not raise the volume of lake water, which is mainly dependent on climatically driven precipitation and evaporation. Instead, a relative base level fall would result, which commonly is accompanied by a reduction of sediment yield (Lambiase and Bosworth, 1995; Ilgard et al., 2005). With increasing subsidence, lacustrine rift basins can evolve under marine conditions with the influx of seawater through narrow straits. Establishment of marine conditions limit turbid mud underflows which otherwise prevail under lacustrine conditions (e.g. Corinth-Pathras, Greece, Reggio-Scilla graben, southern Italy, Pessioratis et al., 2000; Zelilidis et al., 2003).

2.2.3 Late Rift

The late syn-rift is marked by a decline of extensional faulting and the remaining extensional strain is taken up by hard-linked large border fault systems. These border faults are not always bounding the thickest syn-rift depocentres, nor do they correspond to the faults that accumulated the highest displacement rates through rift evolution, given the variability of faulting and subsidence patterns throughout rift development (Gawthorpe et al., 2003; Young et al., 2003). Increased rate of fault-block uplift and erosion can promote the development of intrabasinal fault-block catchment-fed sandy shoreface-fed deep-marine turbidite systems, with slope fans trapped within intra-hangingwall dip slope accommodation (Ravnås and Steel, 1997; Jackson et al., 2011). Large elongate depocentres favour the development of axially-sourced deep-marine clastic systems taking time to reach the distal part of rift basins away from rift margins dominated by fluvio-deltaic clastic systems. Once established, these systems can sustain a stable connection with hinterland and form sediment pathways lingering during the early post-rift (Prosser, 1993; Ravnås and Bondevik, 1997; Alves et al., 2003; Seidler et al., 2004; McArthur et al., 2016). Typically, carbonate systems develop during the late syn-rift onto high-relief fault-block highs remaining at shallow water depth and results in offshore archipelagos away from rift basin margins until clastic sediments trapped into fault-block lows infill accommodation (Bosence, 1998; Cross and Bosence, 2008; Dorobek, 2008; Purkis et al., 2012). The decrease of fault displacement and/or rapid infill and levelling of the fault-related relief with high siliciclastic supply enables subsequent footwall to hangingwall carbonate progradation across low-relief topography. This can result in formation of a larger composite platform, which tend to evolve from a ramp to bypass rimmed shelf margin, whereas elsewhere in the distal part of the basin is characterised by sediment starvation (Leeder and Gawthorpe, 1987; Fraser and Gawthorpe, 1990; Collier and Dart, 1991; Cross et al., 1998; Bosence, 1998; Dorobek, 2008).

2.2.4 Early post-rift

The early post-rift records a reduction of accommodation with decrease of subsidence rate and healing of rift topography which promotes increased sediment bypass towards the basin centre. The rate of healing depends on sediment yield with intrabasinal supply from local fault-block degradation and/or extrabasinal supply from hinterland drainage systems, with increasing control of eustasy and thermal subsidence on sedimentation during the late post-rift (Prosser, 1993; Ravnås and Steel, 1998; Karner and Driscoll, 1999; Alves et al., 2003; Lien, 2005; Gabrielsen et al., 2001; Jarsve et al., 2014; Fig. 2.10).

The syn- to post-rift boundary can be cryptic due the variability of early post-rift sedimentation patterns and stratal geometry that can be similar to the late syn-rift (Nøttvedt et al., 1995; Bosence, 1998; Kyrkjebø et al., 2004; Zachariah et al., 2009; Soares et al., 2012; Jarsve et al. 2014). Furthermore, the cessation of rifting is diachronous at basin-scale and isochronous early post-rift sequences can produce a range of stratal packages due to the long-lived physiographic imprint of rift topography, and inherited accommodation on early post-rift sedimentation. The effects of residual early post-rift deformation (related to compaction, sediment loading or unloading, brittle deformation with thermal subsidence) have the potential to form combined structural-stratigraphic traps with four-way closure and pinchout in the early post-rift strata and can be masked when outpaced by faster rates of thermal subsidence (Doglioni et al., 1998; Cristallini et al., 2006).

Early post-rift deformation can result from various mechanisms. Gravitational faulting driven by sediment loading and erosional unloading (Burov and Poliakov, 2003), or localized “brittle” accommodation of crustal subsidence with residual displacement of major basement-involved faults that can produce small faults, fault growth folds and large-scale monocline folding at basin borders (Sinclair, 1988; Bosence, 1998; Rosas et al., 2007; Monaldi et al., 2008; López-Gamundí and Barragan, 2012; Lohr and Underhill, 2015). Deformation can be induced by far-field stress or compaction, with development of new small faults with few 10s metres to 100s metres displacement, nucleated over syn-rift and pre-rift faults, (Cristallini et al., 2009; Morley, 2015; Morley and Nixon, 2016; Fig. 2.11.).

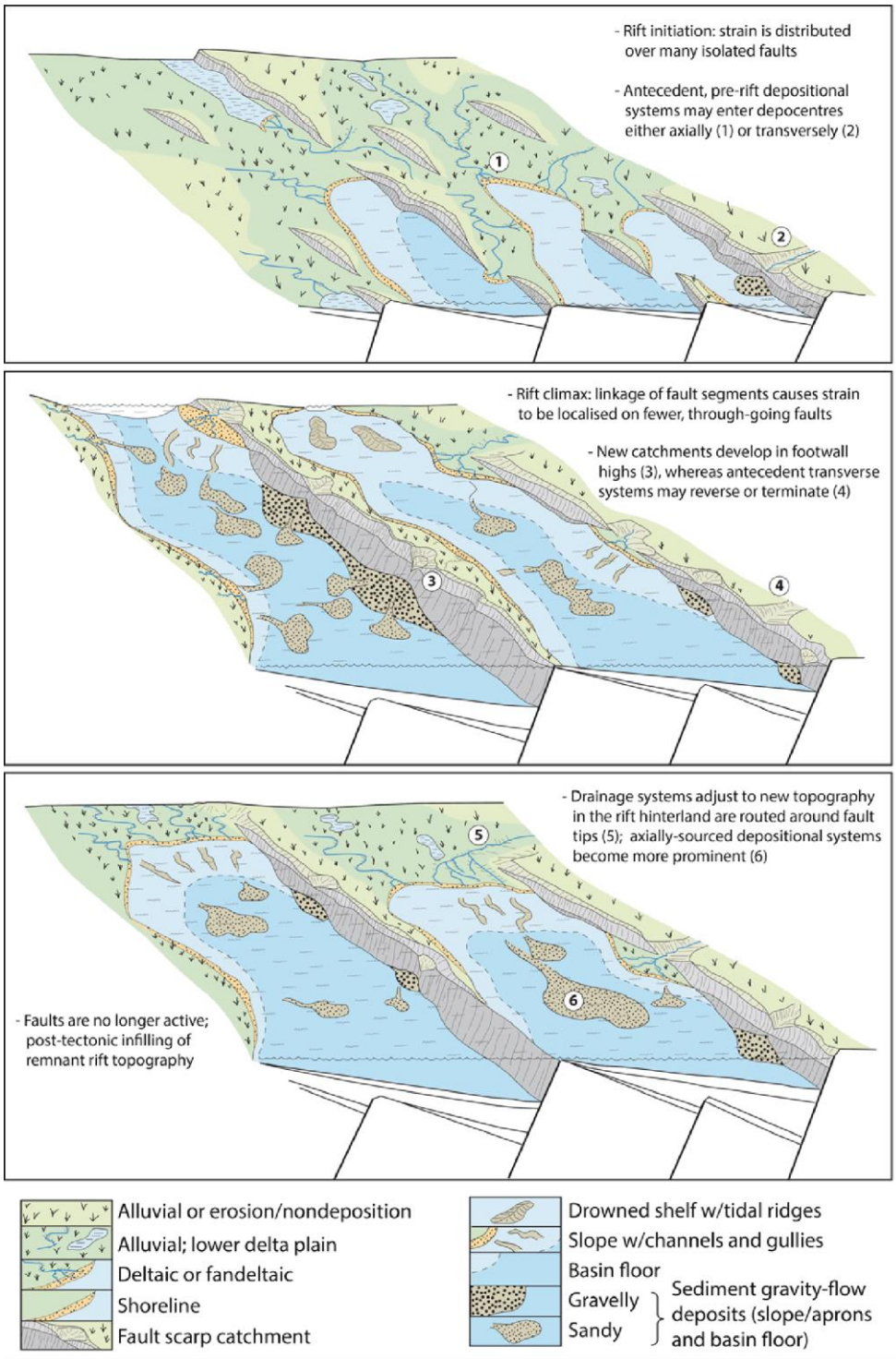

Figure 2.10: Conceptual model for the evolution of sedimentation during rifting from shallow- to deep- marine setting (Henstra et al., 2018; modified after Gawthorpe and Leeder (2000) and Ravnås and Steel (1998). (a) Rift initiation with distributed strain across multiple isolated fault segments. (b) Rift climax and through-going fault phase promoting the development of transverse sedimentary systems. (c) Fault abandonment and development of axial sedimentary systems.

Compaction occurs over short timescales (10^5-10^6 years) with sediment thickness decrease and porosity loss driven by lithostatic and hydrostatic loading within a few hundred metres of burial. The effect of compaction on sedimentation is difficult to distinguish from eustasy, isostatic or tectonic subsidence, despite representing up to a fifth of total basin subsidence (Reynolds et al., 1991; Hunt et al., 1996). Compaction-induced surface deformation during early post-rift sedimentation can induce modification of slope gradient and differential subsidence. This result in stratal thickness changes and multiple erosional and angular unconformities, which can appear similar to effects of tectonic tilting, and/or folding and small-scale faulting, and control facies distribution and stacking patterns.

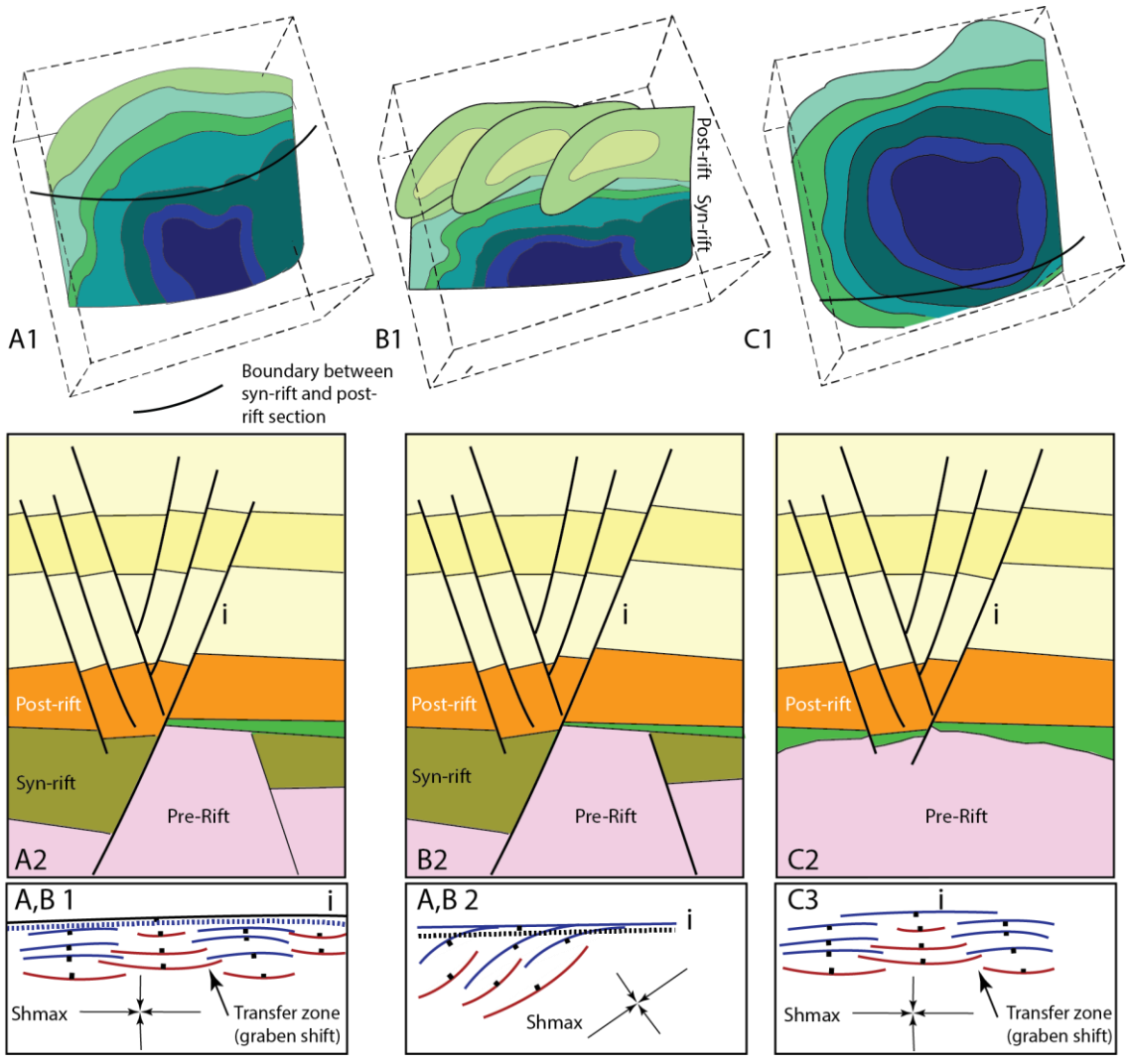

Figure 2.11: Examples of small-scale early post-rift faults in the Pattani and North Malay basins (Morley, 2015) which can be nucleated in the post-rift deposits or which can have relationship with syn-rift faults (A2 and B2)or nucleated above basement highs (C2).

Compaction-related deformation during early post-rift sedimentation can result from different compaction versus sedimentation rates, and/or mechanical compaction related to spatial variations in lithological heterogeneity of buried strata (facies-dependent compaction with variations of porosity-depth gradients lithologies). Furthermore, differential compaction occurs across irregular basement physiography with enhancement of antecedent topography (variable compaction rate between rigid basement, carbonate build-up, volcanic reliefs and overcompacted adjacent hangingwall fills) and natural overcompaction of sediments into fault hangingwalls (Bertram and Milton, 1989; Collier, 1989; Barr, 1991; Cartwright, 1991; Faerseth et al., 1995; Skuce, 1996; Faerseth and Lien, 2002; Carminati and Santantonio, 2005; Cristallini et al., 2006; López-Gamundí and Barragan, 2012; Lohr and Underhill, 2015; Balázs et al., 2017; Fig. 2.12).

Therefore, in early post-rift setting, both inherited rift topography and early post-rift deformation are crucial controls on the development of sedimentary environments. Shallow-marine high-energy areas and/or subaerial exposure are preferentially found on fault-block highs and deeper marine low energy sedimentation in adjacent lows and compaction-induced relief can dictates facies distribution, sediment transport processes and flow routing pathways (Modica and Brush, 2004; López-Gamundí and Barragan, 2012; Lohr and Underhill, 2015). Variations of compaction-induced subsidence can produce local extensional faulting in the early post-rift cover draping topographic highs, forming syn-depositional surface topography able to divert sediment gravity flows which can be misinterpreted as the effects of active extensional faulting (Collier, 1989; Argent et al., 2000; Modica and Brush, 2004; Lohr and Underhill, 2015; Balázs et al., 2017).

Inherited relief (intrabasinal sources), hinterland topography, size of drainage basin (extrabasinal sources), distance of rift basins from sources and slope morphology control the productive supply or starvation of early post-rift basins, and efficient routing or trapping of siliciclastic influx. Inherited structural configuration of transfer zones exerts a more important control during the post-rift than syn-rift evolution. Transfer zones exert a long-lived control on the location of routing pathways, subsurface fluid migration, drainage basins and sediment entry points depending on its evolution. This is mainly in function of the capacity of sediment supply to be cut-off, or outpace and incise fault-growth relief induced

by fault linkage and/or footwall uplift (Gawthorpe and Hurst, 1993; Gupta et al., 1999; Moustafa and Khalil, 2017; Athmer et al., 2011; Moscardelli et al., 2013; Henstra et al., 2016;).

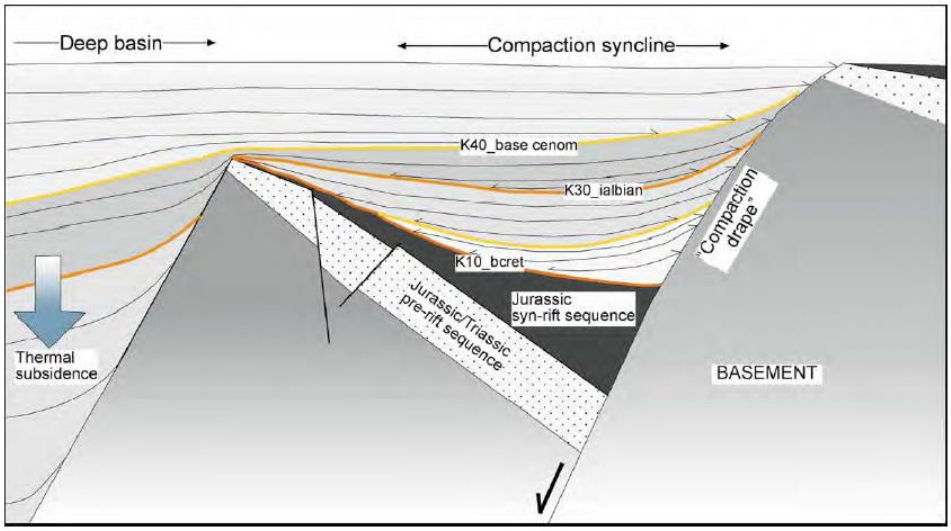

Figure 2.12: Example of early post-rift onlap and compaction-related synclines in a half-graben (Faerseth and Lien, 2002).

Some rift basins inherit a relatively subdued topography when sediment supply is high during the rift climax and late syn-rift, and evolve with little subsidence in the early post-rift, which leads to the development of shallow-marine to continental deposits (Martins-Neto, 2000; Rohais et al., 2016). In contrast, significant inherited rift topography remaining as intrabasinal fault-block islands undergoes prolonged exhumation and degradation, supplying high or low sediment yield according to the exposed bedrock lithology and promotes the preferential development of transverse systems sensitive to residual fault-block movements and differential subsidence (Leeder et al., 2002; McArthur et al., 2013; Muravchik et al., 2014). This produces a deep-water early post-rift basin configuration similar to the late syn-rift until total submergence, onlap and burying of intrabasinal reliefs, and exclusive extrabasinal supply, enable the development of axial systems across a more subdued topography characteristic of a post-rift configuration (Larsen et al., 2001; Zachariah et al., 2009b; Jarsve et al., 2014; McArthur et al., 2016; Henstra et al., 2016).

In contrast, when sedimentation rates are outpaced by the subsidence rate at the end of rifting, the basin undergoes drowning and draping of intrabasinal sources. This promotes sand starvation and development of laterally extensive organic-rich marine mudstone deposits, locally accommodating residual faulting and compaction during the early post-rift (López-Gamundí and Barragan, 2012; Lohr and Underhill, 2015). This underfilled basin configuration results in significant inherited relief, which is progressively healed depending on the rate of extrabasinal sediment supply whichis controlled by the hinterland drainage productivity related to climate and uplift, and sediment bypass or storage. In this case, extrabasinal sediment supply with high sediment yield from a humid climate and/or favourable hinterland configuration plays a critical role on the timing to infill the inherited accommodation and development of sediment balanced to overfilled early post-rift sand-rich depocentres (Takano, 2002; Alves et al., 2003; Yu et al., 2013; Balázs et al., 2017; Marin et al., 2017). Slower infill rates form underfilled to balanced depocentres and isolated thin sand-rich depocentres with long-lived influence of inherited rift topography (Karner and Driscoll, 1999; Argent et al., 2000; Lien, 2005).

2.2.5 Late post-rift

The late post-rift records further infill of inherited accommodation and healing of intrabasinal topography across rift basins, with conformable deposition of tabular strata that onlap onto early post-rift deposits, without complex thickness and facies variations across structures (Prosser, 1993; Leinfelder et al., 1998; Hadlari et al., 2016). This mature post-rift records basin reorganization with bathymetric deepening, drowning of island fault-blocks, and regional slope gradient reduction, which enable transport of large sediment volumes to the basin centre, with eustasy and subsidence as main factors of control (Prosser, 1993; Kjennerud et al., 2001). However, in some rift basins the significant inherited and compaction-enhanced rift topography can have a long-lived influence on sediment routeing and basin-fill architecture, even during the late post-rift sedimentation (Martinsen et al., 2005; Fugelli and Olsen, 2005; Dmitrieva et al., 2018).

2.3 Submarine fans in topographically complex settings

Submarine fans are extensive lobate sand accumulations (lobe complexes) formed by sediment gravity flows exiting confinement at the terminus of a feeder channel-mouth, and develop with variable dimensions, intrinsic characteristics and hierarchy in a range of settings (Normark, 1970; Mutti, 1977; Reading and Richards, 1994; Galloway, 1998; Mattern, 2005; Prélat et al., 2009; Cullis et al., 2018) (Fig. 2.13). The range of size, geometry, architecture and facies in submarine fans are the product of interactions between sediment supply, sea-level changes, and passive or dynamic seabed morphology depending on the tectonic setting.

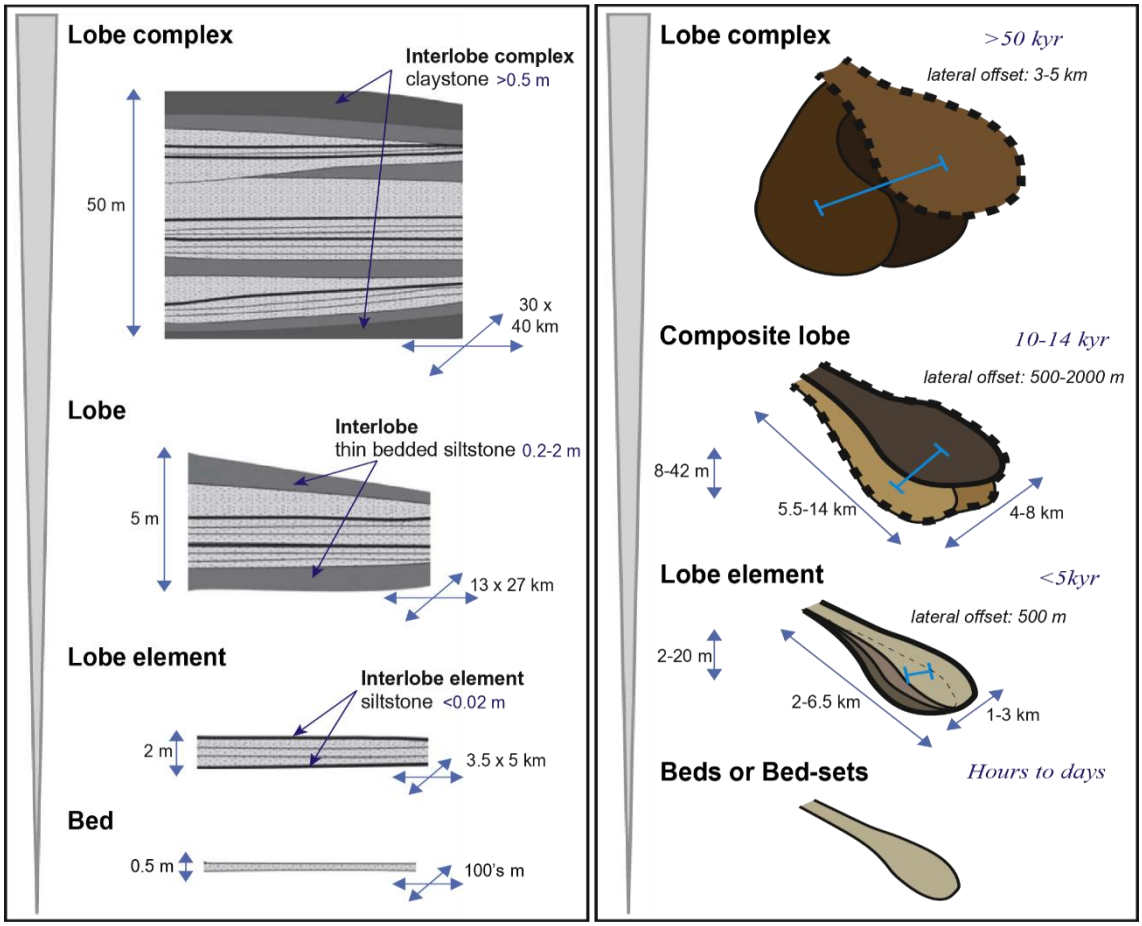

Figure 2.13: Classification of lobes, lobe elements and lobe complexes by Prélat et al. (2009) and Deptuck et al. (2008) used to characterize submarine fan systems (modified after Cullis et al., 2018).

Many authors have pointed out the importance of physiography acting at the same rank as other factors of control on the stratigraphic architecture of sedimentary systems (Ross et al., 1995; Martinsen and Helland-Hansen, 1995; Prather et al., 2003; Cattaneo and Steel, 2003; Veiga et al., 2013). The efficiency of sediment transfer downslope depends on the slope and basin floor accommodation available and the nature of the graded profile. According to the style of tectonic deformation and subsidence versus sedimentation rates, these topographic features exert a control on sediment dispersal and stacking patterns (Smith, 2004; Prather et al., 2012). The volume and composition of sediment gravity flows define their ability to decelerate and deposit sediment across low-gradient slopes (depletive) or erosion and bypass across higher gradient slopes (accumulative) (Smith, 2004).

The effects of seabed topography on the distribution, geometry and evolution of fan architecture in response to infill of above-grade slopes have been observed in a range of topographically complex settings (Satur et al., 2000; Sinclair and Tomasso, 2002; Hooper et al., 2002; Booth et al., 2003; Prather et al., 2003, 2017; Hodgson and Haughton, 2004; Adeogba et al., 2005; Pyles et al., 2008; Covault and Romans, 2009; Cross et al., 2009; Hay, 2012; Marini et al., 2015; Spychala et al., 2015; Jobe et al., 2017; Pinter et al., 2017; Bell et al., 2018).

2.3.1 Intraslope lobes

Sediment routing and partitioning from shelf to slope and basin-floor can result in an increase of sand downslope and development of extensive (>100 km) base-of-slope and basin-floor fans across unconfined basin plains (Mississipi, Twichell et al., 1991; Amazon, Jegou et al., 2008; Zaire, Savoye et al., 2000; Nile, Migeon et al., 2010). Intraslope lobes form in ponded slope accommodation (three dimensionally enclosed basins), or partially confined in perched or healed slope accommodation, or in laterally confined tortuous corridors (Prather et al., 2003, 2017; Smith, 2004) (Fig. 2.14).

Fully confined/ponded systems develop with lower net: gross and commonly lack distal lobe fringe deposits and have thick graded bed tops, as the dilute part of flows cannot override the confining relief, leading to collapse of high-density flows. Progressive smoothing of rugose topography is recorded with a transition

from initial infill of the ponded slope accommodation until flows can bypass and spill across healed slope accommodation and adjust to a new equilibrium profile. This results in a fill-and-spill model, first with deposition of ponded flat lying onlapping “sheet” sandbodies, then superseded by deposition of perched downslope tapering wedge-shaped fill and bypass sequence of sheet sandbodies, channels and mass-transport deposits downlapping onto the ponded sequence (Beaubouef and Friedmann, 2000; Sinclair and Tomasso, 2002; Booth et al., 2003; Prather et al., 2003).

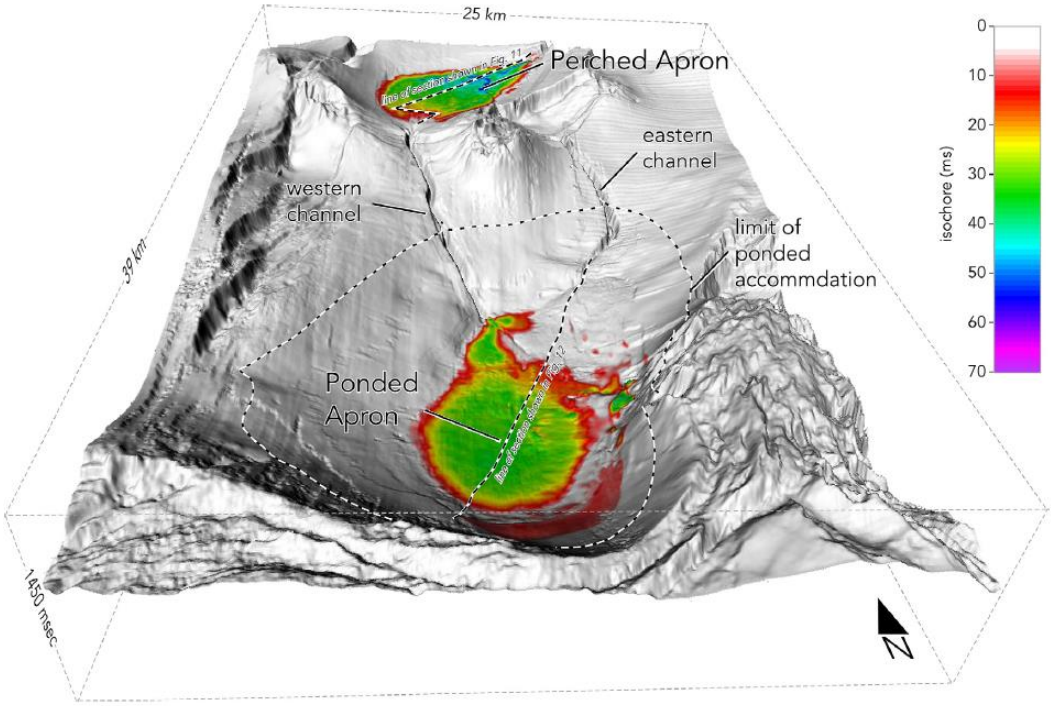

Figure 2.14: Perspective of perched and ponded aprons of the Brazos-Trinity intraslope basin in the Gulf of Mexico (Prather et al., 2017).

In contrast, partially confined systems develop high net: gross successions and lack bed-scale heterogeneity, due to flow stripping and bypass down system of the finer grained dilute flow component. The accumulations are thinner compared with ponded accumulations, given the limited slope accommodation. Partially or weakly confined intraslope fan development is limited by the healed slope accommodation, with preferential sediment trapping across lower gradient steps and bypass across higher gradient ramps, which can result in simple lobe trapping across steps (Ferry et al., 2005; Brooks et al., 2018), or transient fan development when spilling in the downdip outboard basin occurs, and record a

stratigraphic transition upwards of sediment bypass through channel incision, until adjustment to a lower base level (Hooper et al., 2002; Smith, 2004; Adeogba et al., 2005; Gamberi and Rovere, 2011; Deptuck et al., 2012; Hay, 2012; Spychala et al., 2015; Jobe et al., 2017) (Fig. 2.15). In structurally more complex partially confined slope and basin-floor settings, transverse fan systems develop more erratically with common flow deflection (Gervais et al., 2004; Romans et al., 2009; Bourget et al., 2011; Burgreen et al., 2014; Mignard et al., 2019) (Fig. 2.16).

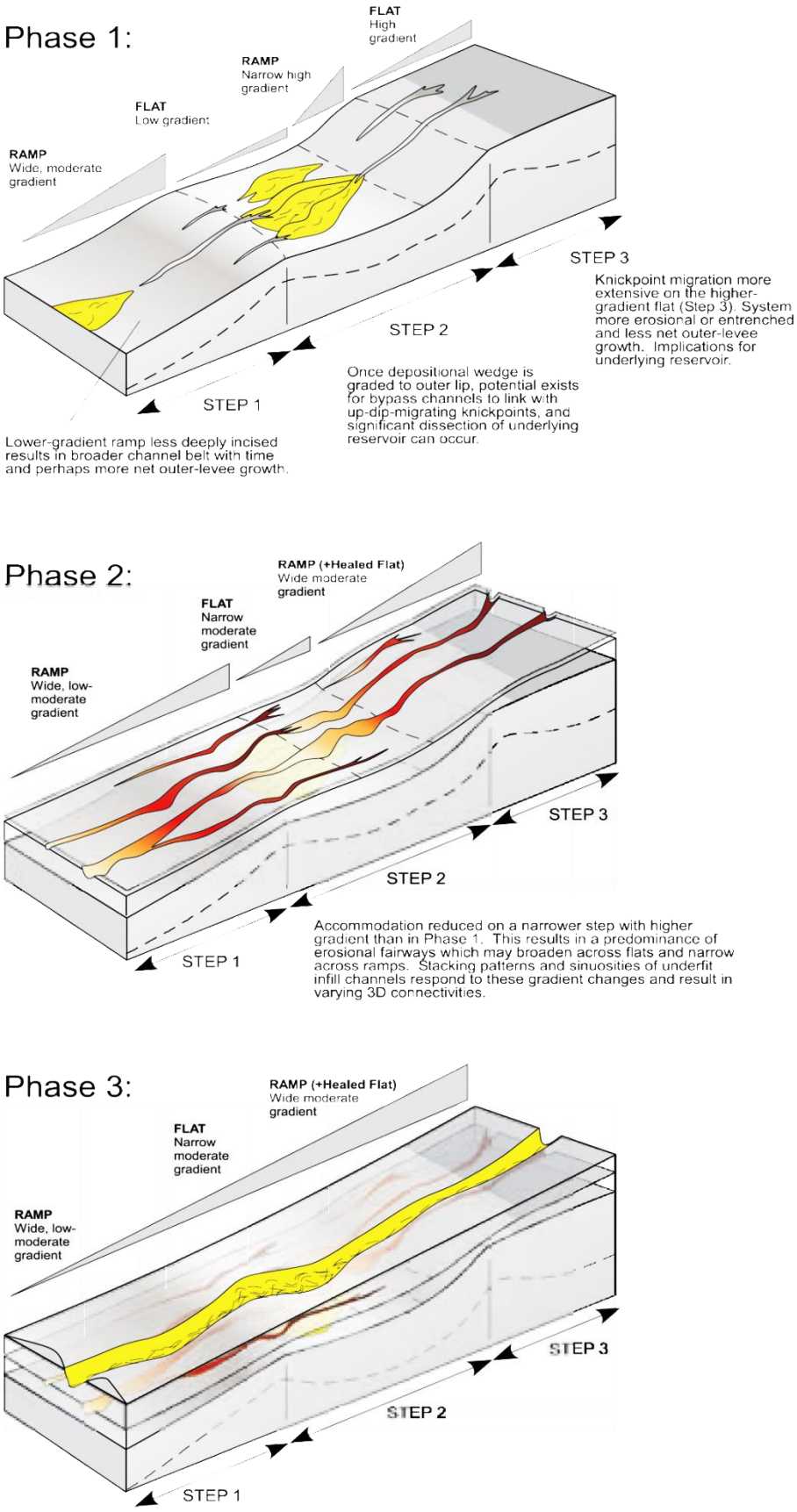

Figure 2.15: Conceptual model for the depositional evolution of a stepped slope profile describing the depositional and erosional response of sediment gravity flows to slope build-up and reduction of accommodation (Hay, 2012).

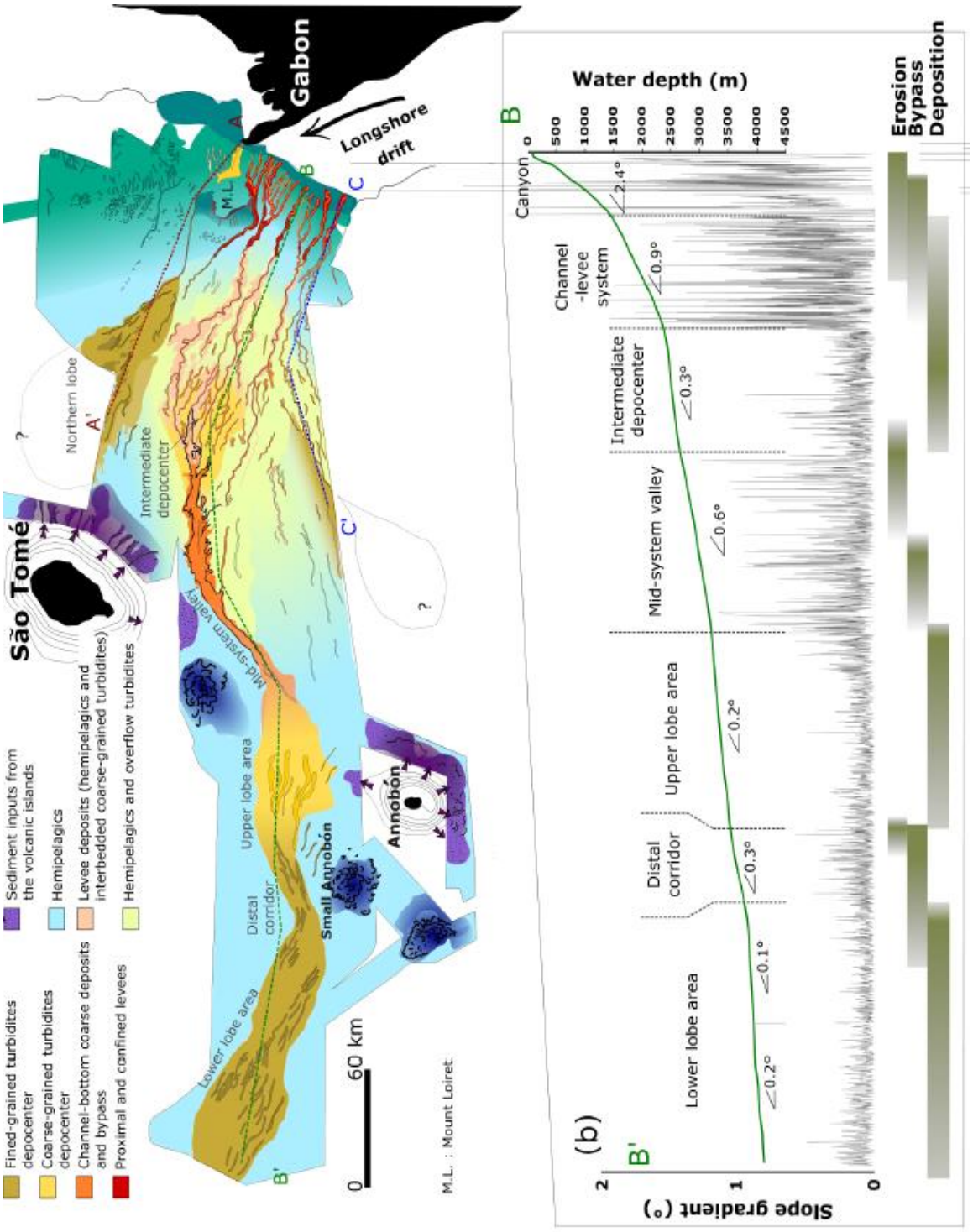

Figure 2.16: Interpretative sketch showing the architecture of the Ogooue along ramp and step slope (a) and bathymetric profile showing the subtle changes of slope gradient (<2) (b) which control changes in sedimentary processes and sand distribution in intraslope basins.

2.3.2 Early post-rift lobes

Narrow rift basin margins have a fixed structural shelf edge position, fronted by a slope with a thin sediment blanket resulting from sediment bypass, or by topographically complex above-grade slopes inherited from rift basin physiography (Leeder et al., 2002; Ford et al., 2007; Helland-Hansen et al., 2012; Strachan et al., 2013; Weiß et al., 2016). Insights on the palaeotopographic configuration, distribution and morphology of early post-rift sand-rich accumulations across complex slopes have been gained from subsurface studies (Argent et al., 2000; Modica and Brush, 2004; Martinsen et al., 2005; Fjellanger et al., 2005; Gjelbeg et al., 2005; Fugelli and Olsen, 2005, 2007; Jackson et al., 2008; López-Gamundí and Barragan, 2012; Moscardelli et al., 2013; Lohr and Underhill, 2015; Dmitrieva et al., 2018; Dodd et al., 2019).

Early post-rift lobes tend to heal the local accommodation of above-grade portions of the slope inherited from rift structures, and share characteristics of partially confined tortuous corridors and structurally controlled intraslope basins bounded by tectonically induced bounding slopes. The early post-rift submarine fan distribution, geometry, architecture, stacking patterns and facies, depends on the inherited rift topography and syndepositional renewal of accommodation controlled by differential sediment loading and compaction across fault-blocks (Argent et al., 2000; Faerseth and Lien, 2002; Modica and Brush, 2004; Fugelli and Olsen, 2007; Jackson et al., 2008; Kane et al., 2010; Lohr and Underhill, 2015) (Fig. 2.17). The geometry of early post-rift submarine fans takes the shape of the confining intraslope accommodation, rather than following established relationships between fan geometry and flow efficiency in unconfined systems (Mutti, 1992; Reading and Richards, 1994; Gardner et al., 2003).

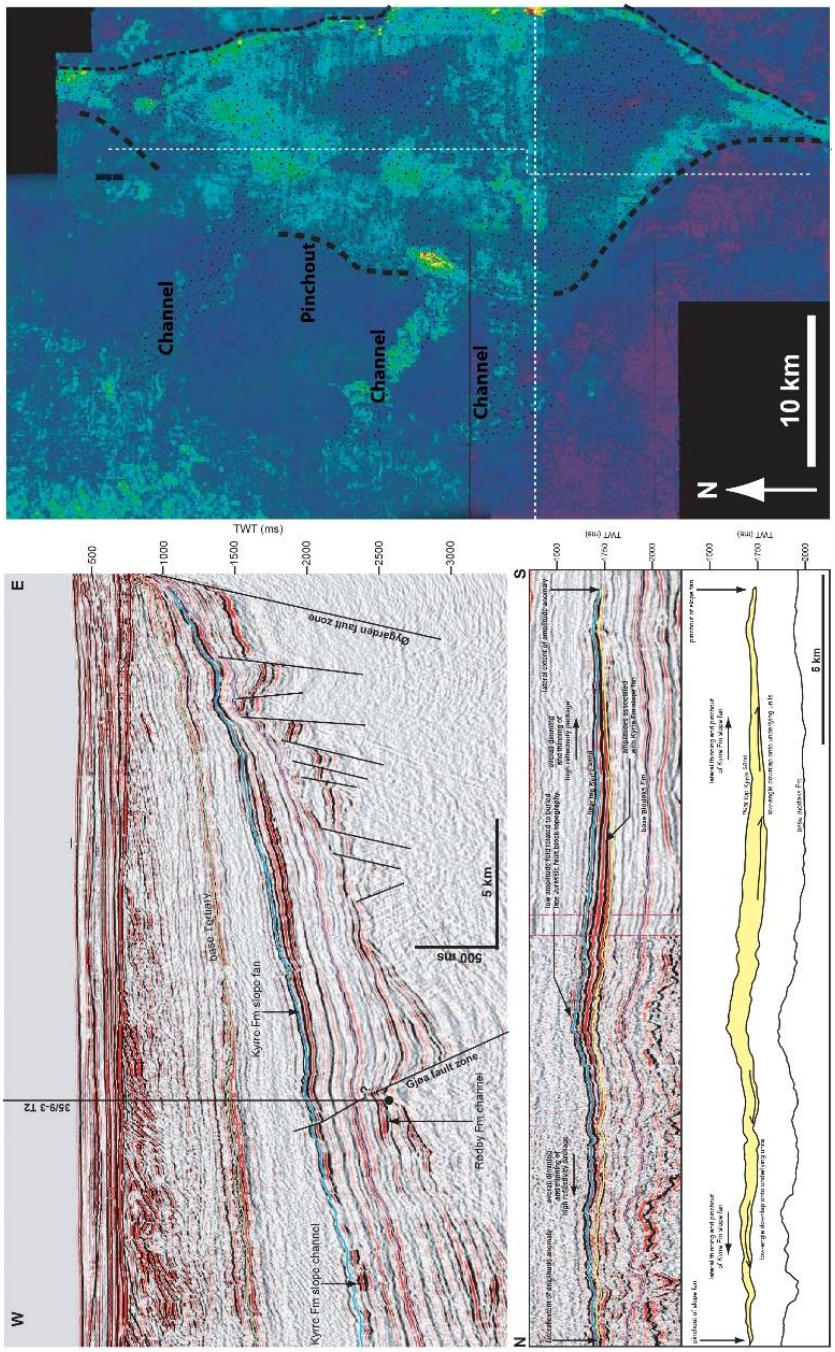

Figure 2.17: Seismic line along-strike the Late Cretaceous Kyrre slope fan across the Måløy Slope and reflection strength amplitude map of depositional systems showing the effect of compaction-related topography onto development of early post-rift sand distribution across the slope (Jackson et al., 2008).

In order to predict the degree of confinement the morphology and topography of the accommodation at the time of deposition needs to be understood. This can be constrained from onlap geometry and facies distributions (Kneller et al., 1999; McCaffrey and Kneller, 2001; Smith, 2004; Gardiner et al., 2006; Amy et al., 2007; Pyles and Jennette, 2009; Bakke et al., 2013; Marini et al., 2015) (Figs 2.18 and 2.19).

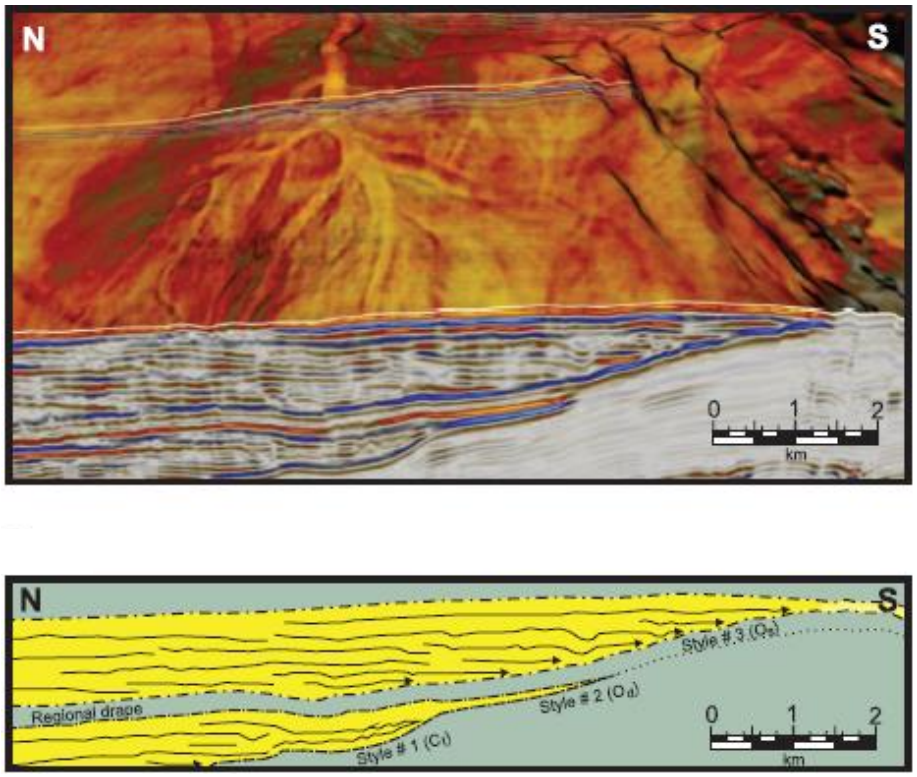

Figure 2.18: Example of lateral onlap of intraslope fan offshore West Africa showing three-dimensional seismic root-mean-square map of stratigraphic traps on a semiconfined basin slope and interpretation sketch showing two sandstone-prone units with different termination styles (Bakke et al., 2013).

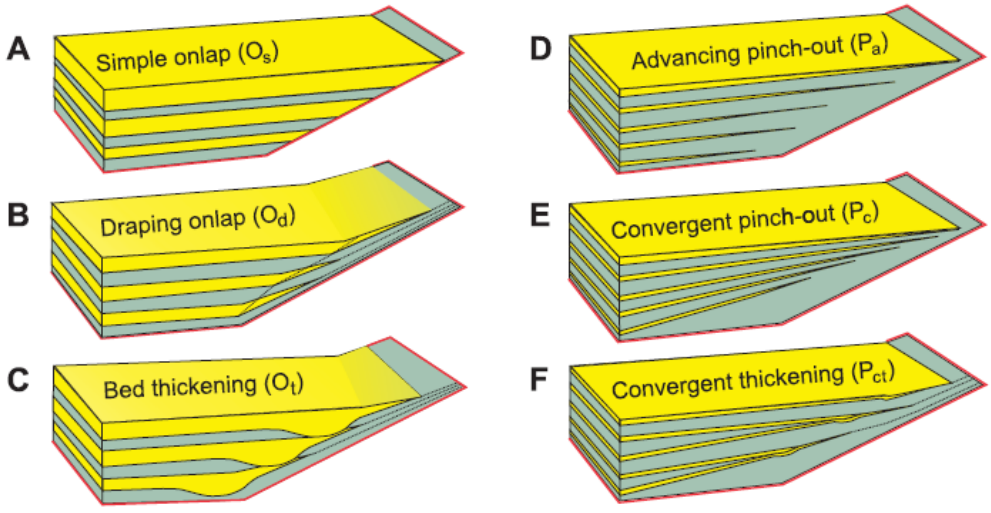

Figure 2.19: Diagram showing the different sandy versus heterolithic pinchout styles (Bakke et al., 2013).

Large volume flows relative to the size of the receiving basin, will interact with bounding slopes and promote onlap at basin margins and/or remobilisation (Haughton, 1994). Smaller volume flows will deposit tapering beds that offset basin margins, with axial to lateral and proximal to distal facies and bed thickness changes. Flows that encounter against oblique lateral or frontal confining slopes, can undergo deceleration, deflect and/or reflect, initiate internal waves (Patacci et al., 2015; Tinterri et al., 2016, Ge et al., 2017) and partially or completely transformation, leading to deposition of hybrid event beds (Smith et al., 2004; Muzzi Magalhaes and Tinterri, 2010; Patacci et al., 2014; Southern et al., 2015; Marini et al., 2015; Bell et al., 2018; Dodd et al., 2019) (Fig. 2.20).

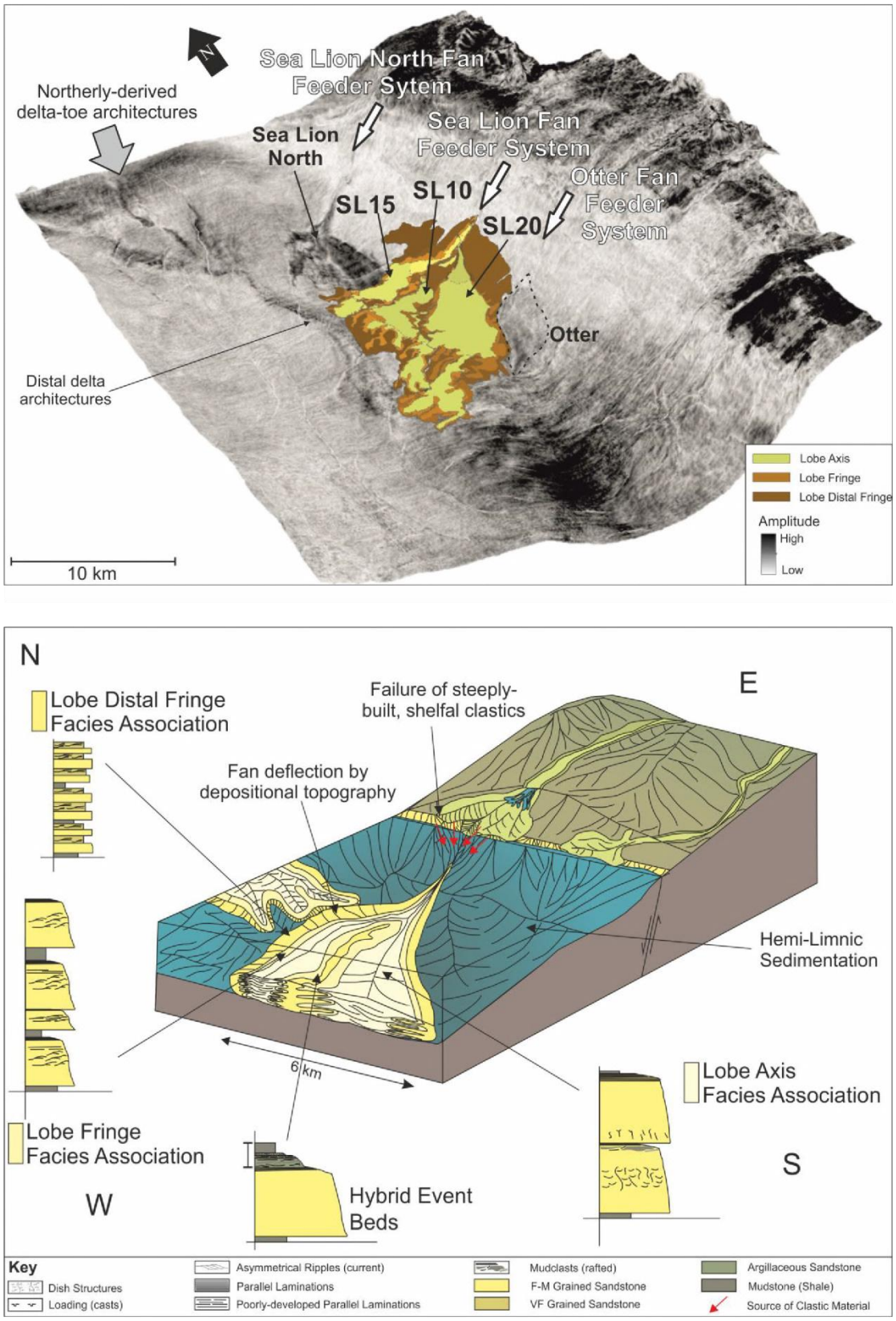

Figure 2.20: Example of early post-rift slope apron type lobes developed in the Sea Lion Fan showing the geometry and distribution of facies associations at the scale of lobes developed in a lacustrine setting (Dodd et al., 2019).

2.3.3 Interactions of sediment gravity flows with seabed topography

The effects of inherited fault relief on sediment gravity flow behaviour (bypass versus deposition, flow transformation, flow trajectory) and the resulting changes in the distribution, nature and thickness of deposit remains poorly constrained (Ferentinos et al., 1988; Alexander and Morris, 1994; Hodgson and Haughton, 2004; Pochat et al., 2007; Athmer, 2010; Weiß et al., 2016; Henstra et al., 2016; Gee et al., 2002; Ge et al., 2017).

Besides controlling submarine fan geometry, architecture and stacking patterns, seabed topography influences the finer scale distribution of depositional and erosional processes and sediment dispersal patterns (Monterey fan, Klaucke et al., 2004; Golo fan, Gervais et al., 2004; Hueneme fan, Romans et al., 2009; Villafranca fan, Gamberi and Rovere, 2011; Makran fan, Bourget et al., 2011; Mignard et al., 2019). Interactions between seabed relief and sediment gravity flows depend of the initial flow rheology, velocity, volume, thickness, and the height orientation, gradient and lateral extent of the topographic relief (Kneller and Branney, 1995). Dilute turbidity currents can override seabed obstacles with limited flow deviation, whereas high-concentration turbidity currents and cohesive debris-flows tend to be deflected and preferentially trapped to adjacent lows (Gee et al., 2002; Bakke et al., 2013) (Fig. 2.21). Interaction with topographic highs (10s m) can promote flow decoupling and deviation of the fluidal and more cohesive flow components. Turbidity currents can be diverted along inherited relief for 100s km, contributing to segregating flow components, with debris-flow deposits updip and deposition of turbidite fans downdip (Modica and Brush, 2004).

Flows passing across an extensional fault can deposit (Alexander and Morris, 1994; Kneller and Branney, 1995) and/or incise (Adeogba et al., 2005; Gamberi and Rovere, 2011) the footwall high, and deposit downdip due to rapid flow expansion and deceleration. Flows passing down a topographic step can undergoe a hydraulic jump at break-of-slope (Komar, 1971; Brook et al., 2018) with change of hydraulic regime (supercritical to subcritical conditions) accompanied by enhanced erosion, bypass, and development of chute and pools, scours, antidune or cyclic steps (Pochat et al., 2007; Bourget et al., 2011; Henstra et al., 2016; Weiß et al., 2016; Ge et al., 2017). Perturbations of flow

structure at a break-of-slope can enhance sediment transport (Gray et al., 2005) or deposition with rapid flow deceleration (Ferentinos et al., 1988; Leppard and Gawthorpe, 2006; Pochat et al., 2007; Henstra et al., 2016).

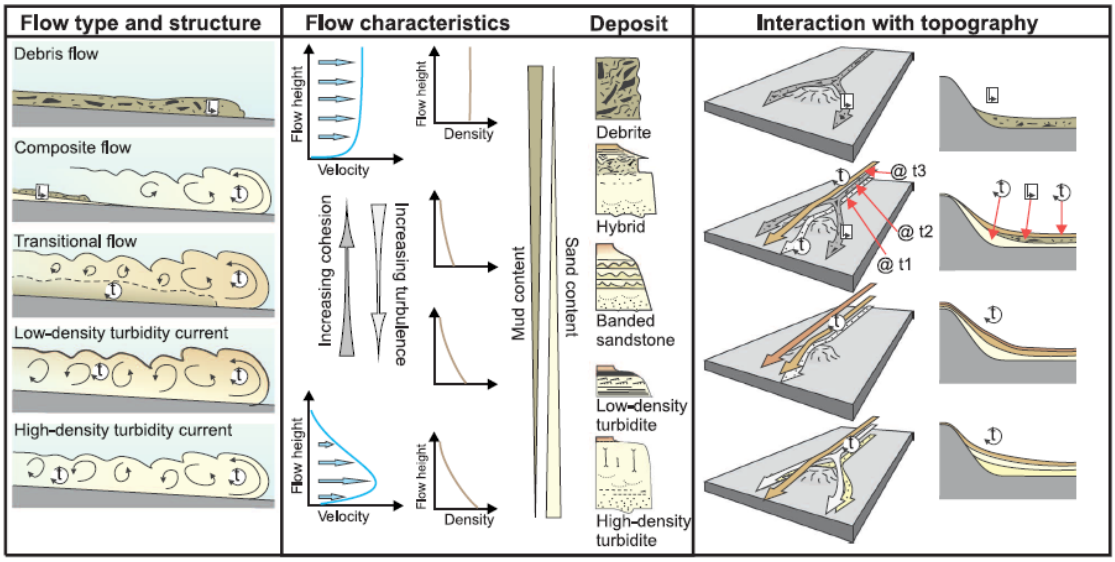

Figure 2.21: Diagram showing the variable interaction of a range of sediment gravity flows with seabed topography, depending on their laminar (L) or turbulent (T) behaviour and co-genetic turbulent-laminar or transitional behaviour, with flow classification after Haughton et al. (2009) (Bakke et al., 2013).

An increase of slope gradient and/or flow constriction enhances grain-size segregation erosion with increased flow turbulence and acceleration (Kneller et al., 1999; McCaffrey and Kneller, 2004). Entrainment of muddy substrate can dampen turbulence and enhance flow deceleration, with development of a quasi-laminar plug in the upper more cohesive part of the flow (Baas et al., 2011; Kane and Pontén, 2012; Baas et al., 2016; Kane et al., 2017; Southern et al., 2017; Dodd et al., 2019; Fig. 2.20). Eroded semi-lithified cohesive muddy substrate can break down into smaller clasts with a lower propensity to produce a significant enrichment of the flow in clay. Flow bulking with increased proportion of clay can dampening flow turbulence (Baas and Best, 2002) and promotes flow partitioning with co-genetic evolution of turbulent and more cohesive flow (Haughton et al., 2003; Talling et al., 2004; Ito, 2008; Hodgson, 2009). At a larger scale, delamination of semi-lithified muddy substrate with injection at the base of flow, scouring and entrainment of larger muddy to heterolithic or sandy clasts and blocks, are even more difficult to mix in flows and remain carried as traction load (Fonnesu et al., 2015). The resultant distribution of sand-rich versus mud-rich

deposits across topography, and the development of bed-scale heterogeneity in potential sand-rich accumulations, can form flow baffles within reservoirs (Amy et al., 2009) and reduce the porosity and permeability of reservoirs (Porten et al., 2016) (Fig. 2.22).

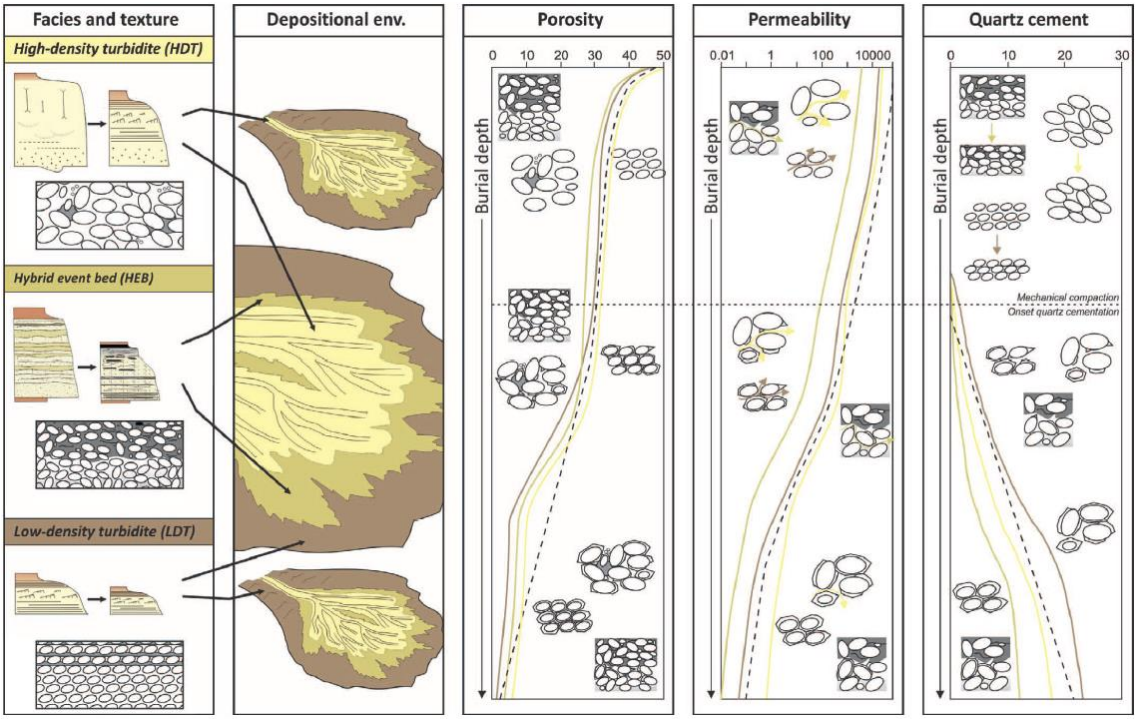

Figure 2.22: Model illustrating the change in porosity, permeability and quartz cementation in High Density Turbidites (HDT), Hybrid Event Beds (HEB) and Low Density Turbidites (LDT). Dashed lines represent previously published depth trends for reservoir sandstones of the Norwegian continental shelf (see Porten et al., 2016). The variability in evolution of reservoir properties with burial is controlled by original sediment composition (grain-size, sorting, detrital clay content and ductile grains) and quartz cementation.

Chapter 3 Introduction to the Neuquén Basin

3.1 Introduction

The Neuquén Basin is a triangular-shaped basin. The western margin runs 700 km and is defined by the Andean magmatic arc, including the Main Andean Cordillera and the Coastal Coridllera of Chilean Andes. The basin is relatively narrow to the north between 31° and 36°S and broadens up to 400 km wide southwards between 36° and 40°S (Fig. 3.1). The basin is bounded to the northeast by the Sierra Pintada belt (San Rafael and Las Matras Block) and to the south by the North Patagonian Massif (Somùn Cura), which represent pre-rift cratonic basement (Uliana and Legarreta, 1993). West of the Andean orogenic front, the Andean sector located along the Main Andean Cordillera underwent strong compressive deformation. In contrast, the Neuquén Embayment east of the Andean orogenic front underwent little compressive deformation due to its foreland position.

The Neuquén Basin comprises a ~7 km thick Triassic to Early Paleogene succession that records post-orogenic thermo-mechanical collapse and volcanic rifting from Late Palaeozoic to Early Jurassic and extensional back-arc sag from Early Jurassic to Early Cretaceous. The basin-fill underwent multiple episodes of Late Cretaceous-Cenozoic structural inversion, with subduction-driven foreland compression that formed the Andean fold and thrust belt and a Cenozoic foreland basin (Legarreta and Uliana, 1991; Vergani et al., 1995; Legarreta and Uliana, 1996; Franzese and Spalletti, 2001; Franzese et al., 2003; Howell et al., 2005; Ramos et al., 2011; Figs 3.2-3.3).

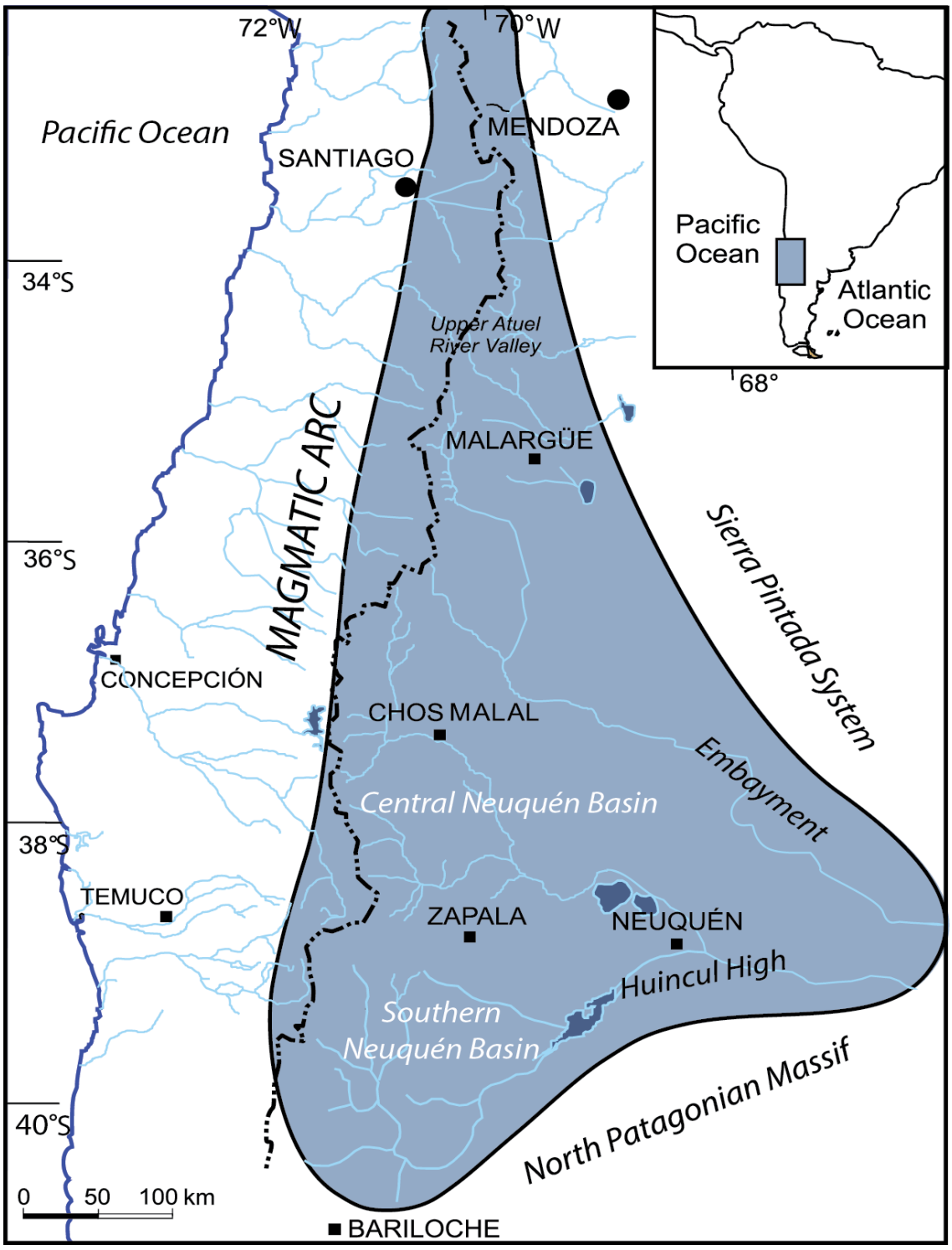

Figure 3.1: Map of the Neuquén Basin.

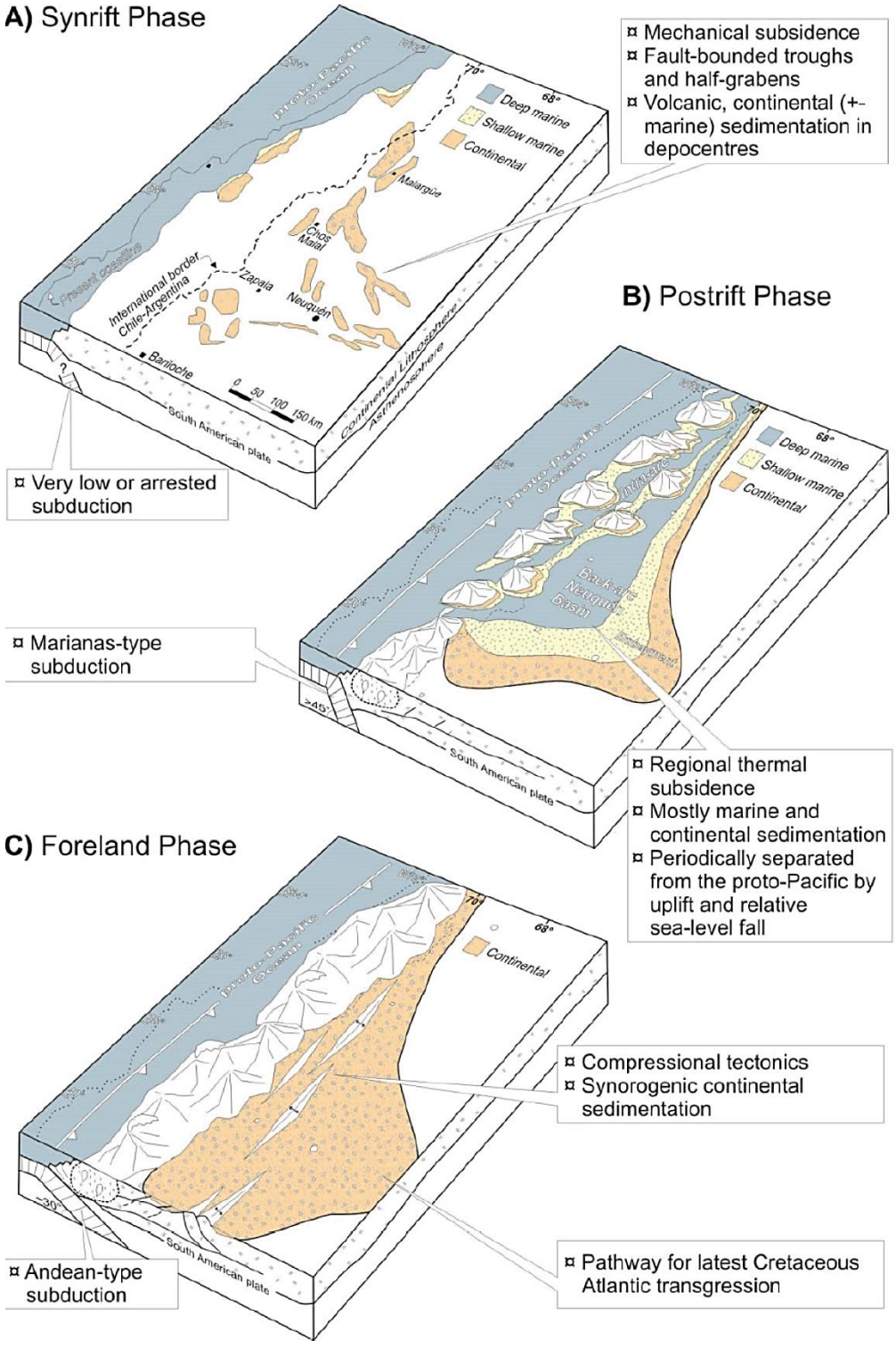

Figure 3.2: Bloc diagrams showing the main stages of basin evolution from Late Triassic to Cenozoic (Howell et al., 2005). (A) Late Triassic-Early Jurassic time with opening of rift basins. (B)Jurassic-Early Cretaceous evolution in a back-arc setting with subduction along the western Gondwana margin. (C) Late Cretaceous Andean uplift and foreland evolution with fold and thrust belt development.

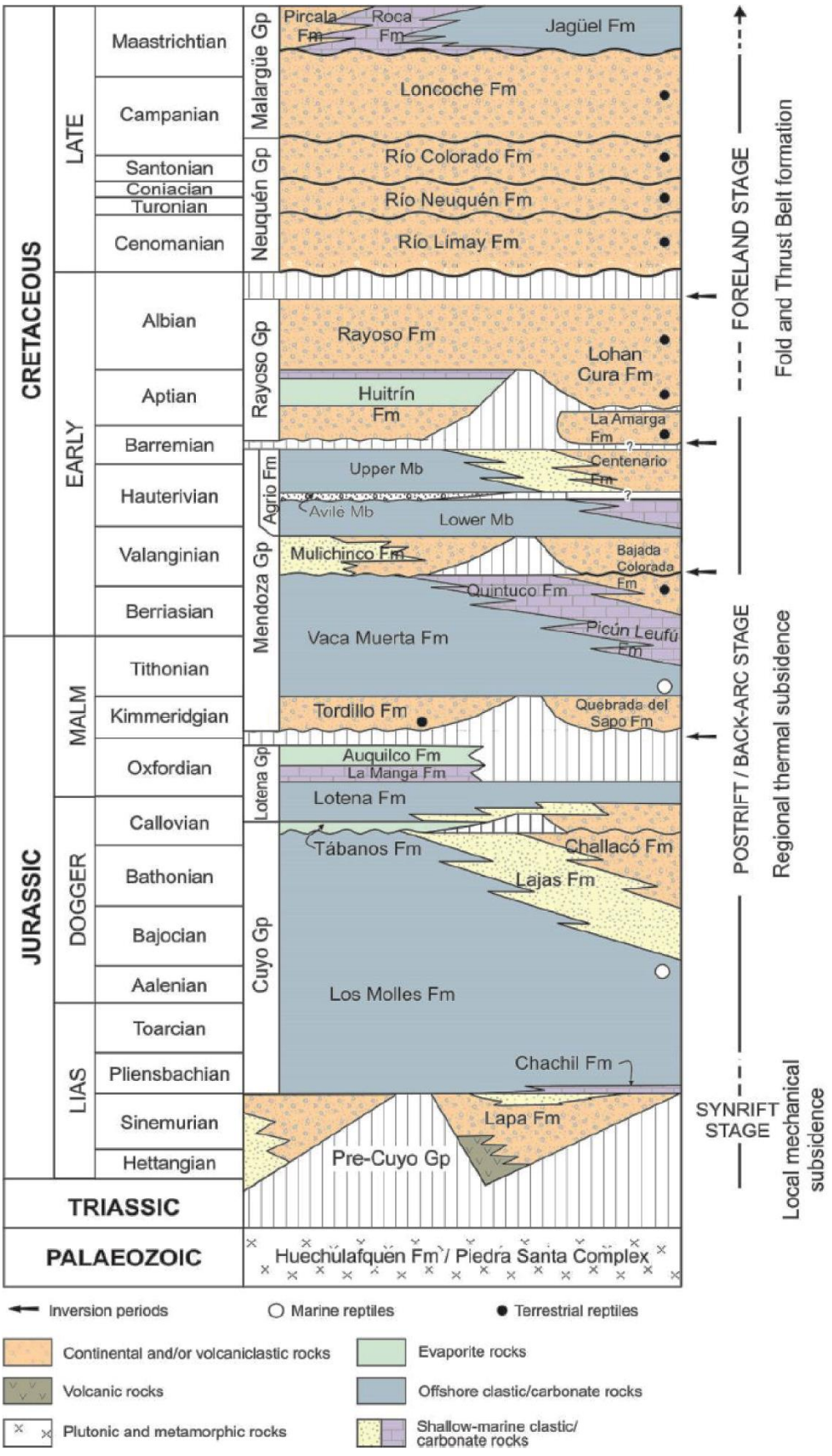

Figure 3.3: Chronostratigraphic chart of the Neuquén Basin (Howell et al., 2005).

3.2 Orogen to rift evolution: Palaeozoic to Early Jurassic

3.2.1 Pre-Andean to Pangea breakup evolution

Several geodynamic models explain the latest Proterozoic to Late Palaeozoic period of crustal accretion that took place prior to intracontinental rifting and Pangea breakup. Initially, a Late Precambrian to Early Cambrian Pampean orogeny formed with continent-continent collision of Cuyania terrane against the Gondwana margin (Rapela et al., 1998; Ramos et al., 2014). This orogen was superseded by the Early Ordovician to Silurian Famatian orogeny, associated with a compressional magmatic arc bounding subduction along the convergent southwestern Gondwana margin (Pankhurst et al., 2006, 2014; Rapela et al., 2016). The Famatian orogeny resulted in collision of the Mesoproterozoic Precordillera or Cuyania terrane (including the San Raphael and Las Matras blocks) with the Paleoproterozoic Pampean orogenic belt (Pampia basement), followed by the Late Devonian-Early Carboniferous collision with the Chilenia terrane during the Chanic orogen (Rapalini, 2005; Llambías and Sato, 2011; Pankhurst et al., 2006, 2014; Ramos, 2008; Ramos et al., 2014; Rapela et al., 2016). Finally, western Gondwana, represented by the Cuyana, Pampia and Chilenia terranes, was accreted to the Patagonian terrane (North Patagonian or Somun Cura Massif) during the Late Carboniferous-Early Permian San Raphael orogen (Mpodozis and Ramos, 1990; Llambías et al., 2003; Ramos, 2008).

The post-orogenic tectonic behaviour of the western Gondwana margin since the Early Permian was contrasted. South of 40°S, the central Patagonian batholith developed with arc magmatism and subduction (Rapela et al., 2005; Echaurren et al., 2017), whereas north of 37°S subduction was interrupted from Permian to Early Triassic (Kay et al., 1989; Mpodozis and Kay, 1992; Llambías et al., 2007). A change in plate boundary conditions, and decrease in compression, resulted from locking of the subduction and slab break-off, with opening of an asthenospheric window. This led to anomalous heating of the upper mantle and large-scale crustal anatexis since Early Permian (Mpodozis and Kay, 1992; Franzese and Spalletti, 2001; Llambías et al., 2003; Pankhurst et al., 2006). Profuse Permo-Triassic magmatism and intracontinental transtension subparallel to the western Gondwana margin accompanied the transition period from

compression to orogenic collapse (Uliana et al., 1989; Franzese and Spalletti, 2001; Ramos, 2008). The Late Permian-Middle Triassic thermomechanical orogenic collapse and opening of continental rift systems was marked by production of large volumes of intermediate and acid magmas. This lead to formation of the volcano-plutonic Choiyoi Province that represents the largest silicic magmatic event of the western Gondwana (from 21°S to 44°S) (Kay et al., 1989; Llambías et al., 2003; Franzese et al., 2003; Ramos et al., 2011).

Late Triassic to Early Jurassic intracontinental rifting (failed rift) lasted ~ 30 Myr across western Gondwana (30°S-40°S), with widespread extensional volcanism associated with bimodal magmatism during a period of very slow subduction along the proto-Pacific margin (Uliana et al., 1989; Mpodozis and Ramos, 1990; Llambías et al., 1990; Tankard et al., 1995; Franzese and Spalletti, 2001; Franzese et al., 2003; Fig. 3.4.). The transition from extensional orogenic collapse to rifting is recorded by a change of volcanic rock composition. This change reflects initial provenance from superficial magmatic chambers that produced large batholiths and ignimbritic fields of the Choiyoi Province, to deep-seated mantelic magmas, which produced less evolved volcanic syn-rift rocks (basalts, andesites, dacites and rhyolites) (Llambías et al., 2003, 2007).

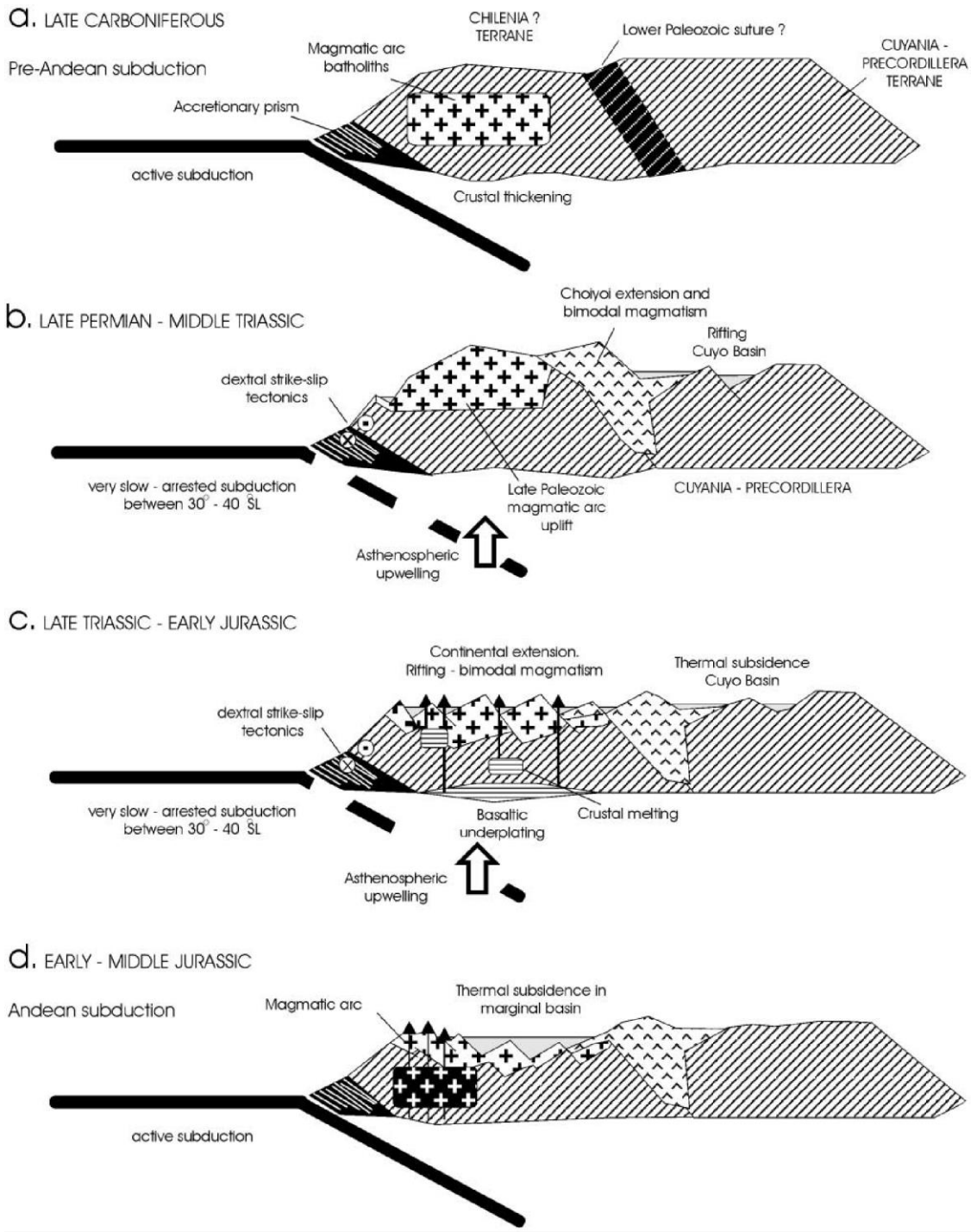

Figure 3.4: Schematic cross section showing the Late Palaeozoic to Middle Jurassic geodynamic evolution of the southwestern Gondwana margin and the Neuquén Basin (Franzese and Spaletti, 2001).

3.2.2 Pre- and syn-rift sedimentation

The pre-rift basement includes Late Devonian-Early Carboniferous low-grade (greenshist) metasedimentary rocks (Piedra Santa Complex) (Franzese, 1995) intruded by Late Carboniferous-Early Permian calco-alkaline plutons

(grabbros to pegmatitic granitoids) (Chachil Plutonic Complex and Cerro Granito, Leanza, 1993). These plutons represent the Choiyoi Group in the southern Neuquén Basin, whereas in the north the Choiyoi Group is represented by Late Permian-Early Triassic silicic igneous rocks (mainly rhyolites and ignimbrites) (Llambías et al., 2003, 2007). The Piedra Santa Complex, and intrusive plutons located in the south of the Neuquén Basin, can be correlated with the Metamorphic Complex of the Coastal Belt (Central Chile), which forms a Devonian-Early Permian igneous-metamorphic belt cored by Carboniferous-Permian granitoids (Franzese, 1995). Prior to deposition of syn-rift deposits, the basement underwent large-scale taphrogeny and regional erosion during a long period of exhumation recorded by the Early-Middle Triassic Huarpican unconformity, with a maximum hiatus of 82 Ma (Llambías et al., 2007; Schiuma and Llambías, 2008).

Late Triassic-Early Jurassic extension developed with effusive and explosive volcanism, which controlled the opening of narrow rift basins (150 km long, 50 km wide) bounded by planar and listric faults with high rates of mechanical and volcano-tectonic subsidence (Franzese and Spalletti, 2001; D'Elia et al., 2018). Syn-rift continental volcano-sedimentary deposits (Norian-Sinemurian) mainly result from primary and reworked volcanic deposits, and form the Precuyano Cycle dated in the South of the Neuquén Basin from 219 to 182 Ma (Rapela et al., 2005; Pángaro et al., 2002; Schiuma and Llambías, 2008). The syn-rift deposits infill rift half-grabens and grabens, with abrupt thickness changes from few metres to 100s m and up to 2 km thick at outcrop (Franzese et al., 2006) and up to 3.6 km thick in subsurface (Pángaro et al., 2002; Bermudez et al., 2002). The Precuyano Cycle is bounded by the Rioatuelican or Intra-Liassic unconformity, which marks the unconformable contact with marine deposits of the Cuyo Group (Pliensbachian-Bathonian) (Gulisano et al., 1984; Gulisano and Gutiérrez Pleimling, 1995; Legarreta and Uliana, 1996; Schiuma and Llambías, 2008; Pángaro et al., 2009; Leanza et al., 2013). Precuyano Cycle successions include basaltic to andesitic and rhyolitic effusive deposits, pyroclastic explosive deposits, epiclastic alluvial-fluvial and playa-lake carbonate deposits, which locally can be rich in organic matter and form productive source rocks (Legarreta and Gulisano, 1995; Pángaro et al., 2002; Bermudez et al., 2002; Muravchik and Franzese, 2005; Franzese et al., 2006, 2007; Schiuma and Llambías, 2008; Muravchik et al., 2011; D'Elia et al., 2012; D'Elia and Martí, 2013; D'Elia et al.,

2015). The stratigraphy of the syn-rift Precuyano Cycle in several depocentres evolves from basaltic and andesitic deposits to rhyolitic and ignimbritic deposits. This records a change from mid- syn-rift climax with mixed mantle-crust sources and basic to mesosilicic magmatism to overlying upper syn-rift climax acid explosive volcanism with silicic magmatism. This evolution reflects a shallower provenance from magmatic reservoirs at the mantle-crust interface through rifting (Franzese et al., 2006; D'Elia, 2010).

3.2.3 Rifting mechanism in the Neuquén Basin

Two main mechanisms were responsible for the transition from regional contraction to extension, which culminated with the Late Triassic-Early Jurassic rifting, but did not reached the point of continental breakup with ocean seafloor spreading. These two processes are: (i) orogenic collapse with the release of excess gravitational potential energy from an unstable, uplifted and thickened lithosphere, and (ii) widespread post-orogenic magmatism and high geothermic gradients that was critical for thermal weakening and mechanical stretching of the lithosphere (Dewey, 1988; Uliana et al., 1989; Ramos and Kay, 1991; Tankard et al., 1995; Franzese and Spalletti, 2001; Llambías et al., 2007). Similar delays (50-60 Ma) between the end of orogeny and onset of extension were required to achieve sufficient thermal relaxation and thermo-mechanical weakening of the lower crust and lithosphere in other post-orogenic rift basins associated with subduction. In such systems, crustal overthickening alone was insufficient to trigger extensional collapse and required additional mantle processes for thermal weakening (Basin and Range province, Liu and Shen, 1998; Rahl et al., 2002; Pannonian and Alboran basins, Houseman et al., 2007; Zhejiang Province of eastern South China, Li et al., 2014). In these systems, strain rate and total extension are proportional to the thermal state of the lithosphere. Therefore, the greatest extension is achieved for a given driving force when thermal relaxation heats the lithosphere to the maximum. This can result in either dominant pure shear or strain partitioning with simple shear when laterally offset weakness zones are present (i.e. high heat flux or thickened zones in the lithosphere) (Braun and Beaumont, 1989).

The presence of basement weakness zones and large-scale intraplate structures inherited form the orogenic collapse controlled the style of brittle deformation in the upper crust, and accommodates extension with considerable strain partitioning during rifting in the southern Neuquén Basin. Crustal decoupling resulted in ductile extension along a décollement surface or master shear zone (~ 12 km depth) in the lower crust and asymmetrical brittle normal faulting in the upper crust, with an estimated stretching factor of β= 1.33 (Sigismondi and Ramos, 2011).

An oblique master shear, located between 16 and 18 km depth within the upper crust (which base is ~ 24 km depth), has also been recognized in the Central Neuquén Basin, dipping 4-5° to 8° from the Bajada de Anelo to the Chihuidos-Las Carceles area (Comingues and Franzese, 2008). Rifting in the Neuquén Basin is also characterized by an asymmetric thermal subsidence pattern with respect to the locus of extension and flexural isostatic compensation (Sigismondi and Ramos, 2011). These features, together with the shift observed between the locus of syn-rift versus post-rift depocentres, do not fit with a uniform pure shear lithospheric stretching model. Instead, they are characteristics of simple shear in non-uniform stretching models (Tucano and Sergipe–Alagoas rift Basin in NE Brazil, Karner et al., 1992) or heterogeneous shear in depth-dependant stretching models associated with volcanism and anomalous thermal subsidence relative to crustal stretching (NW Australian margin rift, Karner and Driscoll, 1999).

Rifting in the Neuquén Basin required minimal extensional stress for rupture of thickened and thermo-mechanically weakened crust and lithosphere. This is characteristic of magma-assisted rifting, which lacks large-scale tectonic subsidence relative to the observed long term and large magnitude thermal subsidence (Taupo Volcanic Zone, Rowland et al., 2010, Red Sea or Gulf of Suez, Buck, 2004). Asthenospheric upwelling, possibly plume generated, induced thermal heating and together with arc magmatism permitted rifting at lower strain rate than normally required for tectonic stretching (Llambías et al., 2007; Sigismondi and Ramos, 2011). The increase of geothermic gradient from the southern to the Central Neuquén Basin, characterised by the patterns of isograde associated with low-grade diastatermal metamorphism of syn-rift deposits (both Precuyano Cycle and Lower Cuyo Group) (Suárez and González, 2018).

The Neuquén Basin rift shares some characteristics with the Basin and Range Province (BRP) region. These include accommodation of extension by strong mechanical decoupling between the crust and upper mantle, widespread magmatism and enhanced lithospheric stretching under high heat flow conditions favourable to lower crustal flow (Westaway, 1998, 2002; Buck, 2004; Morley and Westaway, 2006). However, rifting of the Neuquén Basin fits a wide rift mode of extension, with distributed strain, development of small offset high-angle normal faults in the upper crust, and low-angle master faults rooted at mid crustal depths accumulating large displacement. This pattern is consistent with the relatively moderate thickness of the middle crust and high sedimentation rates involving high overburden pressures and crustal loading (Gartrell, 2001). Therefore, this contrast with the post-orogenic metamorphic core complex mode of extension requires very low crustal loading as sedimentation rates are low and/or outpaced by the extension rate and development of low-angle dipping faults (BRP, Liu and Shen, 1998; Tibet rift, Kapp et al., 2008). High rates of sediment supply induce surface loading and thermal effects increasing subsidence, which promote lower crustal flow from beneath the depocentre towards rift borders. This in turn sustains uplift and development of steeply dipping faults during rifting as seen in the Neuquén Basin and other rifts (Suez Rift, Moretti and Colletta, 1987; Corinth Rift, Westaway, 2002). During the post-rift , sediment-load driven crustal thinning with lower crustal flow will also induce anomalously high thermal subsidence rates (Pattani and Malay Basins, SE Asia, Morley and Westaway, 2006; South China Sea, Clift et al., 2015).

3.2.3 Structural style and deformation of the Neuquén Basin

The Late Triassic-Early Jurassic rift systems are characterized by variable depocentre polarity, vergence and fault orientation across the Neuquén Basin. They developed under a dominant NNE-NE extension direction that controlled most rift systems of the western Gondwana from the Late Palaeozoic to Early Mesozoic. Partitioning of deformation is indicated by variations in structural grain from north to south of the Neuquén Basin. This can be correlated to pre-rift Palaeozoic basement fabrics trending obliquely to the direction of the extensional stress field that induced oblique rifting with reactivation of inherited structures (Franzese and Spalletti, 2001; Franzese et al., 2003; Ramos and Folguera, 2005;

Mpodozis and Ramos, 2008; Silvestro and Zubiri, 2008; Cristallini et al., 2009; Giambiagi et al., 2005; Giambiagi and Martinez, 2008; Yagupsky et al., 2008; Barredo, 2012; Bechis et al., 2010, 2014; Fig. 3.5). Extension lead to the development of normal faults, either parallel or quasi-orthogonal to pre-existing structures striking oblique to the extension direction. This relationship resulted in a combination of strike-slip and en-echelon fault patterns characteristic of oblique rift systems. Upper crust basement fabrics exerted a strong influence on kinematics, geometry and deformation locus of the rift that resulted in the complex faulting and subsidence pattern.

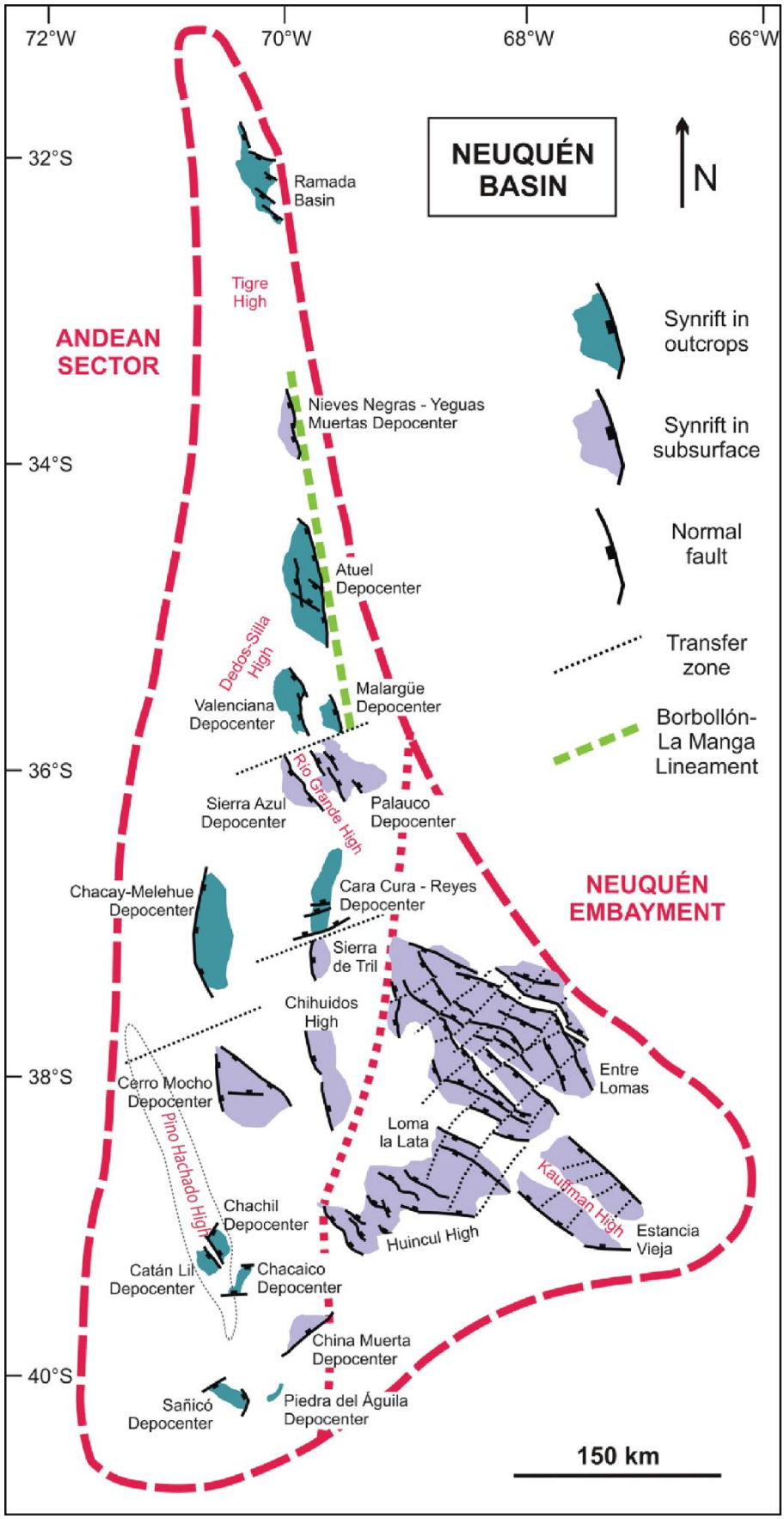

Figure 3.5: Map of the Neuquén Basin showing the distribution of syn-rift depocentres modified after (Bechis et al., 2014).

At the scale of the basin, extensional strain was preferentially accommodated around anisotropies in the upper crust thickened by previous convergence and crustal shortening. These areas formed long-lived zones of deeply rooted crustal thermal heterogeneity and mechanical weakness (intraplate and trans-lithospheric suture zones, foliation, plutonic intrusions) (Franzese and Spalletti, 2001; Comínguez and Franzese, 2005; García Morabito et al., 2011; Mosquera and Ramos, 2006; Mosquera et al., 2011; Yagupsky et al., 2008; Sigismondi and Ramos, 2011; Naipauer et al., 2012; Bechis et al., 2014).

In the northern basin, NNW- to NW-oriented extensional structures are associated with a NNE-SSW stress field, and rift structures propagated subparallel to NNE-and NNW-oriented pre-rift structures (Giambiagi et al., 2005; Giambiagi and Martinez, 2008; Bechis et al., 2009, 2014; Cristallini et al., 2009). In the southern basin, NW- to WNW-oriented structures, organized with relay ramps and intervening NE-oriented transfer faults (10 to 100 km long), are associated with a NNE-SSW to NE-SW oriented stress field (Vergani et al., 1995; Franzese et al., 2006, 2007; Muravchik, 2008, 2014; D'Elia et al., 2012, 2015; Silvestro and Zubiri, 2008;; Naipauer et al., 2012). In the southren basin, the WSW- and WNW-oriented rift structures developed with E-W-oriented reactivation and north-dipping inherited pre-rift structures, whereas NW-oriented structures were oblique to inherited basement trends. NW-oriented structures accommodated the deepest troughs (NE-SW polarity of grabens with dominant vergence towards the E), and WNW-or WSW-oriented structures oblique to the main extensional stress field accommodated the shallowest troughs (N-S polarity of grabens). This pattern is similar to examples of eastern North America basins. Here, reactivated structures controlled the evolution of border faults, which formed shallower depocentres when extension was accommodated with a strike-slip component than when dominated by dip-slip (Schlische 1993).

In the southern Neuquén basin, two main regional-scale basement-related structures are striking: the Huincul High and the Copahue-Pino Hachado Block. The Huincul High is a major ENE-WSW trending structure, which is 250 km long and 120 km wide in its eastern and central part in the subsurface and 60 km wide in its western exhumed part. This structure is a 800 km long regional lineament that constitutes the southern border of the Neuquén Basin and extends in Chile as a series of conspicuous E-W lineaments (Chernicoff and Zappettini, 2004; Ramos, 2008). The Huincul High corresponds to a major intraplate deformation

zone developed along an Early Permian suture (Huincul Fault) inherited from the accretion between the Patagonia and Chilenia-Cuyana terranes of western Gondwana (Chernicoff and Zappettini, 2004; Mosquera and Ramos, 2006; Ramos, 2008; Mpodozis and Ramos, 2008). The Cordillera of Catán-Lil and Chachil correspond to the southwards prolongation of the Copahue-Pino Hachado Block, a pre-rift basement-cored structure bounded by NNW- and NW-oriented faults. These faults were preferentially affected by the Andean compression compared to NE-oriented structures and formed west-verging thrusts that promoted uplift and exposure of Mezozoic depocentres (García Morabito et al., 2011). Such basement-involving structures exerted a control on isopach distribution as they had a considerable influence on post-rift subsidence patterns, and formed preferential sites for differential compaction and folding (Cristallini et al., 2006; Yagupsky, 2009). In the central part of the Neuquén Basin, compaction-induced differential subsidence promoted the development of NW-oriented compaction faults parallel to NW-oriented rift faults, and NW-NNW (N 130-160) oriented en-échelon faults above oblique W-NW-oriented structures (N 110) associated with dextral strike-slip (Silvestro and Zubiri, 2008).

3.3 Back-arc to foreland evolution: Jurassic to Cenozoic

3.3.1 Syn- to post-rift post-rift back-arc evolution

3.3.1.1 Onset of subduction and Early Andean volcanic island arc

During the Late Triassic, the Neuquén Basin was located at its southernmost position (50°S) and reached its northernmost position during the Early Jurassic (Late Pliensbachian-Early Toarcian) (25°S) (Iglesia-Llanos et al., 2006; Iglesia Llanos and Prezzi, 2013). Onset of the Early Andean subduction occurred with oblique SE-oriented convergence of the proto-Pacific oceanic plate (Aluk plate) below the western Gondwana margin, with steep slab and negative trench rollback (Ramos, 1999; Mosquera and Ramos, 2006; Mpodozis and Ramos, 2008; Ramos et al., 2011; Fig. 3.6). The negative trench rollback and generalized extension was related to the northeast absolute motion of the western Gondwana during Early Mesozoic (Ramos, 2010). Subduction was a result of far-field plate stress.

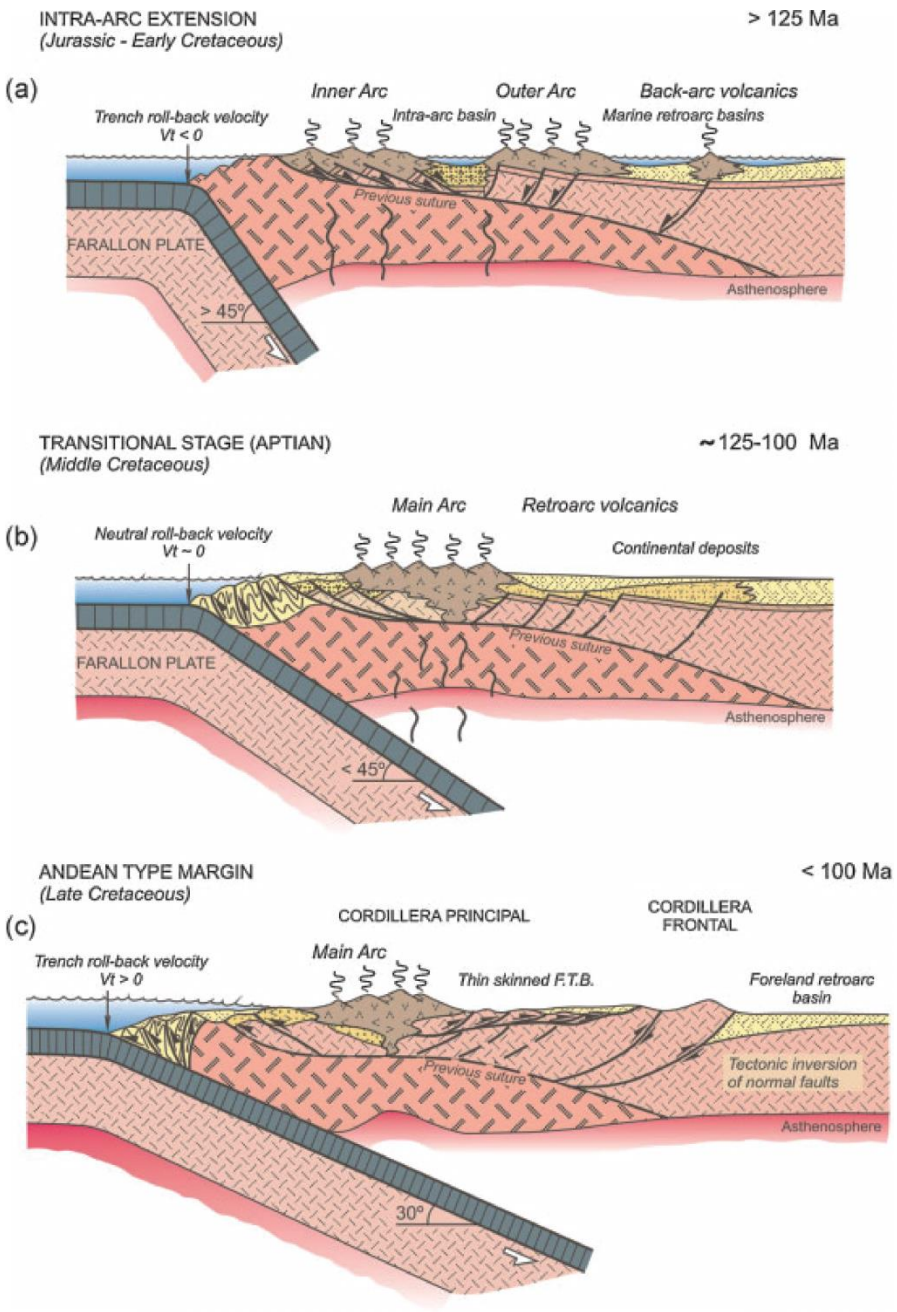

Figure 3.6: Schematic cross sections showing the change from (a) Early Jurassic-Cretaceous intra-arc extension, (b) stationary stage during the Aptian-Albian and (c) Late Cretaceous to present Andean compression (Ramos, 2010.)

Ocean growth occurred along a series of spreading centers between the North and South America, and during Wedell Sea openning as a consequence of the Central Atlantic Magmatic Province hotspot activity and separation Gondwana (Mpodozis and Ramos, 2008). Subduction started along Chile (20-30°S) during the Late Triassic (Rhaetian-Hettangian) (Oliveira et al., 2018), in the Neuquén Basin during the Late Triassic to base of Early Jurassic (Simenumurian-Pliensbachian), and in the Chubut Basin of northern Patagonia (40-45°S) during the Early Jurassic (Early Pliensbachian) (Rapela et al., 2005).

The Early Andean magmatic arc is exhumed along the axis of the Coastal Cordillera of Chile north of 36°S and south of 40°S (Subcordilleran Bahtolith) (Rapela et al., 2005; Llambías et al., 2007). This magmatic arc is represented in the Neuquén Basin near 38°S by Pliensbachian-Early Toarcian tholeiitic basalts with island arc signature (De la Cruz and Suárez, 1997). In the Neuquén Basin, magmatic arc activity was recorded by a range of calc-alkaline volcanic and reworked volcanic deposits emplaced in the Central Neuquén Basin since Late Triassic (Llambías et al., 2007), and in the southern Neuquén Basin along the Huincul High since Late Triassic (Bermudez et al., 2002) to Early Sinemurian (199.0 +-1.5 Ma) (Schiuma and Llambías, 2008). In the southernmost part of the Neuquén Basin arc-related volcanic deposits are recorded since Late Sinemurian (191.7- 2.8 Ma) (Spalletti et al., 2010).

3.3.1.2 Marine flooding of the Andean Basin and syn-to-post-rift transition

The narrow Andean Basin, bounded by to the west by the insular Early Andean magmatic arc, included the Tarapacá, Aconcagua, Neuquén and Chubut back-arc basins developed along the western Gondwana margin and progressively flooded from north to south, from Late Triassic to Early Jurassic (Viciente et al., 2005; Fig. 3.7). Marine transgression from the Panthalassic Ocean started in the northern Peru and Chile since Late Triassic in the Tarapacá and Aconcagua Basins connected to the Taltal Strait (Fantasia et al., 2018). Transgression started in the north of Argentina since the Late Triassic (Hettangian) through the Curepto Gulf (34°S) with flooding of the Atual-Malargüe depocentre (Vicente 2005, 2006; Lanés et al., 2008). The Neuquén Basin was

then flooded during Early Pliensbachian (Gulisano and Gutiérrez Pleimling, 1995; Damborenea et al., 2013; Leanza et al., 2013; Riccardi and Kamo, 2014).

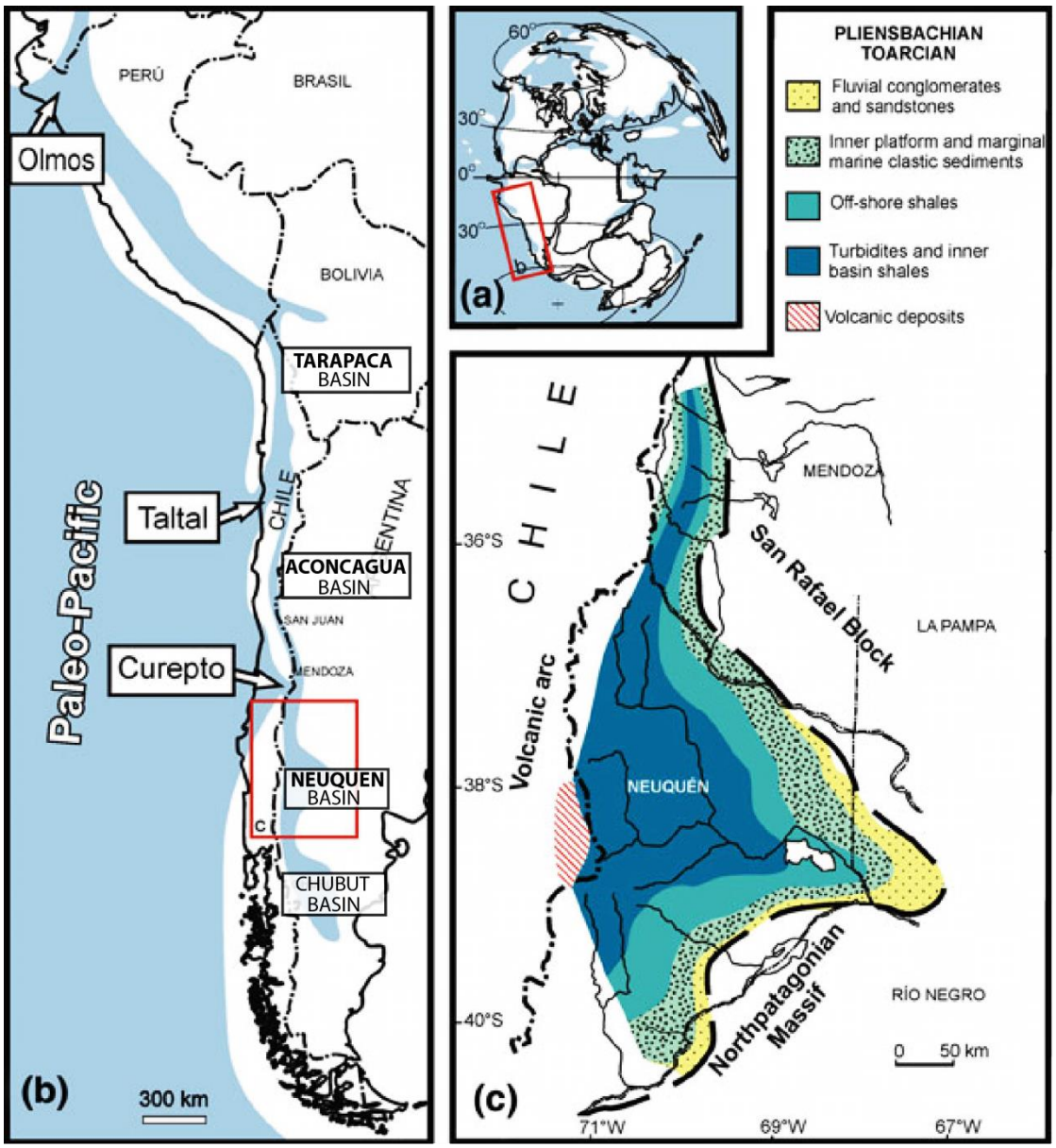

Figure 3.7: Palaeogeographic evolution of the Neuquén Basin with marine flooding during the Early Jurassic (Damborenea et al., 2013). (a) Palaeogeographic reconstruction of the Neuquén Basin as part of the southwestern Gondwana. (b) Representation of the the Early Jurassic palaeoseaway of marine flooding from Peru to the Chubut Basin to the south. (c) Map showing the distribution of depositional environments in the Neuquén Embayment.

Finally, the Early Jurassic sea reached its maximum extent during the Late Pliensbachian-Early Toarcian when flooding the southernmost Chubut Basin (Suárez and Marquez, 2007; Ferrari and Bessone, 2015; Fig. 3.7). The similarity and migration pathways of marine invertebrate fauna suggest a palaeobiogeographic connection between the Neuquén and Chubut basins

during the Late Pliensbachian-Early Toarcian (Damborenea et al., 2013; Ferrari and Bessone, 2015). However, some uncertainties remain on whether these three depocentres were connected to the Panthalassa via a single seaway corresponding to the Curepto Gulf, and/or had separate connections through narrow corridors that dissected the Early Andean volcanic island arc along the western Gondwana margin (Gulisano and Gutiérrez Pleimling, 1995; Viciente et al., 2005; Ferrari and Bessone, 2015). Extension and subsidence resulted in low-relief topography of the Early Andean magmatic arc that contrasts with the present Andean-type arc configuration (Ramos, 2010), the volcanic arc might have acted as a palaeogeographic barrier for marine ingression along the Andean Basin (Viciente, 2005). At the scale of the Neuquén Basin, transgression was enhanced when subparallel to the structural grain and slowed across morphological steps, which led to the development of an epeiric sea across complex Early Jurassic rift topography with local fault-block islands that formed the Neuquén Embayment (Legarreta and Uliana, 1996). The Neuquén Embayment included a central deep-marine basinal depocentre and a series of shallower platform depocentres distributed on its southern margin along the Huincul High.

The Early Jurassic marine transgressive event is recorded by the Lower Cuyo Group. The development of Early Jurassic marine depocentres with flooding of the inherited rift topography and their progressive merging during the Middle Jurassic into a single basin-scale sag depocentre is regarded as a consequence of regional post-rift thermal subsidence (Legarreta and Gulisano, 1989; Gulisano and Gutiérrez Pleimling, 1995; Vergani et al., 1995; Legarreta and Uliana, 1996; Franzese and Spalletti, 2001; Leanza et al., 2013). However, subsurface and outcrop studies have highlighted the heterogeneous spatial decay of normal faulting and volcanism with post-rift onset across the Neuquén Basin. This pattern does not fit the diachronous southwards progression of Early Jurassic marine flooding (e.g. Viciente et al., 2005) nor seem to progress diachronously with younging from north to south (D'Elia et al., 2015). Onset of the post-rift in the Neuquén Basin is recorded during Early Sinemurian in the northernmost area (Lanés et al.,2005, 2008), during Late Pliensbachian-Early Toarcian in the southwest (Sanico-Piedra del Aguila) where volcanism ended since Early Pliensbachian (D'Elia et al., 2015) and during Early to Late Toarcian-Aalenian in the southeast (Huincul High) and northwest (Cordillera del Viento)

(Silvestro and Zubiri, 2008; Pángaro et al., 2006, 2009; Carbone et al., 2011). Volcanism lasted until Early Toarcian, with deposition of subaqueous mixed volcaniclastic-epiclastic deposits, which belong the Lower Cuyo Group recorded to the northwest (Cordillera del Viento, Primavera Fm., Gulisano and Gutiérrez Pleimling, 1995; Llambías et al., 2007) and to the southeast along the Huincul High (Los Molles Fm., Bermudez et al., 2002; Cupen Mahuida Fm., Schiuma et al., 2011). Triassic to Early Jurassic volcanic deposits record an evolution from acidic to less evolved calc-alkaline composition mixing crustal and mantellic sources. This is associated with transition from intraplate rifting to back-arc extension, and progressive migration of volcanism and Early Andean magmatic arc westwards coeval of the syn-to post-rift transition (De la Cruz and Suárez, 1997; Bermudez et al., 2002; Llambías et al., 2007). Southwestward migration of the magmatic arc in the extra Andean Patagonia was accompanied by development of the Chon Aike Magmatic Province. The Chon Aike Province developed from Early to Middle Jurassic (187-162 Ma) with intracontinental extension associated with crustal anatexis and magmatic underplating, and closure of the Chubut Basin during the Middle Jurassic (Rapela et al., 2005; Suárez and Marquez, 2007; Echaurren et al., 2017).

3.3.1.3 Early Jurassic palaeogeographic changes

Early Jurassic was a greenhouse period during which rates and amplitude of eustatic changes were moderate (on the order of 1 m/ kyr, Read, 1995) due to the absence of large continental ice caps at high latitudes. The Early Jurassic marine depocentres had a normal salinity and water circulation despite receiving voluminous freshwater influxes. This point to continuous connection with the Panthalassa Ocean, which enabled migration of certain invertebrate species between the Panthalassa and Tethys (Riccardi, 1991; Damborenea et al., 2013; Ferrari and Bessone, 2015). The latitudinal shift of the Neuquén Basin northwards (from 50°S to 25°S, Iglesia-Llanos et al., 2006, Iglesia Llanos and Prezzi, 2013) is consistent with the southward migration of bivalve distribution boundaries between the Austral and Tethyan Realms of ~700 km (8-10° latitude) observed along the Jurassic western Gondwana margin (Damborenea, 2002; Damborenea et al., 2013; Damborenea and Echevarría, 2015). This paleogeographic change culminated with the local diversification of habitats and increase of species

diversity (34-42°), which reached a peak during the Late Pliensbachian-Early Toarcian (Ballent and Whatley, 2000; Manceñido et al., 2002; Riccardi, 2008, 2011; Damborenea and Echevarría, 2015). This latitudinal change is recorded in the Pliensbachian microflora of Early Jurassic marine deposits which reflect a rise of *Classopollis* pollen from 41.5% in the Sinemurian-Early Pliensbachian, to 91-99% in the Late Pliensbachian (Volkheimer et al., 2008). *Classopollis* pollen is associated with dominant thermophilic conifer vegetation (*Cheirolepidiacean* gymnosperms of lowland vegetation) indicating increasing warmth and aridity with seasonally dry or semi-arid climate (Volkheimer et al., 2008). In the early Late Toarcian, the apparition of a new group of Araucariaceae (*Callialasporites sp.*), which required moist conditions, indicate change towards a more humid climate (Volkheimer et al. 1978, 2008). This period also recorded the occurrence of the TOAE with variable sedimentation rates, important storm activity and warm semi-arid climate which prevailed in the Andean Basin over the southwestern Gondwana (Al-Suwaidi et al., 2016; Fantasia et al., 2018). These conditions altered the deposition of characteristic organic black shale which typically document the TOAE in the northern hemisphere, where a warm and humid climate favoured the development of anoxia (Dera and Donnadieu, 2012).

3.3.2 Late post-rift sag to Andean foreland evolution

The sag phase lasted for ~80 Myr, from Middle Jurassic to Early Cretaceous (Fig. 3.8). By the Late Jurassic, the Andean magmatic arc was fully developed along the western Gondwana margin. Post-rift thermal subsidence was well-established across the basin since the Aalenian, and promoted the development of a single broad extensional back-arc depocentre recorded by the Upper Cuyo Group and controlled by thermal subsidence and eustatic changes with local uplift (Gulisano and Gutiérrez Pleimling, 1995; Legarreta and Uliana, 1996; Vergani et al., 1995; Howell et al., 2005). From the Middle to Late Jurassic, pre-Andean deformation occurred in a regional context of back-arc thermal subsidence during deposition of the Upper Cuyo Group, affected by oblique transpressional reactivation of structures localized along the Huincul High (38-40°S) (Vergani et al., 1995; Gómez-Omil et al., 2002; Pángaro et al., 2006; Mosquera and Ramos, 2006; Mpodozis and Ramos, 2008; Silvestro and Zubiri, 2008; García Morabito

et al., 2011; Naipauer et al., 2012). The SE-oriented oblique subduction motion induced a NNW-NW-oriented transpressive stress field that was accommodated along the ENE-WSW-oriented Huincul High. The high acted as a buttress, and promoted spatial partitioning of transpressional and transtensional deformation (dominant transpressional to the SE and compressional to the SW) (Mosquera and Ramos, 2006; Silvestro and Zubiri, 2008; Mpodozis and Ramos, 2008; Mosquera et al., 2011).

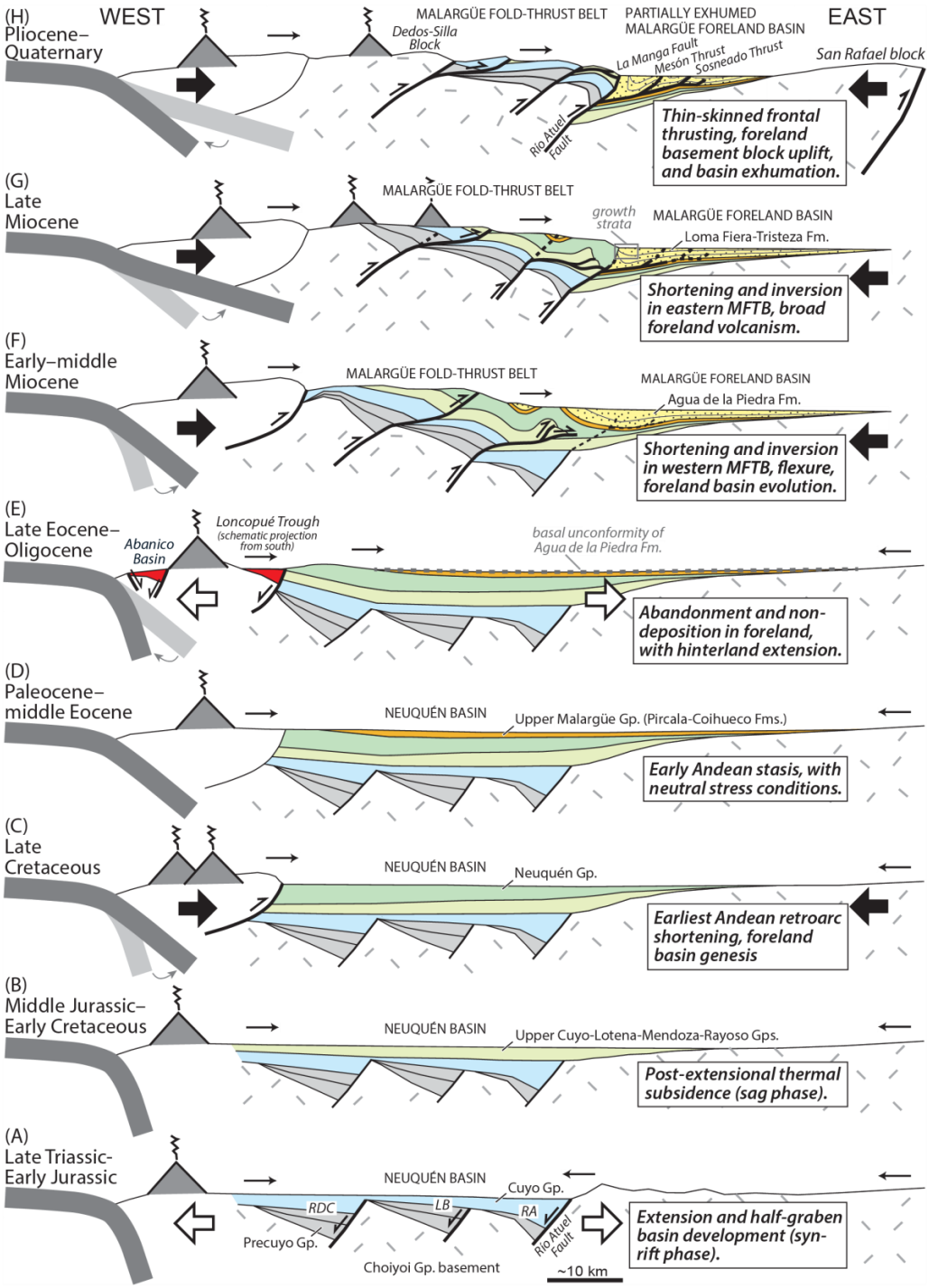

Figure 3.8: Cross sections showing the change of subduction regime and foreland evolution evolution of the Neuquén Basin (Horton et al., 2016).

Early Jurassic (Early Toarcian) to Late Cretaceous deformation was accommodated diachronously from SE to NW, with partial reactivation of rift structures depending on the incidence angle of the transpressive stress field onto pre-existing rift faults, and resulted in limited pure inversion at the exception of WNW-ESE oriented rift faults (Pángaro et al., 2006; Silvestro and Zubiri, 2008). NE-SW,ENE-WSW, and E-W-oriented reverse faults, associated with growth of anticlinal and synclinal folds, formed to accommodate dextral or sinistral slip, with transcurrent reactivation of NW-SE-oriented rift faults or NNW-oriented pre-rift structures (Vergani, 2005; Pángaro et al., 2006; Cristallini et al., 2006; Gómez Omil et al., 2002; Silvestro and Zubiri, 2008). Transpressive and transcurrent tectonic activity along the Huincul High has been related to the development of Intra-Liassic and Intra-Toarcian angular discordances (Mosquera, 2002; Gómez Omil et al., 2002; Pángaro et al., 2006, 2009).

Then a back-arc sag period was marked by local episodes of normal faulting interpreted to record a second rift stage driven by NW-oriented extension related to the opening of the South Atlantic (Vergani et al., 1995; Howell et al., 2005; Mpodozis and Ramos, 2008; Ramos, 2010). This period is recorded during the Late Jurassic by the Lotena Group (Callovian-Kimmeridgian) bounded by the Intra-Callovian and Intra-Malm unconformities, during the Late Jurassic-Early Cretaceous by the Mendoza Group (Kimmeridgian-Barremian), and during the late Early Cretaceous (Barremian-Albian) by the Bajada del Agrio Group.

The changes in proto-Pacific subduction dynamics and far-field stress related to Gondwana breakup, and opening of the Atlantic Ocean, induced a complex post-rift evolution of intra-arc and back-arc basins into foreland basins that led to development of the Andean fold-and-thrust belt (Franzese et al., 2003; Ramos and Folguera, 2005; Ramos, 2010). During the late Early Cretaceous (Albian), a change from negative to positive rollback subduction regime induced a change from overall extension to compression. This change of subduction dynamics occurred due to a shift in convergence direction and/or velocity between the subdued Aluk plate beneath the western Gondwana margin and coeval breakup and opening of the South Atlantic Ocean (Ramos, 1999; Mosquera and Ramos, 2006; Mosquera et al., 2011). The transition from retro-arc flexural subsidence to foreland basin evolution, and final disconnection of the Neuquén Basin from the Pacific Ocean, is recorded with deposition of the Late Cretaceous (Cenomanian-Maastrichtian) Neuquén Group bounded by a

Cenomian-Albian unconformity, and the Paleogene Malargüe Group (Vergani et al., 1995; Howell et al., 2005; García Morabito et al., 2011). The foreland stage records acceleration of convergence with westwards motion of South America and orthogonal reorientation of the subducted plate with a shallower dipping slab. This configuration promoted compression which culminated during the Neogene climax of the Andean orogeny (Ramos and Folguera, 2005; Ramos et al., 2011; Mosquera et al., 2011).

3.4 Syn- to post-rift stratigraphy

The Cuyo Group (Gulisano et al., 1984) comprises two second order depositional sequences separated by the Toarcian-Aalenian boundary: the Early Jurassic transgressive Lower Cuyo Group and Middle Jurassic regressive Upper Cuyo Group (Gulisano and Gutiérrez Pleimling, 1995; Vergani et al., 1995; Legarreta and Uliana, 1996; Burgess et al., 2000; Veiga et al., 2013).

3.4.1 Lower Cuyo Group

The Early Jurassic transgressive deposits of the Lower Cuyo Group corresponds mainly to late syn-rift shallow-marine mixed carbonate or mixed clastic, pyroclastic and epiclastic deposits, emplaced from Early to Late Pliensbachian. This includes respectively, the Chachil Fm. up to 50 m thick in exhumed depocentres, up to ~40 m thick in subsurface (Schiuma and Llambías, 2008) and the Chacaico Fm., 30-190 m thick in exhumed depocentres, and up to ~400 m thick in the subsurface (Pángaro et al., 2009). These shallow-marine deposits are overlain by deep-marine siliciclastic deposits emplaced from Late Pliensbachian to Aalenian (Lower Los Molles Fm., ~200-350 m thick in exhumed depocentres, Paim et al. (2008), and up to 500-1000 m thick in subsurface Gómez Omil et al. (2002)). The deposits of the Chachil and Chacaico Fm. are bounded at their base by the Intra-Liassic unconformity (hiatus from Sinemurian to Pliensbachian). Locally, it corresponds to a flooding surface that forms a sequence boundary for the Early-Late Pliensbachian depositional sequence C1 (Gulisano et al., 1984; Schiuma et al., 2011). The Intra-Liasic and Intra-Toarcian discordance (hiatus from Sinemurian to Early Toarcian) can locally merge on topographic highs where the Chachil or Chacaico formations were not deposited.

In this case, the Los Molles Formation onlaps directly onto syn-rift volcanic Precuyano Cycle or basement deposits which can record up to 150 m of subaerial erosion (see onlap of Lower Los Molles Fm., Bermudez et al., 2002; Pángaro et al., 2002, 2006; Figs 3.9 and 3.10). The Los Molles Fm. can also be locally affected by small-scale compaction faults across rigid basement fault-block highs (Cristallini et al., 2009; Fig. 3.11).

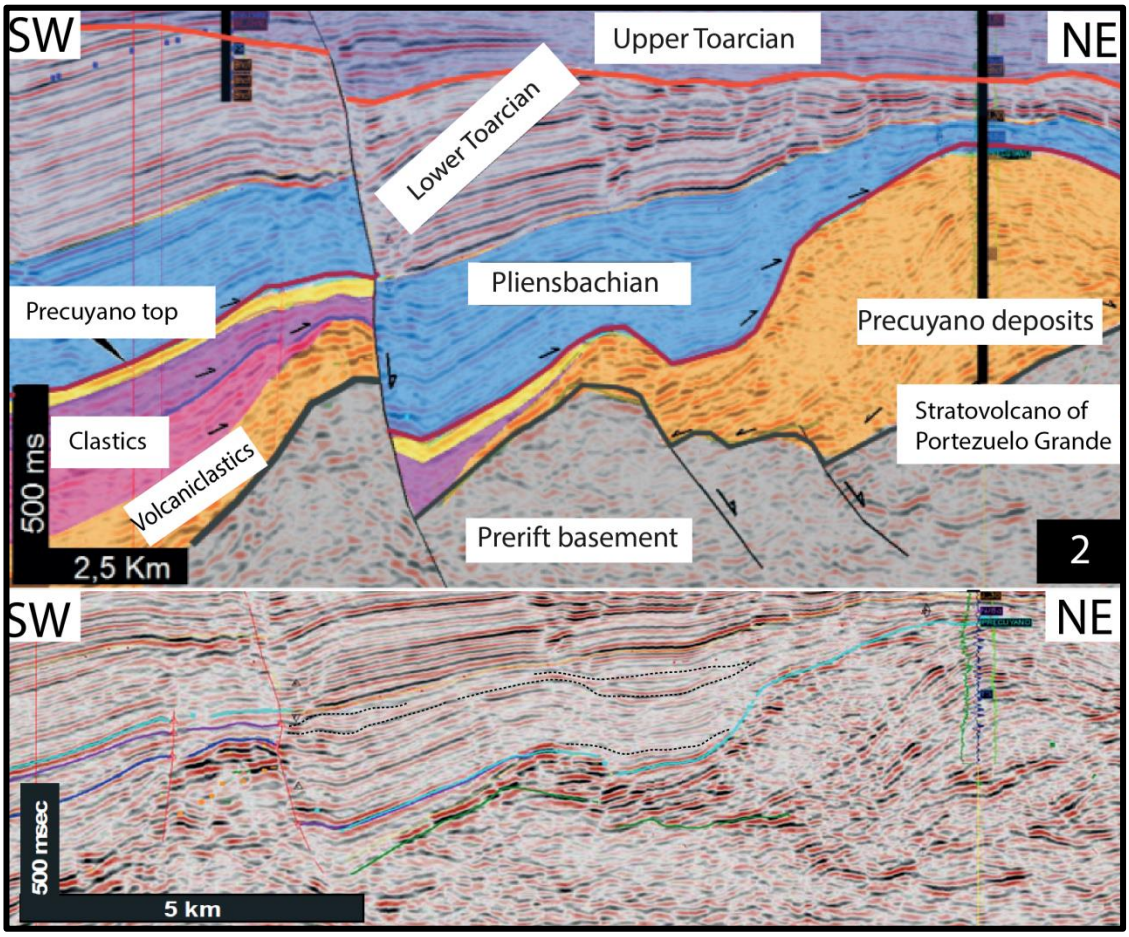

Figure 3.9: SW-NE seismic line in the Portezuelo Grande area modified after Pángaro et al. (2002). Seismic lines show the impact of the distribution of the Precuyano deposits on the sedimentation of the Lower Cuyo Group. Note the stratovolcano (1500 m high) that formed syn-rift relief, which influenced the sedimentation up to Lower Toarcian and produced thickness variations in the Pliensbachian Lower Cuyo Group. The base of the Lower Cuyo Group (Sinemurian-Pliensbachian to Lower Toarcian) is interpreted as a late syn-rift succession that deposited (i) unconformably onlapping onto the erosional angular intra-Liasic discordance at the top of the Precuyano strata; or (ii) conformably where the Precuyo deposits lack due to non-deposition or were not eroded (Pángaro et al., 2009).

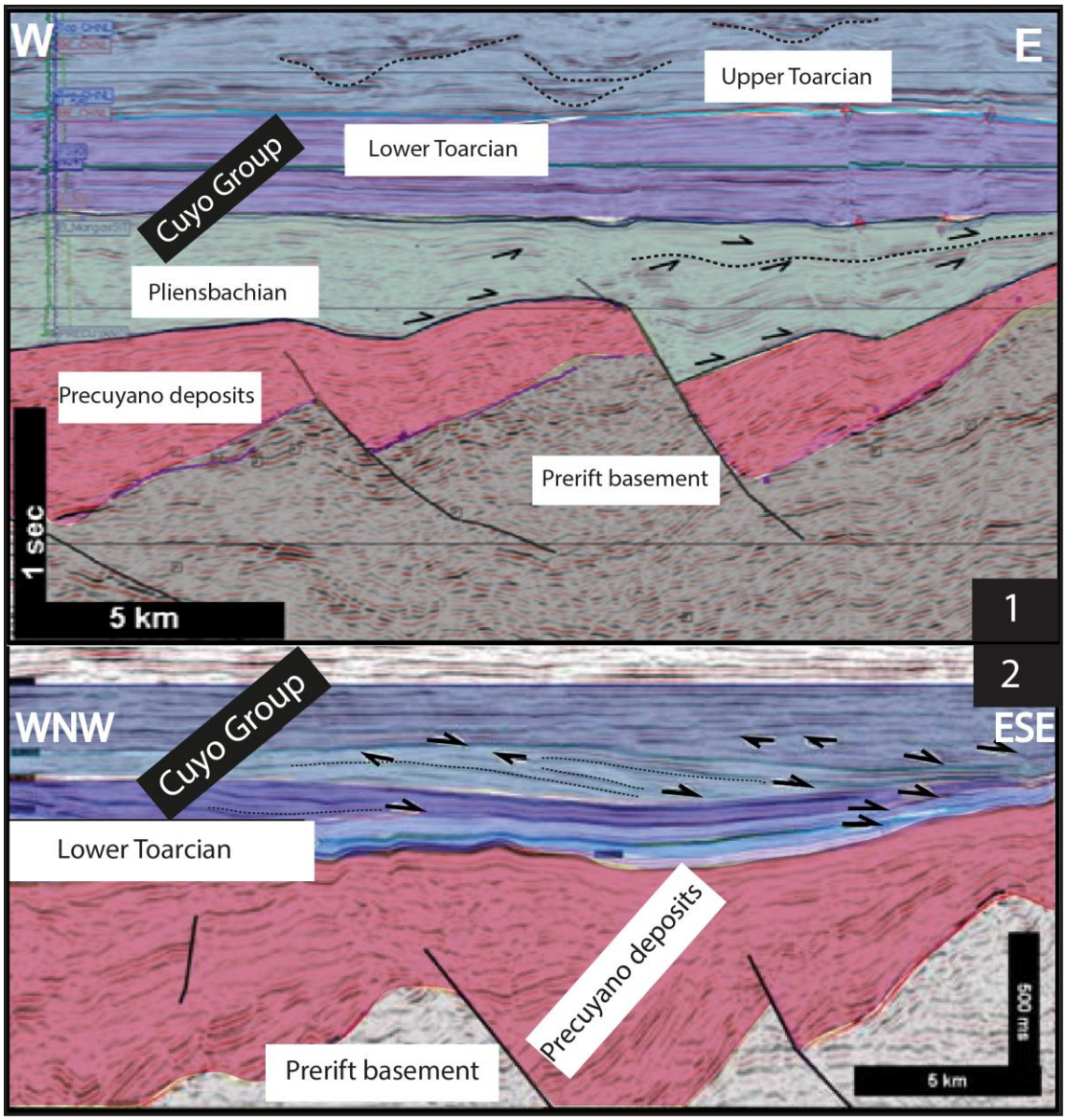

Figure 3.10: (1) W-E seismic line in the Piedra Chenque area and (2) WSW-ENE seismic line in the Aguada Toledo area modified after Pángaro et al. (2006). Seismic lines flattened at the top of Lower Toarcian, and interpreted as sharp rift-sag transition. Line 1 shows along-strike effects of structural palaeohighs (Divisadero Fault anticline) and tectonic subsidence related to rift faults accommodated from Pliensbachian to Upper Toarcian by thickness variations and onlap/toplap in the Lower Cuyo Group. The seismic line (2) shows the hiatus of the Pliensbachian-Early Toarcian Lower Precuyo deposits, interpreted to be the result of short duration rifting in this sector. The Lower Toarcian strata onlap Precuyo deposits and sedimentation could interact up to the Upper Toarcian with palaeoreliefs formed by rotated blocks (Pángaro et al., 2006).

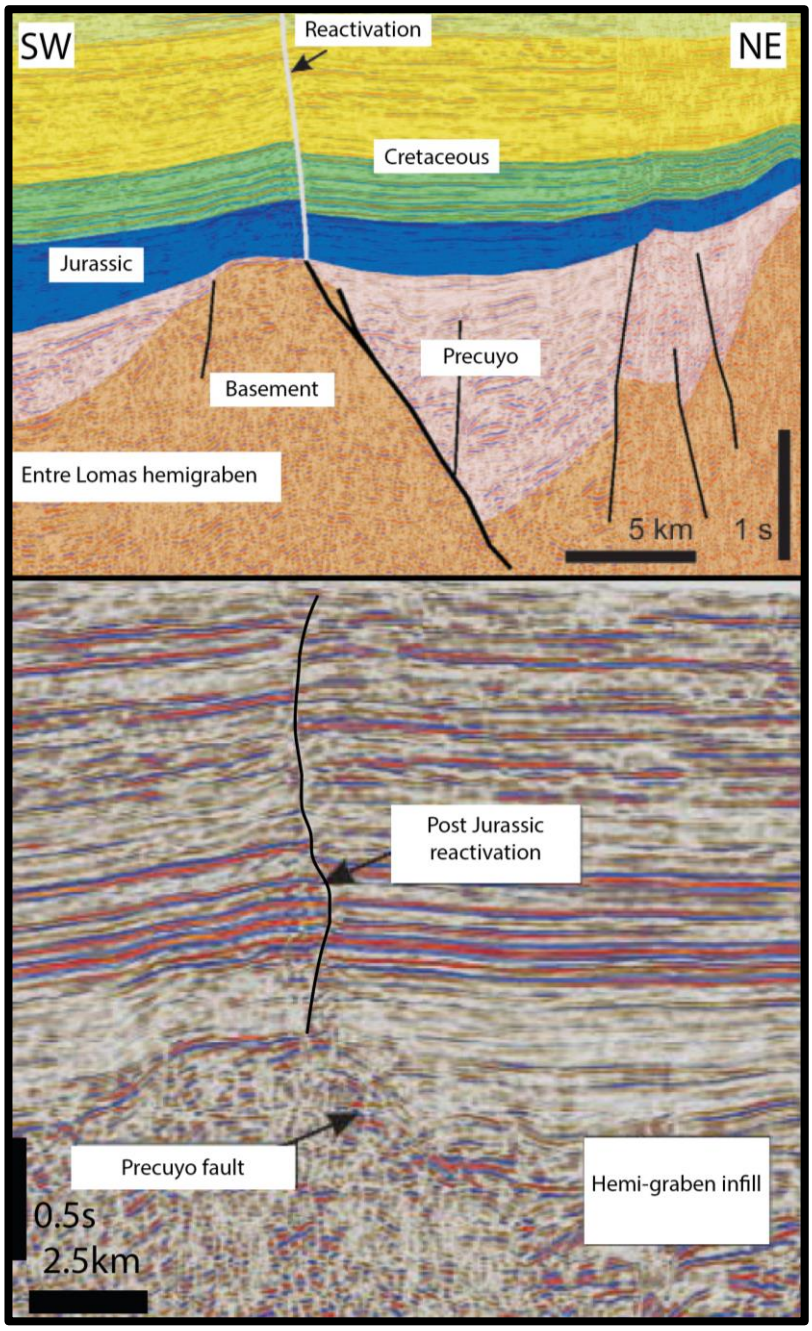

Figure 3.11: SW-NE seismic line in the Entre Lomas SW-NE seismic line in the Entre Lomas area modified after Cristallini et al. (2009). Interpreted and uninterpreted lines evidence normal faulting localized above basement highs and affecting in the Lower Cuyo Group deposits, Faults propagated parallel to NW-oriented Precuyo faults or propagated "en-échelon" above W-NW Precuyo faults. The normal faulting in the Lower Cuyo Group is interpreted as a result of differential compaction produced by abrupt thickness variations of the Precuyano Cycle syn-rift deposits (up to 2000m thickness change across 10 km distance; Entre Lomas-Estancia Vieja).

The equivalent unit to late syn-rift deposits of the Chachil Fm. in the north of the Neuquén Basin corresponds to the upper section of the Puesto Arraya Fm. which marks the base of the early post-rift since Early Sinemurian (Lanés et al., 2008; Giambiagi and Martinez, 2008). In the Central Neuquén Basin, near the Cordillera del Viento, the Chachil Fm. hosts Algoma type BIF mineralisations enriched in sulphur and manganese (Zappettini et al., 2012). In the subsurface along the Huincul High to the south of the Neuquén Basin, the Chacaico Fm. deposited during Late Sinemurian-Early Pliensbachian, and records epiclastic and volcaniclastic sedimentation in shallow-marine environment (Pángaro et al., 2009). Deposits of the Chacaico Fm. are also equivalent to the Cupen Mahuida Fm., which form subaqueous volcanogenic deposits emplaced from Late Pliensbachian to Early Toarcian in a depocentre of the Huincul High (Schiuma et al., 2011). The calc-alkaline composition of Precuyano Cycle deposits and Lower Cuyo Group, including the Chacaico Fm. and some volcaniclastic deposits of the Los Molles Fm., also record magmatic arc volcanism from Late Triassic to Early Jurassic (up to Early Toarcian) in the Cerro Bandera depocentre of the Huincul High (Bermudez et al., 2002).

The Chacaico Fm. is equivalent to fossiliferous marine volcaniclastic deposits of the Primavera Fm. (50-400 m thick) exhumed in the Central Neuquén Basin. This succession comprises basalts, dacites, rhyolites, and reworked volcanic deposits, with a calc-alkaline composition, emplaced with subaerial to subaqueous volcanism during the Late Pliensbachian-Early Toarcian (Gulisano and Gutiérrez Pleimling, 1995; Llambías et al., 2007). In this area, the Precuyano Cycle and Primavera Fm. deposits have been interpreted as part of a Late Triassic to Early Jurassic magmatic arc, equivalent to subduction-accretion complexes developed contemporaneously in the southern Neuquén Basin (~ 38°S) along the Coastal cordillera of Chile (Llambías et al., 2007). These deposits, located near Lonquimay, correspond to Late Pliensbachian-Early Toarcian Icalma Member of the Nacientes del Biobio Fm. They include tholeiitic to calc-alkaline basalts, turbidites including tuffs, breccias and cherts emplaced from subaerial to marine environment (50-100 m water depth) in an intra-arc extensional basin associated with calderas and subaqueous andesitic volcanoes (De la Cruz and Suárez, 1997).

3.4.2 Upper Cuyo Group

The Middle Jurassic is characterized by the development of a post-rift regressive marine to continental system from Aalenian to Callovian (Fig. 3.3 and 3.9). This system prograded from the southern border of the basin towards the northwest or towards the west into the central Neuquén Embayment, with deposition of the Upper Cuyo Group bounded at top by the intra-Callovian regional unconformity (155 Ma) (Dellapé et al., 1979; Gulisano et al., 1984). The progradational system includes Late Toarcian to Bajocian deep-marine siliciclastic slope to basinal deposits (Middle and Upper Los Molles Fm. up to ~750 m thick), shallow-marine deltaic coastal deposits spanning the Bajocian (Lajas Fm. up to ~550 m thick) and fluvial continental deposits spanning the Bathonian (Challaco Fm.). These genetically-related systems, deposited during an eustatic sea-level fall, culminated with deposition of evaporate during the Callovian (Tabanos Fm.) (Gulisano and Gutiérrez Pleimling, 1995; Legarreta and Uliana, 1996; Zavala, 1996; Gómez Omil et al., 2002; Mutti et al., 2003; Martinez et al., 2008; Paim et al., 2008). Progradational sedimentation patterns in the south of the Neuquén Basin contrasts with the continuous transgressive sedimentation pattern that dominated in the northern Neuquén Basin. This contrasted sedimentation pattern might reflect the imbalance between subsidence, eustatism and sedimentation rate (Gulisano and Gutiérrez Pleimling, 1995), and appears to be a consequence of the effects of marine flooding across irregular inherited rift topography at the scale of the Neuquén Basin (Veiga et al., 2013).

3.4.3 Early Jurassic stratigraphic scheme of this study

The present study is focused on refining the stratigraphy of the first second order transgressive sequence defined at large-scale in previous studies: the Lower Cuyo Group (Gulisano and Gutiérrez Pleimling, 1995; Vergani et al., 1995; Legarreta and Uliana, 1996; Burgess et al., 2000) (Fig. 3.12). Stratigraphy of the Early Jurassic Lower Cuyo Group is organized into a late syn-rift megasequence and an early post-rift megasequence, each subdivided into several sequences (J1.1, J1.2, J2.1, J2.2) it can be represented by a range of lithostratigraphic units (1, 2, 3 and 4). Assessing the lateral spatial and temporal changes of units which

can be recorded within a single sequence reflect the natural variability of depositional systems across the studied depocentres.

The late syn-rift megasequence is represented by the J1.1 sequence spanning from Early to Late Pliensbachian. It includes Unit 1 and 2 corresponding either to an alluvial to shallow-marine mixed carbonate-clastic system or fan-deltaic to deltaic system, equivalent to the Chachil Fm. and Chacaico Fm. in the literature.

The early post-rift megasequence is represented by the J1.2 sequence spanning from Late Pliensbachian-Toarcian boundary to late Early Toarcian and the J2.1 sequence spanning from early Late Toarcian to Aalenian. It includes Unit 3 and 4 corresponding to a deep-marine siliciclastic system, equivalent to the Lower Los Molles Fm. in the literature. The Unit 3 which corresponds to organic-rich source rock mudstone associated with a maximum flooding event at the base of the Los Molles Fm. is equivalent to the “Lower Pelitic Member” and also records the Toarcian Oceanic Anoxic Event (TOAE) (Al-Suwaidi et al., 2016; Angelozzi and Pérez Panera, 2016). The Unit 4 which corresponds to the sand-rich part of the Lower Los Molles Fm. is equivalent to the “Upper Pelitic Member”.

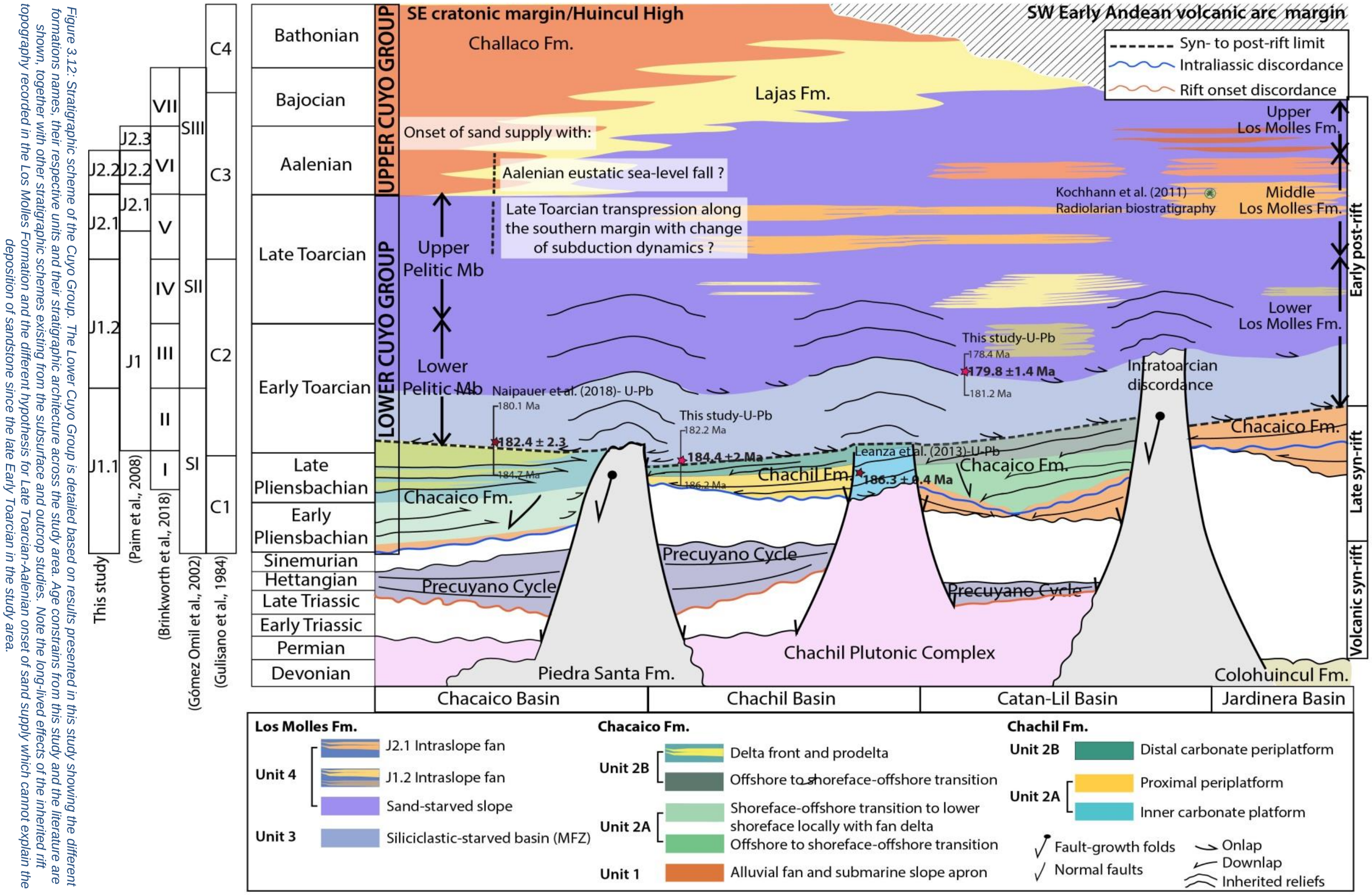

Figure 3.12: Stratigraphic scheme of the Cuyo Group. The Lower Cuyo Group is detailed based on results presented in this study showing the different formations names, their respective units and their stratigraphic architecture across the study area. Age constrains from this study and the literature are shown, together with other stratigraphic schemes existing from the subsurface and outcrop studies. Note the long-lived effects of the inherited rift topography recorded in the Los Molles Formation and the different hypothesis for Late Toarcian-Aalenian onset of sand supply which cannot explain the deposition of sandstone since the late Early Toarcian in the study area.

3.5 Los Molles Fm.

3.5.1 Early Jurassic Lower Los Molles Fm.

The Lower Los Molles Fm. is commonly described as a thick package of deep-marine shales emplaced during rising and highstand sea-level (Gulisano and Gutiérrez Pleimling, 1995; Paim et al., 2008) (Fig. 3.12). Subsurface studies in the Huincul High area have described turbidite lobes in the Lower Los Molles Fm. corresponding to the “Pelitic Member” or “Lower Section” of the Los Molles Fm. (Cruz et al., 1999, 2002; Gómez Omil et al., 2002). The Lower (Pliensbachian-Early Toarcian) and Upper (Early Toarcian-Aalenian) Pelitic Members can be separated by an Intra-Toarcian angular discordance recognized in subsurface (Mosquera, 2002; Gómez Omil et al., 2002; Pángaro et al., 2009). Isolated sealed sandy reservoirs of dry gas and condensates are associated with the higher source rock potential (kerogen type II/III averaging 2 to 4-6% and up to 11% TOC) of the Lower Los Molles Fm., compared to the Middle and Upper Los Molles Fm. (Cruz et al., 1999, 2002; Gómez Omil et al., 2002; Pángaro et al., 2006).

The Lower Los Molles Fm. forms the Late Pliensbachian- early Late Toarcian depositional sequence C2 (Gulisano et al., 1984) or late Early-early Late Toarcian depositional sequence J1 (Paim et al., 2008). J1 and C2 correspond to a second order depositional sequence, which record a transgressive-regressive cycle associated with a major basin wide flooding event recognized in the Huincul High and Catán-Lil area, and in the northern Neuquén Basin. Only recently a seismic stratigraphic study highlighted its internal organization into five different depositional cycles in the eastern part of the Huincul High area (Brinkworth et al., 2018) (Fig. 3.12). The cycle II (Early Toarcian) corresponds to deposits of a deltaic fringe (100-120 m thick) across a submarine ramp and the cycle III (late Early Toarcian) and IV (early Late Toarcian) both record deposition of the first thin clinoforms (50-70 m and up to 300 m thick, prograding 8-12 km/Ma) (Brinkworth et al., 2018). The cycle V (late Late Toarcian) and VI (Early-Middle Aalenian) deposited during a relative sea-level fall, record the formation of thicker and sigmoidal clinoforms (300-500 m thick, prograding 6-8 km/Ma) associated with deltas reaching a well-defined shelf-edge break (~300 m high). Therefore, in the easternmost part of the Huincul High area, the Lower Los Molles Fm.

developed with progradational-aggradational stacking of small deltas oriented to the NW-WSW, first with thin clinoforms across a ~15-20 km wide submarine ramp to intermediate ramp-talus (II-III). These evolved into thicker clinoforms across a well-defined shelf-slope-basin profile (V-VI) but with limited sediment bypass downslope, which resulted in the accumulation of fine-grained distal deposits (Brinkworth et al., 2018).

Towards the west of the Huincul High area, the Lower Los Molles Fm. developed with progradation of narrow alluvial fans and deltaic fringes across a steeper platform-slope-basin profile, with bypass through multiple point sourced feeder conduits. This promoted the accumulation of turbidite lobes towards the NW-NNW (Sequence I-Pliensbachian-Early Toarcian) with a strong control of basement highs and growth faults and folds on the distribution of sand-rich depocentres (Gómez Omil et al., 2002; Pángaro et al., 2006, 2009) (Fig. 3.12). Since the Early Toarcian, progradation of fan deltas (Cutral-Co Member) (Sequence II) in relatively shallow-water (~20 m depth) formed sigmoidal bodies which onlap towards the NE onto the Sequence I and pass distally into mudstone of the Los Molles Fm. (Gómez Omil et al., 2002). These sigmoidal bodies, incised by NNW-oriented canyons, were associated with shelf breaks that nucleated onto rift fault borders (Gómez Omil et al., 2002; Pángaro et al., 2006, 2009). Increased subsidence and large influxes of clastic material in the southeast and western parts of the basin along the Huincul High are linked to transtensional and transpressional tectonics since the Late Toarcian (Gómez Omil et al., 2002; Pángaro et al., 2006, 2009; Silvestro and Zubiri, 2008; García Morabito et al., 2011). Similar compressive or transtensive reactivation of W- and NNW-NW oriented normal faults bounding depocentres (Rahue and Piedra Santa Range) have been interpreted to control the confinement of Early Jurassic depocentres to the west in La Jardinera area (García Morabito, 2010) and as a trigger for the onset of sand supply (Pángaro et al., 2009; Naipauer et al., 2012; Pujols et al., 2018) otherwise regarded as a consequence of a major eustatic sea-level fall (Paim et al., 2008) (Fig. 3.12).

3.5.2 Middle Jurassic Middle and Upper Los Molles

In Gulisano et al. (1984), the Middle and Upper Los Molles Fm. and Lajas Fm. correspond to the depositional sequence C3, and the Challaco Fm. to the depositional sequence C4. In Paim et al. (2008), the Middle and Upper Los Molles Fm., together with the Lajas and the Challaco Fm., form a second order depositional sequence J2 (Fig. 3.12). The Middle and Upper Los Molles Fm., dominated by submarine lobes and channel-fills, have been extensively studied for their organization as large-scale clinoform (200-400 m, inclined 2-4°) deposited with relative sea-level fall (Verzi et al., 2005; Paim et al., 2008; Loss et al., 2018). In Paim et al. (2008), the Middle Los Molles Fm. is subdivided into third order depositional sequences. This includes a Late Toarcian-late Early Aalenian depositional sequence, J2.1, and late Early Aalenian-early Late Aalenian depositional sequence, J2.2.

The Upper Los Molles Fm. forms the early Late Aalenian-Early Bajocian depositional sequence, J2.3. However, these time constraints were arbitrarily placed. A study of radiolarian fauna (Kochhann et al., 2011) has shown that the Toarcian-Aalenian boundary is recorded within the top J2.1 sequence of Paim et al. (2008). This implies that sand-rich deposits of the J2.1 sequence are in fact at least Late Toarcian (Fig. 3.12). The J2.2 and J2.3 sequences correspond to the JC4 sequence recognized in the Sierra Chacaico (Zavala, 1996; García et al., 2006). The J2.1 sequence, which represents the first sandy deposits in the La Jardinera depocentre, is proposed by Paim et al. (2008) as an equivalent of the Cutral-Co Mb or sequence II (Early-Late Toarcian) of Gómez Omil et al. (2002). However, these authors instead associated their sequence III (Aalenian-Early Bajocian) to the sandy turbidite deposits of La Jardinera (Fig. 3.12).

In the subsurface, deposition of the Middle and Upper Los Molles Fm. from Aalenian to Bathonian is recorded by the cycles VII to CIX, which formed an extensive progradational system that progressively infilled accommodation in the basin (Brinkworth et al., 2018; Loss et al., 2018) (Fig. 3.12). Cycle VII records an important palaeogeographic change recognized both in the eastern and western Huincul High area, with an abrupt basinward shift of the shoreline driven by a major relative sea-level fall and “lowstand” sequence. This event is recorded by development of progradational clinoforms (400 m thick, prograding 6-8 km/Ma), including shelf edge deltas, slope channel-fills and turbidite lobes. Large channel

systems (up to 100 m thick) developed preferentially along inherited rift structures across the slope promoting significant sediment bypass and turbidite lobe deposition in the basin, interpreted to form the first “lowstand“ deposits in the westernmost exhumed depocentres along the Huincul High (Gulisano and Gutiérrez Pleimling, 1995; Paim et al., 2008; Loss et al., 2018).

Chapter 4 Evolution from syn-rift carbonates to early post-rift deep-marine intraslope lobes: the role of rift basin physiography on sedimentation patterns

4.2 Introduction

The syn- to post-rift transition is associated with a change from active crustal stretching, typically accommodated by normal faulting and rapid mechanical subsidence, to broad thermal subsidence and decay of normal faulting with cooling of the crust (McKenzie, 1978; Ziegler and Cloetingh, 2004). During the post-rift, the majority of rift-related faults are deactivated. Depending on inherited rift topography, thermal subsidence, and eustatic and climatic changes, the rift may receive immediate early post-rift, or delayed late post-rift extrabasinal sediment (Ravnås and Steel, 1998; Lien, 2005; Soares et al., 2012; Yu et al., 2013; Jarsve et al., 2014; Henstra et al., 2016; Balázs et al., 2017).

Detailed documentation of syn- to post-rift transition stratigraphy is needed to evaluate controls such as inherited rift physiography, change in sediment source area, and to advance existing conceptual models for rift basin-fills. However, the syn- to post-rift transition is difficult to resolve in the subsurface, with low resolution seismic reflection data and sparse well coverage (Kyrkjebø et al., 2004; Lien, 2005; Zachariah et al., 2009; López-Gamundí and Barragan, 2012; Jarsve et al., 2014; Lohr and Underhill, 2015). Consequently, little is known about the architecture, facies distribution, development of bed-scale heterogeneity, and termination style against inherited rift topography of early post-rift deep-marine sand-rich systems that have been documented in the subsurface (Argent et al., 2000; Martinsen et al., 2005; Milton-Worssell et al., 2006; Moscardelli et al., 2013). Outcrop-based studies of ancient deep-water rift basin-fills can provide key information on subseismic stratigraphic architecture and facies distributions during the syn- to post-rift transition, but often lack detailed descriptions of early post-rift sand-rich systems (Surlyk and Korstgård, 2013; Yu et al., 2013; D'Elia et al., 2015; Hadlari et al., 2016).

The aim is to investigate a rare example of an exhumed marine rift depocentre, the Chachil Graben, southwestern Neuquén Basin, west-central

Argentina. The graben-fill records the transition from syn-rift carbonate to post-rift siliciclastic sedimentation during the Early Jurassic evolution of the Neuquén Basin in a back-arc setting. The main objectives are to (i) analyze the stratigraphic architecture of the basin-fill; (ii) evaluate the effects of local and regional controls on sedimentation during the syn- to post-rift transition in the Chachil Graben; and (iii) assess the impact of seabed topography on flow behaviour and the character of lobes during the early post-rift.

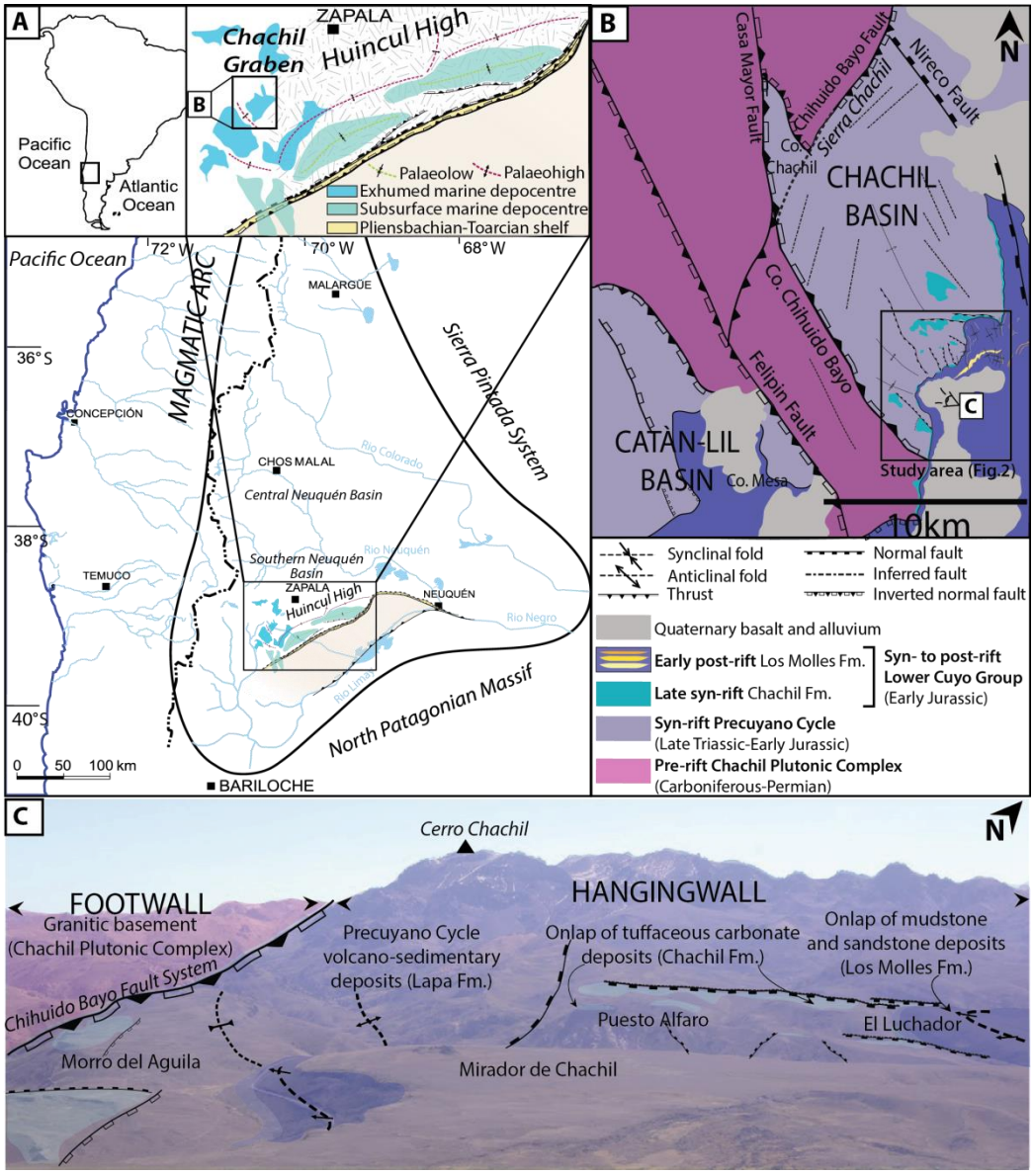

Figure 4.1: A- Map of the Neuquén Basin showing the location of the Chachil Graben detailed in fig. 4.1-B and the Pliensbachian-Toarcian palaeogeographic setting (subsurface palaeoshelf southern border of the Neuquén Basin and depocentres after Gómez Omil et al.*, 2002 and García Morabito* et al.*, 2011). B- Map of the Chachil and Catán-Lil Graben (including structures after Leanza, 1990; Franzese* et al.*, 2006; Muravchik* et al.*, 2014) showing location of the panorama in fig. 4.1-C and detailed geological map of the study area in fig. 4.2-A. C- Panorama from the horst border to the adjacent hangingwall of the Chachil Graben showing structures and spatial distribution of the Lapa, Chachil and Los Molles formations.*

4.3 Geological setting and stratigraphy

The Neuquén Basin, Argentina (36°S-40°S) formed along the southwestern convergent margin of the Gondwana-South American plate, being bound by the Andean volcanic arc to the west, the Sierra Pintada belt to the northeast, and the North Patagonian Massif to the southeast (Fig. 4.1-A). The Neuquén Basin underwent intracontinental rifting from Late Triassic to Early Jurassic, followed by subduction of the proto-Pacific plate and thermal subsidence from Early Jurassic to Early Cretaceous, and subduction-driven foreland evolution characterized the Late Cretaceous-Cenozoic period (Vergani et al., 1995; Legarreta and Uliana, 1996; Franzese and Spalletti, 2001; Howell et al., 2005).

The southwestern Gondwana margin evolved with gravitational collapse of a Late Palaeozoic orogen and widespread magmatism, which played a critical role in thermo-mechanical weakening of the lower crust and lithosphere, which accommodated Late Triassic - Early Jurassic extension with opening of intracontinental volcanic rift basins (Vergani et al., 1995; Legarreta and Uliana, 1996; Franzese and Spalletti, 2001). Extensional faulting with rapid mechanical and volcano-tectonic subsidence (cf. Muravchik et al., 2011) controlled the accumulation of continental volcano-sedimentary successions (Precuyano Cycle; Gulisano et al., 1984). These Late Triassic - Early Jurassic (Norian - Sinemurian) syn-rift continental successions include volcanic effusive, pyroclastic and epiclastic material interbedded with alluvial-fluvial and lacustrine carbonate deposits (Franzese et al., 2006; Muravchik et al., 2011, 2014; D'Elia et al., 2015). Isolated syn-rift depocentres are bound by major pre-rift basement fault-blocks including Late Devonian - Early Carboniferous metasedimentary rocks of the Piedra Santa Fm. (Franzese, 1995), Late Carboniferous - Early Permian calco-alkaline plutons of the Chachil Plutonic Complex (Leanza, 1990) and Late Permian - Early Triassic volcanic terranes of the Choiyoi Group (Llambías et al., 2003).

Transgression of volcanic rift depocentres occurred during the Early Pliensbachian in the Neuquén Basin with flooding from the Panthalassic Ocean and formation of an epeiric sea along the southwestern Gondwana margin (Damborenea et al., 2013; Leanza et al., 2013). The Early Pliensbachian also

recorded the onset of subduction with negative trench rollback, which controlled extension and back-arc subsidence of the Neuquén Basin bounded to the west by the Early Andean volcanic island arc (Franzese and Spalletti, 2001; Mpodozis and Ramos, 2008). Initial development of Early Jurassic marine depocentres was strongly influenced by the rift topography and diachronous syn- to post-rift transition until the Middle Jurassic (Aalenian) (Legarreta and Uliana, 1996; Burgess et al., 2000; Gómez Omil et al., 2002; Veiga et al., 2013). Since Middle Jurassic marine depocentres merged together into a single broad back-arc depocentre controlled by post-rift thermal subsidence (Gulisano and Gutiérrez-Pleimling, 1995; Vergani et al., 1995; Legarreta and Uliana, 1996; Franzese and Spalletti, 2001). The Early to Middle Jurassic evolution of the Neuquén Basin is recorded by the Cuyo Group (Gulisano et al., 1984). It comprises two 2nd order depositional sequences separated by the Toarcian-Aalenian boundary: the Early Jurassic Lower Cuyo Group and Middle Jurassic Upper Cuyo Group (Gulisano and Gutiérrez Pleimling, 1995; Vergani et al., 1995; Legarreta and Uliana, 1996; Burgess et al., 2000). The present chapter is primarily focused on the Early Jurassic transgressive deposits of the Lower Cuyo Group to investigate the local syn- to post-rift transition record in the Chachil Graben (not a basin-scale event, cf. Soares et al., 2012) and effects of inherited rift topography on early post-rift sedimentation.

4.4 Study area and data

Chachil Graben

The study area corresponds to the Chachil Graben located in the southwestern Neuquén Basin which forms the exhumed western part of the Huincul High (Fig. 4.1-A), characterized by a series of NNW-SSE to NW-SE trending half-grabens and grabens inverted and uplifted during the Andean compression (Vergani et al., 1995; Franzese et al., 2006; García Morabito et al., 2011; Muravchik et al., 2011, 2014). The Huincul High is an ENE-WSW oriented intraplate structure which formed the southern shelf-slope margin of the Neuquén Basin during the Early Jurassic, along which marine rift depocentres (see Fig.

4.1-A) with turbidite fan systems developed across a complex rift topography (e.g. Gómez Omil et al., 2002; Pángaro et al., 2009).

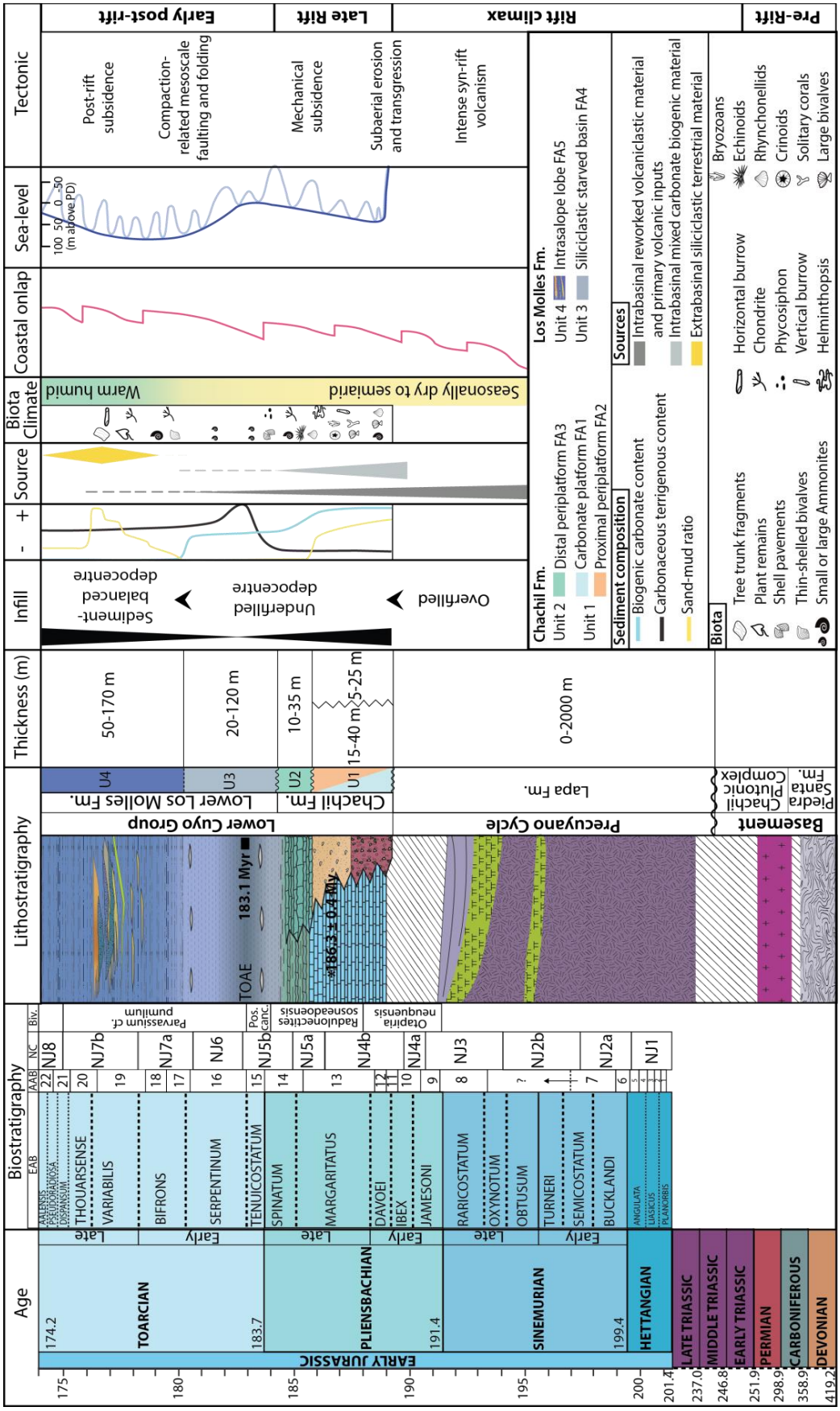

Figure 4.2: Synthetic stratigraphic column representing thickness of lithostratigraphic units, changes in sediment composition and biota, source contribution and interpretations for tectonic stages. Numerical Early Jurassic ages from Ogg et al. *(2016); (NC) nannofossil chronozones (Ballent* et al.*, 2011); Standard European Ammonite Biozone (EAB) and Andean Ammonite Biozone (AAB) numbers (Riccardi, 2008); age at base of the Chachil Fm. (186.3 ± 0.4 Ma from Leanza* et al.*, 2013 and modified after Armella* et al.*, 2016); negative δ13C excursion and TOAE from Al-Suwaidi* et al. *(2016) in the* Tenuicostatum-Dactylioceras hoelderi *zones (AAB 15-16) equivalent to the* Tenuicostatum-Spinatum *EAB and constrained in NJ6 nannofossil chronozone from Angelozzi and Pérez Panera (2016); climate from Volkheimer* et al. *(2008); coastal onlap curve (Legarreta and Uliana, 1996); eustatic sea-level (Haq, 2018).*

The Chachil Graben is a NNW-SSE trending depocentre about 10 km wide and at least 15 km long, although post-rift cover and Cenozoic volcanic rocks overlying syn-rift deposits hamper the clear definition of its eastern margin (Fig. 4.1-B). Its northern margin was controlled by the Chihuido Bayo fault system, which strikes NE-SW and dips to the SE. The Chihuido Bayo fault system extends for 15 km SE from the Cerro Chachil, where it bounds the 5 km wide southern horst border of the Chachil Graben (Figs 4.1-B and C). The Lapa Formation, which represents the syn-rift infill of the Precuyano Cycle in the study area (Fig. 4.2), is <400 m thick along the southern margin of the Chachil Graben and thickens up to 2 km northwards in the graben centre (Franzese et al., 2006). Thickness changes in the Lapa Fm. were controlled by NNW-SSE and minor NE/NNE-SW/SSW striking faults, respectively parallel and oblique to the Chihuido Bayo fault system along the southern horst border of the graben (Fig. 4.1-B). NW-SE and NNW-SSE striking, NE or SW dipping late syn-rift faults subdivide the immediate hangingwall of the graben-horst into several intra-basin highs (Morro del Aguila, Puesto Alfaro, El Luchador and Paine Milla fault-blocks) and intervening lows (Mirador de Chachil and Picún Leufú fault-blocks) (Figs 4.3-A and B).

Data and methodology

A >10 km long NE-SW striking exposure belt into the main hangingwall of the Chachil graben-horst border permits the detailed analysis of sedimentology and stratigraphic architecture, with a focus on stratal geometries, stacking patterns, facies and thickness changes across rift structures. The dataset comprises detailed geological field mapping (Fig. 4.3) using Global Positioning System (GPS) referencing, Digital Terrain Model (DTM) and Unmanned Aerial Vehicle (UAV) surveys, 12 logged vertical sections (1:25 scale) with regular

testing of HCl reaction for carbonate rock composition, 114 strike and dip bedding readings, and 165 palaeocurrent measurements. Bedding measurements were separated into three main geographic zones (Fig. 4.3-A) and by tectono-sedimentary unit (Fig. 4.4).

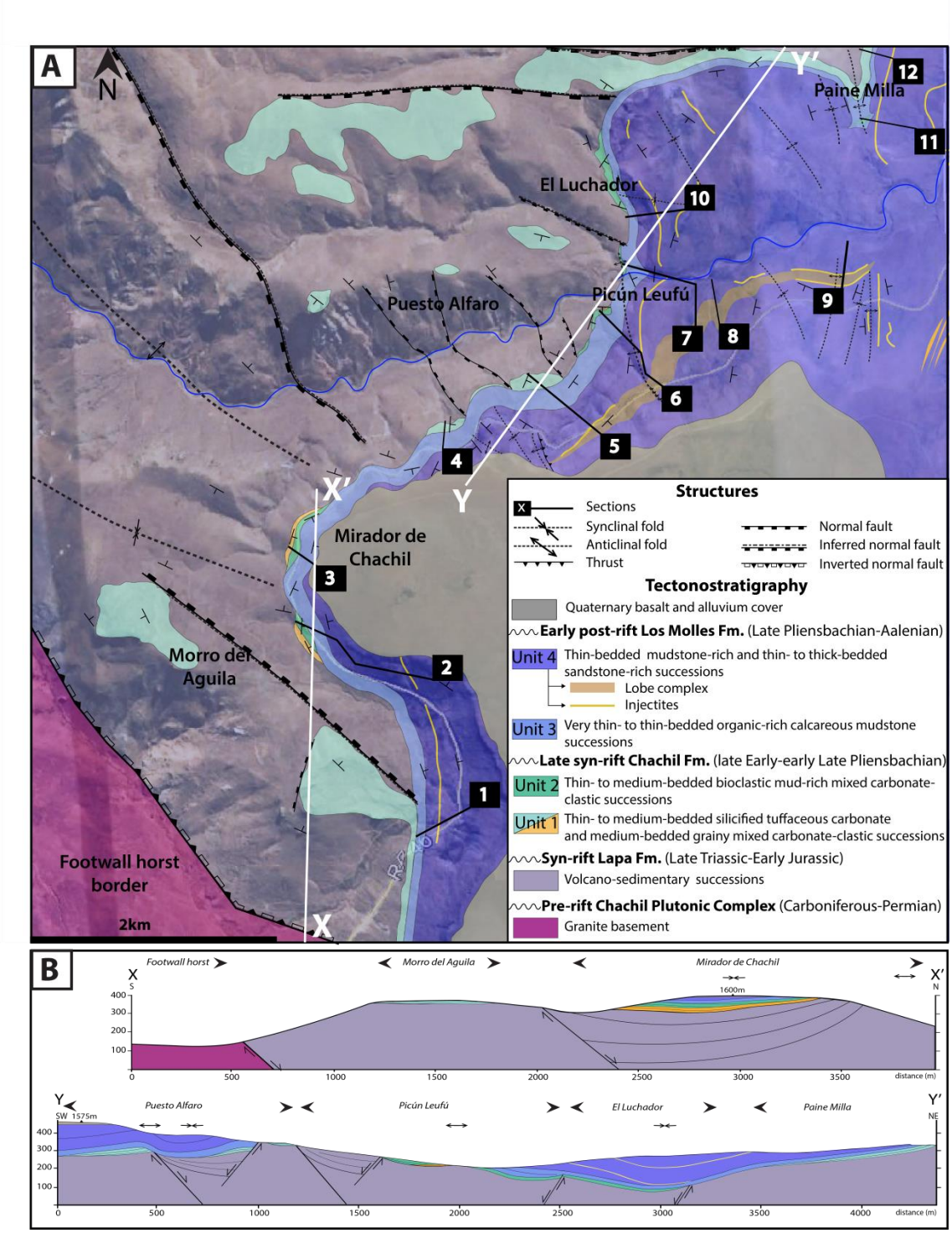

Figure 4.3: A- Detailed map of the Chachil Graben showing the relationship between structures and tectono-sedimentary units of the Chachil and Los Molles formations. B- Cross sections (not restored) indicated on the map with location of structures and locality names.

	Zone SW			Zone Central			Zone NE		
	n	Dip direction	Average strike-dip	n	Dip direction	Average strike-dip	n	Dip direction	Average strike-dip
Unit 4	9	97.4°	N7.4 16.6°E	15	127.7°	N37.7 16.9°E	8	109°	N19 21.1°E
Unit 3	13	126.4°	N36.4 16.8°E	6	126.7°	N36.7 25.1°E	10	111.4°	N21.4 57.4°E
Unit 2	7	98.2°	N8.2 18°E	8	122.7°	N32.7 32.6°E	8	61.5°	N151.5 62.3°E
Unit 1	11	76.8°	N166.8 16.2°E	10	110.3°	N20.3 25.7°E	6	233°	N143 19.5°W
	9	83.5°	N173.5 20.3°E	8	175°	N85 33.6°E			
Lapa Fm.	9	164°	N74 20.5°S	8	21.6°	N111.6 45.8°N	4	261.1°	N171 53.8°W
	9	8.1°	N98.1 23.6°N						

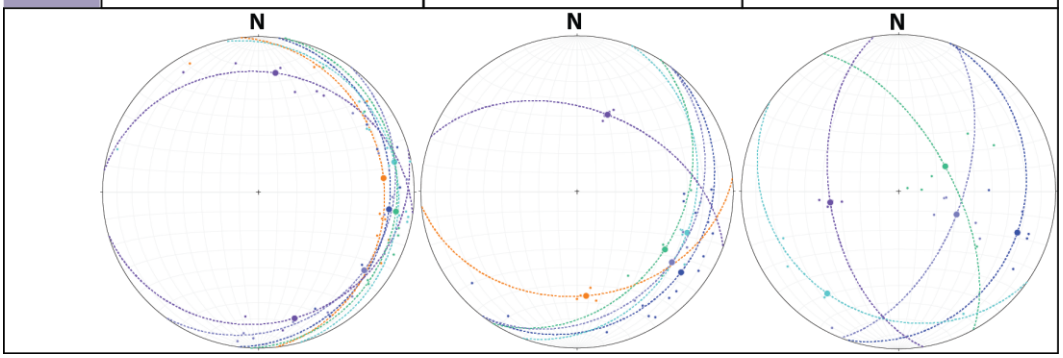

Figure 4.4: Table of the calculated average structural dip and dip direction of mean bedding planes for each tectono-sedimentary unit in each zone realized with Stereonet software. Zone SW includes sections 1-2-3-4, Zone Central includes sections 5-6-7 and Zone NE includes sections 8-9-10. Stereonet diagrams show the mean bedding values for each unit (colours in stereoplots correspond to colours of units in the table), the associated average dip direction vector (bold circle), and all the other dip direction vectors measured (circles).

Results from sections 11 and 12 were not included here given the paucity of data compared to other sections. Mean bedding orientations were calculated for each unit from all measurements taken in a given zone (Appendix 1 and 2), to constrain an average tectonic dip, and dip direction, for each unit in each zone (Fig. 4.4) to help identify dip discordances and subtle unconformities. Palaeocurrent measures (Fig. 4.5) were primarily collected from sole marks including grooves and flute casts, ripples, and dune-scale cross-bedding, and were plotted in rose diagrams to reconstruct the palaeoflow pathways with bedding restored using stereonet software. The presented maps and cross sections are shown across the actual structural and topographic configuration (i.e. no back-stripping).

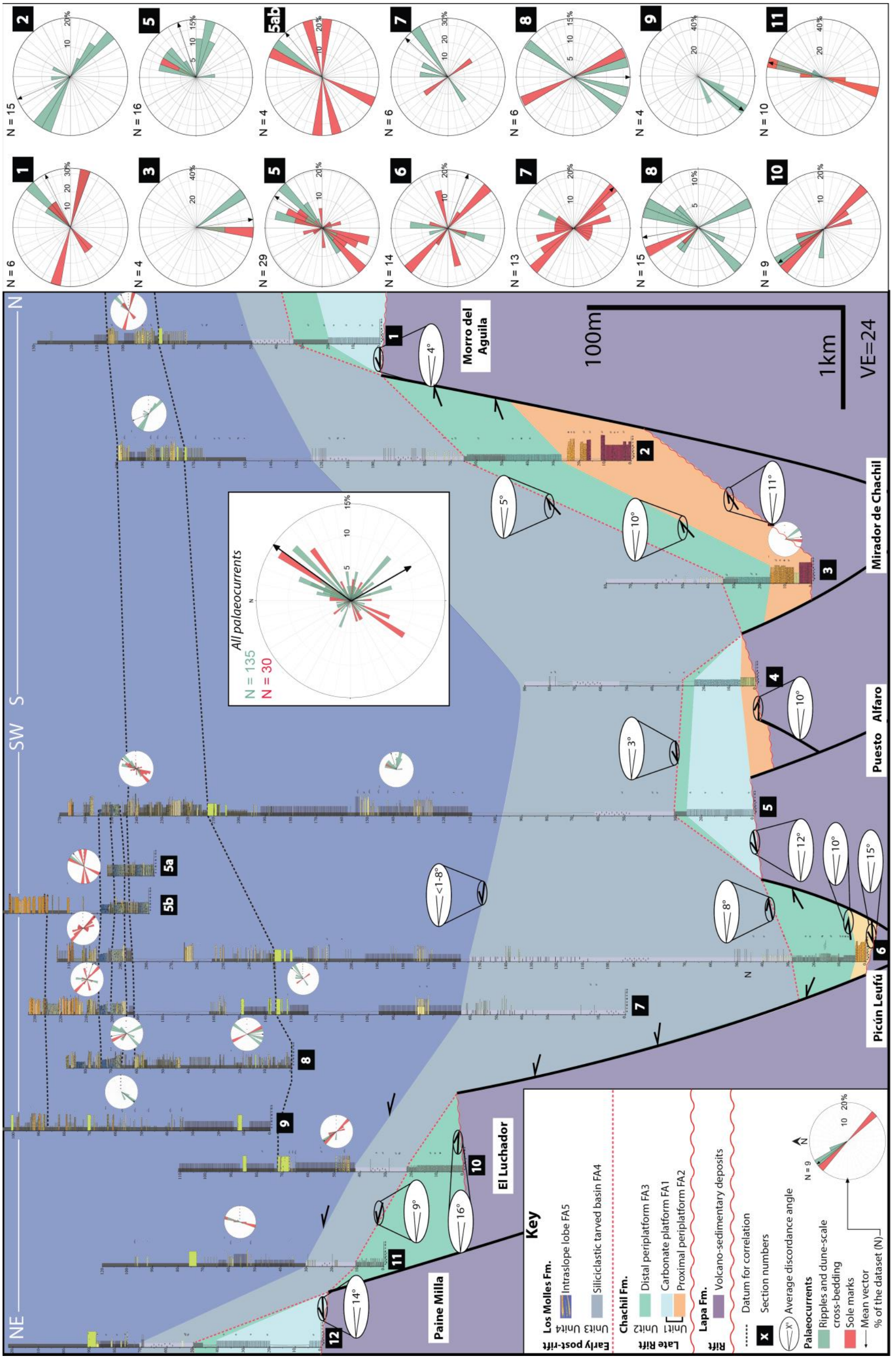

Figure 4.5: Correlation panel (~10 km long transect indicated in fig. 4.3-A), showing relationships between units along the main hangingwall of the graben-horst border, average discordance angles (see fig. 4.4) and palaeocurrent measurements. Each rose diagram presents the detail of sole marks, ripples and dune-scale cross bedding current directions, each corresponding to a different colour indicated in the key. Note that the detailed architecture of the Lapa Fm. is not represented and that vertical offset on faults are approximate. Orientation of sections is located on map fig. 4.3.

The identification of marker beds used for stratigraphic correlation were chosen in Unit 4 (Fig. 4.5) as it deposited across a less complex seabed topography compared to other units and consisted of extensive sandstone packages that could be walked out for several kilometres. Physical correlation of sandstone packages and injectites between logs was also constrained with UAV photo panels.

4.5 Stratigraphy and facies associations

In the study area, the Lower Cuyo Group is represented by the Chachil Fm. (Weaver, 1942) and Los Molles Fm. (Weaver 1931) (Fig. 4.2). Detailed sedimentological analyses allowed the identification of 25 sedimentary facies (Table 4.1) grouped into 5 different facies associations. The Chachil Fm. represents a carbonate system (FA1, FA2, FA3) and the Lower Los Molles Fm. represents a deep-water slope system (FA4, FA5) including intraslope lobes for which subfacies associations have been detailed (FA5.1, FA5.2, FA5.3) (Fig. 4.6). The Chachil Fm. spans the late Early-early Late Pliensbachian based on ammonites of the *Davoei* European Ammonite Biozone (EAB) (*Austromorphites behrendseni* of Andean Ammonite Biozone (AAB number 12)) (Riccardi, 2008), bivalve species of the *Radulonectites sosneadensis* Assemblage Zone (Riccardi et al., 2011) and U-Pb age of 186.3 ± 0.4 Ma (Leanza et al., 2013; Armella et al., 2016) (Fig. 4.2). The presence of *Posidonotis cancellata* (Leanza) in the lower part of Unit 3 indicates onset of deposition of the Lower Los Molles Fm. prior to the latest Pliensbachian, based on the extent of the *Posidonotis cancellata* Assemblage Zone spanning the latest *Spinatum* and *Tenuicostatum* EAB (Fig. 4.2) (cf. Riccardi et al., 2011).

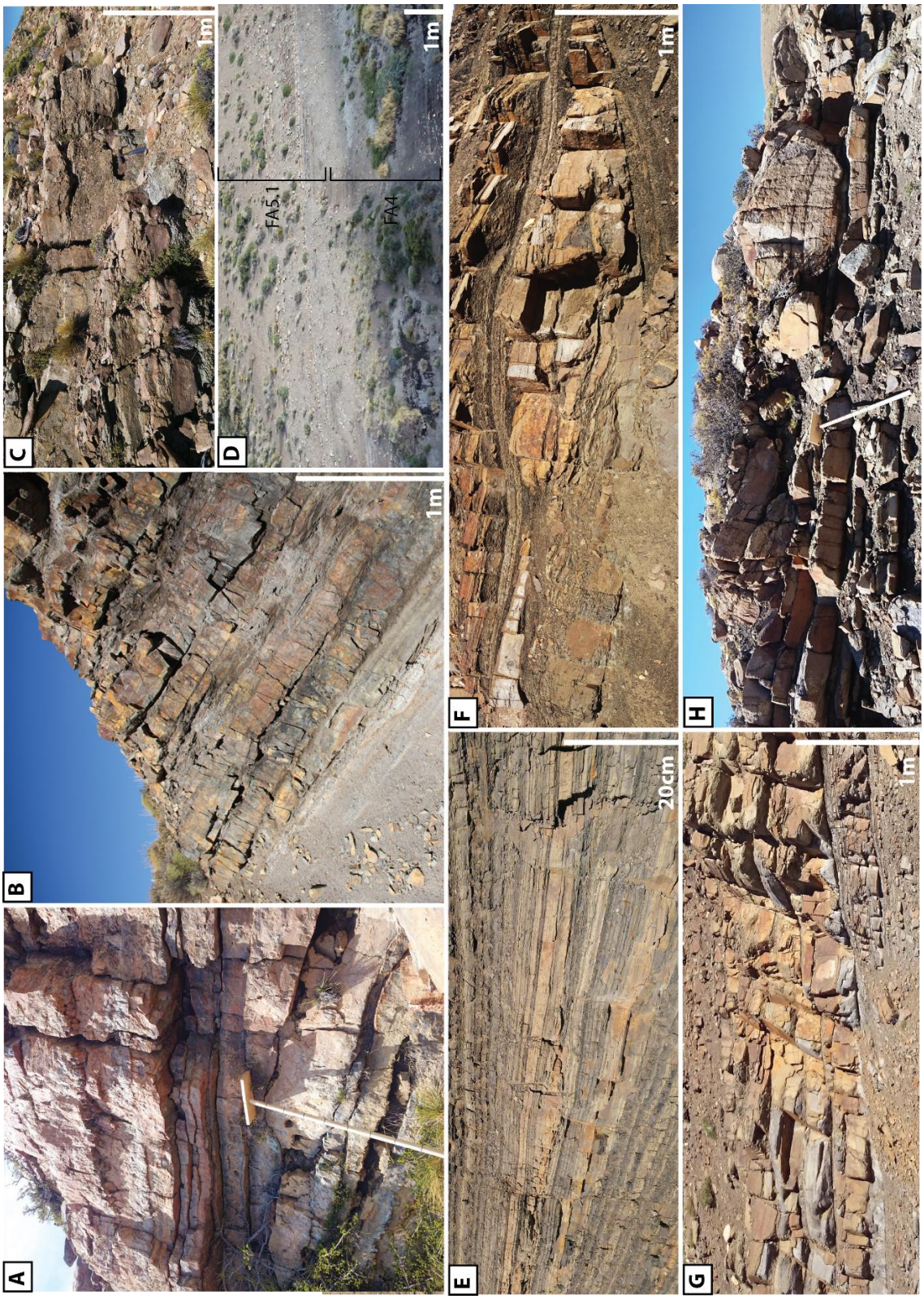

Figure 4.6: Representative photographs of facies associations. A- FA1: Thin- to medium-bedded silicicified carbonate platform successions. B- FA3: Thin- to medium-bedded mud-rich mixed carbonate-clastic successions of distal periplatform. C- FA2: Medium-bedded mixed carbonate-clastic successions of proximal periplatform. D- Transition from FA4 to FA5.1. FA4: Very thin- to thin-bedded calcareous mudstone-dominated successions of siliciclastic-starved basin. E- FA5.1: Thin-bedded muddy heterolithic successions of distal lobe fringe with significant scouring. F- FA5.2: Thin- to medium-bedded sandy heterolithic successions of proximal lobe fringe. G- FA5.3: Medium- to thick-bedded sandstone-dominated successions of dirty lobe axis. H-FA5.3: Medium- to thick-bedded sandstone-dominated successions of cleaner lobe axis.

Facies	Description	Bed thickness/Boundaries	Processes
F1a **Micritic tuffaceous cb**	Wackestone with wispy undulated tuffaceous laminations, semi-infaunal and epifaunal articulated large thick-walled bivalve shells in life position or disarticulated, crinoid ossicles and articulated stems, few siliceous sponge spicules alternating with tuffs (1-10 cm)	(10-35 cm) Tabular, crenulated sharp base and top with *Trypanites* vertical burrows	In-situ biogenic carbonate precipitation and accumulation of biodetrital mud at sea bed with gentle wave-induced reworking near photic depths (<30-50 m) in normal marine, well-oxygenated subtidal environment with frequent ash-falls
F1b **Fossiliferous cb**	Packstone massive or with rare parallel undulose laminations, disarticulated bivalve shells, reworked volcaniclastic Cs grains (qutz, K-Fd) scattered throughout beds and sponge spicules	(50-70 cm) Tabular, wavy sharp base and top, locally with *Helminthopsis* grazing traces	
F2a **Pebbly conglomerate**	VPS matrix-supported polygenic conglomerate of massive VCs-Cs to Ms, with angular to subrounded clasts (reworked vg, qutz, Mds) (0.5-25 cm), pieces of wood (15 cm), disarticulated shells (bivalves, rhynchonellids), crinoid ossicles. Locally clast-supported base	(20-90 cm) Tabular, low erosional relief at base (<10 cm deep) and sharp planar top	Weak gravitational sorting and reworking across short transport distance by non-cohesive hyperconcentrated density flows rich in reworked volcaniclastic material
F2b **Calciturbidite**	MS crudely normally or inversely graded bioclastic Cs-Ms to Fs locally low-angle cross laminated, bearing subrounded Pb (1.5cm) clasts (reworked vg, qutz, K-Fd), bioclasts (thick-walled fragmented shells, crinoids ossicles, fragments of solitary coral (*Montlivaltia*) and bryozoans)	(50-70 cm) Lenticular to lens-shaped, erosional base (up to 15cm deep) and sharp planar or amalgamated top	High-density turbidity currents rich in reworked (allochemical) bioclastic material accumulated below the fair-weather wave base
F2c **Calcarenite**	Grainstone massive dominated by well-rounded Ms- to Fs sized allochems and qutz grains and thin shells (bivalves)	(30-50 cm) Tabular, with subplanar sharp planar base and top with *Skolithos* and *Ophiomorpha* burrows	Concentrated bioclastic grain flows with significant hydraulic bioclastic grain reworking prior to deposition
F3a **Bioclastic cb**	Packstone with reworked volcaniclastic Ms-Fs grains (K-Fd), disarticulated small shells (bivalve, brachiopod) and wavy laminated storm-graded grain-rich layers (1-2 cm)	(15-50 cm) Tabular or locally through-cross bedded, irregular undulated sharp base and top, with *Cylindrichnus* vertical burrows	Storm wave-induced low-density flows reworking and redepositing allochemical biodetrital carbonate material with frequent ash-fall, in a moderate- to low-energy oxygenated environment near or below the storm-wave base
F3b **Spiculitic cb**	Wackestone with mono- and tetraxon siliceous sponge spicules, reworked volcaniclastic Ms-Fs grains (qutz, K-Fd), pumice (1-2 mm), organic intraclasts (2-5 cm) and alternating with marlstone and tuffs (5-10cm)	(30-50 cm) Tabular or lens-shape, sharp base and top with *Chondrite Bollensis* and *Trichichnus*	
F3c **Marlstone**	Marlstone laminated with sponge spicules, tuffaceous and broken shell-ash layers (<0.5 cm), and few large ammonites (15 cm)	(10-60 cm) Flat base and top	
F4a **Calcareous mudstone**	Organic-rich calcareous Mds (pelagic and allochemical biodetrital carbonate silt and clay) alternated with tuffs (1-5 cm), bearing large carbonate concretions (15 cm) and pyrite concretions (5-8cm), bivalve shell pavements including Posidonotis Cancellata (Leanza), small ammonites (2-5 cm)	(5-20 cm) Diffuse or sharp base and top	Pelagic suspension settling with frequent clastic dilution by storm-derived low density carbonate mud plumes and ash-fall in low-energy and poorly oxygenated environment

Table 4.1: Descriptive facies table providing interpretation for depositional processes. Note abbreviations: Cobble (Co), Pebble (Pb), Granule (Gr), Very coarse (VCs) Coarse (Cs) Medium (Ms) Fine (Fs) very fine (VFs) sandstone, Mudstone (Mds), very poorly sorted (VPS), Poorly sorted (PS), Moderately sorted (MS). Volcanics (vg), quartz (qutz), K-feldspar (K-Fd).

Table 4.1. (continue)

Facies	Description	Bed thickness/Boundaries	Processes
F4b	Si massive to normally graded	(5-40 cm) Sharp base and top with *Phycosiphon* and *Chondrite Intricatus*	Storm-induced low-density bioclastic turbidity currents waning with traction-plus-fallout
Calcareous mud-rich siltstone			
F4c	MS normally graded Ms to Fs with low angle planar and current-ripple laminations and with abundant crushed skeletal material	(15-40 cm) Sharp planar or erosional base and sharp top	
Calcareous bioclastic sandstone			
F5.1a	Fissile Mds massive to subtly graded bearing plant nodules (10cm), tiny bivalve moulds and ammonites (5-10 cm)	(1 to 20 cm) Sharp base and subtle gradational top with *Chondrite*	Suspension fallout from fine-grained waning muddy turbidity currents
Massive to subtly graded mudstone			
F5.1b	Mds with parallel to low-angle planar discontinuous laminations of Fs and Si bearing Mds (<0.2-2 cm)	(1 to 20 cm) Sharp base and top	Clay-laden turbulence-modulated low-density flows
Pin-striped laminated mudstone			
F5.1c	Normally graded sandy Si with sandy low-angle laminations and starved current-ripples	(5-20 cm) Sharp base and gradational top	Traction-plus-fallout from low-density turbidity currents
Graded sandy siltstone			
F5.1d	MS normally graded Fs to VFs with planar or wavy laminations and current-ripples, locally carbonaceous-rich.	(5 to 20 cm) Sharp or erosional base (scour-like features) and sharp to gradational top with *Chondrite* and *Planolites*	Tractional reworking beneath low-density turbidity current
Structured fine-grained sandstone			
F5.1e	Massive Ms or FS well-cemented, bearing angular Mds clasts (2-5 cm) and angular heterolithic rafts (10-50 cm) parallel to bedding and calcite-filled spherical vugs (0.2-1cm) levels near bed top	(0.3 to >3.8 m) Stepped sharp base and sharp top with linear wave-crest structures (up to >1m long). that cross-cut mudstone.	Sill injection by slow moving laminar flows
Injected sandstone			
F5.2a	PS Cs-Ms with clay-poor matrix, massive or with subtle normal grading and bearing few deformed subrounded to subangular Mds clasts (0.5-8 cm) near base or throughout. Rare low amplitude dune-scale mud-rich bedforms can be present near top.	(5-80 cm) Planar or irregular erosional base (grooves) and pinch and swell undulated top	Turbulence-modulated transitional flows with propagation of low amplitude bedwaves
Massive mud-poor sandstone			
F5.2b	PS Fs with clayey banding (1-5 mm) alternating light mud-poor and dark mud-rich bands with mudchips and platy mudclasts (<2 cm)	(0.05-0.2 m) Transitional or undulated loaded base (flames) and sharp to transitional top	Turbulence-modulated transitional flows in the upper plane bed regime
Banded muddy sandstone			

Table 4.1. (continue)

Facies	Description	Bed thickness/Boundaries	Processes
F5.2c	PS Ms with patchy mud-rich matrix bearing outsized Cs grains and sheared/deformed Pb Mds clasts (2-25cm) with mudchip rims throughout bed	(20-60 cm) Sharp or erosional and/or sheared base and irregular or pinch and swell undulated top	Transient low to intermediate yield strength sandy debris-flows
Clast-rich muddy sandstone			
F5.2d	Homogeneous massive to slightly graded silty Mds	(10-60 cm) Gradational contact or sharp base-top locally draping scour bedform troughs	Collapse of depletive fluid mud flows
Massive silty mudstone			
F5.2e	VPS patchy muddy Ms-Fs matrix with outsized subangular Gr/Cs lithics, abundant mudchips, deformed sand-streaks, Pb to Co clasts (Mds, Ms) (5-30 cm), heterolithic rafts (80 cm) in the lower sandier part of bed and clast-poor and mud-rich top	(4-6 m) Erosional base scouring into underlying substrate and irregular mounded top	Intermediate yield strength sand-rich debris-flows
Chaotic muddy sandstone			
F5.2f	VPS well-mixed sand-rich mudstone matrix with outsized Cs grains (starry-night like), plant material and subrounded Pb clasts (Mds, Si, Ms with pectens and ostreid shells) (5-50 cm) floating in the muddier upper part of beds	(0.8-5 m) Erosional or sharp base and sharp flat top	High yield strength cohesive muddy debris-flows
Chaotic sandy mudstone			
F5.3a	PS crudely graded Cs-Ms locally with diffuse planar parallel or wavy laminations (1-3 cm) and discontinuous stringers of outsized VCs lithics (Qutz, Fd) and subrounded elongated Gr-Pb clasts (Mds, Si) (1-6 cm).	(0.5 to 1.2m) Erosional (grooves) or sharp or loaded base, and sharp or amalgamated top. Local cross-bedding. *Planolites* and *Chondrite* at top	Turbulence-modulated clay-laden transitional flows with high sediment fallout and suppressed tractional processes
Massive to crudely stratified sandstone			
F5.3b	VPS massive VCs to Cs bearing subangular Gr to Pb clasts (0.2-10 cm) (Mds, Si) with local coarse-tail normal or inverse grading, armoured clasts and bioclasts	(5-50 cm) Erosional base and sharp top	High-density to hyperconcentrated density flows
Granular sandstone			
F5.3c	MS normally graded Cs to Ms structured with anisotropic swaley-like low-angle (<5°) trough-cross-laminations and isotropic (10-25 cm high and wavelengths of few decimetres) or anisotropic hummock-like bedforms	(5-30 cm) Sharp planar base and wavy top	Traction-plus-fallout from high-density combined flows in the upper-stage plane bed field
Graded structured medium sandstone			

FA1: Carbonate platform

Description

FA1 consists of well-stratified, thin- to medium-bedded silicified carbonate successions (10-40 m thick) (Fig. 4.6-A) including laterally extensive thin tuff layers (1-10 cm thick). FA1 onlaps onto volcano-sedimentary syn-rift deposits (Lapa Fm.) of fault-block highs and passes laterally into FA2 in fault-block lows (Figs 4.5 and 4.7).

Thin to medium beds (10-35 cm thick) of micritic tuffaceous carbonate (F1a) have a wackestone texture and wispy, undulose tuffaceous laminations (0.5-1 cm thick). The faunal content in FA1 is dominated by semi-infaunal and epifaunal bivalves (*Kolymonectes weaveri* (Damborenea), *Radulonectites sosneadoensis* (Weaver), *Agerchlamys wunschae* (Marwick), *Weyla bodenbenderi* (Behrendsen), *Weyla alata angustecostata* (R. Philippi), *Chlamys textoria* (Schlotheim), *Antiquilima, Plicatula rapa* (Bayle and Coquand), *Entolium and Pinna* sp.) (see Leanza, 1990).

Bivalve shells (5-10 cm diameter) are either articulated and in life position or gently disarticulated. Shells are associated with well-preserved circular crinoid ossicles (3-5 mm diameter) or articulated stems (2 cm long) and rare siliceous sponge spicules concentrated in micritic levels. Beds are tabular with irregular, crenulated sharp base and top with some vertical burrows (*Trypanites*). Medium beds (50-70 cm thick) of fossiliferous carbonate (F1b) have a packstone texture massive or with rare undulose parallel laminations (0.4-2 cm thick). Disarticulated bivalve shells in broken fragments (5 cm long) and coarse sand-sized reworked volcaniclastic grains (quartz, K-feldspar) are scattered throughout beds (Fig. 4.8A). Beds are tabular with a wavy sharp base and top, locally showing Pascichnia grazing traces (*Helminthopsis*) at the contact with marlstone (F3c) of FA3.

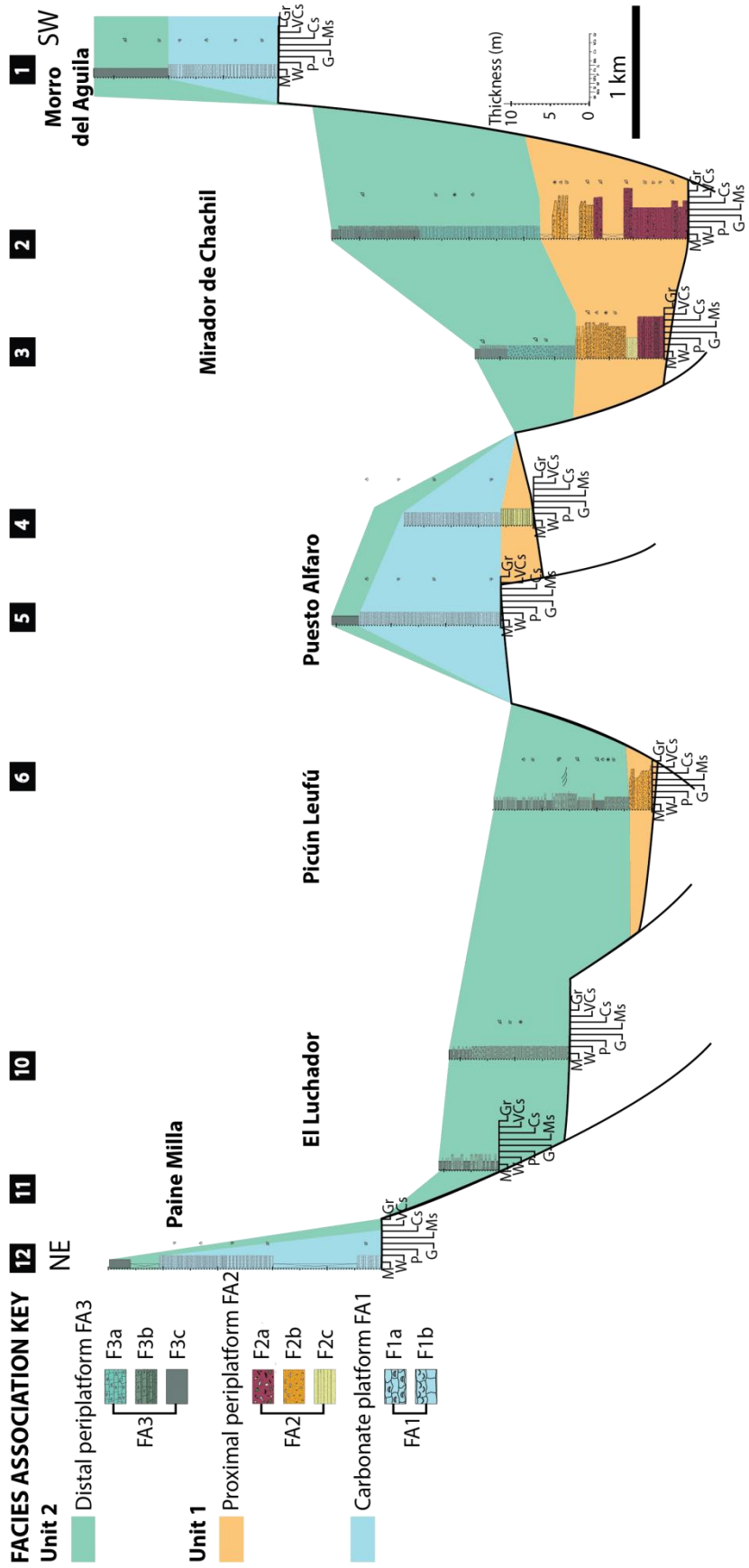

Figure 4.7: Detailed correlation panel showing the internal architecture and spatial facies relationships within Units 1 and 2 (Chachil Fm.); facies are detailed in Table 4.1.

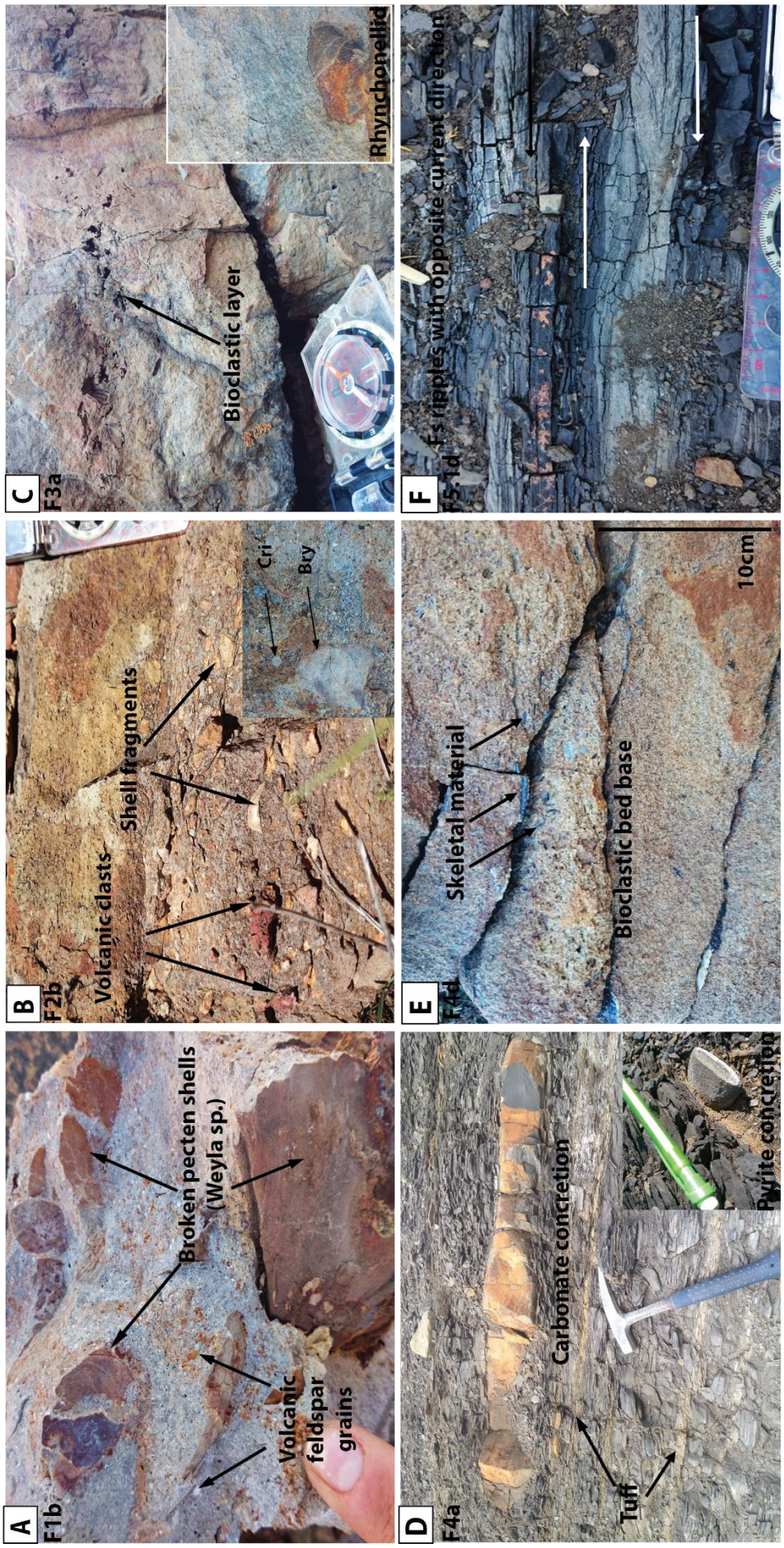
A
F1b
Broken pecten shells (Weyla sp.)
Volcanic feldspar grains
B
F2b
Volcanic clasts
Shell fragments
Cri
Bry
C
F3a
Bioclastic layer
Rhynchonellid
D
F4a
Carbonate concretion
Tuff
Pyrite concretion
E
F4d
Skeletal material
Bioclastic bed base
10cm
F
F5.1d
Fs ripples with opposite current direction

Figure 4.8: Representative photographs of facies. A- Fossiliferous packstone (F1b) bearing reworked volcaniclastic coarse sand-sized grains (K-feldspar) and abundant large broken bivalve shell fragments scattered throughout beds. B- Calciturbidite (F2b) characterized by their crude normal grading and a high proportion of bioclasts (crinoids (Cri), bryozoans (Bry), thick-walled disarticulated shells) with a few reworked volcaniclastic subrounded pebbles. C- Bioclastic packstone (F3a) with reworked volcaniclastic fine to medium sand-sized grains (quartz, K-feldspar) and small disarticulated to broken shells of bivalve and brachiopod concentrated in wavy normally graded grain-rich layers. D- Massive calcareous mudstone (F4a) bearing thin tuff layers, early diagenetic carbonate and pyrite concretions. E- Calcareous bioclastic sandstone (F4c) normally graded with bioclastic base. F- Silty mudstone (F5.1a) interbedded with sandy siltstone current-ripples (F5.1b) locally presenting an opposing palaeocurrent direction.

Interpretation

In the micritic tuffaceous carbonate facies (F1a), the preservation of bivalves in life position or weakly disarticulated indicates no or very little post-mortem transport and together with the small diameter articulated crinoid stems indicates *in-situ* deposition under stable low hydraulic conditions. The abundance and species of large-sized bivalves indicate deposition in a shallow, well-oxygenated and low-energy subtidal environment (cf. Damborenea and Manceñido, 1979, 1992). Resedimented volcaniclastic grains together with parautochthonous broken or disarticulated shells in fossiliferous carbonate (F1b) suggest a wave-induced physical reworking with limited transport. This facies association is interpreted to represent warm-temperate carbonate platform deposits in a low-energy and well-oxygenated subtidal environment periodically influenced by ash-falls. Biodetrital carbonate mud accumulated *in-situ* with skeletal accretion, bioerosion and weak mechanical reworking of organisms that formed a micritic substrate onto fault-block highs which remained near photic depths (<30-50 m) in normal marine waters. Primary volcanic material mixed with carbonate deposits indicates simultaneous explosive volcanic eruptions from the western magmatic arc which is postulated to have intermittently restricted the photic zone and depleted the biota (Armella et al., 2016). The lack of early cementation and binding of these warm-temperate carbonate deposits favoured their reworking and resedimentation into allochemical biodetrital carbonate material into fault-block lows (e.g. Halfar et al., 2004).

FA2: Proximal periplatform

Description

FA2 forms weakly stratified, medium-bedded mixed carbonate-clastic successions (5-28 m thick) (Fig. 4.6-C) restricted to fault-block lows with onlap onto volcano-sedimentary syn-rift deposits (Lapa Fm.) and pass laterally into FA1 onto fault-block highs (Figs 4.5 and 4.7). FA2 includes i) polygenic pebbly conglomerate (F2a), ii) normally graded coarse- to fine-grained calcareous sandstone (F2b) and iii) massive calcarenite (F2c). Pebbly conglomerate (F2a) forms medium to thick beds (20-90 cm thick), with a very poorly sorted, very coarse- to medium-grained sandy matrix bearing abundant granule- to gravel-sized (0.5-25 cm long) and angular to subrounded clasts (reworked pyroclastic and effusive volcanics, quartz, mudstone). Pebbly conglomerate (F2a) also bear a few pieces of wood (up to 15 cm), disarticulated small bivalve and rhynchonellid shells (2-5 cm long) and pentagonal or circular crinoid ossicles (5 mm diameter). Individual beds are tabular with low erosional relief at base (<10 cm deep) and are locally clast-supported with sharp planar top. Medium to thick beds (50-70 cm thick) of moderately sorted, crudely normally or inversely graded calcareous sandstone (F2b) comprise bioclasts, reworked volcaniclastic coarse sand-sized grains (quartz, K-feldspar) and subrounded clasts (1.5 cm long). Bioclasts include thick-walled fragmented shells (2-5 cm long), crinoid ossicles (5 mm diameter), fragments of discoidal robust solitary coral (<5 cm diameter) (*Montlivaltia*, see Gulisano and Gutiérrez Pleimling, 1995) and bryozoan (3 cm diameter) (Fig. 4.8B). Beds can show low-angle cross-laminations and have a broad lenticular to lens-shape (<8 m wide) with erosional base (up to 15 cm deep) and sharp planar top, locally amalgamated. Medium beds (30-50 cm thick) of wel sorted calcarenite (F2c) have a grainstone texture, with well-rounded, medium- to fine-grained skeletal and quartz grains and thin-shelled bivalves (1-2 cm long). Beds have a sharp planar base and top which locally present some vertical burrows (*Skolithos, Ophiomorpha*).

Interpretation

The pebbly conglomerates (F2a) present a very poor sorting of immature reworked volcaniclastic clasts admixed with bioclasts, which indicate a weak gravitational sorting and reworking across short transport distance prior to deposition by subaqueous non-cohesive hyperconcentrated density flows (Drzewiecki and Simó, 2002; Payros and Pujalte, 2008). Calciturbidites (F2b) contain a high proportion of fragmented bioclasts in respect to reworked volcaniclastic material and suggest transport and deposition by high-density turbidity currents, which produced local normal or inverse grading and traction structures (cf. Braga et al., 2001; Payros and Pujalte, 2008). Calcarenites (F2c) reflect intense hydraulic bioclastic grain reworking prior to deposition by concentrated grain flows *(*Drzewiecki and Simó, 2002*;* Halfar et al., 2004). The bioclastic material in this facies association must have been sourced from erosion and reworking of the shallow-water peripheral carbonate platform (FA1). The lack of biodetrital carbonate mud together with mechanical reworking of bioclastic and volcaniclastic material indicate accumulation of proximal periplatform deposits under moderate-energy, below the fair-weather wave base

FA3: Distal periplatform

Description

FA3 corresponds to poorly stratified, medium- to thin-bedded mud-rich mixed carbonate-clastic successions (10-35 m thick) (Fig. 4.6-B) including laterally extensive tuff layers (5-10 cm). FA3 unconformably overlies FA1, with thickening into fault-block lows and thinning across fault-block highs (Fig. 4.7). Thin to medium beds (15-50 cm thick) of bioclastic carbonate (F3a) have a packstone texture, with fine to medium sand-sized reworked volcaniclastic grains (quartz, K-feldspar) and small disarticulated shells of bivalves and brachiopods. Broken shells can be concentrated in wavy laminated normally graded grain-rich layers (1-2 cm thick) (Fig. 4.8C). Individual beds have a tabular geometry with undulated sharp base and top that can show vertical burrows (*Cylindrichnus*) and can be trough cross-bedded. The medium beds (30-50 cm thick) of spiculitic carbonate (F3b) have a wackestone texture containing well-preserved monaxon

and tetraxon siliceous sponge spicules (1-4 mm long) and a few silt- to fine sand-sized reworked volcaniclastic grains (quartz, K-feldspar). Pumice lapillis (1-2 mm diameter) and subrounded organic intraclasts (2-5 cm long) are also found locally. Beds have an irregular tabular or lens-shaped geometry with sharp base and top, locally bioturbated (*Chondrites bollensis, Trichichnus)*. Locally, spiculitic carbonate beds are interbedded with medium beds (10-60 cm thick) of thinly laminated (0.5-5 cm thick) marlstone (F3c), including sponge spicules, tuffaceous and finely comminuted shell hash layers (0.5 cm thick) and rare large ammonites (15 cm diameter).

Interpretation

Normally graded grainy bioclastic layers and rare trough-cross-bedding of bioclastic carbonate (F3a) record episodic storm-wave reworking, which is consistent with oxygenated bottom conditions indicated by the presence of *Cylindrichnus* (Ekdale and Harding, 2015). In contrast, *Chondrite* and *Trichichnus* traces in spiculitic carbonate (F3b) and marlstone (F3c) record a decrease of oxygen levels at the sediment-water interface. In these facies, the well-preserved siliceous sponge megascleres indicate limited transport and support a parautochthonous origin, from a harder carbonate substrate below the storm-wave base. The lower biota diversity (compared to FA1 and FA2) dominated by allochthonous to parautochthonous disarticulated bivalves, brachiopods and siliceous sponges characterizing FA3 supports deposition at greater water depths than FA1 and FA2. Allochemical bioclastic and biodetrital carbonate mud indicate deposition by low-density flows with storm-wave reworking of unconsolidated carbonate platform substrate (FA1) and dilution of frequent volcanic influxes as indicated by pumices and tuffaceous material (D'Atri et al., 1999; Halfar et al., 2004). This facies association represents distal periplatform deposits emplaced under moderate- to low-energy conditions, near or below the storm-wave base, with progressive bathymetric deepening and reduction of oxygen conditions.

FA4: Siliciclastic-starved lower slope

Description

FA4 forms poorly stratified, very thin- to thin-bedded calcareous mudstone-dominated successions (20-120 m thick), which unconformably overlie FA3 and is overlain by FA5 (Fig. 4.6-D), locally affected by significant thickness changes across rift structures (up to 100 m across few kilometres, see Fig. 4.5). Calcareous mudstone (F4a) is massive, with well-preserved carbonaceous matter and mainly composed of dominantly silt- and clay-size *in-situ* pelagic and allochemical biodetrital carbonate material. Very thin- to thin-bedding is monotonous (1-10 and up to 20 cm thick), commonly disrupted by oblate calcareous concretions (<15 cm long) and thin tuff layers (1-5 cm thick). Pyrite is present as discontinuous layers (<0.5 cm thick) parallel to bedding or elliptical oblong concretions (5-8 cm long) (Fig. 4.8D). Faunal content is represented by small ammonites (2-5 cm diameter) and articulated or disarticulated bivalve shells (0.5-2 cm long) distributed along bedding planes, as shell pavements (*Posidonotis cancellata* (Leanza)). Some thin- to medium-beds (5-40 cm thick) of massive to graded calcareous mud-rich siltstone (F4b) and rare graded medium- to fine-grained bioclastic calcareous sandstone (F4c) structured with low-angle planar and current-ripple lamination can be intercalated within mudstone. Bioclastic sandstone beds contain abundant crushed skeletal material and have a sharp planar or erosional base with tool marks and sharp top (Fig. 4.8E). Bioturbation in calcareous mud-rich siltstone (F4b) include small forms of *Chondrite intricatus* and *Phycosiphon* traces.

Interpretation

The thin-bedding, and absence of sedimentary structures, in calcareous mudstone suggest deposition from a biogenic source (McCave, 1984) with intermittent clastic dilution and ash fall. Clastic dilution by low-density flows resulted from storm-induced offshore transport (Schieber, 2016) and deposition of allochemical bioclastic calcareous sandstone and siltstone in the lower part of FA4 could have favoured episodic oxygen influxes. Bioclastic sandstone and siltstone beds record inputs of rare low-density bioclastic-rich turbidity currents

sourced with storm-wave reworking of the drowned carbonate platform (Bouma, 1962; Lowe, 1982). The high organic matter content of type II in the Lower Los Molles Fm. (TOC between 2 and 11%) supports a mixture of marine and terrestrial components (cf. Al-Suwaidi et al., 2016). Preservation of organic matter was favoured under low-oxygen and reducing conditions, which promoted pyrite mineralization and pre-compaction seabed diagenetic processes that formed calcareous concretions, potentially associated with marine flooding and very low sedimentation rates (Taylor et al., 1995). The concentration of juvenile low-oxygen tolerant bivalve specimens (*Posidonotis cancellata* (Leanza), cf. Damborenea et al., 2013) in pavements record episodes of high mortality events and/or condensed surfaces with very low sedimentation rates (Fig. 4.2). Little to no post-mortem bottom current winnowing of bivalves and scarcity of silty and sandy beds support deposition below the storm-wave base, consistent with estimations of palaeobathymetry at base of the Los Molles Fm. between 200 and 400 m (cf. Gómez Omil et al., 2002; Gómez-Pérez et al., 2003).

This facies association records deposition of mixed pelagic and fine-grained carbonate material derived from storm winnowing of the drowned carbonate platforms, redeposited in a sand-starved basinal environment, under low-energy and poorly oxygenated conditions, below the storm-wave base.

FA5.1: Intraslope lobes- Distal lobe fringe

Description

FA5.1 forms well-stratified, thin-bedded muddy heterolithic successions (5-30 m thick) (Fig. 4.6-E) that transitionally overlie FA4 (Fig. 4.6-D). Laterally, FA5.1 can transition and interfinger with packages of FA5.2 and FA5.3. FA5.1 (Fig. 4.9) is dominated by interbedded massive to subtly graded mudstone (F5.1a) and pin-striped laminated mudstone (F5.1b) (1-20 cm thick) including ammonites and small bivalve moulds (indet.) parallel to bedding planes. Pin-striped laminated mudstone (F5.1b) contains parallel to low-angle planar discontinuous laminations of fine sand- and silt-bearing mudstone (0.2-2 cm thick), providing a streaky bedding pattern with sharp grain-size breaks.

Thin to medium beds (5-20 cm thick) of normally graded sandy siltstone (F5.1c) and fine- to very fine-grained sandstone (F5.1d) intercalated in mudstone (F5.1a-b) form heterolithic packages (up to 5 m thick). Graded sandy siltstone (F5.1c) shows low-angle planar laminations and starved current-ripples, which locally record opposing palaeoflow directions (Fig. 4.8F). The sandstone beds (F5.1d) are normally graded, with planar or wavy laminations and current-ripples that can be enriched in carbonaceous material. Beds have sharp planar or irregular base and gradational top, which can show *Chondrite traces*. FA5.1 comprises distinctively greenish-yellowish weathered, well-cemented massive medium- or fine-grained discordant sandstone (F5.1e) (Figs 4.9 and 4.10). These mainly form laterally extensive (5-8 km) subhorizontal bodies (<0.5 to 1.5 m and up to 3.8 m thick) that cross-cut the surrounding mudstone stratigraphy at low-angle (<15°), locally associated with rare thin subvertical bodies (up to 30 cm thick, <1 m wide) (Figs 4.10 and 4.11-A). Discordant sandstone beds can show planar trains of subspheroidal vugs (0.2-1 cm diameter), typically calcite-filled, restricted to the upper part of beds. Beds have sharp planar or stepped base and top and convex-down pinchout terminations. Subangular mudstone clasts (2-5 cm long) and linear wave crests (up to 1-2 m long, 0.-0.4 m wide, 0.1-0.15 m relief and 0.5-1.0 m spacing) oriented NE-SW are locally present on bed top surfaces. Subhorizontal bodies contain large angular rafts of heterolithic strata (10-50 cm and up to >1 m across) found “*in-situ*” with their, long axis parallel to and concordant with bedding of the host stratigraphy.

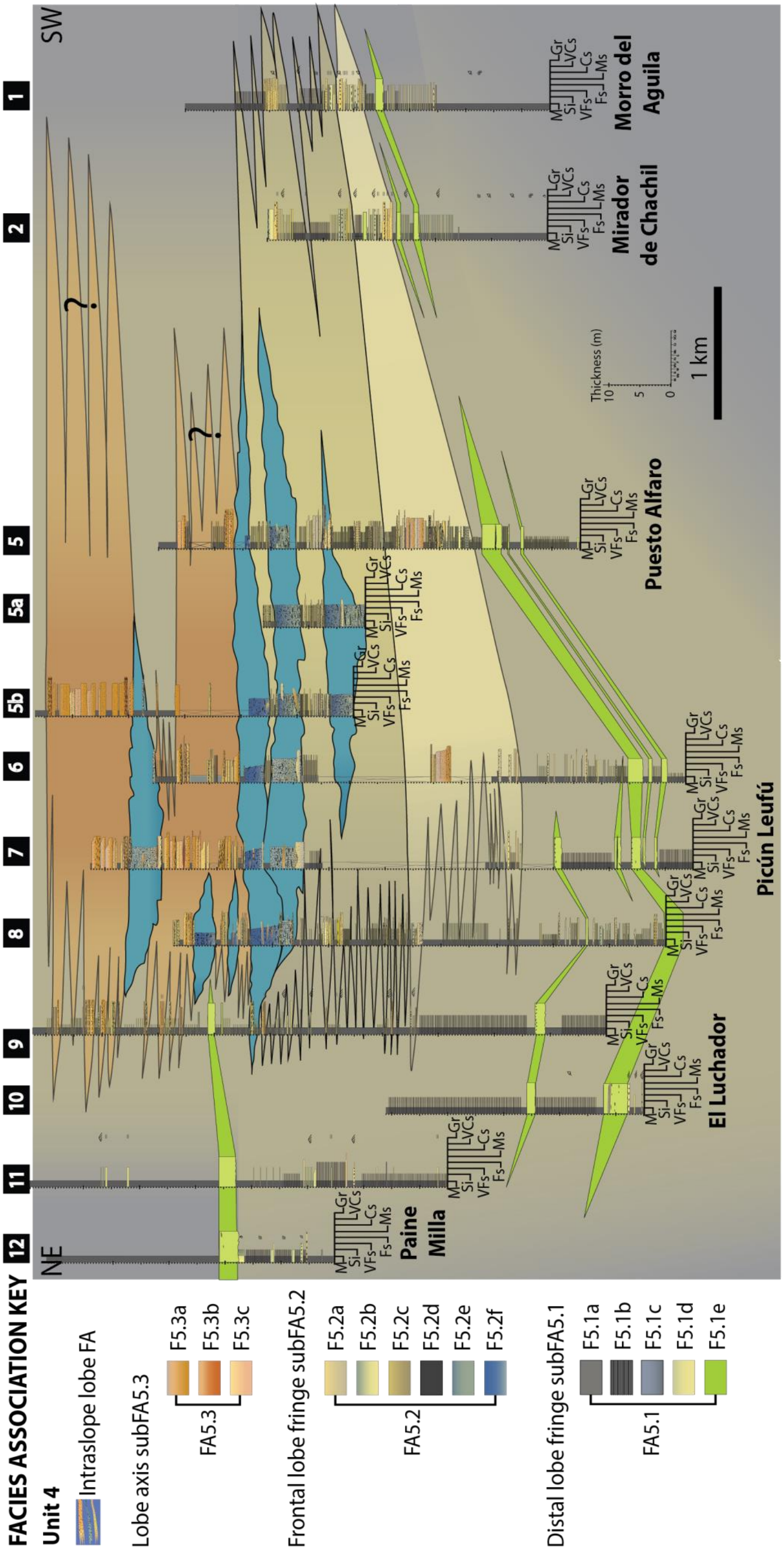

Figure 4.9: Detailed correlation panel showing the internal architecture and spatial facies relationships within Unit 4 (Lower Los Molles Fm.).

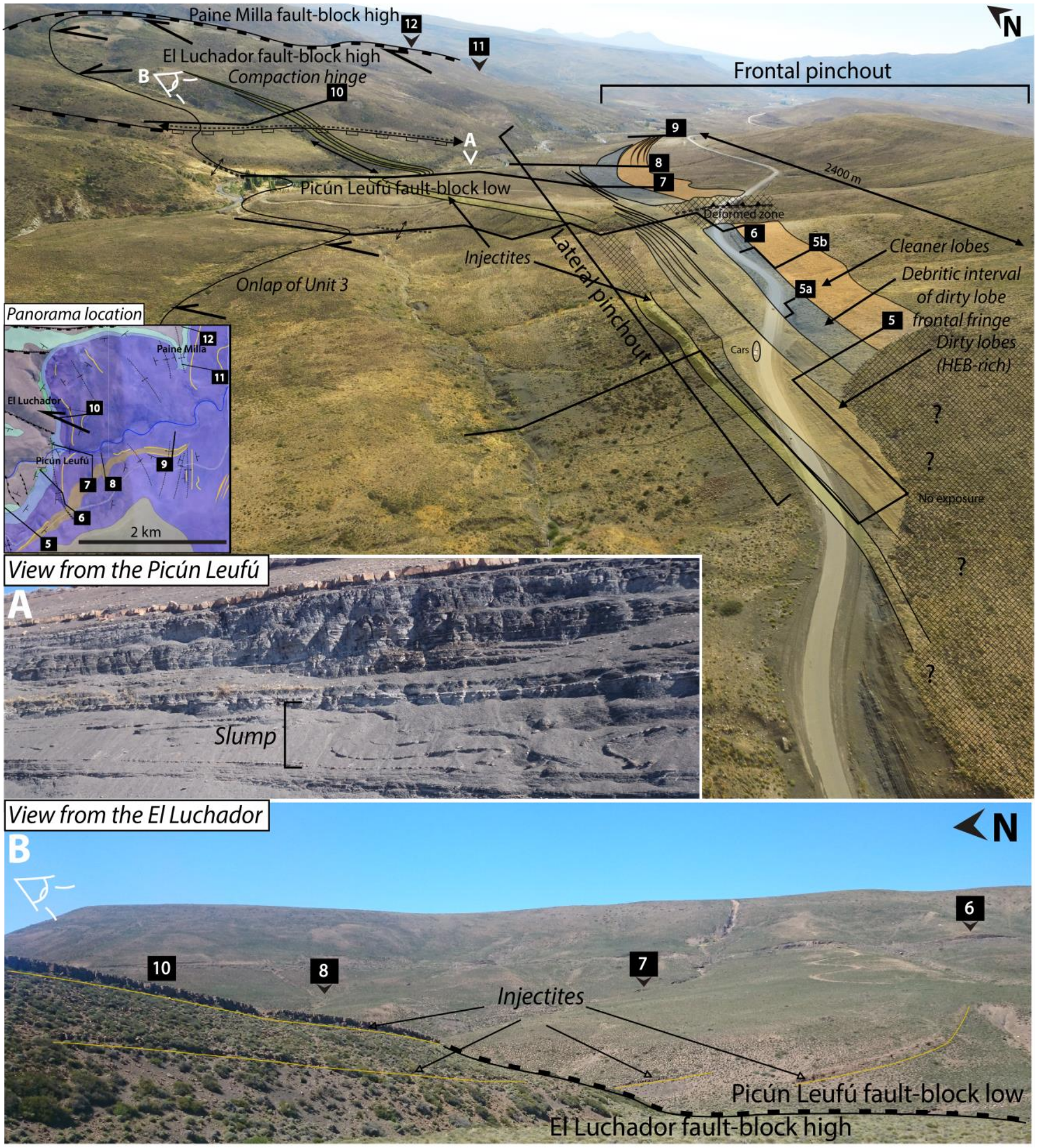

Figure 4.10: Panoramic view from UAV photograph (cars on the road for scale) showing the onlap limit of the Lower Los Molles Fm. (Unit 3) onto the Chachil Fm. (Units 1 and 2), the inferred location of the compaction hinge and distribution of lobe and injectites within Unit 4. Respective lateral and frontal pinchouts are indicated. A- View of slumped mudstone and sandstone interval (1.6 m thick and kilometre-scale). B- View of the stepped sills injectited across the compaction hinge that pinchout across <2 km. Colours for lobes and facies distribution are detailed in fig. 4.9.

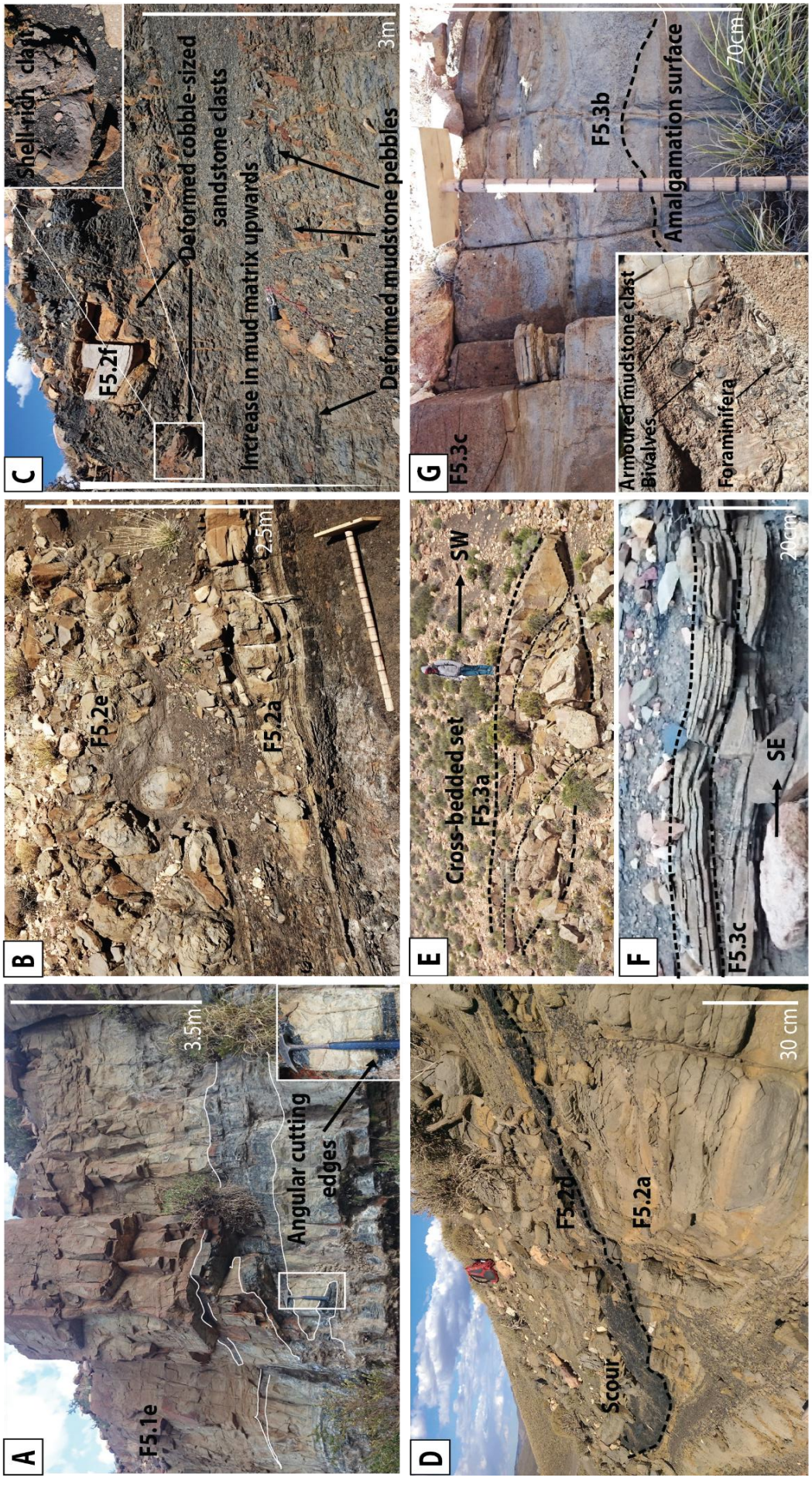
A
F5.1e
3.5m
Angular cutting edges
B
F5.2e
F5.2a
2.5m
C
Shell-rich clast
F5.2f
Deformed cobble-sized sandstone clasts
Increase in mud matrix upwards
Deformed mudstone pebbles
3m
D
F5.2d
F5.2a
Scour
30 cm
E
SW
Cross-bedded set
F5.3a
F
SE
F5.3c
20cm
G
F5.3c
F5.3b
Amalgamation surface
70cm
Armoured mudstone clast
Bivalves
Foraminifera

Figure 4.11: Representative photographs of facies associations. A- Injected sandstone (F5.1e) showing a single injected sill body cutting through mudstone. B- Chaotic muddy sandstone (F5.2e) bearing deformed mudstone and sandstone clasts and heterolithic rafts distributed in a patchy medium- to fine-grained matrix enriched in mud and clast-depleted at top. Bed is scouring and rafting into a pinch and swell, massive, mud-poor sandstone with locally low amplitude dune-scale bedforms developed at top (F5.2a). C- Chaotic sandy mudstone (F5.2f) characterized by a starry night-like matrix with plant material, bearing floating large mudstone, siltstone and sandstone clasts with well-preserved shallow-marine pecten and ostreid shells. D- Massive mud- and clast-poor sandstone division (F5.2a) scoured (0.4 m deep and 3 m wide) and filled by homogeneous massive silty mudstone (F5.2d). E- Massive sandstone (F5.3a) stacked into cross-bedded set of scour fill (up to 5 m long and 1.5-2 m thick). F- Medium-grained sandstone with anisotropic hummock-like bedform showing an asymmetric rounded ripple with low-angle foresets (<5°) draped by sinusoidal parallel laminae sets (F5.3c). G- Amalgamated granular sandstone (F5.3b) grading upwards into medium-grained sandstone with undulose laminations (F5.3c). Armoured mudstone clast with quartz pebbles and surrounding broken bioclasts locally found in granular sandstone (F5.3b) is shown in the frame to the left.

Interpretation

Massive to subtly graded mudstone (F5.1a) suggests deposition from waning fine-grained dilute muddy turbidity currents (Stow and Bowen, 1980). The pin-striped laminated mudstone (F5.1b) was deposited by clay-laden, turbulence-modulated low-density flows, decelerating with possible shear sorting and mixing that formed thin clay- and silt- to sand-bearing stripes (cf. ‘streaky bedding’ of Baas et al., 2016). Graded structured siltstone and sandstone beds (F5.1c, F5.1d) were deposited with tractional reworking beneath intermediate- to low-density turbidity currents allowing differential particle settling (Lowe, 1982; Best and Bridge, 1992). Sparse bioturbation and dissolution of calcitic shells preserved as moulds indicates deposition under poorly oxygenated conditions; as in the oxic zone, organic matter decomposes producing CO_2 and this in turn forms carbonic acid that can lead to dissolution of shells (Aller et al., 1982). The discordant massive sandstone bodies (F5.1e) are interpreted as clastic injectites including minor and thin dykes associated with laterally extensive thick sills (Hurst et al., 2011). The lack of any grading or sedimentary structure, conspicuous cementation and planar trains of subspheroidal vugs suggest polyphased fluid circulation in these sandbodies. Lack of clay matrix, sharp clast margins and “in situ” rafts, indicate the incorporation of lithified host strata during injection of slow moving laminar flows and in other locations, large subangular mudstone clasts mantling top surfaces of sills might result from entrainment and abrasion by erosive injecting flows (Cobain et al., 2015). Muddy heterolithic successions (FA5.1) with narrow grain-size range, beds with gradational top and tabular

extensive geometry for 100s m, lack of amalgamation and sparse bioturbation suggest deposition in a distal lobe fringe setting (Mutti, 1977; Prélat and Hodgson, 2013).

FA5.2: Intraslope lobes- Frontal lobe fringe

Description

FA5.2 comprises thin- to medium-bedded sandy heterolithic successions (<5-25 m thick) (Fig. 4.6-F) that extend for up to 5 kilometres and transitional with FA5.1, vertically and laterally (Fig. 4.9). Beds are rarely amalgamated, and include very poorly sorted sandy mudstone and muddy sandstone facies (i.e. bed divisions) with variable mud matrix and clast content. Bed geometry is irregular, with common lateral facies changes, abrupt thinning with pinchout across <100 m (Figs 4.9 and 4.10). The distinct divisions in individual beds of FA5.2 suggest that these are hybrid event beds (HEBs; *sensu* Haughton et al., 2009) and 3 main bed types are identified (Fig. 4.12).

Type 1 HEBs (F5.2a-F5.2e or F5.2f -F5.2c or F5.1d) (1-7 m thick) comprise a thick (decimetres to metres thick) chaotic muddy sandstone division (F5.2e or F5.2 f) locally either encased between two thinner (10s cm thick) sandier divisions (F5.2a at base and F5.2c or F5.1d at top), or with only the top division present. Typically, the basal sandstone (F5.2a) (30-80 cm thick) is mud-poor, coarse- to medium-grained, and massive with subrounded to subangular mudstone clasts (0.5-8 cm long). The upper part of the sandstone division can show low amplitude dune-scale mud-rich bedforms, and is overlain by a chaotic muddy sandstone (F5.2e) or chaotic sandy mudstone (F5.2f) division (Fig. 4.12). The basal sandy division has an irregular pinch and swell top surface often scoured and filled by homogeneous massive silty mudstone (F5.2d) (10-60 cm thick) (Fig. 4.11-D). Basal sandy divisions (F5.2a) typically pinchout downdip across a few 100s m before the overlying chaotic muddy sandstone pinchout (Fig. 4.11-B and 4.12).

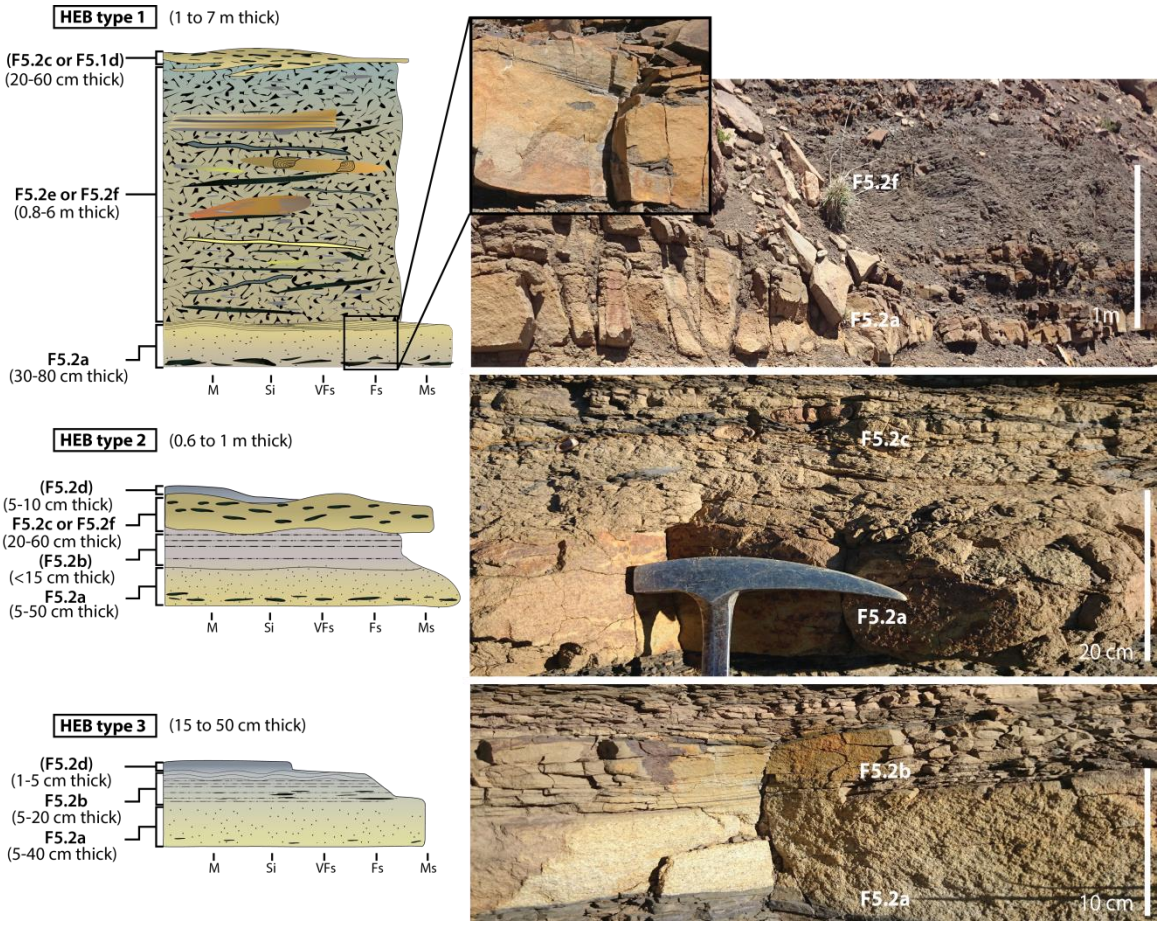

Figure 4.12: Different HEB bed types identified in the intraslope lobes, with some examples in photos. The facies in brackets are only locally present. HEB type 1 comprises a basal massive mud-poor sandstone with low amplitude dune-scale mud-rich bedforms at top (F5.2a) and pinch and swell geometry, sharply overlain and locally scoured by a chaotic muddy sandstone (F5.2e) or sandy mudstone (F5.2f). This is in turn overlain by a clast-rich muddy sandstone (F5.2c) with sheared basal contact, or just draped by structured fine-grained sandstone with planar wavy laminations and current ripples (F5.1d). HEB type 2 comprises a basal massive to laminated mud-poor sandstone (F5.2a), grading into banded muddy sandstone (F5.2b) (that can be absent) and/or a clast-rich muddy sandstone (F5.2c) capped by massive silty mudstone (F5.2d). HEB type 3 comprises a massive mud-poor sandstone (F5.2a) grading into a well-developed banded muddy sandstone (F5.2b) capped by massive silty mudstone (F5.2d).

The chaotic muddy sandstone (F5.2e) (4-6 m thick) is characterized by a very poorly sorted, patchy medium- to fine-grained sand-rich matrix bearing outsized granules and coarse sand grains, abundant mudchips, with erosional base and mounded top (Fig. 4.11-B). The matrix supports pebble- to cobble-sized mudstone and sandstone clasts (5-30 cm long), deformed sand-streaks (30 cm long) and heterolithic rafts (up to 80 cm long), with mud-rich and clast-poor top. The chaotic sandy mudstone division (F5.2f) (0.8-5 m thick) has a very poorly sorted sandy mudstone matrix containing outsized coarse sand grains, plant material and pebble-sized subangular to subrounded mudstone, siltstone and sandstone clasts (5-50 cm long), locally including well-preserved shallow-marine

pecten and ostreid shells (Fig. 4.11-C). The matrix content in these beds increases upwards where the largest clasts are segregated, floating in the matrix (Fig. 4.11-C). Locally, the chaotic division (F5.2e or F5.2f) is overlain by a normally graded sandstone with planar wavy laminations and/or ripples (F5.1d) (<0.2 m thick), or by a clast-rich muddy sandstone (F5.2c) (20-60 cm thick) with irregular bed geometry and a sheared basal contact (shown in Fig. 4.6-F).

Type 2 HEBs (F5.2a-F5.2b-F5.2c-F5.2d) (0.6-1 m thick) comprise a lower, clast- and mud-poor massive sandstone division (F5.2a) (5-50 cm) and an upper poorly sorted argillaceous division of clast-rich muddy sandstone (F5.2c) (20-40 cm thick) (Fig. 4.12). The clast-rich muddy sandstone (F5.2c) consists of poorly sorted chaotic medium-grained sandstone bearing abundant deformed mudstone clasts (2-25 cm long) and mudchips throughout bed. Locally, the upper poorly sorted argillaceous division (F5.2c) overlies a fine-grained banded sandstone division (F5.2b) (<15 cm thick). This banded division is characterized by alternating discontinuous light mud-poor and dark mud-rich bands (1-5 mm up to 2 cm thick) with mudchips, and capped by massive silty mudstone (F5.2d) (5-10 cm thick).

Type 3 HEBs (F5.2a-F5.2b-F5.2d) (15-50 cm thick) comprise a clast- and mud-poor massive sandstone division (F5.2a) (5-40 cm thick) passing upwards into a finer-grained banded sandstone division (F5.2b) (5-20 cm thick) overlain by massive silty mudstone (F5.2d) (few cm thick) (Fig. 4.12).

Interpretation

Type 1 HEBs (Fig. 4.12) are interpreted to reflect deposition from a thick forerunning debris-flow associated with development of a basal concentrated density flow as a result of shear mixing at flow-interfaces (with surrounding seawater) during a single flow event (Amy et al., 2005). In these HEBs, the chaotic muddy sandstone (F5.2e) and sandy mudstone (F5.2f) were likely deposited by intermediate to high yield strength debris-flows, with significant compacted substrate entrainment (Dakin et al., 2013; Talling, 2013). Entrainment of ambient water might have diluted the basal part of the flow enabling substrate erosion and/or hydroplaning (Marr et al., 2001). Fluid mixing at the base of the debris-flow would have played a significant role in decreasing the debris-flow strength below the point it could form a rigid plug flow, resulting in a basal sandy

layer that behaved as a turbulence-modulated clay-laden transitional flow (F5.2a) (Baas et al., 2011). In such a transitional flow, shearing and breaking of clay particles were likely sufficiently high and cohesive bed yield strength sufficiently low, to locally enable bedform development (F5.2a) with propagation of low amplitude bedwaves at the interface with the basal turbulence-modulated transitional flow (Baas et al., 2016). The development of the basal sandy layer, and thus the occurrence of bedforms, as well as variations in the nature of the overlying bed, might be strongly related to lateral changes in debris-flow strength and the irregular erosional behaviour of the debris-flow itself (Talling, 2013). The upper sandy divisions (F5.1d or F5.2c) overlying the debrite might have formed through dilution and shear mixing at the top and front of the debris-flows (Talling et al., 2002; Mohrig and Marr, 2003; Felix et al., 2009). This led either to formation of a turbulent cloud that evolved into a low-density turbidity current (F5.1d), or to increased concentration as a result of mixing with the underlying debris-flow muddy material and evolution into a transient low to intermediate yield strength sandy debris-flow (F5.2c).

In contrast, HEBs 2 and 3, which have similar facies division thickness <1 m (Fig. 4.12), thin across short distances (10s m) and might result from flow bulking through entrainment of clayey substrate, deceleration and flow transformation of an initial high-density turbidity current (Talling et al*.,* 2004*;* Baas et al., 2011; Kane et al., 2017). These HEBs are characterized by banded divisions (F5.2b) deposited in the upper-stage plane bed regime (Baas et al., 2016), well-developed in Type 2 HEBs, and poorly to not developed in Type 3 HEBs at the expense of a debritic division emplaced by a low to intermediate yield strength sandy debris-flow (F5.2c) (Talling et al., 2012). In Type 2 HEBs, the banded division grades upwards into massive silty mudstone (F5.2d) that suggests consolidation after deposition of cohesive silty fluid mud flows (Baas et al., 2011).

Sandy heterolithic successions (FA5.2) show complex spatial facies relationships and bed thickness changes associated with common metre-scale mud-filled scours and hybrid event bed development that record changes in hydrodynamic conditions with variable erosion, deposition and flow transformation, supporting a frontal lobe fringe sub-environment interpretation (Kane et al., 2017; Spychala et al., 2017).

FA5.3: Intraslope lobes- Lobe axis

Description

FA5.3 forms crudely to well-stratified, medium- to thick-bedded sandstone-dominated successions (5-12 m thick) (Figs 4.6-G and H), which transitionally overlie or pass downdip into FA5.2 (Fig. 4.9). Amalgamated contacts with up to 20 cm relief marked by abrupt grain-size breaks and mudstone clasts are common within tabular extensive sandstone packages (1.5-5 m thick), and bed tops can be intensely burrowed by *Planolites and Chondrites*.

Massive to crudely stratified sandstones (F5.3a) form medium to thick beds (0.5 to 1.2 m thick), which are poorly sorted, mud-poor, crudely graded, coarse- to medium-grained and locally structured with diffuse planar parallel or wavy laminations (1-3 cm thick) at top. Beds are often amalgamated, with sharp planar or erosional base (grooves), bearing elongated subrounded lithic granule- to pebble-sized clasts (1-6 cm long). When not amalgamated, beds grade normally to structured medium-grained sandstone (F5.3c) and/or structured fine-grained sandstone (F5.1d). Massive to crudely stratified sandstone beds (F5.3a) are locally stacked into cross-bedded sets (dipping up to 10°, up to 5 m long and 1.5-2 m thick) (Fig. 4.11-E). Granular sandstone (F5.3b) forms thin to medium beds (5-50 cm thick), which are very poorly sorted, very coarse- to coarse-grained and bear abundant subangular granule-sized grains (0.2-0.4 cm) and pebble-size mudstone and siltstone clasts (5-10 cm long) providing an inverse or normal coarse-tail grading to beds. Some mudstone clasts armoured with quartz pebbles and bioclasts including belemnites, bivalves and planktonic foraminifera (*Globorotalia?*) can be found in these beds (Fig. 4.11-G). Beds have erosional base and sharp top, or locally grade upwards into structured medium-grained sandstone (F5.3c). Structured medium-grained sandstone (F5.3c) form thin to medium beds (5-30 cm thick), moderately sorted and normally graded, with non-erosive anisotropic swaley-like low-angle trough-cross-laminations and isotropic (10-25 cm high and wavelengths of few decimetres) or anisotropic hummock-like bedforms. Anisotropic hummock-like bedforms form asymmetric rounded ripples with convex-up lee and stoss side, low-angle foresets (<5°) and are draped by sinusoidal parallel laminae sets (Fig. 4.11-F). F5.3c beds have sharp base and

wavy top overlain by graded structured sandy siltstones (F5.1c) or structured fine-grained sandstone (F5.1d).

Interpretation

Massive to crudely stratified coarse- to medium-grained sandstones (F5.3a) were deposited with high sediment fallout rates that could suppress tractional processes in turbulence-modulated clay-laden transitional flows (Baas et al., 2011). Lower fallout rates and collapse of high-concentration near-bed laminar sheared layers enabled the formation of diffuse laminae (Sumner et al., 2008). Massive granular sandstone with normal or inverse coarse-tail grading (F5.3b) suggests excessive near bed concentration and deposition by high-density to hyperconcentrated density flows (Lowe, 1982; Mulder and Alexander, 2001). Structured medium-grained sandstone (F5.3c) was deposited with traction-and-fallout beneath stratified high-density combined flows, with high sediment fallout rates enabling bedform aggradation in the upper-stage plane bed stability field (Tinterri, 2011). Anisotropic hummock-like structures formed with dominant unidirectional flow component whereas isotropic hummock structures suggest a dominant oscillatory combined flow component (Tinterri, 2011). Given deposition below the storm-wave base, the oscillatory flow component could not originate with surface waves. Alternatively, these bedforms are interpreted to form from interactions of reflected internal wave trains with the near-bed unidirectional flow component, due to flow rebound and deflection against a confining slope (Tinterri, 2011). The effects of confinement and basin configuration are discussed in the section Unit 4.

Medium- to thick-bedded sandstone-dominated successions (FA5.3) comprise amalgamated sandy packages (1.5-5 m thick, ~1-2 kilometres across) of continuous tabular beds with limited basal erosion (<0.6 m deep) and locally narrow and shallow incisional features interpreted as scour-fills (1.5-2 m deep, ~5 m long), suggesting a lobe axis sub-environment (Etienne et al., 2012; Prélat and Hodgson, 2013). The increase in bioturbation intensity compared with FA5.1, marked by burrowed bed base, suggests deposition in a moderately- to well-oxygenated environment, consistent with frequent extrabasinal siliciclastic influxes.

4.6 Synthesis of depositional systems and architecture of tectono-sedimentary units

Genetic facies relationships described in the previous section and stratal relationships across structures allowed four tectono-sedimentary units to be defined (Figs 4.3 and 4.5). Units 1 and 2 belong to the Chachil Fm. and Units 3 and 4 correspond to the Lower Los Molles Fm. Mean bedding dip-directions have been calculated for each unit in the three different geographic zones (Fig. 4.4) in order to show the differences in bed orientation and dip between the different units and structural domains. In each zone, there is a stratigraphic decrease in stratal dip angle, and from a multidirectional dip-direction pattern to a dominant E-SE dip azimuth trend (Fig. 4.4). Analysis of spatial facies distribution, palaeocurrents, thickness changes, stratal bounding surfaces and associated angular relationships between units are used to decipher the late syn-rift to early post-rift evolution of sedimentary systems during the Early Jurassic (Figs 4.2 and 4.13). The terms “proximal” and “distal” refer to the position relative to the graben-horst boundary.

Unit 1

Unit 1 includes carbonate platform deposits (FA1) that onlap onto fault-block highs with an angular unconformity between ~4° and 14°, and proximal periplatform deposits (FA2) that onlap onto fault-block lows with an angular erosional unconformity between ~11° and 15° (Fig. 4.5).

Carbonate platform deposits (FA1) have moderate stratal dip angles (~16 to 25°) with E-SE dip direction on the Morro del Aguila (Zone SW) and Puesto Alfaro (Zone Central) fault-block highs and SW dip direction on the El Luchador fault-block (Zone NE) (Fig. 4.4). Proximal periplatform deposits (FA2) show moderate stratal dip angles (~20°) with E dip direction in the Mirador de Chachil trough (Zone SW) and higher dip angles (~33°) with S dip direction in the Picún Leufú trough (Zone Central) (Fig. 4.4).

The fault-block carbonate platforms (FA1) are detached from the basin margin (*sensu* Bosence, 2005) (Figs 4.7 and 4.13-A), exhibit subtle internal

growth stratal patterns with onlap and pinchout towards the crest of rotated fault-block highs that compartmentalize the immediate hangingwall downdip of the graben-horst border.The Morro del Aguila and the Paine Milla fault-blocks host extensive carbonate platforms (2-5 km length and width, up to 40 m thick) dominated by micritic tuffaceous carbonate (F1a). The platform nucleated on the Puesto Alfaro fault-block highs, and is dominated by fossiliferous laminated carbonate (F1b) (Fig. 4.7). The fauna of Unit 1 records the flourishing of a suspension feeder-dominated carbonate-secreting benthos including subtidal to intertidal encrusters (scleractinian corals, bryozoans, crinoids) and shelly biocalcifiers (bivalves, brachiopods) which insured productivity of the warm-temperate carbonate system (cf. Flügel, 2004). Onto the graben-horst border, a tide-influenced inner carbonate platform with tidal flats and subtidal ponds developed and recorded shallowing-upward cycles with progradation of intertidal and supratidal deposits onto subtidal deposits (Armella et al., 2016). Carbonate sedimentation on the graben-horst border was strongly affected by ash-fall and episodic subaerial exposure indicated by oxide coated surfaces, with Glossifungites ichnofacies representing firmground suites (Armella et al., 2016). Nonetheless, subaerial exposure does not seem to have affected fault-block highs in the graben. Therefore, a combination of subaerial degradation on the horst border and enhanced current erosion of fault-block highs might have controlled extensive reworking of the poorly consolidated carbonate platform deposits (FA1) and volcano-sedimentary substrate into proximal periplatform deposits (FA2).

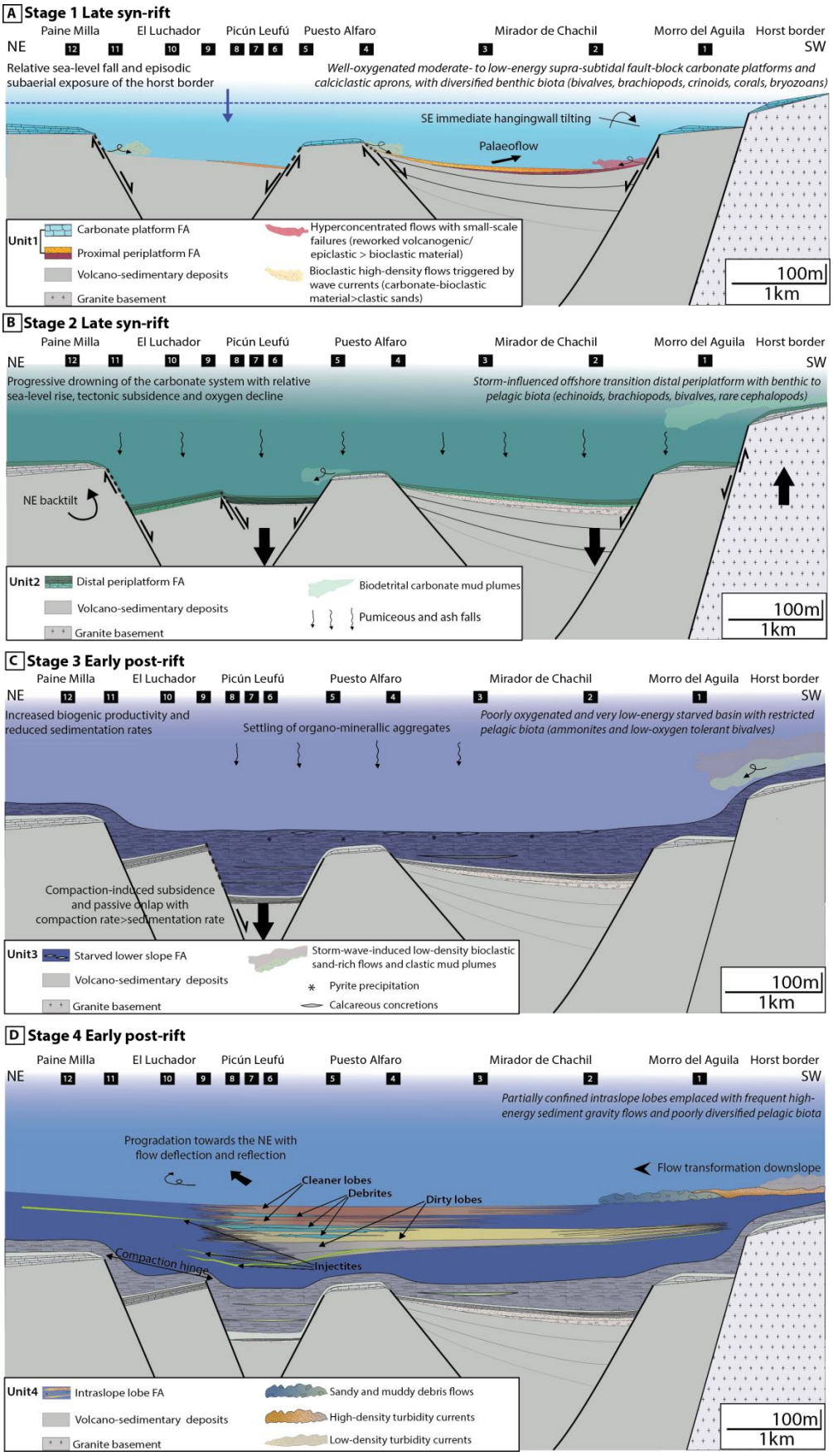

Figure 4.13: Palaeogeographic evolution of the Chachil Graben illustrated in schematic cross sections (not restored) showing changes of depositional setting, facies distribution and inferred fault-block motion during deposition of the units (see the precise timing, fig. 4.2). Section numbers refer to spatial location on the map shown in fig. 4.3-A.

Mixed carbonate-clastic proximal periplatform deposits (FA2) accumulated in the Mirador de Chachil and Picún Leufú troughs with onlap onto volcano-sedimentary syn-rift deposits (Lapa Fm.) and pinchout towards intervening fault-block highs (Figs 4.7 and 4.13-A). The polymict composition of pebbly conglomerates (F2a), dominated by brecciated reworked volcaniclastic material, suggests deposition by hyperconcentrated density flows that originated from small-scale failures triggered by fault-block tilting and destabilization of primary volcanic deposits (Lapa Fm.) (Fig. 4.13-A). Similar deposits interpreted as basal conglomerates of the Chachil Fm. have been recognized in subsurface in the southeast of the Neuquén Basin, and are interpreted as evidence for subaerial exposure and degradation of the Precuyano Cycle deposits (Schiuma and Llambías, 2008). Calciturbidite deposits (F2b) can be compared to carbonate platform-derived calciclastic aprons lacking internal organization and with local development of basal lags in small channel-fills (Braga et al., 2001; Payros and Pujalte, 2008). The stratigraphic increase in proportion and sorting of grainy allochemical carbonate material recorded throughout FA2 might reflect the decreased availability of the volcano-sedimentary syn-rift substrate for reworking due to progressive onlap in fault-block lows.

SSE-oriented palaeocurrents (Fig. 4.5), stratal fanning of proximal periplatform deposits (FA2) in the Mirador de Chachil trough (5 to 25 m thick across 3-4 km) towards the Morro del Aguila fault-block high, and relative sea-level fall and subaerial exposure of the graben-horst border, suggest active faulting and southeastwards tilt of the Mirador de Chachil fault-block low. Facies distribution, depositional geometries and variability of stratal dip azimuths across structures reflect active fault-block rotation during deposition of Unit 1 and support its late syn-rift development (Cross and Bosence, 2008; Dorobek, 2008).

Unit 2

Unit 2 corresponds to mud-rich mixed carbonate-clastic distal periplatform deposits (FA3) that form wedge-shaped packages in fault-block lows, thin drapes across fault-block highs, and onlap onto Unit 1 with an angular unconformity between ~3° and 10° (Fig. 4.5). In the Mirador de Chachil proximal trough (Zone SW) and Picún Leufú distal trough (Zone Central), moderate stratal dip angles (~18 to 32°) and consistent E-SE dip direction of Unit 2 contrast with higher dip

angles (~62°) of deformed strata with NE dip direction across the El Luchador fault-block (Zone NE) (Fig. 4.4).

Bioclastic carbonate (F3a) deposited in the Mirador de Chachil proximal trough shows thinning (20 to 12 m thick across 3-4 km) and onlap onto calciturbidite (F2b) towards the Puesto Alfaro fault-block high (Figs 4.5 and 4.7). These deposits are overlain by interbedded spiculitic carbonate and marlstone (F3b-c) that thin (15 to 5 m thick) towards the Puesto Alfaro fault-block high. Bioclastic carbonate (F3a) also thins (18 to 8 m thick across <2 km) from the El Luchador fault-block high towards the Picún Leufú trough (Figs 4.7 and 4.13-B). Overlying interbedded spiculitic carbonate and marlstone (F3b-c) thin (10 to 5 m thick) from the Picún Leufú trough towards the El Luchador fault-block high (Figs 4.7 and 4.13-B). These deposits present *Chondrite* and *Trichichnus* traces, which record a decrease of oxygen levels at the sediment-water interface. On the Morro del Aguila, Puesto Alfaro and Paine Milla fault-block highs, bioclastic and spiculitic carbonate (F3a-b) are absent, and carbonate platform deposits (F1a-b) are draped by marlstone (F3c) (5-10 m thick) (Figs 4.7 and 4.13-B). This contact is marked by *Pascichnia* grazing traces at the top of carbonate platform deposits representing a condensed surface onto fault-block highs due to sedimentation under poorly oxygenated and relatively deep bottom water conditions (Ekdale and Mason, 1988). A similar situation is observed on the horst border of the graben where the carbonate platform deposits are overlain by marlstone (e.g. Armella et al., 2016).

The stratigraphic deepening recorded by Unit 2 provides strong evidence for fault-controlled subsidence given that tectonically induced relative sea-level changes could outpace the low amplitude and rates of eustatic rise during Early Jurassic greenhouse time (cf. Ravnås and Steel, 1998). Bathymetric deepening promoted rising of the storm-wave base to the level of the most elevated fault-block highs bounding the graben. This promoted extensive reworking of unconsolidated carbonate platforms (FA1) redeposited in fault-block lows as allochemical fine biodetrital carbonate material (FA3) (e.g. Halfar et al., 2004). The thinning- and fining-upward trend of Unit 2 deposits in the Mirador de Chachil and Picún Leufú troughs and thickening towards the Morro del Aguila and Puesto Alfaro fault-block highs dominated by condensed sedimentation support syn-depositional relative sea-level rise and differential subsidence (Fig. 4.13-B). The tectonic differential subsidence pattern suggests an increased displacement

along the graben-horst border fault and localized normal faulting in the graben with formation of the El Luchador fault-block high (Fig. 4.13-B).

Tectonic subsidence and relative sea-level rise outpaced carbonate sedimentation rates and controlled retrogradation of the carbonate system. Drowning of the carbonate system culminated with establishment of a deep-marine environment and reduction of oxygen recorded near the top of Unit 2 at depocentre-scale, from the horst border to the interior of the Chachil graben. The deterioration of chemical and physical conditions with tectonically-induced relative sea-level rise contributed to drowning of the carbonate factory across the entire depocentre undergoing continuous subsidence (e.g. Santantonio, 1994; Ruiz-Ortiz et al., 2004; Navarro et al., 2012).

Unit 3

Unit 3 forms a calcareous mudstone-dominated succession (FA4) which overlies Unit 2 locally with an angular discordance between ~3° to 9° at the graben margins. Dip angles are moderate (~16° to 25°) with general SE dip direction in the Mirador de Chachil proximal trough (Zone SW) and Picún Leufú distal trough (Zone Central), contrasting with higher dip angles (~57°) measured in the deformed strata of the El Luchador fault-block (Zone NE) with some E-SE dip direction (Fig. 4.4).

The base of Unit 3 infills the intrabasinal topography inherited at the top of Unit 2 burying the Puesto Alfaro fault-block highs, and therefore records a change of basin geometry. This is supported by the thinning of Unit 3 (<20 m thick) to the NE across the El Luchador and Paine Milla fault-block highs and to the SW across the Morro del Aguila, and by the thickening (70 to 120 m thick) from the Mirador de Chachil to Picún Leufú trough (Fig. 4.5). The deformed steeply dipping strata of Unit 3 near the El Luchador fault-block (Zone NE) is associated with abrupt mudstone thickening (up to 100 m offset of compacted strata) across less than 2 km from the Paine Milla platform towards the adjacent Picún Leufú trough (Figs 4.5 and 4.13-C). This thickness change occurred across NW-SE striking and SW dipping rift faults involved in the formation of the El Luchador fault-block (Fig. 4.13-B). The potential process that caused small-scale deformation recorded in Unit 3 is discussed.

The occurrence of *Posidonotis cancellata* (Leanza) shell mold pavements in the lower part of Los Molles Fm. has been reported in TOC-rich mudstone of another marine rift depocentre, located 20 km southeast of the Chachil Graben (Al-Suwaidi et al., 2016). Al-Suwaidi et al. (2016) report negative carbon isotope excursions associated with the TOAE during the late *Tenuicostatum*-early *Dactylioceras Hoelderi* Andean Ammonite Biozone (AAB) (Fig. 4.2). The TOAE might be recorded in Unit 3, which spans the latest Pliensbachian-Early Toarcian in the Chachil Graben, marked by a reduction of benthic fauna diversity recorded from Unit 2 to Unit 3 (Fig. 4.2) and variable sedimentation rates related to important storm activity under a warm semi-arid climate (cf. Volkheimer et al., 2008). Similar conditions prevailed over southwestern Gondwana and altered the deposition of organic black shales which documents the TOAE in the northern hemisphere where a warm and humid climate favoured the development of anoxia (Dera and Donnadieu, 2012; Fantasia et al., 2018). The stratigraphic evolution from carbonate to terrigenous mudstone recorded at the top of Unit 3 (Fig. 4.6-D) marks the transition to Unit 4 and indicates an increase of fluvio-deltaic runoff which could be related to climatic change towards more humid conditions from the early Late Toarcian (cf. Volkheimer et al., 2008).

Unit 4

Unit 4 represents a submarine lobe complex (*sensu* Prélat et al., 2009) whose base is transitional with, or sub-concordant to, Unit 3 except around the El Luchador fault-block (Zone NE), where it shows an angular discordance between ~<1-8° (up to 36° onto deformed strata) onto Unit 3. Dip angles of Unit 4 are moderate (~16° to 21°) with consistent E-SE dip direction (Fig. 4.4). Unit 4 shows similar thickness changes as the underlying Unit 3 across structures, thickening (150-170 m thick) from the Mirador de Chachil to the Picún Leufú troughs and thinning (50-100 m) across the Morro del Aguila, El Luchador and Paine Milla fault-block highs (Figs 4.5 and 4.9).

The lower part of Unit 4 dominated by muddy heterolithic strata corresponds to distal lobe fringes (FA5.1) with a low sandstone proportion (Figs 4.9 and 4.10). The upper part of Unit 4 is characterized by a higher proportion of sandstone and includes stacked sandy heterolithic strata in proximal lobe fringes (FA5.2),

sandstone-dominated strata in lobe axes (FA5.3), and minor muddy heterolithic strata in distal lobe fringes (FA5.1) (Fig. 4.9). Individual lobes have a low aspect ratio (1.5-5 m thick, few kms across) and collectively these deposits form a 50-70 m thick, ~5 km minimum wide and 6-8 km long intraslope lobe complex (Figs 4.9 and 4.10). The intraslope lobe complex comprises basal dirty lobes (Fig. 4.6-G), mainly represented by frontal lobe fringe deposits with a high proportion of thin HEBs (mainly type 2 and 3) (Fig. 4.12). The dirty lobe deposits are characterized by a finer grain-size, argillaceous matrix and high clast content. The overlying cleaner lobes (Fig. 4.6-H) include lobe axis deposits with thick HEBs (Type 1) and frontal lobe fringe deposits with few thin HEBs (mainly Type 2). The cleaner lobe deposits are characterized by thicker beds, coarser grain-size and low argillaceous matrix and clast content (Figs 4.9 and 4.13).

The intraslope lobe complex within Unit 4 records a rapid increase of extrabasinal siliciclastic supply, favouring oxygenation and increase of bioturbation intensity and diversity (Figs 4.2 and 4.13-D), consistent with the warming-up humid climate (cf. Volkheimer et al., 2008). The increase in volume and frequency of sand-rich sediment gravity flows over time, associated with the stratigraphic increase in bed thickness and grain-size, amalgamation rate, and increasing sand content upwards in the lobes of Unit 4 suggest progradation of the lobe complex (Crabaugh and Steel, 2004; Macdonald et al., 2011). The slightly shingled pattern of lobe sub-environments, high thickness and facies variability across short distances (100s m) and evidence for palaeoflow reflection and deflection associated with combined flow bedforms, may result from the development of lobes in a partially confined setting (Fig. 4.9). Partial confinement is supported by (i) the variable palaeocurrent directions and abrupt thinning of amalgamated sandstone lobe bedsets (1.5-5 m thick) across a few kilometres, passing down-dip into thinner sandstone beds (10s cm thick) without marked grain-size change or improvement in sorting (thin HEB-rich), (ii) the frontal terminations of these lobe bedsets that offset the abrupt pinchout of metres-thick debrites and (iii) development of a range of combined flow bedforms and of widespread erosion and scouring, even in lobe fringe settings, along lateral margins of lobe complex depocentre (Figs 4.9 and 4.13-D).

Intrabasinal topography inherited across the El Luchador fault-block high formed a S-SW-facing oblique counterslope that influenced sediment gravity flow behavior and direction. Confinement indicators record deviation of the general

NE flow direction mainly towards the SE and rarely SW (Fig. 4.5). This is associated with development of opposite direction current-ripple laminations (Fig. 4.8F) and small-scale anisotropic hummocky-like structures (Fig. 4.11-D) showing azimuth dispersion up to 180° and sole marks (mainly grooves) with average azimuth dispersion of 45° (see palaeocurrents Fig. 4.5). Therefore, the development of combined flows (Tinterri, 2011) is associated with oblique flow reflection and deflection (Kneller, 1991; Amy et al., 2004) against the counterslope flanking the El Luchador fault-block high (Fig. 4.13-D).

The presence of the sill-dominated injectites network stratigraphically above, below and lateral to the lobe complex that onlaps the Paine Milla fault-block high further supports substantial topographic confinement of lobes (e.g. Cobain et al., 2017). Laterally extensive sills (1.5-3.8 m thick, 5-8 km across) step outwards from the lateral lobe complex margins, and split with abrupt pinchout terminations across <1 km above the El Luchador fault-block high (Fig. 4.10). The linear ridges present on the top surface of some sills show a general NE-SW orientation which indicates a NW-SE direction of crack propagation, approximately parallel to the S-SW-facing counterslope (e.g. Kane, 2010). This together with the abrupt pinchout of the sills at this location might reflect the influence of the buried El Luchador fault-block high on the morphology of the injectite complex (e.g. Cobain et al., 2017).

Widespread expulsion of basinal fluids has been reported locally with the formation of methane seepages associated with development of bioherms at the seabed during deposition of the Lower Los Molles Fm. (Gómez-Pérez, 2003). The trigger for injection may have been a combination of (i) deep-seated hot basinal fluid and gas expulsion through rift faults related to mature hydrocarbon plumbing systems in the syn-rift deposits, or sourced from crustal magmatic activity, and (ii) differential loading and compaction of buried strata, contributed to overpressure build-up (e.g. Boehm and Moore, 2002; Kane, 2010).

4.7 Discussion

4.7.1 Early post-rift inherited topography

Depositional patterns in early post-rift strata of the Lower Los Molles Fm. in the Chachil Graben are controlled by local deformation, which is unrelated to regional extensional tectonics. Here, the processes and significance of this deformation are discussed.

Unit 3

Local thickness change at the transition between the Paine Milla-El Luchador fault-blocks and the adjacent Picún Leufú trough must have been accommodated across a major buried/blind rift structure during deposition of Unit 3 (Fig. 4.3-A). The limited facies and thickness changes in Unit 2 across this fault do not support a large bathymetric difference between the El Luchador fault-block high and the adjacent Picún Leufú trough at this time (Figs 4.7 and 4.13-B). Therefore, additional differential subsidence across this fault was required at the end of deposition of Unit 2 to create accommodation associated with the significant thickness change (>100 m compacted strata) observed at this location in the mudstone-dominated succession of Unit 3 (Figs 4.13-B and C). The presence of syn-depositional topography across the fault during deposition of Unit 3 is further supported by the facies change from calcareous mudstone with interbedded siltstone and bioclastic sandstone beds in the Picún Leufú trough, to condensed homogeneous mudstone on the El Luchador and Paine Milla fault-block highs. These facies changes are consistent with compacted sedimentation rates in Unit 3 of 5.3 m/Myr on the structurally elevated fault-block highs, and 35.7 m/Myr in the axis of the Picún Leufú trough, based on measured thickness (Fig. 4.5) and the estimated age of Unit 3 for sedimentation rate (Fig. 4.2). Comparable compacted sedimentation rates are reported for the Kimmeridge Clay Fm. (20-45 m/Myr, cf. McArthur et al., 2013), which similarly formed an extensive, organic-rich mudstone blanket across rift topography in the North Sea. Moreover, stratal geometries of Unit 3 and Unit 4 record the long-lived influence of this fault-block relief, which formed a compaction hinge above the inferred blind fault tip, and that controlled deep-water sediment dispersal during deposition of Unit 4 (Figs 4.13-

D and 4.14). If syn-depositional relief was formed by active extensional tectonics, one might expect near-fault damage (e.g. fracturing and folding), the deposition of coarse-grained event beds in the proximal hangingwall, and abrupt thickness change within Unit 3 in other locations of the graben. None of these are observed, hence other possible controls on the generated relief are considered.

It is suggested that syn-depositional relief developed due to differential compaction of early syn-rift strata of the Lapa Fm. (cf. Franzese et al., 2006) across the pre-existing rift fault bounding the Picún Leufú trough. Thicker deposits at this location compacted more than the thinner succession in the footwall blocks (Paine Milla and El Luchador). In other locations of the Neuquén Basin, small-scale normal faulting, wedging and graben-scale folding of Early Jurassic strata around inherited rift structures are similarly related to differential compaction of the deeply buried syn-rift succession (Cristallini et al., 2006). Compaction-induced surface deformation, including small-scale faulting and large-scale folding, can result from differential compaction across irregular rigid basement topography and/or arise due to lithological heterogeneity (e.g. Barr, 1991; Skuce, 1996; Cristallini et al., 2006; Lohr and Underhill, 2015). Compaction-driven surface deformation proceeds over relatively short timescale (i.e. a few millions of years) and might have outpaced the low sedimentation rate during deposition of Unit 3. This increased the fault scarp relief and the gradient of the hangingwall in the Picún Leufú trough, which exceeded the critical sediment stability threshold (5°) for carbonate muds (cf. Kenter, 1990), triggering gravitational remobilisation and downslope redistribution of fine-grained sediment. As a result, Unit 3 progressively healed the fault-scarp relief (i.e. “parallel onlap fill” Cartwright, 1991). Most critically, our observations indicate that the timing of active (i.e. syn-rift) normal faulting in the Los Molles Fm. could be erroneously inferred based on relatively subtle changes in thickness and facies changes, which instead are controlled by post-rift differential compaction (cf. Carminati and Santantonio, 2005).

Unit 4

Unit 4 is characterized by thinning with onlap updip towards the graben-horst margin, thickening and dipping towards the E-NE into the graben. Unit 4 onlaps onto basin margins defining a broad (~6 km across), NNE-trending, low amplitude monocline, slightly oblique to the NNW-trending graben-horst margin (Figs 4.1-C and 4.3-A). The absence or lack of preserved hangingwall strata above the uplifted graben-horst margin and the gentle dip of Unit 4, together suggest the monocline did not grow in response to horizontal shortening and related basin inversion. Instead, the monocline could have developed during the early post-rift in response to differential compaction across the southern margin of the graben (e.g. Barr, 1991; Cartwright, 1991; Skuce, 1996; Monaldi et al., 2008; López-Gamundí and Barragan, 2012; Lohr and Underhill, 2015). The early post-rift strata recorded differential compaction, with thickening into an area of enhanced accommodation in the centre of the graben, with development of low amplitude, large-scale monoclinal folding and localized formation of a compaction hinge above a rift structure (Figs 4.1-C and 4.10). Therefore, the impact of compaction-induced deformation on early post-rift sedimentation patterns should receive more attention given its potential to form combined stratigraphic and structural traps and influence reservoir distribution (e.g. López-Gamundí and Barragan, 2012; Lohr and Underhill, 2015; Balázs et al., 2017).

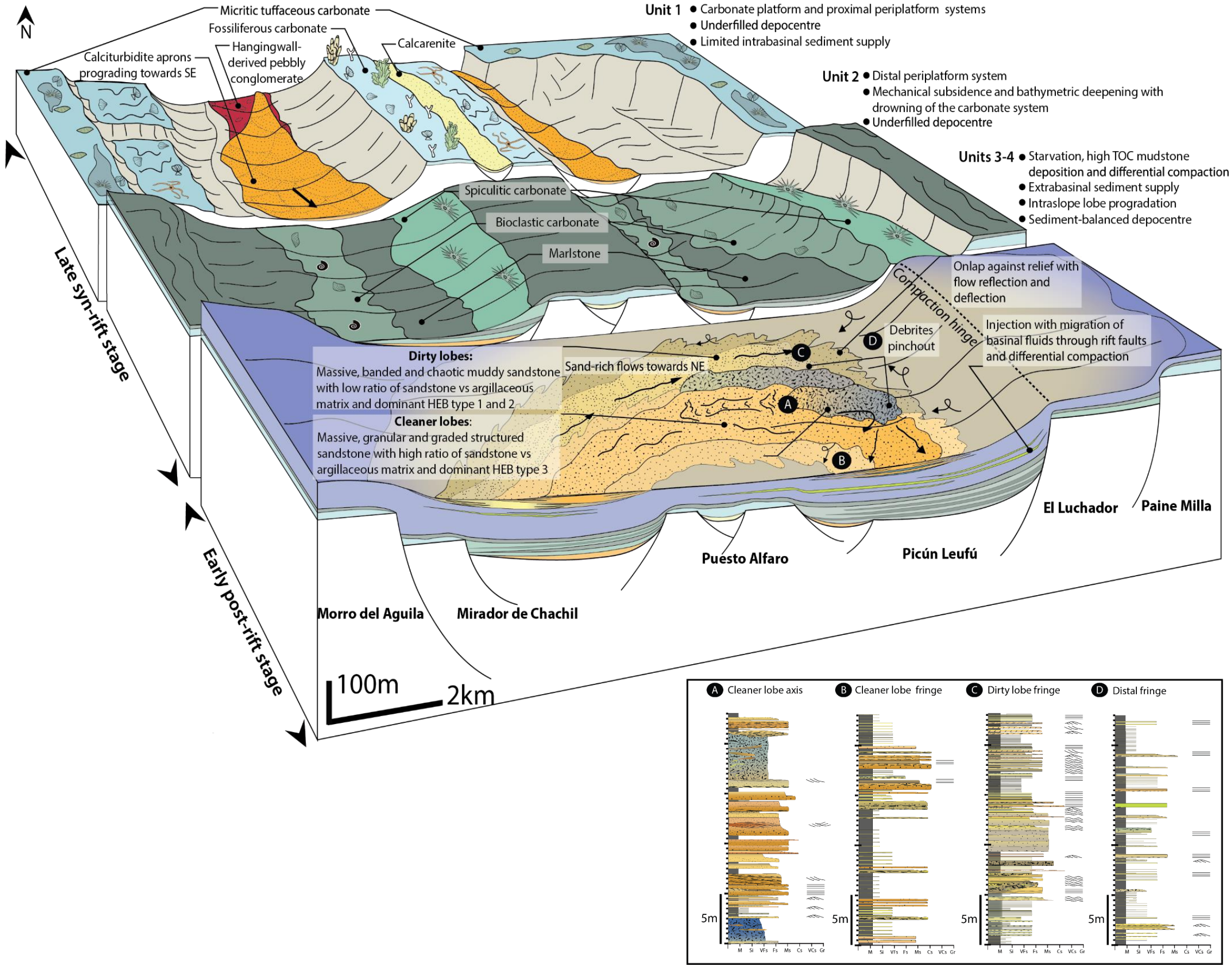

Figure 4.14: Block diagram showing the evolution of sedimentation patterns and interactions with topography in the Chachil Graben from an underfilled to a sediment-balanced depocentre during the syn- to post-rift transition, detailing relationships between facies distribution and structures. Detailed logs in lobes show typical facies association of cleaner lobes rich in HEB type 1 and dirty lobes rich in HEB type 2 and 3, and distal lobe fringe deposits.

4.7.2 Controls on sedimentation during the syn- to post-rift transition

Using outcrops of the Lower Los Molles in the Chachil Graben, a detailed analysis of the stratigraphic record of the transition from active syn-rift extension to tectonically quiescence conditions is provided to characterise the early post-rift. Furthermore, the key role compaction-related deformation has in controlling basin physiography, sediment dispersal and stratigraphic architecture is highlighted. The transition from the late syn-rift to early post-rift is marked by a change from intrabasinal carbonate to extrabasinal siliciclastic sedimentation regime. Stratal stacking patterns changes from retrogradation to progradation, with the depocentre evolving from underfilled to sediment-balanced conditions (Figs 4.2 and 4.14). Rift basin topography, tectonic and climate appear to be the key factors controlling these changes.

Late syn-rift

Linkage of the fault border system of the Chachil Graben early during the rift climax (Franzese et al., 2006), and the presence of resistant granitic and volcanic rocks in the fault footwall might have prevented the development of local drainage catchments during the late syn-rift (Leeder et al., 1998). The relatively low-relief inherited from the overfilled depocentre configuration (*sensu* Muravchik et al., 2011) further limited intrabasinal clastic sediment supply and reworking of volcano-sedimentary syn-rift deposits (Lapa Fm.). In contrast, steeper gradients preserved in the adjacent Catán-Lil Graben promoted intense fault-block degradation and accumulation of late syn-rift fan deltas (Muravchik et al., 2014).

Growth of normal faults during the late syn-rift segmented the immediate hangingwall downdip of the graben-horst border and induced a structural pattern that differed from the rift climax structural configuration (cf. Franzese et al., 2006). These conditions, together with the semi-arid climate (cf. Volkheimer et al., 2008) that was characterised by reduced precipitation, erosion, and both intrabasinal and extrabasinal sediment delivery, permitted the late syn-rift development of the carbonate system in the Chachil Graben (Fig. 4.14). Rapid marine flooding associated with fault linkage and rapid subsidence also suppressed sediment input by reducing the size of intrabasinal drainage catchments. Thus, instead of acting as an efficient clastic intrabasinal source during the late syn-rift and early

post-rift, the horst border of the Chachil Graben underwent rapid marine flooding and acted as a submerged barrier that limited clastic influx in the graben. Fault-block highs controlled the dimensions and morphology of shallow-marine isolated carbonate platforms and prevented their progradation in fault-block lows, which instead received mixed carbonate-clastic deposits reworked from the proximal periplatform (Fig. 4.14). With increasing relative sea-level rise and tectonic subsidence, the carbonate platform supplied greater flux of fine-grained sediment leeward of the graben-horst border (e.g. Dorobek, 2008). This resulted in retrogradation of the system and accumulation of distal periplatform mixed carbonate-clastic mud-rich deposits in fault-block lows, whereas condensed sedimentation occurred over carbonate platform deposits onto fault-block highs (Fig. 4.14). Syn-rift deformation during deposition of the Chachil Fm. prevented the development of fault-block carbonate platforms in down-faulted depressions or the coalescence of the system into a larger composite platform, which would have required tectonic quiescence and subdued fault-related relief (Dorobek, 2008). However, the warm-temperate nature of the carbonate system played a key role in its organisation and evolution across rift structures as the lack of early cementation and binding of these warm-temperate carbonate deposits favoured their reworking and resedimentation into allochemical biodetrital carbonate material into fault-block lows. However, these warm-temperate systems remain poorly documented in rift settings (Gulf of California, Halfar et al., 2004) compared to their tropical counterparts (Gulf of Aden and Suez Rift, Cross and Bosence, 2008). The late syn-rift carbonate sedimentation and drowning of the system, in response to increased rates of fault-controlled subsidence, meant the Chachil Graben evolved into an underfilled depocentre; this had implications for the subsequent development of the early post-rift clastic system (Fig. 4.14).

Early post-rift

During the early post-rift, potential local intrabasinal fault-block sources were rapidly submerged and mud-draped as a consequence of high subsidence rates related to the back-arc evolution of the Neuquén Basin. Local (i.e. intrabasinal) sediment supply with degradation of intrabasinal fault-block highs was limited or absent at this time. This evolution contrasts with many examples of marine rift basins that are characterized by an early post-rift configuration with

local intrabasinal clastic supply driven by subaqueous or subaerial degradation of fault-block highs (e.g. Zachariah et al., 2009; Jarsve et al., 2014; Henstra et al., 2016).

An extrabasinal sediment source for the early post-rift lobes is suggested by the palaeocurrents with respect to rift structures (i.e. axial not transverse) and sandstone composition, which does not reflect transverse supply from the granitic bedrock forming the footwall blocks. The high amount of terrestrial organic material (wood, leaves, carbonaceous fragments), the presence of ostreid-bearing clasts found in some of the mud-rich debrites of dirty lobes (Fig. 4.11-C), and the abundance of armoured mudstone clasts and bioclasts (belemnites, bivalves and planktonic foraminifera) in some sandstones (Fig. 4.11-G), support hinterland-sourced, proximal shelf to slope sediments (Hodgson, 2009; Migeon et al., 2010; Talling et al., 2010). An extrabasinal source with high sediment yield was required to develop the coarsening-upward intraslope lobe succession that prograded in the graben, and caused the Chachil Graben to evolve into a sediment-balanced depocentre during the early post-rift (Figs 4.2 and 4.14). The warm humid climate that prevailed from the early Late Toarcian (cf. Volkheimer et al., 2008) provided conditions suitable for high amounts of erosion and riverine runoff, which together delivered high volumes of sediment towards the basin despite rising sea-level and overall highstand conditions (e.g. Leeder et al., 1998; Yu et al., 2013; Balázs et al., 2017).

The inherited rift topography preserved in the southwestern Neuquén Basin (Legarreta and Uliana, 1996; Burgess et al., 2000; Gómez Omil et al., 2002) would have promoted trapping of clastic material along the shelf-slope system located >20-25 km southeast of the Chachil Graben, close to the hinterland source (see Fig. 4.1-A). This basin configuration, along with the deeply (up to 400 m) submerged inherited rift topography and semi-arid conditions (Fig. 4.2) at the onset of the early post-rift, might have delayed extrabasinal siliciclastic influx in distal depocentres of the southern shelf-slope basin margin system (Fig. 4.2). Consequently, deposition of thick organic-rich calcareous mud across the inherited rift topography occurred in distal depocentres starved of clastic supply. This promoted the long-lived preservation of the rift basin physiography enhanced by differential compaction (Fig. 4.14). In a marine rift basin dominated by extrabasinal sediment supply, inherited rift topography plays a major role in trapping sediment in proximal parts of the basin margin during the early post-rift.

Once proximal depocentres are filled, sediment bypass downslope permits the supply to more distal depocentres (Lien, 2005; Soares et al., 2012). Despite the delayed extrabasinal siliciclastic supply, the development of a distal sand-rich depocentre during the early post-rift in the Chachil Graben indicates that sediment gravity flows might have reached the graben across subdued topography.

4.7.3 Implications for characteristics of early post-rift lobe complexes

The depositional architecture and facies distribution of intraslope lobe complex in the Lower Los Molles Fm. provide rare insights into the interaction of sand-rich sediment gravity flows with inherited early post-rift intrabasinal relief (Haughton et al., 2003; Southern et al., 2017; Dodd et al., 2019). The stratigraphic change from dirty to cleaner lobes (Figs 4.9 and 4.10) could be interpreted to record the variability of lobe environments at an onlap position, with the cleaner lobes representing lobe axis deposits passing downdip into dirty frontal lobe fringe deposits (i.e. time transgressive facies tract onlap of Pyles and Jennette, 2009). Onlap-related trends such as these are interpreted to result from local topographic confinement and HEB development arising from a forced flow transformation (e.g. Pyles and Jennette, 2009; Patacci et al., 2014). However, this lateral trend is not observed, as the cleaner lobes do not pass downdip into the same HEB-rich dirty frontal lobe fringe deposits that they overlie (Figs 4.9 and 4.14). Another potential mechanism for such a stratigraphic change is the progressive healing of intrabasinal relief formed by the compaction hinge obstructing the flow pathway, as early healing of relief could have limited flow interactions with the inherited topography. However, the presence of combined flow bedforms throughout the cleaner lobes supports sustained interactions of flows with the intrabasinal topography, which controlled the routing of flows feeding both dirty and cleaner lobes (Fig. 4.14).

The contrast in facies types and HEB distribution between the dirty and cleaner lobes is interpreted to reflect progradation of the lobe complex with flow interaction and transformation across complex seabed topography). This situation prevailed until the sediment routing system became mature and enabled a reduction of flow interactions with intrabasinal relief, and resulted in only limited transformation of stratified sand-rich flows entering the graben. Widespread

development of bed-scale heterogeneity is recorded in the dirty frontal lobe fringe deposits with the abundance of relatively thin HEBs (type 2 and 3) that have similar thicknesses of facies divisions (Fig. 4.12). Flow transformations giving rise to the deposition of thin HEBs may result from autogenic processes; i.e. through entrainment of muddy substrate that increased flow cohesion and reduced the turbulence. The dirty lobes mark the first stage of development of the intraslope lobe complex, with renewed extrabasinal clastic supply after a protracted period of sand starvation and extensive deposition of organic-rich calcareous mud at onset of the early post-rift. The progressive maturation of sediment dispersal pathways might have suppressed the entrainment of muddy substrate. This is supported by the reduction of thin HEBs (type 2 and 3) (abundant in the dirty lobes) in the thicker-bedded and coarser-grained cleaner lobe axis and frontal fringe deposits (Fig. 4.14). However, thicker HEBs (type 1) containing a well-developed debritic division encased by sandy divisions (Fig. 4.12) are common both in the dirty frontal lobe fringe and cleaner lobe axis. The sporadic distribution of these HEBs, which result from flow transformation with shear mixing at top and base of voluminous, long run-out debris-flows, seem to be the product of flows sourced from a proximal shelf-slope setting (e.g. Hodgson, 2009; Migeon et al., 2010; Talling et al., 2010).

The stratigraphic distribution of HEB type in the intraslope lobe complex is inherent to its evolution as an immature out-of-grade system across complex intrabasinal topography, common during periods of fan initiation and growth (Haughton et al., 2003; Hodgson, 2009). The intraslope lobe complex described here differs from unconfined to weakly confined base-of-slope and basin-floor lobe models (Prélat et al., 2009; Spychala et al., 2017) in terms of its dimensions, architecture and facies distribution (lack of well-defined off-axis subenvironment, facies transition across shorter distance, no spatial HEB segregation in a specific lobe fringe position but random occurrence at any lobe sub-environment, erosion and scouring at lobe complex lateral margins and presence of combined flow bedforms throughout the lobe complex). It is also noteworthy that the low net: gross early post-rift intraslope lobe complex in the Chachil Graben have similarly low aspect ratio (~5 km minimum wide x 6-8 km long x 50-70 m thick) to those previously described (6-10 km x 15-25 km x 10-15 m thick, Spychala et al., 2015; 8 km wide x 8 km long x 120 m thick, Jobe et al., 2017), but are significantly more argillaceous (Fig. 4.9). Intraslope lobes stack vertically, displaying an upwards

increase in grain-size, bed thickness and amalgamation rate, and a decrease in bed-scale heterogeneity. This results in the cleaner lobes having a better potential reservoir quality than the lower dirty lobes. However, the sporadic occurrence of HEBs with thick debrite divisions form extensive intralobe fluid flow baffles throughout the intraslope lobe complex (Fig. 4.14). The characteristics of partially confined intraslope lobes developed in the Los Molles Fm. shows that more investigations of outcrop and subsurface analogues are required to widen the spectrum of intraslope lobes encountered in early post-rift settings (e.g. Southern et al., 2017; Dodd et al., 2019), which might deviate from current facies distribution and architectural models.

4.8 Conclusion

This study highlights the major reorganization of sedimentary systems and physiographic transformation of the rift topography with changes in sedimentation regime and stacking patterns characterizing the syn- to post-rift transition in the Chachil Graben. The late syn-rift evolution of the Chachil Graben into an underfilled depocentre with intrabasinal carbonate sedimentation was controlled by tectonic differential subsidence and rapid bathymetric deepening, which led to retrogradation and drowning of the carbonate system. Subsequent draping of the inherited rift topography by organic-rich calcareous mudstone inhibited intrabasinal sediment supply sources and recorded onset of the early post-rift. Rapid extrabasinal siliciclastic supply enabled the progradation of an extrabasinal-fed intraslope lobe complex and development of the Chachil Graben into a sediment-balanced depocentre.

The architectural consequences of an early post-rift compaction hinge formed across a rift fault-block, which controlled local thickness changes within the organic-rich part of the Lower Los Molles Fm. and acted as an oblique counterslope for sand-rich flows is highlighted. Intraslope lobes evolved in an early post-rift setting with syndepositional relief that induced partial confinement. This promoted lobe progradation and pinchout towards the NE, with shingled stacking of lobe sub-environment and limited facies segregation across lobes with abundant HEBs. The intraslope lobe complex onlaps along the southern graben margin and is associated with injectites stepping towards the compaction hinge. Lateral lobe complex margin is characterized by common erosion with

scouring and combined flow bedform development. Frontal lobe complex margin lack fining or sorting trend and is characterized by gradual pinchout of thin-bedded HEB-rich sandy heterolithics, which offset the abrupt pinchout of thick HEBs with debrites. The low net: gross intraslope lobe complex records a stratigraphic evolution from dirty to cleaner lobes, with a decrease of intralobe bed-scale heterogeneity and sporadic distribution of thick debrites which form significant flow baffles between sandbodies.

There is a need to better constrain the effects of inherited rift topography potentially enhanced by differential compaction, which promote the development of major stratigraphic and combined structural trap with partial confinement of early post-rift lobes. The presented intraslope lobe model demonstrates the risks for reservoir deterioration (i.e. lobe heterogeneity) and post-burial remobilization of reservoirs at onlap margins in topographically complex settings. This study provides a rare analogue for subsurface systems to help characterize the dimensions, facies distributions, terminations and stacking patterns, of both intrabasinal late syn-rift carbonate systems and extrabasinal early post-rift deep-marine sand-rich systems, with evolution of rift topography.

Chapter 5 Deciphering the stratigraphic variability of syn- to post-rift transition successions and physiographic evolution across several basins of the southern Neuquén Basin based on new U-Pb ages in the Los Molles Fm.

5.1. Introduction

The analysis of the interplay between tectonics, eustasy, climate, sediment supply rate and provenance in rift basin-fill patterns requires the identification of genetically linked depositional systems developed during distinct tectonic stages (Gawthorpe et al., 1994; Howell and Flint, 1996; Dorsey and Umhoefer, 2000; Martins-Neto and Catuneanu, 2010). The balance of sedimentation and accommodation can result in overfilled, balanced, underfilled, and starved basin-fill patterns, and reflects the variability of documented early rift, rift climax, late rift and early post-rift stratigraphic signatures in marine rift basins (Prosser, 1993; Ravnås and Steel, 1998). A major weakness of rift basin-fill models is that they do not integrate (i) the effects of volcanism on the tectono-stratigraphic development of depocentres (Muravchik et al., 2011; D'Elia et al., 2018) and (ii) the spatial variability of structural and sedimentological processes associated with the syn- to post-rift stratigraphic transition are widely overlooked (Prosser, 1993; Bosence, 1998; Ravnås and Steel, 1998; Gawthorpe and Leeder, 2000; Withjack et al., 2002; Martins-Neto and Catuneanu, 2010).

Many authors have pointed out the importance of rift basin topography acting at the same rank as other factors of control on the stratigraphic architecture of rift basins (Howell and Flint, 1996; Ravnås and Steel, 1998; Burgess et al., 2000; Young et al., 2003; Jackson et al., 2005, 2011; Veiga et al., 2013; Gawthorpe et al., 2018). However, little emphasis has been placed to date on its evolution and role during the syn- to post-rift transition and this can be rarely demonstrated across multiple rift basins. To date, few studies have examined the detailed nature and variability of late syn-rift and early post-rift depositional systems, and consequently the influence of evolving rift topography (i.e inherited pre-rift tectonic fabrics, fault-block reliefs and lows) on the stratigraphic

development of rift basins is poorly understood, particularly during the early post-rift.

Here, focus is made on changes of Early Jurassic sedimentation during the syn- to post-rift transition coeval with development of the Early Andean volcanic arc, associated with the stepwise marine flooding and decay of syn-rift volcanism across several rift basins of the southwestern Neuquén Basin. The contrasted tectono-stratigraphic development of two exhumed adjacent marine rift basins (Chacaico and Eastern Catán-Lil) in the southwestern part of the Neuquén Basin, are investigated with a <28 km long NW-SE oriented transect along-strike rift structures. The integration of sedimentology, stratigraphic and structural evolution of two basin-fills permits to document stratigraphic units and unpick their individual evolution during the syn- to post-rift transition.

The stratigraphic framework proposed integrates new U-Pb SHRIMP zircon ages in the Los Molles Formation collected from the Eastern Catán-Lil and Chachil Basin. Discussion is focused on (i) the potential factors of control on the temporal and spatial variability of both shallow- and deep-marine sedimentation during the late syn-rift to early post-rift evolution of adjacent depocentres (Eastern Catán-Lil and Chacaico basins) and (ii) the effects of inherited rift topography on the contrasted basin-fill patterns across coeval depocentres of the study area at a regional-scale (Eastern Catán-Lil, Chacaico, Chachil, Western Catán-Lil and La Jardinera basins) and (ii) the palaeogeographic implications for the development of the early post-rift sand-rich depositional system of the Los Molles Formation at the light of the earlier onset of sediment supply presented in this study (since the late Early Toarcian).

A rare level of detail is provided on the variability of depositional environments and sediment dispersal patterns developed in adjacent rift basins but also at a regional-scale, on the migration and linkage of volcanic syn-rift, marine late syn-rift and early post-rift depocentres, changes of sediment supply (intrabasinal versus extrabasinal sources) and mode of sediment dispersal (transverse versus axial systems). This study focused on the syn- to post-rift transition stage complements a gap which is poorly emphasised by classic rift basin models and constitutes a seismic-scale analog which might help to predict the spatial distribution and stratigraphic architecture of early post-rift intraslope systems.

5.2. Geological setting

Intracontinental volcanic rift during the Late Triassic-Early Jurassic led to the opening of a series of rift basins across the southwestern Gondwana, which are now preserved in subsurface or exhumed in the Neuquén Basin, Argentina (36°S-40°S) (Fig. 5.1). Extension and widespread volcanism occurred with the post-orogenic thermo-mechanical collapse of an over-thickened crust inherited from a Palaeozoic period of subduction-collision and accretion of several terranes with the western Gondwana margin (Kay et al., 1989; Tankard et al., 1995; Vergani et al., 1995; Legarreta and Uliana, 1996; Franzese and Spalletti, 2001). Late Triassic to Early Jurassic rifting in the southern Neuquén Basin occurred with NE-SW-oriented extension and local stress field perturbation with reactivation of oblique pre-rift orogenic structures which induced oblique rifting, with development of strike-slip and en-echelon fault pattern (Vergani et al., 1995; Franzese and Spalletti, 2001; Silvestro and Zubiri, 2008; Mpodozis and Ramos, 2008) (Figs 5.1 and 5.2). At basin-scale, the extensional strain was accommodated following simple or heterogeneous shear model, with mechanical decoupling between the crust and upper mantle along pre-rift suture zones rooted at lower crustal or lithospheric depths and lateral offset between the locus of lithospheric thinning and upper crustal brittle faulting (Comínguez and Franzese, 2008; Sigismondi and Ramos, 2011).

Onset of the Early Andean subduction occurred with oblique SE-oriented convergence of the proto-Pacific oceanic plate (Aluk plate) below the western Gondwana margin, with steep slab and negative trench rollback (Ramos, 1999; Mosquera and Ramos, 2006; Mpodozis and Ramos, 2008; Ramos et al., 2011). Activity of the Early Andean magmatic arc started between Late Triassic (Bermudez et al., 2002; Llambías et al., 2007) and Sinemurian-Pliensbachian (De la Cruz and Suárez, 1997; Schiuma and Llambías, 2008; Spalletti et al., 2010). Development of the Early Andean magmatic arc was accompanied by the first marine incursion from the Pacific Ocean which propagated diachronously, first in the north of the Neuquén Basin during the Rhaetian and reaching the southern border of the basin during the Early Pliensbachian (Riccardi, 1991; Damborenea et al., 2013; Leanza et al., 2013). The Early Andean volcanic arc migrated westwards during the Early Jurassic and the syn- to post-rift transition was recorded during the late Early Sinemurian in the north of the Neuquén Basin

(Lanés et al., 2008) and Late Pliensbachian-Early Toarcian in the south (Pángaro et al., 2009; D'Elia et al., 2015). Regional post-rift thermal subsidence controlled the progressive linkage of Early Jurassic marine rift depocentres across the inherited rift topography (e.g Burgess et al., 2000; Gómez Omil et al., 2002). This resulted in the formation of a single sag back-arc depocentre since Middle Jurassic, with local oblique transpressional reactivation of structures localized along the Huincul High (38-40°S) in the south of the Neuquén Basin (e.g Mosquera and Ramos, 2006; Mpodozis and Ramos, 2008; Silvestro and Zubiri, 2008; Naipauer et al., 2012). The sag phase lasted for ~80 Ma from Middle Jurassic to Early Cretaceous, prior to its Late Cretaceous-Cenozoic subduction-driven foreland evolution (Vergani et al., 1995; Gulisano and Gutiérrez Pleimling, 1995; Legarreta and Uliana, 1996; Franzese and Spalletti, 2001; Howell et al., 2005).

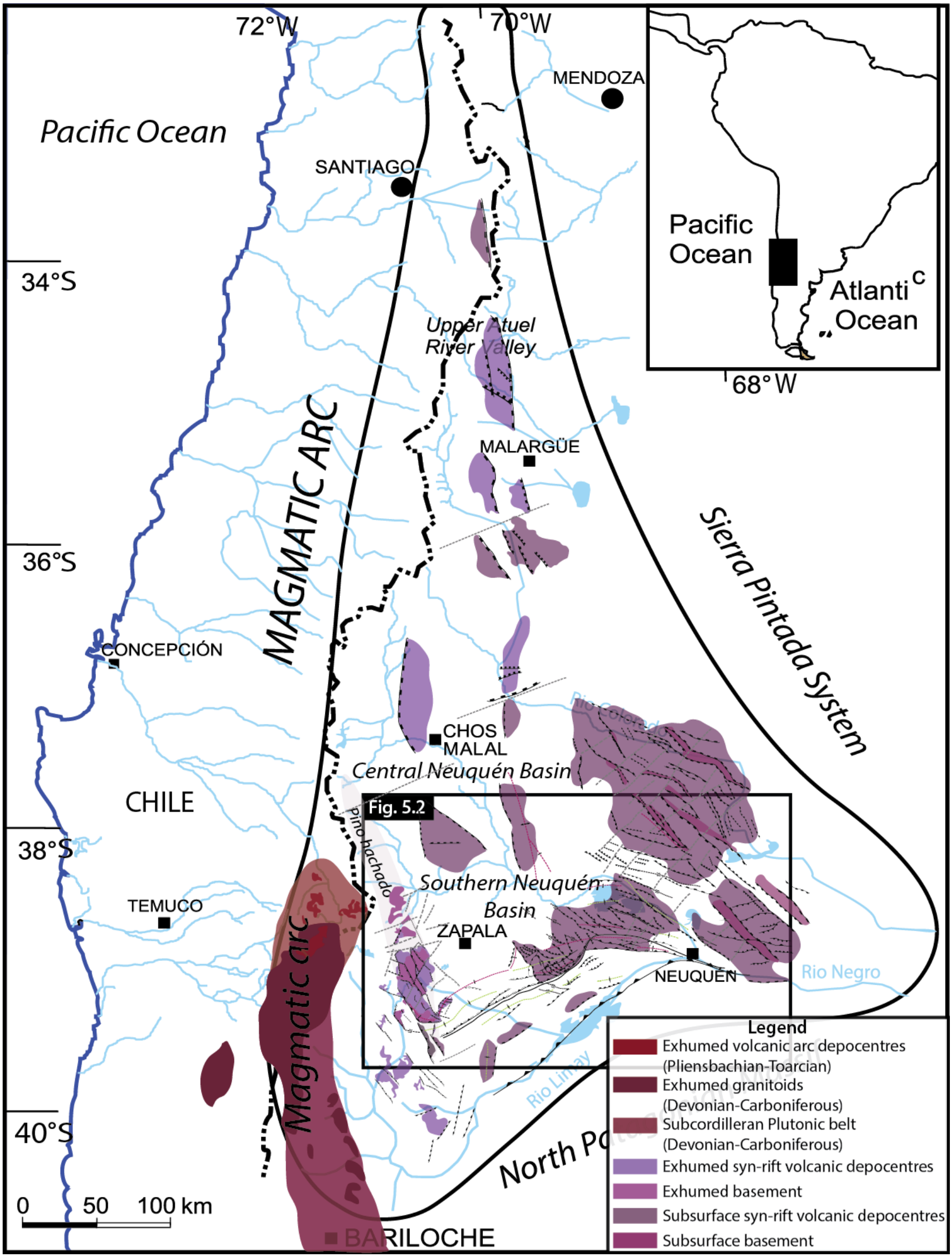

Figure 5.1: General map of the Neuquén Basin showing the distribution of syn-rift volcanic depocentres, basement and structures (after Gómez Omil et al. (2002), Silvestro and Zubiri (2008), Yagupsky (2009), Cristallini et al. (2009),Pángaro et al. (2009), García Morabito et al. (2011), Sigismondi and Ramos (2011), Bechis et al. (2014); location of the Early Andean magmatic arc is after Suárez and Marquez (2007) and volcanic arc depocentres after De la Cruz and Suárez (1997)).

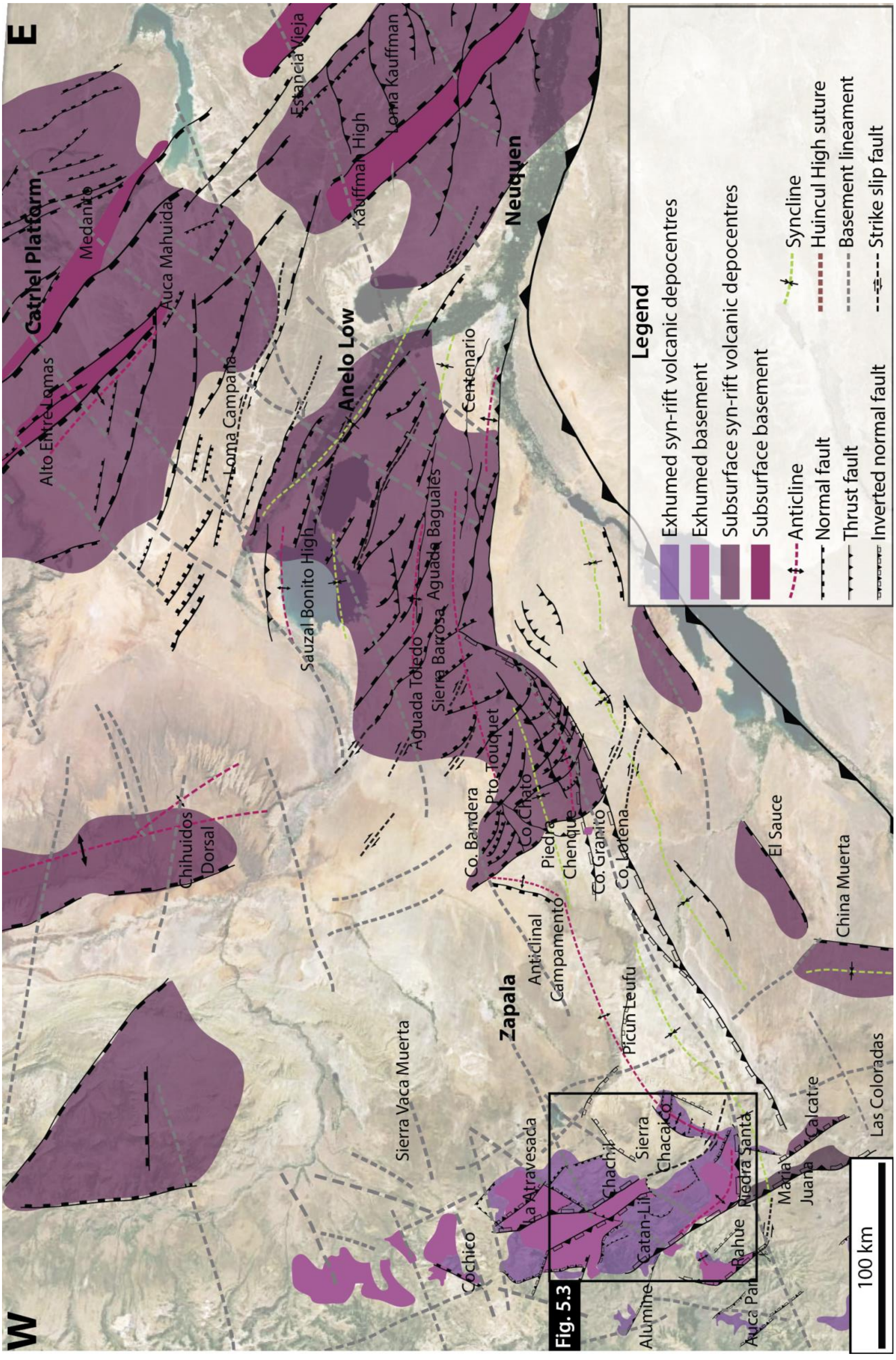

Figure 5.2: Map of the Southern Neuquén Basin showing the structural configuration and distribution of syn-rift volcanic depocentres, basement and structures (after Gómez Omil et al. (2002), Silvestro and Zubiri (2008), Yagupsky (2009), Cristallini et al. (2009),Pángaro et al. (2009), García Morabito et al. (2011), Sigismondi and Ramos (2011), Bechis et al. (2014).)

5.3. Study area and structural framework

5.3.1. Structural framework

The study area located in the southwestern Neuquén Basin comprises five main depocentres which correspond to the Chacaico Basin, the western Catán-Lil Basin, the eastern Catán-Lil Basin, the Chachil Basin and La Jardinera Basin (Fig. 5.3).

The Chacaico Basin (Fig. 5.3) also forms a half-graben (15 km long, 10 km wide) bounded to the north by the E-W striking Cerro Trapial Mahuida fault and to the south by a WNW-ESE striking fault towards which syn-rift strata thickens (Franzese et al., 2007). This depocentre is dissected by some WNW-ESE striking and north or south dipping smaller scale intra-basin faults (few kilometres length). The Rincón del Polo and southern footwall border of the Chacaico Basin are cored by basement metamorphic rocks of the Piedra Santa Range which forms a south-verging anticline, inverted along the E-W striking Las Coloradas Fault (Fig. 5.3). The Sierra Chacaico forms an asymmetric NNE-SSW oriented and west-verging anticline, controlled by a NE striking and east-dipping reverse fault (Franzese et al., 2007). It corresponds to the westernmost exhumed extremity of the Huincul High, an ENE-WSW oriented intraplate structure along which inversion and uplift of a serie of grabens and half-grabens during the Andean compression resulted in the good exposure of syn- to post-rift strata in the study area (García Morabito et al., 2011) (Fig. 5.2).

The Eastern Catán-Lil Basin (Fig. 5.3) forms a small half-graben (10 km long, 5 km wide) developed across the ~5 km long Cerro Mallín de Ibáñez hangingwall block of the NNW-SSE trending granitic basement cored structure which forms the southern extremity of Chachil horst border. The Cerro Mallín de Ibáñez block is segmented by ENE-WSW striking faults (few kilometres length), which are normal to its NNW-SSE striking and SW dipping fault border (Fig. 5.3). This major fault constitutes the southwestern border of the Eastern Catán-Lil Basin, which is bounded to the north by the NE-SW striking SE dipping Tutavel fault towards which syn-rift strata thickens. The northeastern border of this basin lies in subsurface and its southeastern margin corresponds to the Puesto Rincón del Polo basement high bounded by a NE-SW striking fault (Fig. 5.3). The Western Catán-Lil Basin forms a graben (25 km long, 15 km wide) bounded to

the north by the NNW-SSE striking SW dipping Felipin fault and the NE dipping Lonqueo fault, towards which the syn-rift strata thickens (Gulisano and Gutiérrez-Pleimling, 1995; Muravchik et al., 2014).

The Chachil Basin (Fig. 5.3) forms a graben (>15 km long, 10 km wide), bounded by the NNE-SSW and NW-SE striking Chihuido Bayo fault system to the SW and NW, whereas its SE and NE margins are uncertain as lying in the subsurface (Franzese et al., 2006). It comprises multiple NW-SE and NNE-SSW striking smaller faults and folds (cf. Chapter 4). The Chachil syn-rift strata thickens towards the northeast away from the Chachil horst border (5 km wide, >15 km long) controlled by NNW-SE striking Felipin and Chihuido Bayo faults (Fig. 5.3). The La Jardinera Basin (Fig. 5.3) forms a half-graben (15 km long, 10 km wide) bounded to the south by the NNW-SSE striking and NE dipping Rahue fault towards which syn-rift strata thickens and its northern border corresponds to the NNW-SSE striking and NE dipping Lonqueo fault.

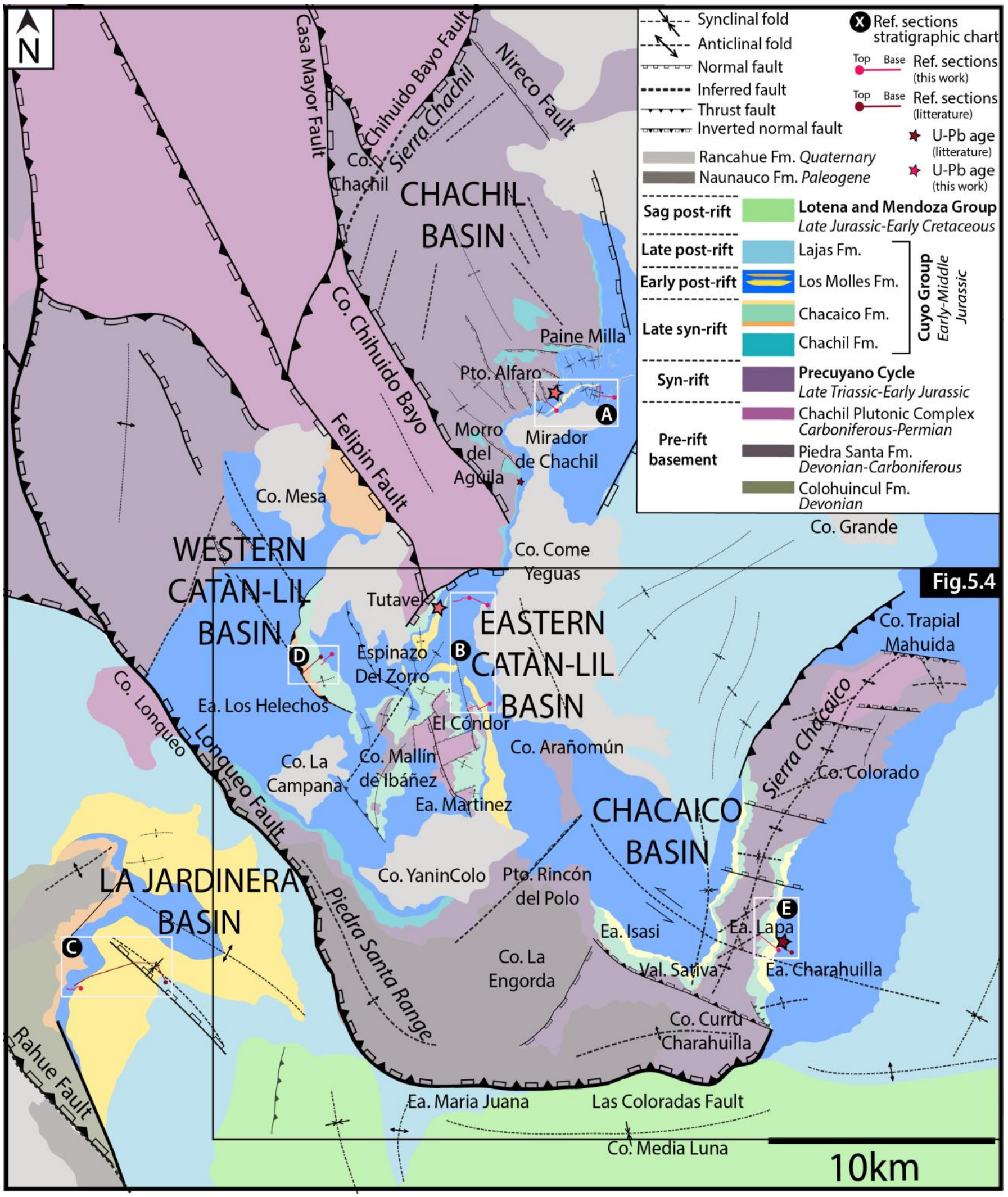

Figure 5.3: Regional geological map of the study area showing the location of the studied depocentres (Chacaico, Eastern and Western Catán-Lil, Chachil, La Jardinera), the location of the large-scale stratigraphic sections collected and U-Pb age data used in the stratigraphic chart of fig. 5.3 and 5.25. The map includes informations after Leanza and Blasco (1990), Gulisano and Gutiérrez-Pleimling (1995), Cucchi et al. (2005), Franzese et al. (2006, 2007), García Morabito et al. (2011) and Muravchik et al. (2014).

5.3.2. Stratigraphy of the study area

The Chacaico, Eastern and Western Catán-Lil, Chachil and La Jardinera basins are bounded by fault borders (5-10s km long) which exhume pre-rift basement in their footwall (Figs 5.3 and 5.4). The pre-rift basement includes Late Carboniferous-Early Permian calco-alkaline plutons (Chachil Plutonic Complex) and Siluro-Devonian to Early Carboniferous low-grade metasedimentary rocks (Piedra Santa formation) and Devonian high to medium grade metamorphic rocks (Colohuincul formation) (Cingolani et al., 2011) (Fig. 5.3). Prior to deposition of syn-rift deposits, the basement underwent large-scale taphrogeny and regional erosion during a long period of exhumation recorded by the Early-Middle Triassic Huarpican unconformity (Llambías et al., 2007; Schiuma and Llambías, 2008).

Syn-rift sedimentation in isolated taphrogenic basins was dominated by intense volcanism with the accumulation of continental volcano-sedimentary successions (Norian-Sinemurian) that form the Precuyano Cycle deposits (Franzese and Spalletti, 2001; Schiuma and Llambías, 2008; D'Elia et al., 2018) (Figs 5.3 and 5.4). The Precuyano Cycle is bounded at top by the Rioatuelican or Intra-Liassic unconformity which marks the unconformable contact with marine deposits of the Cuyo Group (Pliensbachian-Bathonian) (Gulisano and Gutiérrez Pleimling, 1995). Volcanic deposits record an evolution from acidic to less evolved calc-alkaline composition mixing crustal and mantellic sources, associated with the transition from intraplate rifting to back-arc extension since the Early-Late Sinemurian (199.0 ± 1.5 Ma, Schiuma and Llambías, 2008; 191.7 ± 2.8 Ma, Spalletti et al., 2010) and probably earlier since the Late Triassic (Bermudez et al., 2002; Llambías et al., 2007).

The Early-Middle Jurassic evolution of the Neuquén Basin is recorded by two 2nd order depositional sequences (J1 and J2 following Paim et al., 2008) separated by the Toarcian-Aalenian boundary: the Early Jurassic Cuyo Group and Middle Jurassic Upper Cuyo Group (Gulisano and Gutiérrez Pleimling, 1995; Vergani et al., 1995; Legarreta and Uliana, 1996; Paim et al., 2008). In the study area, the Cuyo Group includes the Early Jurassic Chachil, Chacaico and Los Molles formations, and the Middle Jurassic Middle and Upper Los Molles, Lajas and Challaco formations (Gulisano and Gutiérrez Pleimling, 1995; Paim et al., 2008) (Fig. 5.3). The present study focusses on the Early Jurassic Cuyo Group

to characterize syn- to post-rift transition successions exhumed in the southwestern part of the Neuquén Basin (Fig. 5.3).

5.4. Methods

5.4.1. Fieldwork

Detailed mapping in the Chacaico and Eastern Catán-Lil basins using GPS referencing, DTM and Unmanned Aerial Vehicle (UAV) surveys was integrated with previous structural and geological mapping studies (Figs 5.3 and 5.4). Correlation of ten measured large (300-500 m thick) vertical sections logged in detail (1:25 scale) form the basis of a ~28 km long transect oriented NW-SE along-strike with respect to rift structures (Fig. 5.5). This transect includes 3 logs in the Chacaico Basin and 7 logs in the Eastern Catán-Lil Basin which form transects oblique to depositional dip (Fig. 5.5). Most of the facies associations or facies belts and related depositional packages could be tracked on the field due to the good lateral outcrop continuity. In addition, stratigraphic correlations of laterally extensive marker sandstone bed packages in the Los Molles Formation helped to further support log correlations as they could be walked out for several kilometres in the field and constrained with UAV photo panels. Logged vertical sections were used to interpret sedimentary processes, depositional environments and facies associations, and to define the stratigraphic units which belong to the Chacaico (Unit 1 and 2) and Los Molles formations (Unit 3 and 4) (Figs 5.4 and 5.5). Paleocurrent measurements (223 in total) collected from ripple-cross-laminations and dune-scale cross-stratification, as well as from flutes and grooves were plotted in rose diagrams to reconstruct the palaeoflow pathways for each stratigraphic unit (Fig. 5.4). Analysis of facies associations, palaeocurrents, stratal geometries and thickness, and local deformation in relation to structures (faults and folds) were used to determine the influence of tectonism (locus and timing of fault/fold activity and reconstructed structure length) and inherited palaeotopography on sedimentation.

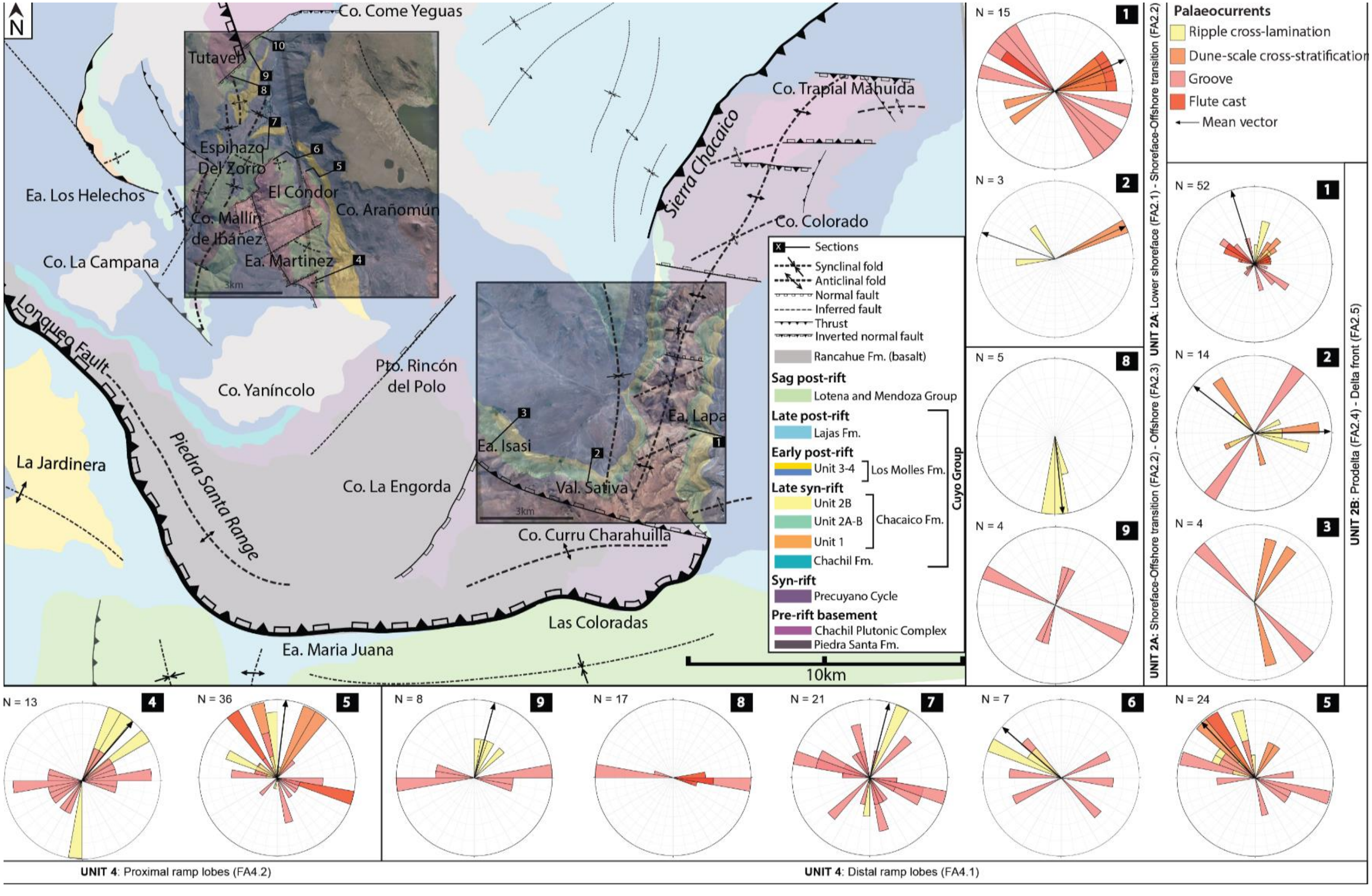

Figure 5.4: Detailed map of the two investigated Eastern Catán-Lil and Chacaico depocentres showing the location of logs collected, spatial distribution of tectono-stratigraphic units presented in this study, and palaeocurrents collected in each of these units.

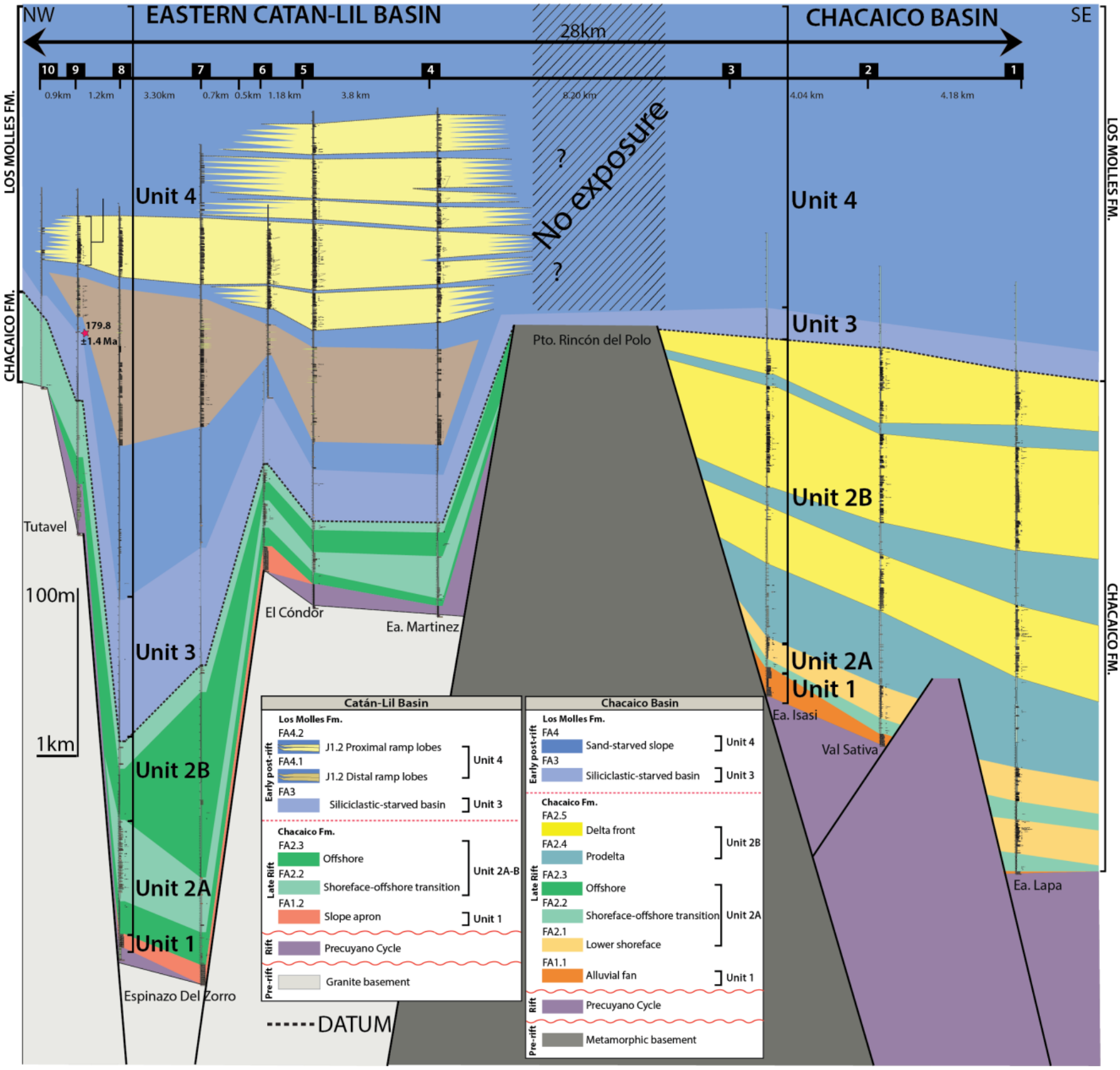

Figure 5.5: Correlation panel showing the spatial distribution of facies associations and relationships between late syn-rift and early post-rift units across structures in each basins (location of logs are shown in the map fig. 5.4), with palaeocurrents and location of the tuff 1 sample. Note that the main datum used to correlated unit is indicated in black dotted line.

The palaeogeographic evolution of the two studied rift basins is based on spatial variations of facies associations and thickness, deformation and onlap/truncation patterns, enabling the evolution of depositional systems across rift structures. The four main stratigraphic units (Unit 1, 2, 3 4) bounded by stratigraphic surfaces which mark major sedimentary changes across basins and their correlation across basins are based on pre-existing geochronologic and biostratigraphic markers including ammonites, nannofossils, and bivalves biozones (Figs 5.3 and 5.6). The refined temporal and stratigraphic framework integrated with new U-Pb concordia ages in the Los Molles Fm. and thickness presented in this chapter also permitted estimation of sedimentation rates (Table 5.1).

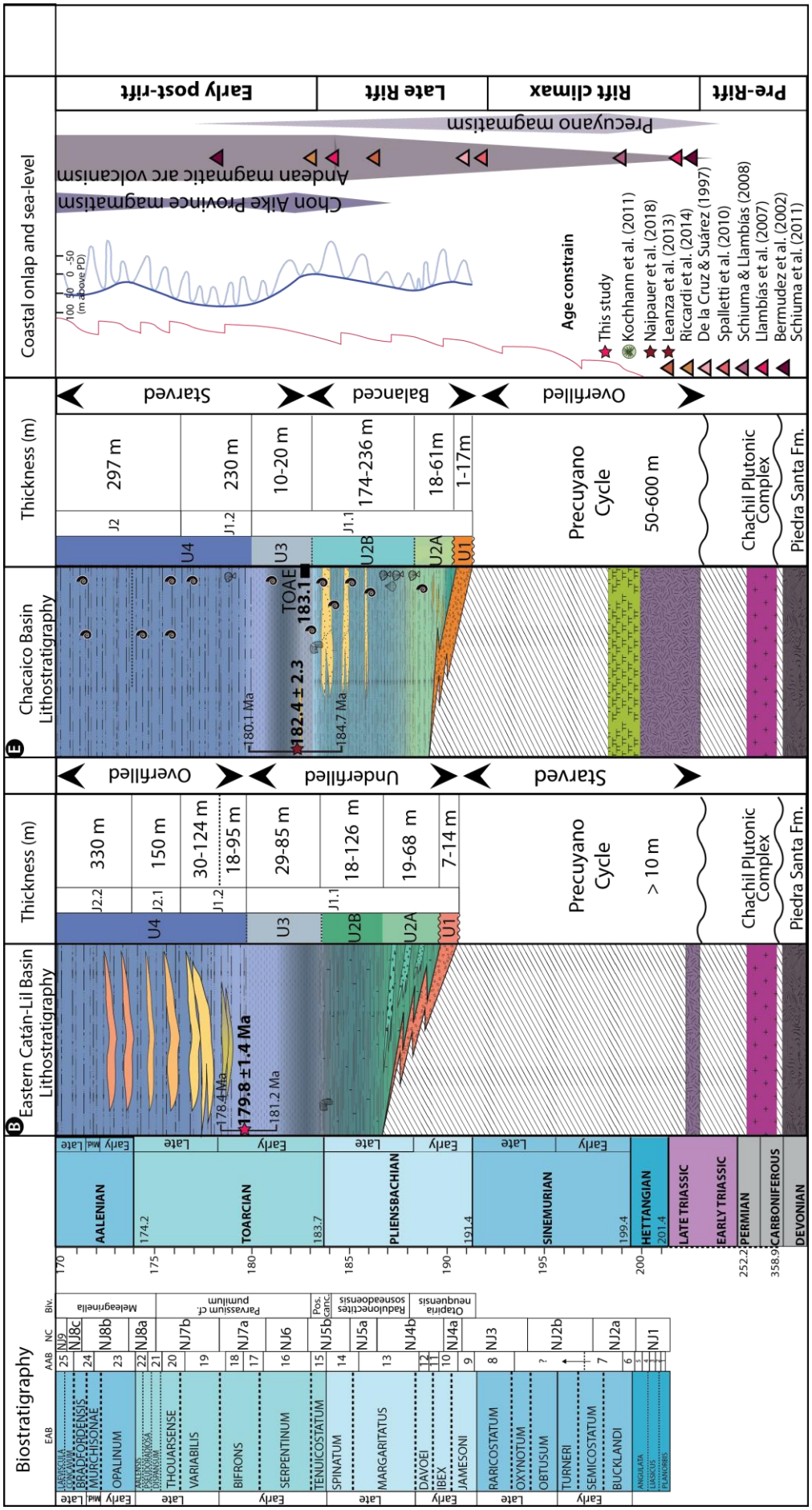
Biostratigraphy
Eastern Catán-Lil Basin Lithostratigraphy
Thickness (m)
Chacaico Basin Lithostratigraphy
Coastal onlap and sea-level
Pre-Rift
Rift climax
Late Rift
Early post-rift
Overfilled
Underfilled
Starved
Balanced
Precuyano Cycle
Chachil Plutonic Complex
Piedra Santa Fm.
330 m
150 m
30-124 m
18-95 m
29-85 m
18-126 m
19-68 m
7-14 m
> 10 m
297 m
230 m
10-20 m
174-236 m
18-61m
1-17m
50-600 m
179.8 ±1.4 Ma
178.4 Ma
181.2 Ma
182.4 ± 2.3
180.1 Ma
184.7 Ma
183.1
TOAE
Chon Aike Province magmatism
Andean magmatic arc volcanism
Precuyano magmatism
Age constrain
This study
Kochhann et al. (2011)
Naipauer et al. (2018)
Leanza et al. (2013)
Riccardi et al. (2014)
De la Cruz & Suárez (1997)
Spalletti et al. (2010)
Schiuma & Llambías (2008)
Llambías et al. (2007)
Bermudez et al. (2002)
Schiuma et al. (2011)

Figure 5.6: Stratigraphic scheme for the Chacaico and Eastern Catán-Lil basins, (see section location fig. 5.3) integrated with available constrains of thickness and fossil data from the literature (Volkheimer, 1973; Gulisano and Gutiérrez-Pleimling, 1995; Franzese et al., 2006, 2007; Paim et al. 2008) and U-Pb zircon ages (186.3 ± 0.4 Ma in the Chachil Graben, Armella et al., 2016 modified from Leanza et al., 2013; 182.4 ± 2.3 Ma in the Chacaico Basin, Naipauer et al., 2018), as well as new U-Pb zircon data provided in this contribution (red stars).Nannofossil chronozones follow Ballent et al. (2011), standard European (EAB) and Andean (AAB) Ammonite biozone numbers follow Riccardi (2008) and bivalve biozones follow Riccardi et al. (2011). The TOAE is placed in the late Tenuicostatum-early Dactylioceras Hoelderi AAB after Al-Suwaidi et al. (2016) and in the NJ6 nannofossil chronozone after Angelozzi and Pérez Panera (2016). Note that the stratigraphic names for intraslope fans follow Paim et al. (2008).

	Depocentre	Min. thickness (m)	Max. thickness (m)	Average thickness (m)	Time (Myr)	Age (Myr)	Average sed. rate (m/Myr)	Min.sed. rate (m/Myr)	Max. sed. rate (m/Myr)
Unit 4 J1.2-J2.1	Chachil		310		10	180-170			31.0
	Catan-Lil		735						73.5
	La Jardinera		650						65.0
Unit 4 J2.1	Chachil		80		3	174-170			26.7
	Catan-Lil		330						110.0
	La Jardinera		325						108.3
Unit 4 J1.2	Chachil		230		6	180-174			38.3
	Catan-Lil		405						67.5
	La Jardinera		325						54.2
	Chacaico		230		6.5	180-173.5			35.4
Unit 4 J1.2B Proximal ramp	Chachil		130		3	177-174			43.3
	Catan-Lil		150						50.0
	La Jardinera		200						66.7
Unit 4 J1.2 Distal ramp	Chachil		100		3	180-177			33.3
	Catan-Lil		255						85.0
	La Jardinera		125						41.7
Unit 3	Chachil	20	120	51.9	4.6	184.4-179.8	11.3	4.3	26.1
	Catan-Lil	29	85	43.7	3.9	183.7-179.8	11.2	7.4	21.8
	La Jardinera	100	200	150.0	6	186-180	25.0	16.7	33.3
	Chacaico	10	20	15	3.7	183.7-180	4.1	2.7	5.4
Unit 2	Chachil	2.5	35	19.1	1.6	186-184.4	12.0	1.6	21.9
	Catan-Lil U2B	18	126	53.4	2	186.5-184.5	26.7	9.0	26.7
	Catan-Lil U2A	19	67.8	38.8	2.5	189-186.5	15.5	7.6	27.1
	La Jardinera								
	Chacaico U2B	174.8	236	203.6	4.3	188-183.7	47.3	40.7	54.9
	Chacaicov U2A	18	61.8	36.4	2	190-188	18.2	9.0	30.9
Unit 1	Chachil	5	40	21.9	4	190-186	5.5	1.3	10.0
	Catan-Lil	7.6	14	10.9	4.4	191.4-187	2.5	1.7	3.2
	La Jardinera	50	350	200.0	4.4	191.4-187	45.5	11.4	79.5
	Chacaico	1.2	17	8.2	1.4	191.4-190	5.9	0.9	12.1

Table 5.1: Summary of units thickness and relative ages used in the stratigraphic chart and to estimate compacted sedimentation rates.

5.4.2. Geochronology

5.4.2.1. Analytical method

Two tuff samples were collected at base and top of the Lower Los Molles Fm. (Unit 3) (i) Tuff 1 at the top of Unit 3 in the Eastern Catán-Lil Basin (39° 15.427'S 70° 34.959'W) and (ii) Tuff 3 at the base of Unit 3 in the Chachil Basin (39° 10.554'S 70° 31.447'W) (Fig. 5.7). Tuff samples of 2 kg each were crushed and grinded to recover zircons at the CIG (Centro de Investigaciones Geológicas). The first step for zircon separation is to use a 140 microns mesh for sieving, washing, and concentration of heavy minerals in the bottom and grooves of the tray, while the light minerals were discarded by its edge. The heavy mineral preconcentrate was washed with ethyl alcohol, recovered by filter paper, and oven-dried. Manual handpicking of 50 zircon grains was carried out under a binocular magnifying glass and stored inside an eppendorf tube to be sent for U-Pb geochronology at Research School of Earth Sciences (RSES) of the Australian National University (ANU). U-Pb dating was carried out using sensitive high-resolution ion microprobe (SHRIMP-SII) following analytical procedures of Williams (1998) and Ireland and Williams (2003). Hand-picked grains (31 grains for Tuff1 and 29 grains for Tuff2) were mounted with standard zircon (Temora-2) in an epoxy disc, ground and polished to expose grain surface for laser ablation (Fig. 5.8-A). Cathodoluminescence imaging was conducted using SEM-EDS (Scanning Electron Microscope with Energy Dispersive Spectroscopy) to characterize idiomorphic zircon crystals (internal texture with oscillatory zoning indicative of igneous origin) inherent to their volcanic provenance, to ensure the absence of inherited cores and define laser ablation spots within well-zoned rims of euhedral grains.

Analytical data were processed using SQUID (Ludwig, 2001a) and ISOPLOT/EX (Ludwig, 2001b), tabulated with isotopic data in Table 5.2. Uranium and thorium abundances have been calculated with reference to SL13 (238 ppm U) and the $^{206}Pb/^{238}U$ ratios have been normalized relative to a value of 0.0668 for the $^{206}Pb/^{238}U$ ratio of the standard zircon Temora-2 of 417 Ma (Black et al. 2004).

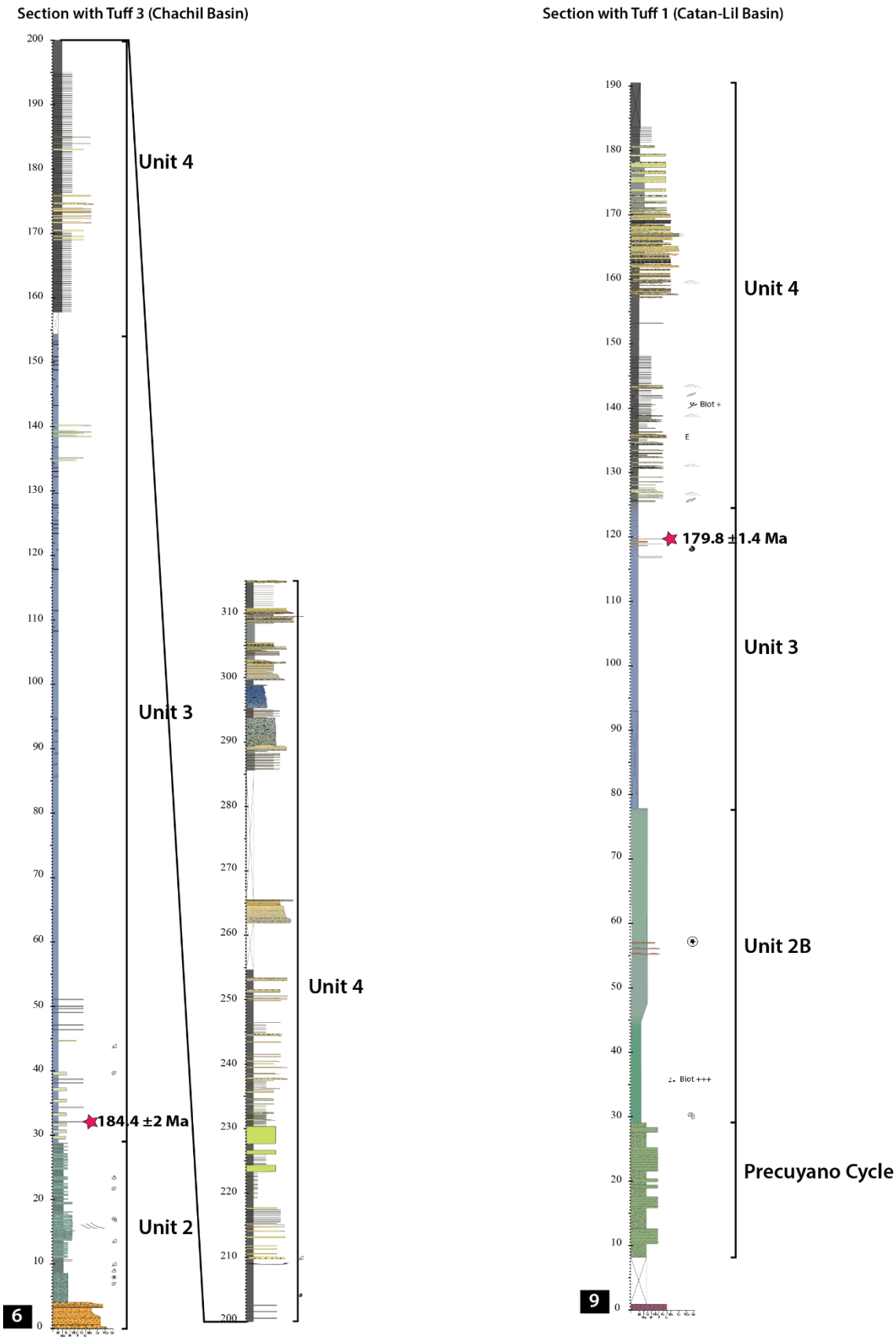

Figure 5.7: Sections located in the Chachil (see location of log in fig. 4.5) and Catán-Lil basins (see location of log in fig. 5.5) indicating the position of the tuff samples analysed in this study, at the base and top of Unit 3 which corresponds to the Lower Los Molles Fm.

5.4.2.2. Results

The concordia ages are calculated with an error on the Temora-2 standard of ± 0.25 % (1σ) for the Tuff 1 and ±0.37 % (1σ) for the Tuff 3, and include 2σ decay constant uncertainties at 95% confidence level (Fig. 5.8). Tuff 1 yielded concordia ages ranging from 185.2 to 171.3 Ma out of 29 zircons with gaussian peak age at 178-179 Ma, and excluding two anomalous inherited grains (out of 31 grains) at 152.2 and 301 Ma with high common Pb (see Table 5.2). The weighted arithmetic mean $^{206}Pb/^{238}U$ age calculated is 179.8 ±1.4 Ma (2σ) and isotopic data points plotted in a concordia diagram show minor deviation (Fig. 5.8-B-C). Tuff 3 yielded concordia ages ranging from 198 to 178 Ma out of 26 zircons with gaussian peak at 186 Ma, and excluding an inherited grain at 221 Ma (out of 29 grains). The weighted arithmetic mean $^{206}Pb/^{238}U$ age calculated is 184.4 ±2 Ma (2σ) and isotopic data points plotted in a concordia diagram show minor deviation (Fig. 5.8-B-C). The results of U-Pb ages obtained and their implications are discussed.

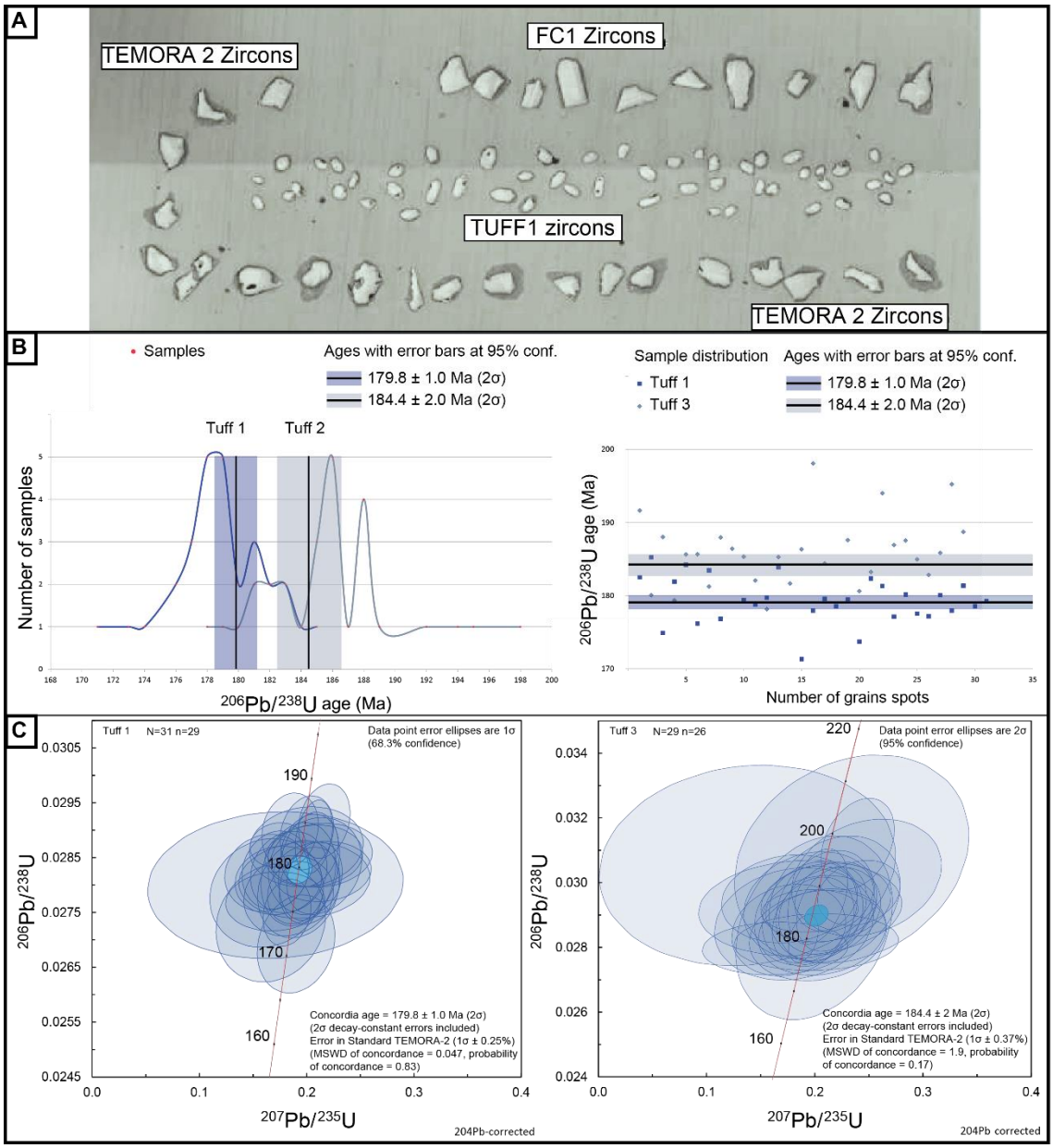

Figure 5.8: U-Pb geochronology results. A- Mount map of the tuff 1 sample zircons analysed and Temora-2 standard zircons. B- Concordia diagram for the tuff 1, with ellipses at 68.3% confidence level (1σ) and concordia diagram for the tuff 3, with ellipses at 95% confidence level (2σ). Blue ellipse represents the centre of the obtained concordia age provided with 95% confidence level. N is the number of zircon grains recovered, n is the number of accepted zircon grains after excluding anomalous grains. MSWD is the Mean Square of Weighted Deviates. C- Diagram showing the frequency of ages and mean age obtained in each samples and diagram showing the distribution of zircon spots realized for each sample.

Sample_Grain.Spot	U (ppm)	Th (ppm)	Th/U	$^{206}Pb^*$ (ppm) (^{204}Pb-corrected)	f_{206} (%)	Total $^{207}Pb^*/^{235}U$ (^{204}Pb-corrected)	± %	Total $^{206}Pb^*/^{238}U$ (^{204}Pb-corrected)	± %	Error correlation	Age (Ma) $^{206}Pb^*/^{238}U$ (^{204}Pb-corrected)	± 1s
TUFF 1												
TUF1_1.1	295	176	0.62	7.3	0.47	0.174	9.9	0.02872	0.9	0.09	182.5	1.6
TUF1_2.1	262	139	0.55	6.6	< 0.01	0.217	7.2	0.02915	1.5	0.21	185.2	2.8
TUF1_3.1	282	186	0.68	6.7	0.20	0.183	8.0	0.02750	1.4	0.18	174.9	2.5
TUF1_4.1	324	203	0.65	8.0	< 0.01	0.204	8.6	0.02862	1.5	0.17	181.9	2.7
TUF1_5.1	303	184	0.63	7.5	0.41	0.186	9.4	0.02899	1.5	0.16	184.2	2.8
TUF1_6.1	202	92	0.47	4.8	0.65	0.172	17.7	0.02771	1.3	0.07	176.2	2.2
TUF1_7.1	491	414	0.87	12.2	< 0.01	0.208	5.4	0.02887	1.5	0.28	183.5	2.8
TUF1_8.1	208	96	0.48	5.0	0.64	0.184	15.0	0.02781	1.7	0.12	176.8	3.0
TUF1_9.1	336	127	0.39	6.9	27.24	~~0.820~~	~~10.7~~	~~0.02389~~	~~4.0~~	~~0.38~~	~~152.2~~	~~6.1~~
TUF1_10.1	174	83	0.49	4.2	0.90	0.164	15.8	0.02822	1.6	0.10	179.4	2.9
TUF1_11.1	256	148	0.60	6.2	< 0.01	0.208	8.2	0.02813	1.5	0.18	178.8	2.7
TUF1_12.1	236	119	0.52	5.7	0.52	0.172	12.0	0.02827	1.6	0.14	179.7	2.9
TUF1_13.1	283	163	0.59	7.0	< 0.01	0.201	8.2	0.02894	1.5	0.19	183.9	2.8
TUF1_14.1	249	156	0.65	10.2	< 0.01	~~0.361~~	~~6.0~~	~~0.04784~~	~~0.9~~	~~0.16~~	~~301.3~~	~~2.7~~
TUF1_15.1	195	93	0.49	4.5	< 0.01	0.191	12.5	0.02693	2.2	0.17	171.3	3.7
TUF1_16.1	66	22	0.35	1.6	0.53	0.172	45.6	0.02799	3.1	0.07	178.0	5.5
TUF1_17.1	191	76	0.41	4.6	< 0.01	0.216	14.0	0.02824	1.3	0.09	179.6	2.2
TUF1_18.1	125	43	0.36	3.0	< 0.01	0.199	20.2	0.02808	1.6	0.08	178.5	2.8
TUF1_19.1	197	100	0.52	4.8	0.18	0.185	12.7	0.02823	1.7	0.14	179.5	3.1
TUF1_20.1	189	61	0.33	4.4	0.77	0.168	20.1	0.02731	2.6	0.13	173.7	4.4
TUF1_21.1	167	70	0.44	4.1	0.02	0.201	17.4	0.02869	1.7	0.09	182.4	3.0
TUF1_22.1	157	53	0.35	3.9	< 0.01	0.208	14.5	0.02852	1.3	0.09	181.3	2.3
TUF1_23.1	186	92	0.51	4.5	0.96	0.163	21.3	0.02786	2.3	0.11	177.1	4.1
TUF1_24.1	181	78	0.45	4.4	< 0.01	0.209	13.7	0.02834	2.0	0.15	180.1	3.6
TUF1_25.1	212	104	0.51	5.1	0.01	0.193	12.9	0.02793	2.1	0.16	177.6	3.6
TUF1_26.1	306	167	0.56	7.3	0.32	0.191	9.0	0.02787	1.3	0.15	177.2	2.3
TUF1_27.1	280	159	0.59	6.8	0.01	0.203	9.2	0.02833	2.3	0.24	180.1	4.0
TUF1_27.2	261	162	0.64	6.3	< 0.01	0.204	9.2	0.02799	1.6	0.18	178.0	2.9
TUF1_28.1	177	58	0.34	4.4	< 0.01	0.214	15.0	0.02854	1.3	0.09	181.4	2.4
TUF1_29.1	234	145	0.64	5.7	0.70	0.175	15.2	0.02808	1.5	0.10	178.5	2.6
TUF1_30.1	247	149	0.62	6.0	0.46	0.193	11.8	0.02819	2.2	0.19	179.2	3.9
TUFF1 concordia age: 179.8 ±1.4 Ma (2σ) (n=29 out of 31) with error in Standard - TEMORA-2 (1σ error of mean was ± 0.25%)												
TUFF 3												
TUFF3_1.1	135	146	1.11	3.51	< 0.01	0.250	11.3	0.03017	2.4	0.2	192	5
TUFF3_2.1	801	953	1.23	19.49	0.19	0.191	2.9	0.02833	1.0	0.4	180	2
TUFF3_2.2	420	259	0.64	10.68	< 0.01	0.204	5.6	0.02960	2.0	0.4	188	4
TUFF3_3.1	130	93	0.74	3.14	< 0.01	0.203	15.3	0.02821	1.3	0.1	179	2
TUFF3_4.1	330	648	2.03	8.28	< 0.01	0.217	6.1	0.02922	1.8	0.3	186	3
TUFF3_5.1	154	146	0.98	3.86	< 0.01	0.207	10.1	0.02922	1.4	0.1	186	3
TUFF3_6.1	181	222	1.27	4.44	< 0.01	0.209	11.5	0.02851	1.9	0.2	181	3
TUFF3_7.1	299	628	2.17	7.60	< 0.01	0.219	6.7	0.02959	1.5	0.2	188	3
TUFF3_8.1	122	100	0.85	3.07	0.15	0.197	12.7	0.02934	2.3	0.2	186	4
TUFF3_9.1	157	250	1.64	3.94	< 0.01	0.197	9.3	0.02917	0.9	0.1	185	2
TUFF3_10.1	174	261	1.55	4.29	< 0.01	0.201	14.7	0.02865	4.0	0.3	182	7
TUFF3_11.1	159	163	1.06	3.83	0.99	0.165	16.6	0.02802	1.2	0.1	178	2
TUFF3_12.1	139	192	1.43	3.47	< 0.01	0.215	8.9	0.02916	1.9	0.2	185	3
TUFF3_13.1	196	213	1.12	4.81	0.29	0.178	12.1	0.02858	2.0	0.2	182	4
TUFF3_14.1	204	374	1.89	5.14	< 0.01	0.212	8.8	0.02933	2.3	0.3	186	4
TUFF3_15.1	385	589	1.58	10.33	< 0.01	0.241	5.7	0.03121	1.8	0.3	198	4
TUFF3_16.1	158	204	1.34	3.93	0.11	0.196	10.5	0.02902	2.1	0.2	184	4
TUFF3_17.1	77	126	1.68	2.31	3.45	~~0.126~~	~~83.4~~	~~0.03483~~	~~3.4~~	~~0.0~~	~~221~~	~~7~~
TUFF3_18.1	225	265	1.22	5.70	0.57	0.178	14.3	0.02953	1.8	0.1	188	3
TUFF3_18.2	122	143	1.22	2.97	< 0.01	0.205	12.6	0.02841	2.0	0.2	181	4
TUFF3_19.1	264	230	0.90	6.54	< 0.01	0.200	7.7	0.02883	1.9	0.2	183	3
TUFF3_20.1	85	128	1.56	2.23	1.74	0.139	40.2	0.03055	4.1	0.1	194	8
TUFF3_21.1	148	271	1.89	3.75	< 0.01	0.212	11.6	0.02942	1.7	0.1	187	3
TUFF3_22.1	153	128	0.86	3.87	< 0.01	0.220	11.2	0.02952	2.7	0.2	188	5
TUFF3_23.1	224	297	1.37	5.60	0.09	0.197	9.1	0.02911	2.2	0.2	185	4
TUFF3_24.1	174	304	1.80	4.30	0.57	0.182	16.4	0.02877	2.4	0.1	183	4
TUFF3_25.1	144	162	1.17	3.62	0.17	0.188	20.4	0.02925	2.0	0.1	186	4
TUFF3_26.1	157	274	1.80	4.16	< 0.01	0.236	18.7	0.03075	4.2	0.2	195	8
TUFF3_27.1	234	323	1.43	5.97	< 0.01	0.243	6.4	0.02971	1.4	0.2	189	3
TUFF3 concordia age: 184.4 ±2.0 Ma (2σ) (n=26 out of 29) with error in Standard - TEMORA-2 (1σ error of mean was ± 0.37%.)												

Table 5.2: Summary of SHRIMP-II U-Pb results for zircons from tuff 1 and 3.

5.5. Facies associations

The Early Jurassic Cuyo Group in the two investigated basins evolve stratigraphically from continental and shallow-marine deposits (Units 1 and 2) to deep-marine deposits (Unit 3 and 4) (Fig. 5.5). Detailed sedimentological analyses in these units allowed identification of 11 facies associations in the Chacaico (FA1.1, FA2.1, FA2.2, FA2.4, FA2.5, FA3, FA4.3) and Eastern Catán-Lil Basin (FA1.2, FA2.2, FA2.3, FA3, FA4.1, FA4.2) where descriptions and interpretations are summarized in the Table 5.3. Note that the use of “epiclastic” refers to deposits with resedimented primary volcanic rocks (cf. White and Houghton, 2006) and that bioturbation index (BI) follows Taylor and Goldring (1993). The terminology used for lobe descriptions (lobe bedset, lobe complex, slope fan) follows Prélat et al. (2009).

Facies association	Sub-associations	Lithology	Flow Interpretation	Ichnofacies and fossils	Environment Interpretation
FA1.1 Alluvial fan (1.2-17 m thick)		Medium-to thick-bedded planar- to cross- stratified pebbly coarse- to medium-grained sandstone (0.2-2.5 n thick), very poorly sorted, with bedload pebble to cobble-sized clasts, with Cc-rich laminations (DXS, PL), erosive concave-up base and sharp top, lenticular amalgamated bedsets (1.2-6.8 m thick, 10-50 m wide) cutting through tuffaceous fine-grained sandstone.	High-concentration and hyperconcentrated flood flows	Plant (Pagiophyllum sp.) BI: 0	Alluvial fan channels in coastal floodplain with freshwater alkaline lakes
		Medium-bedded siliceous carbonate with plant debris, tabular beds within tuffaceous fine-grained sandstone, sharp-bounded	Carbonate precipitation		
FA1.2 Slope apron (7.6-14 m thick)		Thick- to very thick-bedded gravelly very coarse sandstone (1.4-6 m thick), massive, clast-supported with cobble-sized clasts (5-25 cm), tabular to wedge-shaped beds with erosive base and sharp planar top, extensive amalgamated bedsets (7-12 m thick)	Gravelly hyperconcentrated sheet flows	Bivalve disarticulated and broken shells (Kolymonectes coloradoensis) BI: 1 (Skolithos)	Slope apron channels and debrites from coastal to submarine slope, possibly below SWB
		Very thick-bedded gravelly medium-grained sandstone, very poorly sorted, matrix-supported with floating cobble- to boulder-sized clasts (10-50 cm) throughout bed, sheet-like beds with sharp to loaded base and undulated top, extensive amalgamated bedsets (11 m thick)	Poorly cohesive sandy debris-flows		
		Medium-to thick-bedded coarse- to fine-grained sandstone, poorly sorted, normally graded, with bedload pebble-sized clasts (2-5 cm) and rare boulder-sized clasts (up to 40 cm), erosive concave-up base and gradational top, lenticular amalgamated bedsets (1.2 m thick, 5-8 m wide)	High-density SGF		

Table 5.3: Facies association table with bioturbation index (BI) following Taylor and Goldring (1993). RXL: Current ripple-cross-lamination; CRXL: Climbing ripple-cross-lamination; DXS: Dune-scale cross-stratification; PL: Planar lamination; UnL: Undulatory lamination; QPL: Quasi-planar laminations; SiL: Sinusoidal laminations; WR: Wave ripple; HCS: Hummocky cross-stratification; Cc-rich: Carbonacoeus-rich

Table 5.3. (continue)

Facies association	Sub-associations	Lithology	Flow Interpretation	Ichnofacies and fossils	Environment Interpretation
FA2.1 Lower shoreface (13-20 m thick)	Lower shoreface (13-43 m thick)	Bioturbated fossiliferous sandy siltstone thin- to medium-bedded with medium- to fine-grained sandstone (medium HCS and/or WR) and skeletal grainstone (10-40 cm thick) with granule-sized echinoid bioclasts (crinoid-sponge), sharp planar base and undulated wavy top	Wave winnowing fines, and periodic oscillatory current reworking and sand-rich storm-related flows. Skeletal concentrations suggest parautochthonous assemblage, with intense wave reworking and short transport distance from source.	Ammonite and bivalve disarticulated shells (Weyla, Kolymonectes weaveri, Agerchlamys, Entolium), crinoid and echinoids BI: 4-5 (Macaronichnus, Skolithos)	Lower shoreface with proximal tempestites near the FWB, with moderate-energy and well-oxygenated conditions, with local sand supply enabling the development of isolated fan deltaic bottomset sheets and channels
	Fan delta bottomsets (51.8 m thick)	Thin- to medium-bedded epiclastic polymictic volcanogenic coarse- to fine-grained sandstone, poorly sorted, crudely graded, inverse and normal grading, laminated (DXS, PL), capped by muddy siltstone with fine-grained carbonaceous-rich sandy laminations (PL), tabular to lens-shaped beds, sharp or erosive base with granule- and pebble-sized clasts (2-5 cm) and sharp to gradational top	Waning and waxing high- to low-density SGF	Bivalves and ostreids disarticulated shells, crinoids and echinoids broken fragments BI: 3 (Thalassinoides, Planolites, Phycosiphon)	
		Thick-bedded polymictic gravelly coarse- to medium-grained sandstone (0.8-1.2 m thick), very poorly sorted, massive to coarse-tail normally graded. Beds comprise pebble- to cobble-sized clasts (2-20 cm), bioclasts and carbonaceous detritus (0.5-5 cm long), erosive concave-up base and sharp planar top, lenticular amalgamated bedsets (1-.3.5 m thick, 10-20 m wide)	Gravelly high-density to hyperconcentrated SGF		

Facies association	Sub-associations	Lithology	Flow Interpretation	Ichnofacies and fossils	Environment Interpretation
FA2.2 Shoreface-offshore transition (4-54 m thick)		Thin- to medium-bedded, bioturbated muddy siltstone and silty mudstone locally laminated (small HCS 0.1-0.2 m wide, 5-10 cm thick) bearing fossilized wood (up to 15 cm long), interbedded with skeletal packstone-floatstone (0.5-0.15 m thick) with pebble-sized bioclasts (bivalve-crinoid-sponge) and epiclastic polymictic volcanogenic very fine- to fine-grained sandstone, Cc-rich, tabular beds (0.1-0.6 m thick), with sharp planar base and gradational top. Also present epiclastic monomictic volcanogenic breccias (0.5-1.5 m thick) with inverse coarse-tail graded pumices, normal coarse-tail graded pebble-sized feldspar and quartz crystals, tabular to lens-shape beds, with sharp boundaries. Rare medium- to thick-bedded pyroclastic breccias (0.3-0.5 m thick), with inverse graded pumice lapillis, tabular to lens-shape beds, erosive base and sharp planar top.	Wave-enhanced dilute fine-grained SGF and few sand-rich flows, with common oscillatory current reworking. Skeletal concentrations suggest parautochnonous-autochtonous assemblages, with differential reworking, and deposition by waning storm surges. Pyroclastic breccias emplaced with pumiceous density currents and epiclastic monomictic volcanogenic breccias with high-concentration volcaniclastic gravity currents.	Bivalves, crinoid and sponge broken fragments (Posidonotis cancellata present in shell pavements) BI: 3-4 (Helminthopsis, Curvolithus, Thallassinoides, Chondrite Bollensis, Planolites, Skolithos)	Shoreface-offshore transition with distal tempestites, occasional supply of with primary and reworked volcaniclastic material emplaced between the FWB and SWB, with moderate-energy and normal oxygenation conditions

Table 5.3. (continue)

Facies association	Sub-associations	Lithology	Flow Interpretation	Ichnofacies and fossils	Environment Interpretation
FA2.3 Offshore (5-110 m thick)		Thin-bedded siliciastic mudstone with laminated fine-grained sandstone (UnL, PL, RXL) and tuff beds (0.02-0.15 m thick). Mudstone can be silicified banded and with common soft sediment deformation (convolution, folds and loading) and include convex-up convex-down gently disarticulated shell pavements Tabular beds, sharp, loaded or erosive base and sharp planar to undulated top.	Suspension settling and dilute fine-grained SGF. Common gravitational resedimentation, soft sediment deformation, and precipitation of silica-rich fluids at seabed.	Ammonites, bivalves articulated and disarticulated Bi: 2 (Phycosiphon, Chondrites, Cosmorhaphe) Ammonites, bivalves	Offshore with few dilute turbidites and low concentration low ash concentration density flows, below the SWB, under low-energy and fluctuating oxygenation conditions
FA3.1 Prodelta (7-54m)		Medium- to thin-bedded silty mudstone and mudstone, massive or Cc-rich, bearing carbonate concretions and few laminated fine-grained sandstone (small HCS, RXL, PL, UnL) tabular beds (0.2-0.4 m thick) with soft sediment deformation, and bioclastic lens-shaped beds (0.2-0.5 m thick), with loaded or sharp planar base and gradational to sharp top.	Settling and/or collapse of fluid mud flows and traction-plus-fallout from wave-enhanced dilute fine-grained SGF, and infrequent storm-wave reworking. Bioclastic lenses/gullies suggest intense wave reworking mixing parautochthonous assemblages with redeposition by waning storm-wave-induced flows.	Bi: 1-2 (Chondrites, Planolites, Phycosiphon)	Prodelta with low-energy and normal oxygenation conditions

Table 5.3. (continue)

Table 5.3. *(continue)*

Facies association	Sub-associations	Lithology	Flow Interpretation	Ichnofacies and fossils	Environment Interpretation
FA3.2 Delta front (32-61.8 m thick)	Mouthbar axis (5.4-26.8 m thick ~14.3 m)	Medium- to thick-bedded medium- to fine-grained sandstone (0.4-2.2 m thick), well- to moderately sorted, crudely normally graded, local inverse basal grading, lower part massive with granule-sized and few pebble-sized clast stringers (2-8 cm), upper part Cc-rich laminated (PL, QPL, LXL) obliterated by soft sediment deformation. Amalgamated tabular to lens-shaped beds, with convex-down tapering geometry, sharp planar, loaded or erosive base and sharp planar or undulated top. Sandy packages with slight low angle cross stratification include thick amalgamated bedsets (3.8-17.4 m thick) and thick heterolithic or silty mudstone interbeds (0.2-1.2 m thick).	Waning or waxing and waning friction-dominated turbulent jet flows	Bivalves broken shells BI: 1 (Ophiomorpha, Thallasinoides)	Mouthbar and marginal mouthbar deposits associated to shoal-water mouthbar-type delta, under normal marine salinity and high-energy conditions owing to wave and storm-wave influence
	Mouthbar margin (7.6-32 m thick ~12.9 m)	Thin- to medium-bedded, medium- to fine-grained sandstone (0.2-1.2 m thick), moderately to well-sorted, normally graded and laminated (PL, LXL) or ungraded and laminated (QPL, UL, large HCS, combined RXL, WR). Tabular to lens-shape beds, sharp planar or erosive scoured base and sharp planar to undulated wavy top. Interbedded with siltstone, silty mudstone Cc-rich, locally with bioclastic medium- to fine-grained sandstone, poorly sorted, , massive to crudely graded, granule- to pebble-sized bioclasts, Pb lithic clasts at base, lenticular beds (0.2-0.5 m thick, 0.5-1 m wide), erosive concave-up base and sharp planar to gradational top.	Storm-wave reworking under combined unidirectional or pure oscillatory flow conditions and post-storm suspension settling.		

Facies association	Sub-associations	Lithology	Flow Interpretation	Ichnofacies and fossils	Environment Interpretation
FA3. Siliciclastic-starved basinal (10-85 m thick)		Very thin- to thin -bedded calcareous organic-rich mudstone, with carbonate and pyrite concretions, tuff beds, and shell beds with bivalves in life position and ammonites.	Hemipelagic settling from biogenic surface productivity. Rare ash fall. Shell pavements and concretions record low sedimentation rates and/or high mortality episodes	Ammonites and juvenile bivalves (Bositra sp. Agerchlamys, Entolium lunare) BI: 1 (Chondrite Intricatus and cosmorhaphe)	Siliciclastic-starved basin below the SWB, with poorly oxygenated and very low-energy conditions
FA4.1 Distal ramp lobes (18-95 m thick)	Lobe axis (1-4.8 m thick ~2.5 m)	Thick-bedded, medium- to fine-grained sandstone (0.8-2.6 m thick), poorly sorted, massive to crudely normally graded, faint laminated, with rare pebble-sized clasts (2-10 cm) at base of beds, slightly muddier finer-grained top. Tabular beds with sharp planar or loaded base and sharp top.	Clay-rich transitional plug flows with suppressed turbulence	Ammonites BI: 0-1 (Chondrite)	Low sand:mud ratio intraslope lobes, deposited in the distal part of a ramp system, under poorly oxygenated conditions
	Lobe off-axis (6-29 m thick ~16.6 m)	Medium- to thick-bedded, medium- to fine-grained sandstone (0.2-1 m thick), poorly sorted, massive, with deformed pebble-sized clasts (5-10 cm) throughout bed or segregated in the finer-grained muddy upper part. Tabular beds, sharp planar or erosive base and sharp planar or deformed top, interbedded with massive silty mudstone and mudstone	Low strength poorly cohesive sandy debris-flows		
	Lobe fringe (3.4-65 m thick ~16.9m)	Thin- to medium-bedded siltstone and mudstone, with few thin beds of fine-grained sandstone (0.01-0.4 m thick), massive, with pebble-sized clasts (1-5 cm) at top, or normally graded, laminated top (PL, RXL) Tabular beds, sharp planar base and gradational top	Dilute low-density turbulent SGF and few poorly cohesive sandy debris-flows		

Table 5.3. (continue)

Table 5.3. (continue)

Facies association	Sub-associations	Lithology	Flow Interpretation	Ichnofacies and fossils	Environment Interpretation
FA4.2 Proximal ramp lobes (30-124 m thick)	Lobe axis (0.9-11.7 m thick, ~2.3 m)	Medium- to thick-bedded, coarse- to fine-grained sandstone (0.5-2.6 m thick), poorly sorted, lower part massive with stepped laminations and clasts and bioclasts, normally graded. It passes after sharp grain-size break into mud-rich Cc-rich fine-grained sandstone (PL) or is gradationally or sharply overlain after grain-size break by laminated medium- to fine-grained sandstone at top (PL, UnL, SiL, RXL, CRXL). Tabular to mounded amalgamated bedsets (1.2-11.7 m thick, averagely 3 m thick) with irregular loaded or sharp base locally erosive and sharp planar to gradational top. Scoured amalgamated bedsets (0.6-4.4 m thick, averagely 1.8 m thick and 10-50 m wide) with concave-up erosive base (0.5-1 m relief) with basal clast lag or chaotic argillaceous clast-rich sheared base. Local conical clastic pipes through sandstone beds.	High-density SGF and tractional reworking beneath waning dilute turbulent flows with high-suspended load fallout rates, and turbulence-enhanced transitional flows	Ammonites, belemnites and bivalves BI: 2 (Chondrite, Planolites)	High sand:mud ratio intraslope lobes locally channelized, deposited in the proximal part of a ramp system, under normal oxygenated conditions
	Proximal lobe off-axis (2-26.6 m thick, ~14.5 m)	Medium- to thick-bedded, medium- to fine-grained sandstone (0.5-2 m thick), poorly sorted, interbedded with Cc-rich heterolithic RXL fine-grained sandstone, siltstone and mudstone. Medium-grained sandstone, massive lower part or graded into laminated fine-grained sandstone (PL, UnL, DXS, RXL) or medium-grained sandstone massive and clast-rich. Tabular beds, sharp planar locally erosive base and gradational or sharp top.	Waning high- to low-density SGF, clay-rich transitional to quasi-laminar plug flows		

Facies association	Sub-associations	Lithology	Flow Interpretation	Ichnofacies and fossils	Environment Interpretation
FA4.2 Proximal ramp lobes (30-124 m thick)	Distal lobe off-axis (1-22.4 m thick, ~10.1 m)	Thin- to medium-bedded, medium- to fine-grained sandstone (0.2-2 m thick), poorly sorted, interbedded with RXL fine-grained sandstone, siltstone, mudstone. Medium- to fine-grained sandstone, massive to normally graded with Cc-rich laminations (PL, RXL), or massive and/or chaotic argillaceous, clast-rich (2-8 cm). Tabular or lens-shape beds, locally erosive clast-rich base and sharp top.			High sand:mud ratio intraslope lobes locally channelized, deposited in the proximal part of a ramp system, under normal oxygenated conditions
	Lobe fringe (2-10 m thick, ~5.5 m)	Thin- to very-thin-bedded siltstone and mudstone (0.1-0.2 m thick), massive to normally graded, and fine-grained sandstone laminated (RXL-PL). Tabular beds, sharp planar base and gradational top. Locally with cone in cone structures in mudsotne (5-6 cm thick, up to 1.5 m long)	Low-density turbulent SGF and clay-rich transitional plug flows		
FA4.3 Sand-starved slope (450-530 m thick)		Thin- to medium-bedded mudstone and rare siltstone and sandstone (0.05-0.15 m thick), planar laminated or massive, with gradational or sharp top.	Suspension settling and occasional low-density SGF	Ammonites and bivalves (Bositra sp.)	Sand-starved slope below the SWB, with poorly oxygenated and low-energy conditions

Table 5.3. (continue)

5.5.1. Unit 1

Unit 1 comprises two facies associations: alluvial fan deposits (FA1.1) in the Chacaico Basin and proximal slope apron deposits (FA1.2,) in the Eastern Catán-Lil Basin (Table 5.3 and Fig. 5.9). Unit 1 is onlapped by shoreface-offshore transition deposits (FA2.2) of Unit 2A in the Chacaico Basin and offshore deposits (FA2.3) of Unit 2A in the Eastern Catán-Lil Basin (Fig. 5.5).

5.5.1.1. Description

FA1.1

This facies association corresponds to medium- to thick-bedded stratified pebbly sandstone (Fig. 5.9-A) very poorly sorted, coarse- to medium-grained, with wood debris (few cm long) and a high-concentration of subangular to subrounded volcanic, carbonate, metamorphic and granitic pebbles and rare cobbles (up to 10 cm long). Clasts provide a normal coarse-tail grading to beds with crude parallel to low-angle cross-stratification (<10 °), which amalgamate into lenticular bedsets (1.2-6.8 m thick, 10-50 m wide) with erosive concave-up base and sharp planar top (Log 2 Fig. 5.9-A). Bedsets cut through diffusely bedded greenish fine-grained tuffaceous sandstone with locally incised coarse-grained massive sandstone channel-fills (5-10 m thick, 10-20 m wide) (Precuyano Cycle deposits) (cf. Muravchik et al., 2011). Some medium-bedded siliceous carbonates containing wood fragments and well-preserved Araucariaceae plant stems (*Pagiophyllum* sp., Spalletti et al., 1991) can be present within the fine-grained sandstone (Fig. 5.9-B).

FA1.2

This facies association includes clast-supported and matrix-supported gravelly sandstone beds. Thick- to very thick-bedded clast-supported gravelly sandstone beds (1.4-6 m thick) comprise subangular to subrounded granitic, volcanic and siliciclastic cobbles (5-25 cm long) supported by a very poorly sorted, ungraded, coarse to very coarse-grained sandstone matrix. Beds are tabular to wedge-shaped, with erosive base and sharp planar top and commonly

form amalgamated bedsets (7-11.2 m thick). Very thick-bedded matrix-supported gravelly sandstone (3-4 m thick) (Fig. 5.9-C) have a very poorly sorted, ungraded, slightly muddy medium-grained sandstone matrix that support subrounded volcanic and siliciclastic cobbles and boulders (up to 40 cm long). Beds are tabular, with irregular loaded or sharp bases and undulated tops, which can present rare thick abraded bivalve shells (*Kolymonectes coloradoensis,* Gulisano and Gutiérrez-Pleimling, 1995) and form amalgamated bedsets (5-12 m thick) (Log 6 Fig. 5.9-B). They can be overlain by medium- to thick-bedded, poorly sorted and normally graded coarse- to fine-grained sandstone bedsets (0.8-1.2 m thick) (Fig. 5.9-D), bearing subangular volcanic and granitic pebbles concentrated in the lower part of beds. Beds are lenticular, with erosive concave-up base and gradational top that can be burrowed (*Skolithos*, BI: 1) and form amalgamated bedsets (1.2 m thick, 5-8 m wide).

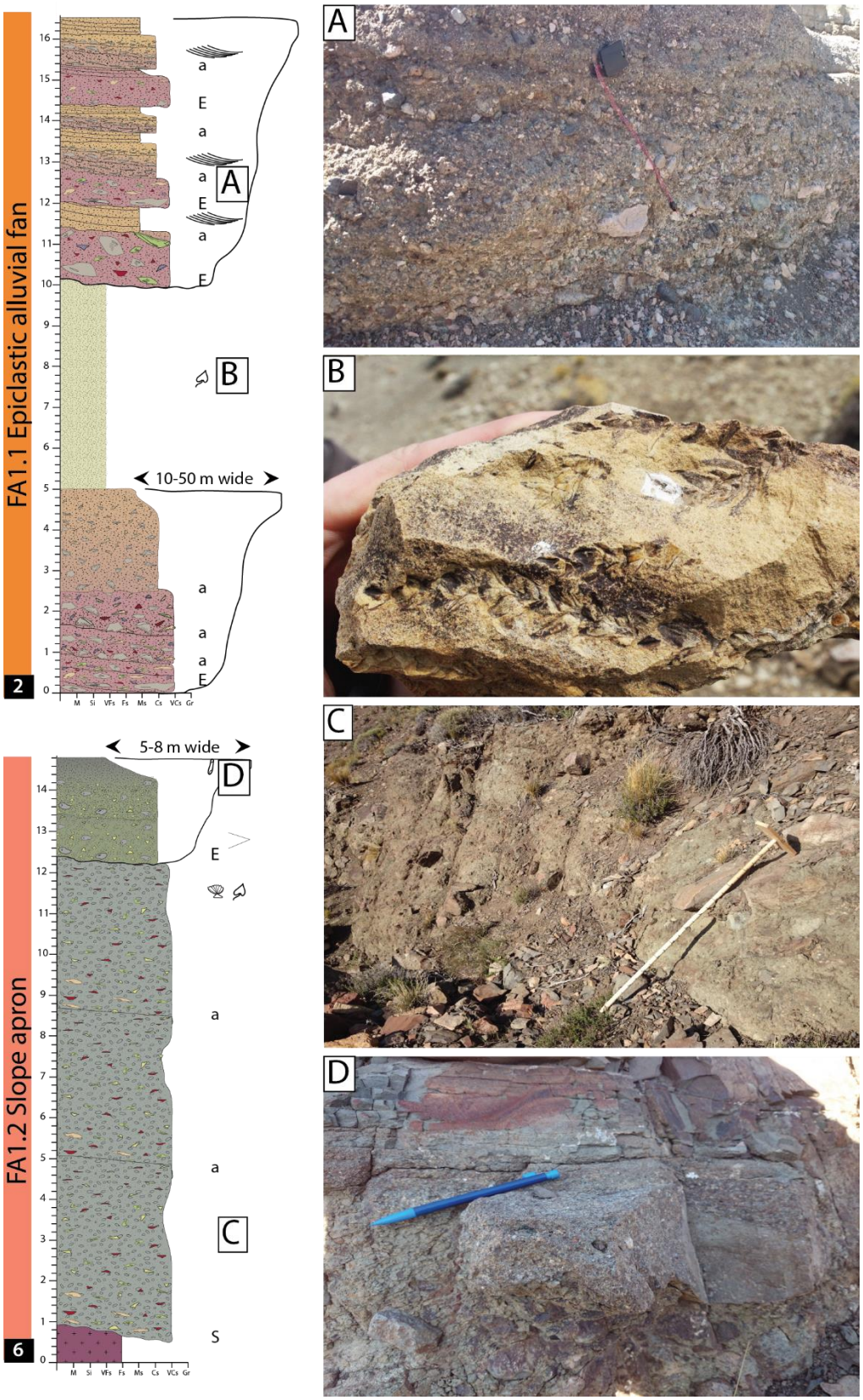

Figure 5.9: A- Medium- to thick-bedded planar- to cross-stratified pebbly sandstone, very poorly sorted, coarse- to medium-grained and bearing normal coarse-tail graded, subangular volcanic, carbonate, metamorphic and granitic pebbles and rare cobbles (FA1.1). B- Siliceous carbonates containing wood fragments and well-preserved Araucariaceae plant stems found in the intervening fine-grained tuffaceous sandstone (FA1.1). D- Very thick-bedded sandstone with a very poorly sorted, ungraded, slightly muddy medium-grained sandstone matrix supporting subrounded volcanic and siliciclastic cobbles and boulders (FA1.2). C- Medium- to thick-bedded, poorly sorted and normally graded coarse- to fine-grained sandstone (FA1.2).

5.5.1.2. Interpretation

FA1.1: Alluvial fans

In stratified conglomerate beds, the differential clast segregation, basal erosion, and tractive structures suggest deposition by high-concentration and hyperconcentrated flood flows (Sohn et al., 1999). The silicified carbonates deposited in freshwater alkaline lakes draining volcanic terrains, with adequate conditions for carbonate precipitation without microbial influence (Wright, 2012). FA1.1 deposits represent channel-fills on small alluvial fans (Blair and McPherson, 1994) in a floodplain environment with freshwater lakes (see also Muravchik et al., 2011).

FA1.2: Slope aprons

The clast-supported conglomerate beds with erosive base, lack of tractional structures, matrix support, and chaotic clast fabric suggest deposition from gravelly hyperconcentrated sheet flows in a subaerial environment (Smith, 1986). In contrast, thick-walled marine bivalves and sparse bioturbation support deposition of matrix-supported conglomerate and normally graded sandstone in a relatively shallow-marine environment. The matrix-supported conglomerate beds lack basal erosion, tractional structures and the random clast fabric in sandy matrix indicate en masse deposition from weakly cohesive sandy debris-flows with sufficient yield strength and buoyancy to support floating clasts (Talling et al., 2012). Coarse- to fine-grained sandstone bedsets show a crude normal grading with clast concentration in the lower part of beds and lenticular geometry with erosive base, which suggest deposition by high-density sediment gravity flows with significant bedload transport and local scouring (Lowe, 1982; Talling et al., 2012). These deposits therefore correspond to submarine clast-rich polymictic conglomerate slope apron deposits (e.g Leppard and Gawthorpe, 2006) probably deposited below the storm-wave base.

5.5.2. Unit 2

Unit 2 includes several facies associations (Table 5.3 and Fig. 5.10). Unit 2A in the Chacaico Basin comprises lower shoreface (FA2.1) and shoreface-offshore transition (FA2.2, 4-54 m thick) deposits onlapped by Unit 2B corresponding to prodeltaic (FA2.4) and delta-front deposits (FA2.5) (Fig. 5.5). Unit 2A and B in the Eastern Catán-Lil Basin comprise shoreface-offshore transition (FA2.2) and offshore deposits (FA2.3) (Fig. 5.5). Both Unit 2A and 2B are onlapped by siliciclastic-starved basinal calcareous mudstone deposits (FA3) in both basins (Fig. 5.5).

5.5.2.1. Description

FA2.1

This facies association corresponds mainly to bioturbated sandy siltstone and sandstone packages (Log 2 Fig. 5.10). The sandy siltstone are diffusely bedded, intensely mottled (*Macaronichnus, Skolithos, Thallasinoides* BI: 4-5), fossiliferous (small ammonites and bivalves) and comprise thin to medium beds of fine- to medium-grained structured sandstone and skeletal grainstone (Fig. 5.10-A). Structured sandstones are well sorted, with ripple-cross-laminations with wave-ripple tops or with anisotropic hummocky cross-stratification (0.2-0.5 m wide and 10-20 cm thick) and also bioturbated (Fig. 5.10-B and C). Skeletal grainstone beds are massive and comprise well sorted, granule-sized bioclasts of crinoid ossicles and sponge spicules in a medium-grained quartzous sandy matrix. Locally, the bioturbated sandy siltstone include some thin to thick event beds of and coarser-grained epiclastic polymictic volcanogenic sandstone (Log 1 Fig. 5.10) They correspond to very poorly sorted, crudely normally graded, coarse- to fine-grained or massive sandstone with dominantly reworked volcaniclastic material and abundant carbonaceous detritus and bioclasts (bivalve and ostreid shells). Biogenic reworking is mainly represented by sharp-walled burrows (*Thalassinoides, Planolites, Phycosiphon*, BI: 3). Basal inverse grading is also common in their massive lower part bearing outsized granules and pebbles. Locally, the upper part of beds contains plane parallel and dune-

scale cross-stratification, capped by carbonaceous-rich fine-grained sandstone to muddy siltstone finely laminated. Non-gravelly sandstone beds are tabular to lens-shaped, with an irregular sharp planar to erosive base, and with sharp or gradational top. Gravelly sandstone beds include subrounded to subangular siliciclastic, volcanic and metamorphic pebbles and cobbles (up to 20 cm long) with normal coarse-tail grading (Fig. 5.10-D) and form lenticular bedsets (1-3.5 m thick, 10-20 m wide), with erosive concave-up bases and planar tops (Log 1 Fig. 5.10).

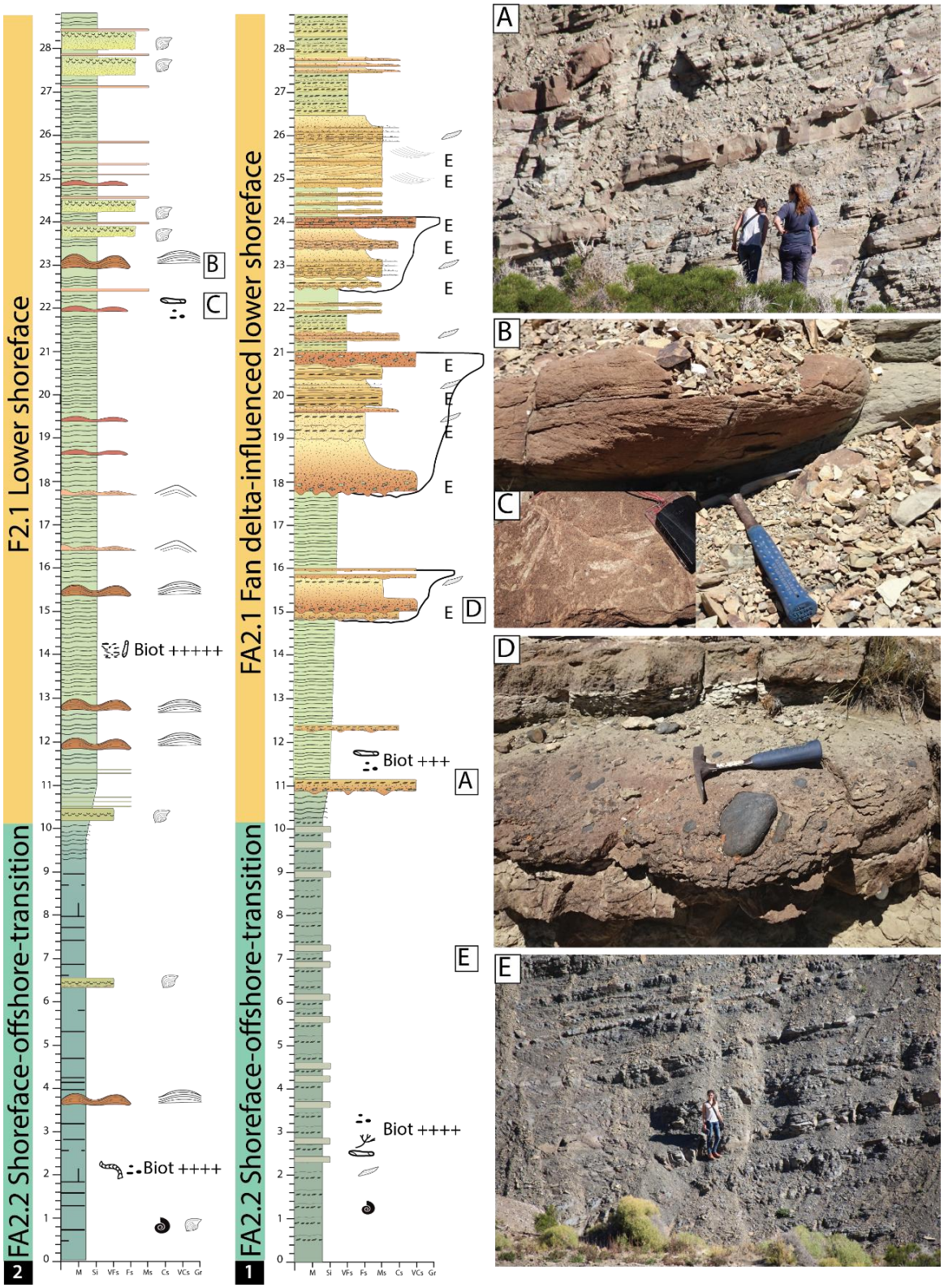

Figure 5.10: A- Succession of highly bioturbated sandy siltstone interbedded with thin to medium beds of fine- to medium-grained structured sandstone and skeletal grainstone (FA2.1). B- Example of anisotropic hummocky cross-stratification in sandstone (FA2.1). C- Thallasinoides bioturbations in sandstone. D- Very poorly sorted, crudely normally graded (with local basal inverse grading), coarse- to fine-grained polymictic gravelly sandstone, bearing subrounded to subangular siliciclastic, volcanic and metamorphic pebbles and cobbles with normal coarse-tail grading in their lower part. E- Moderately bioturbated silty mudstone and muddy siltstone successions (FA2.2).

FA2.2

This facies association is represented by silty mudstone to muddy siltstone packages with uncommon thin to medium-sandstone and breccias beds (Log 1-2 Fig. 5.10, Log 8 Fig. 5.11) and moderate bioturbation (*Helminthopsis, Curvolithus, Thallasinoides, Chondrite Bollensis, Planolites, Skolithos*, BI: 3-4).

The silty mudstone and siltstone deposits (Figs 5.10-E and 5.11-A) commonly have carbonaceous debris (mm-scale), rare fossilized wood and can present convex-up convex-down shell pavements of disarticulated epifaunal bivalves including *Posidonotis cancellata*. They skeletal packstone/floatstone beds contain bed-parallel abraded, disarticulated bivalve shells and other pebble-sized bioclastic material loosely packed in a silty-marly matrix (Fig. 5.11-B). Beds have a sharp planar base and gradational top, with an upward decrease of shell concentration.

The sandstones include coarse-grained epiclastic polymictic graded sandstone beds (Fig. 5.11-C) and very fine- to fine-grained hummocky cross-stratified or massive bioturbated sandstone beds (Fig. 5.11-D). Epiclastic polymictic sandstone beds (Fig. 5.11-C) are massive to normally graded, very poorly sorted, coarse- to fine-grained and structured with thick planar laminations (2-3 cm thick) that show inverse or normal coarse-tail grading of sand- to granule-sized grains, with locally current ripples at top. Beds are tabular, with a sharp planar base and top with *Skolithos* burrows.

Pyroclastic breccias are massive, characterized by inversely graded juvenile pumice lapillis (5 cm long) with intact ragged margins and plastic deformation (flattening) (Fig. 5.11-E). Clasts are arranged with their long-axis subparallel to bed top and are supported in a dark tuffaceous-clayey matrix. These two breccias facies have sharp bases and tops. Epiclastic monomictic volcanic breccias are massive or crudely stratified, with a mixed fine sandy and tuffaceous clayey matrix bearing abundant coarse grain sized angular crystals of feldspar and quartz with inverse coarse-tail grading.

FA2.3

This facies association is composed of thin-bedded siliciclastic mudstone to silty mudstone, with scarce fine-grained sandstone, tuff layers and breccias (Log 8 Fig. 5.11-F). Mudstone-dominated successions can be silicified and form chert with a banded fabric, alternating with whitish siliceous bands. Mudstone are dark grey to greenish, massive or laminated, weakly bioturbated (*Phycosiphon, Chondrite, Cosmorhaphe*; BI: 2) and comprise small ammonites and convex-up disarticulated or articulated shells. Fine-grained sandstone have pinch and swell geometry and internally they show planar parallel and current ripple-cross-laminations (Fig. 5.11-G), locally with convolute laminations and flame structures (Fig. 5.11-H). These beds are tabular, with a sharp planar or loaded base and sharp planar to undulated top. Tuff beds are massive to planar stratified, with a whitish ash matrix and sporadic occurrence of pumice lapillis at top.

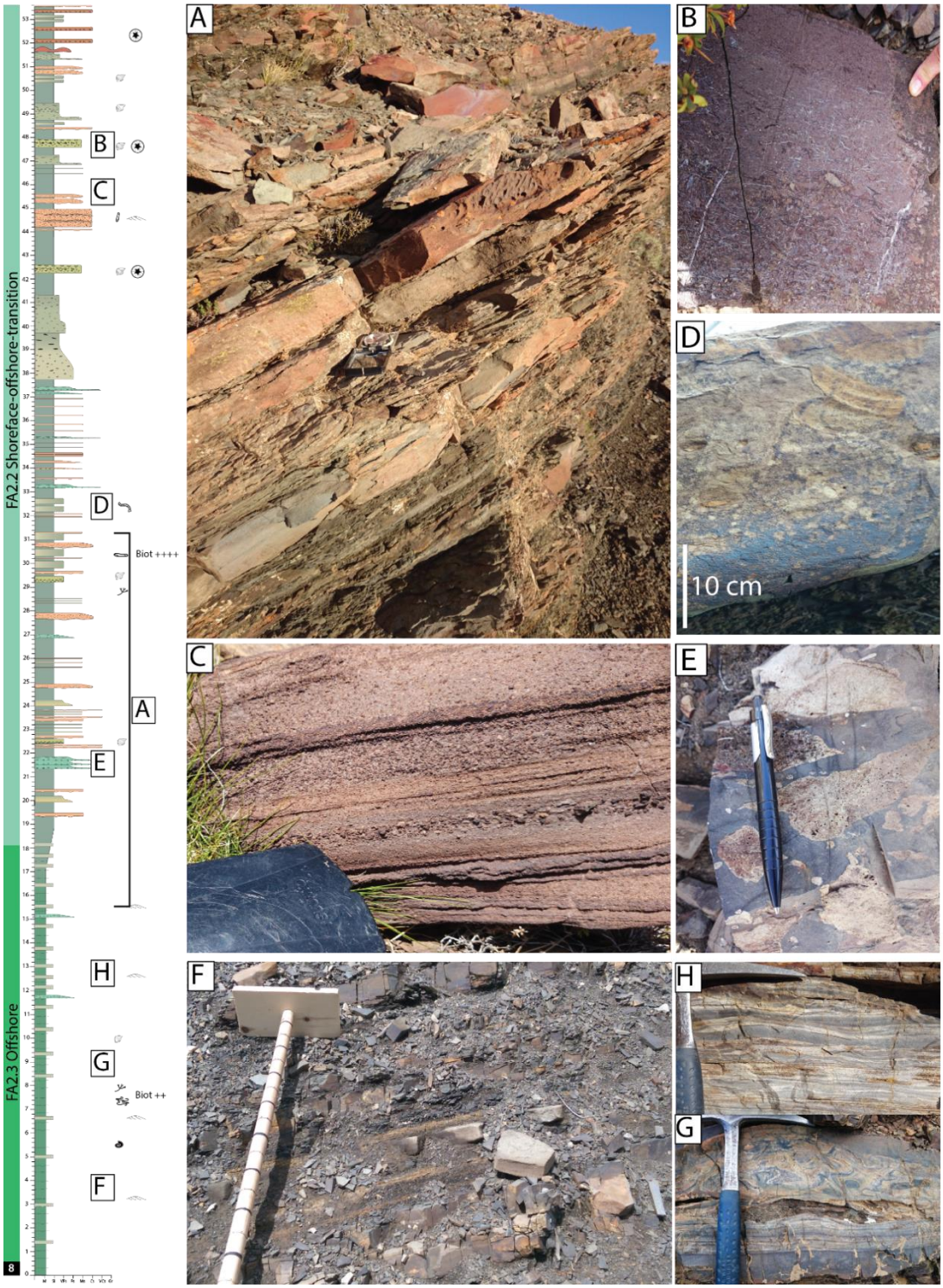

Figure 5.11: A- Thickening and coarsening-upward succession including basal thin-bedded mudstone and silty mudstone (FA2.3) grading upwards into silty mudstone to muddy siltstone packages with uncommon thin to medium sandstone and breccias beds (FA2.4). B-Skeletal packstone-floatstone with normally graded bioclastic material including broken or disarticulated shells, crinoid ossicles and sponge spicules in a silty-marly matrix (FA2.2). C- Very poorly sorted, coarse- to fine-grained polymictic sandstone planar laminated (2-3 cm thick) with inverse or normal coarse-tail grading of sand- to granule-sized grains (FA2.2). D- Very fine- to fine-grained massive bioturbated sandstone including planolites, curvolithus and chondrite (FA2.2). E- Pyroclastic breccia with juvenile pumice lapillis (5 cm long) showing ragged margins floating in a tuffaceous clayey matrix (FA2.2-FA2.3). F- Thin-bedded siliciclastic mudstone to silty mudstone, with scarce fine-grained sandstone, tuff layers and breccias (FA2.3). G- Fine-grained sandstone with planar parallel and current ripple-cross-laminations (FA2.3). H- Fine-grained sandstone with convolute laminations (FA2.3).

FA2.4

This facies association mainly comprises medium- to thin-bedded massive mudstone and planar laminated silty mudstone (Log 1 Fig. 5.12) with abundant organic material (mm-scale), rare ammonites, bivalve shells and low bioturbation (*Chondrite, Planolites, Phycosiphon*; BI: 1-2). Thin to medium and fine-grained sandstone beds and bioclastic sandstone lenses can be present (Fig. 5.12-A). The sandstone beds have undulatory to planar parallel laminations often with soft sediment deformation and loaded or sharp planar base and top (Fig. 5.12-B). Bioclastic lenses form massive, crudely normally graded, medium- to fine-grained sandstone with granule- to pebble-size comminute shell debris and complete shells, randomly oriented and locally mixed with subrounded siltstone pebbles at bed base (Fig. 5.12-C).

FA2.5

This facies association forms sandstone-prone successions including medium- to thick-bedded sandstone with intervening thin- to medium-bedded sandy heterolithics (Log 1 Fig. 5.12). Thick beds of moderately to well sorted, medium- to fine-grained sandstone are massive to weakly normally graded, with local inverse basal grading (Fig. 5.12-A). Beds often show planar to quasi-planar laminations and low-angle cross-laminations often enriched in flat carbonaceous debris (mm- to cm-scale) and commonly affected by soft sediment deformation at bed top. Bed base can show smooth or striated grooves and can bear deformed siltstone and rarely mudstone pebbles. Their top is dominantly unburrowed but can show locally few trace fossils (*Ophiomorpha, Thalassinoides*) (Fig. 5.12-A, inset). These thick sandstone beds are tabular and amalgamated with a blocky grain-size trend (1.2-9 m thick, averagely 3.3 m thick) or have sandy heterolithic interbeds. They form laterally extensive (1-2 km) high sand: mud ratio packages (up to 27 m thick). Thin- to medium-bedded sandy heterolithic packages comprise medium- to fine-grained sandstone (Fig. 5.12-B-D-E), mostly interbedded with massive carbonaceous-rich siltstone and silty mudstone (Fig. 5.12-F, inset). Sandstone beds are normally graded with planar and low-angle cross-laminations or ungraded with quasi-planar to undulatory laminations associated with small isotropic hummocks and symmetrical ripples

with rounded crests (Fig. 5.12-D) or large anisotropic hummocks and asymmetrical rounded ripples with tangential to sigmoidal foresets (Fig. 5.12-E). Beds are tabular to lens-shaped and locally bioturbated (*Thalassinoides, Planolites*; BI: 1).

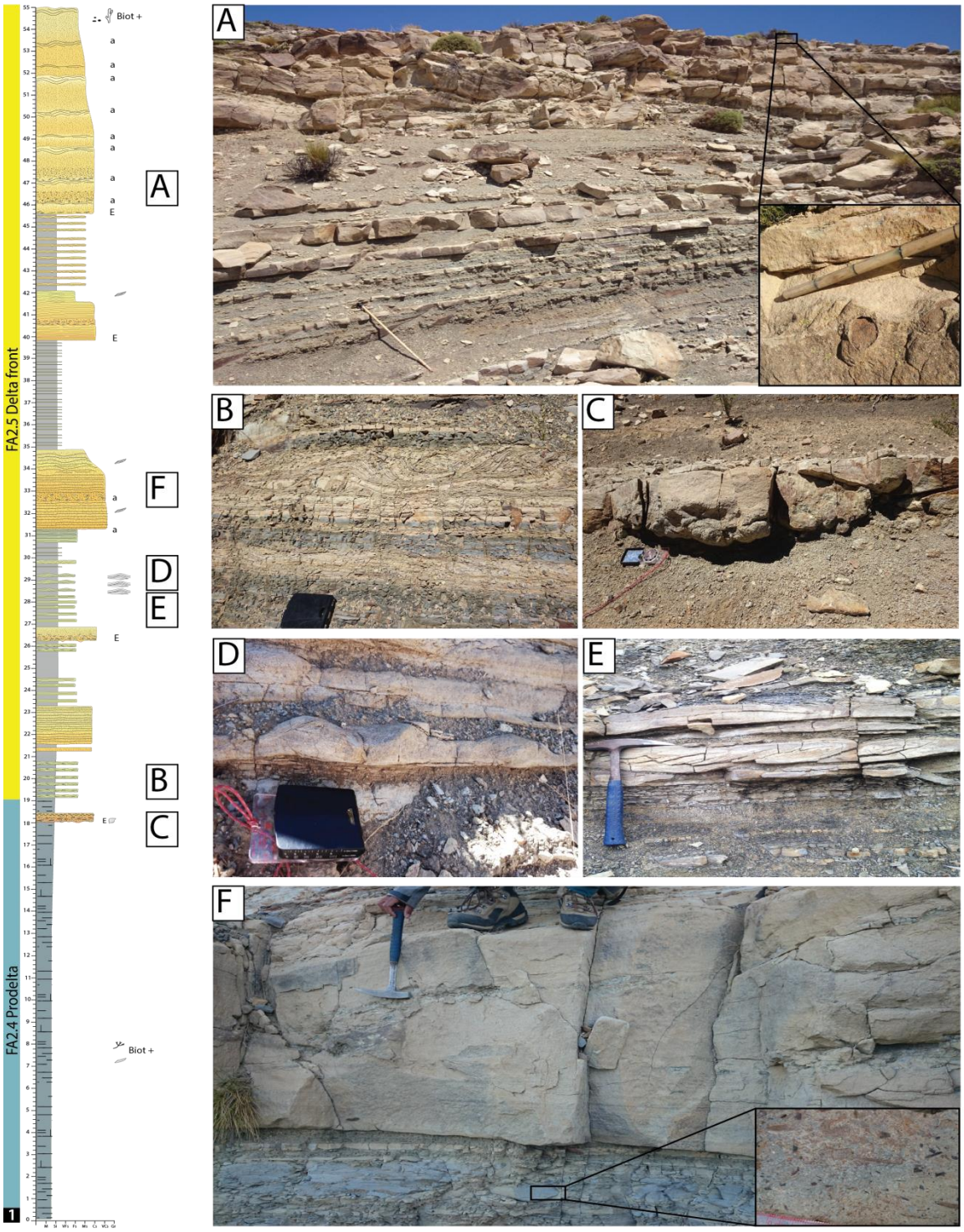

Figure 5.12: A-Thickening- and coarsening-upward succession including medium- to thin-bedded massive mudstone and planar laminated silty mudstone with intervening fine-grained sandstone beds (FA2.4) grading upwards into medium- to thick-bedded sandstone-prone packages (FA2.5). Inset shows bioturbation (Ophiomorpha) at thick sandstone bed top). B-

Fine-grained sandstone beds interbedded with planar laminated silty mudstone, showing undulatory to planar parallel laminations with soft sediment deformation (FA2.4). C- Medium- to fine-grained bioclastic sandstone lenses isolated within massive mudstone showing normal grading of granule- to pebble-size comminute shell debris and complete shells and siltstone pebbles (FA2.5). D- Moderately to well sorted, medium- to fine-grained normally graded sandstone, with planar and low-angle cross-laminations and siltstone pebbles (FA2.5). Inset shows carbonaceous-rich siltstone of sandy heterolithics. E-F Example of medium- to fine-grained sandstone found in sandy heterolithic packages with quasi-planar to undulatory laminations associated with large anisotropic hummocks and asymmetrical rounded ripples with tangential to sigmoidal foresets (E) and symmetrical ripples with rounded crests (F).

5.5.2.2. Interpretation

FA2.1: Lower shoreface

Fine-grained bioturbated sandy siltstone deposited with settling from suspension under fair-weather conditions and HCS or ripple-laminated sandstone deposited with fair-weather- and storm-related processes which moulded relatively large sandy hummocks on the seabed (Cheel and Leckie, 2009). The general abundance and diversity of trace fossils, dominated by deposit and suspension feeders is attributed to the mixed *Skolithos-Cruziana* ichnofacies, with well-oxygenated bottom and interstitial waters (MacEachern et al., 2007). Skeletal grainstone beds bear low diversity, but high-concentration of parautochthonous specimens with high abrasion and fragmentation degree. This points to intense wave reworking and short transport distance prior to deposition by sand-rich storm-related flows as proximal tempestites (Fürsich and Pandey, 2003).

On the other hand, the very poor to poor sorting, erosive base and traction structures and coarse grain size of thick to medium event beds of epiclastic polymictic volcanogenic sandstone contrast with the background fine-grained sandy and silty deposits. Characteristics of these beds often lacking an upper fine-grained bed division and with local basal inverse grading support deposition by high-density sediment gravity flows, with waning and waxing flow behaviour and frequent bypass of the more dilute part of flows (Lowe, 1982). Polymictic gravelly sandstone lacking mud matrix suggests deposition by gravelly high-density to hyperconcentrated flows, with significant sustained bedload transport (Lowe, 1982; Mulder and Alexander, 2001). Sheet to lenticular bed geometries indicate deposition by highly erosive flows with variable confinement and bypass of all, but the coarsest material, which enabled the local development of basal

channel lags (Gardner et al., 2003). These deposits cutting through fine-grained bioturbated sandy siltstone deposits are interpreted as isolated fan delta sandy bottomsets (Nemec and Steel, 1988; Postma 1990).

FA2.1 deposits emplaced in a lower-shoreface environment developed under moderate energy with periodic sediment reworking by storm- and fair-weather-derived processes, locally imprinted by fan-deltaic sand supply, under well-oxygenated conditions enabling intense biogenic activity and, with frequent volcanic input.

FA2.2: Shoreface-offshore transition

Interbedded bioturbated muddy siltstone and silty mudstone reflect dominant settling from suspension during fair-weather wave winnowing and deposition of very fine- to fine-grained sandstone by storm-related flows which moulded relatively small sandy hummocks (Duke et al., 1991; Cheel and Leckie, 2009). The greenish hue of sediment suggests high organic matter content (Uchman and Wetzel, 2011). The relatively low diversity, but locally high-density of trace fossil assemblage dominated by deposit and occasional opportunistic suspension feeders represent a Cruziana ichnofacies under normal oxygenation conditions (MacEachern et al., 2007). Skeletal packstone/floatstone with diverse and fragmented macrofauna beds points towards differential reworking, prior to deposition by waning storm surges as distal tempestites (Fürsich and Pandey, 2003). The thin beds of epiclastic volcanogenic sandstone emplaced with tractional reworking beneath waning, high- to low-density sediment gravity flows (Lowe, 1982) are similar in composition to the sandstone found in FA2.1 and indicate a more distal depositional setting.

The pyroclastic breccias lack traction structures, have sharp planar or locally erosive base, with aligned juvenile pumices at bed top, which suggest subaqueous transport and deposition by water-supported pumiceous density currents (Stewart and McPhie, 2004; Cas and Giordano, 2014). Conversely, the diffuse stratification, and the non-juvenile character and density-controlled settling of volcanogenic clasts indicate deposition of epiclastic monomictic volcanic breccias by stratified high-concentration gravity currents (Watton et al., 2013). Collectively, these facies might record primary pyroclastic and post-eruption resedimentation of freshly deposited loose pyroclastic debris due to

wave reworking and/or slope instability shortly after volcanic eruptions (Watton et al., 2013).

In summary, FA2.2 deposits are interpreted to reflect deposition between the fair-weather wave base and the storm-wave base in a shoreface-offshore transition environment (Reading and Collinson, 1996), characterized by low- to moderate-energy conditions, moderate biogenic activity and normal oxygenation, as well as the frequent input of volcanic-derived material.

FA2.3: Offshore

Mudstone deposited from suspension settling and recorded infaunal activity dominated by grazers and deposit feeders, which indicates a high organic content in sediments. The relatively low intensity of bioturbation in this case might reflect fluctuating oxygenation conditions and Zoophycos ichnofacies (MacEachern et al., 2007). Extensive silicification, chert and siliceous bands indicate precipitation of silica-rich fluids at the seafloor or just below the sediment-water interface. This process might have resulted from enhanced hot thermal fluid circulation leaching silica through volcanic rocks with rapid cooling when mixing with colder seawater during marine flooding (Renaut et al., 2002). The fine-grained sandstones were deposited by dilute low-density sediment gravity flows (Lowe, 1982) and the common soft sediment deformation indicates rapid dewatering and sediment liquefaction after deposition. The tuff beds deposited with suspension fallout of ash clouds, settling of water-logged pumices and low ash concentration density flows (D’Atri et al., 1999).

In summary, FA2.3 successions were deposited below the storm-wave base, under low-energy conditions in a fully marine offshore environment with weak biogenic activity due to fluctuating oxygenation conditions and frequent dilute sediment gravity flows and ash-fall.

FA2.4: Prodelta

The carbonaceous-rich mudstone and silty mudstone with paucity of sedimentary structures suggest deposition with direct settling from hypopycnal plumes during flood peak discharge events and/or with collapse of dense fluid mudflows formed with storm-induced resuspension of flocculated river-flood mud (Ogston et al., 2000; Fan et al., 2004; Traykovski et al., 2007). The fine-grained sandstone beds with common planar to ripple-cross-laminations with soft sediment deformation suggest deposition with traction-and-fallout by unidirectional low-density sediment gravity flows. These could record episodic depositional events related to large river floods.

The bioclastic lenses isolated within mudstone infill gutter casts or scour-shaped depressions. Their gradational bed top, high shell fragmentation with good sorting of diverse parautochthonous specimens suggest intense mechanical wave reworking mixing prior to transport and redeposition by waning storm-wave generated flows (Fürsich and Pandey, 2003). The paucity of sandstone beds often obliterated by soft sediment deformation, scarcity of substrate bioturbation, together with the abundant carbonaceous terrestrial material in these deposits differ from characteristics of offshore deposits (FA2.3). Characteristics of these fine-grained deposits together with lateral association with delta-front deposits (FA2.5) points to high sediment fallout rate at proximity to riverine discharge in a low-energy prodeltaic open-marine environment (MacEachern et al., 2005).

FA2.5: Delta-front

Dominant normal grading, massive to planar and low-angle cross-laminations, local basal erosion and tabular bed geometry with common abrupt pinchout terminations of medium to thick sandstone beds are the main characteristics of this facies association. They suggest deposition under lower and upper plane bed regime via rapidly decelerating high-concentration flows generated with river floods (Wright et al., 1977; Orton and Reading, 1993; Turner and Tester, 2006). The paucity of sand supplied to the prodelta suggest that most of the coarse-grained bedload was deposited in the delta-front by friction-dominated fluvial effluents. Common soft sediment deformation and loading

structures, together with important bed thickness and amalgamation, support high sedimentation rates.

In the sandy heterolithic packages sandstone include anisotropic and isotropic hummocks with quasi-planar to undulatory and low-angle cross-lamination, asymmetrical rounded ripples, symmetrical wave ripples indicative of repeated wave action and storm-wave reworking under combined unidirectional or pure oscillatory flow conditions (Arnott and Southard, 1989; Arnott, 1993; Dumas and Arnott, 2006). The finer-grained carbonaceous siltstone and silty mudstone intervals in this facies association represent post-storm or post-flood suspension settling below the fair-weather wave base, and record low-energy conditions between sandy pulses. Therefore the thin- to thick-bedded sandy heterolithic packages should represent marginal mouthbar subenvironment.

No tide flow indicators have been observed and the absence of syneresis or desiccation cracks and biogenic activity supports normal marine salinity, probably owing to repeated seabed ventilation by geostrophic flows. This is consistent with sporadic and low bioturbation intensity, probably corresponding to an impoverished Cruziana ichnofacies due to high sedimentation rates, water turbidity and storm-wave influence (MacEachern et al., 2005).

FA2.5 is interpreted to represent shoal-water mouthbar-type deltaic depositional setting (Postma and Drinia, 1993; Garcia-Garcia et al., 2006; Ghinassi, 2007) dominated by river floods, spreading over mouthbars with frequent bypass of the finer-grained dilute suspended load in the prodelta and with intermittent record of wave and storm influence.

5.5.3. Unit 3

Unit 3 is represented by one facies association that corresponds to siliciclastic-starved basinal deposits (FA3) both in the Eastern Catán-Lil and Chacaico basins (Table 5.3 and Figs 5.5 and 5.13).

5.5.3.1. Description

FA3

This facies association is dominated by very-thin- to thin-bedded calcareous organic-rich mudstone showing variable carbonate content and relatively high TOC (Al-Suwaidi et al., 2016) (Fig. 5.13). Mudstone include local pyrite layers (<0.5 cm thick), thin tuff layers (1-5 cm thick) and bedding can be disrupted by oblate calcareous concretions (<15 cm long), or scarce bioturbation that mainly correspond to reduced forms (*Chondrite Intricatus*; BI: 1). Thin-shelled juvenile epifaunal bivalves (0.5 cm long) and ammonites (5-20 cm diameter) are mostly concentrated as discontinuous pavements with high-concentration of specimens preserved in life position or disarticulated.

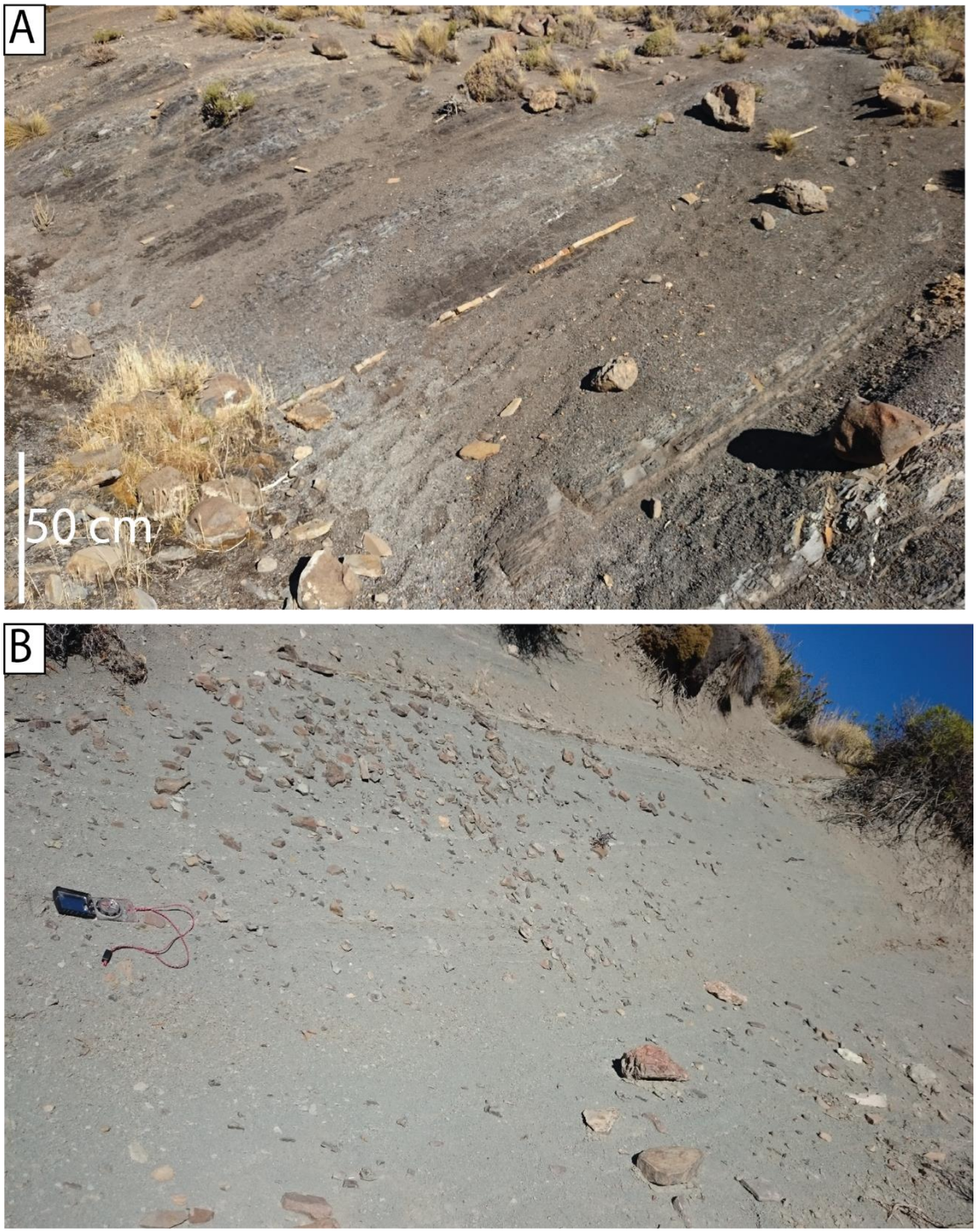

Figure 5.13: A-Thin- to very thin-bedded calcareous organic-rich mudstone found A- in the Catán-Lil Basin, with darker color, concretions and rare tuff beds and B- in the Chacaico basin, with a lighter color as more calcareous and bearing large ammonites deposited parallel to bedding.

5.5.3.2. Interpretation

FA3: Siliciclastic-starved basin

Calcareous organic-rich mud deposited both by settling from hemipelagic biogenic surface productivity (McCave, 1984; Hudson and Martill, 1991) with occasional clastic dilution by ash fall. Low sedimentation rate is suggested by the formation of early cementation carbonate concretions (Taylor et al., 1995) and epifaunal bivalves communities which colonized the seabed (Fürsich and Pandey, 2003). Low energy conditions and deep-marine environment are suggested by the absence of evidence for post-mortem bottom current winnowing of thin-shelled epifaunal bivalves with deposition well-below the storm-wave base (200-400 m, cf. Gómez-Pérez et al., 2003). Shell pavements record maximum condensation probably associated with null to very low clastic input and/or high mortality episodes (Damborenea et al., 2013; Al-Suwaidi et al., 2016). Additionally, the low diversity and scarcity of bioturbation suggest very low oxygen levels, which might have promoted the good preservation of organic matter and support the lack of sediment gravity flows which would have bring oxygenation. Therefore, FA3 represents siliciclastic-starved basinal deposits accumulated way below the storm-wave base, under very low-energy and poorly oxygenated conditions, with rare ash-fall.

5.5.4. Unit 4

Unit 4 is represented by two main facies associations which collectively represent an intraslope fan developed in a ramp-type system recorded in the Eastern Catán-Lil Basin (Figs 5.5 and 5.6) with deposits of distal ramp (FA4.1) and proximal ramp (FA4.2) lobes (Table 5.3 and Figs 5.14 and 5.15). In contrast, in the Chacaico Basin, Unit 4 lacks intraslope fan deposits and mainly consists into sand-starved slope mudstone-dominated deposits (FA4.3) (Figs 5.5 and 5.6).

5.5.4.1. Description

FA4.1

This facies association is mostly composed of poorly sorted, matrix-rich, medium- to fine-grained sandstone with a tabular geometry, which can be amalgamated or interbedded with subordinated mudstone and are rarely bioturbated (*Chondrite*; BI: 1). It is possible to distinguish three types of packages having different mean bed thickness and sandstone-mudstone relationships (Log 7 Fig. 5.14).

Thick-bedded sandstone packages mainly consist into massive to crudely normally graded sandstone, locally with faint planar laminations and bearing few mudstone pebbles and cobbles (up to 10 cm long) often found in the lower part of beds (Fig. 5.14-A). Beds have a sharp planar or loaded base, and sharp top, and can form laterally extensive (several kilometres) amalgamated packages (1-4.8 m thick, averagely 2.5 m thick). However, medium- to thick-bedded packages of sandstone regularly interbedded with massive silty mudstone and mudstone dominates. These sandstone bear numerous deformed mudstone pebbles distributed through the beds or near bed top (Fig. 5.14-B) and have sharp planar, and sometimes irregular erosive base that may have grooves, with sharp top (Fig. 5.14-A and B). Some massive sandstone beds depleted of any sedimentary structures cross-cut the surrounding mudstone-prone strata at low-angle with abrupt pinchout terminations. They have a stepped base and deformed undulated top surface mantled by mudstone clasts and which can show grooves and

plumose structures. These sandstone beds are locally cross-cutted by thin subvertical sandstone bodies (few cm-thick, ~1 m wide).

Finally, thin- to medium-bedded mustone-dominated heterolithic packages (Fig. 5.14-C) include silty mudstone, mudstone and fine-grained sandstone either normally graded with planar and/or current ripple laminations or massive with small subrounded deformed mudstone pebbles at top.

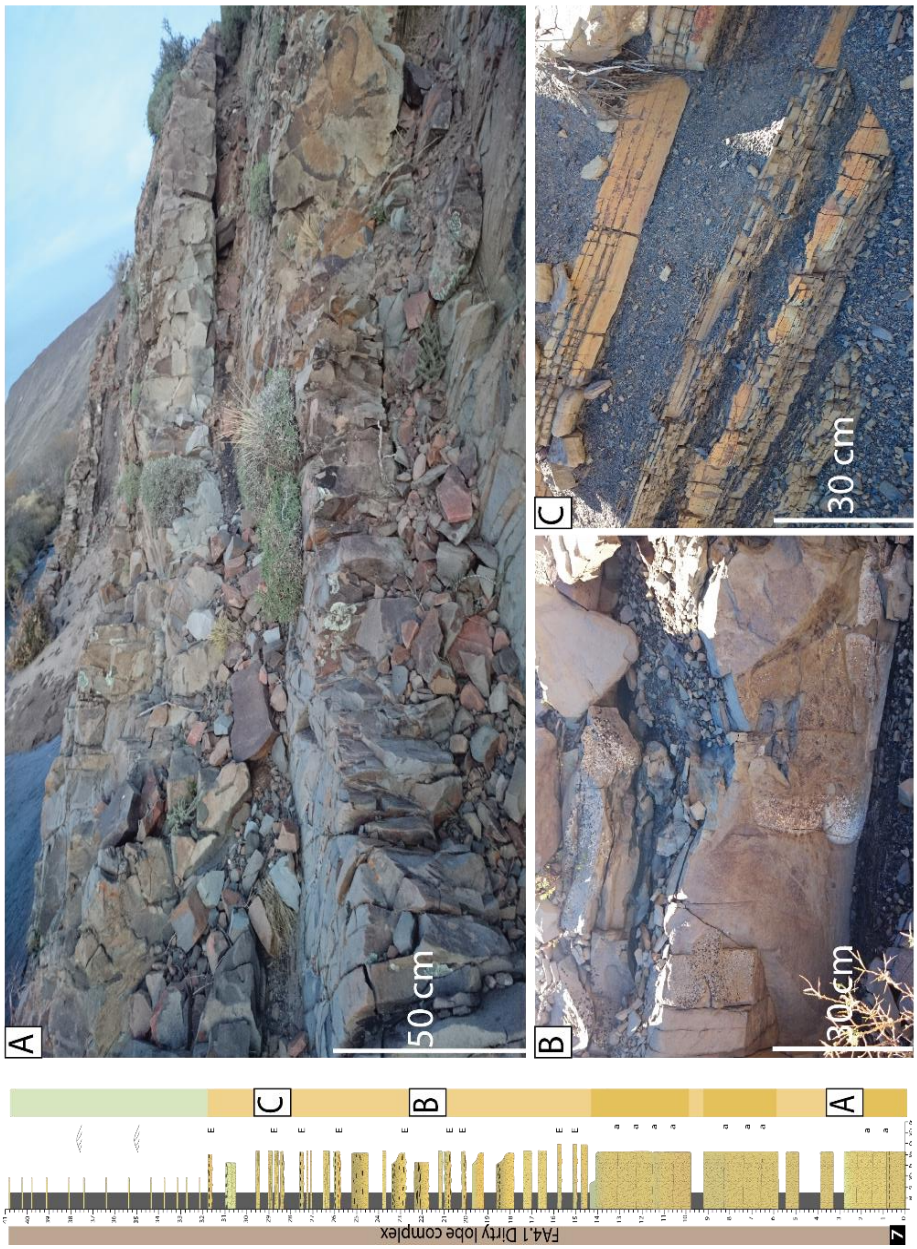

Figure 5.14: A- Thick-bedded, poorly sorted, matrix-rich, medium- to fine-grained sandstone with a tabular geometry, internally massive to crudely normally graded, locally with faint planar laminations, bearing few mudstone clasts in the lower part of beds. B- Medium- to thick-bedded, poorly sorted, matrix-rich, medium- to fine-grained sandstone interbedded with massive silty mudstone and mudstone. Sandstone bear deformed mudstone pebbles distributed through the beds or near bed top, and with sharp base and deformed top. C-Thin- to medium-bedded mufstone-dominated heterolithics including including silty mudstone, mudstone and fine-grained sandstone that can be normally graded with planar laminations or massive with small subrounded deformed mudstone pebbles.

FA4.2

FA4.2 is mostly composed of poorly sorted, matrix-poor, coarse- to medium- or fine-grained sandstone, amalgamated or interbedded with subordinated mudstone, showing relatively low bioturbation (*Chondrite, Planolites*; BI: 2-3). Four different types of packages can be defined in this facies association according to bed thickness and sandstone-mudstone relationships (Log 5 Fig. 5.15).

Medium- to thick-bedded sandstone packages consist of poorly sorted, crudely normally graded sandstones (Fig. 5.15-A). The lower part of beds is mainly massive, locally with stepped laminae (1-2 cm thick). Outsized (very coarse) lithic grains, siltstone and/or mudstone pebbles, and bioclasts can be present near bed base. These beds can be bipartite and after a sharp grain-size break pass stratigraphically into finer-grained and muddier upper part with parallel planar lamination enriched in carbonaceous material (Fig. 5.15-B). Otherwise, it passes gradationally or with grain-size break into finer-grained sandstone with current ripples and/or climbing ripples (Fig. 5.15-C) and/or parallel planar to undulatory or sinusoidal laminations that can be carbonaceous-rich and form isotropic and anisotropic hummock-like bedforms (Fig. 5.15-D). In places, sandstone beds can show massive medium-grained, calcite-cemented conical clastic pipes widening upwards. Sandstone beds have a loaded (with flame structures) or sharp planar base, locally erosive (up to 20 cm relief, flute cast, grooves), and with sharp planar or gradational top commonly deformed. These sandstone have a tabular to slightly mounded geometry and commonly form laterally extensive (several kilometres) amalgamated packages (1.2-11.7 m thick, averagely 3 m thick) (Fig. 5.15-A and B). Locally, the erosive bed base can form scours (0.5-1 m relief, few to tens metres across) locally marked by a clast lag or a chaotic argillaceous and clast-rich sheared basal interval (Fig. 5.15-E).

Medium- to thick-bedded sandstone-dominated heterolithic packages comprise non-amalgamated medium- to fine-grained sandstone with subordinated finer grained interbeds. Sandstone beds are normally graded, with parallel planar to undulatory laminations at the top (Fig. 5.15-D), or less commonly with dune-scale cross-stratification or current ripple-cross-laminations. Beds are tabular, with sharp planar base, locally erosive, and with sharp or gradational top. Some matrix-rich massive and clast-rich sandstone beds are also

present. The finer-grained interbeds consist of massive siltstone and mudstone, or thin-bedded with current ripple laminated sandstone reach in carbonaceous material.

Thin- to medium-bedded sandstone-dominated heterolithic packages consist of interbedded medium- to fine-grained sandstone, massive siltstone and carbonaceous-rich mudstone (Fig. 5.13-F). Sandstone beds are either massive, locally with few mudstone clasts or normally graded with parallel plane to undulatory and current ripple-cross-laminations. Some rare mudstone clast-rich argillaceous chaotic sandstone beds can occur alone, or just form the upper part of bipartite beds or encasing sandstone (sandwiched beds, Talling et al., 2013).These sandstone beds are tabular with sharp planar base and sharp or gradational top.

Thin- to very thin-bedded mudstone-dominated heterolithic packages comprise siltstone and mudstone locally with massive to normally graded fine-grained sandstone beds with carbonaceous-rich planar and current ripple-cross-laminations. Beds are tabular, with sharp planar base and sharp or gradational top, and are commonly found in between sandy packages. Cone-in-cone structures and calcite-filled fractures can be observed in the mudstone.

FA4.3

This facies association is dominated by thin- to medium-bedded siliciclastic mudstone and siltstone bearing terrestrial fine plant material, with rare thin planar laminated or massive sandstone beds. Ammonites and small thin-shelled bivalves (*Bositra sp.*) can be found in mudstone.

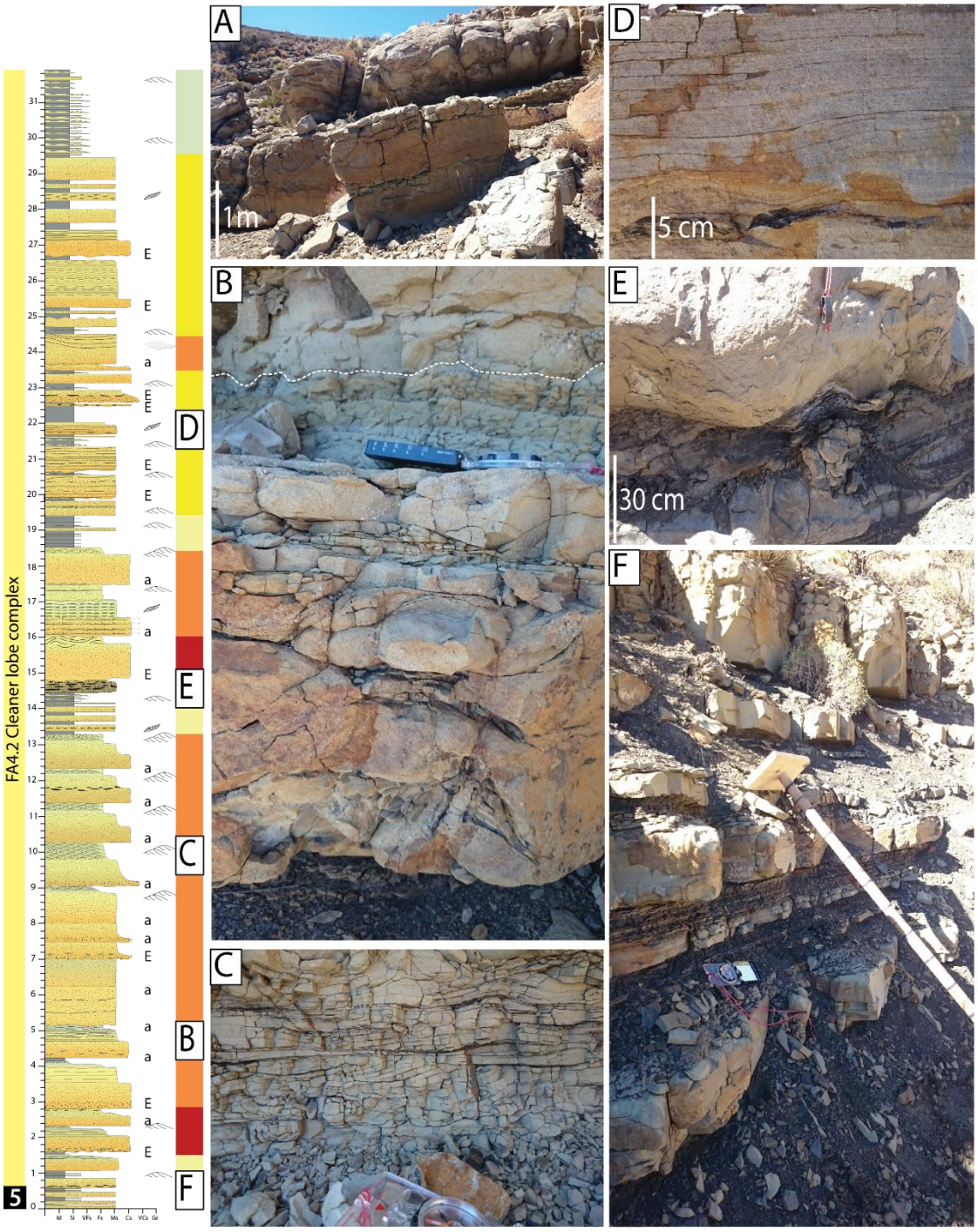

Figure 5.15: A- Medium- to thick-bedded, poorly sorted, matrix-poor, coarse- to medium-grained sandstone with a tabular to mounded geometry, internally massive with outsized (very coarse) lithic grains, siltstone and/or mudstone pebbles and bioclasts near irregular erosive bed base and with sharp top. B-Coarse to medium-grained crudely normally graded sandstone bed, with a massive clast-bearing lower part and a finer-grained muddier upper part with parallel planar lamination enriched in carbonaceous material. Note the sharp grain-size break between the lower and upper bed part and the amalgamated bed top highlighted with white dot line. C-Example of finer-grained structured upper part of beds with carbonaceous-rich parallel planar and climbing ripple laminations. D-Example of finer-grained structured upper part of beds parallel planar to undulatory laminations. Note the darker carbonaceous material. E- Chaotic argillaceous and clast-rich sheared basal interval which marks the concave-up scoured base of a thick sandstone bed. F- Thin- to medium-bedded sandstone-dominated heterolithic packages consist of interbedded medium- to fine-grained sandstone internally planar laminated and with sharp planar base and top, massive siltstone and carbonaceous-rich mudstone.

5.5.4.2. Interpretation

FA4.1: Distal ramp lobes

Characteristics of thick-bedded matrix-rich and clast-poor sandstone, with crude normal grading, massive or with faint planar laminations, suggest deposition with rapid collapse of clay-rich transitional plug flows (Baas et al., 2009). The clast-rich sandstone of medium- to thick-bedded packages, with a weak to absent grading and variable argillaceous matrix and deformed mudstone clast content record substrate entrainment prior to deposition by low-strength, poorly cohesive sandy debris-flows (Talling et al., 2012).

The few amalgamated sandstone bedsets might represent lobe axis subenvironment whereas the interbedded sandstone and silty mudstone which dominates this facies association 4.1 should correspond to a lobe off-axis subenvironment (Prélat et al., 2009). The thin- to medium-bedded mudstone-dominated heterolithic deposits with normally graded and structured fine-grained sandstone emplaced with more dilute and turbulent low-density sediment gravity flows (Lowe, 1982). In contrast, the massive clast-bearing sandstones found in these heterolithic deposits were emplaced by thin poorly cohesive sandy debris-flows (Talling et al., 2012). These packages represent a lobe fringe subenvironment (Mutti, 1977; Prélat et al., 2009). The massive sandstone beds cross-cutting the surrounding mudstone-prone strata at low-angle with abrupt pinchout terminations are interpreted as clastic sills injected by erosive flows with entrainment of lithified mudstone clasts which can be found mantling bed top (Cobain et al., 2015). The thin subvertical sandstone bodies that can cross-cut those laterally extensive sills are interpreted accordingly as clastic dykes.

The matrix-rich lobes are characterized by the general paucity of traction structures, lack of common erosional basal surfaces, poor sorting and deformed mudstone clasts throughout or in the upper part of beds. This supports dominant deposition by transitional to debris-flows with a poor capacity for downstream sorting, consistent with the poor spatial segregation of facies across these lobes. Characteristics of FA4.1, with occasional amalgamated sandstone and dominant heterolithic facies suggest development of low sand: mud ratio sandy lobes in intraslope setting under poorly oxygenated conditions. This facies association

might represent the distal part of a deep-marine ramp system (Heller and Dickinson, 1985; Postma, 1990).

FA4.2: Proximal ramp lobes

Characteristics of medium- to thick-bedded matrix-poor sandstone points to deposition beneath high-density sediment gravity flows, with high bed aggradation rate and significant tractional reworking beneath waning dilute turbulent flows (Lowe, 1982; Leclair and Arnott, 2005; Sumner et al., 2008). Locally, undulatory or sinusoidal and climbing ripple laminations record deposition with a high rate of suspended load fallout (Jobe et al., 2012) and together with commonly deformed bed tops indicate high sedimentation rates.

Hummock-like bedforms formed through traction-and-fallout beneath stratified high-density combined flows, with high sediment fallout rates enabling bedform aggradation in the upper-stage plane bed stability field (Tinterri, 2011). Anisotropic hummock-like structures formed with a dominant unidirectional flow component, whereas the more common isotropic hummock-like structures suggest a dominant oscillatory combined flow component (Tinterri, 2011). Given deposition below the storm-wave base, the oscillatory flow component could not originate with surface waves. Therefore, these bedforms are interpreted to form from interactions of internal wave trains with the near-bed unidirectional flow component, due to flow reflection and deflection against a confining slope (Tinterri, 2011).

Common grain size break at top of thick massive sandstone beds suggest sediment bypass (Stevenson et al., 2015). Some crudely graded bipartite sandstone beds have a finer-grained, carbonaceous-rich and muddier planar laminated upper part which suggest emplacement by turbulence-enhanced transitional flows (Baas et al., 2009). Facies characteristics and amalgamation of thick tabular to mounded bedsets and channelforms associated with scoured base support deposition with abrupt decrease in confinement, in a lobe axis environment (Etienne et al., 2012).

Medium- to thick-bedded and thin- to medium-bedded sandstone-dominated heterolithics were mainly deposited by waning high- to low-density sediment gravity flows (Mulder and Alexander, 2001). Massive clast-rich sandstone beds with variable mud matrix found in both of these heterolithic successions record

also deposition by clay-rich transitional to quasi-laminar plug flows (Baas et al., 2009). The presence of weakly erosive, structured and normally graded sandstone with some clast- and matrix-rich sandstone beds, and the well-preserved finer-grained interbeds suggest deposition in lobe off-axis subenvironment (Prélat et al., 2009). The thicker sandstone beds with thin finer-grained interbeds and their close spatial association with amalgamated sandstone packages could reflect a proximal off-axis setting whereas the thinner sandstone beds with thicker finer-grained interbeds might represent a distal off-axis setting.

Thin- to very thin-bedded mudstone-dominated heterolithics were mainly deposited with suspension fallout and tractional reworking beneath low-density turbidity current (Stow and Bowen, 1980; Lowe, 1982) and minor clay-rich transitional plug flows (Baas et al., 2009). The dominant thin beds with fine grain size, lacking erosion and with gradational tops indicate deposition in a lobe fringe environment (Mutti, 1977; Prélat et al., 2009).

The diagenetic differences and morphology of the clastic pipes with the host sandstone suggests that they might correspond to fossilized vertical fluid flow conduits (Buck and Goldring, 2003; Ross et al., 2011), similar to non-textural pipes with pervasive carbonate cementation (e.g Wheatley and Chan, 2018). Cone-in-cone structures developed with fibrous calcite growth (which has been replaced by pyrite) due to vertical tensile stress induced by overpressure, with hydraulic fracturation and calcite precipitation (Cobbold et al., 2013).

The matrix-poor lobes are characterized by well-developed erosion with local scouring, common traction structures and graded bed top that can be deformed, and local presence of grain-size breaks in beds. These features indicate deposition by higher-energetic waning flows able to achieve turbulence, locally with some bypass, which contributed to enable better spatial facies segregation across lobes.

In contrast with FA4.1, these characteristics together with the coarser-grain size and common amalgamation of sandstone, suggests the development of high sand: mud ratio lobes in intraslope setting, which should represent the proximal part of a relatively deep-marine ramp system (Heller and Dickinson, 1985; Postma, 1990).

FA4.3: Sand-starved slope

These fine-grained deposits represent mainly deposition by suspension settling and dilute sediment gravity flows transporting terrestrial plant material. in a low-energy deep-marine environment. FA4.3 is mudstone-dominated and accumulated way below the storm-wave base, under low-energy and poorly oxygenated conditions. Given the spatial association with intraslope deposits of FA4.1 and 2 well constrained by ammonite biostratigraphy (Volkheimer, 1973; Gulisano and Gutiérrez-Pleimling, 1995), FA4.3 should represent their sand-starved slope counterpart.

5.6. Synthesis of depositional systems

Unit 1

In the Chacaico Basin, Unit 1 is characterized by stratified pebbly sandstone channel-fills that incise tuffaceous sandstone in the Lapa and Isasi sector (Figs 5.4 and 5.5). These deposits can pass laterally into lacustrine siliceous plant-rich carbonates in between the Val Sativa and Isasi sectors. The intercalation of high-energy flood deposits and coeval of freshwater lake sedimentation, suggest deposition on alluvial fan systems (FA1.1) (Fig. 5.9-A-B) in a relatively low-gradient floodplain environment in the Chacaico Basin (Blair and McPherson, 1994). The variable clast roundness and mixing suggests a relatively long storage in catchments and/or long transport distance with intense mechanical erosion prior to deposition (Muravchik et al., 2011).

In the Eastern Catán-Lil Basin, Unit 1 corresponds to slope apron deposits (FA1.2) (Fig. 5.9-C-D), including clast-supported gravelly sandstone onto footwalls in the Tutavel sector (Fig. 5.16), and matrix-supported gravelly sandstone developed across subaqueous footwall to immediate hangingwall slope in the of Espinazo Del Zorro sector and around the Cerro Mallín de Ibáñez (Figs 5.4 and 5.5). These subaqueous slope aprons record the first evidence of marine transgression in these sectors, whereas the Tutavel footwall was emerged. The wider clast size range and less diverse lithologies indicate limited abrasion and sorting prior to remobilization of unconsolidated volcanic deposits, with short transport distance and/or and rapid deposition. This suggests deposition of slope aprons across steeper slope gradients than in the Chacaico

Basin, with subaerial to subaqueous fault-block degradation potentially related to fault activity (Leppard and Gawthorpe, 2006). The paucity of plant remains (dominated by conifers) suggests warm semi-arid to seasonally dry climatic conditions during deposition of Unit 1, supported by the well-preserved fresh angular feldspar and quartz grains with limited chemical weathering (Blair and McPherson, 1994; Leeder et al., 1998). In such conditions, development of the vegetal cover might have been hampered by the previous volcanic eruptions, and favoured remobilization of loose tephra during infrequent but heavy rainfall episodes (Muravchik et al., 2011; Palmer et al., 1993).

The epiclastic nature of these deposits in both basins is supported by the occurrence of varied clast lithologies (volcanic, carbonate, granitic, metamorphic, siltstone, wood debris). Heterogeneity in clast shapes, sizes and lithologies between the two basins suggest different catchment bedrocks, storage period and morphologies. Palaeoflows recorded within Unit 1 in both basins suggest development as fault transverse dispersal systems, with a patchy distribution along fault strike consistent with local late syn-rift tectonic control. This is supported by stratal relationships with Unit 1 unconformably overlying the granitic basement and Precuyano Cycle volcanic syn-rift deposits, with a limited dip extent into immediate hangingwalls and pinchout towards the footwall highs (Fig. 5.16). The lack of axial drainage systems might be a direct consequence of their deposition after the main phase of fault linkage and formation of master basin border faults (Gawthorpe et al., 2000; Muravchik et al., 2014).

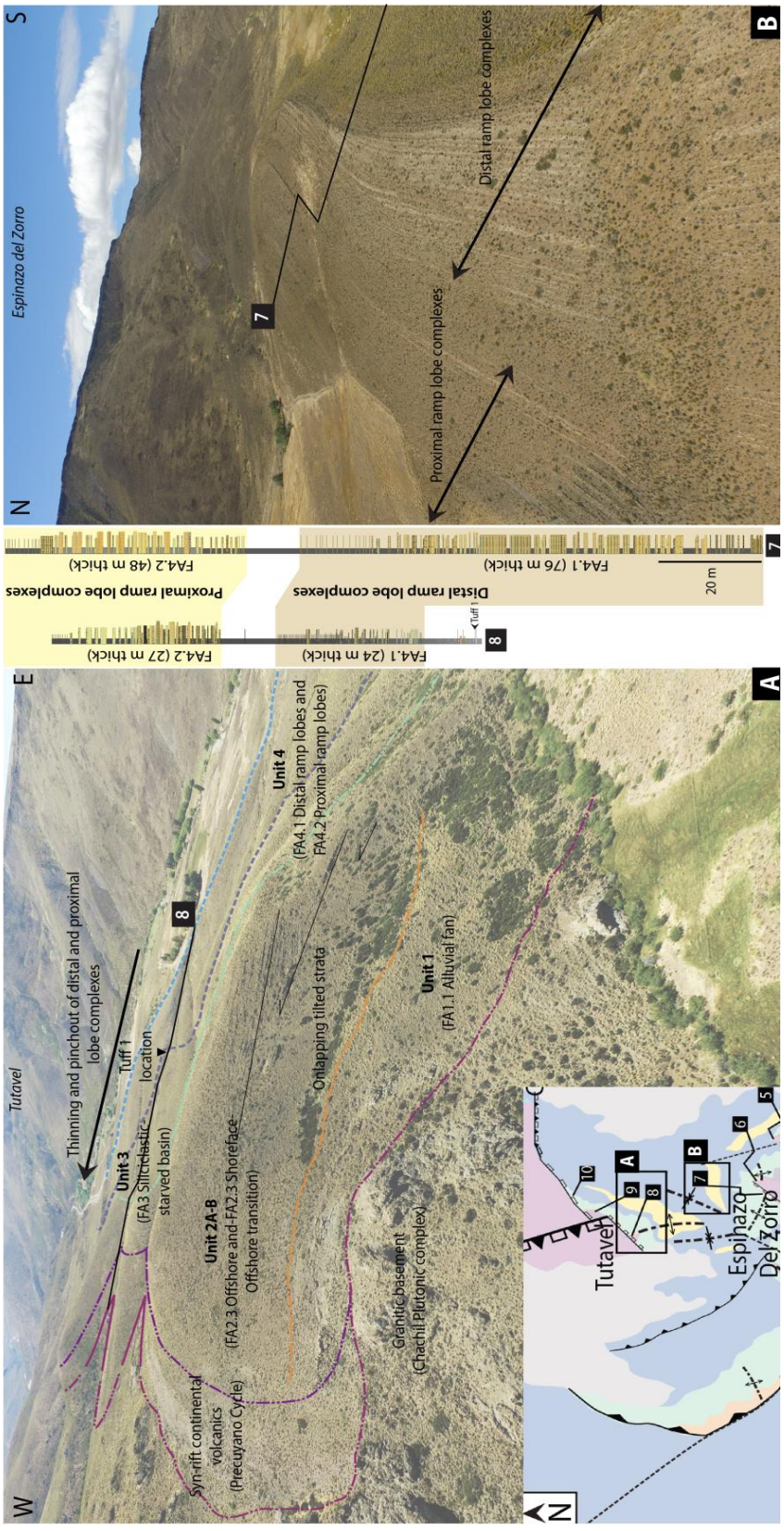

Figure 5.16: Outcrop in the Tutavel sector (left) showing stratal relationships between units with onlap of the fine-grained strata of Unit 2A showing internal angular discordances onto alluvial fan deposits of Unit 1 unconformably overlying the granitic basement and Precuyano Cycle volcanic syn-rift deposits. Stratal dip angle decreases in overlying mudstone and sandstone of Unit 3 and 4. Note that distal ramp lobes of Unit 4 thin and pinchout towards the basin fault border northwestwards. Logs 8 and 7 shown in the correlation panel of figure 4 show thinning of proximal and distal ramp lobes from the Espinazo del Zorro to Tutavel sector. Location of the tuff 1 is also indicated.Location of the two outcrops A and B is shown on inset map (cf. fig. 5.4).

Unit 2

Unit 2A

In the Chacaico Basin, Unit 2A comprises high to moderately bioturbated fossiliferous shoreface-offshore transition deposits (FA2.2), coarsening upwards into sandy lower-shoreface deposits (FA2.1) (Fig. 5.9 and 5.17). Locally, intercalated coarser-grained fan-deltaic sandy bottomset deposits (FA2.1) developed in the tectonically over steepened Lapa sector and to the NW of the Isasi sector (Figs 5.4 and 5.5). In the Chacaico Basin, Unit 2A extends as wedge-shaped packages that show (i) thickening of shoreface-offshore transition deposits (FA2.2) and (ii) thinning with onlap of fan-deltaic deposits (FA2.1), towards the flank of a NE-SW trending blind fault growth anticline fold in the Precuyano Cycle volcanic deposits (Fig. 5.18). This fold is few kilometres wide, parallel to the trend syn-rift faults which controlled the syn-rift, which are oblique to the main NNE-SSW trend of the Sierra Chacaico anticline (Fig. 5.4). Fan-deltaic channels of Unit 2A stack towards the SE, away from the growth fold and can be offset by syn-depositional antithetic and synthetic small-scale normal faults (Fig. 5.18). All these features should record surface tilting and stratal rotation associated with unbreached fault growth fold development (e.g Gawthorpe et al., 1997; Jackson et al., 2005). Given the proximity of the fan deltas to terrestrial source and the similar coarse grain size, very poor sorting, clast shapes and immature sediment composition to epiclastic alluvial fans deposits that pinchout downdip, they might represent bottomsets developed in a relatively shallow-marine environment (Figs 5.10 and 5.18). Development of fan deltas into relatively shallow-water (~ 50 m depth) are also interpreted from time-equivalent subsurface deposits located near the Puesto Touquet (see location Fig. 5.1) (Gómez Omil et al., 2002).

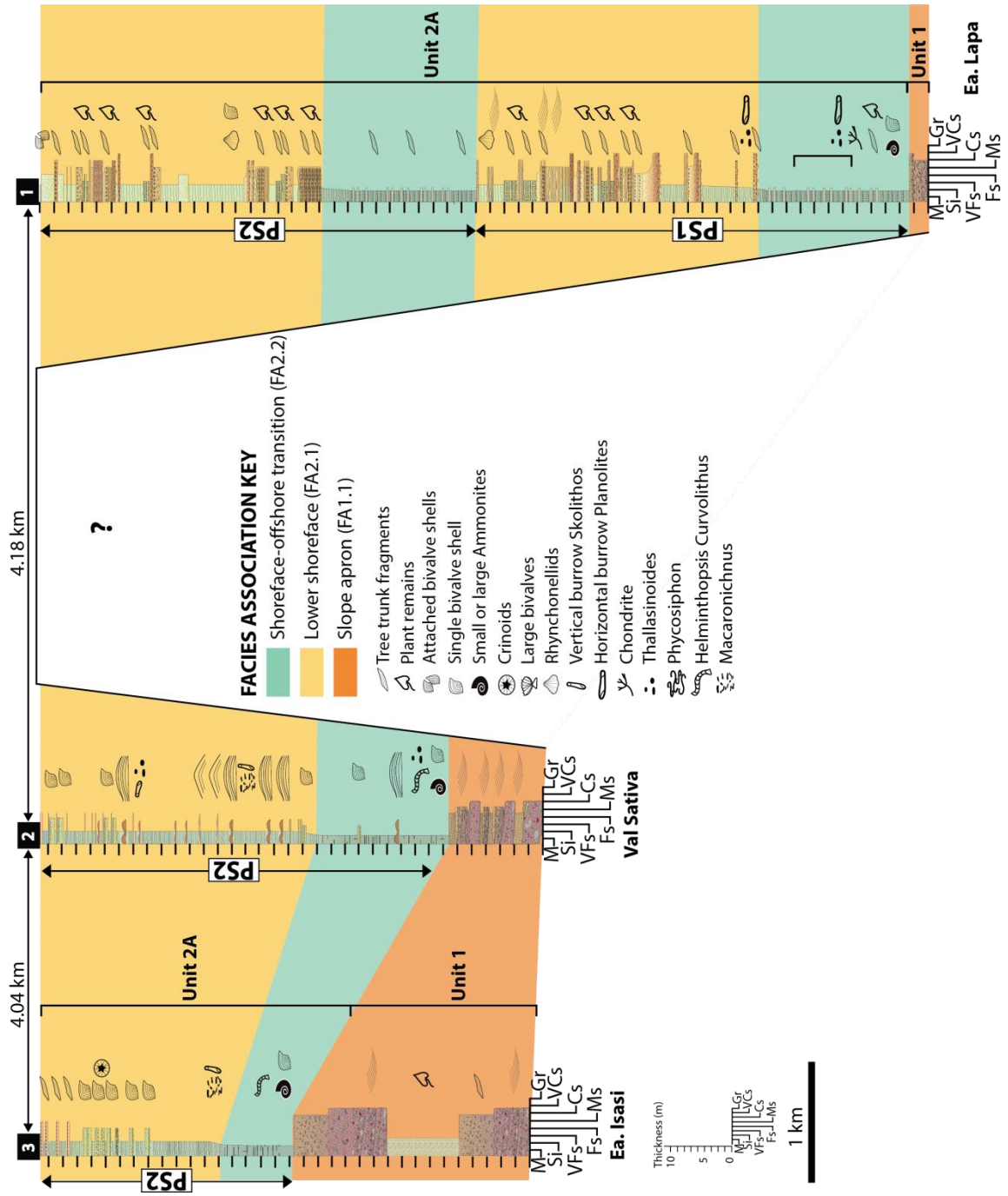

Figure 5.17: Detailed spatial relationships between FA1.1, FA2.1 and FA2.2 in the Chacaico Basin.

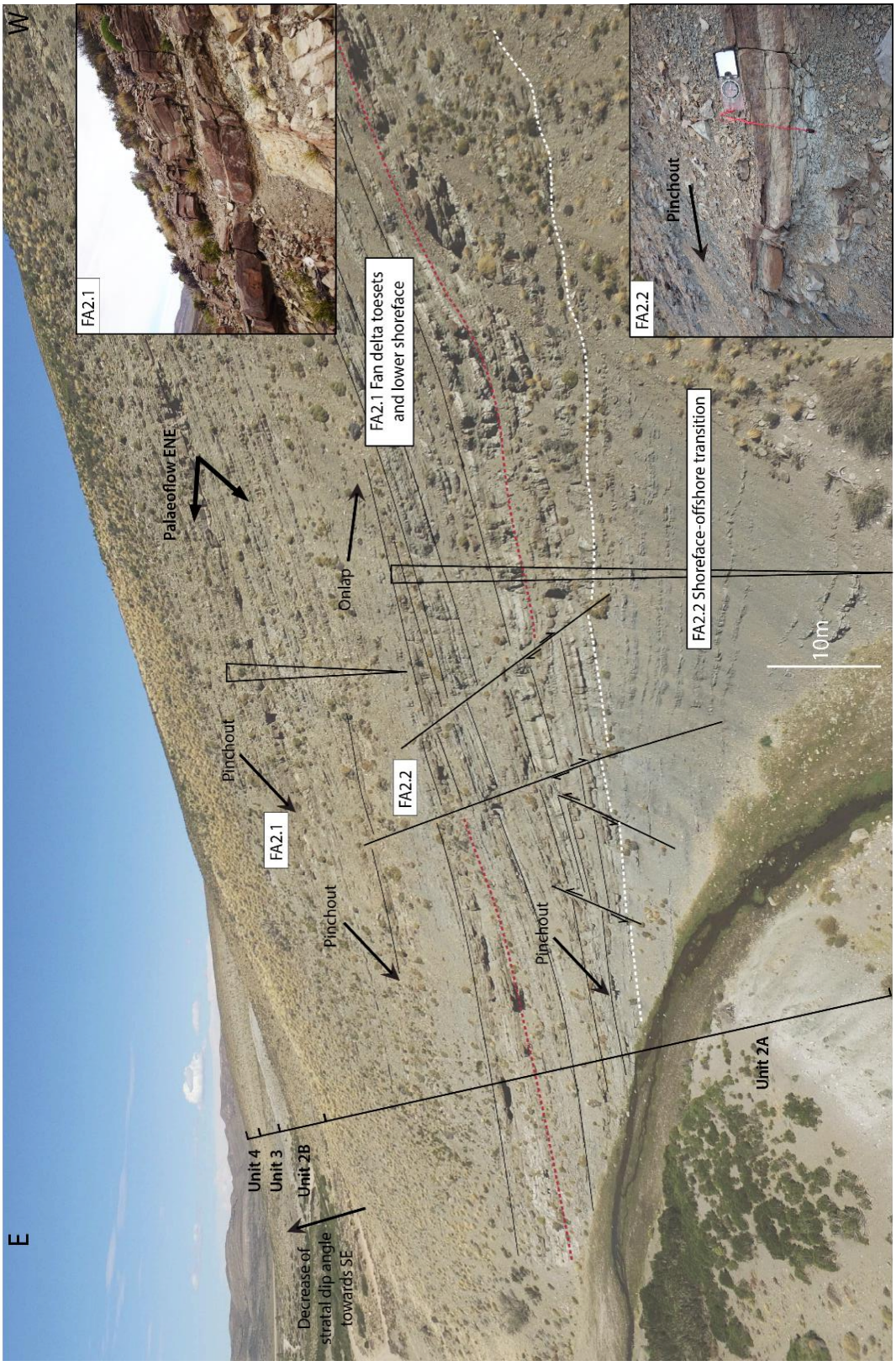

Figure 5.18: Outcrop in the Lapa sector showing successions which pass upwards from shoreface-offshore transition to fan-deltaic bottomsets in lower shoreface deposits (Unit 2A), with thickening of shoreface-offshore transition deposits and fan-deltaic deposits onlapping towards the flank of a NE-SW trending blind fault growth fold in the Precuyano Cycle volcanic deposits. Note channelforms (red dotted lines) stacked towards the SE, away from the growth fold and local offset by syn-depositional antithetic and synthetic small-scale normal faults and the stratal decrease of dip angles southeastwards in overlying deltaic (Unit 2B) and deep-marine siliciclastic-starved basinal mudstone (Unit 3) and sand-starved slope mudstone deposits (Unit 4).

The lack of slope aprons supports deposition of Unit 2A across relatively subdued rift topography in the Chacaico Basin. Palaeoflows indicate progradation of fan deltas towards the ENE and NW (Figs 5.4 and 5.5), transverse to master fault segments. These line-sourced fan deltas which developed in the Isasi and Lapa sectors are part of a storm- and wave-dominated mixed carbonate-siliciclastic shelf system, including more protected shallow-marine environments with high biogenic productivity that permitted the development of carbonate systems. This was recorded with the formation of detached carbonate platforms and carbonate-clastic periplatform systems in the most elevated fault-blocks of the Chachil Basin (Leanza et al., 2013) (cf. Chapter 4). Wave and storm-wave currents indicate a WNW-ESE direction which is parallel to the orientation of the southern fault border of the Chacaico Basin (Figs 5.4 and 5.5). Wave and storm-wave agitation might have prevailed over fluvial influence and played a crucial role preventing strong variations of turbidity and salinity induced by fresh-water influxes which would not be tolerated by stenohaline ammonoids, echinoids and crinoids communities which were abundant bioclasts in deposits of Unit 2A (cf. Damborenea et al., 2017). The abundant plant debris in Unit 2A points to erosion of a vegetated coastal plain that might reflect the onset of a climatic change towards more humid and warmer conditions than during deposition of Unit 1.

In the Eastern Catán-Lil Basin, Unit 2 successions are interpreted as shoreface-offshore transition and offshore deposits (FA2.2 and FA2.3) (Fig. 5.19), with sandier shoreface-offshore transition deposits in Unit 2A than in Unit 2B (Figs 5.5 and 5.11). Evidence for resedimentation processes, soft sediment deformation and both primary and epiclastic volcaniclastic deposits suggest intrabasinal supply from nearby volcanic eruptions and slope instability potentially associated with high slope gradients. Additionally, primary volcanic input and extensive recrystallization and silicification of fine-grained sediments of Unit 2A in the Eastern Catán-Lil Basin resulted from effects of hydrothermal fluid circulation which increased dissolved silica concentrations and alkalinisation of water chemistry (Renaut et al., 2002). The accumulation of large amount of fine-grained material in this unit results from delivery of fine terrigenous and reworked volcanic particles at mouths of alluvial fan catchments. The composition of epiclastic polymictic volcanogenic sandstone of Unit 2 might indicate distal influxes from the fan-deltaic systems of the Chacaico Basin, and support the development of Unit 2A in the Eastern Catán-Lil Basin in a relatively sand-starved

and deeper environment, at distance from the main sediment entry points. Unit 2 shows onlap onto Unit 1 and Precuyano Cycle syn-rift footwall deposits, with multiple stratal discordances and wedging towards the NE from the Martinez to Espinazo del Zorro sector (Fig. 5.16). The maximum thickness of Unit 2 in the Espinazo del Zorro sector suggests maximum mechanical subsidence and increase of accommodation in this location (Figs 5.4 and 5.5). Along-strike stratal thickening towards the NW, from El Cóndor high to the Espinazo Del Zorro and Tutavel sectors indicate deposition across a structural platform in the Martinez and El Cóndor sectors (Figs 5.4 and 5.5). Stratal geometry with onlap and thinning towards fault footwalls showing internal angular discordances (Fig. 5.16) and palaeoflows towards the S and NW-SE mainly transverse to faults footwalls (Fig. 5.4), support syn-depositional hangingwall fault-block tilting during deposition of Unit 2A.

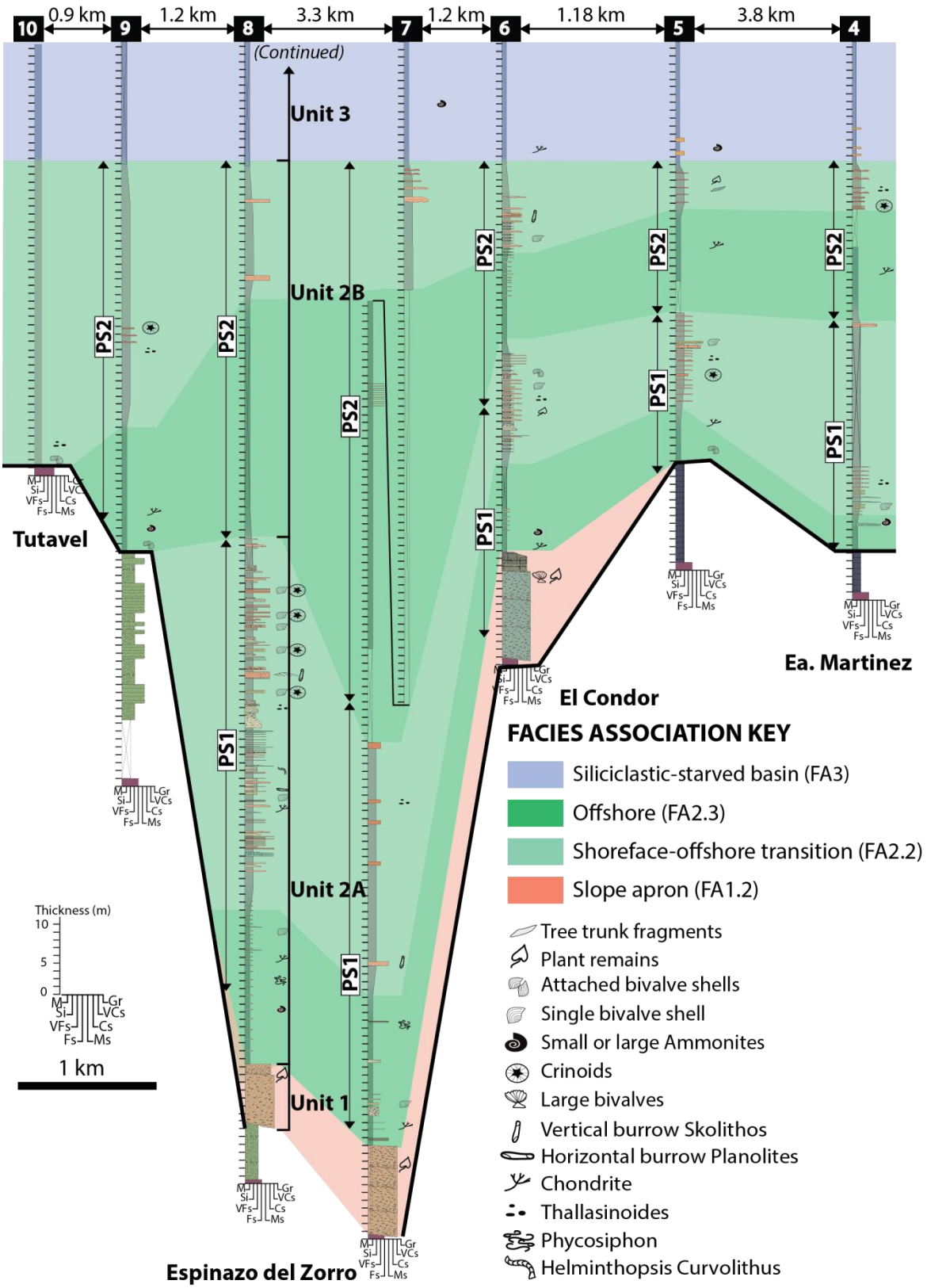

Figure 5.19: Detailed spatial relationships between FA1.2, FA2.2, FA2.3 and FA3 in the Chacaico Basin.

Unit 2B

In the Chacaico Basin, Unit 2B includes successions of mudstone-dominated prodeltaic deposits (FA2.4) coarsening upwards into sandy delta-front deposits (FA2.5) (Figs 5.12 and 5.20). Given the lack of gravelly material and widespread gravitational resedimentation typical of steep delta slopes (i.e. Gilbert-type), these deltaic deposits are interpreted to form shoal-water mouthbar-type deltas (Postma and Drinia, 1993; Garcia-Garcia et al., 2006; Ghinassi, 2007). In the Chacaico Basin, Unit 2B has not been observed to onlap or drape across syn-rift or basement rocks which were subdued and buried beneath Unit 2A. Unit 2B onlaps onto Unit 2A, with upward decrease of stratal dip angle which might indicate the decreased or arrest of fold growth in the Lapa sector, and supports the fact that this feature cannot be related to post-depositional fault drag folding otherwise Unit 2B deposits would be deformed as well and all the Unit 2 would present some reverse faults (Fig. 5.18).

The deltaic deposits of Unit 2B also seem to thicken from the Isasi to Lapa sector and towards the Cerro Colorado location (Fig. 5.4). Longitudinal onlap and stratal thickening of Unit 2B deposits northeastwards along the Sierra Chacaico suggest basin lengthening through time and syn-depositional increase of subsidence in this direction (e.g. Schlische, 1993). Subsidence was probably controlled by the main basin-border fault in the Cerro Trapial Mahuida area, which contrasts somehow with thickening of volcanic syn-rift Precuyano Cycle deposits southwards towards the Curru Charahuilla basin fault border (Franseze et al., 2007). This is also supported by rotation of the dominant unidirectional palaeoflow direction ranging between NW-NNE as the main progradation direction, with subordinate ESE direction that might correspond to combined flow directions (Figs 5.4 and 5.5). The influence of storm-waves and wave-induced oscillatory flows reflect the development of the deltaic system in a high-energy, open-marine embayment (Ravnås and Bondevik, 1997).

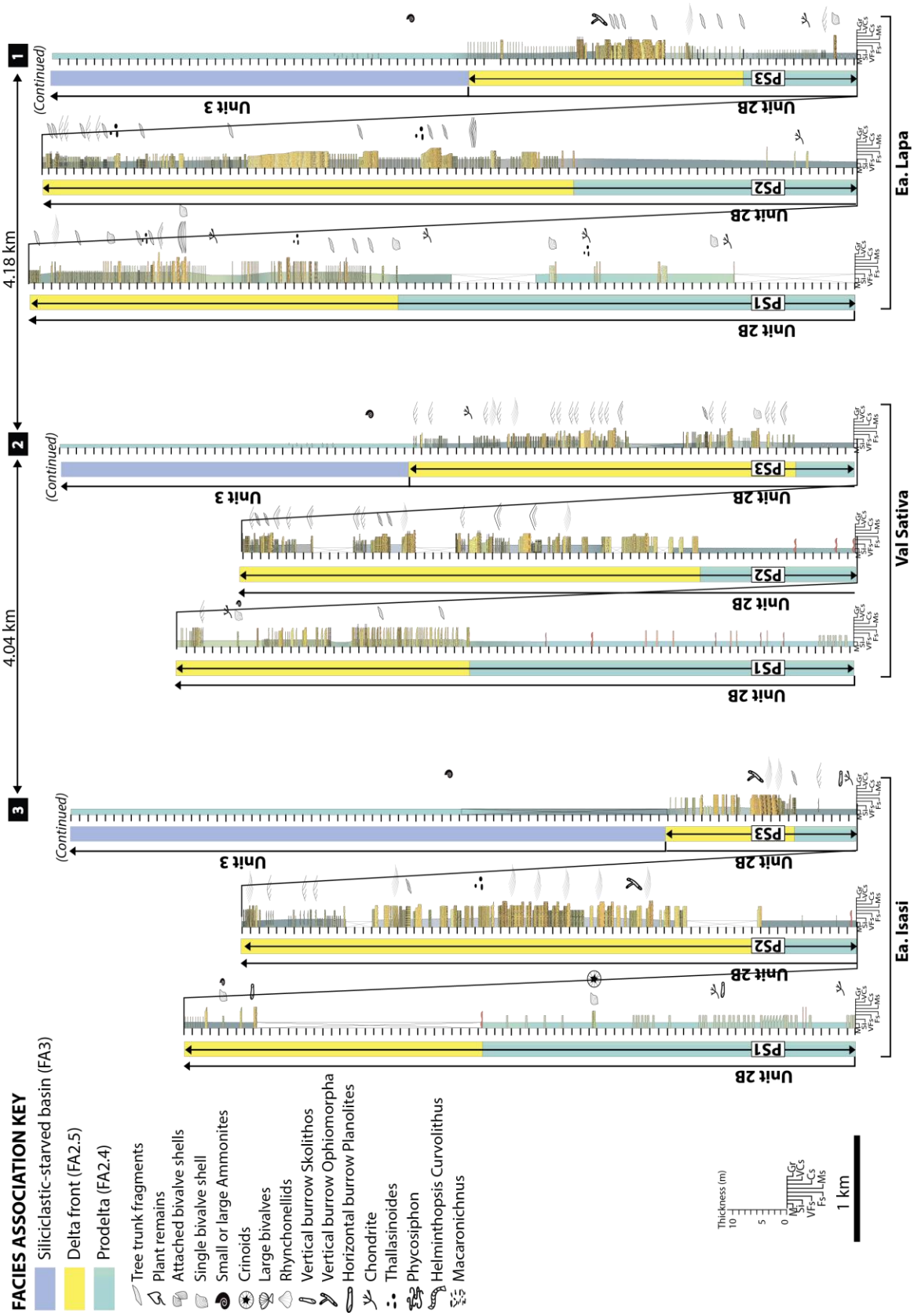

Figure 5.20: Detailed spatial relationships between FA2.4, FA2.5 and FA3 in the Chacaico Basin.

Unit 3

In the Chacaico Basin, siliciclastic-starved basinal mudstone deposits of Unit 3 (FA3) overlie prodelta deposits (FA2.4) of Unit 2B (Figs 5.5 and 5.20). These deposits record a condensed period of sedimentation related to an abrupt shut down of siliciclastic influx, without evidence for gravitational resedimentation or normal faulting which discards tectonic activity. In the Eastern Catán-Lil Basin, Unit 3 is also characterized by siliciclastic-starved basinal calcareous organic-rich mudstone (FA3) deposited under very low-energy and poorly oxygenated conditions (Fig. 5.13). Unit 3 can be observed to gently onlap Unit 2A in fault hangingwalls and to drape onto basement and Precuyano Cycle volcanic footwall deposits (Figs 5.16 and 5.19). As Unit 3 heals part of the inherited accommodation and relief at top of Unit 2A, it can present significant local thickness changes with thickening of up to 55 m between the El Cóndor high and Tutavel sectors (Fig. 5.5). Given that in the Chacaico sector, TOC measurements in the Lower Los Molles Fm. (nearly at the base of Unit 3) enabled identification of the Toarcian Oceanic Anoxic Event record (Al-Suwaidi et al., 2016; Angelozzi and Pérez Panera, 2016), Unit 3 in the Eastern Catán-Lil Basin should also record this regional event.

Unit 4

In the Chacaico Basin, Unit 3 is overlain by siliciclastic mudstone deposits including rare thin beds of sandstone (Gulisano and Gutiérrez-Pleimling, 1995) laterally equivalent to Unit 4 in the Catán-Lil Basin and therefore records the lack or paucity of sand influxes in slope mudstone dpeosits at this location (Fig. 5.5).

In contrast, in the Eastern Catán-Lil Basin, the succession of Unit 4 comprises a lower succession interpreted as distal ramp lobes (FA4.1) (Figs 5.14 and 5.21) that are “precursor” to the overlying sandier succession interpreted as proximal ramp lobes (FA4.2) (Figs 5.15 and 5.23). Both distal and proximal ramp lobe successions are separated from each other by a laterally extensive mudstone unit (2.2-6.3 m thick) (Fig. 5.5). These deposits are collectively interpreted as reflecting the development and evolution of a deep-marine intraslope fan (Figs 5.4 and 5.5) developed across a relatively low-gradient ramp-

type system. Unit 4 gradationally overlies Unit 3, with progressive development of the intraslope fan towards the N-NE from the Martinez to Tutavel sectors (Figs 5.4 and 5.5).

The distal ramp lobe succession (FA4.1) corresponds to lobe complexes (Prélat et al., 2009) which formed two small depocentres thickening in topographic lows of the Martinez and Espinazo Del Zorro sectors, and thinning across the El Cóndor fault-block which formed an inherited relief at the top of Unit 3 (Figs 5.4 and 5.5). The two small distal ramp lobe complexes are characterized by the presence of sill-dominated clastic injectites stepping outwards lobe complexes margins adjacent to inherited buried topographic highs. This spatial relationship might reflect the deposition of these lobe complexes with substantial confinement that promoted post-depositional remobilization with differential loading and compaction of buried strata that increased overpressure (Cobain et al., 2017).

These narrow and thick distal ramp lobe complexes (individually averaging 32 m thick and traced over 1.5-4.5 kilometres downdip) include thick lobes (1-4.8 m thick, averagely 2.5 m thick) which pass into lobe fringe deposits across 10s m to <100 m close to topography of the El Cóndor and Tutavel sectors limited by the Tutavel fault border (Figs 5.5 and 5.16). Several units of distal ramp lobe complexes can show an internal thinning-upward trend, which could reflect a discrete retrogradational pattern (Fig. 5.16), but overall their vertical stacking suggest aggradation of the system (Fig. 5.21). The lack of well-organized lobe stacking patterns which might be compensational, or lateral thickness and grain-size trends, the low sand: mud ratio and low amalgamation rate (ranging between 17.5 and 53.3%, averaging 27.7%) is characteristic of the distal ramp lobe complexes (Fig. 5.23). This, together with the scatter of palaeocurrents (Fig. 5.4) which vary between NW and NE direction might be related to effects of confinement by inherited intrabasinal mud-draped relief until the accommodation available was filled.

The well-developed bed-scale heterogeneity consists into matrix-rich and abundant deformed mudstone clasts in these lobe complexes (see FA4.1). This could reflect initial muddy substrate entrainment with erratic routeing pathways of the first sediment gravity flows that could reach this part of the basin after travelling across a rugose slope. Characteristics of these deposits also suggest deposition by low volume, high efficiency, clay-rich transitional plug flows with

dampened turbulence (Baas et al., 2009). In these flows, high-suspended clay content could have played a significant role in delaying settling velocities for the medium-grained sediment fraction that could be transported across long distance (Gladstone et al., 1998; Al Ja'Aidi et al., 2004; Baas et al., 2009).

The proximal ramp lobe succession (FA4.2) form lobe complexes deposited as a single and larger depocentre across intraslope topography subdued with deposition of the precursor distal ramp lobe complexes (Fig. 5.5). The proximal ramp lobe complexes thin and fine from the Martinez and El Cóndor sector, towards the Tutavel sector showing a spatial transition from typical matrix-poor sandstone facies of proximal ramp lobes (FA4.2) to matrix-rich sandstone facies of distal ramp lobes (FA4.1) (Fig. 5.23). This suggests a transition to lobe complex margins towards the NW slope flanking the northern Tutavel fault border, which might have contained the proximal ramp lobe depocentre in the Eastern Catán-Lil Basin (Figs 5.16 and 5.23).

The proximal ramp lobe complexes also individually thin and onlap from the Martinez sector towards the Puesto Ricón del Polo horst suggesting confinement of the proximal ramp lobe depocentre along the southeastern horst margin of the Eastern Catán-Lil Basin (Fig. 5.22). At the scale of lobe complexes, the lateral switching of successive lobe complexes towards the SE could reflect compensational stacking and increase in accommodation into the Martinez sector that is also suggested by the onlap pattern of lobe complexes shifting away from the Puesto Ricón del Polo horst margin (Fig. 5.22). Overall, the stacking pattern of proximal ramp lobe complexes reflects progradation towards the N/NE, followed by aggradation/compensation and southwards retrogradation with backstepping of the system upslope (Figs 5.4 and 5.23).

The subdued depocentre configuration led to deposition of more laterally extensive and thinner lobe complexes (individually averaging 24.5 m thick and traced over 5 to 8.5 km downdip) than the precursor distal ramp lobe complexes (Figs 5.4 and 5.23). These proximal ramp lobe complexes show a higher sand: mud ratio, amalgamation rate (averaging up to 46.5%) and more widespread erosion in their axis than the distal ramp lobe complexes (Fig. 5.23). Individual proximal ramp lobe complexes can show an asymmetric coarsening- and thickening-upward and fining- and thinning-upward trend, which might reflect progradation followed by retrogradation of lobe complexes, with discrete compensation of individual lobes (Fig. 5.23). It is also possible to identify better-

defined facies segregation across lobes between the weakly amalgamated margin of lobe complexes which has a low amalgamation rate averaging 27.7% and the centre of lobe complexes which has a higher amalgamation rate averaging 46.5% (Fig. 5.23).

Characteristics of proximal ramp lobes (see FA4.2) indicate deposition by larger volume and lower efficiency, well-stratified high-concentration flows, able to achieve greater turbulence than the sluggish flows that deposited the distal ramp lobes, enabling significant traction and high bed aggradation rate. The proximal ramp lobe complexes also have a better-defined internal organization of subfacies associations (see FA4.2). This includes vertical thickness and grain-size trends and lateral downdip thinning and fining over a few kilometres, with enrichment in dirty beds and transition into matrix-rich sandstone towards lobe complex margins (Fig. 5.23). The convergent onlap terminations of lobe complexes and the common occurrence of hummock-like bedforms point to some degree of containment with flow reflection and deflection against a confining slope (Kneller, 1991; Amy et al., 2004; Tinterri, 2011).

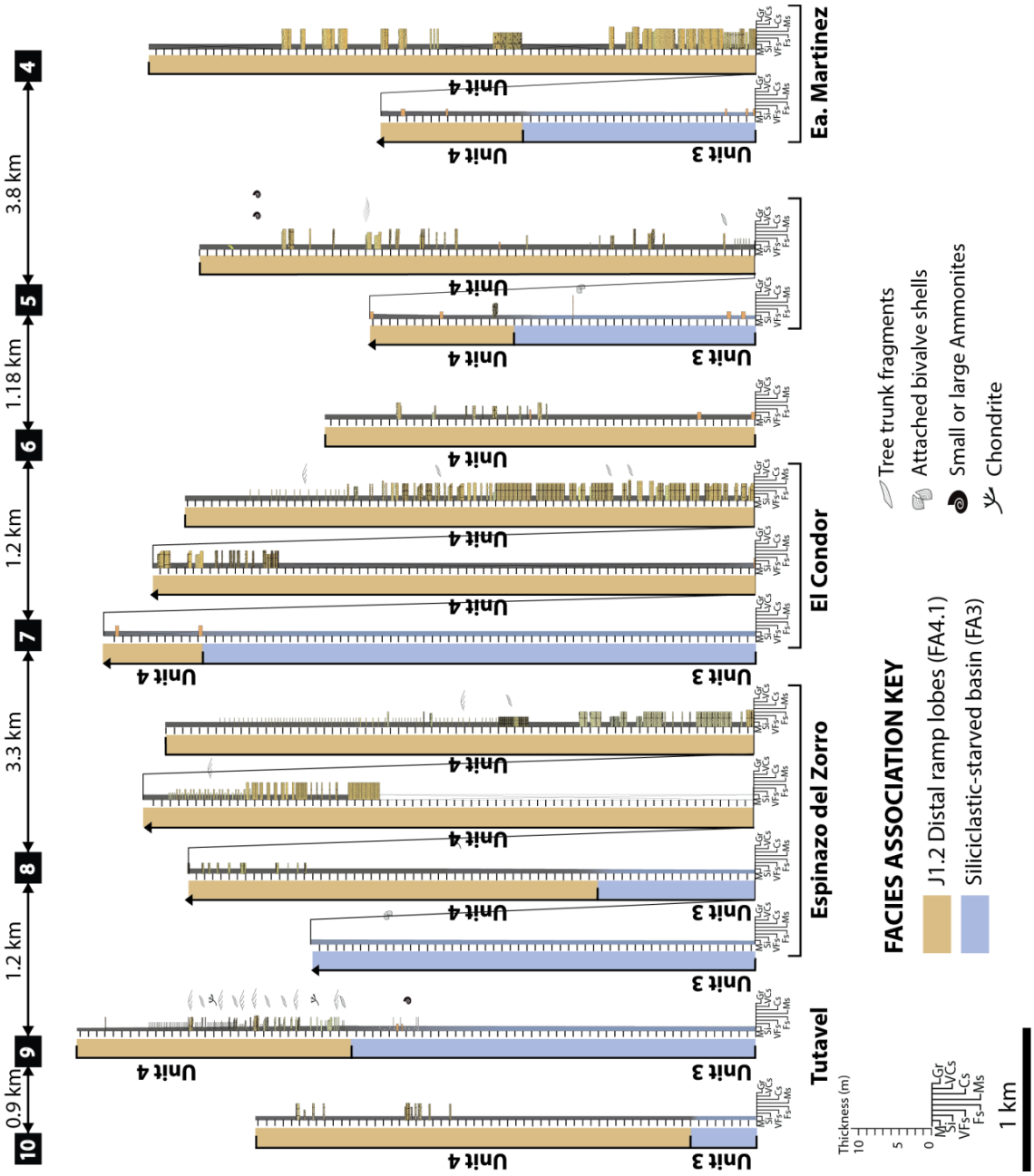

Figure 5.21: Detailed sections of the J1.2 distal ramp lobe complexes of Unit 4.

Figure 5.22: Outcrop view of onlapping proximal ramp lobe complexes (shown in fig. 5.23) towards the lateral basin margin. Location of the outcrop is shown on inset map (cf. fig. 5.4).

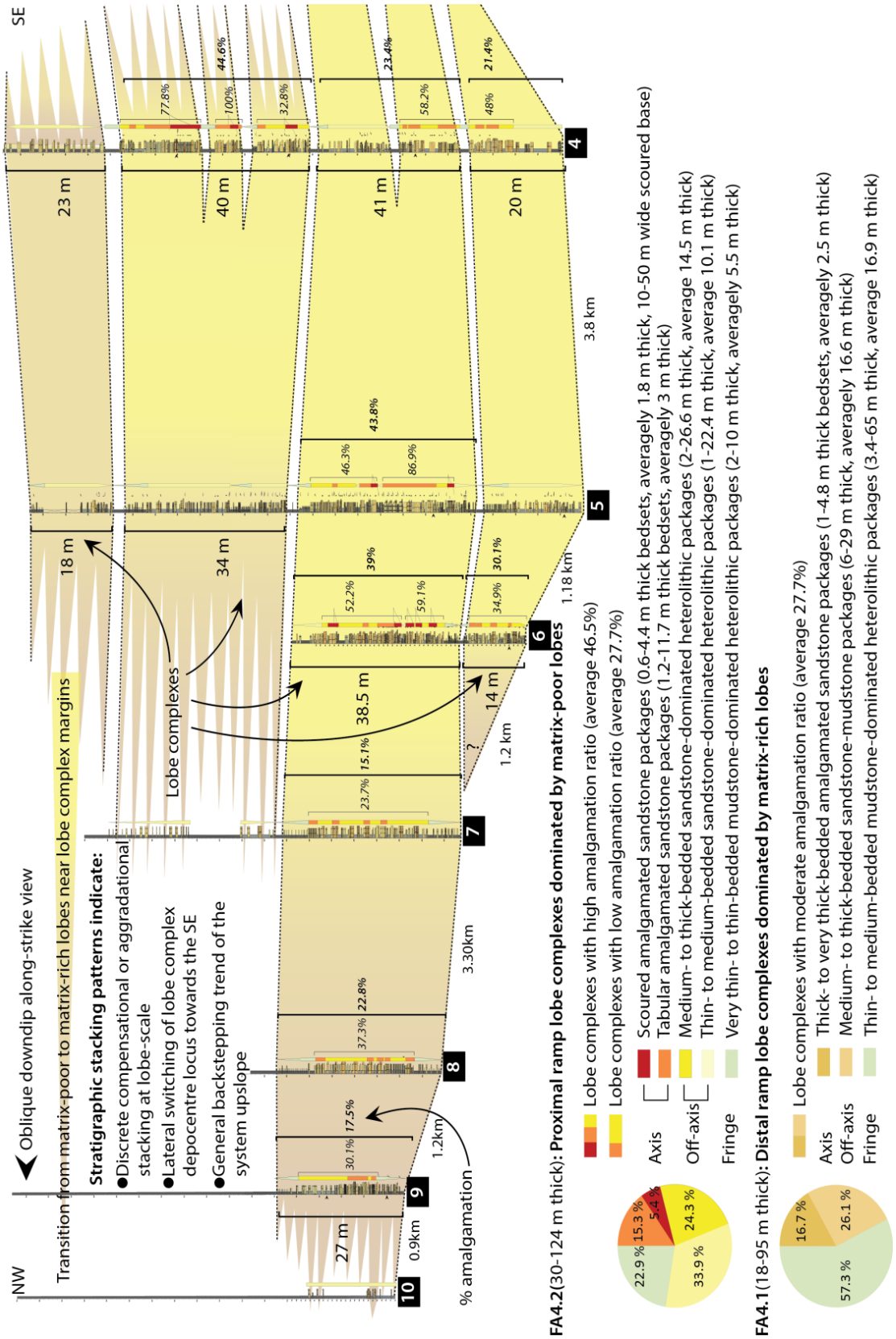

Figure 5.23: Detailed correlations showing the distribution of axis, off-axis and fringe facies associations in proximal ramp lobe complexes including the amalgamation rate in percentages and thicknesses. Quantitative diagrams in both distal and proximal ramp lobe deposits show the differences in the total proportions of facies association measured in the two types of lobe complexes, with a dominant occurrence of fringe and off-axis deposits in distal ramp lobes compared with proximal ramp lobes which are dominated by lobe axis and off-axis deposits. Note that lobe complexes with high amalgamation ratio include scours and channelforms in comparison with lobes having a lower amalgamation ratio and common finer-grained interbeds.

5.7. Stratigraphic architecture

5.7.1. J1.1 sequence

In the present study, the J1.1 sequence including Unit 1, 2 and 3 (Figs 5.6 and 5.24) corresponds to the transgressive cycle of a 2nd order sequence (equivalent to J1 sequence in Paim et al. (2008)),. It is bounded at base by a 2nd order sequence boundary that corresponds to the Intra-Liassic unconformity at top of the Precuyano Cycle deposits (Fig. 5.24). This unconformity corresponds to a transgressive surface overlying continental conglomerate deposits of Unit 1 in the Chacaico Basin and bounding the base of submarine conglomerate deposits (Unit 1) in the Eastern Catán-Lil Basin (Fig. 5.24). The top of this sequence corresponds to the top of Unit 3 which represents the maximum flooding zone (MFZ) and is bounded by a major flooding surface in both basins (Fig. 5.24). In the Eastern Catán-Lil and Chacaico Basin, the J1.1 sequence is represented by a siliciclastic storm- and wave-dominated shoreface to offshore system (Unit 2A) replaced in time by a deltaic system (Unit 2B). The facies of this sequence are significantly different in the Chachil Basin in which sedimentation is dominated by carbonates which form a detached carbonate platform and periplatform system (Fig. 5.24).

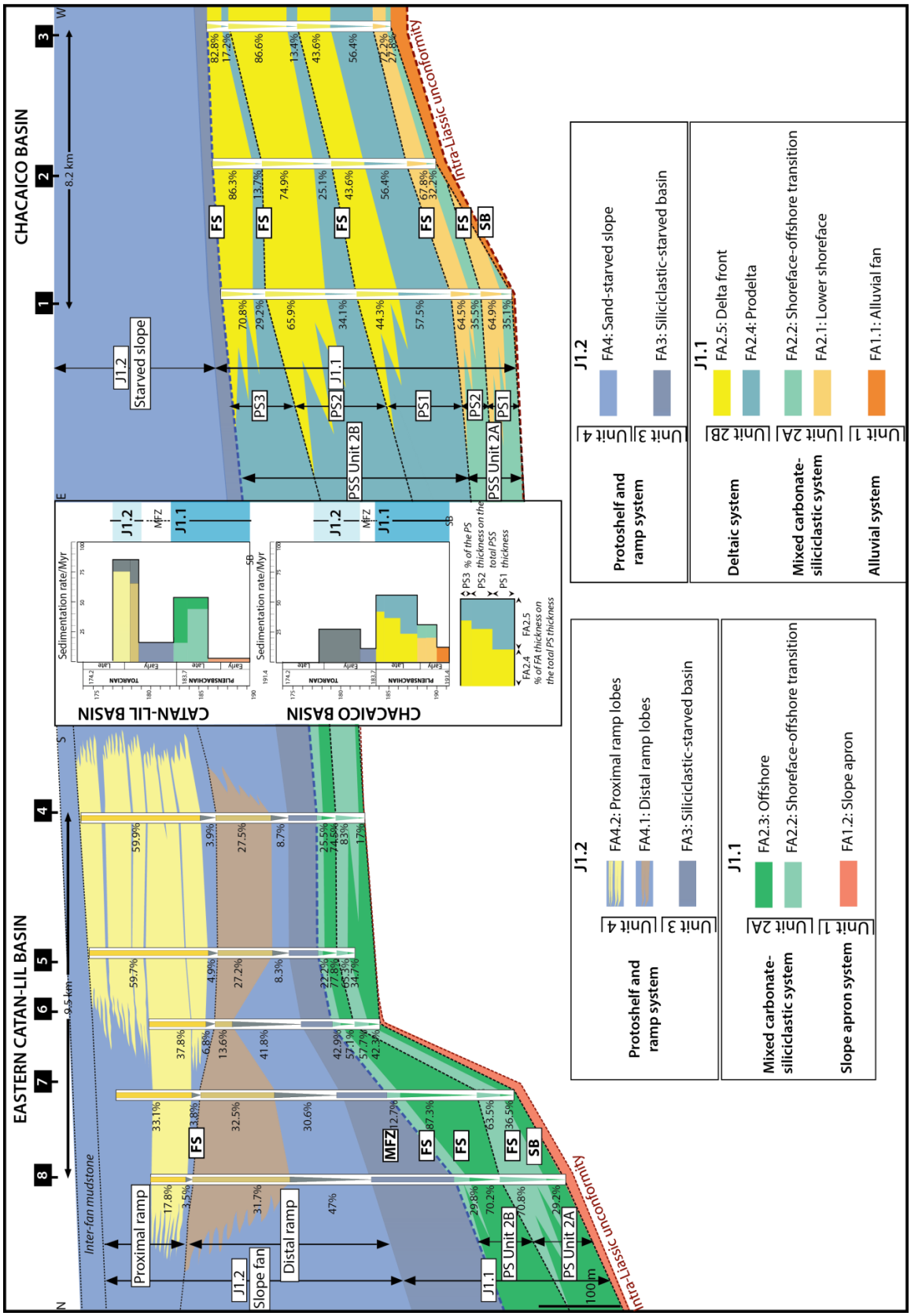

Figure 5.24: Stratigraphic scheme showing the interpreted parasequences (PS), parasequence sets (PSS) bounded by Flooding Surfaces (FS) and the main sequences J1.1 and J1.2. The early post-rift is recorded by Unit 3 which represents a Maximum Flooding Zone (MFZ) recorded both across the Chacaico and Eastern Catán-Lil basins. Distribution of facies associations with their respective percentage are indicated for each parasequence. Compacted sedimentation rates (calculated from Table 5.1) are also shown for each parasequence.

In the Chacaico Basin the J1.1 sequence includes five parasequences and two parasequences recognized in the Eastern Catán-Lil Basin. Parasequences are stacked vertically and bounded by non-erosive flooding surfaces and the facies association percentages calculated for each parasequence are shown in the Fig. 5.24. Despite the refined stratigraphic framework (Figs 5.5, 5.6 and 5.24), the physical correlation of individual parasequences between the two basins is uncertain as they cannot be traced across the basement footwall of the Puesto Rincón del Polo which isolated the Chacaico from the eastern part of the Eastern Catán-Lil Basin (Figs 5.4 and 5.5). However they can be integrated in a proximal-distal transect as they record respectively the proximal and distal evolution of coeval sedimentary systems and factors of control in both basins.

In the Chacaico Basin, Unit 2A comprises up to two parasequences (18-31 m thick) recording a vertical transition upwards from shoreface-offshore transition to sandier lower shoreface deposits (Fig. 5.18 and 5.24). As the ratio of lower shoreface deposits relative to shoreface-offshore transition decrease upwards, they are grouped in a parasequence set with a retrogradational pattern (Fig. 5.24). The parasequence set boundary represents a major flooding surface and a change in the dominant depositional environment.

The overlying Unit 2B in the Chacaico Basin comprises three sand-rich parasequences (40.8-97 m thick) (Fig. 5.24). Individually, parasequences record a shallowing upward trend, from muddy prodelta to sandy delta-front deposits topped by a marine flooding surface. Alternations of sand and mud, and the decrease in amalgamation rate within delta-front deposits of individual parasequence might result from fluctuations in sand discharge with short-term variations of frequency of storm or river flood events and/or minor rising pulses of relative sea-level (Hampson, 2000; Hampson and Storms, 2003). The consecutive three parasequences show a vertical decrease of individual parasequence thickness and increase in the thickness ratio of delta-front deposits at the expense of prodelta deposits (Fig. 5.24). Hence, they represent a parasequence set with aggradational to slight progradational pattern. The first two parasequences could record a coeval increase in the rate of relative sea-level rise and sediment supply counterbalancing the transgression, whereas the thinner third one could record a decrease in the rate of relative sea-level rise and/or an increase in the rate of sediment supply. The top of the parasequence

set is represented by a large-scale flooding event recognized all across the two basins (i.e, base of Unit 3 Fig. 5.24).

In the Eastern Catán-Lil Basin, Unit 2 comprises two fine-grained and thicker parasequences represented by Unit 2A and B (18-126 m thick) which both records a vertical transition upwards from offshore to shoreface-offshore transition deposits (Fig. 5.24). The parasequence set of Unit 2B in the Eastern Catán-Lil Basin records very little sand supply despite being coeval to prodelta and delta-front parasequence set of the Chacaico Basin (Figs 5.5, 5.6 and 5.24). That might be a consequence of the long-lived topographic high of the Puesto Rincón del Polo sector which isolated the two depocentres. The paucity of flows which could bypass the Chacaico Basin also suggests dominant trapping of coarse grained sediments in the delta which is characteristic of low-gradient shoal-water mouthbar-type delta (Postma and Drinia, 1993). The parasequences stack vertically with an increasing thickness, and an increase of the thickness ratio of offshore deposits at the expense of shoreface-offshore transition deposits (Fig. 5.24). Therefore, retrogradational stacking reflects deposition of this parasequence set with an increase in accommodation and sediment supply outpaced by the rate of relative sea-level rise, which might be the result of local mechanical subsidence.

Major marine flooding is recorded at the base of Unit 3 by the accumulation of siliciclastic-starved basinal mudstone onto offshore and offshore-transition deposits in the Eastern Catán-Lil Basin, and onto delta-front deposits in the Chacaico Basin (Fig. 5.24). In the Chacaico Basin, maximum marine flooding resulted in drowning of the previous deltaic system (Unit 2B) and long-term deposition of carbonate-dominated mudstone (Unit 3). The shallow-marine deltaic system was abandoned as it could not re-establish and transit again across the shelf to supply sand in the Chacaico Basin after backstepping landward with marine flooding. In the Eastern Catán-Lil Basin, Unit 3 overlies shoreface-offshore transition and offshore deposits of Unit 2A, therefore the facies shift associated with marine flooding is less important than in the Chacaico Basin (Figs 5.6 and 5.24). These calcareous organic-rich mudstone deposited and draped inherited intraslope topography and as a result, they presently show local thickness variations across basins of the study area (Fig. 5.6). These fine-grained sediments accumulated under very poorly oxygenated conditions and U-Pb age constraints provided in the present study indicates that it should record

the Toarcian Oceanic Anoxic Event (TOAE) which has been constrained with ammonite biostratigraphy in the Chacaico Basin (Damborenea et al., 2013; Al-Suwaidi et al., 2016) in time-equivalent deposits (Fig. 5.6). This interval records very low sedimentation rates (5-35 m/Myr based on compacted thickness, Table 5.1) with mainly biogenic sedimentation and maximum condensation during a period of generalized sea-level rise. Hence, all the characteristics of Unit 3 can be regarded as recording the maximum fllooding zone associated with regional transgression (Fürsich and Pandey, 2003) (Fig. 5.6 and 5.24).

5.7.2. J1.2 sequence

The J1.2 sequence corresponds to the regressive cycle of the 2nd order sequence J1 in Paim et al. (2008), represented by the Unit 4 (Figs 5.6 and 5.24). J1.2 is bounded at top by the basal surface of the next intraslope fan J2.1 sequence.

Unit 4 record intraslope fan development in the Eastern Catán-Lil Basin, with progradation, aggradation and retrogradation that should reflect fan initiation, growth and retreat (Figs 5.23 and 5.24). Fan initiation occurs with deposition of the “precursor” distal ramp lobe complexes infilling accommodation, forming the first local sandy lobe depocentres with substantial confinement by mud-draped inherited intraslope topography. The distal ramp lobe depocentres mainly record successive stacking of lobe complexes with aggradation and final retrogradation associated with shut down of the system. Subsequent renewed fan growth and retreat is recorded by deposition of the proximal ramp lobe complexes (including the basal mudstone unit) (Fig. 5.23) with partial confinement across a more subdued intraslope topography and progressively healing and leveling remnant inherited intrabasinal relief (Figs 5.5 and 5.24). The proximal ramp lobe depocentre mainly record successive stacking of lobe complexes with progradation, aggradation with lateral compensation and final retrogradation associated with upslope backstepping and shut down of the system. The laterally extensive mudstone interval separating the distal ramp lobe complexes from the proximal ramp lobe complexes might record an intermittent decrease of sand supply which could reflect abandonment of the intraslope fan with major avulsion of the feeder system or variation of sediment supply at source. Therefore, the sequential organization of Unit 4 can be interpreted as comprising two smaller-

scale sequences, each bounded at base by a flooding surface and respectively represented by the distal ramp lobe complexes (FA4.1) and the proximal ramp lobe complexes (FA4.2) (Figs 5.5 and 5.24). Major shut down of sediment supply to the intraslope fan in the Eastern Catán-Lil Basin is recorded with widespread deposition of a thick interfan mudstone succession (15-70 m thick) (*sensu* Prélat et al., 2009).

In contrast, in the Chacaico Basin, Unit 4 records deposition of a significant thickness of siliciclastic mudstone accumulated until the Aaleanian (230 m thick, Volkheimer, 1973) contemporaneously of the development of the J1.2 intraslope fan recorded by Unit 4 in other basins (Fig. 5.25). Sand-starvation in this eastern basin suggests that shallow-marine deltaic system was abandoned as it could not re-establish and transit again across the shelf and might have switched laterally eastwards (see Gómez Omil et al., 2002).

5.7.3. Summary and implications for the syn- to post-rift transition

The changes in stratigraphic architecture and stacking patterns recorded by the evolution of sedimentary systems and sources during the syn- to post-rift transition also reflect key changes of shelf-slope basin physiography. The evolution of sedimentary systems in the J1.1 sequence records a great variability of sedimentation patterns, which might reflect the disorganization and multiplicity of systems developed across the irregular basin topography during transgression (Figs 5.25). It includes two main parasequence sets which record a progressive reduction in the rate of transgression, marked by an increase of individual parasequence thickness that could result from an increase of sediment supply with contribution of both intrabasinal (siliciclastic and volcanic arc-related) and cratonic extrabasinal sources, and/or a decrease of tectonic subsidence (from Unit 2A to B) (Fig. 5.24). This sequence should record shelf margin accretion with a rising trajectory during a period of relative sea-level rise with different expressions in each depocentres. This result in the coeval development of a fan-deltaic and deltaic system in the most proximal rift depocentre fed by a southeastern extrabasinal source (according to palaeocurrents) related to the hinterland supply across the cratonic basin margin adjacent to the Chacaico Basin. In contrast, dominance of a mixed carbonate-siliciclastic system is

characteristic of depocentres distal to the cratonic basin margin, which instead received limited sediment supply from extrabasinal cratonic sources and more form intrabasinal sources reaching the Eastern Catán-Lil Basin.

In contrast, the J1.2 sequence records regression during a period of slow relative sea-level rise or stand-still, with stacking of intraslope fan over former basinal mudstone deposits of regional extent that record a major marine flooding event (Fig. 5.24). The intraslope fan develops with the rapid renewal of sediment supply from a volcanic arc-related extrabasinal source (according to palaeocurrents). This extrabasinal source was different to the one that permitted the development of the deltaic system in the Chacaico depocentre, which then remained a sand-starved depocentre (Figs 5.6 and 5.24). The intraslope fan evolves stratigraphically from precursor distal ramp to proximal ramp lobe complexes which infill the inherited intrabasinal accommodation and heals topography in the Catán-Lil depocentre, prior to shut down of extrabasinal sediment supply from the southeastern cratonic basin margin. Therefore, the evolution of sedimentation with intraslope fan deposition recorded the establishment of a deep-marine sandy low-gradient ramp-type system, which permitted extrabasinal sediment supply from a source located to the south-southwest (according to palaeocurrents); this is consistent with growth of the proto-shelf island arc basin margin. Therefore, the syn-to post-rift transition is characeterized by a major reorganization of sedimentary systems with progressive levelling the inherited rift basin topography, change of from mixed intrabasinal-extrabasinal to extrabasinal source contribution, and change of source location after the major marine flooding event marking onset of the early post-rift.

5.8. Discussion

5.8.1. Chronostratigraphy: Revision of the stratigraphic framework at the light of new U-Pb ages

This section re-emphasises the stratigraphic framework and clarifies the type of marine deposits representing the Chacaico and Los Molles Fm., based on sedimentation patterns observed across several depocentres (Fig. 5.25). Unit 1 and 2 of this study (Figs 5.5 and 5.24) correspond to the Chacaico Fm. deposited during Early to Pliensbachian-Toarcian boundary in the Eastern Catán-Lil and Chacaico Basin (Figs 5.3 and 5.25), following the original definition of the Chacaico Fm. in the Chacaico Basin (Volkheimer, 1973). However, all deposits of the Chacaico Fm. have sometimes been integrated as the base of the Los Molles Fm. (which is in this study defined at the base of Unit 3 and including Unit 4) across all the study area (Gulisano and Gutiérrez Pleimling, 1995). This is also seen in several subsurface studies with the integration of carbonate and pyroclastic deposits (that belong to the Unit 2 of this study) at the base of the Los Molles Fm. (Gómez Omil et al., 2002; Bermudez et al., 2002; Schiuma et al., 2008). The Chacaico Fm. should record respectively, shallow-marine fan-deltaic to deltaic deposits, and deep-marine offshore-transition to offshore mudstone-dominated deposits (Unit 2) influenced by active volcanism (primary or reworked volcanic influx). The Chacaico Fm. should also lack deep-marine slope or basin-floor submarine sandstone lobes. In contrast, the base of the Los Molles Fm. should be recognized as deep-marine siliciclastic-starved organic-rich calcareous basinal mudstone (Unit 3) associated with major marine flooding, which evolve into submarine fan sandstone and mudstone deposits (Unit 4).

In the Chacaico Basin, a late Early Toarcian age of the TOAE in the Lower Los Molles Fm. has been constrained in the lower part of Unit 3 based on TOC measurements and biostratigraphy (*Dactylioceras hoelderi* Ammonite Andean Biozone-16, Al-Suwaidi et al., 2016; NJ6 Nannofossil Zone, Angelozzi and Pérez Panera, 2016) (Figs. 5.25). This same stratigraphic level in the Unit 3 was also sampled for U-Pb dating which provided a maximum depositional weighted mean age calculated for the youngest volcanic zircons at 182.4 ± 2.3 Ma (1σ) (Naipauer et al., 2018) (Fig. 5.25). Therefore, according to geochronology and ammonite biostratigraphy, Unit 3 started to deposit from Early Toarcian in the Chacaico

Basin (Volkheimer, 1973) and should be taken as the base of the Los Molles Fm. (Figs 5.5 and 5.25)

In the Chachil Basin, the obtained U-Pb SHRIMP concordia ages indicate deposition of the Tuff 3 at base of Unit 3 occurred at 184.4 ±2 Ma (2σ) (Figs 5.7 and 5.8), which implies a latest Pliensbachian age for the base of the Los Molles Fm. (Fig. 5.25). This is also supported in the Eastern Catán-Lil Basin, as the age of the base of the Los Molles Fm. can be estimated near the Late Pliensbachian-Toarcian boundary given the occurrence of *Posidonotis cancellata* (Leanza) near the top of Unit 2B, based on the timing of the *Posidonotis cancellata* Assemblage Zone (cf. Riccardi et al., 2011) (Fig. 5.25). In the Eastern Catán-Lil Basin, the Tuff 1 deposited at the top of Unit 3 occurred at 179.8 ±1.4 Ma (2σ) (Figs 5.7 and 5.8) which implies a late Early Toarcian age for the Unit 3-Unit 4 boundary in the Los Molles Fm. (Fig. 5.25). Therefore, biostratigraphic and U-Pb ages (including error margins) means that the deltaic system of the Chacaico Basin (Unit 2B) was contemporaneous with offshore to shoreface-offshore transition deposits accumulated in the Eastern Catán-Lil Basin (Unit 2B) (Figs 5.5 and 5.24). This shows the variability of sedimentation between the two studied marine rift basins during the Pliensbachian (Fig. 5.6).

These results implies that siliciclastic-starved calcareous basinal mudstone (Unit 3) were deposited more or less contemporaneously across late syn-rift depocentres of the study area, and suggest the record of a major flooding event during the early-mid Early Toarcian, associated with onset of the early post-rift (Fig.5.25). In a general perspective, it permits to change previous assumptions of some other authors who adopted a late Early Toarcian age to the base of the Los Molles Fm. both in the La Jardinera Basin (Paim et al., 2008), Chachil Basin and even from the southern to central Neuquén Basin (Cucchi et al., 2005; Leanza et al., 2013). The U-Pb ages obtained in the present chapter also point the diachronous character of the base of the Los Molles Fm. at basin-scale. This is shown by the U-Pb age (~182.3 Ma) obtained at top of the Chachil Fm. in the Chacay Melehue Basin of the central Neuquén Basin (see location Fig. 5.1), which indicates a maximum Early Toarcian age for the base of the Los Molles Fm. (Riccardi and Kamo, 2014).

Finally, the late Early Toarcian age for the Unit 3-Unit 4 boundary implies the development of intraslope fan of the Los Molles Fm. earlier in the Catán-Lil Basin than interpreted in the La Jardinera Basin. In this basin, the first deep-

marine intraslope sandy deposits have been placed at the boundary between the two 2nd order sequences J1-J2 (here equivalent to the boundary Unit 3-4) defined by Paim et al. (2008) after Gulisano and Gutiérrez-Pleimling (1995). This sequence boundary was advocated in order to support a scenario where sand supply is related with the Toarcian-Aalenian sea-level fall, and therefore related to eustatic control on sedimentation, without biostratigraphic control (Paim et al., 2008). However, the study of radiolarian biostratigraphy sampled in the same section measured by Paim et al. (2008) permitted the Toarcian-Aalenian boundary to be placed ~150 m above the base of the first sandy lobe deposits, which form their J2.1 sequence (belonging to the 2nd order sequence J2) (Kochhann et al., 2011) (Fig. 5.25). Therefore, the Toarcian-Aalenian boundary is not located at the J1-J2 boundary, but instead at the top of the J2.1 sequence, and means that sandy deposits of J2.1 should have been deposited at least during the Late Toarcian (Fig. 5.25). This result is consistent with the obtained U-Pb ages that support sand deposition started since the late Early Toarcian in the Catán-Lil Basin. Therefore sand supply occurred during the regressive cycle of the 2nd order sequence J1, earlier than previously thought, which is therefore named here J1.2 (Fig. 5.25).

This has implications for previous models (Paim et al., 2008) that highlighted the boundary between the sequence J1 and J2 (equivalent here to the boundary between Unit 3 and 4), which was interpreted to mark an abrupt increase of sand supply associated with the syn- to post-rift transition in the La Jardinera Basin. However, the new U-Pb ages presented here highlight the diachroneity of sand supply and intraslope fans development between basins, and should not be taken as a lithostratigraphic record of the onset of early post-rift. The new U-Pb ages permit to revise the stratigraphic scheme for the Early Jurassic Cuyo Group and its implications for controls on the sediment supply given that the J1-J2 sequence boundary appears to be older than previously assumed and might also be diachronous across basins (Fig. 5.25).

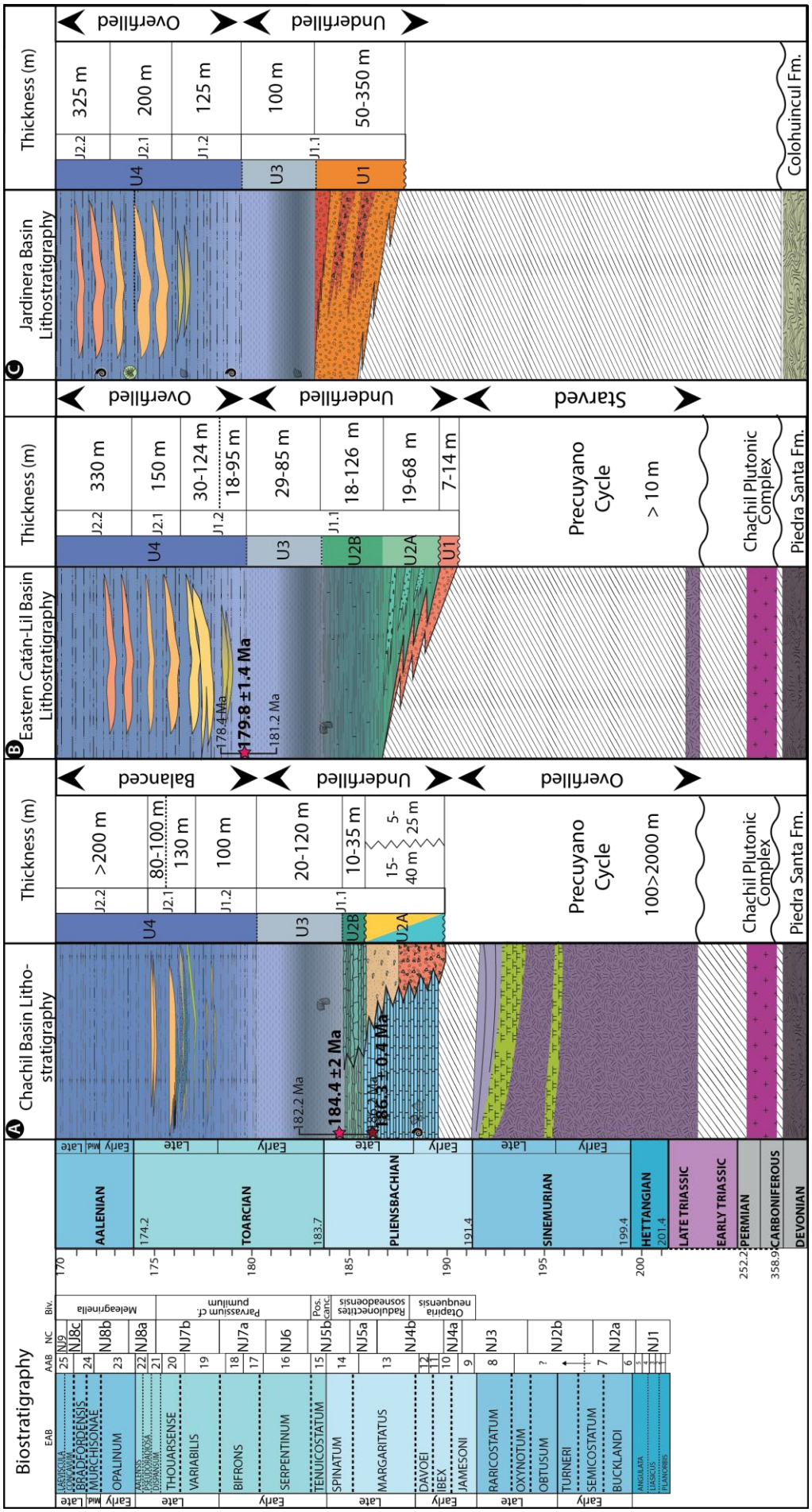
Biostratigraphy
A Chachil Basin Litho-stratigraphy
B Eastern Catán-Lil Basin Lithostratigraphy
C Jardinera Basin Lithostratigraphy
Thickness (m)
Balanced
Underfilled
Overfilled
Starved
U4
U3
U2B
U2A
U1
J2.2
J2.1
J1.2
J1.1
>200 m
80-100 m
130 m
100 m
20-120 m
10-35 m
15-40 m
5-25 m
330 m
150 m
30-124 m
18-95 m
29-85 m
18-126 m
19-68 m
7-14 m
325 m
200 m
125 m
100 m
50-350 m
Precuyano Cycle
100>2000 m
> 10 m
Chachil Plutonic Complex
Piedra Santa Fm.
Colohuincul Fm.
182.2 Ma
184.4 ±2 Ma
186.3 ± 0.4 Ma
178.4 Ma
179.8 ±1.4 Ma
181.2 Ma
AALENIAN
TOARCIAN
PLIENSBACHIAN
SINEMURIAN
HETTANGIAN
LATE TRIASSIC
EARLY TRIASSIC
PERMIAN
CARBONIFEROUS
DEVONIAN

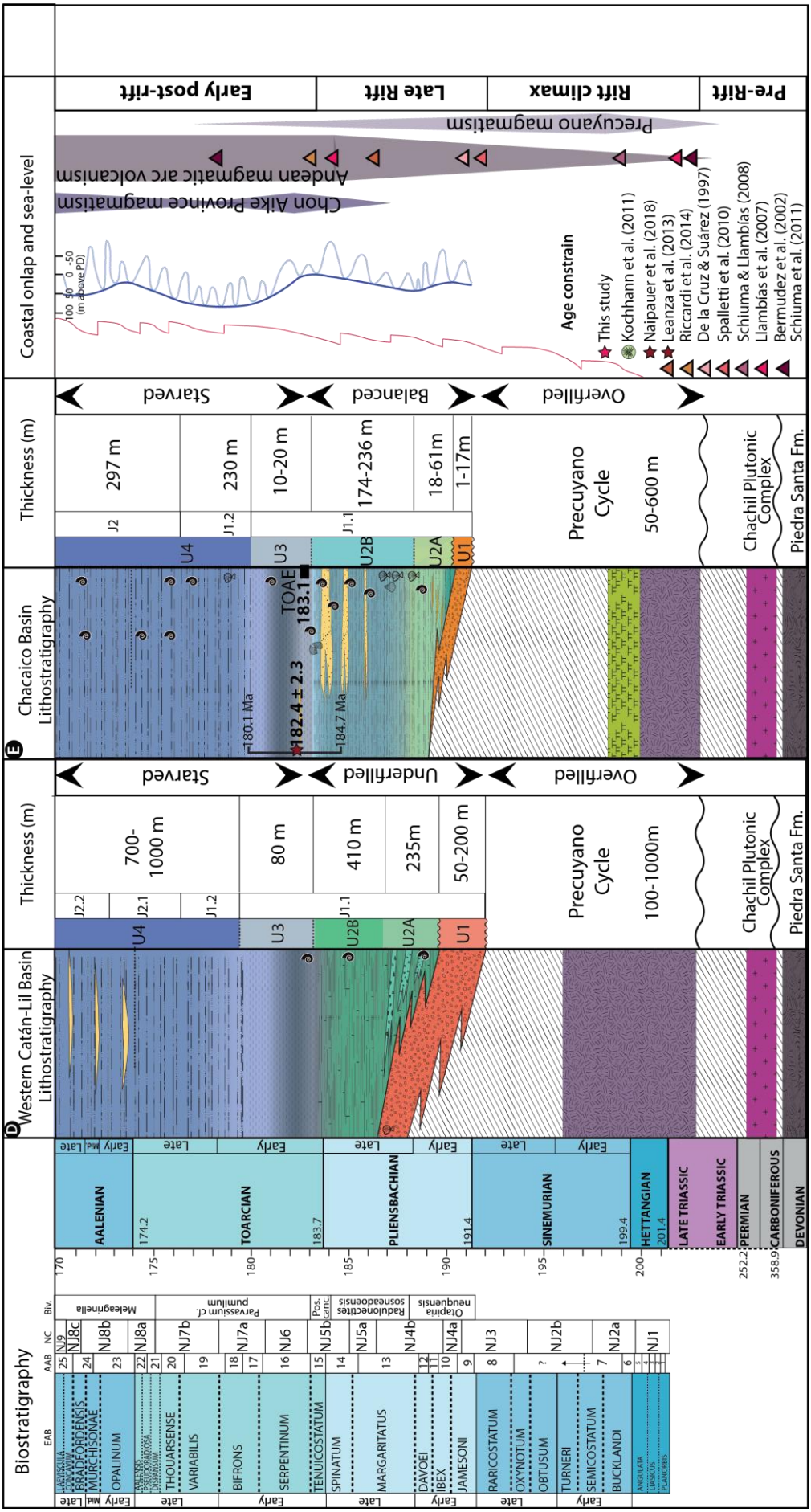
Biostratigraphy
Western Catán-Lil Basin Lithostratigraphy
Thickness (m)
Chacaico Basin Lithostratigraphy
Thickness (m)
Coastal onlap and sea-level
Pre-Rift
Rift climax
Late Rift
Early post-rift
Precuyano magmatism
Andean magmatic arc volcanism
Chon Aike Province magmatism
Age constrain
This study
Kochhann et al. (2011)
Naipauer et al. (2018)
Leanza et al. (2013)
Riccardi et al. (2014)
De la Cruz & Suárez (1997)
Spalletti et al. (2010)
Schiuma & Llambías (2008)
Llambías et al. (2007)
Bermudez et al. (2002)
Schiuma et al. (2011)
Overfilled
Underfilled
Balanced
Starved
Precuyano Cycle
100-1000m
50-600 m
Chachil Plutonic Complex
Piedra Santa Fm.
700-1000 m
80 m
410 m
235m
50-200 m
297 m
230 m
10-20 m
174-236 m
18-61m
1-17m
182.4 ± 2.3
180.1 Ma
184.7 Ma
183.1
TOAE
AALENIAN
TOARCIAN
PLIENSBACHIAN
SINEMURIAN
HETTANGIAN
LATE TRIASSIC
EARLY TRIASSIC
PERMIAN
CARBONIFEROUS
DEVONIAN

Figure 5.25: Stratigraphic scheme for the five main basins in the study area, integrated with available constrains of thickness and fossil data from the literature (Volkheimer, 1973; Gulisano and Gutiérrez-Pleimling, 1995; Franzese et al., 2006, 2007; Paim et al. 2008) and U-Pb zircon ages (186.3 ± 0.4 Ma in the Chachil Graben, Armella et al., 2016 modified from Leanza et al., 2013; 182.4 ± 2.3 Ma in the Chacaico Basin, Naipauer et al., 2018), as well as new U-Pb zircon data provided in this contribution (red stars).Nannofossil chronozones follow Ballent et al. (2011), standard European (EAB) and Andean (AAB) Ammonite biozone numbers follow Riccardi (2008) and bivalve biozones follow Riccardi et al. (2011). The TOAE is placed in the late Tenuicostatum-early Dactylioceras Hoelderi AAB after Al-Suwaidi et al. (2016) and in the NJ6 nannofossil chronozone after Angelozzi and Pérez Panera (2016). Note that the stratigraphic names for intraslope fans follows Paim et al. (2008). See location of sections on map fig. 5.3.

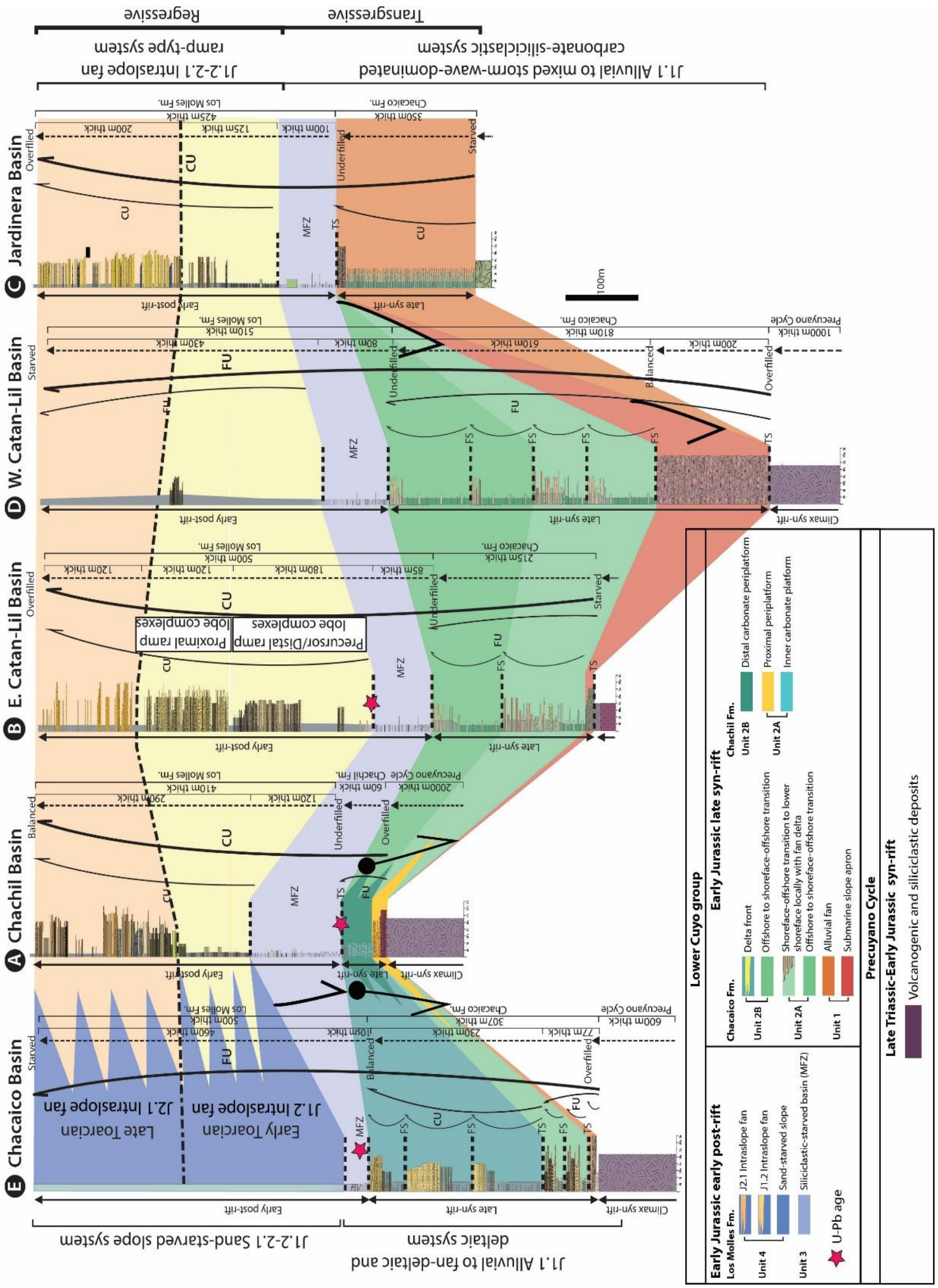

Figure 5.26: Correlation of lithostratigraphic units across the five depocentres of the study area showing the different sedimentary systems developed across depocentres, with indication of units thickness, basin-fill trends, sequences and nomenclature with formations. Constrains of volcanic syn-rift thickness data from the literature (Gulisano and Gutiérrez-Pleimling, 1995; Franzese et al., 2006, 2007) and J2.1 sequence thickness after Paim et al. 2008 with J1.1 and J1.2 sequences thickness measured from the present study) and U-Pb zircon ages (186.3 ± 0.4 Ma in the Chachil Graben, Armella et al., 2016 modified from Leanza et al., 2013; 182.4 ± 2.3 Ma in the Chacaico Basin, Naipauer et al., 2018), as well as new U-Pb zircon data provided in this contribution (red stars).Note the maximum thickness are indicated (see range of thickness in fig. 5.25).

5.8.2. Evolution of syn- to post-rift sedimentation at a regional-scale

A synthesis of the stratigraphic architecture and palaeogeographic changes recorded by the Early Jurassic Cuyo Group is provided at a regional-scale, across the Eastern and Western Catán-Lil, Chacaico, Chachil and La Jardinera basins, based on large-scale measured sections and complementary data from the literature (Figs 5.25 and 5.26).

5.8.2.1. Late syn-rift sedimentation (Early-Late Pliensbachian)

The late syn-rift recorded with the Chacaico and Chachil formations is characterized by the heterogeneity of sedimentation regimes ranging from subaerial coastal plain and lacustrine, to mixed shallow-marine carbonate and clastic, and deltaic systems (Figs 5.25 and 5.26). The development of a range of different depositional systems with a complex spatial organization resulted in significant along-strike fault variability of depositional environments and multiplicity of related sedimentary processes, similar to the Suez rift (Gupta et al., 1999; Young et al., 2003; Jackson et al., 2005; Leppard and Gawthorpe, 2006; Cross and Bosence, 2008). The late syn-rift deformation was mainly accommodated with fault-block tilting (Figs 5.16 and 5.18) with thinning and onlapping across blind faults, stratal dipping into the hangingwall and with unbreached fault growth fold development with sedimentation rate outpacing fold growth rate (Fig. 5.18) (e.g Gawthorpe, 1997; Lewis et al., 2015; Khalil and McClay, 2018).

During the late syn-rift, the Chacaico Basin evolved as an overfilled depocentre, which promoted the accumulation of intrabasinal fault-block catchment-fed alluvial fans, fluvial channels and lacustrine carbonates of alluvial plain of Unit 1, sandy shoreface with intervening fan-deltaic bottomset deposits and deltaic deposits of Unit 2 (~190-300 m thick) (Figs 5.27, 5.28 and 5.29). In this basin, the development of low-gradient systems might have been promoted by the limited inherited rift topography and overfilled conditions that resulted from significant accumulation of Precuyano Cycle volcanic deposits (50-600 m thick, Franzese et al., 2007; Muravchik et al., 2011) (Figs 5.25 and 5.26). The eastern part of the Eastern Catán-Lil Basin developed across a granitic basement

structure which outcrops from the Cerro Mallin de Ibànez-Martinez sector to the Tutavel sector to the northwest, where it links with the Chachil Basin horst border bounded by the Felipin and Chihuido Bayo Fault (Fig. 5.3). The Eastern Catán-Lil Basin recorded the influence of this granitic basement high dissected by normal faults, which formed a major accommodation zone across which a very limited thickness (<10 m thick) of Precuyano Cycle volcanic deposits accumulated (Figs 5.25 and 5.26). This granitic horst separated the Eastern Catán-Lil Basin from the overfilled syn-rift volcanic depocentre of the Chachil Basin (10-2000 m thick, Franzese et al., 2006) (Fig. 5.3). The Chachil Basin evolved during the late syn-rift into an underfilled depocentre dominated by mixed carbonate-clastic deposits of Unit 1 and 2, which recorded the influence of ash-fall from the volcanic arc (cf. Chapter 4) (Figs 5.27, 5.28 and 5.29). The Western Catán-Lil Basin, bounded by the Lonqueo Fault to the southwest and the Felipin Fault to the northeast, recorded overfilled syn-rift basin-fill condition with accumulation of significant thickness of Precuyano Cycle volcanic deposits (100-1000 m thick) (cf. Gulisano and Gutiérrez-Pleimling, 1995; Muravchik et al., 2014) (Figs 5.25 and 5.26). Here, the late syn-rift strata is associated with thinning of footwall and hangingwall-derived alluvial fans and slope apron deposits of Unit 1 (7-14 m to 50-200 m thick) away from basin bounding basement highs. In contrast, sand-starved offshore to shoreface-offshore transition deposits of Unit 2 (37-194 m to 235-410 m thick) are thickening into growth synclines towards the centre of the Eastern and Western Catán-Lil Basin and record both intrabasinal siliciclastic and pyroclastic source contribution (Figs 5.28 and 5.29). The southwestern basin of La Jardinera (Fig. 5.3) lacks Precuyano Cycle volcanic deposits and formed a starved to underfilled late syn-rift depocentre which recorded deposition of pyroclastic monomictic breccias and polymictic conglomerates of Unit 1 (50- >350 m thick) above metamorphic basement cored fault hangingwalls and lack Unit 2 deposits (Figs 5.25, 5.26 and 5.27).

In contrast to the Chacaico and Chachil Basin, which were overfilled, significant late syn-rift accommodation enabled the development of balanced to underfilled conditions in the Catán-Lil and La Jardinera Basin (Figs 5.25 and 5.26). The inherited rift topography promoted the development of high-gradient transverse systems which formed narrow submarine slope apron conglomeratic fringes restricted to footwall and immediate hangingwall fault-blocks (Unit 1) (Fig. 5.27). The composition of sediments and characteristics of clasts indicate very

short sediment transport distance from intrabasinal sources which might have correspond to isolated small drainage basins developed along footwall fault-blocks (e.g Muravchik et al., 2014). The hard granitic and volcanic fault-block bedrock lithologies of footwalls and the semi-arid climate (Volkheimer et al., 2008) might have contributed to limit sediment supply and the coarse grain-size of removed material prevented water turbidity (Fig. 5.28). Similarly to the Gulf of Suez (Cross and Bosence, 2008) these conditions permitted the coeval development of carbonate systems in the Chachil Graben, which evolved as an underfilled late syn-rift depocentre (cf. Chapter 4) (Fig. 5.29). In contrast, the proximity of multiple point sources with extrabasinal supply from a cratonic hinterland along the shoreline of the Chacaico Basin permitted the development of a transverse deltaic system across a low-gradient basin margin previously healed by alluvial fan deposits and its evolution into a sediment-balanced depocentre (Fig. 5.29).

Permanent reshaping of rift landscapes by volcanic-related processes inhibited the development of long-live and large drainage catchments during the late syn-rift. In non-volcanic rift basins drainage catchments form major inherited intrabasinal sources that can allow identification of the location of subsequent depocentres (e.g Gawthorpe et al., 2018). Therefore feedbacks between syn-rift volcanism, tectonism and sedimentation (e.g Muravchik et al., 2011; D'Elia et al., 2018) contributed to limit sediment supply during the late syn-rift and conditioned the inherited accommodation and slope gradients. This resulted in a complex distribution of sedimentary environments, involving coeval intrabasinal (siliciclastic and volcanic-arc related) and cratonic extrabasinal sources (Figs 5.27, 5.28 and 5.29) feeding transverse systems.

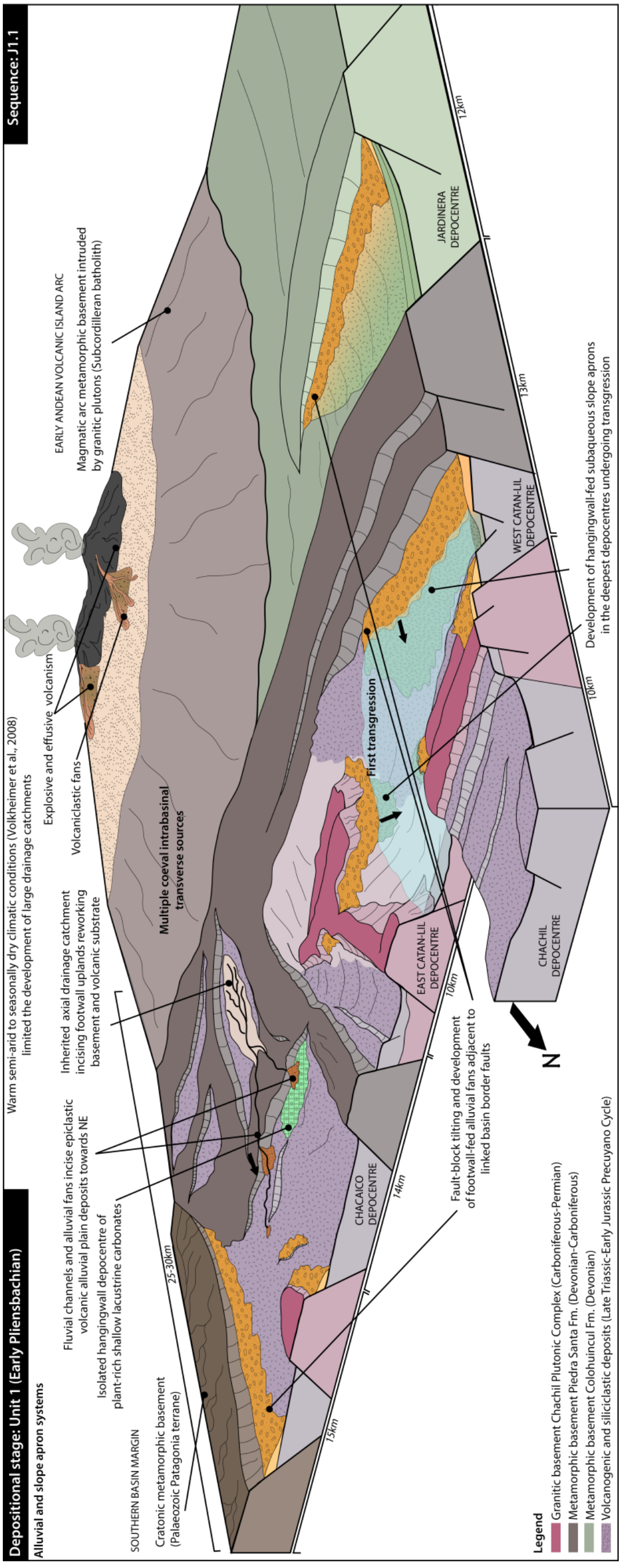

Figure 5.27:Palaeogeographic block diagram of the studied depocentres of the southwestern Neuquén Basin representing the Early Pliensbachian configuration during late syn-rift deposition of the Unit 1 with first transgression.

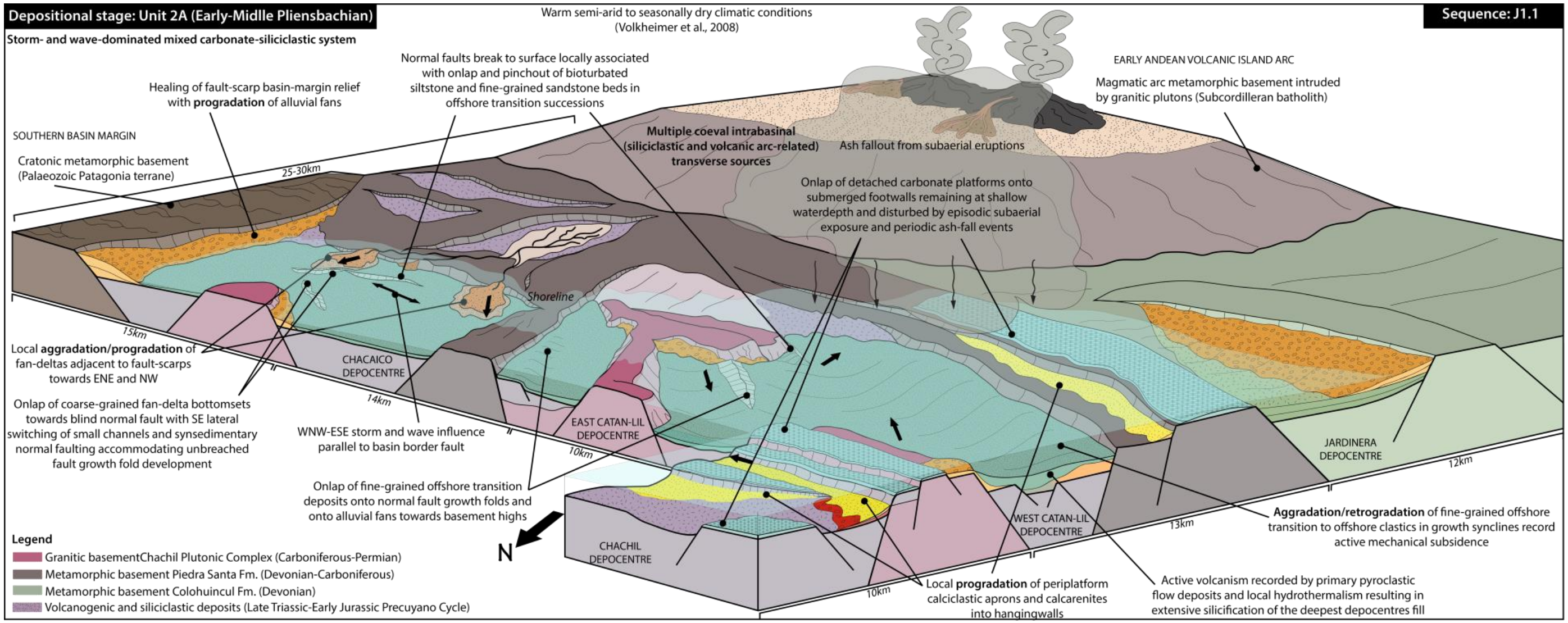

Figure 5.28: Palaeogeographic block diagram of the studied depocentres of the southwestern Neuquén Basin representing the Early-Middle Pliensbachian configuration during late syn-rift deposition of the Unit 2A with transgression and formation of fault-block ilsands.

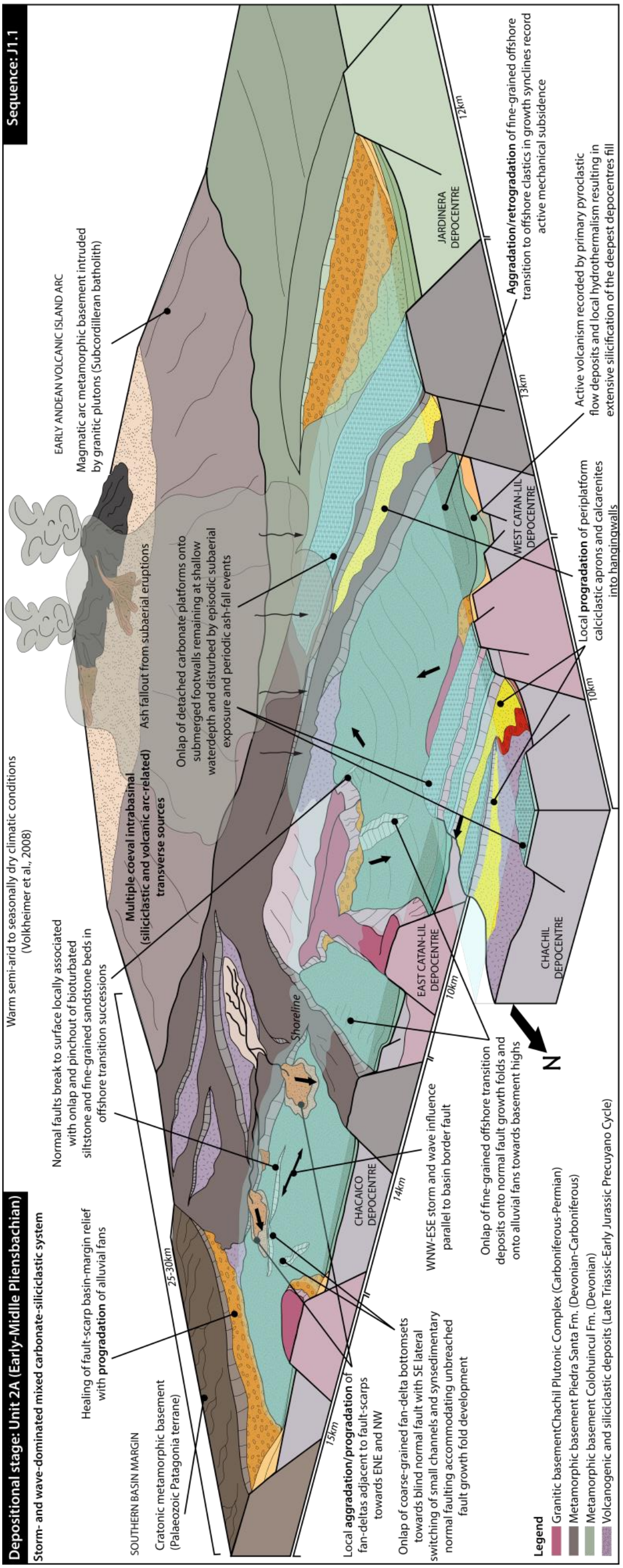

Figure 5.29: Palaeogeographic block diagram of the studied depocentres of the southwestern Neuquén Basin representing the Middle-Late Pliensbachian configuration during late syn-rift deposition of the Unit 2B with generalized flooding of fault-block islands.

5.8.2.2. Early post-rift sedimentation (Early Toarcian-Aalenian)

Onset of the early post-rift is recorded with a major marine flooding event and establishment of basinal calcareous organic-rich mudstone deposits (Unit 3) draping across late syn-rift inherited rift topography of all the basins (Catán-Lil, Chacaico, Chachil, La Jardinera) (Fig. 5.30). Stratal geometries are mainly characterized by further onlap of late syn-rift deposits, and directly onto granitic basement and Precuyano Cycle syn-rift volcanic footwalls, with gentle wedging and dipping into the hangingwall and passive onlap fill pattern (Fig. 5.30). Given the lack of indicator of major normal faulting or tectonic activity in these mudstone deposits and their regional extent, early post-rift thermal subsidence associated with major marine flooding might explain this abrupt change of sedimentation pattern (Figs 5.25 and 5.26).

Dominant accumulation of calcareous organic-rich mudstone suggests that the late syn-rift shallow-marine systems were drowned and mud-draped and promoted the cut-off of intrabasinal and extrabasinal sources associated with the cratonic basin margin (Fig. 5.30). This enhanced the underfilled character of deep-marine distal depocentres such as the Catán-Lil and Chachil Basin, which were already dominated by fine-grained clastic or carbonate sedimentation during the late syn-rift (Figs 5.28 and 5.29). The starved evolution of the studied basins permitted to record the effects of differential compaction of buried volcano-sedimentary deposits across fault-block highs which enhanced the inherited rift topography during the early post-rift (e.g Cristallini et al., 2006) (cf.Chapter 4). A range of fluid flow features are also recorded in that unit, including methane seeps associated with stromatholithic bioherms in the Chacaico Basin (cf. Gómez-Pérez, 2003) (Fig. 5.30). The seepages might have formed with migration of deep-seated overpressured basinal fluids through rift faults, either from crustal magmatic sources and/or with a thermogenic-biogenic origin related to hydrocarbon expulsion during early burial (Gómez-Pérez, 2003).

The renewed late Early Toarcian extrabasinal sand supply from the Early Andean volcanic island arc basin margin permitted the development of two sand-rich intraslope fans (J1.2 and J2.1) (Unit 4), which developed as axial systems with sediment routeing by inherited rift topography (Figs 5.31, 5.32 and 5.33). This permitted the early post-rift evolution of underfilled rift depocentres into

sediment-balanced and overfilled depocentres like the Eastern Catán-Lil, Jardinera and Chachil Basin (Figs 5.25 and 5.26). In contrast, sand-starvation and mudstone deposition prevailed in the Chacaico and Western Catán-Lil Basin.The evolution of sedimentation in the Chacaico Basin also shows that basin margin-attached deltaic systems that established during the late syn-rift do not always sustain a stable connection with the hinterland and form sediment pathways into the early post-rift (Prosser, 1993; Alves et al., 2003; Seidler et al., 2004; McArthur et al., 2016).

The intraslope fan (J1.2) developed as part of a low-gradient ramp-type system flanking the low-relief Early Andean volcanic island arc (Fig. 5.31). The first precursor lobe complexes of this intraslope fan were trapped in depressions of mud-draped inherited topography in the Eastern Catán-Lil Basin, whereas other depocentres underwent sand-starvation. Substantial confinement resulted in thinning and pinchout at lobe complex margins, with common post-depositional remobilization and injection close to intrabasinal relief (Fig. 5.31). These relatively small lobe complexes form low net: gross successions of mainly matrix-rich sandstone, and record aggradation and retrogradation of the most distal part of a low-gradient ramp-type system (Fig. 5.31). The subsequent renewed progradation of that intraslope fan was recorded with deposition of lobe complexes that formed high to moderate net: gross successions of mainly matrix-poor sandstone, which represent the proximal part of the low-gradient ramp-type system (Fig. 5.32). These larger lobe complexes progressively levelled the remaining intrabasinal relief, with depocentre widening during infill. This phase is characterized by initial progradation and aggradation of lobe complexes with compensational stacking, until backstepping of the system and shut down of sand supply. Preferential stacking of lobe complexes occurred in accommodation inherited along an interbasinal horst between the Chacaico and Eastern Catán-Lil Basin, where the largest accommodation was available (Fig. 5.32). If intrabasinal topography was levelled in the Eastern Catán-Lil Basin and permitted compensational stacking of lobe complexes (J1.2), interbasinal horsts bounding the basin induced some confinement recorded by thinning with convergent onlap near the margins of lobe complexes (Fig. 5.22). These lobe complexes deposited in a weakly confined setting, with flows interacting with subtle seabed topography that resulted in the development of a range of combined flow bedforms. Depocentre confinement by the interbasinal horst between the Chachil and

Eastern Catán-Lil Basin resulted in overspilling of dilute flows and accumulation of lobe complexes fringes in the downdip outboard and formerly sand-starved Chachil Basin (Fig. 5.32). In parallel, the first sand-rich flows reaching the formerly starved La Jardinera Basin promoted the development of small precursor lobe complexes trapped in topographic lows with substantial confinement. This also resulted in thinning and pinchout at lobe complex margins, with common post-depositional remobilization and injection close to intrabasinal relief (Fig. 5.32).

The intraslope fan (J2.1) developed as part of a higher-gradient ramp-type system flanking a steeper flexural arc margin (Fig. 5.33). The intraslope fans prograded across healed topography of the Eastern Catán-Lil Basin and La Jardinera Basin with deposition of lobe complexes that formed low to moderate net: gross successions of matrix-rich sandstone (Fig. 5.33). Preferential stacking of lobe complexes occurred with aggradation and lateral compensation of the previous intraslope fan in the Eastern Catán-Lil Basin. The system prograded towards the most distal Chachil Basin with bypass and erosion across the Chachil interbasinal horst, as relief was levelled (Fig. 5.33). If intrabasinal topography was smoothed by deposition of the former intraslope fan (J1.2) in the Eastern Catán-Lil Basin, enabling weak confinement and thinning with subtle onlap of lobe complex margins, this was not the case in the Chachil Basin. Compaction-enhanced relief was long-lived in sand-starved distal depocentres such as the Chachil Basin, and influenced the development of intraslope fans with partial confinement by intrabasinal relief. This resulted in thinning with erosive pinchout at lobe complex margins, with widespread development of HEBs and debrites that form significant bed-scale heterogeneity, associated with a range of combined flow bedforms and scouring along lateral depocentre margins. These configurations are also marked by the development of large plurikilometric clastic sills close to intrabasinal relief (cf. Chapter 4) (Fig. 5.33).

The thickest Early Toarcian-Early Aalenian accumulation of early post-rift intraslope fan deposits (J1.2-J2.1, Unit 4) occurred across a major granitic basement accommodation zone in the Eastern Catán-Lil Basin (up to 735 m thick) and metamorphic basement accommodation zone in the La Jardinera Basin (up to 650 m thick, Paim et al., 2008) (Figs 5.25 and 5.26). The thickness pattern of intraslope fans across these basins shows that the proximal depocentres, with

respect to the presumed extrabasinal volcanic arc-related source, were infilled first, enabling progressive depocentre widening with leveling of intrabasinal topography (Figs 5.31 and 5.32). Once the relief was healed, the intraslope fan could shift from proximal to more distal depocentres with sediment bypass and erosion across subtle remnant interbasinal relief that recorded the influence of compaction-enhanced topography in the formerly sand-starved distal depocentres such as in the Chachil Basin (Fig. 5.33). Consequently, a more reduced total sandstone thickness accumulated in the Chachil Basin (up to 330 m thick). This highlights the role of inherited rift topography, from interbasinal pre-rift basement highs such as the Chachil and Rincón del Polo horst borders or from compaction-enhanced intrabasinal syn-rift fault-block highs such as in the Chachil Basin (Figs 5.31, 5.32 and 5.33). The variety of early post-rift lobe complexes developed successively in each basin was mainly dependent upon the degree of confinement induced by inherited topography. The differential and diachronous sand supply in those basins led to a time transgressive healing of topography and therefore contemporaneous accumulation of lobe complexes with different characteristics (terminations, facies segregation, stacking patterns). Inherited slope topography might also have impacted flow routing pathways from source to sink as seen in other complex early post-rift rift basins (Modica and Brush, 2004; López-Gamundí and Barragan, 2012; Lohr and Underhill, 2015).

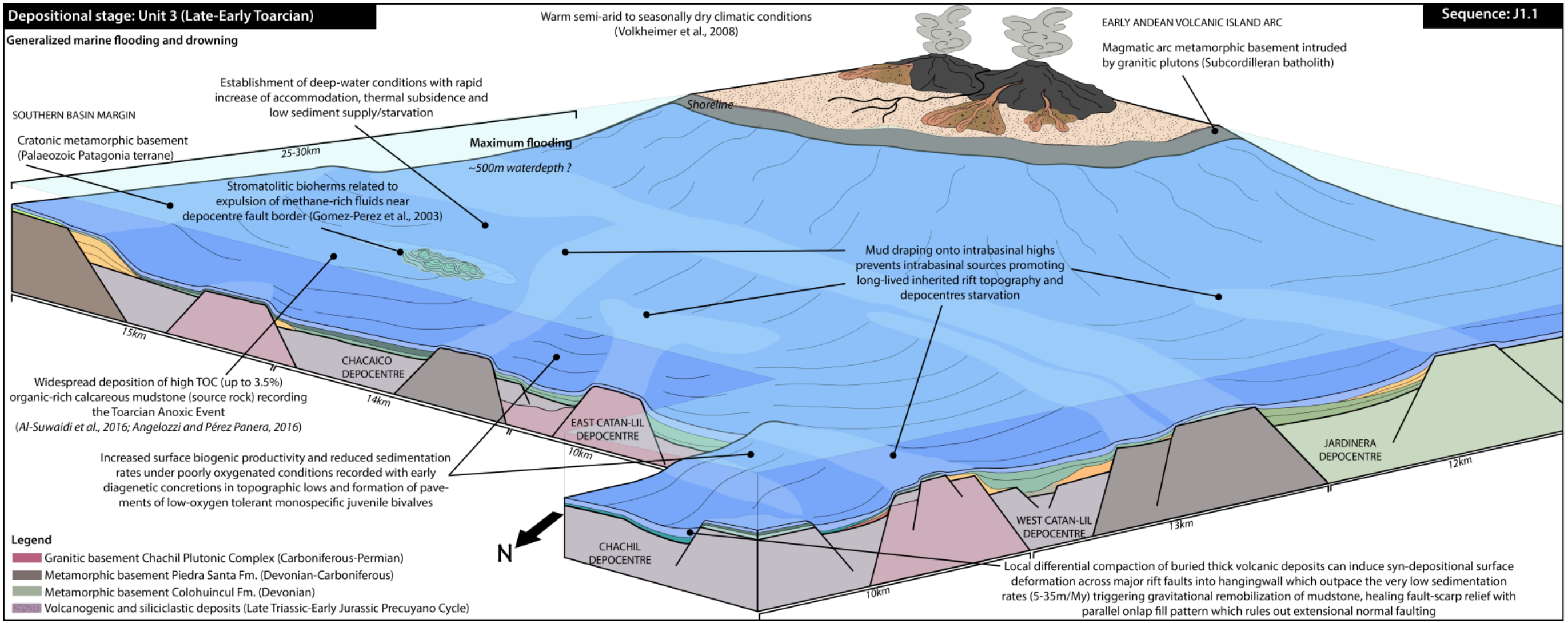

Figure 5.30: Palaeogeographic block diagram of the studied depocentres of the southwestern Neuquén Basin representing the Late-Early Toarcian configuration during onset of the early post-rift associated with maximum marine flooding at regional-scale and deposition of the Unit 3.

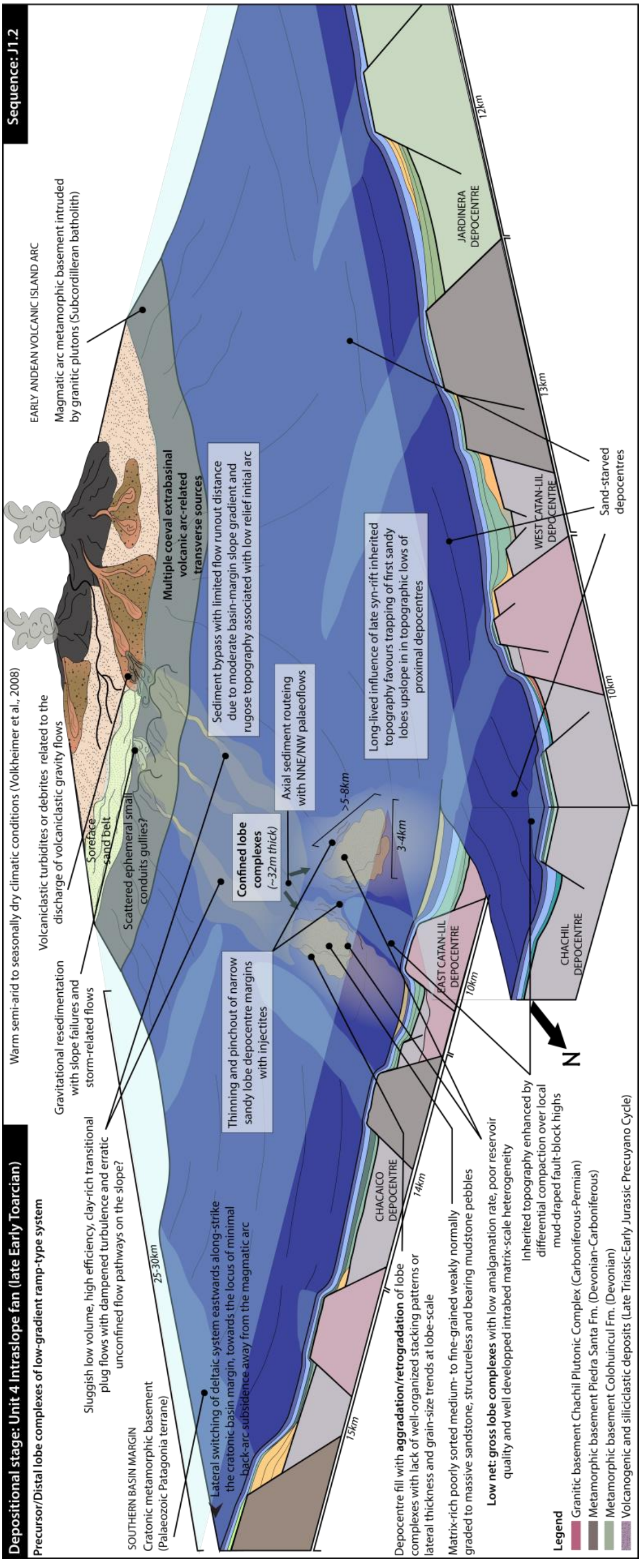

Figure 5.31: Palaeogeographic block diagram of the studied depocentres of the southwestern Neuquén Basin representing the late Early Toarcian configuration during the early post-rift deposition of the low-gradient distal ramp lobe complexes recording initiation of the J1.2 intraslope fan of Unit 4.

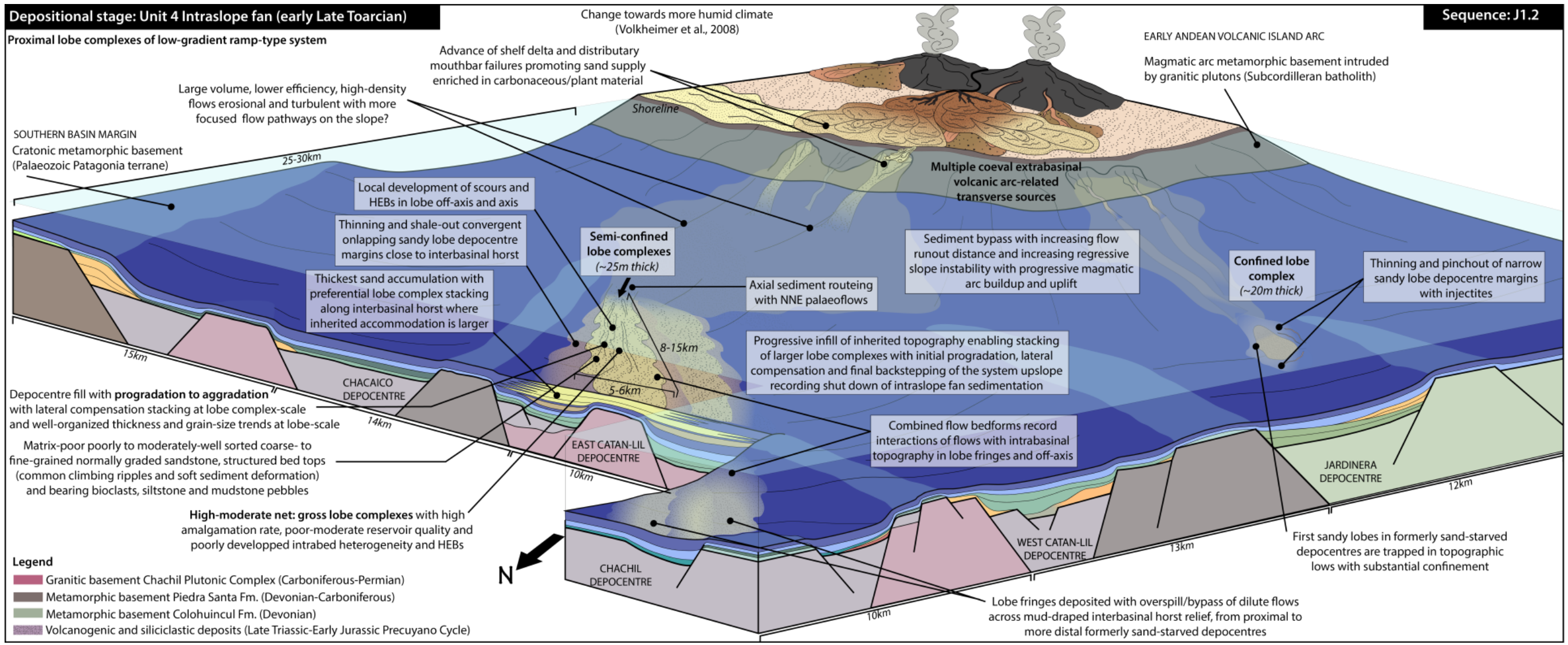

Figure 5.32: Palaeogeographic block diagram of the studied depocentres of the southwestern Neuquén Basin representing the early Late Toarcian configuration during the early post-rift deposition of the low-gradient proximal ramp lobe complexes recording basinwards progradation of the J1.2 intraslope fan of Unit 4.

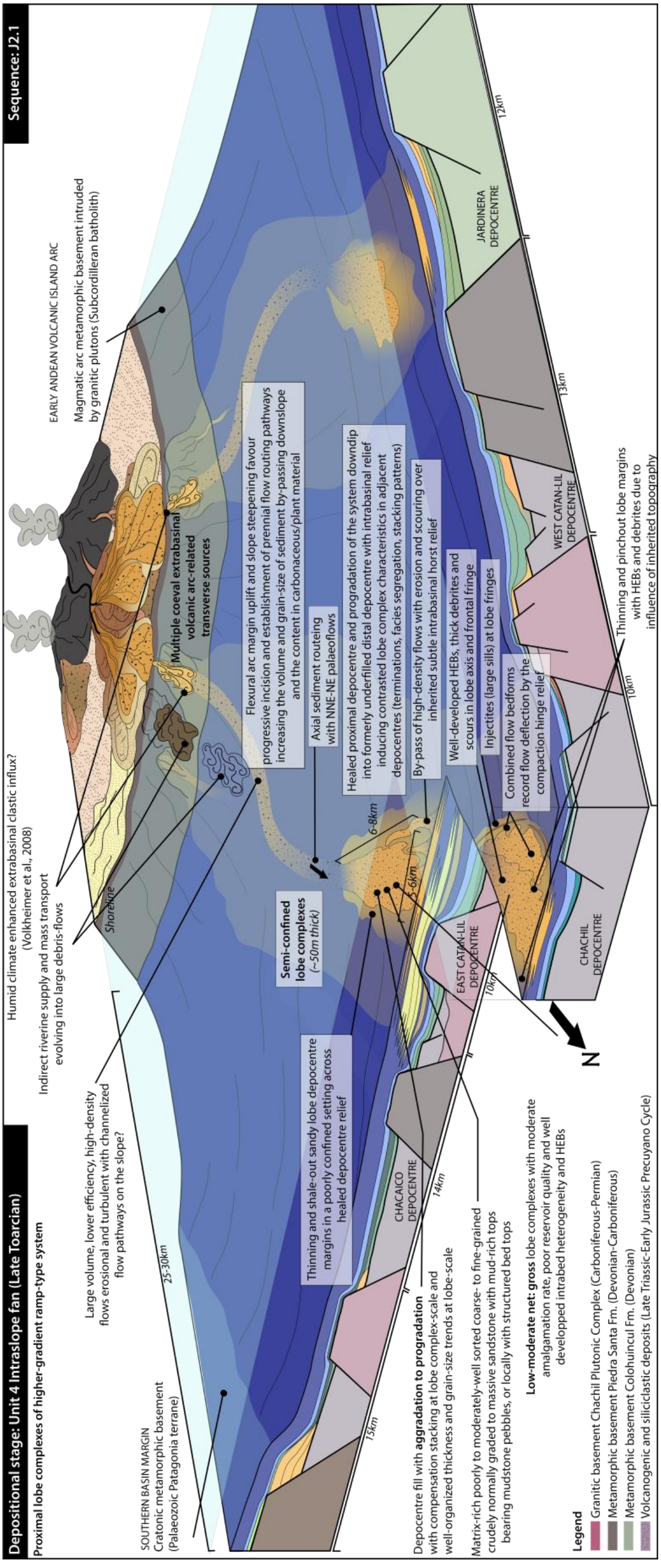

Figure 5.33: Palaeogeographic block diagram of the studied depocentres of the southwestern Neuquén Basin representing the Late Toarcian configuration during the early post-rift deposition of the higher-gradient proximal ramp lobe complexes recording basinwards progradation of the J2.1 intraslope fan of Unit 4

5.8.3. Effects of inherited rift topography during the syn- to post-rift transition

The syn-to post-rift stratigraphic architecture and evolution of marine basin-fill patterns (discussed in the previous section) can be contrasted between adjacent basins (Figs 5.25 and 5.26). The Chacaico Basin-fill records the development of a balanced syn-rift continental volcanic to overfilled late syn-rift marine depocentre and evolution into an underfilled-starved early post-rift depocentre. The Western Catán-Lil basin-fill records development of a balanced to overfilled continental syn-rift volcanic to balanced late syn-rift marine depocentre and early post-rift sand-rich depocentre. The Eastern Catán-Lil basin-fill records development of an underfilled continental syn-rift volcanic to balanced late syn-rift marine depocentre, which evolves into an overfilled early post-rift sand-rich depocentre localized across a former accommodation zone between two basins. The Chachil basin-fill records the development of an overfilled syn-rift continental volcanic and underfilled late syn-rift marine depocentre and evolution into a balanced early post-rift depocentre. The La Jardinera basin-fill records the development of an underfilled continental syn-rift volcanic and late syn-rift marine depocentre and evolution into an overfilled early post-rift depocentre. Therefore, the stratigraphic architecture of late syn-rift systems was clearly impacted by the inherited accommodation space and major basement footwall highs which acted as long-lived topographic barriers between basins. During the early post-rift, inherited rift topography was totally flooded, healed by mudstone and locally enhanced by compaction-related deformation. Intraslope relief exerted a continuous influence on the development of early post-rift sand-rich systems, until the spatial linkage of these systems across individual basins (Figs 5.25 and 5.26).

The differences of inherited basin accommodation and physiography, which conditioned the development of late syn-rift and early post-rift systems, were linked to variations in magma supply across volcanic syn-rift depocentres (e.g Muravchik et al., 2011; D'Elia et al., 2018). In addition, the syn-rift sedimentation and thickness pattern across basins of the study area were directly related with the orientation of their border faults with respect to the main extensional NE-SW stress field. Basins bounded by NNW-SSE striking faults formed the deepest basins, whether they remained underfilled (La Jardinera

Basin) or were balanced to overfilled (Catán-Lil and Chachil Basin) (Figs 5.25 and 5.26). In contrast, basins bounded by WNW-SSE and E-W striking faults, which developed with reactivation of inherited E-W pre-rift structures oblique to the main extensional stress field, formed the shallowest basins (Chacaico Basin). Therefore the configuration and basin-fill patterns of rift basins and their spatial distribution was intimately related to local perturbation of the extensional stress field by pre-rift structures. The pre-rift structural template also dictated the organization of the main interbasin highs across the rift system, which acted as topographic barriers and had a long-lived influence on sedimentation and thickness distribution through rift evolution and controlled early post-rift intraslope fan development (Chachil horst border, Puesto Rincón del Polo-Piedra Santa, Rahue blocks) (Figs 5.25 and 5.26).

The early post-rift depocentres can develop with a change of polarity (thickening towards the NE-NNE) compared to the syn-rift depocentres (thickening towards the S-SW) in the La Jardinera and Western Catán-Lil Basin, or can develop across former basement-cored accommodation zone as seen in the Eastern Catán-Lil Basin. At a broader scale, the distribution of early post-rift intraslope fans show the basins that formed basement accommodation zones during the syn-rift, therefore lacking significant accumulations of volcanic syn-rift deposits, formed ideal traps for subsequent early post-rift sandy depocentres (Figs 5.25 and 5.26). This is recorded by the early post-rift sand-starvation of the Chacaico Basin and Western Catán-Lil Basin, which accumulated the thickest volcanic syn-rift and late syn-rift deposits in their southwestern part. In contrast, the development of the thickest early post-rift intraslope fan successions occurred in the basins with reduced thickness of late syn-rift deposits including the Eastern Catán-Lil, La Jardinera and Chachil Basin (Fig. 5.26). Therefore, besides contrasting basin-fill and thickness patterns across basins, the syn-to post-rift transition is also associated with the migration and spatial offset of syn-rift versus early post-rift depocentres (Fig. 5.26).

The stacking between syn-rift and post-rift depocentres observed at a regional-scale, with early post-rift sagging away from syn-rift depocentre axis, does not fit the uniform pure shear lithospheric stretching model (cf. McKenzie, 1978). Instead, this reflects asymmetric thermal subsidence with respect to the locus of extension that has implications for the prediction of the distribution of early post-rift sandy depocentres in a back-arc setting.

5.8.4. Early post-rift depositional system

The early post-rift development of intraslope fans at a regional-scale in the study area occurred with coeval growth of the Early Andean volcanic island arc system that formed the southeastern basin margin (Figs 5.31, 5.32, 5.33). This might have promoted the development of a proto-shelf lacking a shelf-break and low-gradient slope dissected by gullies enabling sediment bypass, as delta-fed submarine ramp fan systems (Heller and Dickinson, 1985; Postma, 1990). Ramp-type margins commonly bound moderately deep intracratonic basins, with a moderate slope gradient between the shelf edge and the proximal ramp bypass of sediment supplied from line- or multiple point-sources (Heller and Dickinson, 1985; Postma, 1990; Surlyk and Noe-Nygaard, 2001; Eschard et al., 2004) (Figs 5.31, 5.32, 5.33). This contrast with sedimentary shelves that have higher shelf-to-basin relief with steep slope and well-defined shelf-break commonly associated with point-source sediment supply through major feeder channels and development of basin-floor fans (Reading and Richards, 1994). Equally, this contrasts with rift basins having a high-relief structural shelf promoting direct sediment bypass towards the basin-floor (Bell et al., 2008; Strachan et al., 2013).

Sand supply and accumulation across the proximal ramp is dependent upon delta-front progradation and shelf width, which determines the timing for deltas to reach the margin and therefore for sediment supply or trapping across the shelf. In rift basins, sediment supply tend to be naturally enhanced by the limited capacity for sediment storage across narrow structural shelves and the high sediment yield expected from small catchment basins flanked by high-relief hinterlands (Blum and Hattier-Womack, 2009; Strachan et al., 2013). Therefore, thickening and coarsening stratigraphic evolution from the intraslope fans J1.2 to J2.1 could reflect an evolution from ramp-type to shelf-break type margin, as seen in the East Greenland rift systems (Surlyk and Noe-Nygaard, 2001). However, this scenario is unlikely during the Early Jurassic, given that the formation of a well-defined shelf-break in the southern Neuquén Basin occurs during the Middle Jurassic and along the cratonic southern basin margin. Shelf-break formation is recognized from subsurface data along the Huincul High showing the Aalenian-Bathonian progradation of shelf edge deltas with development slope channels and canyons and basin-floor fans, as a consequence of a relative sea-level fall (Gómez Omil et al., 2002; Brinkworth et al., 2018; Loss et al., 2018).

During the Early Jurassic, little to no sand reached the basin-floor as the shelf, slope and basin-floor segments were not connected, and therefore no Early Jurassic basin-floor fans could develop. This is well-recorded along the cratonic southern basin margin to the west of the Huincul high (Figs 5.1 and 5.2). Here, drowning of the deltaic system and lateral switching of the system eastwards along-strike on the cratonic southern basin margin induced sand starvation of the Chacaico Basin from the late Early Toarcian (Fig. 5.31, 5.32, 5.33). This Late Pliensbachian deltaic system was superseded by Early-Late Toarcian development of fan deltas nucleated onto a narrow structural shelf that fed multiple point-sourced intraslope fans trapped across a topographically complex slope, updip of the starved basin-floor (Gómez Omil et al., 2002; Pángaro et al., 2009). Therefore the stratigraphic evolution recorded by intraslope fans of the Los Molles Fm. in the study area are more likely to reflect the “distal” signature of aggradation and progradation of deltaic systems developed along the Early Andean volcanic island arc basin margin (Figs 5.31, 5.32, 5.33). This evolution could also involve a maturation of routeing pathways across the slope which could be related with the change in lobe dimensions, sand: mud ratio, stacking patterns, facies distribution and development of bed-scale heterogeneity between the precursor distal ramp and proximal ramp lobe complexes (Figs 5.31, 5.32, 5.33) (cf. Chapter 6).

5.8.5. Early post-rift sediment supply

The preservation of inherited rift topography and the subsidence rate during the syn- to post-rift transition mainly condition the potential for prevailing intrabasinal or extrabasinal source contribution and dominant development of transverse versus axial transport systems (Figs 5.27-5.33). In turn, sediment yield of intrabasinal sources with local fault-block degradation and/or extrabasinal supply from hinterland drainage systems determines the rate of healing inherited rift topography and early or late post-rift timing for the formation of sand-rich depocentres. Rapid bathymetric deepening (minimum 200-400 m water depth, cf. Gómez Omil et al., 2002; Gómez-Pérez et al., 2003) at the onset of the early post-rift promoted the drowning and mud draping of inherited rift topography (Fig. 5.30). Rift basins undergoing high subsidence rate and early post-rift mud draping of the inherited rift topography acted to prevent fault-block high degradation and

intrabasinal sediment supply (Lien, 2005; Soares et al., 2012) which could otherwise heal the inherited relief (Zachariah et al., 2009; Jarsve et al., 2014). In these conditions, sediment supply rate and accumulation of early post-rift fans in a given basin depends upon their distance from hinterland sources (proximal versus distal) (Figs 5.31, 5.32, 5.33). Therefore early post-rift sediment supply can require far-field tectonic plates which can induce uplift and source rejuvenation (Takano, 2002; Marin et al., 2017) and/or favourable eustatic sea-level variation and/or productive hinterland climate (Alves et al., 2003; Yu et al., 2013; Balázs et al., 2017).

In the study area, the onset of early post-rift sediment supply is associated with deposition of a 400 m thick regressive sandy succession of slope rise and slope deposits making the bulk of the 2nd order sequence J2 is inferred to be driven by a major eustatic sea-level fall (Paim et al., 2008). Therefore the U-Pb ages obtained with the present work have shown that the sand supply is younger (late Early Toarcian) than previously supposed (Fig. 5.25) and eustatic control cannot be invoked to explain the cause of Early Jurassic sand supply.

In the southern Neuquén Basin, the effects of transpressional fault reactivation are commonly invoked to explain the Middle to Late Jurassic sand supply with uplift and erosion along the Huincul High (Pángaro et al., 2009; Naipauer et al., 2012; Pujols et al., 2018). Again, in the study area sand supply started prior to the inversion premises and if sediment supply would have been sourced from the Huincul High area or the NE Patagonian Massif, one might expect sediment supply coming from the southeast of the basin. This would be consistent with a WNW-NW or NNW progradation of in Early Jurassic sand-rich systems of the Los Molles Fm., as documented in the subsurface along the Huincul High (Gómez Omil et al., 2002; Brinkworth et al., 2018). However, the NNE/NE palaeocurrent directions of sandy systems developed in the Catán-Lil and Chachil Basin (Fig. 5.4) and NE-ENE palaeocurrent in the La Jardinera Basin (cf. Burgess et al., 2000; Paim et al., 2011) indicate that sediment supply instead should come from a source located to the southwest, where the Early Andean volcanic arc developed (Figs 5.31, 5.32, 5.33).

Early Jurassic volcanogenic sediment production promoted rapid sediment supply towards the NE (De la Cruz and Suárez, 1997) which could have controlled the late Early Toarcian development of early post-rift sand-rich systems of the Catán-Lil, Chachil Basin and La Jardinera in a transitional intra-arc to back-

arc setting (Bermudez et al., 2002; Llambías et al., 2007). Sediment were likely sourced from Early Jurassic littoral calderas, subaqueous (50-100 m water depth) andesitic volcanoes, volcaniclastic aprons and deltaic systems that developed along the submerged Early Andean volcanic arc at ~30-50 km from the study area (De la Cruz and Suárez, 1997) (Figs 5.31, 5.32, 5.33). Volcanism, together with the warm humid climate since the early Late Toarcian (cf. Volkheimer et al., 2008), might have provided suitable conditions to accumulate critical amounts of (volcanic-epiclastic) sands at the shelf edge bounding the volcanic arc. Volcanic arcs form topographically dynamic regions where magmatically-driven surface uplift and high sediment accumulation rates might have promoted gravitational instabilities. Gravitational resedimentation across the slope might have resulted from autogenic volcanic-driven eruptions, hydrothermalism, subduction-induced earthquakes and surface uplift, and allogenic factors related to and storm waves and/or enhanced climatic erosion and relative sea-level changes (De la Cruz and Suárez, 1997; Manville et al., 2009; Shumaker et al., 2018; Clare et al., 2018).

Given the NNE-NE progradation of early post-rift sandy systems of the Los Molles Fm., with Early Jurassic sediment supply derived from the westerly-located Early Andean volcanic arc, and the conspicuous lack of shelf-break until the Middle Jurassic, it seems counter-intuitive to interpret them as basin-floor deposits genetically related to a NNW-NW prograding shelf-break system that developed along the Huincul High (cf. Vann, 2013; Tudor, 2014). Therefore, the highlighted characteristics, stratigraphic architecture and age of Early Jurassic intraslope fans of the Los Molles Fm. outcropping in the study area, including the Catán-Lil and Chachil but also La Jardinera Basin (cf. Paim et al., 2011), warns against the extrapolation of these facies models for subsurface reservoir assessment of Middle Jurassic basin-floor fans (e.g Loss et al., 2018).

5.9. Conclusion

This study demonstrates the variability of the syn-to post-rift signature recorded by the stratigraphic architecture and evolution of marine basin-fill patterns at a regional-scale in the southwestern Neuquén Basin, This is well-recorded by the contrasted tectono-stratigraphic development of two exhumed adjacent marine rift basins (Chacaico and Eastern Catán-Lil) which has been constrained with new U-Pb SHRIMP zircon ages in the Los Molles Formation. The late syn-rift is recorded by the development of a transgressive sequence culminating with major marine flooding, which shows a complex distribution of depositional environments and contrasted retrogradational or aggradational to progradational sedimentation patterns, with changes in stratigraphic architecture across rift basins. The early post-rift is mainly recorded by a regressive sequence, with progradation of ramp-type sandy system since the late Early Toarcian. This lead to diachronous development of intraslope fans that consist into series of lobe complexes progressively healing the inherited topography from proximal to distal basins.

The syn-to post-rift transition was associated with a change in shelf-slope physiography and source, with transition from intrabasinal and extrabasinal, to exclusively extrabasinal sediment supply, and a change in the mode of sediment dispersal from dominantly transverse to axial transport systems. The local intrabasinal and extrabasinal sources that fed transverse systems during the late syn-rift were deactivated due to mud-draping associated with major marine flooding during onset of the early post-rift. During the early post-rift, renewed extrabasinal sediment supply is interpreted as a distal signal of volcanogenic sediment production, and reworking and supply from deltaic systems developed along the narrow shelf that flanked the back-arc side of the Early Andean magmatic arc.

At regional-scale, differences of tectono-stratigraphy and basin-fill patterns result from the effects of inherited rift topography and accommodation space on the successive development of syn-rift, late syn-rift and early post-rift depocentres. This is well-recorded by the compensational thickness pattern (i.e. the thickest early post-rift depocentres stack above the thinnest syn-rift depocentres) and an individual change of polarity (i.e. spatial shift of the late syn-rift versus early post-rift depocentre axis) of late syn-rift and early post-rift

depocentres in the Eastern and Western Catán-Lil, Chacaico, Chachil and La Jardinera basins, Pre-rift inherited structures also exerted a long-lived influence on sedimentation that controlled the distribution, geometry, and evolution of late syn-rift and early post-rift depocentres. Finally, local relief inherited from rift topography and/or locally enhanced by compaction-related deformation, played a key role in the distribution and types of early post-rift lobe complexes, which developed through levelling of topography and timing of linkage of intraslope fan sandy depocentres across basins. Lobe complexes can show variable characteristics (dimensions, termination style, stacking patterns, facies) across depocentres, depending on the topographic confinement and interactions of flows with intra- and interbasinal reliefs at time of deposition.

This study highlights the effects of rapid physiographic modification of rift topography through rift evolution, of pre-rift inheritance and volcanism on the stratigraphic architecture of the syn- to post-rift transition, from individual basin-fill patterns to depocentre migration at regional-scale. Outcomes on early post-rift lobe complexes which developed through levelling of topography can be used to predict the distribution pattern and characteristics of seismic-scale analog intraslope systems developed with variable topographic confinement.

Chapter 6 Textural and compositional analysis of sandstone in the Early Jurassic Los Molles Formation

6.1. Introduction

Compositional and textural maturity of sediments is a function of the type of source material, residence time and weathering in the drainage basin, and the system efficiency for physical sorting and partitioning of grains from source to sink, according to autogenic (e.g., provenance mixing, sedimentary and hydraulic processes) and allogenic controls (e.g., tectonism, eustasy, volcanism). Sandstone composition and textural characteristics can be a useful tool to identify changes in provenance and palaeogeographic setting. In a rift setting, small catchment basins (<100 km long) are flanked by mountainous hinterlands associated with high sediment yield and low storage potential (e.g Millimann and Syvitski 1992; Castelltort et al., 2004; Blum and Hattier-Womack, 2009) that promote extrabasinal sediment supply and inherited relief can form intrabasinal sediment sources. In rift basins, the distance from source areas and slope physiography control sediment supply or starvation, and routing or storage of sediment in time and space, which can be more challenging to predict when associated with active volcanism (Marsaglia et al., 2016; Shumaker et al., 2018).

The Neuquén Basin is bounded to the west by a volcanic arc and to the south and east by cratonic blocks. This makes it an ideal place to document detrital mineralogy and textural characteristics in relation to stratigraphic units (e.g Garzanti, 1991; Ingersoll and Cavazza, 1991; Armorosi and Zuffa, 2011; Ciccioli et al., 2014; Tentori et al., 2016) and to investigate changes in the provenance of late syn-rift and early post-rift sandstone. In this context, understanding sediment source areas, dispersal patterns and depositional processes which determine sediment composition and textural and mineralogical maturity, is important to predict temporal and spatial changes in the quality of reservoir sandstones. Additionally, characteristics of early post-rift lobe complexes are poorly known, mainly due to the paucity of exhumed examples and resolution limitations of subsurface examples (Argent, 2000; Fugelli and Olsen, 2007; Southern et al., 2017; Dodd et al., 2019). Therefore, two intraslope fans of the Los Molles Fm.

are investigated to document differences in petrofacies in relation with stratigraphic architecture and characteristics of lobe complexes (dimensions, termination style, stacking patterns, facies, combined flow bedforms and bed-scale heterogeneity).

6.2. Geological setting

Intracontinental volcanic rifting of the Neuquén Basin occurred from Late Triassic to Early Jurassic, after a period of post-orogenic extension-transtension along the southwestern Gondwana margin, which formed syn-rift grabens and half-grabens filled with continental and lacustrine volcano-sedimentary successions (Vergani et al., 1995; Legarreta and Uliana, 1996; Franzese and Spalletti, 2001; Howell et al., 2005). The first marine incursion from the proto-Pacific Ocean occurred since the Pliensbachian, with coeval growth of the Early Andean magmatic arc along the western margin of Gondwana (Riccardi, 1991; Viciente, 2005; Damborenea et al., 2013). This transgression was recorded with development of Early Jurassic and late syn-rift, carbonate and siliciclastic deltaic or fan-deltaic shallow-marine sedimentation in the southern Neuquén Basin (Gulisano and Gutiérrez Pleimling, 1995; De la Cruz and Suárez, 1997; Gómez Omil et al., 2002; Leanza et al., 2013; D'Elia et al., 2015).

Marine flooding and bathymetric deepening with onset of thermal subsidence since the Early-Late Toarcian, promoted the linkage of isolated late syn-rift depocentres across inherited rift topography. This lead to the establishment of early post-rift deep-marine siliciclastic sedimentation along the southern margin of the Neuquén Basin, mainly represented by intraslope fans developed in an intra-arc to back-arc setting, with influence of inherited and/or compaction-enhanced intrabasinal topography. The investigated exhumed Early Jurassic marine depocentres (Chacaico, Eastern Catán-Lil and Chachil) in the southwestern part of the Neuquén Basin (Fig. 6.1) recorded the transition from shallow-marine late syn-rift deposits of the Chacaico and Chachil formations, to deep-marine early post-rift deposits of the Los Molles Formation (Fig. 6.2). The well-constrained Early Jurassic stratigraphic framework with ammonite and bivalve biostratigraphy, and U-Pb volcanic zircon ages (cf. Chapter 5), enables the petro-stratigraphic evolution of the compositional and textural characteristics

of sandstone of the Chacaico and Los Molles Fm. This permits to refine sediment provenance, sediment pathways and palaeogeographic setting and insights into the stratigraphic architecture and different characteristics of early post-rift intraslope fans hosted in the Los Molles Formation across several rift basins (Fig. 6.2).

The Early Jurassic transgression created a large marine embayment within the Neuquén Basin. The basin was bounded by a SSW-NNE oriented palaeocoastline formed by the Early Andean island arc system (De la Cruz and Suárez, 1997), a SW-NE oriented palaeocoastline along the Huincul High, an inherited structure from a suture zone between accreted Palaeozoic terranes (Silvestro and Zubiri, 2008) which bounded the North Patagonian Massif (Fig. 6.1). Therefore, both the North Patagonian Massif, a late Palaeozoic metamorphic highland, and the western Coastal Cordillera and Subcordilleran batholith, which corresponds to the metamorphic basement and intrusive plutons of the Early Andean magmatic arc, formed the main crystalline basement sources in the southern Neuquén Basin (Rosenfeld and Eppinger, 1993; Burgess et al., 2000). Other sources in this region include uplifted basement blocks of Permian igneous rocks (Choiyoi Cycle), syn-rift volcanic deposits of the Precuyano Cycle exhumed ~100 km south of the study area (Sanico formation including basaltic, andesitic, rhyolitic volcanic rocks), and Early Jurassic (177 and 189 Ma) silicic igneous rocks from the Chon Aike Province developed with intraplate extensional magmatism in the extra-Andean Patagonia (Naipauer et al., 2018).

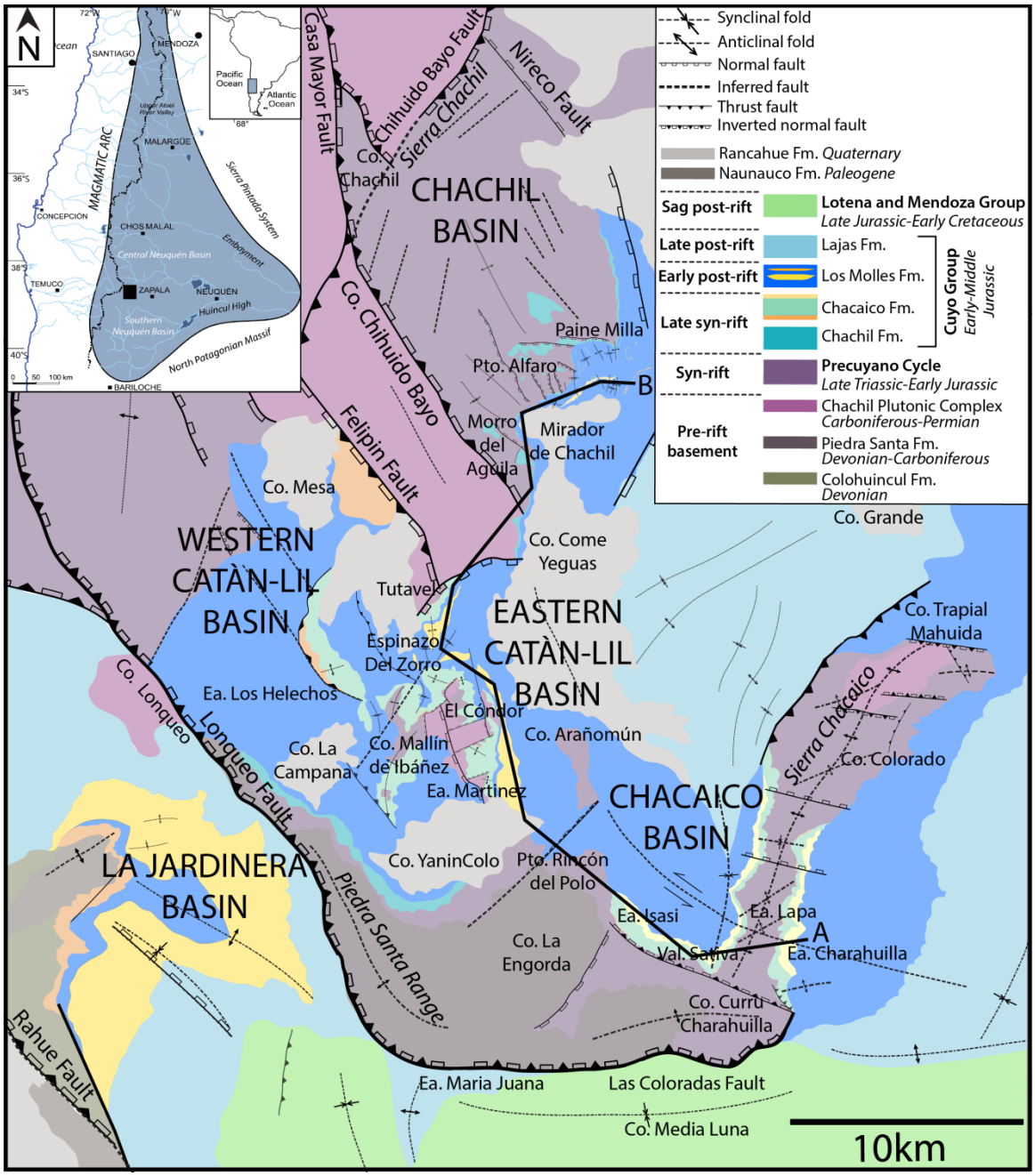

Figure 6.1: Map of the Neuquén Basin showing the location of the study area (A) and the regional geological setting with location of the correlation panel across the Chacaico, Eastern Catán-Lil and Chachil basins (dark line AB).

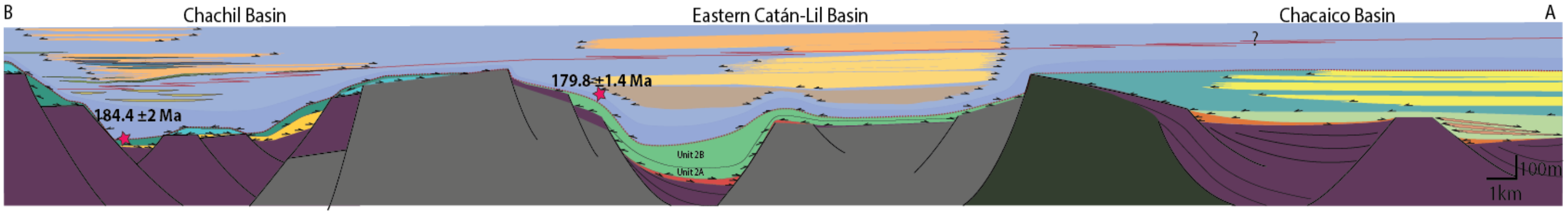

Lower Cuyo group

Early Jurassic early post-rift

Unit 4 — J2.1 Intraslope fan
Unit 4 — J1.2 Intraslope fan
Unit 4 — Sand-starved slope
Unit 3 — Siliciclastic-starved basin
J1-J2 sequence boundary
Syn- to post-rift transition
U-Pb age

Early Jurassic late syn-rift

Unit 2B — Prodelta and delta-front
Offshore to Shoreface-offshore transition
Distal carbonate periplatform
Unit 2A — Shoreface-offshore transition to Lower shoreface with fan delta
Offshore to Shoreface-offshore transition
Unit 2A — Proximal periplatform
Inner carbonate platform
Unit 1 — Alluvial fan
Submarine slope apron

Precuyano Cycle

Late Triassic-Early Jurassic syn-rift

Volcanogenic and siliciclastic deposits

Basement

Carboniferous-Permian pre-rift

Granitic rocks (Chachil Plutonic Complex)

Siluro-Devonian-Carboniferous pre-rift

Metamorphic rocks (Piedra Santa Fm.

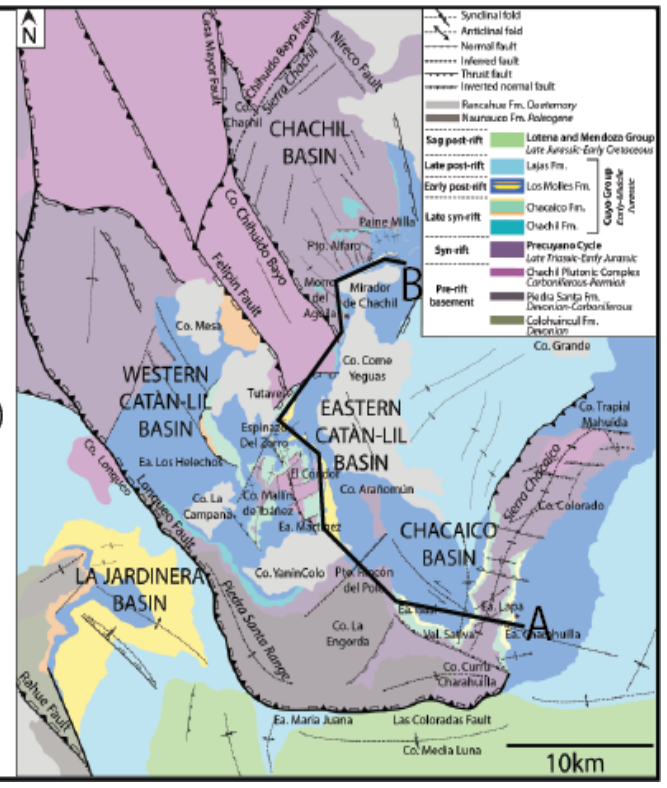

Figure 6.2: Cross section showing the stratigraphic architecture across the three studied depocentres (see Chatper 4 and 5 for descritpions of units) which is detailed in fig. 6.3.

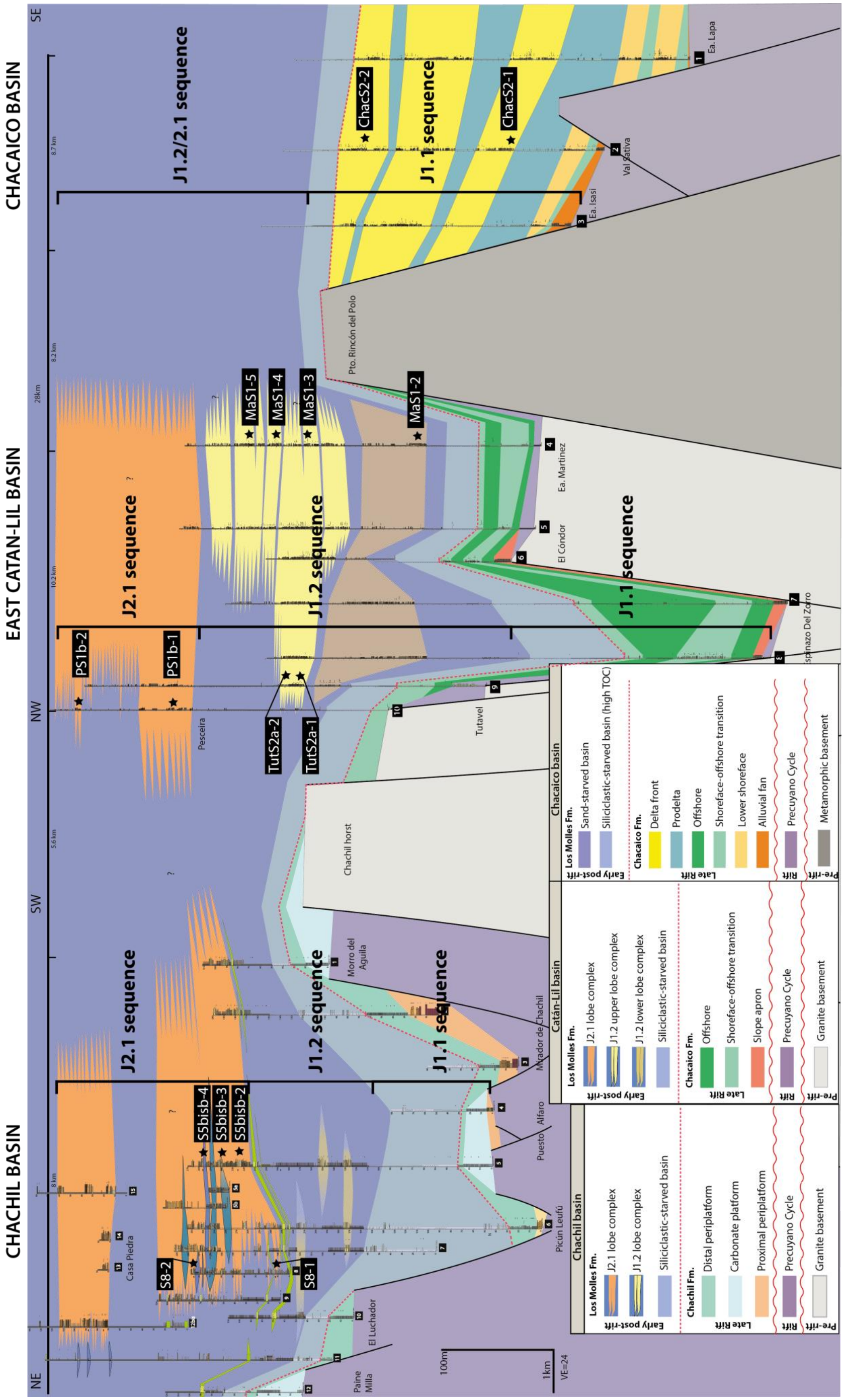

Figure 6.3: Correlation panel showing the stratigraphic framework across the three studied basins and the location of the sandstone sampled in lobe complexes which belong to J1.1, J1.2 and J2.1 sequences See detailed location of logs in Chapter 4 and 5..

6.3. Methods

This study uses 15 petrographic thin sections extracted from 15 different hand samples which location and names are indicated in vertical sections (Fig. 6.3 and Table 6.1) that were collected in three distinct stratigraphic units (J1.1, J1.2 and J2.1). The stratigraphic evolution of stratigraphic units is constrained by a correlation panel including 3 vertical sections in the Chacaico Basin, 7 vertical sections in the Eastern Catán-Lil Basin and 17 vertical sections in the Chachil Basin, forming a 40 km long panel (Fig. 6.3) (cf. Chapter 4 and 5). Facies analysis was conducted based on qualitative field observations (grain and clast composition, grain size and roundness, the ratio of grains to matrix, grading and sorting of deposits) and distribution of facies associations and stratigraphic architecture were defined for each stratigraphic unit. Thin sections are used to define the compositional and textural characteristics of sandstones, analyse petrofacies and interpret provenance.

The thin section slices were cut vertically from base to top of the given samples and analysed at the Centre of Geological Investigations Laboratory (CIG) of the National University of La Plata, Argentina and at the University of Leeds, UK. Serial acquisition of digital images were taken at high magnification (4x) in plane (PPL) and cross polarized (XPL) transmitted light using a digital-camera equipped microscope and processed with the Leica software. Digital images (0.5-0.8 cm large and 2-3 cm long) were acquired with high magnification given the distortion effect toward the edges of the frame at low magnification. The images were stitched with the Photoshop software into high-resolution photomosaic slices covering 1 - 1.5 cm^2 areas on each thin sections. Photomozaic slices (PPL and XPL) were used to proceed to semi-automatic digital point counting with the JMicrovision V1.27 software Java™ (Roduit, 2008) (see also Ilyah, 2013; Rossi and Moussaoui, 2014) and simultaneous grain identification under the microscope.

Percentage abundance of component grains were defined with 600 modal point counts per thin section, including intergranular space and framework grains, following the Gazzi-Dickinson method to minimize the dependence of modal composition on grain size Dickinson (1970). Samples were collected in the lower part of beds (except for two samples collected in the upper part of beds) to avoid distortion in the quantitative analysis of detrital modes due to modal variability

induced by size-density hydraulic sorting of minerals (Ingersoll et al., 1984; Garzanti and Vezzoli, 2003; Garzanti et al.; 2009). Additionally, most of the coarser grains in samples are monocrystalline and/or aphanitic (rare phaneritic grains), and therefore the compositional bias related to hydraulic segregation of the coarser-grained particles was reduced.

For each slice, the 600 points counted were stochastically distributed across an aleatory grid with a minimum interpoint distance larger than the maximum grain size fraction to avoid counting the same grain twice (van der Plas and Tobi, 1965). This number of point counts is twice the number of point counts required for a standard deviation of 5.5% or less (at the 95% confidence level) for any measured volumetric percentage of mineral or porosity components (Stanton and Wilson, 1994). Grains-size was qualitatively assessed using the Udden-Wentworth standard grain-size scale defining sand as particles between 0.063 and 2 mm, roundness/shape and sorting were assessed by visual comparison on digital image slices following Beard and Weyl (1973) (Table 6.1).

Cement and matrix were counted separately, and grain types were classified according to several petrographic categories defined by Zuffa (1985) based on composition (carbonate versus non-carbonate) and spatial relationships (intrabasinal versus extrabasinal). Textural subdivision of metamorphic lithics follows (Garzanti and Vezzoli, 2003) and volcanic grains were categorized using criteria defined by Dickinson (1970) to help distinguish the relative proportion of mafic, intermediate, and felsic components, and their palaeovolcanic (epiclastic) or neovolcanic origin follows criteria of Critelli and Ingersoll (1995). Thin section staining for feldspar identification was not necessary as their good preservation permitted differentiation based on their twinning. Point-count categories are defined in Appendix 6-7-8, and recalculated parameters are shown in Table 6.2.

Ternary diagrams are used to discriminate any compositional change or trend between the different sequences and to relate compositional signature to provenance source (stable craton, basement uplift, magmatic arc, recycled orogen). A range of regeneration modal diagrams with components characteristic of the main source areas are used to define petrofacies as sandstone of similar composition. These are defined with recalculated percentages of a range of different parameters and ratio of different grain types, which can highlight specific stratigraphic petrologic intervals (Dickinson and Rich, 1972). The recalculated

parameters are those of Dickinson (1970, 1985), Zuffa (1985), Critelli and Le Pera (1994) and Critelli and Ingersoll (1995).

Sample name	Total point counted	Bed thickness	Sample position	Modal grain size	Sorting	Grain shape
ChaS2-1	558	0.2	Lower part bed	Lower medium-Upper fine	Well to moderately sorted	Subangular-subrounded
ChaS2-2	642	1	Lower part bed	Upper-lower medium	Moderately-well sorted	Subangular
MaS1-1	607			Upper-lower fine	Moderately -poorly sorted	Subangular
MaS1-2	607	0.9	Lower part bed	Upper medium-Lower coarse	Poorly to very poorly sorted	Subangular to subrounded
MaS1-3	621	0.8	Lower part bed	Upper medium-Lower coarse	Poorly sorted	Subangular to subrounded
MaS1-4	619	1.2	Lower part bed	Lower/upper coarse-Upper medium	Very poorly-poorly sorted	Subangular to subrounded
MaS1-5	608	1.8	Upper part bed	Lower fine-upper very fine	Moderately sorted	Subangular
TutS2a-1	618	0.4	Lower part bed	Upper fine	Moderately sorted	Subangular
TutS2a-2	607	0.4	Lower part bed	Upper-lower fine	Moderately sorted	Subangular
PS1b-1	632	2.3	Upper part bed	upper fine-lower medium	Moderately sorted	Angular subangular
PS1b-2	607	0.4	Lower part bed	lower coarse-upper medium	poorly sorted	Subangular
S5bisb-2	606	0.4	Lower part bed	upper medium-lower coarse	Moderately-poorly sorted	Subangular
S5bisb-3	622	0.4	Lower part bed	lower coarse	moderately-poorly sorted	Subangular to subrounded
S5bisb-4	625	0.4	Lower part bed	lower medium	poorly sorted	Angular subangular
S8-1	623	0.2	Lower part bed	upper-lower medium	moderately sorted	Subangular
S8-2	647	0.4	Lower part bed	upper-lower medium	moderately sorted	Subangular

Sample name	Total point counted	Bed thickness	Cement %	Matrix %	Petrofacies
ChaS2-1	558	0.2	8.4	19.1	Litharenite
ChaS2-2	642	1	14.7	1.8	Litharenite
MaS1-1	607				
MaS1-2	607	0.9	4	17.3	Feldspathic litharenite
MaS1-3	621	0.8	21.1		Feldspathic litharenite
MaS1-4	619	1.2	23.6	10.2	Feldspathic litharenite
MaS1-5	608	1.8	14.3	24.5	Litharenite
TutS2a-1	618	0.4	6.8	26.2	Feldspathic litharenite
TutS2a-2	607	0.4	44.3		Litharenite
PS1b-1	632	2.3	10.4	11.4	Litharenite
PS1b-2	607	0.4	36.6	3.1	Feldspathic litharenite
S5bisb-2	606	0.4	4.8	35.3	Litharenite
S5bisb-3	622	0.4	24.8	27.7	Litharenite
S5bisb-4	625	0.4	2.6	26.9	Feldspathic litharenite
S8-1	623	0.2	25.2	25.2	Feldspathic litharenite
S8-2	647	0.4	11.1	21	Litharenite

Table 6.1: Table showing the different textural characteristics of sandstone samples and their petrofacies.

Sample name	QtFL			QmFLt			QmKP			P	F	P/F	LvlsLm			QpLvLsm			LvfLvmLvv		
	Qt	F	L	Qm	F	L+Qp	Qm	K	P				Lv	Ls	Lm	Qp	Lv	Lsm	Lvf	Lvm	Lvv
ChaS2-1	47	10	43	41	10	48	80	7	13	29,00	43	0,67	78	22	1	11	69	20	77	23	0
ChaS2-2	41	17	42	35	17	48	68	8	24	57,00	75	0,76	76	23	1	11	68	21	72	24	0
MaS2	37	20	43	28	20	52	59	5	36	71,00	81	0,88	66	31	3	17	55	28	63	37	0
MaS3	42	19	40	30	19	51	62	10	29	58,00	78	0,74	76	24	1	22	59	19	62	35	2
MaS4	48	14	38	32	14	55	69	12	18	28,00	47	0,60	53	45	2	30	37	33	55	43	1
MaS5	38	18	45	33	18	50	65	3	32	52,00	57	0,91	69	31	0	10	62	28	80	20	0
TutSa-1	47	20	33	42	20	38	68	4	28	55,00	63	0,87	98	0	2	15	83	2	89	11	0
TutSa-2	50	13	37	43	13	43	77	3	21	31,00	35	0,89	93	7	0	16	78	6	80	20	0
PS1-1	41	16	43	36	16	47	69	4	27	67,00	76	0,88	96	4	0	9	87	4	82	18	0
PS1-2	53	19	28	35	19	46	64	3	33	59,00	64	0,92	73	26	1	39	45	16	86	14	0
S5bis-B-2	35	17	48	29	17	54	63	6	31	42,00	50	0,84	57	43	0	11	51	38	48	48	2
S5bis-B-3	59	9	33	42	9	49	83	0	17	23,00	23	1,00	71	26	3	33	49	18	90	25	0
S5bis-B-4	40	20	40	31	20	49	61	3	36	68,00	73	0,93	85	15	0	19	69	13	67	32	1
S8-1	52	21	27	35	21	44	63	11	26	52,00	74	0,70	71	29	0	38	44	18	61	39	0
S8-2	41	15	44	33	15	51	68	2	30	49,00	52	0,94	43	63	0	15	37	48	75	25	0

Table 6.2: Table showing the recalculated parameters for ternary diagrams.

6.4. Stratigraphic units

6.4.1. Characteristics of sandstone lobe complexes

In the study area, the J1.1 sequence which belongs to the Chacaico Fm. corresponds to an Early-Late Pliensbachian shallow-marine shoal-water mouthbar-type delta-front system deposited with transgression during the Late Pliensbachian in the Chacaico depocentre (Figs 6.1, 6.2 and 6.3). The J1.2 and J2.1 sequences which belong to the Los Molles Fm. form two distinct intraslope fans that developed with normal regression of a deep-marine ramp-type system from the late Early Toarcian to Aalenian, in the Eastern Catán-Lil and Chachil depocentre (Figs 6.1, 6.2 and 6.3). The J1.2 sequence includes a lower and upper intraslope lobe complexes with different characteristics, interpreted respectively as distal and proximal ramp lobe deposits (cf. Chapter 5). The terminology used for lobe descriptions (lobe, lobe complex, fan) follows Prélat et al. (2009).

J1.1 sequence Delta-front lobes

Description

The J1.1 sequence includes delta-front lobes of amalgamated (1.2-9 m thick, ~3.5 m thick) (Fig. 6.4) lens-shaped to tabular sandstone beds thinning with common convex-down tapering, which can present sandy heterolithic interbeds. Sandstone beds (0.2-1.2 m thick) are medium- to fine-grained, well to moderately sorted, and massive to weakly normally graded, with local basal inverse grading. Beds are structured with planar to undulatory and low-angle cross-laminations, isotropic and anisotropic hummocky bedforms, rare convex-down ripples with tangential foresets or symmetrical ripples. Beds commonly contain subrounded siltstone pebbles and bioclasts in their lower part, and have carbonaceous-rich upper part (mm- to cm-scale), locally with plant fragments and disturbed by soft sediment deformation. Beds have sharp or deformed (loaded) base, locally erosive and sharp bed tops. There is no bed-scale heterogeneity developed. These lobes stack into lobe complexes (~14.3 m thick) with a high amalgamation and high sand: mud ratio, and commonly form thickening-upward successions.

Figure 6.4: J1.1 delta-front lobes in the Chacaico Basin and inset showing massive to planar laminated sandstone with enrichment in carbonaceous fragments near bed top (inset).

Interpretation

Delta-front lobes characteristics suggest that they were deposited under lower and upper plane bed regime, by waning high-concentration flows generated with river floods (Wright et al., 1977; Orton and Reading, 1993; Turner and Tester, 2006). Common soft sediment deformation and loading structures, together with important bed thickness and amalgamation, support high sedimentation rates. Hummocky structures, asymmetrical and symmetrical wave ripples record intermittent storm-wave reworking under combined unidirectional or pure oscillatory flow conditions (Arnott and Southard, 1989; Arnott, 1993; Dumas and Arnott, 2006) and frequent bypass of the finer-grained dilute part of flows in the prodelta.

J1.2 sequence Intraslope fan lobes

Description: Lower J1.2 lobes

The lower lobes of the J1.2 sequence (Fig. 6.5) correspond to laterally extensive (several kilometres) tabular sandstone beds rarely amalgamated (~2.5 m thick) and often interbedded with subordinated mudstone. Sandstone beds (0.2-4.8 m thick) are medium- to fine-grained, poorly sorted, massive or crudely normally graded and matrix-rich. Beds contain deformed mudstone pebbles in their upper part, or throughout the entire bed, with rare current ripple and planar laminations toward bed top. Beds have sharp or rare erosive base and sharp top. Heterogeneity is matrix-scale, and bed-scale heterogeneity induced by chaotic muddy sandstone is not common (0.4 m thick). The lobes stack into lobe complexes (~32 m thick) traced over 1.5-4.5 km downdip, with low amalgamation and low sand: mud ratio, with a thinning- and fining-upward pattern or without any thickness trend. Lobe complex terminations show thinning with abrupt pinchout.

Figure 6.5: J1.2 lower lobes, corresponding to medium- to fine-grained massive to planar laminated sandstone locally bearing deformed mudstone clasts.

Interpretation Lower J1.2 lobes

The lower lobes of the J1.2 sequence were mainly emplaced with high efficiency and high-concentration flows with dampened turbulence including clay-rich transitional plug flows (Baas et al., 2009) and low strength sandy debris-flows (Talling et al., 2012), which collapsed. The lack of consistent stacking pattern, showing lobe-scale compensation and lobe complex-scale aggradation, in these low sand: mud ratio lower lobe complexes with low amalgamation and widespread matrix-scale bed heterogeneity, might represent the distal part of the intraslope fan system (cf. Chapter 5). Some seabed relief inducing relatively high confinement by intrabasinal relief and basin margins is suggested by the common abrupt pinchout lacking lateral thickness and grain-size trends and associated with clastic injectites (sills and dykes) at lobe complex margins (cf. Chapter 5).

Description Upper J1.2 lobes

The upper lobes of the J1.2 sequence (Fig. 6.6) correspond to laterally extensive (several kilometres) tabular to mounded sandstone beds amalgamated (~3 m thick) or interbedded with subordinated heterolithic strata. Sandstone beds (0.5-2.6 m thick) are coarse- to fine-grained, poorly to very poorly sorted, matrix-poor, and normally graded and structured, or less commonly massive with clast-rich bed tops. Beds commonly contain subrounded siltstone and deformed mudstone pebbles, bioclasts (belemnite, ammonites and shells). Carbonaceous-rich material (mm- to cm-scale) is disseminated in laminations. Typically, beds are bipartite, including a massive lower division with outsized grains, locally with some stepped laminations, and either a muddier upper division enriched in carbonaceous material with planar laminations, or a finer-grained upper part with planar to sinusoidal and undulatory laminations associated with isotropic and anisotropic hummock-like bedforms, and/or current ripples or climbing current ripples. Dune-scale cross-stratification can also occur. Beds have sharp, loaded, or erosive scoured bases with basal clast-rich division (few metres thick, 10s m width). Bed tops are sharp or gradational into muddy siltstone. Bed-scale heterogeneity is developed locally, with occurrence clast-rich chaotic muddy sandstone beds (0.2-0.4 m thick) found at the base of lobe complexes. These lobes stack into lobe complexes (~24.5 m thick) with a high amalgamation and

high sand: mud ratio and often with well-defined thickening- and coarsening-upwards, or thinning- and fining-upwards patterns. Lobe complex terminations show thinning and fining in convergent onlap, either with local development of bedforms near lateral lobe complex margins or with transition into matrix-rich sandstone near frontal lobe complex margins.

Interpretation Upper J1.2 lobes

The upper lobes of the J1.2 sequence were deposited by lower efficiency and stratified high-density sediment gravity flows with greater turbulence, commonly enabling significant traction and development of high sediment fallout rate features (sinusoidal laminations, climbing ripples, soft sediment deformation) (Lowe, 1982; Leclair and Arnott, 2005; Sumner et al., 2008). Less commonly deposits record the contribution of turbulence-enhanced transitional flows (Baas et al., 2009). The upper lobe complexes formed as a single and larger depocentre in the Eastern Catán-Lil basin across subdued intraslope topography after deposition of the precursor lower lobe complexes (cf. Chapter 5). The well-defined stacking patterns show lobe-scale compensation and initial NNE lobe complex-scale progradation, followed by aggradation with slight compensation. The consistent stacking pattern in these high sand: mud ratio upper lobe complexes with high amalgamation, localised erosion in their axis, and segregation of bed-scale heterogeneity at the stratigraphic base of each lobe complex, might indicate the proximal part of the intraslope fan system (cf. Chapter 5). The common convergent onlap associated with occurrence of a range of bedforms (HCS-like and climbing ripples) at lateral lobe complex margins or with increase of matrix-scale heterogeneity at frontal lobe complex margins, suggest moderate confinement by basin margins (cf. Chapter 5).

Figure 6.6: J1.2 upper lobes, corresponding to coarse- to fine-grained, normally graded sandstone with erosional base.

J2.1 sequence Intraslope fan lobes

Description J2.1 lobes

The lobes of the J2.1 sequence (Fig. 6.7.) correspond to laterally extensive (several kilometres) tabular to mounded (pinch and swell) sandstone beds amalgamated (~1.5-5 m thick), or interbedded with subordinated heterolithic strata. Sandstone beds (0.3-1.2 m thick) are very coarse to medium- to fine-grained, very poorly to poorly sorted, matrix-rich, and massive to crudely stratified, clast-rich or weakly normally graded with structured bed tops. Beds can show normal or inverse coarse-tail grading and common grain-size breaks. Beds can show planar to sinusoidal parallel laminations, current ripples, local dune-scale cross-stratification, but also banding, convex-down ripples, isotropic and anisotropic HCS-like bedforms. Locally, planar laminations and ripples can be carbonaceous-rich (mm-scale) and armoured clasts and exotic bioclasts are also observed. Matrix-scale heterogeneity is common in thin-bedded sandy lobe fringe deposits. Bed-scale heterogeneity is well-developed in these lobes, with a range of thin (15-50 cm thick) to medium to thick (0.6-1 m thick) or thick (4-7 m thick) hybrid event beds (HEB), including massive, banded and chaotic muddy sandstone bearing abundant mudstone, sandstone and heterolithic clasts

(pebble to cobble-sized). HEB bed geometry is irregular, with common lateral facies changes, abrupt thinning with pinchout across <100 m. Beds have sharp or erosive bases (grooves) associated with scours (1.5-2 m deep, ~5 m long) and have sharp tops. Erosion and scouring is common both in heterolithic lobe fringe and sandy lobe axis deposits. These lobes stack into lobe complexes (~50-70 m thick) with moderate amalgamation, and low to moderate sand: mud ratio, with thickening- and coarsening-upward or thinning- and fining-upward patterns. Lobe complex terminations show thinning (but not fining) with erosive pinchout, associated with scouring and widespread hybrid event beds (HEB) and local combined flow bedform (HCS-like, convex-down ripples) near lateral lobe complex margins and gradual pinchout of HEB-rich thin-bedded sandstone that offset abrupt thick HEB pinchout near frontal lobe complex margins.

Figure 6.7: J2.1 lobes, corresponding to coarse or very coarse-grained sandstone, massive or crudely graded, with abundant mudstone clasts.

Interpretation J2.1 lobes

The lobes of the J2.1 sequence were formed by flows with high sediment fallout rates that could suppress tractional processes in turbulence-modulated clay-laden transitional flows (Baas et al., 2011) and by high-density to hyperconcentrated density flows (Lowe, 1982). Hummock-like bedforms and convex-down ripple bedforms differ from true well sorted fine-grained HCS

emplaced in shallow-marine environment by oscillatory flows. These bedforms formed with traction-and-fallout beneath stratified high-density combined flows, with high sediment fallout rates enabling bedform aggradation in the upper-stage plane bed stability field and are associated with oscillatory combined flow component due to flow reflection and/or deflection (Tinterri, 2011).

HEBs emplaced with a range of transient low to intermediate yield strength sandy debris-flows and associated turbulence-modulated transitional flows (Baas et al., 2016). The general abundance of deformed subangular to angular intrabasinal mudstone clasts in these deposits reflect substrate entrainment and flow transformation, which resulted in a range of HEBs. Stacking patterns show lobe-scale compensation and progradation, with N/NE lobe complex-scale progradation across the interbasin high between the Eastern Catán-Lil and Chachil basins. This was permitted by healing and levelling of inherited topography with deposition of the previous J1.2 intraslope fan (cf. Chapter 5). The J2.1 intraslope fan mainly consists into mudstone clast-rich coarse-grained sandstone lobes in the proximal Eastern Catán-Lil Basin. These facies are equivalent to HEB-rich finer-grained matrix-rich to matrix-poor sandstone lobes deposited downdip in the Chachil Basin, after bypass across seabed relief of the buried horst margin (Fig. 6.3).The erosive pinchout of these lobe complexes is associated with scouring and widespread hybrid event beds (HEB) and local combined flow bedform (HCS-like, convex-down ripples) at lateral lobe complex margins, and gradual pinchout of HEB-rich thin-bedded sandstone that offset abrupt thick HEB pinchout at frontal lobe complex margins. These termination styles indicate partial confinement by intrabasinal relief and basin margins (cf. Chapter 4).

6.4.2. Delta-front and intraslope fan sandstone petrofacies and textural characteristics

For each sample collected from delta-front and intraslope fan sandstones, grain-size, sorting, grain shape and matrix content are provided in Table 6.1. Bias related to particle grain-size, sorting and composition dependence on facies (Garzanti et al., 2009) was monitored by collecting samples from the lower part of beds. Two samples were collected in the finer-grained upper part of beds (PS1-1 and MaS1-5) and in the distal part of the system (TutS2a-1 and 2).

Detrital modes or petrofacies were identified using standard diagram QtFL (Heller and Dickinson, 1985) and QmFLt diagrams (Folk et al., 1980) to emphasise sandstone compositional maturity based on the relative abundances of quartz, feldspar and lithic grains, and on LvLmLs diagram to identify the main lithic components (Fig. 6.8). On a QmFLt diagram, sandstones sampled in the Los Molles Fm. plot as feldspathic-litharenites (7 samples) with an average Qm-F-Lt% = 33-19-47, and litharenites (8 samples) with an average Qm-F-Lt% = 37-14-49 (Fig. 6.8). Using the refined QtFL diagram refined by Weltje (2006), deposits plot as lithoquartzoze arenites (6 samples) with an average Qt-F-L% = 47-14-38, and quartzolithic arenites (9 samples) with an average Qt-F-L% = 38-16-47 (Fig. 6.8). This shows that there is no major change in sandstone compositional maturity through the stratigraphy, apart from an increase in sandstone maturity distally in the J1.2 sequence in samples TutS2a-1 and 2, which are enriched in quartz (Fig. 6.8). Based on the textural definition scheme of Dott (1964) separating sandstones from wackes with a threshold of 15 % matrix, 5 samples are arenites as they have <15% clay matrix (average of 6% matrix) and 9 samples are wackes as they have between 17-35% clay matrix (average of 25%) (Table 6.1 and Fig. 6.9).

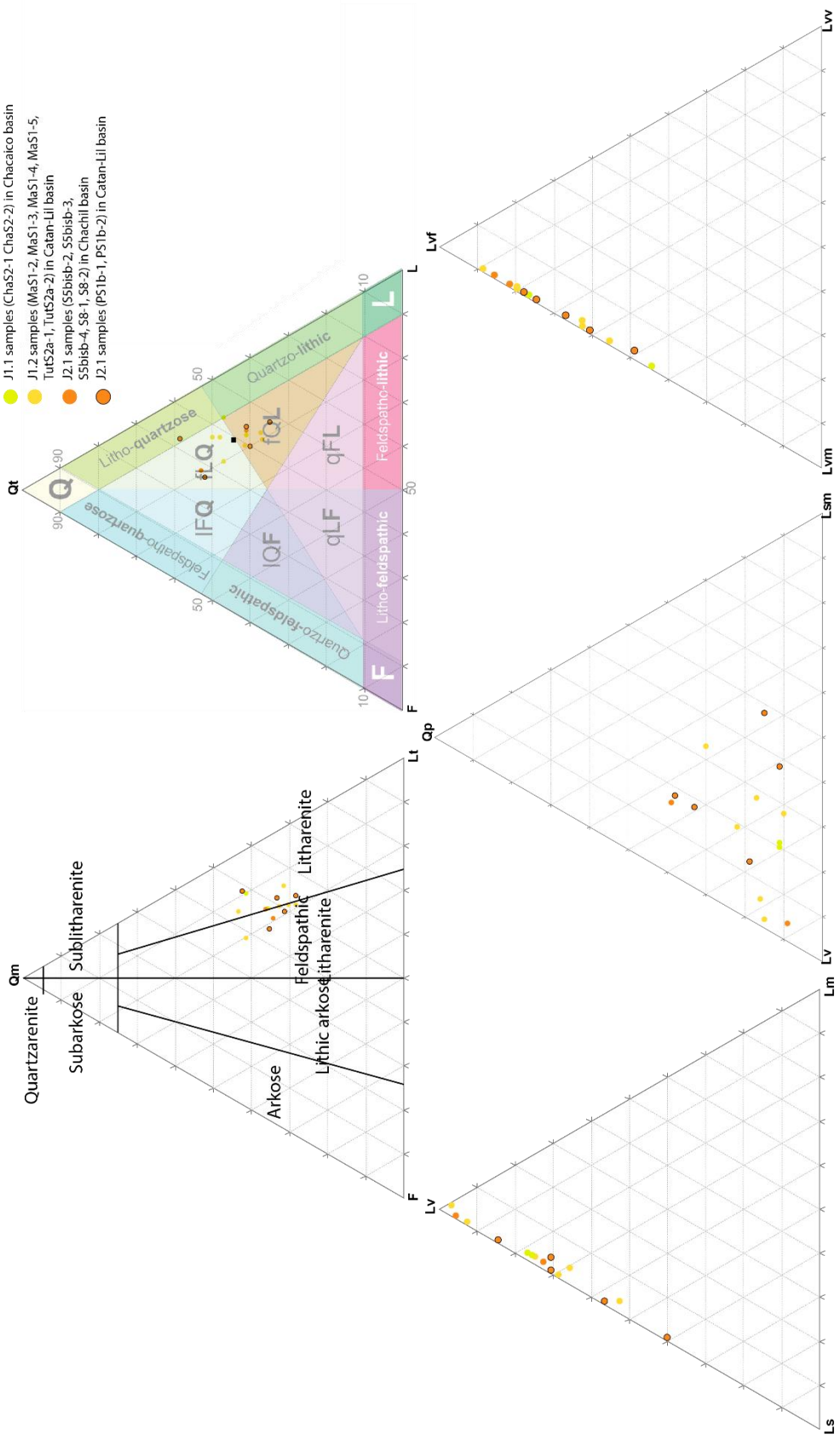

Figure 6.8: Samples distribution in standard diagram QtFL (Heller and Dickinson, 1985) and QmFLt diagrams (Folk et al., 1980) to emphasise sandstone compositional maturity based on the relative abundances of quartz, feldspar and lithic grains. Diagrams showing the proportions of different lithics including volcanic, metamorphic and sedimentary grains (LvLmLs), polycrystalline quartz, volcanic lithics and sedimentary and metamorphic lithics (Qp, Lv, Lsm) and the proportions of different types of volcanic lithics including felsitic, microlitic and vitric grains.

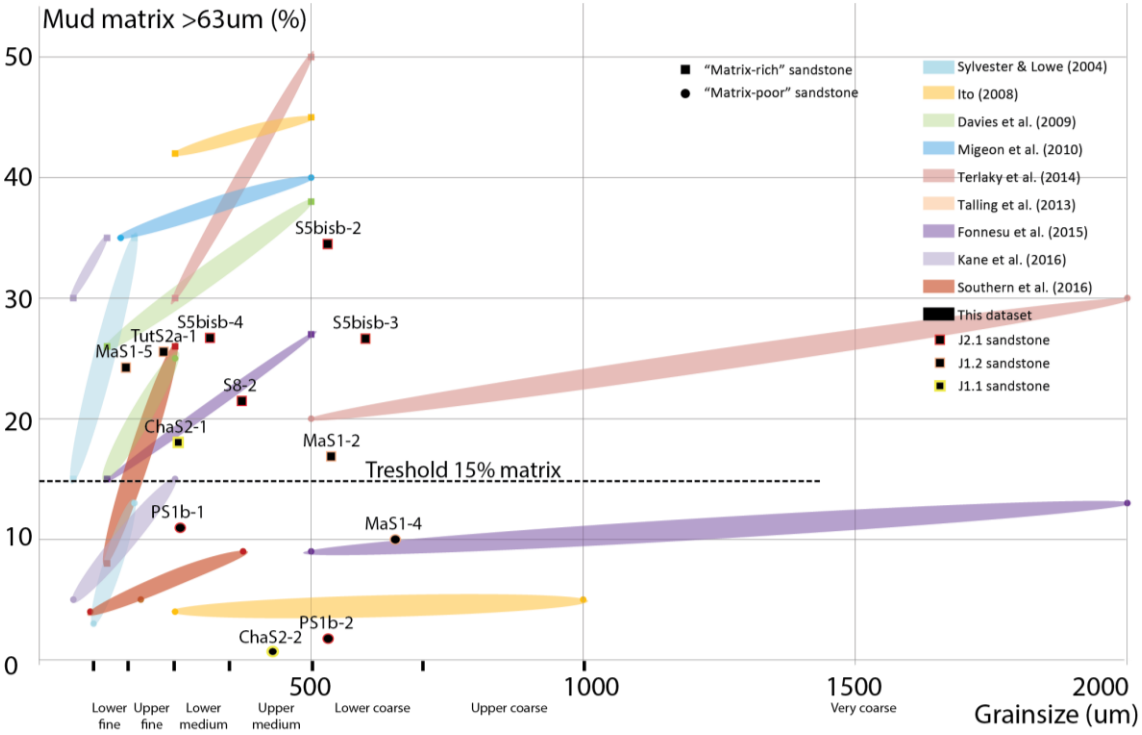

Figure 6.9: Diagram showing the relationships between grain-size and matrix content of sandstones. The sampled sandstone of the Los Molles Formation have relatively high matrix content in comparison to other "matrix-rich" examples from the literature, and are above the 15% matrix threshold of Dott (1964) separating sandstones from wackes. Note that samples in the upper part of beds are not included.

The J1.1 sequence in the Chacaico Basin include two samples (Fig. 6.10) collected in the lower part of beds and correspond both to litharenites, ranging from upper medium to upper fine grain-size sandstone, well- to moderately-sorted with subangular grains and with 1.8 and 19.1% of matrix content (Fig. 6.9). The J1.2 sequence includes six samples collected in the Eastern Catán-Lil Basin (Figs 6.11, 6.12, 6.13). Four are feldspathic litharenites collected in the lower part of beds and range from lower coarse to upper medium-grained sandstone, poorly to very poorly sorted with subangular to subrounded grains and with 10.2 to 17.3 % matrix content (MaS1-2, MaS1-3, MaS1-4) (Fig. 6.9), whereas for the sample collected in the distal part of the system sandstone is upper fine-grained, moderately sorted, with subangular grains and up to 26% matrix content (TutS2a-1) (Fig. 6.9).

The J1.2 sequence includes two litharenites that range from upper-lower fine-grained to upper very fine-grained sandstone, moderately sorted with subangular grains, and were collected in the distal part of the system (TutS2a-2) and in the upper part of a bed with up to 24.5% matrix content (MaS1-5). The J2.1 sequence includes seven samples, with two samples collected in the

Eastern Catán-Lil Basin (PS1b-1, 2) (Fig. 6.14) and five samples collected in the Chachil Basin (S5bisb-2, 3, 4, S8-1 and 2) (Figs 6.15 and 6.16). Three are feldspathic arenites collected in the lower part of beds, ranging from lower coarse to lower medium sandstone, poorly to moderately sorted, with subangular to angular grains and with 26.9 and 3.1 % matrix content (S5bisb-4, S8-1 and PS1b-2) (Fig. 6.9). Four samples correspond to litharenites, with three collected in the lower part of beds that range from lower coarser to upper-lower medium-grained sandstone, moderately to poorly sorted with subangular grains, and with 21 to 27.7 % matrix content (S5bisb-2, 3, S8-2) (Fig. 6.9). The litharenite sample collected in the upper part of bed (PS1b-1) (Fig. 6.14) corresponds to lower medium-upper fine-grained sandstone, moderately sorted with subrounded to angular grains and up to 11.4 % matrix content (Fig. 6.9).

The finer-grained samples in the J1.1 and J1.2 sequence tend to be litharenites and the coarser-grained samples are felspathic litharenites, whereas in the J2.1 sequence the finer-grained samples are feldspathic litharenites and the coarser-grained samples are litharenites (Table 6.1). The finer-grained samples display a better sorting, but with angular to subangular grain roundness compared with the coarser-grained samples that are poorly to very poorly sorted with subangular to subrounded grains (Table 6.1). The coarser and outsized grains correspond to upper and lower coarse quartz (commonly monocrystalline) and microlitic or felsitic volcanic lithics. There is a slight difference in matrix content between the feldspathic litharenite (average matrix content ~18%) and litharenite petrofacies (average matrix content ~21.4%) when comparing samples collected in the lower part of beds and a control on grain-size depending on the proximal-distal stratigraphic position of samples (Table 6.1).

The deltaic sandstones of the J1.1 sequence have modal medium grain size, well to moderate sorting with low matrix content averaging 10.4%, and equal cement proportion averaging 11.5%. The intraslope fan sandstone have a modal medium-coarse grain size and are poorly to very poorly sorted with variable, but overall higher matrix content (ranging from 10.2-35.3%). The sandstone of J1.2 sequence have high matrix content averaging 18% and lower cement proportion averaging 12%, whereas sandstone of the J2.1 sequence are more matrix-rich averaging 27.2% with average of 16.5% cement (only samples showing both

matrix and cement and collected in the lower part of beds are considered in the average percentages for matter of comparison). These differences are not related to grain size change given that both sequences have similar modal grain-size and sorting, nor vary with the thickness of the sampled bed ranging from medium to thick beds (0.2-1.2 m thick for the compared samples) (Table 6.1). Moreover, the sampled sandstone and their host bed thickness patterns show that they do not necessarily correlate with reservoir quality and grain size or matrix content.

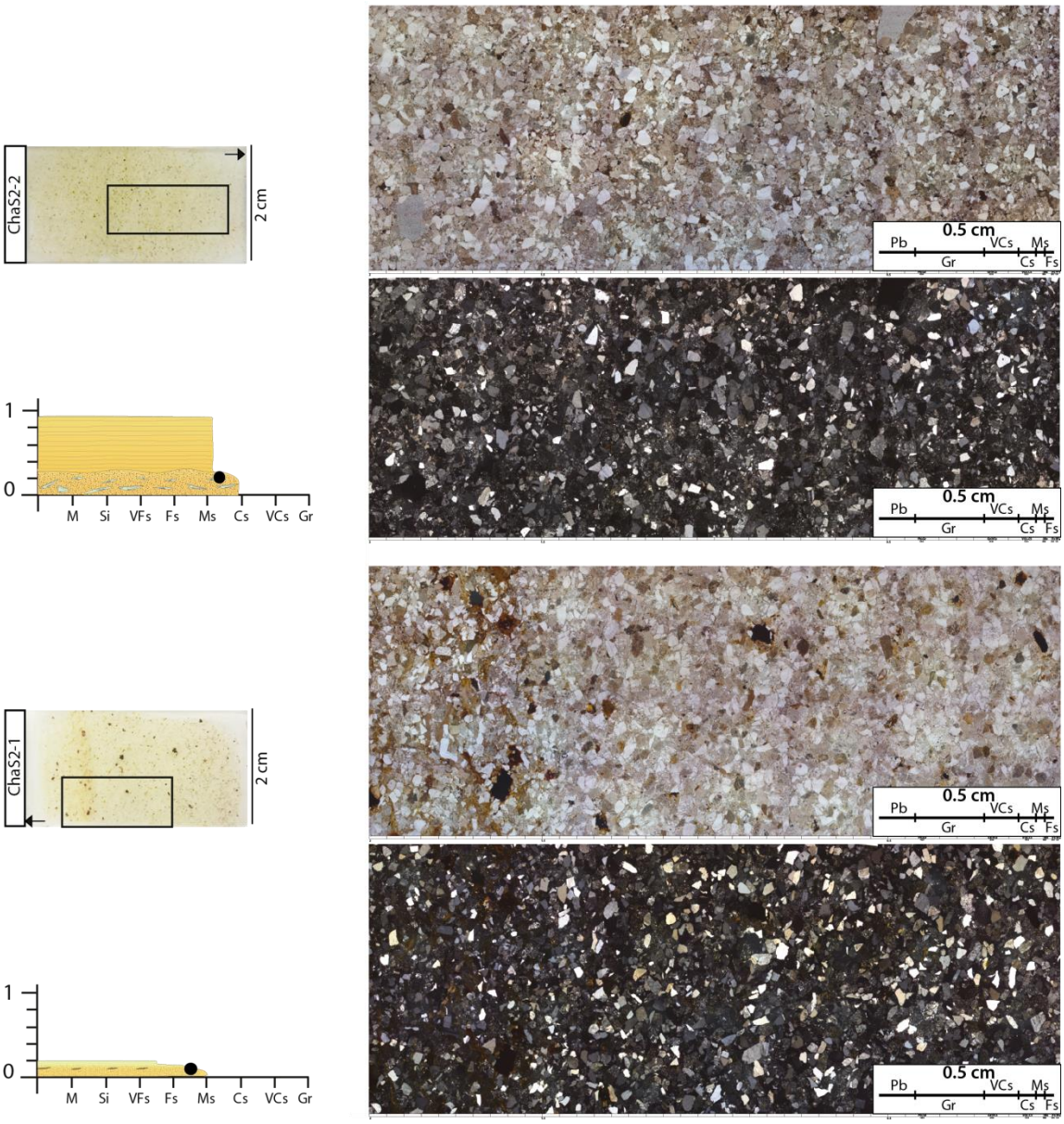

Figure 6.10: Thin section with localisation of the sample in sandstone beds of the J1.1 delta-front lobes in the Chacaico Basin, and photomosaic slices. Location of the imaged slice is shown on the thin section.

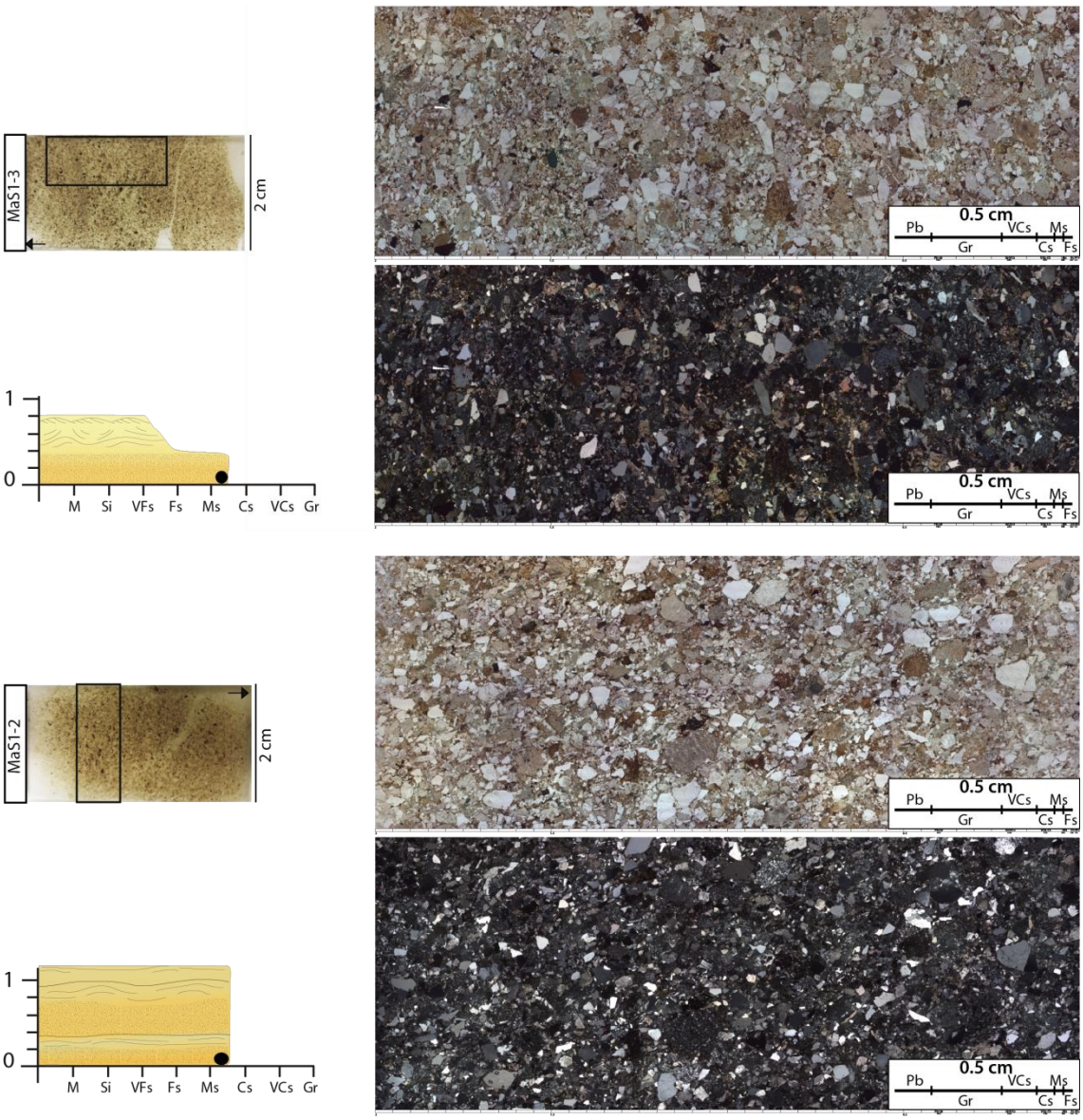

Figure 6.11: Thin section with localisation of the sample in sandstone beds of the J1.2 lower and upper lobes in the Eastern Catán-Lil Basin, and photomosaic slices. Location of the imaged slice is shown on the thin section.

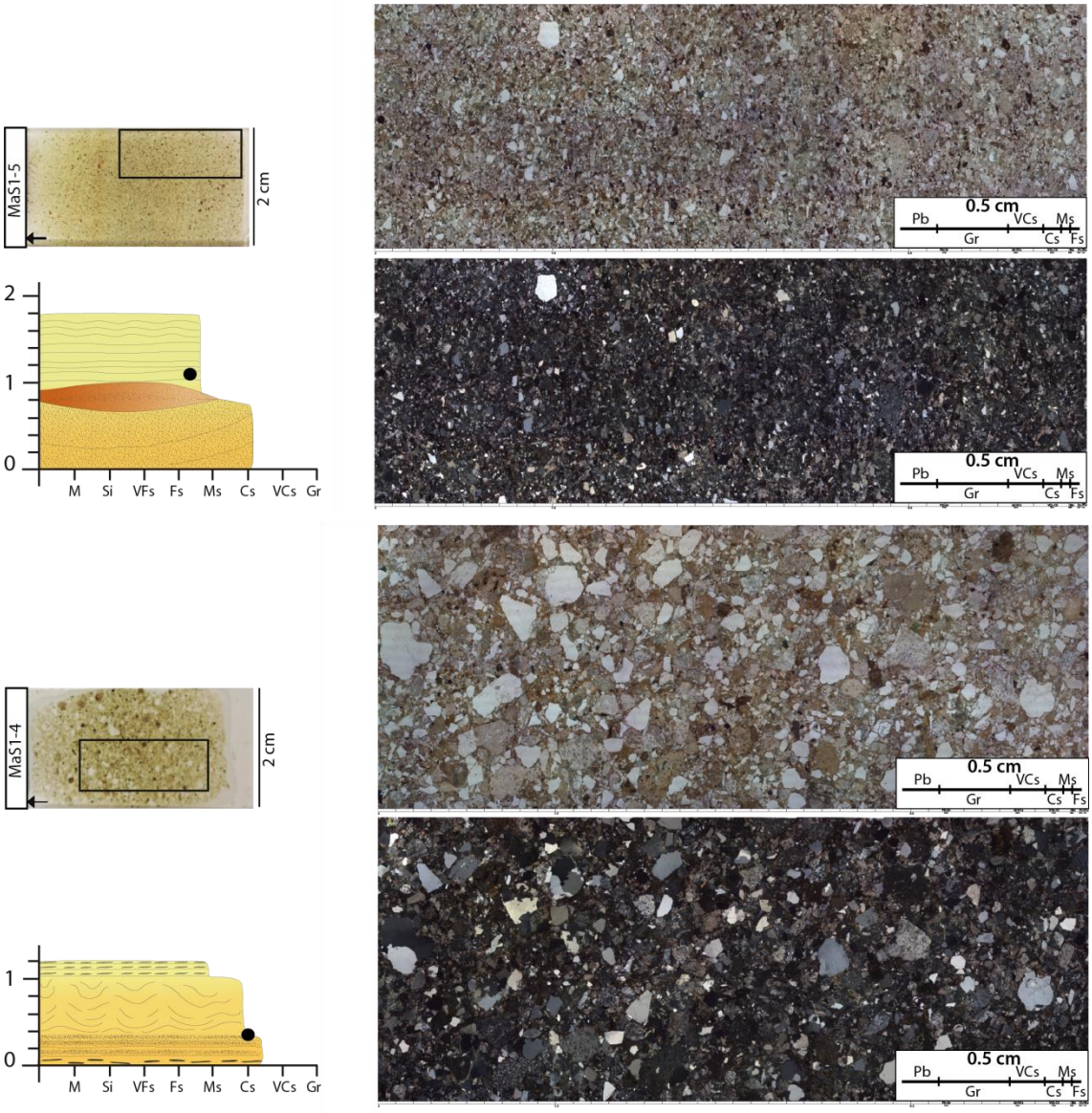

Figure 6.12: Thin section with localisation of the sample in sandstone beds of the J1.2 upper lobes in the Eastern Catán-Lil Basin, and photomosaic slices. Location of the imaged slice is shown on the thin section.

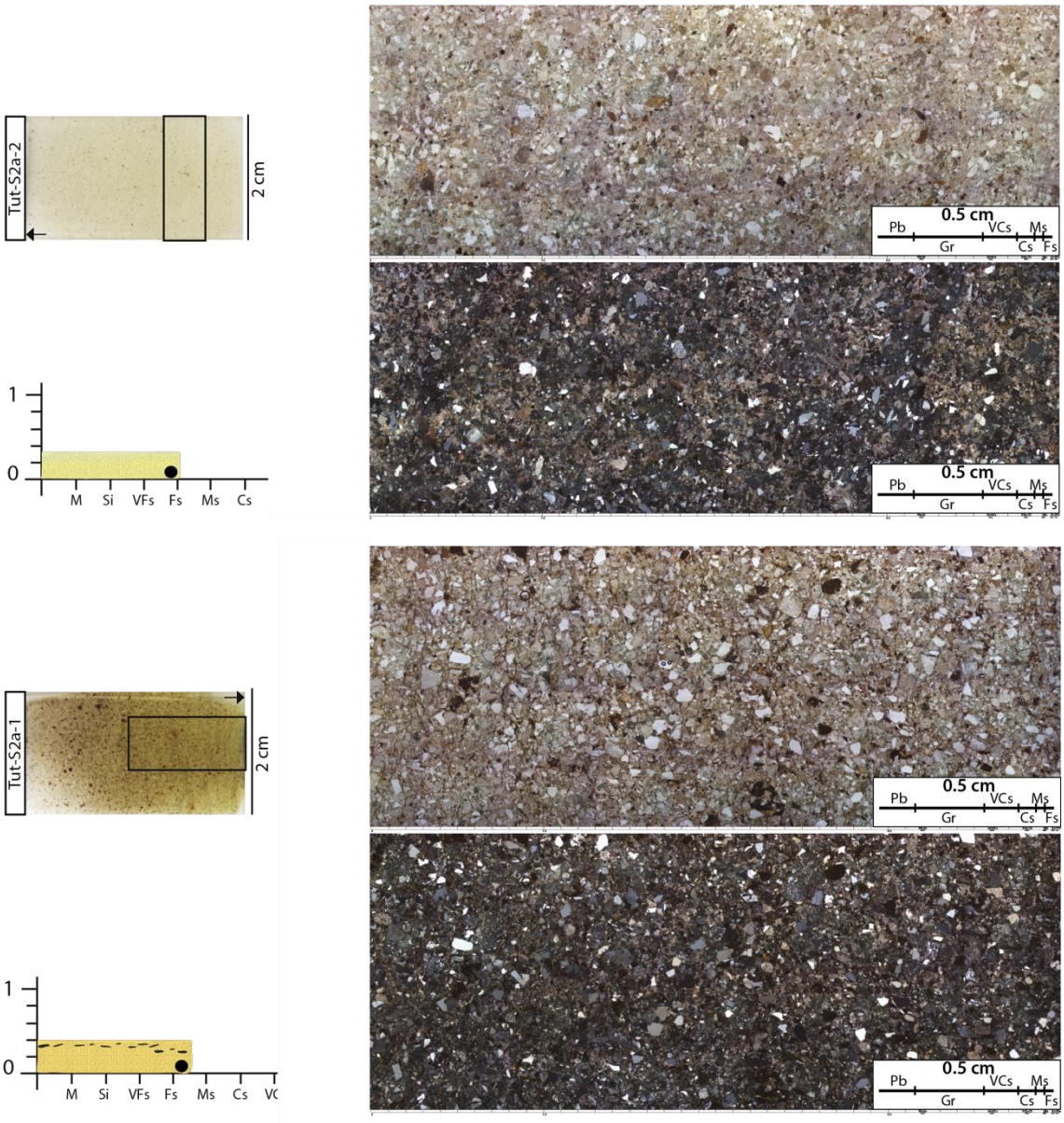

Figure 6.13: Thin section with localisation of the sample in sandstone beds of the J1.2 upper lobes in the distal part of the system in the Eastern Catán-Lil Basin, and photomosaic slices. Location of the imaged slice is shown on the thin section.

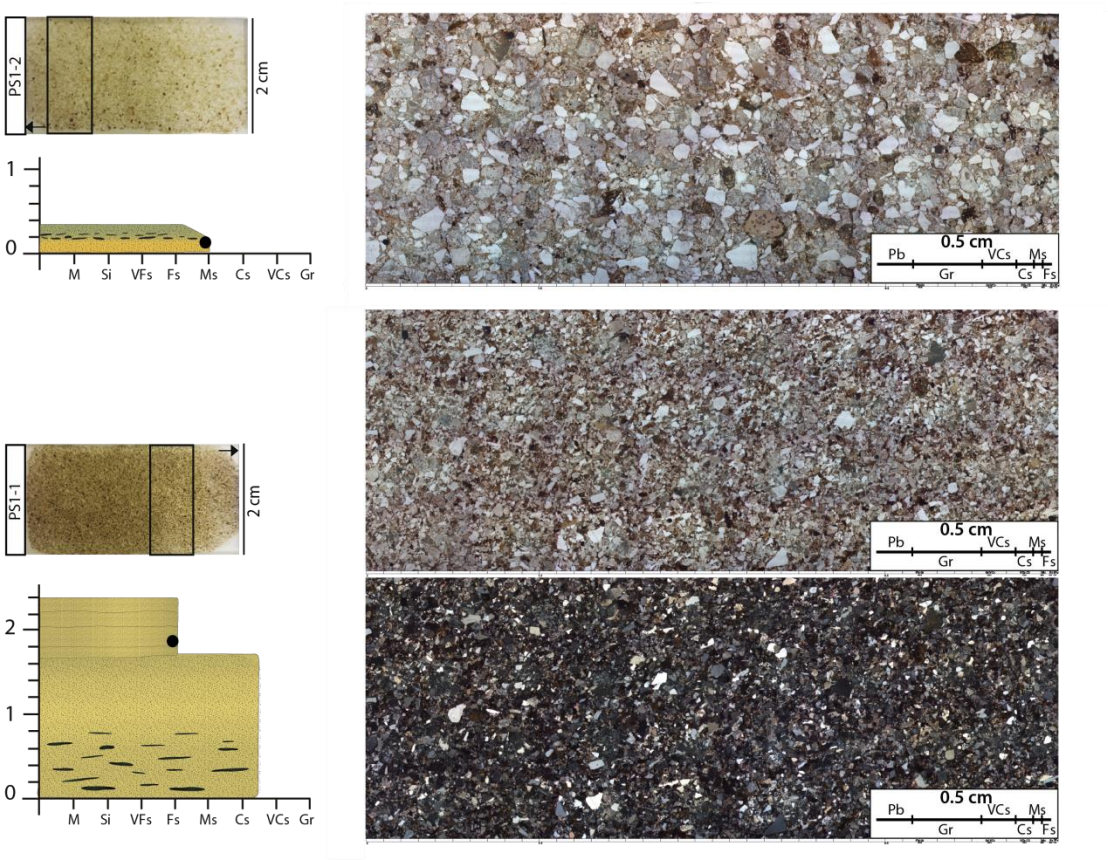

Figure 6.14: Thin section with localisation of the sample in sandstone beds of the J2.1 lobes in the Eastern Catán-Lil Basin, and photomosaic slices. Location of the imaged slice is shown on the thin section.

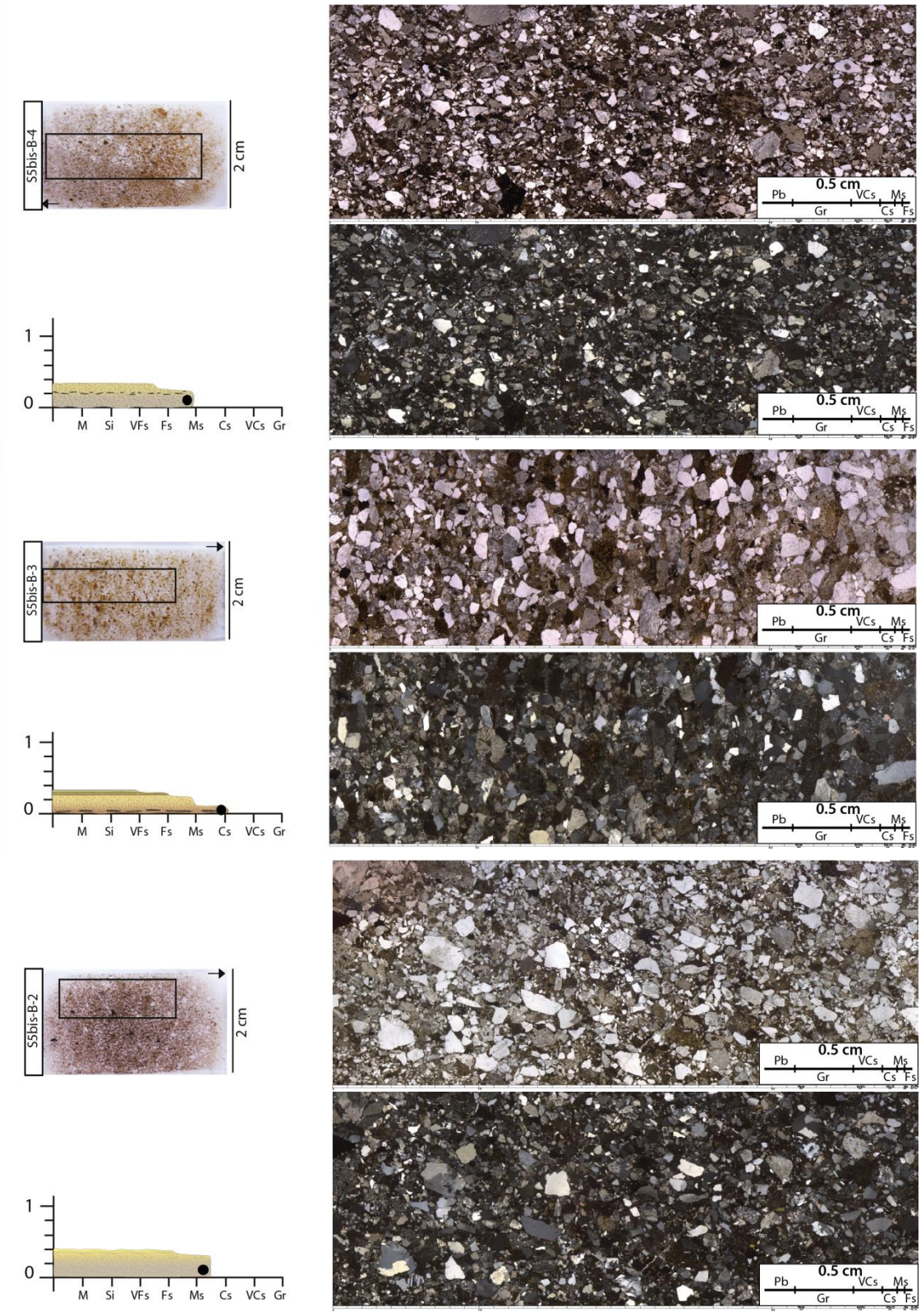

Figure 6.15: Thin section with localisation of the sample in sandstone beds of the J2.1 lobes in the Chachil Basin, and photomosaic slices. Location of the imaged slice is shown on the thin section.

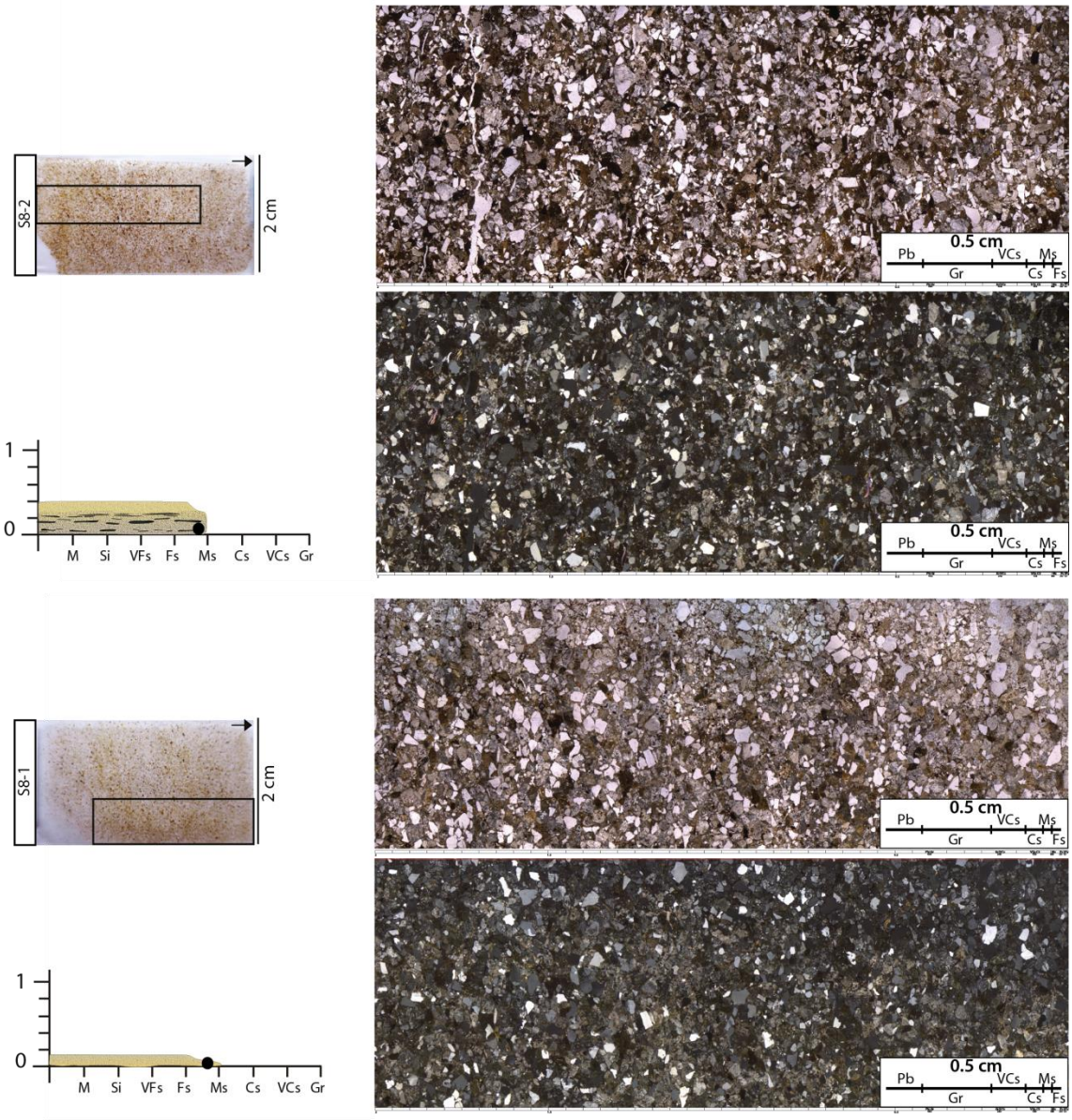

Figure 6.16: Thin section with localisation of the sample in sandstone beds of the J2.1 lobes in the Chachil Basin, and photomosaic slices. Location of the imaged slice is shown on the thin section.

6.4.3. Sandstone composition

Grains

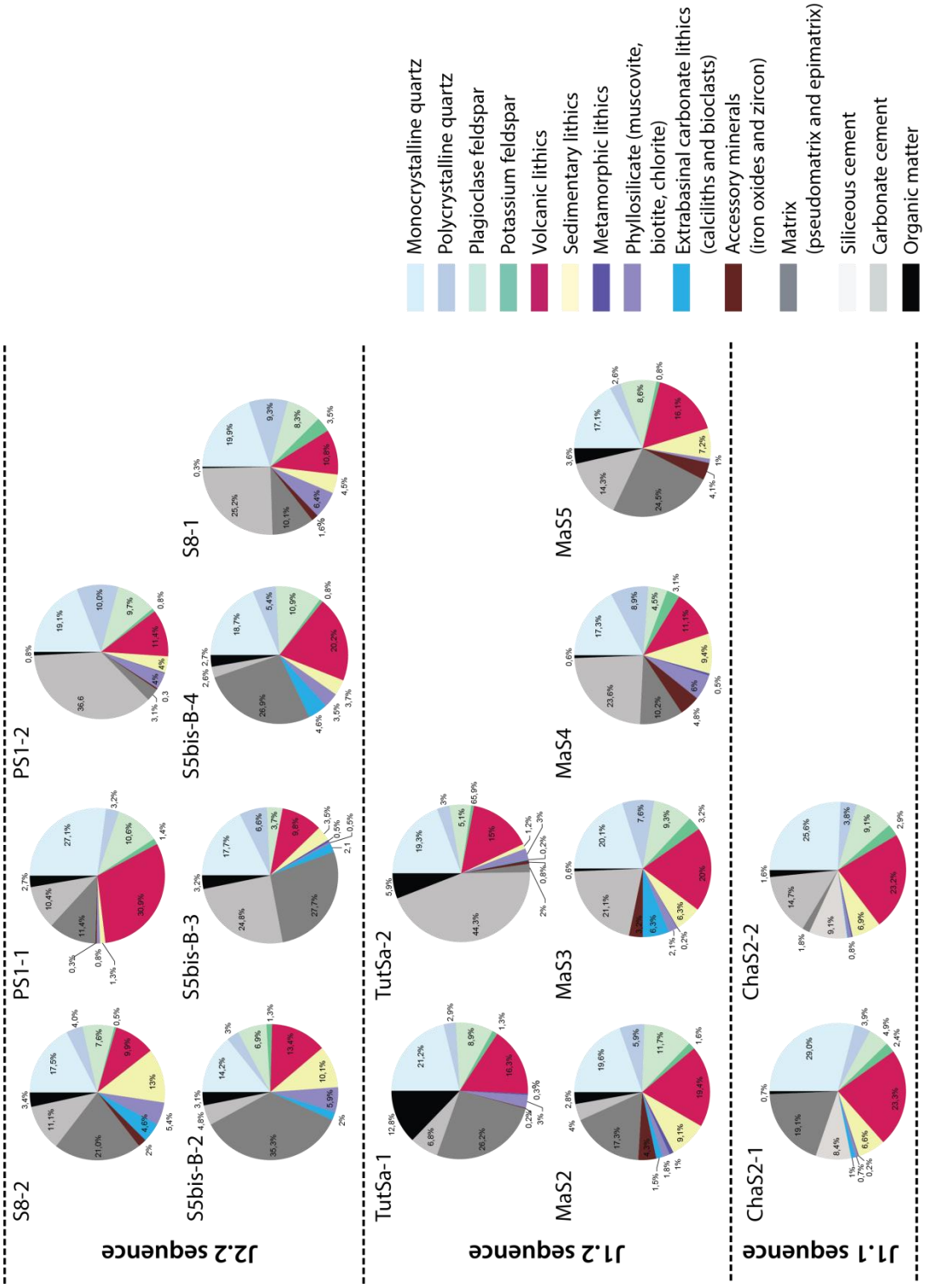

Figure 6.17: Compositional pie charts showing the distribution of the main component grain classes in samples of the J1.1, J1.2 and J2.1 sequences (see percentages in Appendix 6-7-8).

The sandstones are mainly composed of lithics and monocrystalline quartz (Qm ranges from 14.2-29 % of the total counted points in each sample (Table 6.1)), which dominate over polycrystalline quartz (Qp ranges from 2.6-10 % of the total counted points in each sample (Table 6.1)) (Fig. 6.17). Monocrystalline quartz corresponds to subeuhedral angular to subrounded grains including the finest and coarsest grain sizes and can show straight or undulatory extinction (angle < 5 °) and less frequent occurrence of vesicles and partial resorption embayments (Figs 6.18 and 6.19). Polycrystalline quartz corresponds to subangular to subrounded grains, which can be unstrained and granular coarse crystalline quartz (<2-5 crystals) (53%) straight to curved intercrystal boundaries, or strained to foliated fine crystalline quartz (>3-5 crystals) (47%) with and crenulated sutured intercrystal boundaries that can show stylolites (percentages refer to total count of this class Table 6.1) (Figs 6.18 and 6.19).

Monocrystalline components consist into individual grains or occur as phenocrysts or xenocrysts in lithic grains, dominated by monocrystalline quartz (mean Qm-K-P%Qm = 68), plagioclase feldspar (mean Qm-K-P%P = 27) and few potassium feldspar (mean Qm-K-P%K = 6) (Table 6.2) (Fig. 19). Feldspar plagioclase is the dominant feldspar as P/F ratio is comprised between 0.6 and 1 (Table 6.2), with average ratio of 0.84 that outpaces the threshold ratio of 0.75 used to define volcanic-derived sandstone (Dickinson, 1970). Plagioclase feldspar crystals form medium to coarse sized subangular grains with common polysynthetic twinning (albite) and microlites or laths in volcanic lithics with common simple twinning (sanidine) and can present sieve textures and replacement by calcite or sericitization (Pg-Fd ranges from 3.7-11 % of the total counted points in each sample). Potassium feldspar correspond to medium or fine tabular orthoclase crystals monocrystalline or with carlsbad twinning and common perthitic or less common myrmekite texture, and minor coarse microcline crystals with tartan twinning (K-feldspars ranges from 0.5-3.5% of the total counted points in each sample).

Sandstone contain volcanic (LvLsLm%Lv ranges from 43-98%), sedimentary (mainly shale and siltstone) (LvLsLm%Ls, 4-45%) and metamorphic lithics (LvLsLm%Lm, 0-3.5%) (mean Lv-Ls-Lm% = 74-26-1) (Fig. 6.8). The ratio of total volcanic lithics to total lithics Lv/Lt ranges between 0.4 and 0.9 (averaging 0.6) as they are the dominant types of lithic grains in sandstone (Lv ranges from

2.6-10 % of the total counted points in each sample). Volcanic lithics show a range of textures associated with different magma compositions, including as major components felsitic grains (Lv%Lvf ranges from 11-48%), microlitic grains (Lv%Lvm, 53-97%), lathwork grains (Lv%Lvl, 47-90%) and vitric grains (Lv%Lvv, 0-2%) (mean Lvf- Lvm- Lvv% = 72.5-27-0.5) (Figs 20 and 21). Felsitic volcanic lithics are characterized by a felsophyric silicic groundmass of meso- to cryptocrystalline non-fibrous quartz (chert) commonly associated with siliceous recrystallization and bearing variable amount of meso- and phenocrysts (quartz, plagioclase), either showing granular (Lv%Lvf gr, 53-85%, averaging 68%) or seriate textures (Lv%Lvf se, 0.7-9.8%, averaging 3.8% in samples). Microlitic volcanic lithics are characterised by a variable amount of plagioclase microlites scattered in aphanitic devitrified groundmass, showing trachytic fluidal textures or pilotaxitic texture when microlites are interwoven without specific orientation (Lv%Lvmi pi-tra, 10-42%, averaging 22.7% in samples). Some volcanic grains can also show lathwork or hyalopilitic textures, with plagioclase phenocrysts and microlaths scattered in aphanitic devitrified or isotropic glassy groundmass (Lv%Lvmi lat-hya, 1-11%, averaging 5.3% in samples). Vitric and pumiceous volcanic lithics are scarce (Lv%Lvv-pu, 0-2.4%, averaging 0.5% in samples). Glass is often devitrified with common development of spherulitic and fibrous siliceous textures (with chalcedony**)** or locally preserved as yellowish-brownish aphanitic glassy grains. Pyroclastic grains can form brownish preserved juvenile pumices with irregular margins and tube vesicles or non-welded tuffaceous clasts with fine-grained ash matrix is often replaced by clay or cryptocrystalline chert with sericitization or siliciclization.

Sedimentary and metamorphic lithics are found in less abundant proportions (Fig. 6.17) as Ls ranges from 0-13% and Lm ranges from 0.2-1% of the total counted points in each sample. Sedimentary lithic fragments include subrounded to subangular fine to coarse-sized grains of shale (ranging from 1.4-15.8%, averaging 6.3% in samples) and siltstone (ranging from 0.4-1.7%, averaging 0.3% in samples), with dominant shale (95%) over siltstone grains (5%) (percentages refer to total count of this class) (Fig. 6.19). Metamorphic lithics mainly consist into subrounded medium grains of phyllite, aphanitic slate with preferential foliation, strained medium-grained gneiss and less common schist including muscovite and polycrystalline quartz (mean Lmsl-Lmphyl-Lmsch-Lmgn % = 16.7-55.6-16.7-11.1) (Figs 6.18 and 6.21).

Organic matter ranges from 0.3-12.8% of the total counted points in each sample (Fig. 6.17). It includes dark brown to black phytoclasts in the form of lath-shaped biostructured plant debris (with residual membraneous tissues and cell walls) (Fig. 6.21), opaque massive equant to blade shaped organic matter and brownish-orangey translucent amorphous flaky or speckled organic matter (Fig. 6.19). Organic matter fragments are dominated by opaque structureless (46%) and structured phytoclasts (25%) over amorphous organic matter (29%) (percentages refer to total count of this class), and commonly degraded with oxidization associated with fine disseminated pyrite indicative of oxidizing conditions and distance form terrestrial source (Tyson, 1993).

Minor framework grains include phyllosilicates and calciliths (Fig. 6.17). Phyllosilicates comprise micas (90%), biotite (6%) and detrital chlorite (4%) (percentages refer to total count of this class) and phyllosillicates range from 0.7-6.4% of the total counted points in each sample (Fig. 6.18). Calciliths correspond to medium-grained subrounded to subangular intrabasinal carbonate grains, which mainly consist into large equant calcite crystals with simple twinning, granular sparitic calcite (>30 um) or microsparite (4-30 um) associated with shell bioclasts and calciliths ranges from 1-6.3% of the total counted points in each sample (Fig. 6.19). Accessory heavy minerals (Fig. 6.17) are mainly iron oxide opaque grains (potentially pyrite and chromite) and non-opaque minerals mostly zircons which together ranges from 0.2-5.3% of the total counted points in each sample (Fig. 6.18 and 6.19).

Figure 6.18: A-Example of MaS2 thin section showing quartz grains including monocrystalline non undulose (QmnU) and spherulitic (QSph) quartz with resorption embayments characteristic of volcanic rocks, muscovite (MS), feldspar with pertithe (KOp), plagioclase feldspar with polysynthetic twinning (Pg) and microlitic volcanic lithics with pilotaxitic texture (Lvmpi), felsitic volcanic lithics with granular texture (Lvfgr) and recrystallized devitrified pumice grains (Lvpu) with remnant shard walls. Note the cryptocrystalline cement and pseudomatrix around grains. B-Example of PS1 thin section showing quartz grains monocrystalline non-undulose (Qmnu) and undulose (QmU) and polycrystalline (Qp) with sutured internal boundaries, muscovite (Ms), zircon crystal (Zr), metamorphic lithic (Lmg), plagioclase feldspar (Pg) locally with sericitized margins (Pgse), microlitic volcanic lithics including pilotaxitic texture (Lvmpi) and vitric fragment (Lvvgl), amorphous organic matter (Moam) and calcite crystals (CaC). Note the drusy calcite cement and dissolution replacement of feldspars with calcite. C- Example of MaS3 thin section showing quartz grains monocrystalline non-undulose (Qmnu) and polycrystalline (Qpf), plagioclase feldspar (Pg), muscovite (Ms), felsitic volcanic lithic with microcrystalline texture (Lvfmi) and extensive calcite cement.

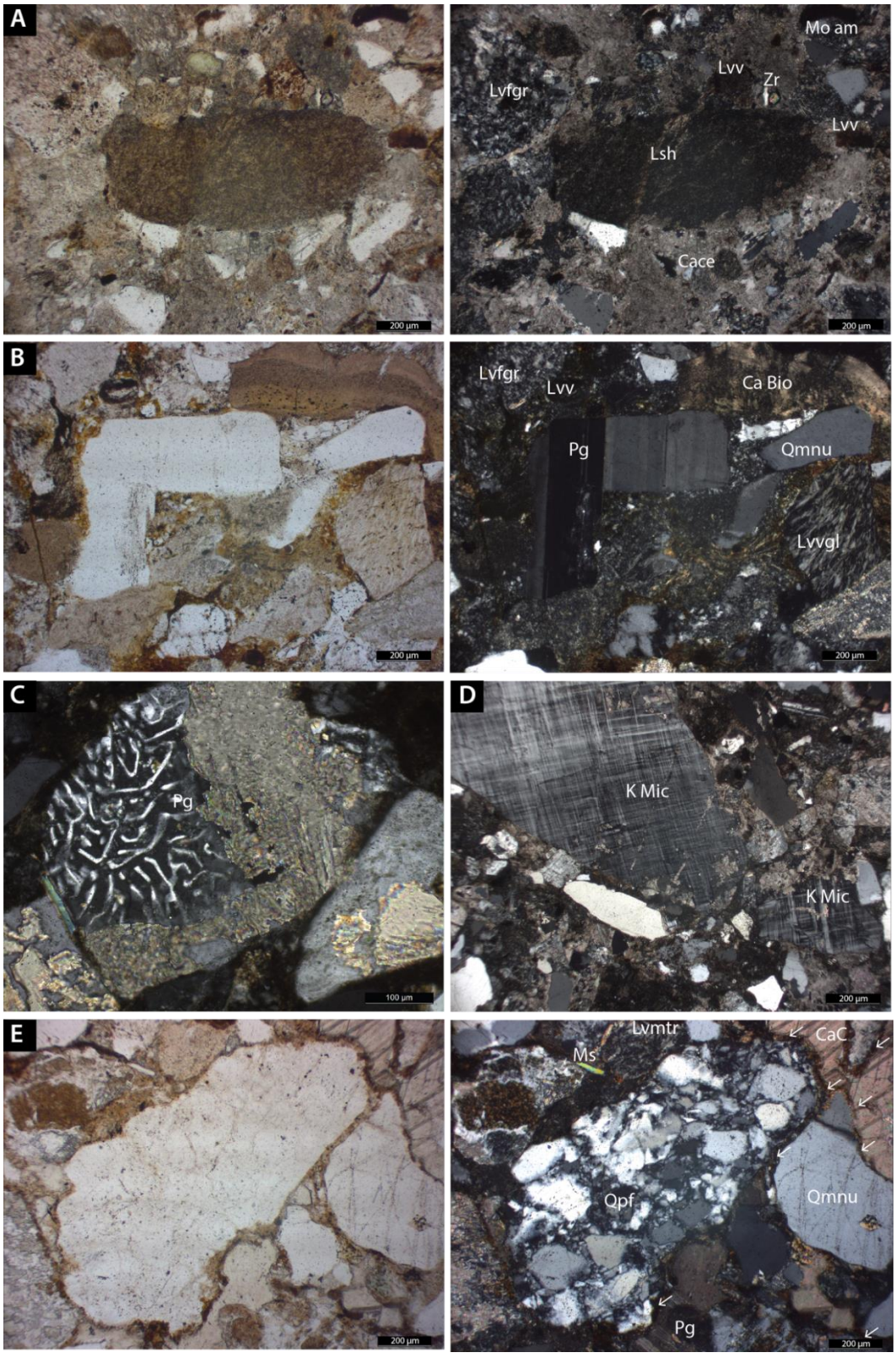

Figure 6.19:A-Example of MaS3 thin section showing a fragment of pumice (Lvpu) with spherulitic devitrification preserving tube vesicles and recrystallized cryptocrystalline texture. Note the pseudomatrix. B-Example of MaS4 thin section showing a glassy volcanic lithic (Lvvgl) with typical ragged margins and felsitic fragment with granular texture (Lvfgr).C-Example of MaS4 thin section showing microlitic volcanic lithic with trachytic texture (Lvmtr) and devitrification texture of glassy fragment (Lvvgl).Note the drusy calcite cement.D-Example of MaS4 thin section showing microlitic volcanic lithic with lathwork (Lvml) and trachytic texture (Lvmtr) and felsitic volcanic lithic with recrystallized microcrystalline texture (Lvfmi).

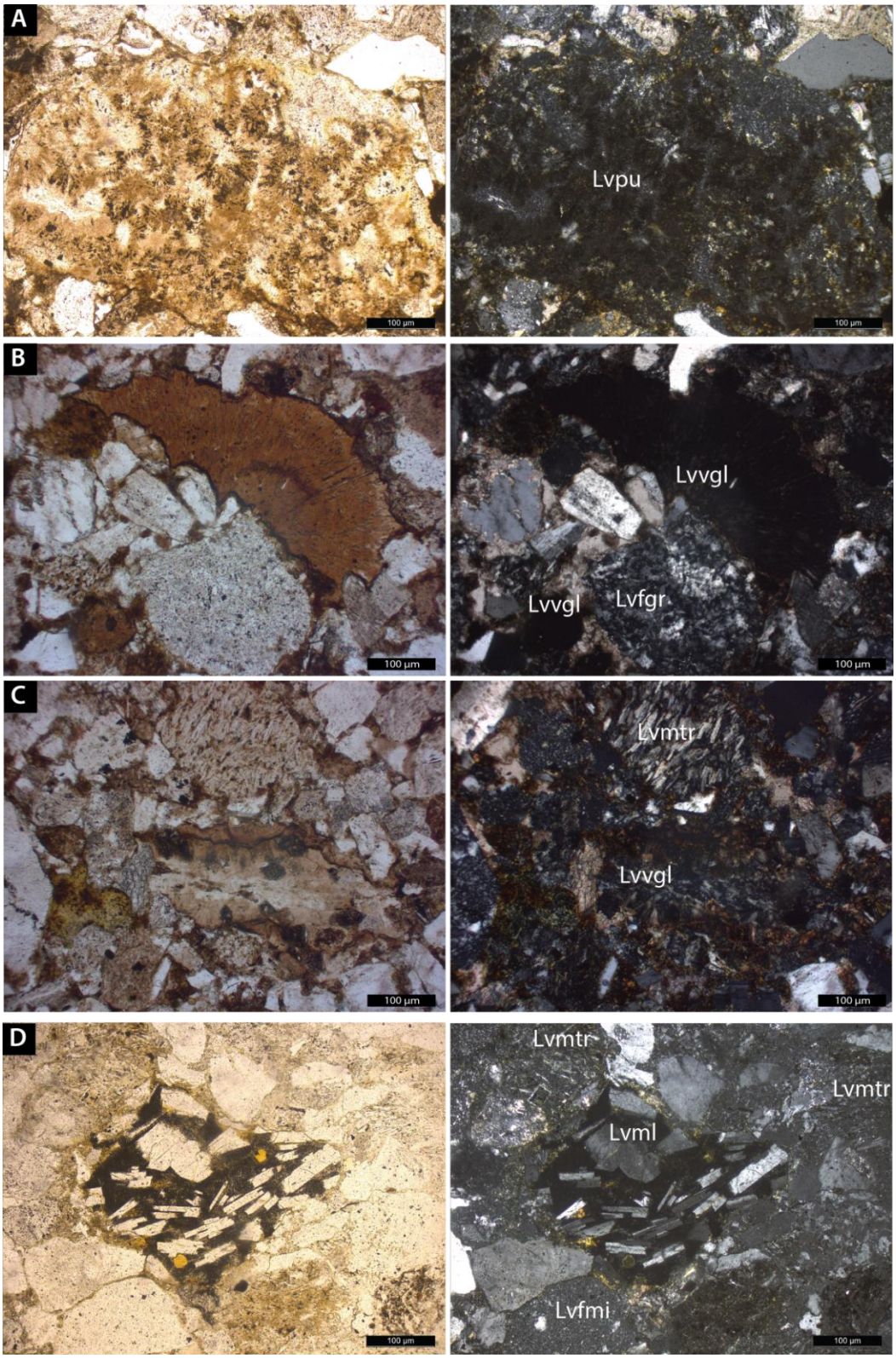

Figure 6.20:A-Example of S5bisB2 thin section showing a fragment of structured organic matter. Note associated iron oxydes. B-Example of TutS1 thin section showing a fragment of pumice (Lvpu) with spherical devitrification with preserved tubes.C-Example of MaS2 thin section showing microlitic volcanic lithics with pilotaxitic texture (Lvmpi) including polycrystalline quartz (Qp) and euhedral feldspar phenocryst with a sieve texture with glass inclusions (Pgs), plagioclase crystal (Pg) and metamorphic lithic (Lmg).

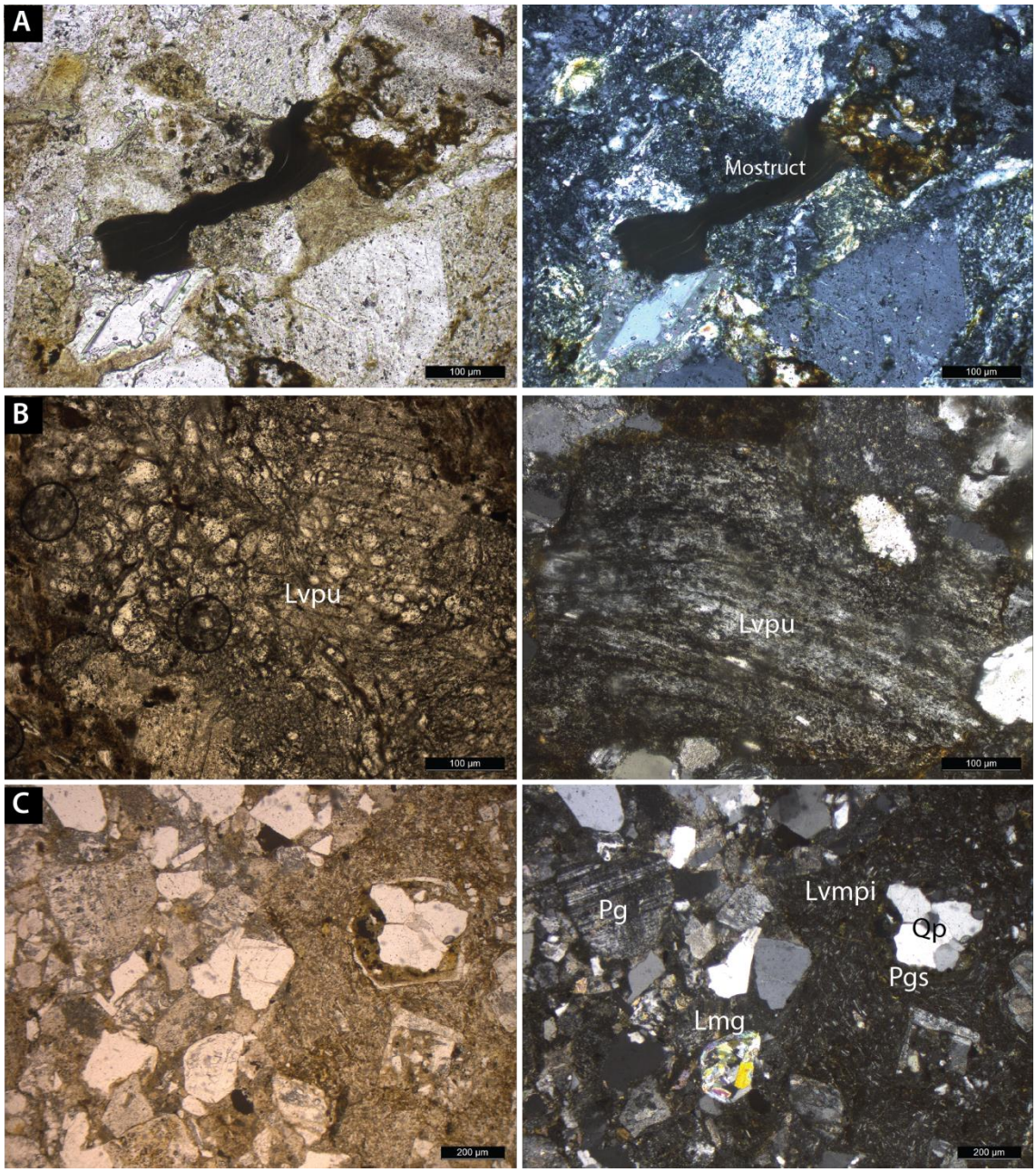

Figure 6.21:A-Example of MaS1 thin section showing sedimentary lithic shale (Lsh), volcanic lithics with vitric (Lvv) and felsitic granular texture (Lvfgr), zircon (Zr), amorphous organic matter fragment (Moam) and extensive drusy calcite cement.B-Example of ChaS2 thin section showing subhedral plagioclase crystal fragment (Pg), quartz grain monocrystalline non-undulose (Qmnu), bioclast calcilith (Ca Bio), volcanic lithic with felsitic granular texture (Lvfgr), vitric amygdule (Lvv) and spherulitic vitroclastic texture of glassy volcanic fragment (Lvvgl). Note the extensive intergranular siliceous recrystallization and paucity of calcite cement.C-Example of MaS1 thin section showing myrmekite vermicular texture of plagioclase feldspar characteristic of plutonic rocks and dissolution replacement calcite.D-Example of PS1 thin section showing microcline potassium feldspar with tartan twinning present as oversized grains.E-Example of PS1 thin section showing quartz grain monocrystalline non undulose (QmnU), polycrystalline (Qpf), microlitic volcanic lithic with trachytic texture (Lvmtr), calcite crystals (CaC), muscovite (Ms), plagioclase feldspar (Pg). Note the clay rim type coating and dissolution features (arrows).

Matrix and cement

Most of samples are texturally immature and matrix and/or cement framework supported (represent 22 to 52% of the total counted points in samples, averaging 32.8 %), (Fig. 6.17) owing to the abundance of subangular grains, poor sorting and non-uniformity of grain-size. Dominant point to tangential contacts between mechanically rigid grains, lacking straight-sutured contacts and stylolites associated with tight grain fabric and the occupation of the intergranular space with matrix and/or cement suggest early cementation and limited mechanical compaction.

Clay matrix (2-35% of the total counted points in samples, averaging 18%) (Fig. 6.17) mainly consists into pseudomatrix of crushed and squeezed mudstone and devitrified volcanic grains that form primary matrix. Detrital intergranular epimatrix consists into cryptocrystalline silica and clay aggregates related to dissolution of the mudstone and devitrified volcanic clasts between other lithic grains (*sensu* Dickinson, 1970).

Authigenic cement occluding primary intergranular porosity commonly consists into diagenetic microsparite and blocky sparry calcite (large single crystals), and minor occurrence of drusy calcite around some grains (2-44% of the total counted points in samples, averaging 17%). Less commonly cryptocrystalline and microcrystalline quartz cement occur (represent up to 9 % of the total counted points in only two samples) and scarce authigenic quartz overgrowths can be found. Secondary intragranular porosity formed with diagenetic alteration of chemically unstable grains includes feldspar grains and early cementation calcite filling, and abundant devitrification features in volcanic lithic grains with replacement by clay minerals, fibrous chalcedony and zeolite and meso- to crypto- and microcrystalline quartz. The presence of authigenic quartz is consistent with burial temperatures > 80° (Walderhaugh, 1994) which could reach between 175 and 200° in the study area and in subsurface of the southern Neuquén Basin (Suárez and González, 2018).

6.5. Analysis of compositional stratigraphic trends

Sandstone samples were plotted on standard QtFL, QmFLt and QmKP diagrams to emphasise provenance (Fig. 6.22 and Table 6.2). In the QtFL

provenance diagram (Dickinson et al., 1983), samples plot in the recycled orogenic field. In the QmFLt diagram (Dickinson et al., 1983), 5 samples plot in the transitional continental field (1 sample of the J1.1 sequence, 2 samples of the J1.2 sequence, 2 samples of the J2.1 sequence), 6 samples plot in the mixed field (1 sample of the J1.1 sequence, 2 samples of the J1.2 sequence, 3 samples of the J2.1 sequence) and 4 in the dissected arc field (2 samples of the J1.2 sequence, 2 samples of the J2.1 sequence). In the QmKP provenance diagram (Dickinson and Suczek, 1979) detrital modes of all sequences are located in the transitional recycled orogen field.

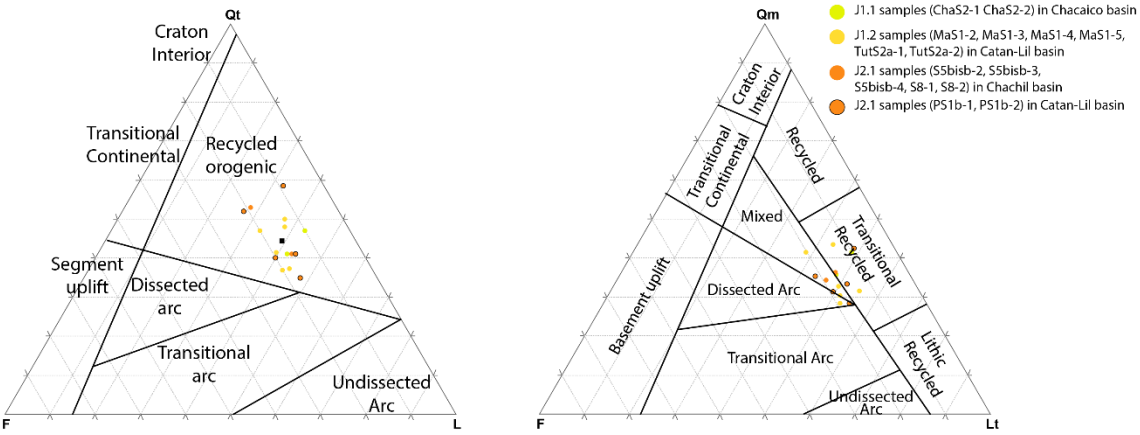

Figure 6.22: Standard provenance diagrams of QtFL and QmFLt to emphasise provenance (Dickinson, 1983).

The ternary diagrams do not permit to highlight any major change of source and such detailed analysis must be complemented with bulk-sediment, multi-mineral and single mineral analysis (Garzanti, 2016). The changes in proportions of types of quartz, feldspars, volcanic, metamorphic and sedimentary lithics permitted to identify several discrete changes of detrital composition within and across sequences. Therefore the changes of framework grains are analysed based on variations of average percentages calculated for each classes by sequence (Fig. 6.23) and based on comparative curves for the total of grains counted by samples in sequences (Fig. 6.24).

Non-undulatory and unstrained monocrystalline quartz, which can be associated with extrusive igneous (basalt, andesite, rhyolite) and pyroclastic rocks (Blatt and Christie, 1963), is consistently found in larger proportions than other monocrystalline or polycrystalline quartz grains. Other monocrystalline quartz grains include grains with an undulatory extinction associated with

provenance from low-grade metamorphic rocks (Basu et al., 1975) and quartz grains with vesicles and partial resorption embayments associated with a volcanic origin. The significant stratigraphic diminution of monocrystalline quartz (average J1.1=27.3%, J1.2=19.1%, J2.1=19.2%) is mainly related to the decrease of non-undulatory quartz grains (average J1.1=19.21%, J1.2=15.77%, J2.1=13.72%) and of spherulitic volcanic quartz grains with vesicles (average J1.1=0.32%, J1.2=0.32%, J2.1=0.16%) (Figs 6.23 and 6.24).

This evolution, is coeval with the increase of undulatory quartz (average J1.1=7.9%, J1.2=3.46%, J2.1=5.37%) and polycrystalline quartz (average J1.1=3.9%, J1.2=5.1%, J2.1=5.9%) (Figs 6.23 and 6.24). The abundance of non-undulatory monocrystalline quartz as a framework grain, even if its proportions decreases stratigraphically, might be associated with recycling of volcanic rocks but given that these grains are often associated with second sedimentary cycle they should not be used solely to infer source rock (Blatt and Christie, 1963). However, its decrease is correlated with the decrease of spherulitic quartz and volcanic lithics (average J1.1=23.3%, J1.2=16.3%, J2.1=15.2%), suggesting recycling from volcanic source rock (Precuyano Cycle deposits) and might record a diminution of palaeovolcanic source rock contribution through time (Figs 6.23 and 6.24).

Undulatory and less stable polycrystalline quartz grains, which are more prone to mechanical breakdown can provide indication on the type of plutonic or metamorphic source rock, and their stratigraphic increase indicate enrichment in immature grains of primary sedimentary cycle. There is a stratigraphic increase of undulatory monocrystalline quartz and coarse-grained polycrystalline quartz (average J1.1=1.5%, J1.2=1.5%, J2.1=3.8%) over fine-grained strained polycrystalline quartz (average J1.1=2.37%, J1.2=2.69%, J2.1=2.85%) (Figs 6.23 and 6.24). Both undulatory monocrystalline and coarse polycrystalline quartz might reflect a plutonic origin, whereas fine polycrystalline quartz is more likely to have a low- to medium-grade metamorphic origin (Blatt et al., 1980). Therefore, the stratigraphic evolution in immature quartz grain proportions should record an increase in plutonic source contribution, with a relative decrease of metamorphic source contribution. This could be related with variable proportions of metamorphic lithics (found in low proportions) from J1.2 to J2.1 (average J1.1=0.2%, J1.2=0.5%, J2.1=0.3%), mainly dominated by slate and phyllite

grains indicative of a low-grade metamorphic rock provenance (Figs 6.23 and 6.24).

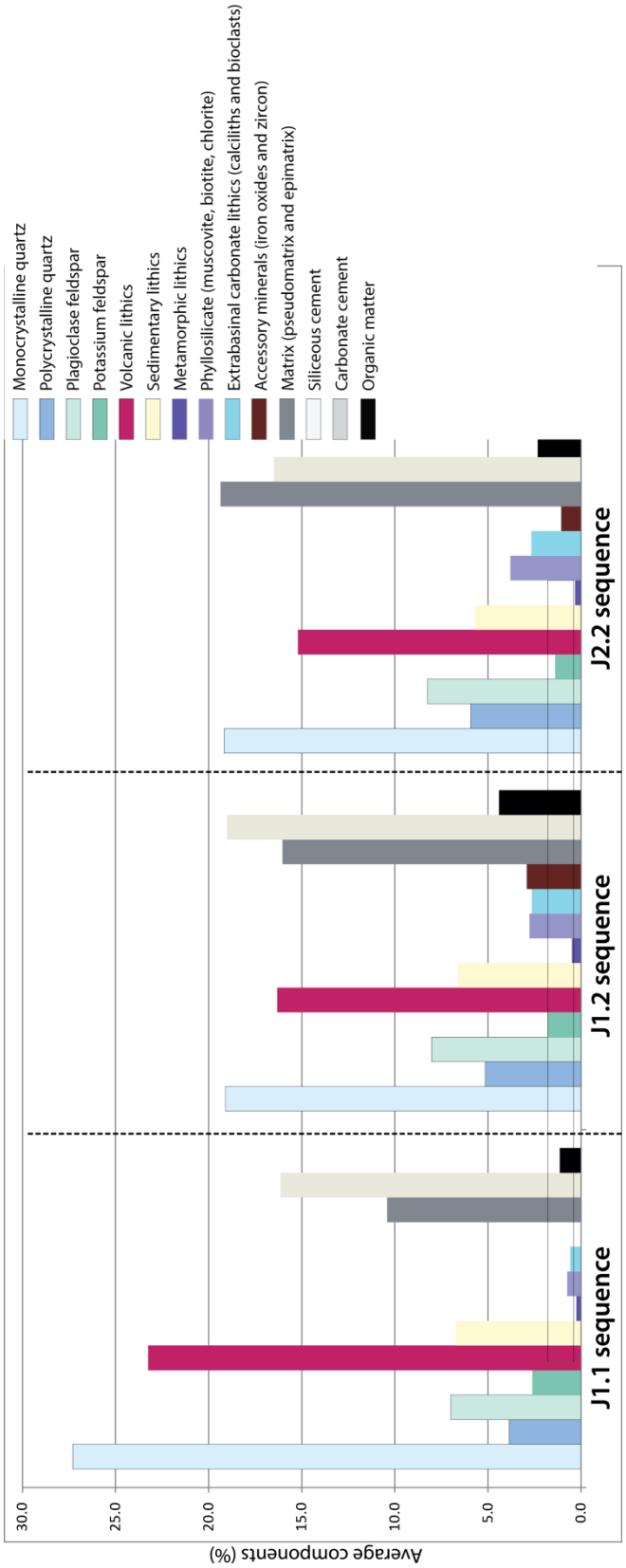

Figure 6.23: Histogram showing the distribution of average percentages of component grain classes (see Appendix 6-7-8) for each sequence highlighting the compositional variability.

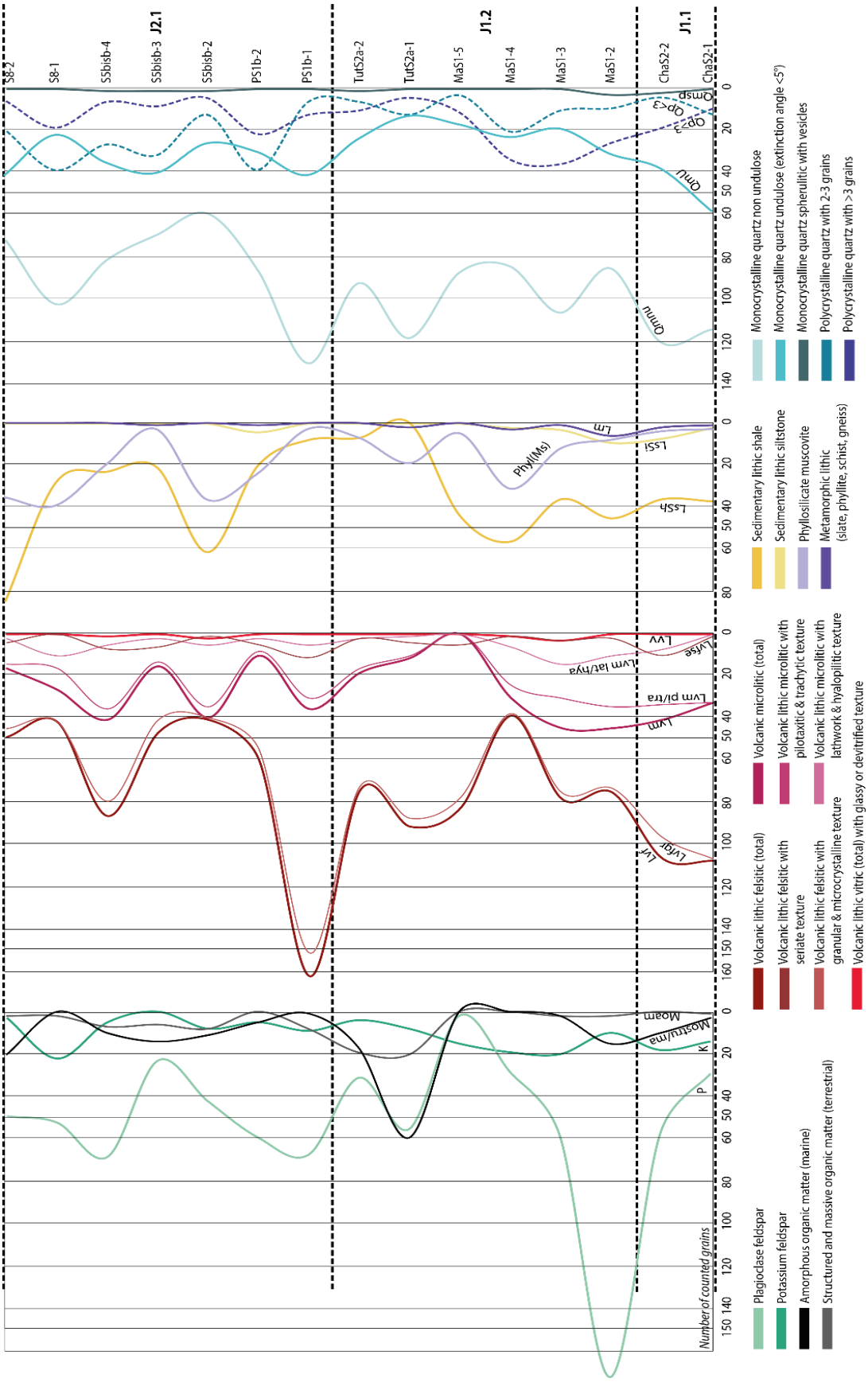

Figure 6.24: Composition curves of specific types of grains of component grain classes.

The stratigraphic increase of phyllosilicates (especially muscovite) (average J1.1=0.7%, J1.2=2.8%, J2.1=3.8%), which are virtually absent of the J1.1 sequence and increase from J1.2 to J2.1 sequence, with undeformed or foliated aspect, should reflect a plutonic origin. The fragile nature of micas flakes could explain their destruction in a high-energy deltaic environment associated with the J1.1 sequence. However, the combined increase of coarse polycrystalline quartz, micas and occurrence of feldspar grains with intergrowth textures of quartz and feldspar (myrmekite, perthite) are characteristic of acid plutonic rocks, support the increase of plutonic source rock provenance. This is also consistent with the high proportions and stratigraphic increase of plagioclase feldspar (J1.1=7%, J1.2=8%, J2.1=8.2%), which could be associated with crystalline plutonic rocks or with acid to intermediate volcanic rocks. In contrast, the proportions of potassium feldspar, including microcline characteristic of upper crustal felsic plutonic rocks, tend to decrease stratigraphically (average J1.1=2.6%, J1.2=1.8%, J2.1=1.4%) and might reflect their propensity for chemical weathering at source (Figs 6.23 and 6.24).

The proportion of felsitic volcanic lithics is large, but with a stratigraphic decrease from sequence J1.1 to J1.2 and J2.1 (average J1.1=17.3%, J1.2=11.7%, J2.1=11.1%) (Figs 6.23 and 6.24). In contrast, the microlitic volcanic lithics decrease moderately (average J1.1=6.5%, J1.2=4.5%, J2.1=4.2%) and vitric lithics, which are in minor proportions due to devitrification processes, show a slight increase (average J1.1=0%, J1.2=0.4%, J2.1=0.2%). The high proportions of felsitic volcanic lithics with granular textures (Fig. 6.24) suggest a main silicic volcanic source typical of dacite and rhyolite, whereas seriate textures indicate a subordinate intermediate volcanic source typical of dacite and andesite (Dickinson, 1970; Critelli and Ingersoll, 1995). This is consistent with dominance of microlitic volcanic grains with pilotaxitic and trachytic textures indicative of intermediate volcanic source typical of andesite, and subordinate lathwork and halopilitic textures, suggesting intermediate to basic volcanic source typical of andesite and basalt. The vitric volcanic grains and pyroclasts are absent from the J1.1 sequence and appear in the J1.2 and 2.1 sequences (Fig. 6.24). The remnant of yellowish-brownish, non-vesicular sideromelane glass reflects palagonitisation and permits to infer an intermediate to mafic magma chemistry characteristic of basalt and andesite (Marsaglia and Ingersoll, 1992). However, abundant devitrification and dissolution features affected most of the chemically

unstable pumice, tuffaceous and glassy vitric volcanic grains but also felsitic grains, with replacement by authigenic silicates and siliceous minerals (fibrous chalcedony or crypto- to microcrystalline chert). These processes reduced the proportions of volcanic lithics at the expense of metamorphosed volcanic grains and contributed to increase the proportion of authigenic epimatrix in sandstone. The paucity of fresh angular grain edges or fluidal morphologies (welded or banded textures, well-preserved cuspate or platy glass shard shapes) and preservation of minor broken vitric fragments (including palagonitic sideromelane glass), together with the tractive sedimentary structures and grading, attest of emplacement by cold flows and abrasion of volcanic grains with transport (Fisher and Schmincke, 1984). The heterogeneity of composition and grain-size of polymictic epiclastic volcanic grains, their normal alteration, subangular to subrounded grain morphology and similar grain-size as non-volcanic terrigenous grains points a dominant non-coeval origin, with erosion of volcanic bedrock (White and Houghton, 2006).

The felsic components (colourless glass, monocrystalline quartz, felsitic grains) are found in major quantities in syn-rift deposits associated with bimodal magmatism (Marsaglia and et al., 1995) and could reflect recycling of bimodal palaeovolcanic deposits of the Precuyano Cycle (Bermudez et al., 2002; Muravchik et al., 2011; D'Elia et al., 2018). The high content of such acidic volcanic fragments, which has been recognized in sandstones the Los Molles Formation of the Chacaico Basin (J1.1 sequence) has been interpreted as sourced from the Marifil formation based on compatible zircon isotope signatures (Naipauer et al., 2018). These deposits formed the Chon Aike Igneous Province, which developed with intraplate magmatism in the extra-Andean Patagonia in the North Patagonian Massif ~100 km south of the study area (Naipauer et al., 2018). However, the relatively stable amount in microlitic volcanic lithics in sandstone precludes a purely felsic source and indicate admixed felsic and intermediate-mafic composition provenance (Fig. 6.24).

The composition of volcanic grains and their stratigraphic evolution could reflect erosion of bimodal volcanic products associated with subaerial felsic volcanic centres developed with extension across the dissected volcanic arc (Marsaglia et al., 1991). This would be consistent with supply from Early Jurassic deposits described across the Early Andean volcanic island arc including subaerial andesitic-dacitic volcanoes, which coexisted with intermediate-silicic

composition calderas located ~30 km west from the study area (e.g De la Cruz and Suárez, 1997). The presence of preserved angular vitric fragments (basaltic glass) and other pyroclastic particles suggest potential reworking of neovolcanic grains (Critelli and Ingersoll, 1995), which might be related to explosive arc magmatism (Marsaglia and Ingersoll, 1992). Additionally, the very low proportions of vitric grains might be underestimated due to devitrification and replacement by authigenic phases. Similarly, the high proportions of felsitic granular volcanic grains could be a product of post-burial devitrification of felsic glass and/or could reflect the sensitivity of mafic or vitric volcanic lithics to weathering and breaking during transport (Critelli et al., 2002). Therefore, the possibility that the high content in monocrystalline quartz and felsitic volcanic grains (especially with granular texture) (Fig. 6.24) could reflect the proximity to a felsic-dominated volcanic source bedrock is taken with caution here, as enrichment in felsic grains could be a function of weathering and transport or devitrification processes.

The sandstones indicate a mixed source composition of volcanic and magmatic arc basement (metamorphic and granitic plutonic) consistent with the scatter of samples plotted across three different provenance fields in the QmFLt diagram (Fig. 6.22). The overprint of diagenetic alteration onto detrital composition is moderate and mainly consists of dissolution of chemically unstable grains (aphanitic volcanic and shale lithics), whereas the feldspar and micas crystals are often well preserved, meaning that the proportions of volcanic grains might be underestimated (Fig. 6.24). Additionally, the proportions of shale lithics also might be underestimated given that they were transformed into pseudomatrix with mechanical compaction. If included in the category of sedimentary lithics it would shift the provenance field of the sandstones to the transitional arc field, both in the QtFL and QmFLt diagrams (Fig. 6.22). The detailed analysis of component grains permitted to highlight mixing and overwhelming of volcanic source with increased plutonic, and minor metamorphic basement source contribution recorded from sequence J1.1 to J2.1, enabling to discuss a potential change of source provenance from J1.1 to J1.2-2.1 sequences.

6.6. Discussion

6.6.1. Source provenance

The compositional modes identified in the three sequences J1.1, J1.2 and J2.1 of the Early Jurassic Los Molles Formation indicate high monocrystalline quartz, volcanic lithics (dominated by felsitic grains) and feldspar plagioclase content, with subordinate sedimentary lithics (shale and siltstone) and polycrystalline quartz (Figs 6.17 and 6.23). The sandstone are compositionally immature, including both high proportions of both stable monocrystalline quartz and microcrystalline felsitic volcanic lithics, and unstable aphanitic volcanic lithics, polycrystalline quartz, feldspars and micaceous crystals (Fig. 6.24). Sandstones are also texturally immature, with average matrix content in sequences ranging from 10 to 20%, with dominant subangular to angular grain shapes and poor to very poor sorting (Fig. 6.9 and Table 6.1). These characteristics, together with the presence of delicate amorphous organic matter and structured plant debris suggest a moderate physical grain abrasion during transport, and therefore relatively short transport distance from the source.

The J1.1 sequence shows higher proportions of monocrystalline non-undulatory and spherulitic quartz grains than the J1.2-2.1 sequences which have higher proportions of monocrystalline undulatory quartz and coarse polycrystalline quartz. This stratigraphic increase of immature grains is associated with an increase of phyllosilicates micaceous and feldspar grains with intergrowth textures from J1.1 to J1.2-J2.1 sequences. In addition, the J1.1 shows higher amounts of felsitic over microlitic volcanic lithic grains and higher proportion of felsitic grains in comparison with J1.2-2.1 sequences which record a slight increase of vitric and pyroclastic volcanic lithic grains. This evolution might reflect a change of source from dominant bimodal palaeovolcanic syn-rift and metamorphic rocks of cratonic basement, with subordinate decrease of metamorphic rocks sourced material at the expense of acidic plutonic rocks of magmatic arc basement (Fig. 6.25). The depositional setting and more mature compositional and textural characteristics of the J1.1 sequence suggests sediment source from the North Patagonian Massif hinterland and development as part of a SW-NE oriented deltaic system along-strike the southern margin of the Neuquén Basin (cf. Gómez Omil et al., 2002) (Fig. 6.25). This is consistent

with the N-NW palaeocurrents recorded by delta-front deposits of the J1.1 sequence and N-NE palaeocurrents recorded by intraslope fan deposits of the J1.2 and 2.1 sequences. In contrast, the immature compositional and textural characteristics of sandstone of the J1.2-2.1 sequences provide little support for a mature (secondary cycle) cratonic signature represented by metamorphic highlands of the North Patagonian Massif (cf. Rosenfeld and Eppinger, 1993; Burgess et al., 2000).

The signature of basement source with a stratigraphic increase of immature grains (first sedimentary cycle) from sequence J1.1 to J1.2-2.1 and compositional trends should reflect a change of source. The J1.2-2.1 sequences would record sediment supply with denudation of the magmatic arc batholith, with progressive unroofing of plutonic arc roots as a result of subduction-triggered uplift and exhumation (Marsaglia and Ingersoll, 1992) (Fig. 6.25). The compositional immaturity of sandstones in J1.2-2.1 sequences indicate a relatively low degree of chemical weathering associated with a short residence time in the drainage basin, despite the development of a humid climate since the early Late Toarcian (Volkheimer et al., 2008) that could have promoted weathering of chemically unstable grains. This immaturity might be also related to low storage time of sediment on the shelf, with limited exposure to hydrodynamic processes of high-energy coastal environment, with coeval growth of a magmatic arc system and back-arc subsidence involving sediment transport from short watersheds.

The different source provenances and depositional environments are consistent with enhanced preservation of organic matter in the intraslope fans of the J1.2-2.1 sequences rather than in the delta-front deposits of the J1.1 sequence (average J1.1=1.1%, J1.2=4.4%, J2.1=2.3%) (Fig. 6.22). This could reflect the difference of depositional environment, as a function of oxygenation and sedimentation rate, consistent with high sediment supply rates and rapid burial after depositional under oxygen-poor and low-energy conditions in intraslope fans. Similarly, the increase of matrix content in sandstone from delta-front to intraslope fan deposits (average J1.1=10.4%, J1.2=16%, J2.1=19.4%, including all samples by sequence) (Fig. 6.22) might reflect more intense reworking of grains and cleaning of sandstone in a higher energy environment for delta-front sandstone than for intraslope fan sandstone (Fig. 6.25). The overall stratigraphic increase of calcareous cement proportions in samples (average

J1.1=7.4%, J1.2=19%, J2.1=16.5%) could be related to the preservation or dissolution of carbonate intrabasinal grains (average J1.1=0.6%, J1.2=2.6%, J2.1=2.7%) (Fig. 6.22). There might also be a proximal-distal stratigraphic trend well recorded in the J1.2 sequence, which reveals a change of composition with selective transport and increase of terrestrial blade-shaped phytoclasts and decrease of polycrystalline quartz and shale grains (Fig. 6.24). This could reflect the higher buoyancy of organic matter fragments (Tyson, 1995) and the mechanical breakdown of fragile grains with longer transport distance recorded at sequence scale.

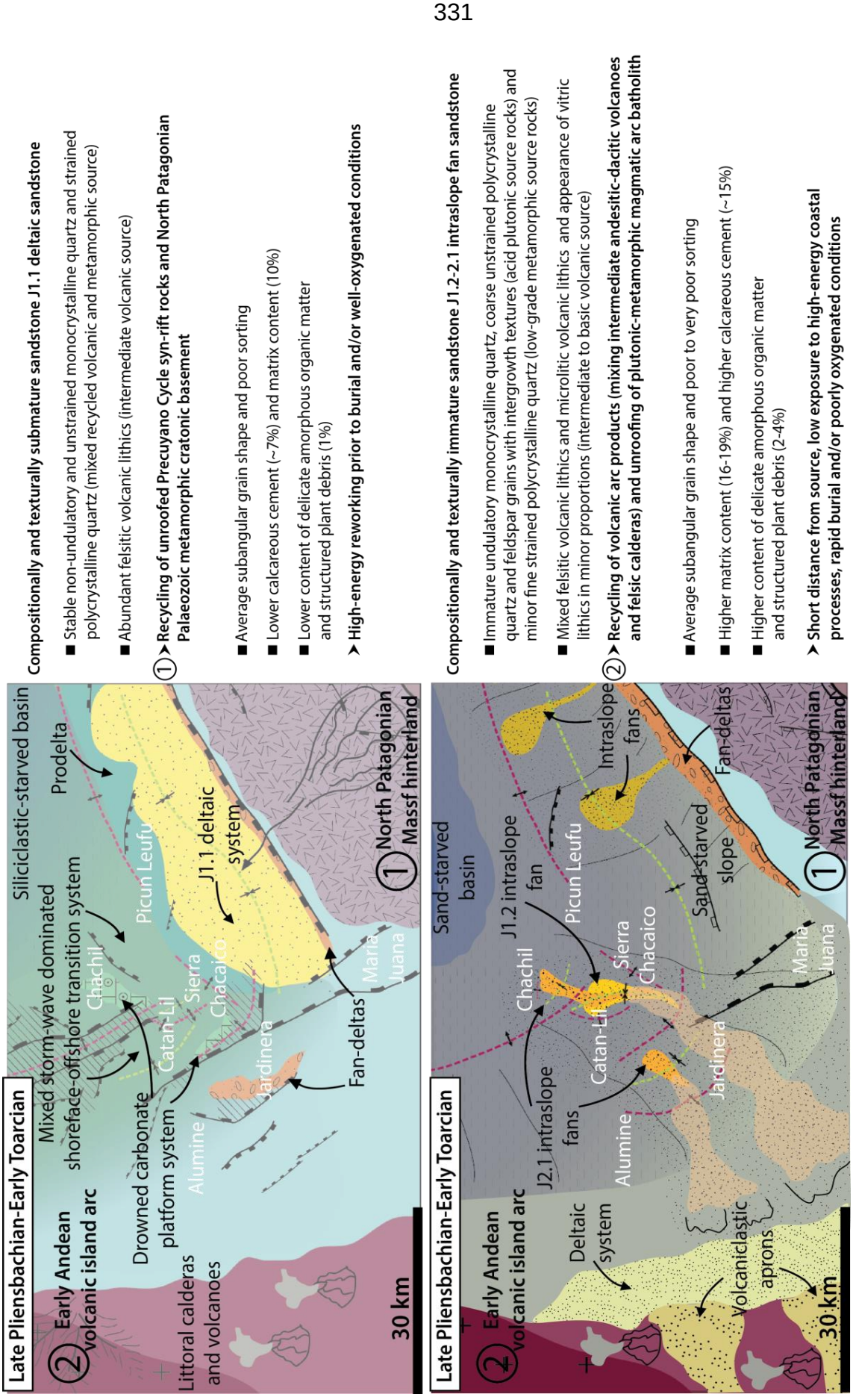

Figure 6.25: Palaeogeographic evolution maps showing the development of the J1.1 deltaic system and of the J1.2 and 2.1 intraslope fan system with their respective sediment sources and petrographic characteristics.

6.6.2. Implications for sediment supply from the Early Andean volcanic island arc margin

The two investigated intraslope fans (J1.2-2.1 sequences) of the Early Jurassic Los Molles Fm. consist into compositionaly and texturally immature sandstone (matrix-rich or matrix-poor) point to dominant deposition by relatively high efficiency, high-concentration flows respectively, with dampened turbulence (e.g clay-rich transitional plug flows and low strength sandy debris-flows) or with enhanced turbulence. The mud matrix content highlighted in sandstone lobes of the J1.2 (~18%) and J2.1 (~27.2%) sequences contrast with the sandstones described by Paim et al. (2008) in the La Jardinera depocentre (Fig. 6.1). The La Jardinera sandstones were described as having a clean texture and very fine-grained sandy matrix lacking the silt and clay sediment fraction, but with abundant mudstone clasts. The lack of fine-grained sediment fraction has been interpreted to reflect flow separation at the mouth of distributary channels and deposition by poorly efficient flows (Paim et al., 2011). Instead, the sandstone characteristics support a weak flow capacity for sorting and flow ignition, consistent with deposition across a moderate to gentle slope in a ramp-type setting that lacked slope channels, which could segregate the fine sediment fraction through flow stripping and overspill. The lack or poorly developed feeder conduits across the slope also implied a reduced sediment transport distance and sediment storage across the slope.

Ramp-type basin margins tend to develop small-scale and shallow gullies at the shelf edge, which deepen and widen with increased sediment supply and/or flow volume and erosional strength of delta-front sourced flows (Surlyk and Noe-Nygaard, 2001; Sanchez et al., 2012; Prélat et al., 2015). Flows could have initiated via gravitational resedimentation of deltaic deposits fringing the structural narrow shelf, which limited capacity for sediment storage and might have promoted accumulation of critical amounts of sand and enhanced sediment supply independently of relative sea-level change (Burgess and Hovius, 1998; Helland-Hansen et al., 2012; Strachan et al., 2013). In these conditions, sediment supply could occur with destabilization of coastal deposits accumulated with abruptly decelerating hyperpycnal flows at river-mouths, with sediment-laden surface river plumes exiting river-mouths with sediment settling and reconcentration, triggering dense turbulent underflows (Parsons et al., 2001;

Clare et al., 2016). None of the observed sandstone deposit indicates deposition by sustained flows with fluctuating waxing-waning behaviour, characteristic of direct river-fed hyperpycnal flows with exceptional sediment concentrations that can directly plunge downslope as they overcome the higher seawater density (Mulder et al., 2003).

Tectonic uplift and widening of the growing Early Andean volcanic island arc, with accumulation of several kilometre-thick volcaniclastic successions, might have permitted sediment supply of primary and reworked epiclastic or volcaniclastic material in Early Jurassic intra-arc and marginal arc basins (Fig. 6.25). Submarine shelves and slopes bounding volcanic arcs are characterized by rapid accumulation rates of sediments with high excess pore-fluid pressures prone to gravitational resedimentation with frequent slumping and mass flows. Therefore, sediment failure could be induced with cyclic wave loading and erosion (Noda and Tuzino, 2007; Horikawa and Ito, 2009), earthquakes, dynamic topographic uplift, or collapse related to magma intrusion and extrusion and slope steepening with rapid aggradation of volcanic deposits (Schneider, 2000; Watt et al., 2014). This would have been combined with frequent subaqueous and subaerial eruptions of andesitic-dacitic volcanoes, which coexisted with intermediate-silicic calderas (e.g De la Cruz and Suárez, 1997).

The large volume of volcanic sediment supply during eruptions could generate eruption-fed pyroclastic density flows discharges into the sea and ash fallout (Cas and Wright, 1991). Syn- and post-eruptive weathering, erosion transport and reworking of volcanic sediments by deltaic systems might have promoted rapid accumulation and destabilization across the narrow shelf bounding the Early Andean volcanic arc at ~30-50 km from the study area (De la Cruz and Suárez, 1997) (Fig. 6.25). This could produce sediment gravity flows laden with reworked volcaniclastic material, which could carve slope gullies (Chiocci and Casalbore, 2011; Carey and Schneider, 2011). The rapid segregation of volcanic particles into sand and mud that forms cohesive matrix could enhance entrainment of slope material along with transport (Watt et al., 2014). In these flows, the high-suspended clay content might have reduced the difference of density between interstitial water and fines and the coarser-grained particles, and played an important role in delaying settling velocities for coarse-grained sediment fraction and increasing flow run-out distance (Gladstone et al., 1998; Gardner et al., 2003; Al Ja'Aidi et al., 2004).

6.6.3. Stratigraphic architecture of intraslope fans of the Los Molles Formation

6.6.4. Change recorded within an intraslope fan sequence (J1.2)

The stratigraphic evolution from the lower distal ramp to upper proximal ramp lobe complexes recorded within intraslope fan J1.2 in the Eastern Catán-Lil Basin includes an increase of lobe complex dimensions and in sand: mud ratio and a change from unorganized stacking patterns to organized progradation and aggradation with lobe complex compensation (Fig. 6.3). This evolution reflects a change of deposition across an irregular to smoothed seabed topography, which permitted development of wider, longer and thinner lobe complexes. The differences in petrofacies and characteristics of lobe complexes (dimensions, termination style, stacking patterns, facies, combined flow bedforms and bed-scale heterogeneity) which have been described are consistent with changes in stratigraphic architecture (Fig. 6.3).

At lobe-scale, the stratigraphic increase in grain-size and bed thickness, and change in facies with decrease in detrital mud matrix content in sandstone suggest deposition with an increase of flow volume and decrease in flow efficiency from distal to proximal ramp lobes. A decrease in flow efficiency could be related to less erosive flow behaviour, which incorporated less muddy substrate material admixed as fine-grained particles in the flows, or to erosion of a more compact substrate incorporated into flows as durable clasts consistant with textural changes and variation of clast content from distal to proximal ramp lobes. Increase in flow volume would require an increase in sediment supply rate and/or decrease of flow run-out distance from their main sediment source. An increase in sediment supply rate could be driven by a change at source, with increase of catchment size or change of catchment bedrock type increasing erodibility and sediment flux, climate change increasing precipitation and erosion rates and/or increased volcanic sediment production (Leeder et al., 1998; Collier et al., 2000; Garzanti et al., 2001; Schneider et al., 2016). The similar composition modes in the J1.2 sequence do not support changes of source, and cannot be related to climatic change towards more humid conditions which occurred after deposition of the J1.2 sequence, in the Late Toarcian (Volkheimer et al., 2008).

A complementary aspect to consider is the maturation of sediment routeing pathways throughout intraslope fan development (unchannelized versus channelized flows), which could have both led to a decrease of flow efficiency and an increase of flow volume. Initial high efficiency unchannelized flows undergoing erratic routeing pathways and lengthening of conduits through time could explain the initial stage of intraslope fan development recorded by the dirty matrix-rich lobe complexes of distal ramp, analogous to frontal or disconnected lobes from other systems (e.g. Gutiérrez Paredes et al., 2017; Shumaker et al., 2018). These flows might have entrained an uncompacted fine-grained substrate, incorporated in flows as watery soft muddy substrate easily admixed into flows as clay flocs promoting flow cohesion and transformation (Baas et al., 2009) well-recorded by the dirty lobe facies. Subsequent cleaner matrix-poor lobe complexes of the proximal ramp developed across a subdued seabed relief, with an increase of sediment supply rate which could reflect progressive channelization of flows through slope gullies and deposition proximal to the feeder channel-mouth until system retreat and abandonment.

In ramp-type systems, sand supply and accumulation across the proximal ramp is dependent upon delta-front progradation and shelf width, and determines the timing for deltas to reach the margin and therefore for sediment supply or trapping across the shelf (Heller and Dickinson, 1985; Burchette and Wright, 1992; Helland-Hansen, 2012). Therefore, the stratigraphic evolution recorded by the intraslope fan J1.2 would be consistent with the interpretation of vertical stacking of clean above dirty lobe complexes as a result of intraslope fan progradation, which might also reflect the distal signature of delta progradation at the shelf-edge along the Early Andean volcanic island arc basin margin (cf. Chapter 5). This evolution might involve a maturation of routeing pathways across the slope which might be related with the recorded variation of flow type and behaviour (efficiency, volume, stratification) with an increase in flow energy and capacity in the deposits from the precursor distal to proximal ramp lobe complexes.

6.6.5. Change recorded across intraslope fan sequences (J1.2-J2.1)

Intraslope fans recorded the evolution of the system with influence of topography on the sediment partitioning, reflected in their stratigraphic architecture and facies.

Relief interacted with flows inducing a certain confinement at lobe complex-scale and acting as palaeogeographic barriers which controlled the timing for linkage of sandy depocentres across basins through time (Fig. 6.3). Inherited topography was an important control on individual lobe complex pinchout style, reflecting the development of each intraslope fan with stratigraphic decrease of confinement. This is well-recorded at scale of the J1.2 intraslope fan, by the change from abrupt pinchout with common clastic injectites characteristic of distal ramp lobe complex terminations, to convergent onlap with common lateral bedform development or frontal enrichment in matrix-rich sandstone characteristic of proximal ramp lobe complex terminations. In the J2.1 intraslope fan, lateral lobe complex margins are characterized by erosive pinchout with scouring, widespread HEBs and bedform development, whereas frontal lobe complex margins show a more gradual pinchout of HEB-rich thin-bedded sandstone that offset abrupt thick HEB pinchout (cf. Chapter 4). Therefore, differences in lobe complex dimensions and termination styles between the J1.2 and J2.1 intraslope fans suggest development of the J2.1 intraslope fan with stronger confinement by intrabasinal relief and basin margins. This pattern is consistent with the overall evolution of sandy depocentre linkage across inherited rift basin topography (cf. Chapter 5).

The progressive healing of intrabasinal topography of the Eastern Catán-Lil depocentre during deposition of the J1.2 intraslope fan promoted overspill, and subsequent bypass and progradation of the J2.1 intraslope fan from the Eastern Catán-Lil to the downdip Chachil basins. This is consistent with the stratigraphic facies changes at the scale of both J1.2 and J2.1 intraslope fans, with an evolution from dirty matrix-rich to cleaner matrix-poor sandstone and coarsening upwards trend, both associated with individual fan progradation. Additionally within the J2.1 intraslope fan, some proximal to distal differences apply as sandstone lobes in the proximal Eastern Catán-Lil Basin, tend to be coarser-grained and with lower matrix content than the HEB-rich sandstone lobes deposited downdip in the Chachil Basin, after bypass across seabed relief. This

suggests that the stratigraphic distribution of bed-scale heterogeneity is associated with development of lobes across inherited intrabasinal relief until healing of topography, recorded both from base to top and from proximal to distal part of the J2.1 intraslope fan.

Facies change is also observed at larger-scale across several depocentres from J1.2 to J2.1 intraslope fans, which record a marked coarsening of sediment grain size up to granule- and very coarse-outsized grains, and increase of mudstone clast content at the expense of siltstone clasts and bioclasts and in average matrix content in sandstone (~18% matrix content in J1.2 sequence and ~27.2% matrix content in J2.1 sequence). Sediment composition and palaeoflows permitted to consider a potential source area to the southwest, along the volcanic arc which was bounded by fan-deltaic systems and volcaniclastic aprons (De la Cruz and Suárez, 1997) (Fig. 6.25). However, given the consistent composition of sediments, the increase in grain-size is unlikely to be driven by a change of bedrock lithology. Alternatively, this could have resulted from changes in climate towards more humid conditions during the early Late Toarcian, with increasing precipitation and erosion rates (Volkheimer et al., 2008), and/or with an increase in slope gradient favouring the transport of coarse-grained particles farther from the source (Strachan et al., 2013), which could have been triggered with enhanced subsidence and source uplift. An increase of slope gradient could be consistent with progressive effect of slope healing and aggradation-progradation of the system, until the development of a proper shelf-break during the Aalenian (cf. Brinkworth et al., 2018). Progressive slope steepening through time with the combined uplift and growth (widening) of the active magmatic arc, together with increase of adjacent back-arc subsidence, might have promoted progradation of the ramp-type system and the stratigraphic change observed from J1.2 to J2.1 intraslope fan facies characteristics.

Conclusion

The petro-stratigraphic evolution of the compositional and textural characteristics of Early Jurassic sandstone of the Chacaico and Los Molles Fm. and palaeocurrent constraints suggest different extrabasinal source contribution. The late syn-rift deltaic sandstone (Chacaico Fm.) were likely sourced from southeastern hinterland along the cratonic basin margin. In contrast, early post-rift intraslope fans sandstone (Los Molles Fm.) might record a distal signal of arc-related volcanogenic sediment production, with reworking and supply from multiple source ramp system along the southwestern narrow shelf flanking the Early Andean volcanic island arc. Petrographic work, although focused on provenance, permitted to identify a better potential reservoir quality for late syn-rift deltaic sandstone sourced from the cratonic basin margin (North Patagonian Massif) than for early post-rift intraslope fan sandstone sourced from the magmatic arc basin margin.

The two investigated intraslope fans consist into compositionaly and texturally immature sandstone (matrix-rich or matrix-poor) is consistent with their deposition in a ramp-type setting by relatively high efficiency, high-concentration flows with a weak flow capacity for sorting and flow ignition. The overall stratigraphic changes in individual facies and characteristics of lobe complexes (dimensions, termination style, facies, combined flow bedforms and bed-scale heterogeneity) in Early Jurassic intraslope fans of the Los Molles Fm. are not related to a change of source, but to their stratigraphic evolution with evolving topography. The stratigraphic evolution recorded by the intraslope fan J1.2 with vertical stacking of clean above dirty lobe complexes reflects intraslope fan progradation. Facies characteristics of distal ramp matrix-rich lobe complexes are associated with initial high efficiency unchannelized flows undergoing erratic routeing pathways across the slope. Characteristics of subsequent proximal ramp matrix-poor lobe complexes record progradation of the system with progressive channelization of flows through slope gullies and increase of sediment supply rate. The facies changes (increasing grain-size, bed-scale heterogeneity and matrix-scale heterogeneity) recorded from J1.2 to J2.1 intraslope fan is associated with progradation of the ramp-type system and healing of slope topography across basins. Progradation of the system is interpreted to reflect

maturation of routeing pathways across the slope and progressive slope steepening through time promoted by the combined uplift and growth (widening) of the active Early Andean magmatic arc, together with increase of adjacent back-arc subsidence.

Finally, the distribution of bed-scale heterogeneity and termination style of lobe complex margins points to development of J1.2 and J2.1 fans with changing confinement and interactions of seabed relief with flows depending on deposition across underfilled or healed seabed topography. Therefore, the two intraslope fans, despite having similar composition and provenance, can show markedly different facies distributions across lobes and bed-scale heterogeneity development, and termination style at lobe complex margins. This have implications for predicting the types of stratigraphic traps and reservoir quality and can be used for analog early post-rift sandy systems developed across above-grade slopes inherited from rift basin physiography.

Chapter 7 Discussions and conclusions

This study aimed to (i) refine and extend established models of sedimentation in marine rift basin-fills, discuss the interplay of controls during the syn- to post-rift transition, and (ii) develop models for early post-rift lobe complexes, from documenting the Early Jurassic stratigraphic record of the Los Molles Formation that is exhumed across several depocentres of the southern Neuqén Basin, Argentina. Here, a series of key over-arching questions are examined, integrating the work covered in chapters 4 to 6.

7.1 What factors controlled the temporal and spatial variability of the syn- to post-rift transition sedimentation?

7.1.1 Intrabasinal topography

At the scale of the several depocentres studied in the southern Neuquén Basin, the detailed stratigraphic architecture, the distribution of interpreted depositional environments, and the stratigraphic evolution of sand-rich systems identified: (i) a late syn-rift delta-front setting related to the Huincul High shelf-slope system (invetsigated in the Chacaicop Basin), and (ii) an early post-rift deep-marine slope setting as part of a ramp-type system (investigated in the Catán-Lil and Chachil Basin) (Fig. 7.1). The first system was developed obliquely or transverse to the dominant NW-SE orientation of rift structures, whereas the second one was axial to rift structures. Both systems highlight the influence of inherited topography at depocentre-scale on flow routeing and sediment dispersal and stacking patterns. At regional-scale inherited topography controlled the distribution of depocentres, and led to coarse-grained sediment starvation of some basins until the relief was completely healed, enabling the spatial linkage of sand-rich depocentres.

The major structures that formed inherited relief correspond to pre-rift basement-cored structures that exerted an important control on flow routeing, and therefore late syn-rift and early post-rift sedimentation (cf. Chapter 4 and 5). Furthermore, the orientation of pre-rift structures with respect to the extensional stress field played an important role in the configuration and spatial distribution

of shallow versus deep rift basins (Chacaico versus Chachil or Catán-Lil basins). This impacted late syn-rift and early post-rift thickness led to contrasting basin-fill patterns (Fig. 7.1). Pre-rift structures played a key role providing long-lived inherited seabed relief as they formed preferential sites for differential compaction and related deformation (small-scale faulting, large-scale folding), although these processes could also occur across syn-rift faults bounding major intrabasinal highs (e.g., in the Chachil Basin).

Rift topography controlled the late syn-rift juxtaposition of different contemporaneous depositional environments developed across an irregular topography, until major marine flooding. During the early post-rift, the effects of interbasin highs were recorded in the distribution and architecture of intraslope fan deposits, until the system could fill accommodation and heal the relief (cf. Chapter 5). This introduced the new notion that all early post-rift lobe systems of the Los Molles Formation did not develop synchronously in depocentres. Therefore inherited and/or enhanced topography from pre-rift structures largely influenced the distribution and progradation of intraslope fans, and the timing for spatial linkage of early post-rift depocentres across topography (Fig. 7.1). The orientation of the topographic relief with respect to the main direction of system progradation was key, as flow oblique to parallel relief could change flow pathways, whereas transverse relief could prevent sediment bypass downdip (Prather et al., 2003; Smith, 2004).

Current rift basin models do not integrate the effects of topography on dominantly fine-grained sedimentation, which can control the distribution of prodelta, offshore, and basinal deposits having subtle, but crucial differences for the prediction of spatial source rock distribution (see later discussion on the “base" of the Los Molles Formation) but which also plays a major role in the development of deep-marine sand-rich systems. The present study helps to highlight these gaps in rift basin models, improving their accuracy in the prediction of fine-scale source rock distribution, bed-scale heterogeneity development and reservoir potential, and trap type (stratigraphic versus combined structural-stratigraphic) across multiple adjacent depocentres. The integration of regional stratigraphy across several basins at a regional-scale demonstrates that the onset of the early post-rift occurs with major marine flooding (Fig. 7.1). In contrast with other marine rift basin models, this shows that basin starvation and bathymetric deepening is not the only signature of rift climax or late rift

sedimentation, and that onset of sand supply in a formerly starved rift basin should not be used as a characteristic signature of the immediate post-rift to interpret the syn-to post-rift transition boundary (Prosser, 1993; Ravnås and Steel, 1998). In rift basin models the development of large axial turbidite systems is often related to lingering of sediment supply from local intrasbasinal sources (e.g exposed footwall highs), in an early post-rift basin configuration analog to late syn-rift (e.g Zachariah et al., 2009; Jarsve et al., 2014; Henstra et al., 2016) (Fig. 7.1). Alternatively, when extrabasinal sources are active during the late syn-rift, long-lived large drainage catchments permit to predict the location of subsequent early post-rift depocentres as they form inherited sources (Prosser, 1993; Ravnås and Steel, 1998) (Fig. 7.1). In the study area, the development of early post-rift sandy depocentres occurs after drowning of intrabasinal sources and mud-drapping of intrabasinal reliefs, with onset of extrabasinal sediment supply from the magmatic arc. Basin margin-attached deltaic systems which formed the extrabasinal source established during the late syn-rift, are not sustaining a stable connection with depocentres during early post-rift. Increased back-arc subsidence might have promoted the lateral shift of deltaic source along-strike the cratonic basin margin towards the locus of minimal backarc subsidence away from the magmatic arc which resulted in the cut-off of extrabasinal cratonic source in the study area (Fig. 7.1). Therefore, evolution of rift basins in a back-arc setting involved a rapid spatial and temporal change of extrabasinal source contribution along-strike basin margins in relation to the development of the magmatic arc.

The distribution of early post-rift sandy depocentres across accommodation zones formed by pre-rift inherited structures that segmented the syn-rift depocentres is offset from the locus of volcanic syn-rift and late syn-rift depocentres. The development of early post-rift depocentres is largely controlled by the inherited topography, leading to evolution of adjacent sand-starved underfilled and sand-supplied balance to overfilled rift basins. The stratigraphic variability of the syn- to post-rift transition and distribution of early post-rift sandy depocentres show that adjacent rift basins with similar climatic or tectonic conditions can develop contrasted basin-fill patterns (Fig. 7.1). This is mainly interpreted as a response to the physiographic evolution of rift basin topography through rift evolution, which is largely underemphasised in tectono-stratigraphic

rift basin models (Prosser, 1993; Gabrielsen et al., 1995; Ravnås and Steel, 1998, Gawthorpe and Leeder, 2000).

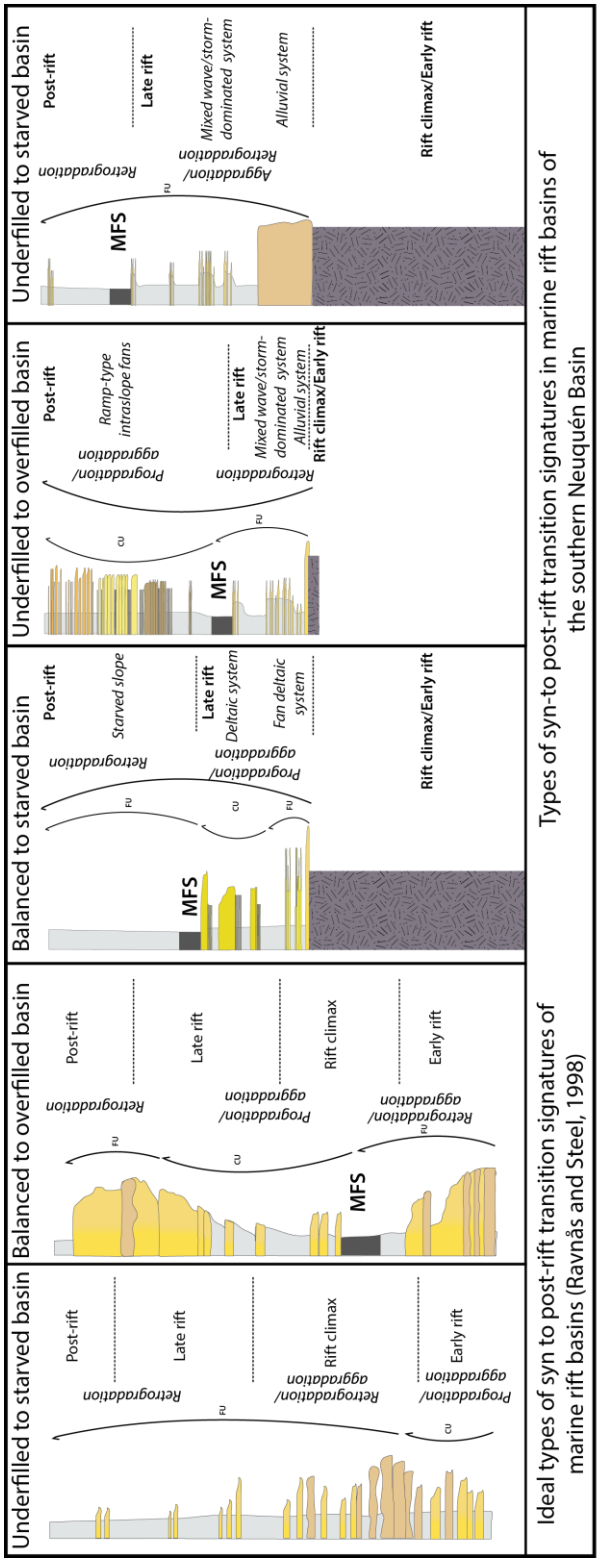

Figure 7.1: Comparison of different syn- to post-rift transition characteristics with changing conditions of intrabasinal-extrabasinal sediment supply, position (proximal versus distal) with respect to basin margin and early post-rift subsidence.

Study of the syn-to post-rift sedimentary record in the southern Neuquén Basin has shown that the changes in rift topography during decreased extension and onset of thermal subsidence, appear as the dominant controlling factor on the intrinsic variability of depositional systems . It is important to refine rift basin models, including the effects of topography on sediment gravity flow behaviour, and the generation or enhancement of relief due to early post-rift compaction-related deformation, which might have different implications depending on the shallow- or deep-marine setting (Fig. 7.1). At a larger-scale, basin margin physiography and topographic relief controls sediment routeing and partitioning from the shelf, through the slope to the basin-floor. The changes of basin margin physiography also control the rate of transgression during the early post-rift (Veiga et al., 2013), and therefore the distribution and variability of coeval shallow- versus deep-marine systems along the basin margin. Therefore the early post-rift palaeogeographic evolution of the southern Neuquén Basin margin provides a unique case study to assess the effects of along-strike changes in basin margin physiography on the variability of depositional systems with transgression and regression, across variable slope gradients and with variable seabed relief.

7.1.2 Sediment supply

Another control on the record of the syn- to post-rift transition in rift basins is the inherited basin configuration, which conditions the potential for intrabasinal versus extrabasinal sediment supply and distance from the sediment source (Fig. 7.1). This has consequences on the timing for healing of the inherited rift topography, and on the location of sand-rich deposits and sedimentological characteristics of these sand-rich deposits (long extrabasinal versus short intrabasinal transport distance).

At the scale of single depocentres, study of the Early Jurassic stratigraphic record has shown that the syn- to post-rift transition can be marked by a change from intrabasinal to extrabasinal sediment supply (e.g., in Chachil and Catán-Lil basins; Chapters 5 and 6), whereas in other basins extrabasinal sediment supply starts earlier during the late syn-rift (Chacaico Basin; Chapter 5). The timing for extrabasinal sediment contribution across depocentres, even if a similar distance to the sediment source areas, is directly dependent on the inherited topography.

When sediment supply shuts down during the early post-rift, in the basin which received extrabasinal sand-supply during the late syn-rift, extrabasinal sediment supply reached in turn the basins which were formerly sand-starved during the late syn-rift. Therefore there was a reciprocal relationship across depocentres in the loci of sediment supply or sand-starvation (Fig. 7.1). This shows the complications related to the contribution of different extrabasinal sediment sources and routeing pathways in adjacent depocentres during the syn- to post-rift transition, which would be difficult to predict without petrographic and palaeocurrent constraint.

The switching from late syn-rift extrabasinal sediment supply to early post-rift sand-starvation in the Chacaico depocentre correlates with the arrival of extrabasinal sand supply in the formerly sand-starved Catán-Lil, Chachil and La Jardinera depocentres. This change occurred after a major marine flooding event that is recognized at the scale of the southern Neuquén Basin margin (Gómez Omil et al., 2002; D'Elia et al., 2015). Major marine flooding also decreased early post-rift intrabasinal source contribution, as mud draping of rift topography deactivated intrabasinal fault-block sources in all the studied depocentres (Fig. 7.1). Therefore, instead of generating intrabasinal sediment gravity flows during the syn-to post-rift transition (Zachariah et al., 2009; Jarsve et al., 2014), relief acted as topographic barriers for flows, and controlled the timing of sediment supply in a given depocentre.

Established rift basin models consider inherited rift topography for its potential to form effective intrabasinal sources. However, in this case topography was covered and acted as a palaeogeographic barrier, which is poorly emphasised in these models despite the implications for the development of intraslope fans. Additionally, the direct application of predictive rift basin-fill models, which suggest the onset of extrabasinal sand supply as a characteristic signature of the immediate post-rift in numerous basins is risky (Prosser, 1993; Ravnås and Steel, 1998). Following this logic, both the Chacaico and the Los Molles Formation would be interpreted as early post-rift, based on the fact that they both record the onset of extrabasinal sediment supply, whereas the present study demonstrate that they developed diachronously. This argument has been used to place the syn- to post-rift transition boundary in the La Jardinera depocentre (Paim et al., 2008). In the absence of regional constraint on depocentre evolution, care should be taken when interpreting the syn-to post-rift

transition boundary in a single depocentre. The implications for late syn-rift versus early post-rift trap prediction in the subsurface, where little constraint is available or when deformation is of subseismic scale, are discussed further in detail.

7.2 What are the characteristics of the syn-to post-rift transition signature?

7.2.1 Depocentre-scale perspective

In the studied depocentres in the southern Neuquén Basin (Chacaico, La Jardinera and Western Catán-Lil), the late syn-rift and early post-rift depocentres develop through migration and change of polarity (thickening towards the NE-NNE) compared to the volcanic syn-rift depocentres (thickening towards the S-SW). The early post-rift depocentres can also develop across former basement-cored accommodation zones lacking (or with negligible) volcanic syn-rift strata, as seen in the Eastern Catán-Lil Basin (cf. Chapter 5).

Late syn-rift strata onlaps or wedges towards basement and late syn-rift faults, showing internal discordances between successive packages due to syn-depositional tilting and blind fault growth folding (cf. Chapter 5). Locally, some new fault networks could develop and dissect the volcanic deposits into the main hangingwall of some basins, changing the inherited volcanic syn-rift topographic configuration during the late syn-rift. This structural evolution differs from several rift basins in which late syn-rift extension is accommodated over fewer, but larger border faults, onto which strain should localise (Gawthorpe et al., 2003; Dorobeck, 2008).

The early post-rift deposits onlap passively onto late syn-rift deposits and across basement footwall blocks, healing the inherited accommodation. They also show consistent dip away from the main basin border fault footwalls, with shallowing-upwards in stratal dips. Additionally, early post-rift strata can be affected by mesoscale (metre-scale) normal faults mostly located above basement highs interpreted as the effects of compaction-related deformation (cf. Chapter 4). Onset of the early post-rift with major marine flooding and siliciclastic starvation (recorded by Unit 3), induced a period of very slow accumulation rates. During this period the effects of differential compaction were recorded by thickness changes in mudstone (up to 100 m thick) across buried rift structures with local small-scale deformation as seen in the Chachil Basin (cf. Chapter 4).

Compaction-related deformation recorded in depocentres did not induce variations of depositional environment and sedimentation around basement highs (e.g. López-Gamundi and Barragan, 2012). This suggests that compaction-induced deformation rates did not outpace thermal subsidence rates during the early post-rift. Instead, thermal subsidence rates might have been high during the early post-rift and could mask the effects of differential compaction (e.g. Doglioni et al., 1995, 1998; Morley, 2001; Cristallini et al., 2006).

7.2.2 Basin-scale perspective

This study has clarified and refined the spatial distribution and timing of subtle extension versus compaction-related features in the Early Jurassic stratigraphy of southern Neuquén Basin to better understand the syn- to post-rift transition record in the region (cf. Chapter 4 and 5). The spatial variability and stratigraphic architecture of depositional systems and basin-fill patterns highlight active fault-block tilting and fault growth folding during the Chachil and Chacaico formations (Unit 1 and 2A) and the base of the Los Molles Formation (Unit 2B). This implies that the late syn-rift lasted until the latest Pliensbachian, whereas onset of the early post-rift is recorded since the latest Pliensbachian-earliest Toarcian, with a major marine flooding event. These findings differ from previous interpretations that suggested the onset of early post-rift would be represented by a marine transgression and deposition of a carbonate system represented by the Chachil Formation, marking a large-scale event recorded from north to south at the scale of the Neuquén Basin (Leanza et al., 2013). The first marine transgression of the Neuquén Basin is diachronous from north to south. This should not be taken as the syn-to post-rift transition marker as it might reflect the diachronous development of the Early Andean magmatic arc form north to south until the Early Toarcian (Suarez and De la Cruz, 1997; Llambias et al., 2007; Oliveros et al., 2018).

Some previous authors have assumed diachroneity of the syn-to post-rift transition, from north to south of the Neuquén Basin (D'Elia et al., 2015), because the onset of the early post-rift occurred in the Sinemurian in the north (Lanés et al., 2008) and during the Early-Late Toarcian in the south (Pángaro et al., 2009). However, at the scale of the Neuquén Basin, the spatial pattern of decaying volcanism and extensional faulting did not follow a simple latitudinal pattern, as it

lasted until the Late Toarcian in the central and southeastern Neuquén Basin because of a thermal anomaly (Suarez and De la Cruz, 1997; Bermudez et al., 2002; Llambias et al., 2007; Schiuma et al., 2011). This raises the question of whether or not, at basin-scale, the syn- to post-rift transition sequence that records deposition from the decay of extension (Sinemurian to Early Toarcian) to complete thermal relaxation (Aalenian) should be regarded as part of the late syn-rift sequence, as they are not attributable to the basin-scale end of rifting *sensu stricto* (cf. Soares et al., 2012).

D'Elia et al. (2015) used some examples of small-scale normal faulting (few metres) developed in mudstone and sandstone heterolithic strata at the base of the Early Jurassic Cuyo Group (Middle section of their TSUIII, equivalent to Unit 3 in Chapter 5 of this study) in the Sañico depocentre located in the southernmost part of the Neuquén Basin. Therefore, they place the syn- to post-rift boundary at the Pliensbachian-Toarcian limit, similarly to this study, consistent with the synchronous onset of the early post-rift in the southern Neuquén Basin. Furthermore, the syn- to post-rift transition might not rely on the presence of mesoscale faults as these features might be due to deformation, related to compaction that does not reflect active extension, as shown in this study (cf. Chapter 4). Therefore, it is crucial to distinguish the evolution of depositional systems at a regional-scale, and the influence and distribution of subtle extensional deformation such as fault-induced growth folds versus compaction-related deformation, as it can have consequences for interpretation of the relative timing and diachroneity of the syn- to post-rift transition.

At regional-scale, the stacking pattern of the syn-rift and post-rift depocentres with spatial offset and change of depocentre polarity also departs from previous assumptions that thickness of the post-rift Early Jurassic strata simply matches the syn-rift Precuyano Cycle thickness patterns to infer active extensional faulting until the Aalenian (Vergani et al., 1995). Instead, early post-rift sagging away from syn-rift depocentres axis is consistent with accommodation of extension with lateral offset between the locus of lithospheric thinning and upper crustal brittle faulting (cf. Chapter 5). This pattern might reflect extension with mechanical decoupling between the crust and upper mantle, and consequent asymmetric thermal subsidence with respect to the locus of extension that is observed at a larger scale in the basin (Sigismondi et al., 2012). The rapid change to high magnitude thermal subsidence from syn-rift mechanical

subsidence to thermal subsidence recorded with the rapid deep-marine evolution of early post-rift depocentres, should reflect enhanced back-arc subdidence of the Neuquén Basin shortly after the onset of subduction. This evolution is different from other “cool” failed rifts (East African Rift, North Sea Rift, Suez Rift) and is characteristic of the post-rift evolution of many extensional back-arc basins involving more complex subsidence-related processes (Doglioni, 1995; Morley and Westaway, 2006; Baur et al., 2014) than in conventional stretching models.

7.3 What were the timing and source for early post-rift sand supply, and their implications for palaeogeographic evolution of the Southern Neuquén Basin margin?

7.3.1 Revised timing of sand supply in the Early Jurassic Los Molles Formation

The new age constraints from this study show that the onset of extrabasinal sand supply cannot be attributed to the effects of structural inversion, as commonly assumed for the Los Molles Formation, because it is recorded since the Late Pliensbachian in the Chacaico Basin (cf. Chapter 5). There, late syn-rift deltaic systems were developed under significant extrabasinal sand supply and possibly humid climate (Volkheimer, 2008). Later, during the late Early Toarcian, sand-rich, early post-rift deep-water systems were developed in the Catán-Lil and Chachil basins (and probably as well in the La Jardinera Basin), most likely under highstand sea-level conditions and high thermal subsidence. This contrasts with previous assumptions that sand-rich systems started to accumulate from the Middle Jurassic, with sediment supply induced by major eustatic falls (Gulisano and Gutiérez-Pleimling, 1995; Legarretta and Uliana, 1996; Paim et al., 2008) or with localized inversion with transpression induced by subduction dynamics (Naipauer et al., 2012; Pujols et al., 2018). In the present study, climate might have influenced sediment supply. However, the U-Pb ages obtained have also shown that extrabasinal sediment supply started prior to the early Late Toarcian evolution of climate towards more humid and warmer conditions (Volkheimer et al., 2008).

Sediment composition and palaeoflow data permit a new source area to be considered, along the volcanic arc to the southwest that was bounded by fan-deltaic systems, volcaniclastic aprons and deltaic system (De la Cruz and Suarez, 1997) mixing volcanic arc-derived, volcanic syn-rift derived and crystalline basement-derived sources. Maximum sediment supply rates (from compacted thicknesses) range between 67 m/Myr during deposition of the older intraslope fan J1.2 and 110 m/Myr during deposition of the intraslope fan J2.1 (cf. Chapter 5). These sedimentation rates are in the lower range of rates expected with the rapid and short-lived development of sand-rich early post-rift systems, ranging between 100 and 250 m/Myr (Yu et al., 2013). These results show that

extrabasinal sediment production was independent on any other allogenic controlling factor and contrast with sequence stratigraphic prediction that suggest sediment trapping across the shelf under transgressive, and to a lesser extent, highstand conditions. The development of sand-rich intraslope fans across a delta-fed ramp-type system constitutes a departure from depositional sequence models that emphasise accumulation of low-density sediment gravity flow deposits with delta progradation under highstand conditions (cf. Chapter 5 and 6). Moreover, the occurrence of sediment supply during both transgressive and highstand conditions could reflect changes in the rates of volcanogenic sediment production and reworking (Ito et al., 1998; Schneider, 2000; Chiocci and Casalbore, 2011). This shows that in post-rift settings associated with active magmatic arc development, an interplay of allogenic and autogenic factors should be considered as controls on sediment supply rates in rift basins (Takano, 2002; Alves et al., 2003; Yu et al., 2013; Balázs et al., 2017; Marin et al., 2017).

7.3.2 Insights from the palaeogeographic evolution of the Southern Neuquén Basin margin

At the scale of the southern Neuquén Basin margin, the detailed study of the types of lobes in deltaic and deep-marine intraslope fan systems of the Chacaico and Los Molles Formation has shown the record of two different types of systems during the late syn-rift and early post-rift (Fig. 7.2 and 7.3) (cf. Chapter 5). These two systems are: (i) deposits which belong to a central WSW-ENE orientated system presently lying in the subsurface along the Huincul High located along the cratonic basin margin, and (ii) deposits which belong to a western SW-NE orientated system located in the back-arc side of the magmatic arc basin margin. In the western system, the Toarcian intraslope fans developed after major marine flooding of a former Late Pliensbachian deltaic system, considered as the lateral continuity of the central sand-rich systems recognized in the subsurface (Gómez Omil et al., 2002) (Figs 7.2 and 7.4). This deltaic system might therefore represent the contribution of sediment supply from the central system associated with the Huincul High in the studied depocentres. However, the Toarcian development of intraslope fans in the central system with NW palaeoflows, and in the western system with NNE-NE palaeoflows, precludes a genetic relationship between these two contemporaneous systems (cf. Chapter

5). This shows that the studied depocentres record both the late syn-rift extrabasinal sediment supply from the central system (Late Plienbachian) and the early post-rift extrabasinal sediment supply from the western system (late Early Toarcian) due to the spatial variability of source contribution during the syn- to post-rift transition (Fig. 7.2 and 7.3).

Intraslope fans of the studied depocentres belong to a deep-marine sandy ramp-type system (Figs 7.3 and 7.4) that developed in the western part of the southern basin margin during the Toarcian, prior to shelf-break development during the Middle Jurassic (cf. Brinkworth et al., 2018). In the central system, the Toarcian intraslope fans developed downdip fan deltas associated with a narrow shelf (Gómez Omil et al., 2002). This contrasts with the eastward configuration of the southern basin margin, which recorded the development of a SW-NE-orientated sand-rich deltaic system with WNW palaeoflow, that remained in a shallow-marine setting associated with a wider shelf (Brinkworth et al., 2018) (Figs 7.2 and 7.4). This system compised relatively small-scale deltaic sandy clinoforms (50-300 m thick) and muddy deltaic fringes developed during Early-Late Toarcian along a low-gradient ramp lacking downdip intraslope fans (Brinkworth et al., 2018). It also evolved since the latest Toarcian-Early Aalenian into thicker shelf-edge deltaic clinoforms (300-500 m thick) with shelf-break nucleation (Brinkworth et al., 2018) (Figs 7.3 and 7.4).

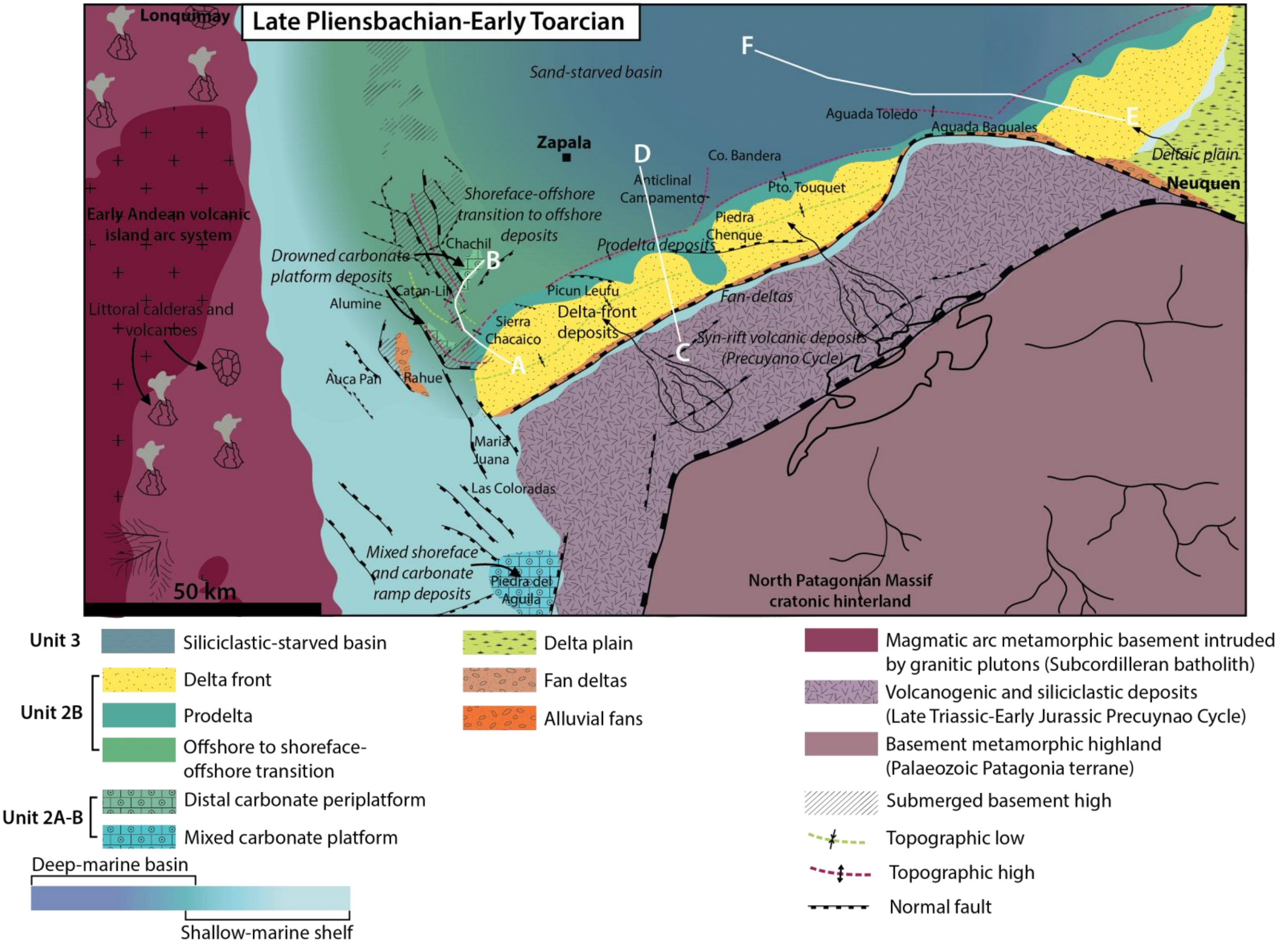

Figure 7.2: Late Pliensbachian-Early Toarcian palaeogeographic map of the Southern Neuquén Basin margin after Gómez Omil et al. (2002) and Brinkworth et al. (2018). Note the seismic-scale cross sections indicated correspond to fig. 7.4.

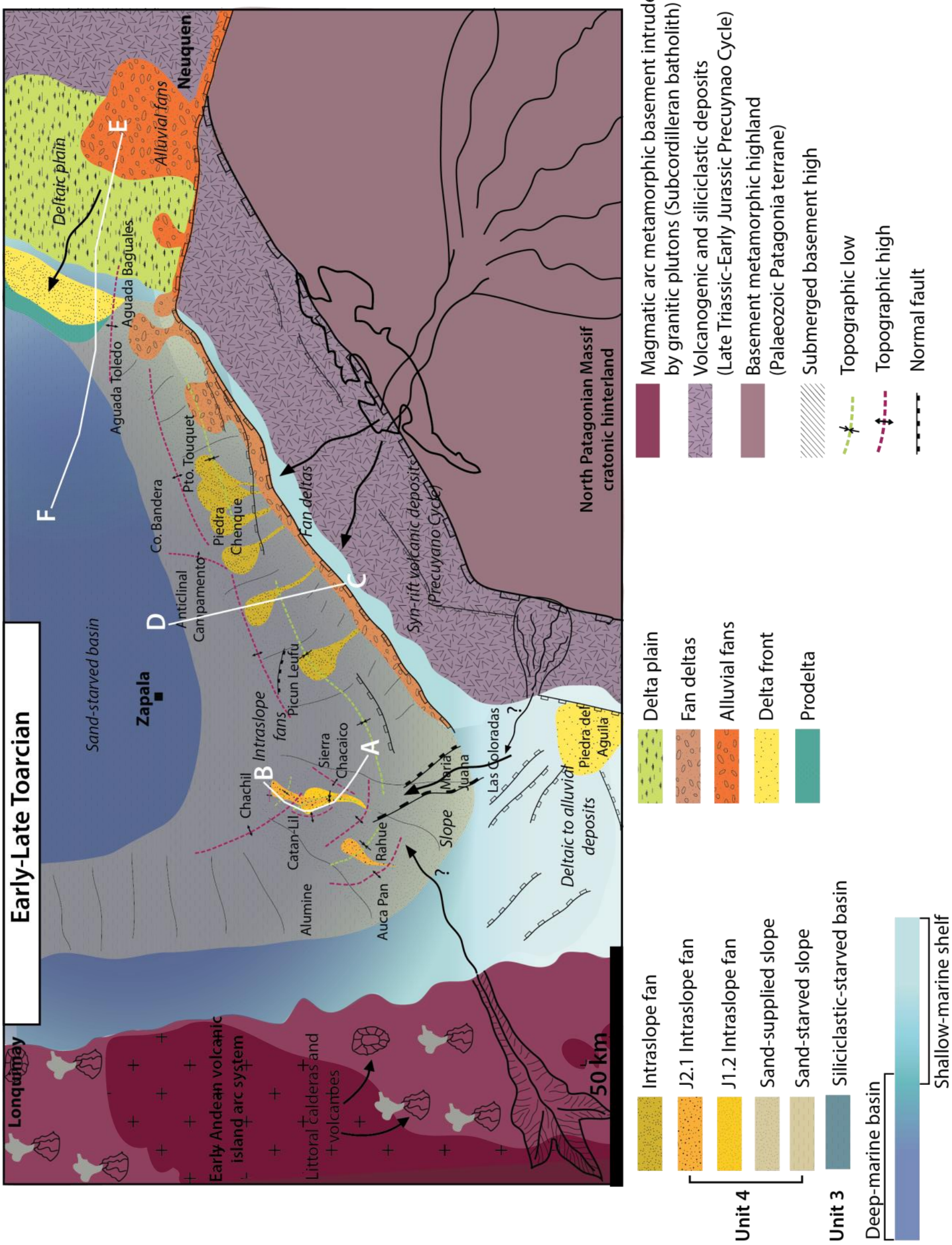

Figure 7.3: Early-Late Toarcian palaeogeographic map of the Southern Neuquén Basin margin after Gómez Omil et al. (2002) and Brinkworth et al. (2018). Note the seismic-scale cross sections indicated correspond to fig. 7.4.

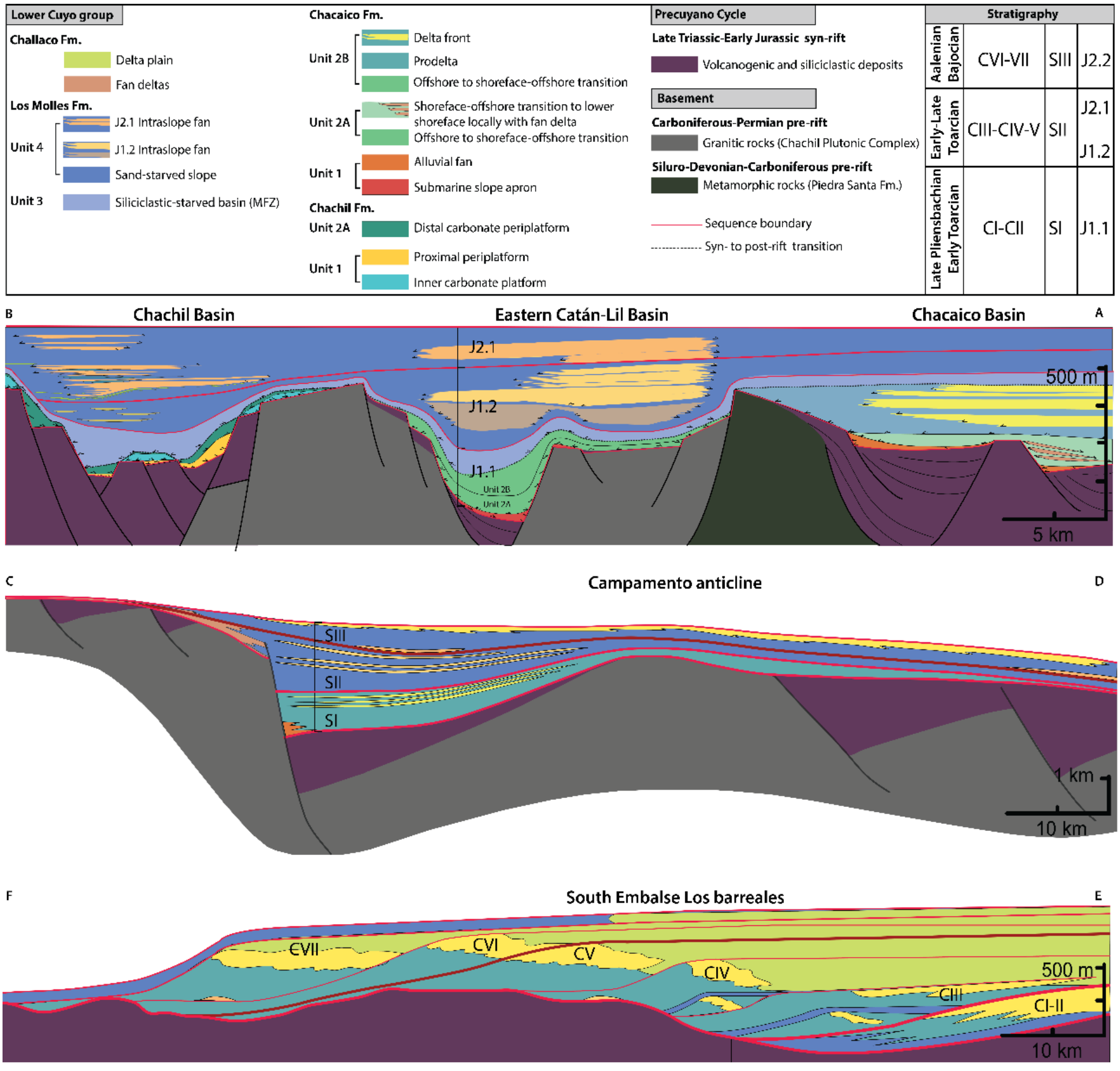

Figure 7.4: Comparative sections seismic neuquen southern margin

The presence of intraslope fans in the central system associated with a steeper basin margin physiography than for the eastern system shows the role of slope gradient and shelf width (cf. Strachan et al., 2013) on the development of deep-marine intraslope fans in early post-rift setting (Figs 7.3 and 7.4). This suggests that sediment supply of the western intraslope fans from a relatively narrow shelf area favoured sediment transfer downslope. The western intraslope fans in the studied depocentres could not be physically related with their updip feeder system, which was exhumed and eroded with the Andean foreland evolution of the basin. However, their development during rapid early post-rift subsidence in the back-arc side adjacent to the Early Andean magmatic arc basin margin and under highstand sea-level conditions, contrasts with the prevalence of deltaic sedimentation in the eastern system due to limited subsidence and a wider shelf along the cratonic basin margin (Figs 7.2 and 7.3). This shows the control of differential subsidence in the back-arc setting, decreasing eastwards away from the magmatic arc.

Intraslope fans recorded (i) the evolution of the system with influence of topography on sediment partitioning recorded in their stratigraphic architecture and facies distribution within basins but also across several basins, and (ii) the general progradation of the system through time with coarsening of sediment grain size from J1.2 to J2.1 intraslope fans (cf. Chapter 5). Slope steepening through time is recorded by the evolution of this low- to higher-gradient ramp-type system and might reflect increased subsidence in the vicinity of the volcanic island arc, with uplift and growth (widening) of the magmatic arc relief with active volcanism. Therefore, the main intrabasinal factors that controlled the Toarcian evolution of western early post-rift intraslope fans of the southern basin margin were healing of topography and increasing slope angle driven by the increase of basin subsidence and magmatic arc basin margin uplift and/or the build-up of depositional shelf-edge relief. This evolution contrasts with some other rift basin margins, which evolve with the development of narrow combined structural-sedimentary shelves (<2-15 km wide) with a well-defined shelf-slope break nucleated and/or amplified by a pre-existing structural relief bounded by relatively steep slopes (Bell et al., 2008; Strachan et al., 2013) (Figs 7.1 amd 7.3). In such high shelf- to basin-relief configurations, enhanced by sustained syn-rift basin subsidence and starvation, efficient sediment bypass across steep out-of-grade

slopes is the dominant process and promotes the rapid development of detached basin-floor fans or base-of-slope aprons in sediment-underfilled basins (Helland-Hansen et al., 2012; Strachan et al., 2013; Dodd et al., 2019) (Fig. 7.1).

The development of rift basins with high shelf- to basin-relief is inherent to their syn-rift flooding and establishment of deep-marine conditions with mechanical subsidence. In contrast, in the Neuquén Basin deep-marine conditions established with rapid thermal subsidence behind an active magmatic arc with a generalized early post-rift maximum marine flooding, resulting in the development of a deep-marine basin bounded by lower gradient shelf-to-basin-relief. This promoted, starvation of the true basin-floor of the Neuquén Basin at that time (Fig. 7.3) and sand storage across the slope, in contrast with rift basins having a higher gradient shelf- to-basin-relief. This is supported by the new U-Pb ages presente din this study, showing that the Toarcian intraslope lobes of the western system developed prior to establishment of the Middle Jurassic shelf-slope-basin-floor system(Fig. 7.4). Therefore care should be taken when applying basin-floor fan models to interpret Early Jurassic sand-rich systems along the southern basin margin (cf. Chapter 5).

7.3.3 Implications of sandstone source type for hydrocarbon reservoirs distribution along the Southern Neuquén Basin margin

The findings of this study have several implications for subsurface reservoirs, traps, and source rock prediction. Correct identification of the syn- to post-rift boundary is key for the assessment of late syn-rift versus early post-rift isopach thickness maps and associated types of traps. The defined “base” of the Los Molles Formation in many subsurface is Late Pliensbachian in age and therefore should instead be identified as the Chacaico Fm. (cf. Chapter 5). Following this view it can be either late syn-rift or early post-rift, which has implications in subsurface for both the prediction of the thickness and distribution of source rocks and the type of combined stratigraphic-structural or stratigraphic traps and reservoir quality of sandbodies within the Los Molles Formation.

This study permits to better define what should correspond to the base of the Los Molles Formation (Unit 3) (cf. Chapter 5), which should be constrained as a stratigraphic marker of regional extent that have been recognized at outcrop and records major marine flooding. This event marked a change in sedimentation

across the study area and at regional-scale, which is associated with thermal subsidence effects and onset of the early post-rift. From a source rock perspective, the sedimentary variability recognized at the base of the “Los Molles Formation” (when not differentiated between the Chacaico or Chachil Fm. deposits) has implications for the identification of the mudstone with “higher source rock potential” tracked in subsurface studies (Gómez Omil et al., 2002; Pángaro et al., 2006). Indeed, it could correspond to a range of “mudstone” deposits at outcrop including siliciclastic offshore (Catán-Lil Basin), delta-front and prodelta (Chacaico Basin), or siliciclastic-starved basinal deposits associated with maximum marine flooding (Chachil Basin) deposits, which can be late syn-rift or early post-rift (cf. Chapter 5).

From a reservoir perspective this requires to consider (i) late syn-rift combined traps as subsidence is associated with onlap and thickening of delta-front sandstone and prodelta mudstone (Chacaico Basin; Chapter 5) towards the basin border fault, and (ii) early post-rift stratigraphic traps related to effects of inherited and compaction-enhanced rift topography on the stratigraphic architecture and characteristics of intraslope fans (Chachil and Catán-Lil Basin; Chapter 4 and 5). Petrographic work (cf. Chapter 6), although focused on provenance, has shown that significant differences exist between intraslope fan and delta-front sandstone characteristics from architecture, to bed-scale and reservoir-scale, depending on source provenance (Figs 7.2 and 7.3). These characteristics show the importance of constraining the source, depositional environment and inherited topography at time of deposition of “sandbodies” in the Los Molles Formation along the southern basin margin. For instance, moderately sorted delta-front deposits (J1.1 sequence) with extrabasinal cratonic basin margin source record better reservoir quality than overall poorly to very poorly sorted intraslope fans, which can be matrix-poor (J1.2 sequence) or matrix-rich (J2.1 sequence) (cf. Chapter 6).

In the deltaic system which presents the best potential reservoir quality, stratigraphic traps could be associated with pinchout of sandbodies within prodeltaic deposits. However, the poor spatial connectivity and amalgamation rate in the delta-front sandstone might form targets of limited volume. Traps in the intraslope fan system would be associated with low-aspect ratio amalgamated lobe complex terminations/margins. They can form volumetrically larger amalgamated sand-rich packages thinning with onlap or abrupt pinchout

across just a few kilometres, forming stratigraphic and/or combined trap with variable reservoir quality and risk for hydrocarbon leakage at their downdip and lateral terminations (cf. Chapter 4 and 5).

Considering spatial relationships between the western magmatic arc margin-fed and central cratonic margin-fed intraslope fan systems, shows the risk for stacking of northeastward prograding western intraslope fans, with northwestwards prograding intraslope fans (Figs 7.2 and 7.3). It might be difficult to distinguish the different types of intraslope fans and their respective provenance determines differences in reservoir quality. In the studied depocentres, if the Late Pliensbachian deltaic system (J1.1 sequence) did not switch laterally, therefore starving the slope in the Chacaico Basin, both central and western intraslope fan systems would have developed contemporaneously during the Toarcian, and this scenario is likely to have occurred later with progradation of both systems. In the subsurface, the risk for interfingering and stacking of axial sandy systems sourced from the magmatic arc basin margin and transverse sandy systems sourced from the cratonic basin margin along the southern Neuquén Basin has significant implications for the prediction of reservoir quality.

The differences between intraslope fans characteristics inherent to their depositional configuration and degree of confinement/interaction with topography also needs to be considered. The main controls on the net: gross and reservoir quality of investigated intraslope fans in the Early Jurassic Los Molles Fm. are the degree of inherited topography on which depends of confinement at basin margins, and interaction with seabed relief. For instance sandstone beds in the J1.2 intraslope fan sequence have a lower matrix content and dominant gradational bed tops compared with coarser-grained sandstone with dominant sharp tops of the J2.1 intraslope fan sequence. The latter deposits present a higher risk for development due to bed-scale heterogeneity related to the stratigraphic distribution of (i) thin hybrid event beds near lobe complex margins, and (ii) hybrid event beds with thick debrites (several metres thick) forming flow baffles in stacked lobe axis and fringe deposits (cf. Chapter 4). Furthermore, within the J2.1 intraslope fan, some proximal to distal differences also apply. For instance, thin- to medium-bedded sandstone located updip in the proximal Eastern Catán-Lil Basin, which might record sediment bypass (Stevenson et al., 2015), tend to be coarser-grained and with lower matrix content than the thicker-

bedded sandstone located downdip in the Chachil Basin. Therefore, the effects of topography on stratigraphic architecture need to be taken into account due to the implications for sediment bypass and/or developing and trapping hybrid event beds, and termination style of lobe complex margins near intrabasinal relief. Here, two intraslope fans, despite having similar composition and provenance, lobe dimensions and geometry, can show markedly different facies distributions across lobes and bed-scale heterogeneity development. Furthermore, the thickness patterns of lobes and sandstone grain-size (coarser versus finer) does not fit with reservoir quality (e.g. coarser-grained beds are not always the thickest beds, thick beds can have more matrix than thinner beds, the coarser-grained sandstone lobes of the J2.1 sequence have the highest matrix content and include more hybrid event bed deposits compared with finer-grained sandstone lobes of the J1.2 sequence) (cf. Chapter 6).

7.4 What are the characteristics of early post-rift intraslope fan deposits of the Early Jurassic Los Molles Formation and how do they compare to other deep-marine sandy systems?

7.4.1 Facies characteristics of lobes in the Early Jurassic Los Molles Formation

The outcomes of the present study provide rare insights into the subseismic characteristics of early post-rift intraslope lobes formed in perched or healed slope accommodation that are not captured by current deep-marine rift basin models. Sediment gravity flows respond to inherited seabed topography, which can induce partial flow confinement, sediment bypass or storage, and changes in sediment gravity flow behaviour including flow deflection and reflection. General characteristics of lobes in intraslope fans of the Early Jurassic Los Molles Fm. include poor to very poor sorting with variable fine to very coarse grain-size, plant material and mud matrix content (average 18% for sandstone of the J1.2 intraslope fan and 27% for sandstone of the J2.1 intraslope fan) (cf. Chapter 6). The coarser grain-size range, poor sorting and variable matrix content of these sand-rich deposits permit comparison with other intraslope fans and base-of-slope and basin-floor fans developed with the influence of seabed topography.

Sandstones can record the presence or not of outsized granule fraction, grain-size breaks, high sediment fallout rate features (sinusoidal laminations, climbing ripples, soft sediment deformation), exotic combined flow bedforms related to flow reflection or deflection (convex-down ripples with tangential foresets, isotropic and anisotropic HCS-like bedforms), and clayey banding and low amplitude dune-scale bedforms (cf. Chapter 5 and 6) (Fig. 7.5). Overall, the mud matrix content and poor to very poor sorting of sandstone suggest variable but high efficiency flows, able to transport a relatively coarse-grained sediment fraction, but with a limited flow capacity for sediment sorting, probably due to the limited flow run-out distance. The occurrence of clast-rich and matrix-rich facies, including hybrid event beds with thick debrite divisions, points to deposition by a range of turbulent to turbulence-supressed clay-rich transitional flows, quasi-laminar plug flows and sandy debris-flows with variable strength (Baas et al., 2009, 2011; Talling et al., 2012) (cf. Chapter 4 and 6). The limited segregation of these cohesive deposits and bed-scale heterogeneity compared with less or non-

cohesive sandy deposits might be related with the development of lobes across a moderate slope gradient, with seabed relief that was not favourable for flow ignition and enhanced flow deceleration (Fig. 7.5). This resulted in deposition across the slope with no sediment bypass towards the basin-floor (cf. Chapter 5) (Fig. 7.3). The early post-rift lobe complexes can show poorly organized to random bed thickness and grain-size trends in finer-grained lobe complexes in the distal part of the system (distal part of J1.2). In contrast, thinning- and fining-upwards trends, sometimes with basal coarsening- and thickening-upwards trends, characterise coarser-grained lobe complexes in the proximal part of the system (J2.1 and proximal part of J1.2). Their differences relate to the high matrix (distal part of J1.2 and J2.1) versus low matrix content of sandstones (proximal part of J1.2), low sand: mud ratio (distal part of J1.2 and J2.1) versus high sand: mud ratio of lobe complexes (proximal part of J1.2), paucity (J1.2) versus abundance of hybrid event beds and scouring (J2.1) and abundant (J1.2) or moderate (J2.1) development of combined flow bedforms (cf. Chapter 6).

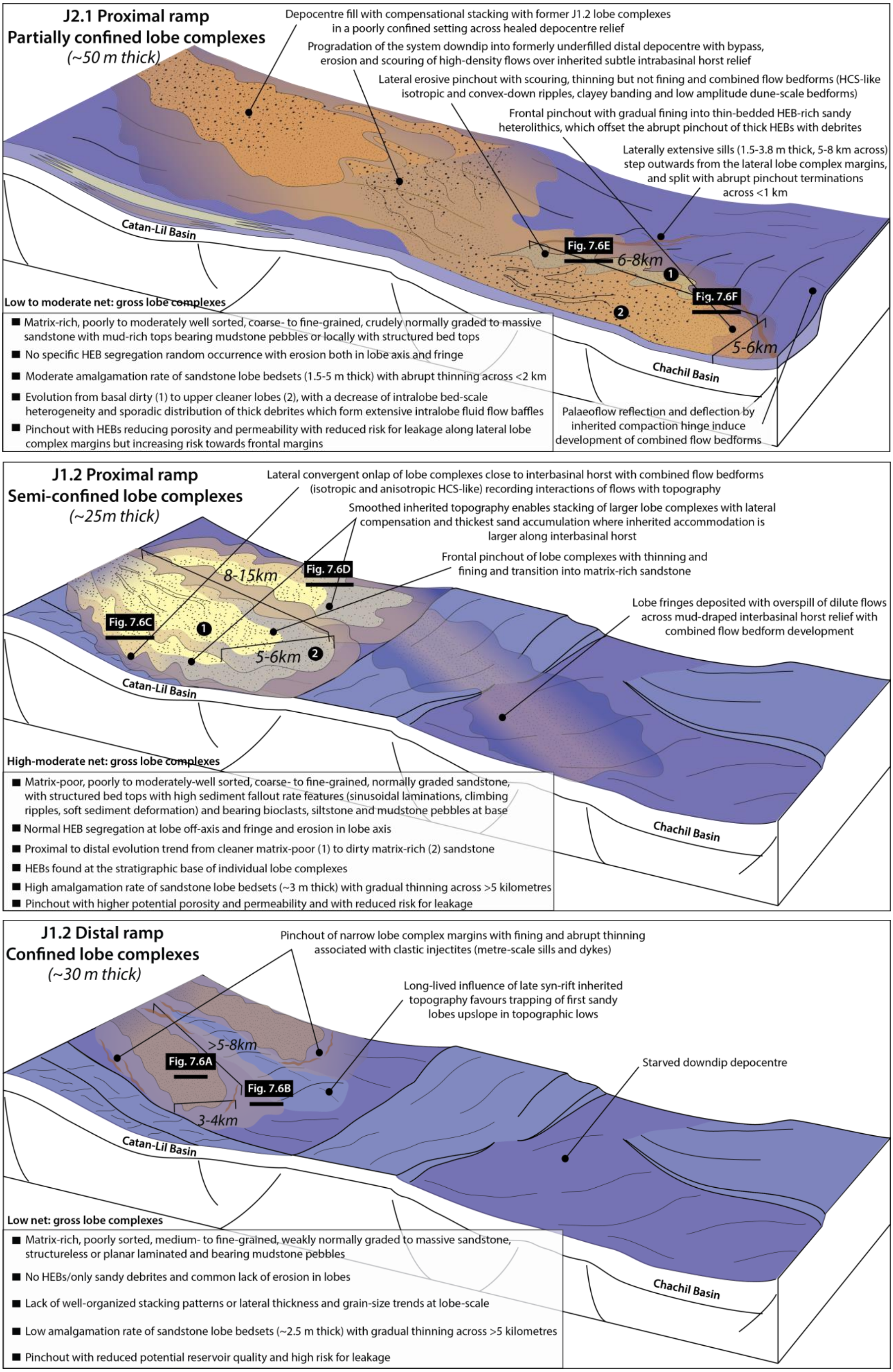

Figure 7.5: Bloc diagrams showing the evolution of lobe complexes with healing of inherited rift topography by J1.2 to J2.1 intraslope fans, and summarizing their main characteristics. Termination pinchout styles shown in fig. 7.6 are indicated.

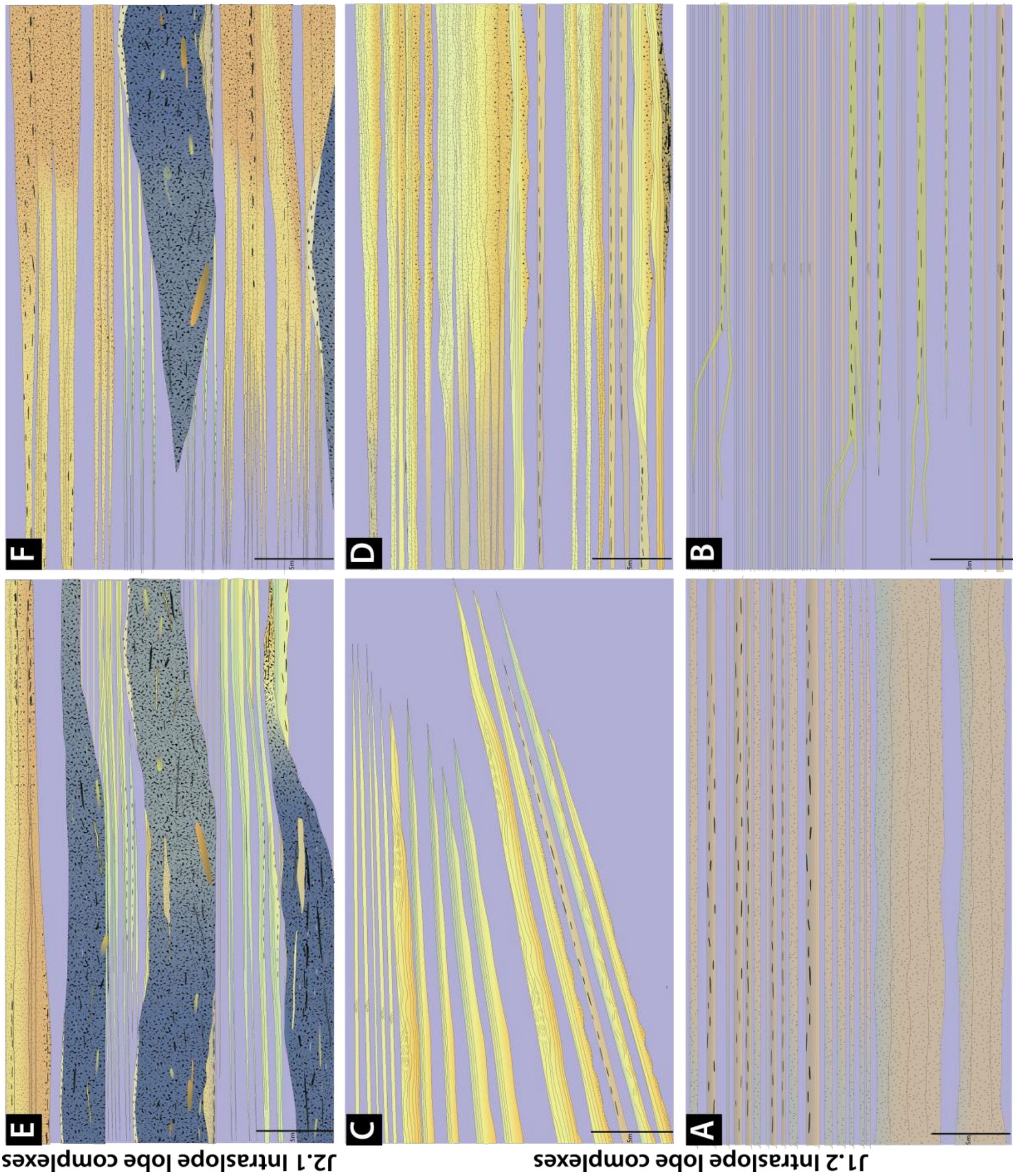

Figure 7.6: Schematic cross sections of termination pinchout styles indicated in fig. 7.5. Abrupt pinchout of matrix-rich sandstone associated with post-depositional remobilization and injection is recorded from depocentre (A) to lateral and frontal margins (B) of J1.2 distal ramp lobe complexes. J1.2 proximal ramp lobe complexes show lateral convergent onlap near depocentre horst border (C) and frontal pinchout with transition from matrix-poor to matrix-rich sandstone and increase in bed-scale heterogeneity (D). J2.1 proximal ramp lobe complexes record lateral pinchout with erosion, scouring and HEB development (E) and frontal termination with abrupt pinchout of thick HEBs offset by thin-bedded matrix-rich sandstone. Vertical scale is 5 metres.

The terminations of intraslope lobe complexes offset basin margins, and show spatial thickness changes (Fig. 7.6). Changes can be associated with i) abrupt sandstone pinchout without significant fining associated with remobilization and injection (sills and dykes) near frontal and lateral lobe complex margins, with high confinement by intrabasinal relief and basin margins (distal ramp lobe complexes in J1.2) (Fig. 7.6-AB), or ii) with convergent onlaps with sandstone fining and thinning with bedform (HCS-like, climbing ripples, soft sediment deformation) development near lateral lobe complex margins and enrichment in matrix-scale heterogeneity near frontal lobe complex margins, with moderate confinement by basin margins (proximal ramp lobe complexes in J1.2) (Fig. 7.6-CD), or iii) with erosive pinchout with relatively coarse-grained sandstone thinning but not fining, with scouring and hybrid event bed (HEB) development near lateral margins and frontal lobe complex margins, with partial confinement by intrabasinal relief and basin margins (proximal ramp lobe complexes J2.1) (Fig. 7.6-EF).

The abrupt pinchout is associated with reduced potential reservoir quality due to presence of matrix-scale heterogeneity, enrichment in mudstone clasts and cementation associated with clastic injectites near lateral and frontal lobe complex margins (distal ramp lobe complexes in J1.2) (cf. Chapter 5 and 6) (Figs 7.5 and 7.6-AB). Injectites pinchouts have been recognized in oblique updip pinchout of basin-floor lobes as increasing the risk for hydrocarbon leakage (Cobain et al., 2017). In contrast, the structured and gradual fining towards convergent onlap implies better potential reservoir quality near lateral lobe complex margins (Figs 7.5 and 7.6-CD). The lack of, or poorly developed matrix-scale heterogeneity restricted to frontal lobe complex margins and the lack of bed-scale heterogeneity (HEBs are confined to the stratigraphic base of lobe complexes) implies a higher potential porosity and permeability with reduced risk for leakage in the convergent onlap configuration (proximal ramp lobe complexes in J1.2) (cf. Chapter 5 and 6).

The erosive pinchout with thinning (but not fining) and HEB development implies a lower potential reservoir quality near lateral lobe complex margins due to the widespread development of bed-scale heterogeneity (Figs 7.5 and 7.6-EF). Improvement of potential reservoir quality near frontal lobe complex margins is related to the offset of abrupt pinchout of thick HEB by the gradual pinchout of thin-bedded sandstone with matrix-scale heterogeneity. The widespread

presence of HEBs implies high matrix content in sandstone reducing porosity and permeability, reducing risk for leakage along lateral lobe complex margins, but with increased risk towards frontal margins. In addition, the risk for leakage is also increased by the development of large-scale injectite complex (sill-dominated) near the stratigraphic base of lobe complex (cf. Chapter 4). Both terminations are indicative of local high confinement by basin margins and frontal intrabasinal relief and their difference should be related to the orientation of the confining topography (cf. Chapter 4) (Fig. 7.5). The lack of fining trends that can be observed towards lobe complex margins (in J2.1) is a feature recognized in intraslope lobes associated with bypass of finer grained flow components across relief (Spychala et al., 2015; Jobe et al., 2017). This is consistent with the distribution of small scours and channel forms in the coarser-grained lobes (J2.1 and to a less extent in the proximal part of J1.2), which might have served as ephemeral conduits for bypass of the most energetic flows downdip and can be found in intraslope lobes (Hay, 2012; Spychala et al., 2015) (Fig. 7.7). The lack of fining trends towards lobe complex margins and the coarser grain-size of matrix-rich sandstone (J2.1) could also result from the clay-rich character of sediment gravity flows that can promote the transport of coarser-grained particles and increase flow run-out distance (Gladstone et al., 1998; Gardner et al., 2003; Al Ja'Aidi et al., 2004).

7.4.2 Comparison of intraslope lobe complex dimensions, stacking patterns and termination style of the Early Jurassic Los Molles Formation with other basin-floor and intraslope systems

The dimensions of individual early post-rift lobe complexes (~25-32 m thick in J1.2 min 5-15 km long, min 5-6 km wide and 50-70 m thick in J2.1, min 6-8 km long, min 5-6 km wide) are comparable to basin-floor lobe complexes of the Karoo Basin (10-50 m thick; Prélat and Hodgson 2013; Spychala et al., 2017), which are of greater areal extent (40 km long, 30 km wide) (Prélat et al., 2009) (Fig. 7.7). Their thickness is also sensible to other lobe complexes of large intraslope fans developped in a similar ramp-type stepped slope setting with subtle change of slope gradient but which are of greater areal extent (40 m thick, 100 km long, 40 km wide) (Mignard et al., 2019) (Fig, 7.7). They are much thinner, but of similar extent to ponded turbidite systems of the Gulf of Mexico (70-100 m thick, 10-16

m long, 6-12 m wide) (Covault et al., 2009) or across the western Nigeria delta slope (70-120 m thick, 8 km long, 8 km wide) (Jobe et al., 2017) (Figs 7.7 and 7.8). Their dimensions are similar to other well constrained intraslope lobe complexes found in the Karoo Basin (10-15 m thick, 15-25 km long, 6-10 km wide) (Spychala et al., 2015) but they remain thicker (Fig. 7.8). Their thickness and dimensions are more similar to other early post-rift intraslope lobe complexes including examples of the Maloy Slope of the northern North Sea (Jackson et al., 2008) and base-of-slope systems of the North Falkland basin (Dodd et al., 2019) and East Greenland (Henstra et al., 2016) (Fig. 7.7).

Lobes have a tabular to mounded lobe geometry and low-aspect ratio, slightly larger in the J1.2 intraslope fan (~2.5-3.5 m thick, 5-8 km long, ~2-5 km wide) than in the J2.1 intraslope fan (1.5-5 m thick, 4-6 km long, ~1-4 km wide). The thickness range of intraslope lobes are much smaller than basin-floor lobes of the Karoo Basin (3-14 m thick, 21-31 km long, 8-18 km wide), or similar unconfined mud-rich basin-floor systems, which form elongate and relatively thin lobes (Prélat et al., 2010) (Fig. 7.7) . In contrast, the studied early post-rift lobes have similar spatial extent range as highly confined lobes of the Golo Fan system but are much thinner (14-38 m thick, 5-14 km long, 3-8 km wide), than the Kutai Fan system (22-47 m thick, 3-12 km long, 1-7 km wide) (Prélat et al., 2010) (Fig. 7.8). Again, the dimensions of individual lobes across the western Nigeria delta slope are the better analogue to the lobes of the Los Molles Formation (<2 m thick, 8 km long, 5 km wide) (Jobe et al., 2017) and therefore they might record deposition by smaller volume flows in larger depocentres, with partial confinement (Fig. 7.8).

This is consistent with progradational to aggradational stacking of the lobe complexes with compensational stacking indicative of lobe size being small relative to basin area at the time of deposition. Nonethless, it is also consistent with some flow confinement at basin margins given termination styles ranging from subtle onlap to abrupt pinchout, and the range of exotic combined flow bedforms, hybrid event bed distribution and diverse palaeocurrents recording variable effects of flow interactions with topography. Aggradational to progradational stacking patterns are common in intraslope lobes influenced by the containment of slope morphology (Covault and Romans, 2009; Spychala et al., 2015; Marini et al., 2015) and contrast with compensational stacking that is more common in basin-floor lobes developed in unconfined setting (Prélat et al.,

2009). Compensational patterns can also arise due to the subtle influence of lobe depositional relief in basin-floor lobes (Klaucke et al., 2004; Gervais et al., 2006) or in base-of-slope apron lobes (Dodd et al., 2019).

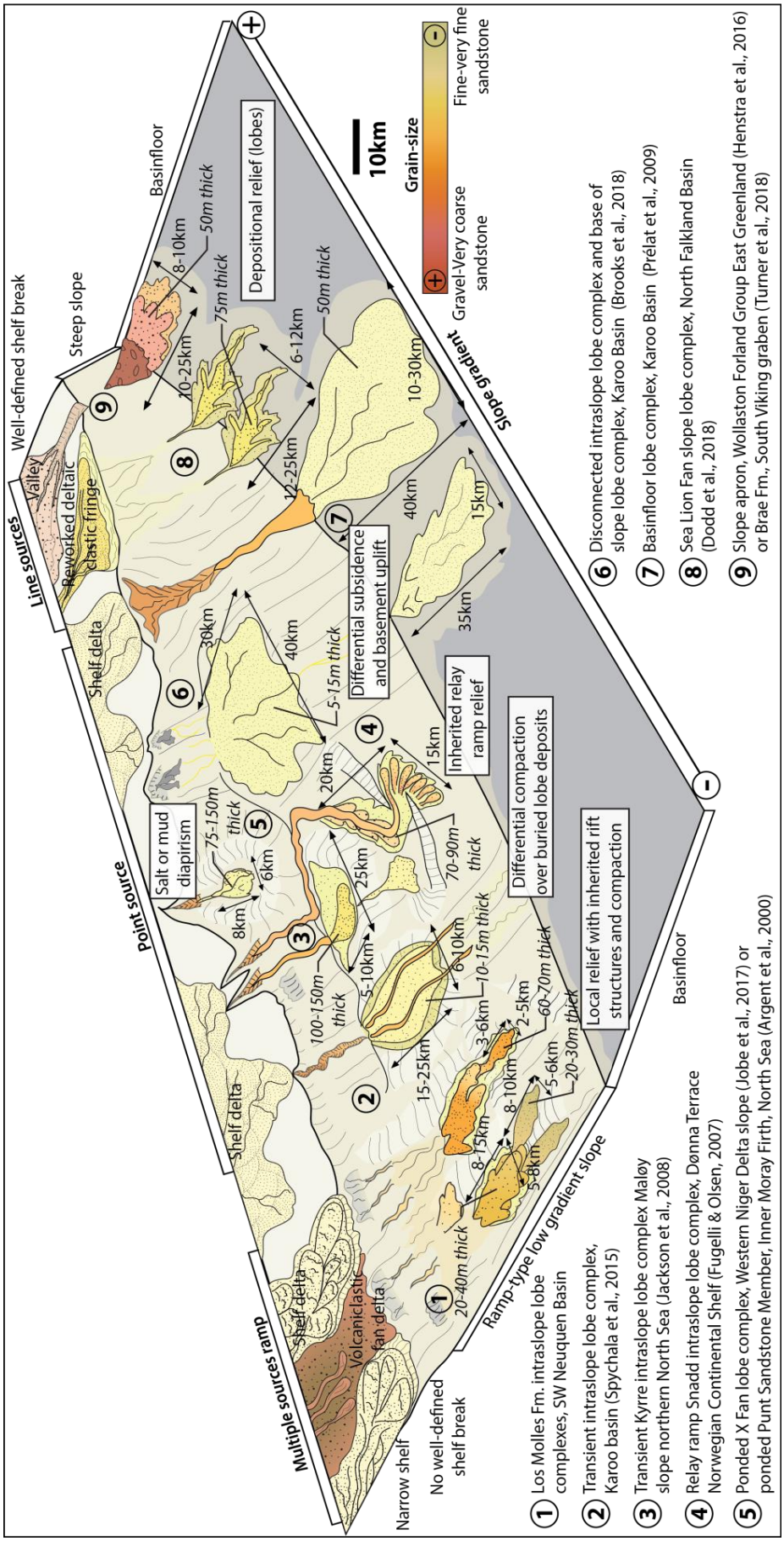

Figure 7.7: Synthetic bloc diagram showing a range of intraslope, slope apron and basin-floor lobe complexes to compare dimensions, depositional setting and grain-sizes, with characteristics of the ramp-type lobe complexes of the Los Molles Formation.

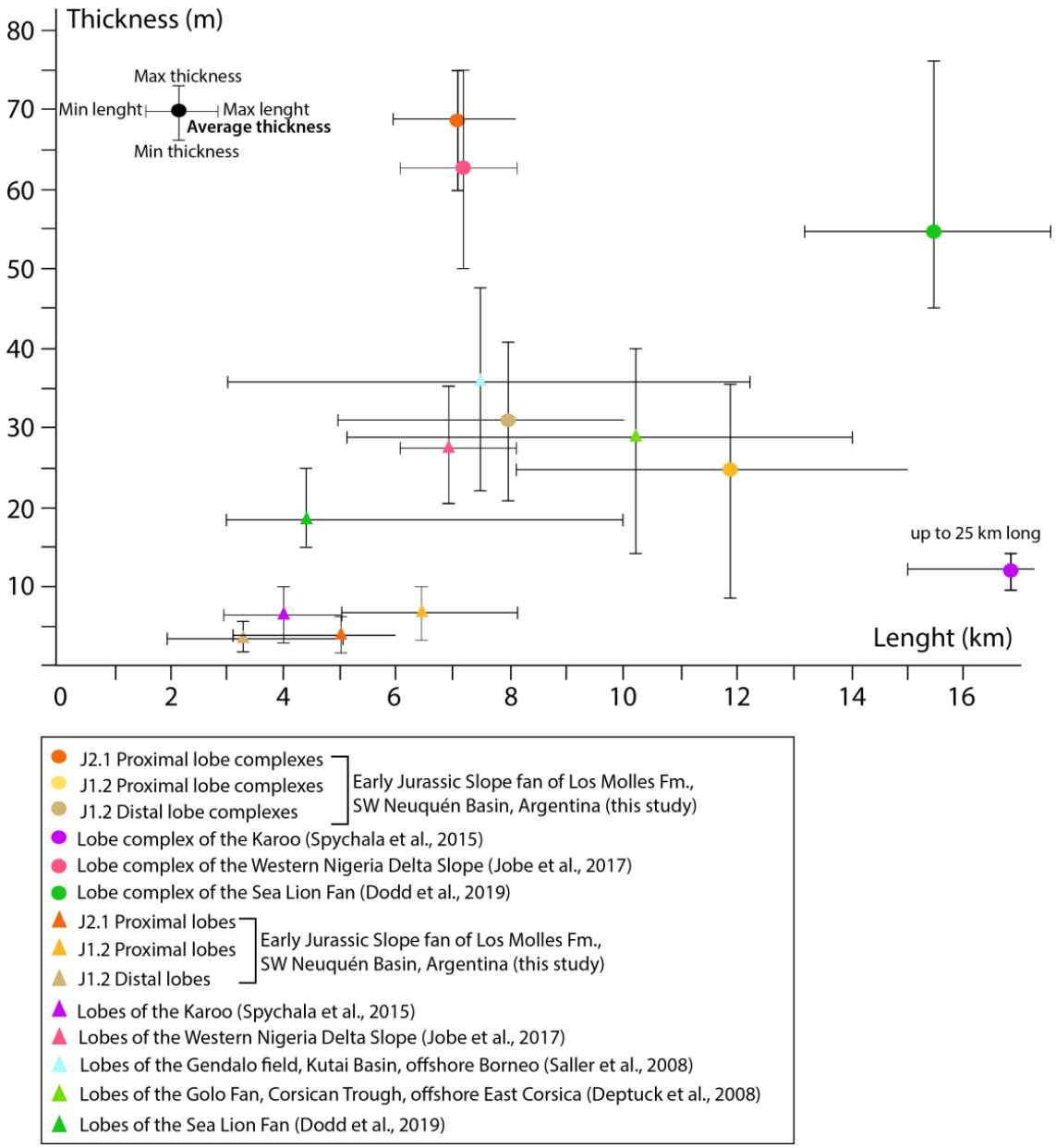

Figure 7.8: Diagram comparing the dimensions of a range of intraslope lobe complexes with lobe complexes of the Los Molles Formation.

7.4.3 Controls on confinement and development of bed-scale heterogeneity in intraslope lobe complexes of the Early Jurassic Los Molles Formation

The differences in J1.2 versus J2.1 lobe complex dimensions fans of the Los Molles Fm. (~25-32 m thick in J1.2 min 5-15 km long, min 5-6 km wide and 50-70 m thick in J2.1, min 6-8 km long, min 5-6 km wide) and high or low net: gross successions are consistent with deposition in contrasted topographic configurations (Fig. 7.5). Intraslope fans of the Los Molles Fm. do not show evidence for full confinement, with a strict fill-and-spill stratigraphic architecture including thick wedge-shaped successions of ponded sheet sandbodies downlapped by bypass channels and mass-transport deposits, typical of three-dimensional ponding (Prather et al., 1998; Beaubouef and Friedmann, 2000; Sinclair and Tomasso, 2002; Booth et al., 2003) (Fig. 7.7). The pinchout and onlap pattern of intraslope fans of the Los Molles Fm. indicate rather moderate to subtle confinement towards basin margins, with a stratigraphic architecture indicative of fine-grained dilute flow stripping in the downdip outboard basins, and intraslope fan progradation as accommodation is healed and relief is levelled (Fig. 7.6). These features are more characteristic of partial confinement with a low ratio of flow size to receiving basin size in perched or healed slope settings with limited slope accommodation (Prather et al., 2003; Smith, 2004). However, the accumulation pattern of high net: gross lobe successions lacking bed-scale heterogeneity, expected in these settings is not observed here as intraslope lobe complexes form low to high net: gross successions due to the variable development of matrix- to bed-scale heterogeneity and effects of topographic confinement.

Intraslope fan successions of the Los Molles Fm. show well-developed matrix-scale heterogeneity throughout lobe complexes with dirty pinchout margins with injectites (distal ramp lobe complexes of J1.2 sequence), bed-scale heterogeneity segregated a the stratigraphic base of lobe complexes with cleaner onlap margins (distal ramp lobe complexes of J1.2 sequence), or matrix- and bed-scale heterogeneity widespread throughout lobe complexes, including towards dirty pinchout margins (lobe complexes of J2.1 sequence) (Figs 7.5 and 7.6). Bed-scale heterogeneity is recorded by deposition of a range of thin to medium HEB types showing segregation towards the frontal fringe of lobe complex in the J1.2 intraslope fan (Fig. 7.6-CD). In contrast, thin to very thick

HEBs occur at lobe fringes and lobe axis, showing inefficient segregation in the J2.1 intraslope fan (Fig. 7.6-EF). This departs from the common recognition of bed-scale heterogeneity segregated radially towards lobe fringes in basin-floor lobes, which is used as an indicator of better-quality reservoir sandstone developed upstream in the system (Haughton et al., 2009; Kane and Pontén, 2012; Kane et al., 2017; Spychala et al., 2017).

As intraslope lobe complex terminations are not specifically associated with systematic development of bed-scale heterogeneity restricted to basin bounding slopes (Pyles and Jennette, 2009; Patacci et al., 2014; Southern et al., 2015), confinement was not the main control for bed-scale heterogeneity development. Flow confinement by lateral basin margins with deflection and reflection, and initiation of internal waves (Patacci et al., 2015; Tinterri et al., 2016, Ge et al., 2017) led to the development of combined flow bedforms near lateral lobe complex margins of the J1.2 and J2.1 intraslope fans. The distribution pattern of matrix- to bed-scale heterogeneity in intraslope lobe complexes of the Los Molles Fm. is consistent with the sensitivity of clay-rich transitional flows and debris-flows to local intrabasinal relief . This might have promoted preferential trapping of more cohesive deposits, including hybrid event beds, close to the site of flow perturbation by seabed relief (Gee et al., 2002; Modica and Brush, 2004). The erratic HEB distribution throughout the J2.1 lobe complex in the Chachil Basin is consistent with progradation of the system with sediment bypass and erosion across seabed relief inherited from the horst border of the Chachil Basin (cf. Chapter 5) (Fig. 7.5). In contrast, the discrete organized HEB distribution locally present at the stratigraphic base of the J1.2 intraslope lobe complexes in the Eastern Catán-Lil Basin supports deposition across subdued intrabasinal relief with little flow perturbation (Fig. 7.5).

Chapter 8 Conclusions

This study documents the sedimentology and tectono-stratigraphic architecture of the syn- to post-rift transition and to characterize the different types of early post-rift lobes in the Los Molles Formation in several exhumed Early Jurassic marine rift basin-fills of the southwestern Neuquén Basin in Argentina. The main outcomes permitted marine rift models to be extended to back-arc settings and highlighted the effects of physiographic evolution of rift basin topography. Its role is largely underemphasised in tectono-stratigraphic rift basin models, despite being crucial for the exploration of deep-marine post-rift plays and reservoir quality.

Sedimentological characteristics and timing of deposition of the Chachil, Chacaico and Los Molles Fm. have been refined, and the spatial distribution and timing of subtle extension versus compaction-related features have been clarified in order to define the syn- to post-rift transition across basins. The syn- to post-rift transition was marked by a major reorganization of depositional systems across inherited rift topography associated with a change in shelf-slope physiography and source. This implied a transition from late syn-rift mixed intrabasinal (intrarift derived) and extrabasinal (cratonic derived) transverse systems with short sediment routeing (alluvial to lacustrine, fan-deltaic, deltaic and mixed siliciclastic-carbonate), to early post-rift exclusively extrabasinal (magmatic arc derived) axial turbidite systems with longer sediment routeing.

New age constraints from this study show that extrabasinal sediment supply permitted (i) the development of a deltaic system since the Late Pliensbachian in the Chacaico Basin during the late syn-rift and (ii) the first deep-marine intraslope fans, which started to deposit since the late Early Toarcian in the study area during the early post-rift. Therefore, based on the timing of development and provenance data, this work precludes a genetic relationship between the deltaic system that developed since the late syn-rift along the southeastern cratonic basin margin, and intraslope fans that accumulated since the early post-rift in the back-arc side of the southwestern magmatic arc basin margin. This contradicts previous models in which the first sandy lobes of the Los Molles Formation attributed to the Late Toarcian, were interpreted to record extrabasinal sand supply from the southeastern basin margin with (i) major eustatic sea-level fall

and/or (ii) response to structural inversion with transpression induced by a change in subduction dynamics.

In terms of sediment source, the study of the Early Jurassic stratigraphy across the investigated depocentres has shown that the syn- to post-rift transition can be marked by a change from intrabasinal to extrabasinal sediment supply (e.g., in Chachil and Catán-Lil basins). In contrast, in adjacent basins where extrabasinal sediment supply starts earlier during the late syn-rift (Chacaico Basin), the early post-rift instead record starvation associated with cut-off of extrabasinal sediment supply due to migration of systems along basin margin and increase of back-arc subsidence near the magmatic arc. In both cases, the local intrabasinal and extrabasinal sources that fed late syn-rift systems were deactivated due to mud-draping associated with major marine flooding and onset of the early post-rift. This maximum flooding event is marked by the deposition of an organic-rich mudstone succession that marks the base of the Los Molles Fm. and is diachronous at the scale of the Neuquén Basin.

During the early post-rift, renewed extrabasinal sediment supply in the study area is interpreted as a distal signal of arc-related volcanogenic sediment production with reworking and supply from deltaic systems developed along the narrow shelf flanking the Early Andean volcanic island arc. Indeed, stratigraphic, petrographic and palaeocurrent constraints suggest that in the study area the provenance of sandstone lobes in the Los Molles Fm. is more consistent with extrabasinal supply from magmatic arc basin margin. Petrographic work, although focused on provenance, also permitted better potential reservoir quality to be identified for late syn-rift deltaic sandstone sourced from the southeastern cratonic basin margin than for early post-rift intraslope fan sandstone sourced from the southwestern magmatic arc basin margin. This study demonstrates the contribution of different extrabasinal sources (cratonic versus magmatic arc origin) and implications for the different spatial distribution of late syn-rift and early post-rift sandy depocentres, as reservoir quality depends on the type of source. In the subsurface, distinguishing the types of lobes and their respective provenance might be difficult. Therefore the risk for interfingering and stacking of axial sandy systems sourced from the magmatic arc basin margin and transverse sandy systems sourced from the cratonic basin margin, could have implications for the prediction of reservoir quality along the southern Neuquén Basin margin.

In terms of rift basin models, the syn- to post-rift basin-fill signatures and predictive spatial distribution of sandy early post-rift accumulations across rift topography differ markedly from intracratonic rift basins, and record relatively low sedimentation rates (60-110 m/Myr) compared with other examples of early post-rift sandy systems (~150 m/Myr). Such particularities are inherent to the long-lived influence of volcanic rifting and inherited topography on the sedimentation, important early post-rift back-arc subsidence rates and multiple active extrabasinal sediment sources. One of the most striking effects is the long-lived influence of pre-rift inherited structures on the distribution, geometry and evolution of late syn-rift and early post-rift depocentres with contrasting basin-fill patterns. This resulted in the migration of the locus of syn-rift, late syn-rift and early post-rift depocentres showing a compensational thickness pattern (i.e. the thickest early post-rift depocentres stack above the thinnest syn-rift depocentres) and individual change of depocentres polarity (i.e. spatial shift of the late syn-rift versus early post-rift depocentre axis). Therefore, early post-rift intraslope fans were mainly distributed offset from syn-rift depocentres in basins that formed across basement accommodation zones during the syn-rift, and which accumulated little or lacking volcanic syn-rift deposits.

Outcomes of the present study provide rare insights into the subseismic characteristics of early post-rift intraslope lobes formed in perched or healed slope accommodation that are not captured by current marine rift basin models. At a regional-scale, early post-rift intraslope fans developed as axial systems, from proximal to distal basins, with initial trapping of sand in depocentres proximal from the source. Progressive healing of intrabasinal relief and levelling of interbasinal relief that acted as long-lived palaeogeographic barriers enabled overspill, bypass and progradation of intraslope fans into more distal sand-starved depocentres, while some adjacent depocentres remained sand-starved. This shows that inherited topography locally enhanced by compaction-related deformation (small-scale faulting, large-scale folding) played a key role by forming long-lived inherited seabed relief that largely influenced the timing for spatial linkage of early post-rift sandy depocentres. This implies that early post-rift intraslope fans of the Los Molles Formation t developd diachronously across depocentres, and deposited across underfilled or healed slope topography with

different characteristics. Intraslope fans developed across a low- to moderate-gradient ramp-type system flanking the magmatic arc basin margin, whereas the true basin-floor of the Neuquén Basin remains sand-starved during the Early Jurassic. The overall stratigraphic evolution and individual facies characteristics of Early Jurassic intraslope fans of the Los Molles Fm. reflect the maturation of sediment routeing pathways and slope steepening due to magmatic arc uplift and increasing adjacent back-arc subsidence.

At the scale of individual depocentre, this study demonstrates the role of inherited rift and compaction-enhanced topography on the stacking patterns and types of early post-rift lobe complexes comprised in intraslope fans. Depending on the difference of available inherited topography and accommodation in adjacent depocentres, coeval intraslope lobe complexes developed with variable degree of confinement and interactions of sediment gravity flow behaviour with seabed relief. The implications of these parameters on the variability of lobe complex characteristics (dimensions, termination style, stacking patterns, facies, exotic combined flow bedforms and bed-scale heterogeneity) have been highlighted. Three main termination styles of intraslope lobe complexes have been identified: (i) abrupt pinchout of matrix-rich sandstone without significant fining and associated with remobilization and injection at lateral and frontal lobe complex margin, (ii) convergent onlap of matrix-poor sandstone with fining and thinning, with exotic combined flow bedform development at lateral lobe complex margin and with development of matrix-scale heterogeneity at frontal lobe complex margin, or (iii) erosive pinchout of matrix-rich relatively coarse-grained sandstone with thinning but not fining, with a certain degree of scouring associated with widespread hybrid event bed and exotic combined flow bedform development near lateral lobe complex margin and with abrupt pinchout of thick hybrid event beds offset by gradual pinchout of HEB-rich thin-bedded sandstone near frontal lobe complex margin. Lobe complex characteristics and termination styles have implications for the prediction of stratigraphic traps, hydrocarbon leakage and reservoir quality that are difficult to assess in subsurface. Analogues for the Early Jurassic part of the Los Molles Fm. should consider early post-rift intraslope fans with variable degree of confinement induced by inherited topography, complex spatial distribution and multiple extrabasinal sources, which differ from models of currently applied unconfined basin-floor fan models.

Perspectives for future research from a proposed involve the elaboration of detailed intraslope lobe characteristics. This involves fine-scale assessment of facies and HEB type distribution at lobe-scale (Markov chain analysis), petrographic characterization of bed-scale heterogeneity and quantification of bed thinning rates with restoration of slope angles towards lobe complex margins in order to constrain the variability in the degree of confinement. Finally, refinement of the stratigraphic architecture of intraslope fans can be integrated with UAV photogrammetric models and borehole drilling to better constrain the dimensions and architecture of intraslope fans in subsurface in the study area.

References

Acocella, V., Spinks, K., Cole, J., Nicol, A., 2003. Oblique back arc rifting of Taupo Volcanic Zone, New Zealand. Tectonics 22. https://doi.org/10.1029/2002TC001447

Adeogba, A.A., McHargue, T.R., Graham, S.A., 2005. Transient fan architecture and depositional controls from near-surface 3-D seismic data, Niger Delta continental slope. Am. Assoc. Pet. Geol. Bull. 89, 627–643. https://doi.org/10.1306/11200404025

Al-Suwaidi, A.H., Hesselbo, S.P., Damborenea, S.E., Manceñido, M.O., Jenkyns, H.C., Riccardi, A.C., Angelozzi, G.N., Baudin, F., 2016. The Toarcian Oceanic Anoxic Event (Early Jurassic) in the Neuquén Basin, Argentina: A Reassessment of Age and Carbon Isotope Stratigraphy. J. Geol. 124, 171–193. https://doi.org/10.1086/684831

Al Ja'Aidi, O.S., McCaffrey, W.D., Kneller, B.C., 2004. Factors influencing the deposit geometry of experimental turbidity currents: implications for sand-body architecture in confined basins, in: Lomas, S.A., Joseph, P. (Eds.), Confined Turbidite Systems. Geological Society, London, Special Publications. pp. 45–58. https://doi.org/10.1144/GSL.SP.2004.222.01.04

Alexander, J., Morris, S., 1994. Observations on Experimental, Nonchannelized, High-Concentration Turbidity Currents and Variations in Deposits Around Obstacles. J. Sediment. Res. A64, 899–909. https://doi.org/10.1306/D4267F00-2B26-11D7-8648000102C1865D

Allen, P.A., Allen, J.R., 2013. Basin Analysis: Principles and Application to Petroleum Play Assessment, 3rd editio. ed. Wiley-Blackwell.

Aller, R.C., 1982. Carbonate Dissolution in Nearshore Terrigenous Muds: The Role of Physical and Biological Reworking. J. Geol. 90, 79–95. https://doi.org/10.1086/628652

Alves, T.M., Manuppella, G., Gawthorpe, R.L., Hunt, D.W., Monteiro, J.H., 2003. The depositional evolution of diapir- and fault-bounded rift basins: examples from the Lusitanian Basin of West Iberia. Sediment. Geol. 162, 273–303. https://doi.org/10.1016/S0037-0738(03)00155-6

Amorosi, A., Zuffa, G.G., 2011. Sand composition changes across key boundaries of siliciclastic and hybrid depositional sequences. Sediment. Geol. 236, 153–163. https://doi.org/10.1016/j.sedgeo.2011.01.003

Amy, L.A., Kneller, B.C., McCaffrey, W.D., 2007. Facies architecture of the Grès de Peïra Cava, SE France: landward stacking patterns in ponded turbiditic basins. J. Geol. Soc. London. 164, 143–162. https://doi.org/10.1144/0016-76492005-019

Amy, L.A., McCaffrey, W.D., Kneller, B.C., 2004. The influence of a lateral basin-slope on the depositional patterns of natural and experimental turbidity currents, in: Joseph, P., Lomas, S.A. (Eds.), Deep-Water Sedimentation in the Alpine Basin of SE France. New Perspectives on the Grès d'Annot and Related Systems. Geological Society, London, Special Publications. pp. 311–330. https://doi.org/10.1144/GSL.SP.2004.221.01.17

Amy, L.A., Peachey, S.A., Gardiner, A.A., Talling, P.J., 2009. Prediction of hydrocarbon recovery from turbidite sandstones with linked-debrite facies: Numerical flow-simulation studies. Mar. Pet. Geol. 26, 2032–2043. https://doi.org/10.1016/j.marpetgeo.2009.02.017

Amy, Peakall, J., Talling, P.J., 2005. Density- and viscosity-stratified gravity currents: Insight from laboratory experiments and implications for submarine flow deposits. Sediment. Geol. 179, 5–29. https://doi.org/10.1016/j.sedgeo.2005.04.009

Angelozzi, G.N., Pérez Panera, J.P., 2016. Calcareous nannofossils from Los Molles Formation (Pliensbachian-Aalenian), Neuquén Basin, Argentina, in: Jurassic Calcareaous Nanofossil

Workshop, Lyon. pp. 6–11.

Argent, J.D., Stewart, S.A., Underhill, J.R., 2000. Controls on the Lower Cretaceous Punt Sandstone Member, a massive deep-water clastic deposystem, Inner Moray Firth, UK North Sea. Pet. Geosci. 6, 275–285. https://doi.org/10.1144/petgeo.6.3.275

Armella, C., Leanza, H.A., Corfu, F., 2016. Synsedimentary ash rains and paleoenvironmental conditions during the deposition of the Chachil Formation (Pliensbachian) at its type locality, Neuquén Basin, Argentina. J. South Am. Earth Sci. 71, 82–95. https://doi.org/10.1016/j.jsames.2016.07.002

Armitage, J.J., Allen, P.A., 2010. Cratonic basins and the long-term subsidence history of continental interiors. J. Geol. Soc. London. 167, 61–70. https://doi.org/10.1144/0016-76492009-108

Arnott, R.W.C., 1993. Quasi-Planar-Laminated Sandstone Beds of the Lower Cretaceous Bootlegger Member, North-Central Montana: Evidence of Combined-Flow Sedimentation. J. Sediment. Res. 63, 488–494. https://doi.org/10.1306/D4267B31-2B26-11D7-8648000102C1865D

Athmer, W., 2010. Syn-tectonic emplacement of deep-marine reservoir sands at rifting margins including a case study from the Vøring Basin. PhD thesis, Technische Universität Clausthal, Clausthal-Zellerfeld, Germany.

Athmer, W., Gonzalez Uribe, G.A., Luthi, S.M., Donselaar, M.E., 2011. Tectonic control on the distribution of Palaeocene marine syn-rift deposits in the Fenris Graben, northwestern Vøring Basin, offshore Norway. Basin Res. 23, 361–375. https://doi.org/10.1111/j.1365-2117.2010.00494.x

Athmer, W., Luthi, S.M., 2011. The effect of relay ramps on sediment routes and deposition: A review. Sediment. Geol. 242, 1–17. https://doi.org/10.1016/j.sedgeo.2011.10.002

Audin, L., Manighetti, I., Tapponnier, P., Métivier, F., Jacques, E., Huchon, P., 2001. Fault propagation and climatic control of sedimentation on the Ghoubbet Rift Floor: insights from the Tadjouraden cruise in the western Gulf of Aden. Geophys. J. Int. 144, 391–413. https://doi.org/10.1046/j.0956-540x.2000.01322.x

Baas, J.H., Best, J.L., 2002. Turbulence Modulation in Clay-Rich Sediment-Laden Flows and Some Implications for Sediment Deposition. J. Sediment. Res. 72, 336–340. https://doi.org/10.1306/120601720336

Baas, J.H., Best, J.L., Peakall, J., 2016. Predicting bedforms and primary current stratification in cohesive mixtures of mud and sand. J. Geol. Soc. London. 173, 12–45. https://doi.org/10.1144/jgs2015-024

Baas, J.H., Best, J.L., Peakall, J., 2011. Depositional processes, bedform development and hybrid bed formation in rapidly decelerated cohesive (mud-sand) sediment flows. Sedimentology 58, 1953–1987. https://doi.org/10.1111/j.1365-3091.2011.01247.x

Baas, J.H., Best, J.L., Peakall, J., Wang, M., 2009. A Phase Diagram for Turbulent, Transitional, and Laminar Clay Suspension Flows. J. Sediment. Res. 79, 162–183. https://doi.org/10.2110/jsr.2009.025

Bakke, K., Kane, I.A., Martinsen, O.J., Petersen, S.A., Johansen, T.A., Hustoft, S., Jacobsen, F.H., Groth, A., 2013. Seismic modeling in the analysis of deep-water sandstone termination styles. Am. Assoc. Pet. Geol. Bull. 97, 1395–1419. https://doi.org/10.1306/03041312069

Balázs, A., Burov, E., Matenco, L., Vogt, K., Francois, T., Cloetingh, S., 2017a. Symmetry during the syn- and post-rift evolution of extensional back-arc basins: The role of inherited orogenic structures. Earth Planet. Sci. Lett. 462, 86–98. https://doi.org/10.1016/j.epsl.2017.01.015

Balázs, A., Granjeon, D., Matenco, L., Sztanó, O., Cloetingh, S., 2017b. Tectonic and Climatic Controls on Asymmetric Half-Graben Sedimentation: Inferences From 3-D Numerical Modeling. Tectonics

36, 2123–2141. https://doi.org/10.1002/2017TC004647

Balázs, A., Matenco, L., Magyar, I., Horváth, F., Cloetingh, S., 2016. The link between tectonics and sedimentation in back-arc basins: New genetic constraints from the analysis of the Pannonian Basin. Tectonics 35, 1526–1559. https://doi.org/10.1002/2015TC004109

Ballent, S., Concheyro, A., Náñez, C., Pujana, I., Lescano, M., Carignano, A.P., Caramés, A., Angelozzi, G., Ronchi, D., 2011. Microfósiles Mesozoicos Y Cenozoicos, in: Relatorio Del XVIII Congreso Geológico Argentino, Neuquén. pp. 489–528.

Ballent, S.C., Whatley, R., 2000. The composition of Argentinian Jurassic marine ostracod and foraminiferal faunas: Environment and zoogeography. Geobios 33, 365–376. https://doi.org/10.1016/S0016-6995(00)80164-3

Barr, D., 1991. Subsidence and sedimentation in semi-starved half-graben: a model based on North Sea data. Geol. Soc. London, Spec. Publ. 56, 17–28. https://doi.org/10.1144/GSL.SP.1991.056.01.02

Barredo, S.P., 2012. Geodynamic and Tectonostratigrafic Study of a Continental Rift: The Triassic Cuyana Basin, Argentina, in: Sharkov, E. (Ed.), Tectonics - Recent Advances. pp. 99–130. https://doi.org/10.5772/49958

Basu, A., Young, S.W., Suttner, L.J., James, C.W., Mack, G.H., 1975. Re-evaluation of the Use of Undulatory Extinction and Polycrystallinity in Detrital Quartz for Provenance Interpretation. SEPM J. Sediment. Res. 45, 873–882. https://doi.org/10.1306/212F6E6F-2B24-11D7-8648000102C1865D

Baur, J., Sutherland, R., Stern, T., 2014. Anomalous passive subsidence of deep-water sedimentary basins: a prearc basin example, southern New Caledonia Trough and Taranaki Basin, New Zealand. Basin Res. 26, 242–268. https://doi.org/10.1111/bre.12030

Beard, D.C., Weyl, P.K., 1973. Influence of Texture on Porosity and Permeability of Unconsolidated Sand. Am. Assoc. Pet. Geol. Bull. 57, 349–369.

Beaubouef, R.T., Friedmann, S.J., 2000. High Resolution Seismic/Sequence Stratigraphic Framework for the Evolution of Pleistocene Intra Slope Basins, Western Gulf of Mexico: Depositional Models and Reservoir Analogs, in: Weimer, P. (Ed.), Deep-Water Reservoirs of the World. SEPM Society for Sedimentary Geology. Society of economic paleontologists and mineralogists, pp. 40–60. https://doi.org/10.5724/gcs.00.15.0040

Bechis, F., Cristallini, E.O., Giambiagi, L.B., Yagupsky, D.L., Guzmán, C.G., García, V.H., 2014. Transtensional tectonics induced by oblique reactivation of previous lithospheric anisotropies during the Late Triassic to Early Jurassic rifting in the Neuquén basin: Insights from analog models. J. Geodyn. 79, 1–17. https://doi.org/10.1016/j.jog.2014.04.010

Bechis, F., Giambiagi, L., García, V., Lanés, S., Cristallini, E., Tunik, M., 2010. Kinematic analysis of a transtensional fault system: The Atuel depocenter of the Neuquén basin, southern Central Andes, Argentina. J. Struct. Geol. 32, 886–899. https://doi.org/10.1016/j.jsg.2010.03.009

Bell, R.E., McNeill, L.C., Bull, J.M., Henstock, T.J., 2008. Evolution of the offshore western Gulf of Corinth. Geol. Soc. Am. Bull. 120, 156–178. https://doi.org/10.1130/B26212.1

Bell, R.E., McNeill, L.C., Bull, J.M., Henstock, T.J., Collier, R.E.L., Leeder, M.R., 2009. Fault architecture, basin structure and evolution of the Gulf of Corinth Rift, central Greece. Basin Res. 21, 824–855. https://doi.org/10.1111/j.1365-2117.2009.00401.x

Bellahsen, N., Fournier, M., D'Acremont, E., Leroy, S., Daniel, J.M., 2006. Fault reactivation and rift localization: Northeastern Gulf of Aden margin. Tectonics 25. https://doi.org/10.1029/2004TC001626

Bermudez, A., Delpino, D., Pángaro, F., 2002. Volcanismo de arco asociado a procesos de subducción – extensión durante el Triásico Superior – Jurásico Inferior (Precuyano). Área Cerro Bandera, Cuenca Neuquina, Argentina. V Congr. Explor. y Desarro. Hidrocarburos.

Bertram, G.T., Milton, N.J., 1988. Reconstructing basin evolution from sedimentary thickness; the importance of palaeobathymetric control, with reference to the North Sea. Basin Res. 1, 247–257. https://doi.org/10.1111/j.1365-2117.1988.tb00020.x

Best, J., Bridge, J., 1992. The morphology and dynamics of low amplitude bedwaves upon upper stage plane beds and the preservation of planar laminae. Sedimentology 39, 737–752. https://doi.org/10.1111/j.1365-3091.1992.tb02150.x

Bialas, R.W., Buck, W.R., 2009. How sediment promotes narrow rifting: Application to the Gulf of California. Tectonics 28. https://doi.org/10.1029/2008TC002394

Black, L.P., Kamo, S.L., Allen, C.M., Davis, D.W., Aleinikoff, J.N., Valley, J.W., Mundil, R., Campbell, I.H., Korsch, R.J., Williams, I.S., Foudoulis, C., 2004. Improved 206Pb/238U microprobe geochronology by the monitoring of a trace-element-related matrix effect; SHRIMP, ID–TIMS, ELA–ICP–MS and oxygen isotope documentation for a series of zircon standards. Chem. Geol. 205, 115–140. https://doi.org/10.1016/j.chemgeo.2004.01.003

Blair, T.C., McPherson, J.G., 1994. Alluvial Fans and their Natural Distinction from Rivers Based on Morphology, Hydraulic Processes, Sedimentary Processes, and Facies Assemblages. J. Sediment. Res. Vol. 64A, 450–489. https://doi.org/10.1306/D4267DDE-2B26-11D7-8648000102C1865D

Blatt, H., Christie, J.M., 1963. Undulatory Extinction in Quartz of Igneous and Metamorphic Rocks and Its Significance in Provenance Studies of Sedimentary Rocks. J. Sediment. Res. 33, 559–579. https://doi.org/10.1306/74D70EBB-2B21-11D7-8648000102C1865D

Blatt, H., Middleton, G., Murray, R., 1980. Origin of Sedimentary Rocks, 2nd ed. Englewoods Cliffs, N.J.: Pentice-Hall.

Blum, M.D., Hattier-Womack, J., 2009. Climate Change, Sea-Level Change, and Fluvial Sediment Supply to Deepwater Depositional Systems, in: Kneller, B., Martinsen, O.J., McCaffrey, B. (Eds.), External Controls of Deep-Water Depositional Systems. SEPM Special Publication. SEPM (Society for Sedimentary Geology), pp. 15–39. https://doi.org/10.2110/sepmsp.092.015

Boehm, A., Moore, J.C., 2002. Fluidized sandstone intrusions as an indicator of Paleostress orientation, Santa Cruz, California. Geofluids 2, 147–161. https://doi.org/10.1046/j.1468-8123.2002.00026.x

Booth, J.R., Dean, M.C., DuVernay III, A.E., Styzen, M.J., 2003. Paleo-bathymetric controls on the stratigraphic architecture and reservoir development of confined fans in the Auger Basin: central Gulf of Mexico slope. Mar. Pet. Geol. 20, 563–586. https://doi.org/10.1016/j.marpetgeo.2003.03.008

Bosence, D., 2005. A genetic classification of carbonate platforms based on their basinal and tectonic settings in the Cenozoic. Sediment. Geol. 175, 49–72. https://doi.org/10.1016/j.sedgeo.2004.12.030

Bosence, D.W.J., 1998. Stratigraphic and sedimentological models of rift basins, in: Purser B.H., Bosence D.W.J. (Eds.), Sedimentation and Tectonics in Rift Basins Red Sea:- Gulf of Aden. Springer, Dordrecht. https://doi.org/10.1007/978-94-011-4930-3

Bouma, A.H., 1962. Sedimentology of Some Flysch Deposits. A Graphic Approach to Facies Interpretation.

Bourget, J., Zaragosi, S., Ellouz-Zimmermann, N., Mouchot, N., Garlan, T., Schneider, J.-L., Lanfumey, V., Lallemant, S., 2011. Turbidite system architecture and sedimentary processes along topographically complex slopes: the Makran convergent margin. Sedimentology 58, 376–406.

https://doi.org/10.1111/j.1365-3091.2010.01168.x

Braga, J.C., Martin, J.M., Wood, J.L., 2001. Submarine lobes and feeder channels of redeposited, temperate carbonate and mixed siliciclastic-carbonate platform deposits (Vera Basin, Almeria, southern Spain). Sedimentology 48, 99–116. https://doi.org/10.1046/j.1365-3091.2001.00353.x

Braun, J., Beaumont, C., 1989. Contrasting Styles of Lithospheric Extension: Implications for Differences Between the Basin and Range Province and Rifted Continental Margins: Chapter 5: Concepts, in: Tankard, A.J., Balkwill, H.R. (Eds.), Extensional Tectonics and Stratigraphy of the North Atlantic Margins. pp. 53–79.

Brinkworth, W., Vocaturo, G., Loss, M.L., Mortaloni, E.M., Giunta, D.L., Massaferro, J.L., 2018. Estudio cronoestratigráfrico y evolución paleoambiental del Jurásico Inferior-Medio en el engolfamiento de la cuenca Neuquina, Argentina, in: X Congreso de Exploración y Desarrollo de Hidrocarburos. Sessiones Generales: "Energía y Sociedad, Aliados Inseparables". pp. 597–622.

Brooks, H.L., Hodgson, D.M., Brunt, R.L., Peakall, J., Poyatos-Moré, M., Flint, S.S., 2018. Disconnected submarine lobes as a record of stepped slope evolution over multiple sea-level cycles. Geosphere 14, 1753–1779. https://doi.org/10.1130/GES01618.1

Brun, J.P., 1999. Narrow rifts versus wide rifts: inferences for the mechanics of rifting from laboratory experiments. Philos. Trans. R. Soc. London. Ser. A Math. Phys. Eng. Sci. 357, 695–712. https://doi.org/10.1098/rsta.1999.0349

Brune, S., 2016. Rifts and Rifted Margins, in: Duarte, J.C., Schellart, W.P. (Eds.), Plate Boundaries and Natural Hazards. pp. 11–37. https://doi.org/10.1002/9781119054146.ch2

Buck, S.G., Goldring, R., 2003. Conical Sedimentary Structures, Trace Fossils or Not? Observations, Experiments, and Review. J. Sediment. Res. 73, 338–353. https://doi.org/10.1306/091602730338

Buck, W.R., 2015. The Dynamics of Continental Breakup and Extension, in: Schubert, G. (Ed.), Treatise on Geophysics. Elsevier, pp. 325–379. https://doi.org/10.1016/B978-0-444-53802-4.00118-4

Buck, W.R., 2004. Consequences of asthenospheric variability on continental rifting, in: Karner, G.D., Taylor, B., Driscoll, N.W., Kohlstedt, D.L. (Eds.), Rheology and Deformation of the Lithosphere at Continental Margins. Columbia University Press, New York, pp. 1–31.

Buck, W.R., 1991. Modes of continental lithospheric extension. J. Geophys. Res. Solid Earth 96, 20161–20178. https://doi.org/10.1029/91JB01485

Burchette, T.P., Wright, V.P., 1992. Carbonate ramp depositional systems. Sediment. Geol. 79, 3–57. https://doi.org/10.1016/0037-0738(92)90003-A

Burgess, P.M., Flint, S., Johnson, S., 2000. Sequence stratigraphic interpretation of turbiditic strata: An example from Jurassic strata of the Neuquén basin, Argentina. Geol. Soc. Am. Bull. 112, 1650–1666. https://doi.org/10.1130/0016-7606(2000)112<1650:SSIOTS>2.0.CO;2

Burgess, P.M., Gurnis, M., Moresi, L., 1997. Formation of sequences in the cratonic interior of North America by interaction between mantle, eustatic, and stratigraphic processes. Geol. Soc. Am. Bull. 109, 1515–1535. https://doi.org/10.1130/0016-7606(1997)109<1515:FOSITC>2.3.CO;2

Burgess, P.M., Hovius, N., 1998. Rates of delta progradation during highstands: consequences for timing of deposition in deep-marine systems. J. Geol. Soc. London. 155, 217–222. https://doi.org/10.1144/gsjgs.155.2.0217

Burgess, P.M., Moresi, L.N., 1999. Modelling rates and distribution of subsidence due to dynamic topography over subducting slabs: is it possible to identify dynamic topography from ancient strata? Basin Res. 11, 305–314. https://doi.org/10.1046/j.1365-2117.1999.00102.x

Burgreen, B., Graham, S., 2014. Evolution of a deep-water lobe system in the Neogene trench-slope

setting of the East Coast Basin, New Zealand: Lobe stratigraphy and architecture in a weakly confined basin configuration. Mar. Pet. Geol. 54, 1–22. https://doi.org/10.1016/j.marpetgeo.2014.02.011

Burov, E., Poliakov, A., 2003. Erosional forcing of basin dynamics: new aspects of syn- and post-rift evolution, in: Nieuwland, D.A. (Ed.), New Insights into Structural Interpretation and Modelling. Geological Society, London, Special Publications. pp. 209–223. https://doi.org/10.1144/GSL.SP.2003.212.01.14

Burov, E., Poliakov, A., 2001. Erosion and rheology controls on synrift and postrift evolution: Verifying old and new ideas using a fully coupled numerical model. J. Geophys. Res. Solid Earth 106, 16461–16481. https://doi.org/10.1029/2001JB000433

Carbone, O., Franzese, J.R., Limeres, M., Delpino, D., Martínez, R., 2011. El Ciclo Precuyano (Triásico Tardío - Jurásico Temprano) En La Cuenca Neuquina. Relat. del XVIII Congr. Geológico Argentino, Neuquén 63–76.

Carey, S.N., Schneider, J.-L., 2011. Volcaniclastic Processes and Deposits in the Deep-Sea, in: Hneke, H., Mulder, T. (Eds.), Developments in Sedimentology. pp. 457–515. https://doi.org/10.1016/B978-0-444-53000-4.00007-X

Carminati, E., Santantonio, M., 2005. Control of differential compaction on the geometry of sediments onlapping paleoescarpments: Insights from field geology (Central Apennines, Italy) and numerical modeling. Geology 33, 353–356. https://doi.org/10.1130/G21262.1

Carroll, A.R., Bohacs, K.M., 1999. Stratigraphic classification of ancient lakes: Balancing tectonic and climatic controls. Geology 27, 99–102. https://doi.org/10.1130/0091-7613(1999)027<0099:SCOALB>2.3.CO;2

Cartwright, J., 1991. The kinematic evolution of the Coffee Soil Fault. Geol. Soc. London, Spec. Publ. 56, 29–40. https://doi.org/10.1144/GSL.SP.1991.056.01.03

Cas, R.A., Wright, J. V, 1991. Subaqueous pyroclastic flows and ignimbrites: an assessment. Bull. Volcanol. 53, 357–380. https://doi.org/10.1007/BF00280227

Cas, R.A.F., Giordano, G., 2014. Submarine Volcanism: a Review of the Constraints, Processes and Products, and Relevance to the Cabo de Gata Volcanic Succession. Ital. J. Geosci. 133, 362–377. https://doi.org/10.3301/IJG.2014.46

Castelltort, S., Pochat, S., Van Den Driessche, J., 2004. Using T–Z plots as a graphical method to infer lithological variations from growth strata. J. Struct. Geol. 26, 1425–1432. https://doi.org/10.1016/j.jsg.2004.01.002

Cattaneo, A., Steel, R.J., 2003. Transgressive deposits: a review of their variability. Earth-Science Rev. 62, 187–228. https://doi.org/10.1016/S0012-8252(02)00134-4

Cheel, R.J., Leckie, D.A., 1993. Hummocky Cross-Stratification, in: Wright, V.P. (Ed.), Sedimentology Review/1. Blackwell Publishing Ltd., Oxford, UK, pp. 103–122. https://doi.org/10.1002/9781444304534.ch7

Chernicoff, C.J., Zappettini, E.O., 2004. Geophysical Evidence for Terrane Boundaries in South-Central Argentina. Gondwana Res. 7, 1105–1116. https://doi.org/10.1016/S1342-937X(05)71087-X

Chiocci, F.L., Casalbore, D., 2011. Submarine gullies on Italian upper slopes and their relationship with volcanic activity revisited 20 years after Bill Normark's pioneering work. Geosphere 7, 1284–1293. https://doi.org/10.1130/GES00633.1

Ciccioli, P.L., Marenssi, S.A., Limarino, C.O., 2014. Petrology and provenance of the Toro Negro Formation (Neogene) of the Vinchina broken-foreland basin (Central Andes of Argentina). J. South Am. Earth Sci. 49, 15–38. https://doi.org/10.1016/j.jsames.2013.10.003

Cingolani, C.A., Zanettini, J.C.M., Leanza, H.A., 2011. El basamento ígneo y metamórfico. Relat. del XVIII Congr. Geológico Argentino, Neuquén 37–47.

Clare, M.A., Hughes Clarke, J.E., Talling, P.J., Cartigny, M.J.B., Pratomo, D.G., 2016. Preconditioning and triggering of offshore slope failures and turbidity currents revealed by most detailed monitoring yet at a fjord-head delta. Earth Planet. Sci. Lett. 450, 208–220. https://doi.org/10.1016/j.epsl.2016.06.021

Clare, M.A., Le Bas, T., Price, D.M., Hunt, J.E., Sear, D., Cartigny, M.J.B., Vellinga, A., Symons, W., Firth, C., Cronin, S., 2018. Complex and Cascading Triggering of Submarine Landslides and Turbidity Currents at Volcanic Islands Revealed From Integration of High-Resolution Onshore and Offshore Surveys. Front. Earth Sci. 6. https://doi.org/10.3389/feart.2018.00223

Clift, P.D., Brune, S., Quinteros, J., 2015. Climate changes control offshore crustal structure at South China Sea continental margin. Earth Planet. Sci. Lett. 420, 66–72. https://doi.org/10.1016/j.epsl.2015.03.032

Cloetingh, S., Willett, S.D., 2013. TOPO-EUROPE: Understanding of the coupling between the deep Earth and continental topography. Tectonophysics 602, 1–14. https://doi.org/10.1016/j.tecto.2013.05.023

Cobain, S.L., Hodgson, D.M., Peakall, J., Shiers, M.N., 2017. An integrated model of clastic injectites and basin floor lobe complexes: implications for stratigraphic trap plays. Basin Res. in press, 1–20. https://doi.org/10.1111/bre.12229

Cobain, S.L., Peakall, J., Hodgson, D.M., 2015. Indicators of propagation direction and relative depth in clastic injectites: Implications for laminar versus turbulent flow processes. Geol. Soc. Am. Bull. 127, 1816–1830. https://doi.org/10.1130/B31209.1

Cobbold, P.R., Zanella, A., Rodrigues, N., Løseth, H., 2013. Bedding-parallel fibrous veins (beef and cone-in-cone): Worldwide occurrence and possible significance in terms of fluid overpressure, hydrocarbon generation and mineralization. Mar. Pet. Geol. 43, 1–20. https://doi.org/10.1016/j.marpetgeo.2013.01.010

Collier, R.E.L., 1989. Tectonic evolution of the Northumberland Basin; the effects of renewed extension upon an inverted extensional basin. J. Geol. Soc. London. 146, 981–989. https://doi.org/10.1144/gsjgs.146.6.0981

Collier, R.E.L., Dart, C.J., 1991. Neogene to Quaternary rifting, sedimentation and uplift in the Corinth Basin,Greece. J. Geol. Soc. London. 148, 1049–1065. https://doi.org/10.1144/gsjgs.148.6.1049

Collier, R.E.L., Leeder, M.R., Trout, M., Ferentinos, G., Lyberis, E., Papatheodorou, G., 2000. High sediment yields and cool, wet winters: Test of last glacial paleoclimates in the northern Mediterranean. Geology 28, 999–1002. https://doi.org/10.1130/0091-7613(2000)28<999:HSYACW>2.0.CO;2

Collier, R.E.L., Thompson, J., 1991. Transverse and linear dunes in an Upper Pleistocene marine sequence, Corinth Basin, Greece. Sedimentology 38, 1021–1040. https://doi.org/10.1111/j.1365-3091.1991.tb00369.x

Comínguez, A.H., Franzese, J.R., 2008. Central Neuquén basin: some deep-seismic indicators of the rift stage development, in: Actas Del XVII Congreso Geológico Argentino, Jujuy. pp. 754–755.

Comínguez, A.H., Franzese, J.R., 2005. The deep seismic structure of the central Neuquén Basin , Argentina, in: 6th International Symposium on Andean Geodynamics (ISAG). Barcelona, pp. 178–181. https://doi.org/2-7099-1575-8

Conti, B., Perinotto, J.A. de J., Veroslavsky, G., Castillo, M.G., de Santa Ana, H., Soto, M., Morales, E., 2017. Speculative petroleum systems of the southern Pelotas Basin, offshore Uruguay. Mar. Pet.

Geol. 83, 1–25. https://doi.org/10.1016/j.marpetgeo.2017.02.022

Contreras, J., Zühlke, R., Bowman, S., Bechstädt, T., 2010. Seismic stratigraphy and subsidence analysis of the southern Brazilian margin (Campos, Santos and Pelotas basins). Mar. Pet. Geol. 27, 1952–1980. https://doi.org/10.1016/j.marpetgeo.2010.06.007

Corti, G., van Wijk, J., Cloetingh, S., Morley, C.K., 2007. Tectonic inheritance and continental rift architecture: Numerical and analogue models of the East African Rift system. Tectonics 26. https://doi.org/10.1029/2006TC002086

Covault, J.A., Graham, S.A., 2010. Submarine fans at all sea-level stands: Tectono-morphologic and climatic controls on terrigenous sediment delivery to the deep sea. Geology 38, 939–942. https://doi.org/10.1130/G31081.1

Covault, J.A., Romans, B.W., 2009. Growth patterns of deep-sea fans revisited: Turbidite-system morphology in confined basins, examples from the California Borderland. Mar. Geol. 265, 51–66. https://doi.org/10.1016/j.margeo.2009.06.016

Crabaugh, J.P., Steel, R.J., 2004. Basin-floor fans of the Central Tertiary Basin, Spitsbergen: relationship of basin-floor sand-bodies to prograding clinoforms in a structurally active basin, in: Lomas, S.A., Joseph, P. (Eds.), Confined Turbidite Systems, Geological Society, London, Special Publications. pp. 187–208. https://doi.org/10.1144/GSL.SP.2004.222.01.10

Cristallini, E., Tomezzoli, R., Pando, G., Gazzera, C., Martínez, J.M., Quiroga, J., Buhler, M., Bechis, F., Barredo, S., Zambrano, O., 2009. Controles precuyanos en la estructura de la Cuenca Neuquina. Rev. la Asoc. Geológica Argentina 65, 248–264.

Cristallini, E.O., Bottesi, G., Gavarrino, A., Rodríguez, L., Tomezzoli, R., Comeron, R., 2006. Synrift geometry of the Neuquén Basin in northeastern Neuquén Province, Argentina Ernesto. Geol. Soc. Am. Spec. Pap. 407, 147–161. https://doi.org/10.1130/2006.2407(07).

Critelli, S., Ingersoll, R. V., 1995. Interpretation of neovolcanic versus palaeovolcanic sand grains: an example from Miocene deep-marine sandstone of the Topanga Group (Southern California). Sedimentology 42, 783–804. https://doi.org/10.1111/j.1365-3091.1995.tb00409.x

Critelli, S., Le Pera, E., 1994. Detrital modes and provenance of Miocene sandstones and modern sands to the Southern Apennines thrust-top basins (Italy). J. Sediment. Res. A64, 824–835. https://doi.org/10.1306/D4267ED8-2B26-11D7-8648000102C1865D

Critelli, Salvatore, Le Pera, E., Galluzzo, F., Milli, S., Moscatelli, M., Perrotta, S., Santantonio, M., 2007. Interpreting siliciclastic-carbonate detrital modes in foreland basin systems: An example from Upper Miocene arenites of the central Apennines, Italy, in: Arribas, J., Critelli, S., Johnsson, M.J. (Eds.), Provenance and Petrogenesis: Perspectives from Petrography and Geochemistry. Geological Society of America Special Paper. Geological Society of America, pp. 107–133. https://doi.org/10.1130/2006.2420(08)

Critelli, S., Marsaglia, K.M., Busby, C.J., 2002. Tectonic history of a Jurassic backarc-basin sequence (the Gran Cañon Formation, Cedros Island, Mexico), based on compositional modes of tuffaceous deposits. GSA Bull. 114, 515–527. https://doi.org/10.1130/0016-7606(2002)114<0515:THOAJB>2.0.CO;2

Cross, N.E., Bosence, D.W.J., 2008. Tectono-Sedimentary Models For Rift-Basin Carbonate Systems, in: Controls on Carbonate Platform and Reef Development. SEPM (Society for Sedimentary Geology), pp. 83–105. https://doi.org/10.2110/pec.08.89.0083

Cross, N.E., Bosence, D.W.J., Purser, B.H., 1998. The tectono-sedimentary evolution of a rift margin carbonate platform: Abu Shaar, Gulf of Suez, Egypt., in: Purser, B.H., Bosence, D.W.J. (Eds.), Sedimentation and Tectonics in Rift Basins: Red Sea–Gulf of Aden. Chapman and Hall, London, pp. 271–295.

Cross, N.E., Cunningham, A., Cook, R.J., Taha, A., Esmaie, E., El Swidan, N., 2009. Three-dimensional seismic geomorphology of a deep-water slope-channel system: The Sequoia field, offshore west Nile Delta, Egypt. Am. Assoc. Pet. Geol. Bull. 93, 1063–1086. https://doi.org/10.1306/05040908101

Cruz, C., Boll, A., Gómez Omil, R., Martínez, E.A., Arregui, C., Gulisano, C., Laffite, G.A., Villar, H.J., 2002. Hábitat de hidrocarburos y sistemas de carga los molles y vaca muerta en el sector central de la cuenca neuquina. Argentina, in: 5° Congreso de Exploración y Desarrollo de Hidrocarburos (Mar Del Plata).

Cruz, C.E., Robles, F., Sylwan, C.A., Villar, H.J., 1999. Los sistemas petroleros jurásicos de la Dorsal de Huincul, Cuenca Neuquina, Argentina, in: IV Congreso de Exploración y Desarrollo de Hidrocarburos, Mar Del Plata, IAPG. Tomo I. pp. 175–195.

Cucchi, R., Leanza, H.A., Repol, D., Escosteguy, L., González, R., Danieli, J.C., 2005a. Hoja Geológica 3972-IV, Junín de los Andes. Provincia del Neuquén. Programa Nacional de Cartas Geológicas de la República Argentina a escala 1:250.000. Inst. Geológia y Recur. Miner. Serv. Geológico Min. Argentino.Buenos Aires 357, 102. https://doi.org/0328-2333

Cucchi, R., Leanza, H.A., Repol, D., Escoteguy, L., González, R., Danieli, J.C., 2005b. Hoja Geológica 3972-IV, Junín de los Andes, Provincia del Neuquén (escala 1: 250.000). Inst. Geológia y Recur. Miner. Serv. Geológico Min. Argentino. Boletín 357. Buenos Aires 357, 102. https://doi.org/0328-2333

Cullis, S., Colombera, L., Patacci, M., McCaffrey, W.D., 2018. Hierarchical classifications of the sedimentary architecture of deep-marine depositional systems. Earth-Science Rev. 179, 38–71. https://doi.org/10.1016/j.earscirev.2018.01.016

D'Atri, A., Dela Pierre, F., Lanza, R., Ruffini, R., 1999. Distinguishing primary and resedimented vitric volcaniclastic layers in the Burdigalian carbonate shelf deposits in Monferrato (NW Italy). Sediment. Geol. 129, 143–163. https://doi.org/10.1016/S0037-0738(99)00098-6

D'Elia, L., 2010. Caracterización estratigráfica y estructural de la evolución temprana (sin-rift y post-rift inicial) del margen sur de la Cuenca Neuquina entre Sañicó (Neuquén) y el río Limay (Río Negro). PhD thesis, Universidad Nacional de La Plata,La Plata, Argentina. https://doi.org/ISBN: 978-950-34-0769-1

D'Elia, L., Bilmes, A., Franzese, J.R., Veiga, G.D., Hernández, M., Muravchik, M., 2015. Early evolution of the southern margin of the Neuquén Basin, Argentina: Tectono-stratigraphic implications for rift evolution and exploration of hydrocarbon plays. J. South Am. Earth Sci. 64, 42–57. https://doi.org/10.1016/j.jsames.2015.09.004

D'Elia, L., Martí, J., 2013. Caldera events in a rift depocentre: an example from the Jurassic Neuquén basin, Argentina. J. Geol. Soc. London 170, 571–584. https://doi.org/10.1144/jgs2012-116

D'Elia, L., Martí, J., Muravchik, M., Bilmes, A., Franzese, J.R., 2018. Impact of volcanism on the sedimentary record of the Neuquén rift basin, Argentina: towards a cause and effect model. Basin Res. 30, 311–335. https://doi.org/10.1111/bre.12222

D'Elia, L., Muravchik, M., Franzese, J.R., Lopez, L., 2012. Tectonostratigraphic analysis of the Late Triassic-Early Jurassic syn-rift sequence of the Neuquen Basin in the Sanico depocentre, Neuquen Province, Argentina. Andean Geol. 39, 133–157. https://doi.org/10.5027/andgeoV39N1-a07

Dakin, N., Pickering, K.T., Mohrig, D., Bayliss, N.J., 2013. Channel-like features created by erosive submarine debris flows: Field evidence from the Middle Eocene Ainsa Basin, Spanish Pyrenees. Mar. Pet. Geol. 41, 62–71. https://doi.org/10.1016/j.marpetgeo.2012.07.007

Damborenea, S.E., 2002. Jurassic evolution of Southern Hemisphere marine palaeobiogeographic units based on benthonic bivalves. Geobios 35, 51–71. https://doi.org/10.1016/S0016-6995(02)00048-7

Damborenea, S.E., Echevarría, J., 2015. Palaeolatitudinal gradients along the southeastern Palaeo-Pacific margin and the distribution of Early Jurassic bivalves. Vol. Jurassica 13, 3–16. https://doi.org/10.5604/17313708.1148552

Damborenea, S.E., Echevarría, J., Ros-Franch, S., 2013. Southern Hemisphere Palaeobiogeography of Triassic-Jurassic Marine Bivalves, Seaways and Landbridges: Southern Hemisphere Biogeographic Connections Through Time, SpringerBriefs in Earth System Sciences. Springer Netherlands, Dordrecht. https://doi.org/10.1007/978-94-007-5098-2

Damborenea, S.E., Manceñido, M.O., 1992. A comparison of Jurassic marine benthonic faunas from South America and New Zealand. J. R. Soc. New Zeal. 22, 131–152. https://doi.org/10.1080/03036758.1992.10420811

Damborenea, S.E., Manceñido, M.O., 1979. On the palaeogeographical distribution of the pectinid genus weyla (bivalvia, lower jurassic). Palaeogeogr. Palaeoclimatol. Palaeoecol. 27, 85–102. https://doi.org/10.1016/0031-0182(79)90095-6

Dawers, N.H., Underhill, J.R., 2000. The Role of Fault Interaction and Linkage in Controlling Synrift Stratigraphic Sequences: Late Jurassic, Statfjord East Area, Northern North Sea1. Am. Assoc. Pet. Geol. Bull. 84, 45–64. https://doi.org/10.1306/C9EBCD5B-1735-11D7-8645000102C1865D

de la Cruz, R., Suárez, M., 1997. El Jurásico de la cuenca de Neuquén en Lonquimay, Chile; Formación Nacientes del Biobío (38-39 degrees S). Rev. Geológica Chile 24, 3–24. https://doi.org/-

Deptuck, M.E., Sylvester, Z., O'Byrne, C., 2012. Pleistocene Seascape Evolution Above a "Simple" Stepped Slope—Western Niger Delta. Appl. Princ. Seism. Geomorphol. to Cont. Base-of-Slope Syst. Case Stud. from Seafloor Near-Seafloor Analog. SEPM Soc. Sediment. Geol. Spec. Publ. 99, 199–222. https://doi.org/10.2110/pec.12.99.0199

Dera, G., Donnadieu, Y., 2012. Modeling evidences for global warming, Arctic seawater freshening, and sluggish oceanic circulation during the Early Toarcian anoxic event. Paleoceanography 27. https://doi.org/10.1029/2012PA002283

Dewey, J.F., 1988. Extensional collapse of orogens. Tectonics 7, 1123–1139. https://doi.org/10.1029/TC007i006p01123

Dickinson, W.R., 1985. Interpreting Provenance Relations from Detrital Modes of Sandstones. Proven. Arenites. NATO ASI Ser. (Series C Math. Phys. Sci. 148, 333–361. https://doi.org/10.1007/978-94-017-2809-6_15

Dickinson, W.R., 1970. Interpreting Detrital Modes of Graywacke and Arkose. J. Sediment. Res. 40, 695–707. https://doi.org/10.1306/74D72018-2B21-11D7-8648000102C1865D

Dickinson, W.R., Beard, L.S., Brakenridge, G.R., Erjavec, J.L., Ferguson, R.C., Inman, K.F., Knepp, R.A., Lindberg, F.A., Ryberg, P.T., 1983. Provenance of North American Phanerozoic sandstones in relation to tectonic setting. GSA Bull. 94, 222–235. https://doi.org/10.1130/0016-7606(1983)94<222:PONAPS>2.0.CO;2

Dickinson, W.R., Rich, E.I., 1972. Petrologic Intervals and Petrofacies in the Great Valley Sequence, Sacramento Valley, California. GSA Bull. 83, 3007–3024. https://doi.org/10.1130/0016-7606(1972)83[3007:PIAPIT]2.0.CO;2

Dickinson, W.R., Suczek, C.A., 1979. Plate Tectonics and Sandstone Compositions. Am. Assoc. Pet. Geol. Bull. 63, 2164–2182. https://doi.org/10.1306/2F9188FB-16CE-11D7-8645000102C1865D

Dmitrieva, E., Jackson, C.A.L., Huuse, M., Kane, I.A., 2018. Regional distribution and controls on the development of post-rift turbidite systems: insights from the Paleocene of the eastern North Viking Graben, offshore Norway, in: Bowman, M., Levell, B. (Eds.), Petroleum Geology OfNW Europe: 50 Years OfLearning – Proceedings Ofthe 8th Petroleum Geology Conference. Geological

Society, London, Petroleum Geology Conference Series. pp. 147–170. https://doi.org/10.1144/PGC8.31

Do Couto, D., Gorini, C., Jolivet, L., Lebret, N., Augier, R., Gumiaux, C., D'Acremont, E., Ammar, A., Jabour, H., Auxietre, J.L., 2016. Tectonic and stratigraphic evolution of the Western Alboran Sea Basin in the last 25Myrs. Tectonophysics 677–678, 280–311. https://doi.org/10.1016/j.tecto.2016.03.020

Dodd, T.J.H., McCarthy, D.J., Richards, P.C., 2019. A depositional model for deep-lacustrine, partially confined, turbidite fans: Early Cretaceous, North Falkland Basin. Sedimentology 66, 53–80. https://doi.org/10.1111/sed.12483

Doglioni, C., 1995. Geological remarks on the relationships between extension and convergent geodynamic settings. Tectonophysics 252, 253–267. https://doi.org/10.1016/0040-1951(95)00087-9

Doglioni, C., Dagostino, N., Mariotti, G., 1998. Normal faulting vs regional subsidence and sedimentation rate. Mar. Pet. Geol. 15, 737–750. https://doi.org/10.1016/S0264-8172(98)00052-X

Dorobek, S.L., 2008. Carbonate-platform facies in volcanic-arc settings: Characteristics and controls on deposition and stratigraphic development, in: Draut, A., Clift, P.D., Scholl, D.W. (Eds.), Formation and Applications of the Sedimentary Record in Arc Collision Zones: Geological Society of America Special Paper. Geological Society of America, pp. 55–90. https://doi.org/10.1130/2008.2436(04)

Dorsey, R.J., Umhoefer, P.J., 2000. Tectonic and eustatic controls on sequence stratigraphy of the Pliocene Loreto basin, Baja California Sur, Mexico. Geol. Soc. Am. Bull. 112, 177–199. https://doi.org/10.1130/0016-7606(2000)112<177:TAECOS>2.0.CO;2

Dott, R.H., 1964. Wacke, Greywacke and Matrix—What Approach to Immature Sandstone Classification? J. Sediment. Petrol. 34, 625–632.

Drzewiecki, P.A., Simó, J.A., 2002. Depositional processes, triggering mechanisms and sediment composition of carbonate gravity flow deposits: examples from the Late Cretaceous of the south-central Pyrenees, Spain. Sediment. Geol. 146, 155–189. https://doi.org/10.1016/S0037-0738(01)00171-3

Ducassou, E., Migeon, S., Mulder, T., Murat, A., Capotondi, L., Bernasconi, S.M., Mascle, J., 2009. Evolution of the Nile deep-sea turbidite system during the Late Quaternary: influence of climate change on fan sedimentation. Sedimentology 56, 2061–2090. https://doi.org/10.1111/j.1365-3091.2009.01070.x

Duffy, O.B., Brocklehurst, S.H., Gawthorpe, R.L., Leeder, M.R., Finch, E., 2015. Controls on landscape and drainage evolution in regions of distributed normal faulting: Perachora Peninsula, Corinth Rift, Central Greece. Basin Res. 27, 473–494. https://doi.org/10.1111/bre.12084

Duke, W.L., Arnott, R.W.C., Cheel, R.J., 1991. Shelf sandstones and hummocky cross-stratification: New insights on a stormy debate. Geology 19, 625–628. https://doi.org/10.1130/0091-7613(1991)019<0625:SSAHCS>2.3.CO;2

Dumas, S., Arnott, R.W.C., 2006. Origin of hummocky and swaley cross-stratification - The controlling influence of unidirectional current strength and aggradation rate. Geology 34, 1073–1076. https://doi.org/10.1130/G22930A.1

Ebinger, C.J., Casey, M., 2001. Continental breakup in magmatic provinces: An Ethiopian example. Geology 29, 527–530. https://doi.org/10.1130/0091-7613(2001)029<0527:CBIMPA>2.0.CO;2

Echaurren, A., Oliveros, V., Folguera, A., Ibarra, F., Creixell, C., Lucassen, F., 2017. Early Andean tectonomagmatic stages in north Patagonia: insights from field and geochemical data. J. Geol.

Soc. London. 174, 405–421. https://doi.org/10.1144/jgs2016-087

Ekdale, A.A., Harding, S.C., 2015. Cylindrichnus concentricus Toots in Howard, 1966 (trace fossil) in its type locality, Upper Cretaceous, Wyoming. Ann. Soc. Geol. Pol. 85, 427–432. https://doi.org/10.14241/asgp.2015.018

Ekdale, A.A., Mason, T.R., 1988. Characteristic trace-fossil associations in oxygen-poor sedimentary environments. Geology 16, 720–723. https://doi.org/10.1130/0091-7613(1988)016<0720:CTFAIO>2.3.CO;2

Elliott, G.M., Jackson, C.A.L., Gawthorpe, R.L., Wilson, P., Sharp, I.R., Michelsen, L., 2017. Late syn-rift evolution of the Vingleia Fault Complex, Halten Terrace, offshore Mid-Norway; a test of rift basin tectono-stratigraphic models. Basin Res. 29, 465–487. https://doi.org/10.1111/bre.12158

Eschard, R., Albouy, E., Gaumet, F., Ayub, A., 2004. Comparing the depositional architecture of basin floor fans and slope fans in the Pab Sandstone, Maastrichtian, Pakistan, in: Lomas, S.A., Joseph, P. (Eds.), Confined Turbidite Systems, Geological Society, London, Special Publications. pp. 159–185. https://doi.org/10.1144/GSL.SP.2004.222.01.09

Etienne, S., Mulder, T., Bez, M., Desaubliaux, G., Kwasniewski, A., Parize, O., Dujoncquoy, E., Salles, T., 2012. Multiple scale characterization of sand-rich distal lobe deposit variability: Examples from the Annot Sandstones Formation, Eocene–Oligocene, SE France. Sediment. Geol. 273–274, 1–18. https://doi.org/10.1016/j.sedgeo.2012.05.003

Faerseth, R.B., Lien, T., 2002. Cretaceous evolution in the Norwegian Sea—a period characterized by tectonic quiescence. Mar. Pet. Geol. 19, 1005–1027.

Faerseth, R.B., Sjøblom, T.S., Steel, R.J., Liljedahl, T., Sauar, B.E., Tjelland, T., 1995. Tectonic controls on bathonian-volgian syn-rift successions on the visund fault block, northern north sea, in: Steel, R.J., Felt, V.L., Johannessen, E.P., Mathieu, C. (Eds.), Sequence Stratigraphy on the Northwest European Margin, Norwegian Petroleum Society Special Publication. pp. 325–346. https://doi.org/10.1016/S0928-8937(06)80074-3

Falvey, D.A., 1974. The development of continental margins in plate tectonic theory. J. Aust. Pet. Prod. Explor. Assoc. 14, 95–106. https://doi.org/10.1016/B978-0-444-42530-0.50012-3

Fan, S., Swift, D.J.P., Traykovski, P., Bentley, S., Borgeld, J.C., Reed, C.W., Niedoroda, A.W., 2004. River flooding, storm resuspension, and event stratigraphy on the northern California shelf: observations compared with simulations. Mar. Geol. 210, 17–41. https://doi.org/10.1016/j.margeo.2004.05.024

Fantasia, A., Föllmi, K.B., Adatte, T., Bernárdez, E., Spangenberg, J.E., Mattioli, E., 2018. The Toarcian Oceanic Anoxic Event in southwestern Gondwana: an example from the Andean Basin, northern Chile. J. Geol. Soc. London. 175, 883–902. https://doi.org/10.1144/jgs2018-008

Favalli, M., Chirico, G.D., Papale, P., Pareschi, M.T., Boschi, E., 2009. Lava flow hazard at Nyiragongo volcano, D.R.C. Bull. Volcanol. 71, 363–374. https://doi.org/10.1007/s00445-008-0233-y

Felix, M., Leszczyński, S., Ślączka, A., Uchman, A., Amy, L., Peakall, J., 2009. Field expressions of the transformation of debris flows into turbidity currents, with examples from the Polish Carpathians and the French Maritime Alps. Mar. Pet. Geol. 26, 2011–2020. https://doi.org/10.1016/j.marpetgeo.2009.02.014

Ferentinos, G., Papatheodorou, G., Collins, M.B., 1988. Sediment Transport processes on an active submarine fault escarpment: Gulf of Corinth, Greece. Mar. Geol. 83, 43–61. https://doi.org/10.1016/0025-3227(88)90051-5

Ferrari, S.M., Bessone, S., 2015. Una nueva localidad marina de edad jurásica temprana en la cuenca sudoccidental del Chubut, Argentina. Andean Geol. 42, 349–363.

https://doi.org/10.5027/andgeoV42n3-a04

Ferry, J.N., Mulder, T., Parize, O., Raillard, S., 2005a. Concept of equilibrium profile in deep-water turbidite system: effects of local physiographic changes on the nature of sedimentary process and the geometries of deposits, in: Hodgson, D.M., Flint, S.S. (Eds.), Submarine Slope Systems: Processes and Product. Geological Society, London, Special Publications. pp. 181–193. https://doi.org/10.1144/GSL.SP.2005.244.01.11

Ferry, J.N., Parize, O., Mulder, T., Raillard, S., 2005b. Sedimentary architecture and growth pattern of turbidite systems in distal part of a median fan; example of the Upper Miocene sedimentary sequence of the Lower Congo basin. Geodin. Acta 18, 145–152. https://doi.org/10.3166/ga.18.145-152

Fetter, M., De Ros, L.F., Bruhn, C.H.L., 2009. Petrographic and seismic evidence for the depositional setting of giant turbidite reservoirs and the paleogeographic evolution of Campos Basin, offshore Brazil. Mar. Pet. Geol. 26, 824–853. https://doi.org/10.1016/j.marpetgeo.2008.07.008

Finch, Emma, Gawthorpe, R., 2017. Growth and interaction of normal faults and fault network evolution in rifts: insights from three-dimensional discrete element modelling, in: Finch, E., Gawthorpe, R.L. (Eds.), The Geometry and Growth of Normal Faults. Geological Society, London, Special Publication. pp. 219–248. https://doi.org/10.1144/SP439.23

Fisher, R. V., Schmincke, H.-U., 1984. Pyroclastic Rocks. Springer Berlin Heidelberg, Berlin, Heidelberg. https://doi.org/10.1007/978-3-642-74864-6

Fjellanger, E., Surlyk, F., Wamsteeker, L.C., Midtun, T., 2005. Upper cretaceous basin-floor fans in the Vøring Basin, Mid Norway shelf, in: Wandås, B.T.., Nystuen, J.P., Eide, E., Gradstein, F. (Eds.), Onshore-Offshore Relationships on the North Atlantic Margin, Proceedings of the Norwegian Petroleum Society Conference, Norwegian Petroleum Society Special Publications. pp. 135–164. https://doi.org/10.1016/S0928-8937(05)80047-5

Flügel, E., 2004. Microfacies of Carbonate Rocks, Analysis, Interpretation and Application. Berlin.

Fonnesu, M., Haughton, P., Felletti, F., McCaffrey, W., 2015. Short length-scale variability of hybrid event beds and its applied significance. Mar. Pet. Geol. 67, 583–603. https://doi.org/10.1016/j.marpetgeo.2015.03.028

Ford, M., Le Carlier de Veslud, C., Bourgeois, O., 2007. Kinematic and geometric analysis of fault-related folds in a rift setting: The Dannemarie basin, Upper Rhine Graben, France. J. Struct. Geol. 29, 1811–1830. https://doi.org/10.1016/j.jsg.2007.08.001

Fossen, H., Rotevatn, A., 2016. Fault linkage and relay structures in extensional settings—A review. Earth-Science Rev. 154, 14–28. https://doi.org/10.1016/j.earscirev.2015.11.014

Franke, D., 2013. Rifting, lithosphere breakup and volcanism: Comparison of magma-poor and volcanic rifted margins. Mar. Pet. Geol. 43, 63–87. https://doi.org/10.1016/j.marpetgeo.2012.11.003

Franzese, J., Spalletti, L., Gómez Pérez, I., Macdonald, D., 2003. Tectonic and paleoenvironmental evolution of Mesozoic sedimentary basins along the Andean foothills of Argentina (32°–54°S). J. South Am. Earth Sci. 16, 81–90. https://doi.org/10.1016/S0895-9811(03)00020-8

Franzese, J.R., 1995. El Complejo Piedra Santa (Neuquén, Argentina): parte de un cinturón metamórfico neopaleozoico del Gondwana suroccidental. Rev. Geológica Chile 22, 193–202.

Franzese, J.R., Spalletti, L.A., 2001. Late Triassic–early Jurassic continental extension in southwestern Gondwana: tectonic segmentation and pre-break-up rifting. J. South Am. Earth Sci. 14, 257–270. https://doi.org/10.1016/S0895-9811(01)00029-3

Franzese, J.R., Veiga, G.D., Muravchik, M., Ancheta, M.D., D''Elía, L., 2007. Estratigrafía de "sin-rift" (Triásico Superior-Jurásico Inferior) de la Cuenca Neuquina en la sierra de Chacaico, Neuquén,

Argentina. Rev. Geológica Chile 34, 49–62. https://doi.org/10.4067/S0716-02082007000100003

Franzese, J.R., Veiga, G.D., Schwarz, E., Gómez-Pérez, I., 2006. Tectonostratigraphic evolution of a Mesozoic graben border system: the Chachil depocentre, southern Neuquen Basin, Argentina. J. Geol. Soc. London 163, 707–721. https://doi.org/10.1144/0016-764920-082

Fugelli, E.M.G., Olsen, T.R., 2007. Delineating confined slope turbidite systems offshore mid-Norway: The Cretaceous deep-marine Lysing Formation. Am. Assoc. Pet. Geol. Bull. 91, 1577–1601. https://doi.org/10.1306/07090706137

Fugelli, E.M.G., Olsen, T.R., 2005. Screening for deep-marine reservoirs in frontier basins: Part 1—Examples from offshore mid-Norway. Am. Assoc. Pet. Geol. Bull. 89, 853–882. https://doi.org/10.1306/02110504029

Fürsich, F.T., Oschmann, W., 1993. Shell beds as tools in basin analysis: the Jurassic of Kachchh, western India. J. Geol. Soc. London. 150, 169–185. https://doi.org/10.1144/gsjgs.150.1.0169

Fürsich, F.T., Pandey, D.K., 2003. Sequence stratigraphic significance of sedimentary cycles and shell concentrations in the Upper Jurassic–Lower Cretaceous of Kachchh, western India. Palaeogeogr. Palaeoclimatol. Palaeoecol. 193, 285–309. https://doi.org/10.1016/S0031-0182(03)00233-5

Gabrielsen, R.H., Kyrkjebø, R., Faleide, J.I., Fjeldskaar, W., Kjennerud, T., 2001. The Cretaceous post-rift basin configuration of the northern North Sea. Pet. Geosci. 7, 137–154. https://doi.org/10.1144/petgeo.7.2.137

Gabrielsen, R.H., Steel, R.J., Nøttvedt, A., 1995. Subtle traps in extensional terranes; a model with reference to the North Sea. Pet. Geosci. 1, 223–235. https://doi.org/10.1144/petgeo.1.3.223

Galloway, G.E., 1998. Siliciclastic Slope and Base-of-Slope Depositional Systems: Component Facies, Stratigraphic Architecture, and Classification. Am. Assoc. Pet. Geol. Bull. 82, 569–595. https://doi.org/10.1306/1D9BC5BB-172D-11D7-8645000102C1865D

Gamberi, F., Rovere, M., 2011. Architecture of a modern transient slope fan (Villafranca fan, Gioia basin–Southeastern Tyrrhenian Sea). Sediment. Geol. 236, 211–225. https://doi.org/10.1016/j.sedgeo.2011.01.007

García-García, F., Fernández, J., Viseras, C., Soria, J.M., 2006. Architecture and sedimentary facies evolution in a delta stack controlled by fault growth (Betic Cordillera, southern Spain, late Tortonian). Sediment. Geol. 185, 79–92. https://doi.org/10.1016/j.sedgeo.2005.10.010

García Morabito, E., 2010. Tectónica y estructura del retroarco andino entre los 38°15’ y los 40°S. PhD thesis, Universidad de Buenos Aires, Buenos Aires, Argentina.

García Morabito, E., Götze, H.-J., Ramos, V.A., 2011. Tertiary tectonics of the Patagonian Andes retro-arc area between 38°15’ and 40°S latitude. Tectonophysics 499, 1–21. https://doi.org/10.1016/j.tecto.2010.10.020

García, V.M., Quattrocchio, M.E., Zavala, C.A., Martínez, M.A., 2006. Palinofacies, paleoambientes y paleoclima del Grupo Cuyo (Jurásico Medio) en la Sierra de Chacaico, Cuenca Neuquina, Argentina. Rev. Española Micropaleontol. 38, 269–288.

Gardiner, A.R., 2006. The variability of turbidite sandbody pinchout and its impact on hydrocarbon recovery in stratigraphically trapped fields, in: Allen, M.R., Goffrey, G.P., Morgan, R.K., Walker, I.M. (Eds.), The Deliberate Search for the Stratigraphic Trap. Geological Society, London, Special Publications. pp. 267–287. https://doi.org/10.1144/GSL.SP.2006.254.01.14

Gardner, M.H., Borer, J.M., Melick, J.J., Mavilla, N., Dechesne, M., Wagerle, R.N., 2003. Stratigraphic process-response model for submarine channels and related features from studies of Permian Brushy Canyon outcrops, West Texas. Mar. Pet. Geol. 20, 757–787. https://doi.org/10.1016/j.marpetgeo.2003.07.004

Garrett, S.W., Atherton, T., Hurst, A., 2000. Lower Cretaceous deep-water sandstone reservoirs of the UK Central North Sea. Pet. Geosci. 6, 231–240. https://doi.org/10.1144/petgeo.6.3.231

Gartrell, A.P., 2001. Crustal rheology and its effect on rift basin styles. Tecton. Model. A Vol. Honor Hans Ramberg. GSA Mem. 193, 221–233. https://doi.org/10.1130/0-8137-1193-2.221

Garzanti, E., 2016. From static to dynamic provenance analysis—Sedimentary petrology upgraded. Sediment. Geol. 336, 3–13. https://doi.org/10.1016/j.sedgeo.2015.07.010

Garzanti, E., 1991. Non-Carbonate Intrabasinal Grains in Arenites: Their Recognition, Significance, and Relationship to Eustatic Cycles and Tectonic Setting. J. Sediment. Res. 61, 959–975. https://doi.org/10.1306/D4267816-2B26-11D7-8648000102C1865D

Garzanti, E., Andò, S., Vezzoli, G., 2009. Grain-size dependence of sediment composition and environmental bias in provenance studies. Earth Planet. Sci. Lett. 277, 422–432. https://doi.org/10.1016/j.epsl.2008.11.007

Garzanti, E., Vezzoli, G., 2003. A Classification of Metamorphic Grains in Sands Based on their Composition and Grade. J. Sediment. Res. 73, 830–837. https://doi.org/10.1306/012203730830

Garzanti, E., Vezzoli, G., Andò, S., Castiglioni, G., 2001. Petrology of Rifted-Margin Sand (Red Sea and Gulf of Aden, Yemen). J. Geol. 109, 277–297. https://doi.org/10.1086/319973

Gawthorpe, R.L., Fraser, A.J., Collier, R.E.L., 1994. Sequence stratigraphy in active extensional basins: implications for the interpretation of ancient basin-fills. Mar. Pet. Geol. 11, 642–658. https://doi.org/10.1016/0264-8172(94)90021-3

Gawthorpe, R.L., Hardy, S., Ritchie, B., 2003a. Numerical modelling of depositional sequences in half-graben rift basins. Sedimentology 50, 169–185. https://doi.org/10.1046/j.1365-3091.2003.00543.x

Gawthorpe, R.L., Hurst, J.M., 1993. Transfer zones in extensional basins: their structural style and influence on drainage development and stratigraphy. J. Geol. Soc. London. 150, 1137–1152. https://doi.org/10.1144/gsjgs.150.6.1137

Gawthorpe, R.L., Jackson, C.A.., Young, M.J., Sharp, I.R., Moustafa, A.R., Leppard, C.W., 2003b. Normal fault growth, displacement localisation and the evolution of normal fault populations: the Hammam Faraun fault block, Suez rift, Egypt. J. Struct. Geol. 25, 883–895. https://doi.org/10.1016/S0191-8141(02)00088-3

Gawthorpe, R.L., Leeder, M.R., 2000. Tectono-sedimentary evolution of active extensional basins. Basin Res. 12, 195–218. https://doi.org/10.1111/j.1365-2117.2000.00121.x

Gawthorpe, R.L., Leeder, M.R., Kranis, H., Skourtsos, E., Andrews, J.E., Henstra, G.A., Mack, G.H., Muravchik, M., Turner, J.A., Stamatakis, M., 2018. Tectono-sedimentary evolution of the Plio-Pleistocene Corinth rift, Greece. Basin Res. 30, 448–479. https://doi.org/10.1111/bre.12260

Gawthorpe, R.L., Sharp, I., Underhill, J.R., Gupta, S., 1997. Linked sequence stratigraphic and structural evolution of propagating normal faults. Geology 25, 795–798. https://doi.org/10.1130/0091-7613(1997)025<0795:LSSASE>2.3.CO;2

Ge, Z., Nemec, W., Gawthorpe, R.L., Hansen, E.W.M., 2017. Response of unconfined turbidity current to normal-fault topography. Sedimentology 64, 932–959. https://doi.org/10.1111/sed.12333

Gee, M.J.R., Masson, D.G., Watts, A.B., Mitchell, N.C., 2002. Passage of debris flows and turbidity currents through a topographic constriction: seafloor erosion and deflection of flow pathways. Sedimentology 48, 1389–1409. https://doi.org/10.1046/j.1365-3091.2001.00427.x

Gervais, A., Savoye, B., Piper, D.J.W., Mulder, T., Cremer, M., Pichevin, L., 2008. Present morphology and depositional architecture of a sandy confined submarine system: the Golo turbidite system

(eastern margin of Corsica), in: Lomas, S.A., Joseph, P. (Eds.), Confined Turbidite Systems. Geological Society, London, Special Publications. pp. 59–89. https://doi.org/10.1144/gsl.sp.2004.222.01.05

Ghinassi, M., 2007. The effects of differential subsidence and coastal topography on high-order transgressive–regressive cycles: Pliocene nearshore deposits of the Val d'Orcia Basin, Northern Apennines, Italy. Sediment. Geol. 202, 677–701. https://doi.org/10.1016/j.sedgeo.2007.08.002

Giambiagi, L., Martinez, A.N., 2008. Permo-Triassic oblique extension in the Potrerillos-Uspallata area, western Argentina. J. South Am. Earth Sci. 26, 252–260. https://doi.org/10.1016/j.jsames.2008.08.008

Giambiagi, L., Suriano, J., Mescua, J., 2005. Extensión multiepisódica durante el Jurásico temprano en el depocentro Atuel de la cuenca neuquina. Rev. la Asoc. Geológica Argentina 60, 524–534.

Gjelbeg, J., Martinsen, O.J., Charnock, M., Møller, N., Antonsen, P., 2005. The reservoir development of the Late Maastrichtian–Early Paleocene Ormen Lange gas field, Møre Basin, Mid-Norwegian Shelf, in: Doré, A.G., Vining, B.A. (Eds.), Petroleum Geology: North-West Europe and Global Perspectives—Proceedings of the 6th Petroleum Geology Conference. Geological Society, London, Petroleum Geology Conference Series. pp. 1165–1184. https://doi.org/10.1144/0061165

Gladstone, C., Phillips, J.C., Sparks, R.S., 1998. Experiments on bidisperse, constant-volume gravity currents: propagation and sediment deposition. Sedimentology 45, 833–843. https://doi.org/10.1046/j.1365-3091.1998.00189.x

Göğüş, O.H., 2015. Rifting and subsidence following lithospheric removal in continental back arcs. Geology 43, 3–6. https://doi.org/10.1130/G36305.1

Goldsworthy, M., Jackson, J., Haines, J., 2002. The continuity of active fault systems in Greece. Geophys. J. Int. 148, 596–618. https://doi.org/10.1046/j.1365-246X.2002.01609.x

Gómez-Pérez, I., 2003. An Early Jurassic deep-water stromatolitic bioherm related to possible methane seepage (Los Molles Formation, Neuquén, Argentina). Palaeogeogr. Palaeoclimatol. Palaeoecol. 201, 21–49. https://doi.org/10.1016/S0031-0182(03)00508-X

Gómez-Vasconcelos, M.G., Villamor, P., Cronin, S., Procter, J., Palmer, A., Townsend, D., Leonard, G., 2017. Crustal extension in the Tongariro graben, New Zealand: Insights into volcano-tectonic interactions and active deformation in a young continental rift. GSA Bull. 129, 1085–1099. https://doi.org/10.1130/B31657.1

Gómez Omil, R., Schmithalter, J., Cangini, A., Albariño, L., Corsi, A., 2002. El Grupo Cuyo en la Dorsal de Huincul, consideraciones estratigrafias, tectonicas y petroleras. Cuenca Neuquina. 5° Congr. Explor. y Desarro. Hidrocarburos (Mar del Plata).

Gray, T.E., Alexander, J., Leeder, M.R., 2005. Quantifying velocity and turbulence structure in depositing sustained turbidity currents across breaks in slope. Sedimentology 52, 467–488. https://doi.org/10.1111/j.1365-3091.2005.00705.x

Grundvåg, S.-A., Johannessen, E.P., Helland-Hansen, W., Plink-Björklund, P., 2014. Depositional architecture and evolution of progradationally stacked lobe complexes in the Eocene Central Basin of Spitsbergen. Sedimentology 61, 535–569. https://doi.org/10.1111/sed.12067

Gulisano, C.A., Gutiérrez Pleimling, A.R., 1995. Field Guide. The Jurassic of the Neuquén Basin. a) Neuquén Province, Asociación Geológica Argentina, Serie E.

Gulisano, C.A., Gutiérrez Pleimling, A.R., Digregorio, J.H., 1984. Esquema estratigráfico de la secuencia jurásica del oeste de la provincia del Neuquén, in: IX Congreso Geológico Argentino, Bariloche. pp. 236–259.

Gupta, S., Underhill, J.R., Sharp, I.R., Gawthorpe, R.L., 1999. Role of fault interactions in controlling synrift sediment dispersal patterns: Miocene, Abu Alaqa Group, Suez Rift, Sinai, Egypt. Basin Res. 11, 167–189. https://doi.org/10.1046/j.1365-2117.1999.00300.x

Gutiérrez Paredes, H.C., Catuneanu, O., Hernández Romano, U., 2017. Sequence stratigraphy of the Miocene section, southern Gulf of Mexico. Mar. Pet. Geol. 86, 711–732. https://doi.org/10.1016/j.marpetgeo.2017.06.022

Hadlari, T., Midwinter, D., Galloway, J.M., Dewing, K., Durbano, A.M., 2016. Mesozoic rift to post-rift tectonostratigraphy of the Sverdrup Basin, Canadian Arctic. Mar. Pet. Geol. 76, 148–158. https://doi.org/10.1016/j.marpetgeo.2016.05.008

Halfar, J., Ingle, J.C.J., Godinez-Orta, L., 2004. Modern non-tropical mixed carbonate-siliciclastic sediments and environments of the southwestern Gulf of California, Mexico. Sediment. Geol. 165, 93–115. https://doi.org/10.1016/j.sedgeo.2003.11.005

Hall, R., Morley, C.K., 2004. Sundaland basins, in: Clift, P., Kuhnt, W., Wang, P., Hayes, D. (Eds.), Continent-Ocean Interactions Within East Asian Marginal Seas. AGU Geophysical Monograph Series. pp. 55–85. https://doi.org/10.1029/149GM04

Hamlyn, J.E., Keir, D., Wright, T.J., Neuberg, J.W., Goitom, B., Hammond, J.O.S., Pagli, C., Oppenheimer, C., Kendall, J.M., Grandin, R., 2014. Seismicity and subsidence following the 2011 Nabro eruption, Eritrea: Insights into the plumbing system of an off-rift volcano. J. Geophys. Res. Solid Earth 119, 8267–8282. https://doi.org/10.1002/2014JB011395

Hampson, G.J., 2000. Discontinuity Surfaces, Clinoforms, and Facies Architecture in a Wave-Dominated, Shoreface-Shelf Parasequence. J. Sediment. Res. 70, 325–340. https://doi.org/10.1306/2DC40914-0E47-11D7-8643000102C1865D

Hampson, G.J., Storms, J.E.A., 2003. Geomorphological and sequence stratigraphic variability in wave-dominated, shoreface-shelf parasequences. Sedimentology 50, 667–701. https://doi.org/10.1046/j.1365-3091.2003.00570.x

Haq, B.U., 2018. Jurassic Sea-Level Variations: A Reappraisal. GSA Today 4–10. https://doi.org/10.1130/GSATG359A.1

Haughton, P., Davis, C., McCaffrey, W., Barker, S., 2009. Hybrid sediment gravity flow deposits – Classification, origin and significance. Mar. Pet. Geol. 26, 1900–1918. https://doi.org/10.1016/j.marpetgeo.2009.02.012

Haughton, P.D.W., 1994. Deposits of deflected and ponded turbidity currents, Sorbas Basin, Southeast Spain. J. Sediment. Res. A64, 233–246. https://doi.org/10.1306/D4267D6B-2B26-11D7-8648000102C1865D

Haughton, P.D.W., Barker, S.P., McCaffrey, W.D., 2003. 'Linked' debrites in sand-rich turbidite systems - origin and significance. Sedimentology 50, 459–482. https://doi.org/10.1046/j.1365-3091.2003.00560.x

Hay, D.C., 2012. Stratigraphic Evolution of a Tortuous Corridor From The Stepped Slope of Angola, in: Application of the Principles of Seismic Geomorphology to Continental-Slope and Base-of-Slope Systems: Case Studies from Seafloor and Near-Seafloor Analogues. SEPM (Society for Sedimentary Geology), pp. 163–180. https://doi.org/10.2110/pec.12.99.0163

Helland-Hansen, W., Steel, R.J., Somme, T.O., 2012. Shelf genesis revisited. J. Sediment. Res. 82, 133–148. https://doi.org/10.2110/jsr.2012.15

Heller, P.L., Dickinson, W.R., 1985. Submarine ramp facies model for delta-fed, sand-rich turbidite systems. Am. Assoc. Pet. Geol. Bull. 69, 960–976.

Henstra, G.A., Grundvåg, S.-A., Johannessen, E.P., Kristensen, T.B., Midtkandal, I., Nystuen, J.P.,

Rotevatn, A., Surlyk, F., Sæther, T., Windelstad, J., 2016. Depositional processes and stratigraphic architecture within a coarse-grained rift-margin turbidite system: The Wollaston Forland Group, east Greenland. Mar. Pet. Geol. 76, 187–209. https://doi.org/10.1016/j.marpetgeo.2016.05.018

Hinsken, S., Ustaszewski, K., Wetzel, A., 2007. Graben width controlling syn-rift sedimentation: the Palaeogene southern Upper Rhine Graben as an example. Int. J. Earth Sci. 96, 979–1002. https://doi.org/10.1007/s00531-006-0162-y

Hodgson, D.M., 2009. Distribution and origin of hybrid beds in sand-rich submarine fans of the Tanqua depocentre, Karoo Basin, South Africa. Mar. Pet. Geol. 26, 1940–1956. https://doi.org/10.1016/j.marpetgeo.2009.02.011

Hodgson, D.M., Haughton, P.D.W., 2004. Impact of syndepositional faulting on gravity current behaviour and deep-water stratigraphy: Tabernas-Sorbas Basin, SE Spain. Geol. Soc. London, Spec. Publ. 222, 135–158. https://doi.org/10.1144/GSL.SP.2004.222.01.08

Holmes, A.A.J., Rodgers, D.W., Hughes, S.S., 2008. Kinematic analysis of fractures in the Great Rift, Idaho: Implications for subsurface dike geometry, crustal extension, and magma dynamics. J. Geophys. Res. 113. https://doi.org/10.1029/2006JB004782

Hooper, R.J., Fitzsimmons, R.J., Grant, N., Vendeville, B.C., 2002. The role of deformation in controlling depositional patterns in the south-central Niger Delta, West Africa. J. Struct. Geol. 24, 847–859. https://doi.org/10.1016/S0191-8141(01)00122-5

Horikawa, K., Ito, M., 2009. Non-uniform across-shelf variations in thickness, grain size, and frequency of turbidites in a transgressive outer-shelf, the Middle Pleistocene Kakinokidai Formation, Boso Peninsula, Japan. Sediment. Geol. 220, 105–115. https://doi.org/10.1016/j.sedgeo.2009.07.002

Houseman, G.A., Gemmer, L., 2007. Intra-orogenic extension driven by gravitational instability: Carpathian-Pannonian orogeny. Geology 35, 1135–1138. https://doi.org/10.1130/G23993A.1

Howell, J.A., Flint, S.S., 1996. A model for high resolution sequence stratigraphy within extensional basins, in: Hwell, J.A., Aitken, J.F. (Eds.), High Resolution Sequence Stratigraphy: Innovations and Applications. Geological Society, London, Special Publications. pp. 129–137. https://doi.org/10.1144/GSL.SP.1996.104.01.09

Howell, John A., Schwarz, Ernesto, Spalletti, Luis A., Veiga, Gonzalo D., 2005. The Neuquén Basin: an overview, in: Veiga, G.D., Spalletti, L.A., Howell, J.A., Schwarz, E. (Eds.), The Neuquén Basin, Argentina: A Case Study in Sequence Stratigraphy and Basin Dynamics, Geological Society, London, Special Publications. pp. 1–14. https://doi.org/10.1144/GSL.SP.2005.252.01.01

Hudson, J.D., Martill, D.M., 1991. The Lower Oxford Clay: production and preservation of organic matter in the Callovian (Jurassic) of central England, in: Tyson, R.V., Pearson, T.H. (Eds.), Modern and Ancient Continental Shelf Anoxia, Geological Society, London, Special Publications. pp. 363–379. https://doi.org/10.1144/GSL.SP.1991.058.01.23

Huismans, R.S., Beaumont, C., 2014. Rifted continental margins: The case for depth-dependent extension. Earth Planet. Sci. Lett. 407, 148–162. https://doi.org/10.1016/j.epsl.2014.09.032

Hunt, D., Allsop, T., Swarbrick, R.E., 1996. Compaction as a primary control on the architecture and development of depositional sequences: conceptual framework, applications and implications, in: Howell, J.A., Aitken, J.F. (Eds.), High Resolution Sequence Stratigraphy: Innovations and Applications. Geological Society, London, Special Publications. pp. 321–345. https://doi.org/10.1144/GSL.SP.1996.104.01.18

Hurst, A., Scott, A., Vigorito, M., 2011. Physical characteristics of sand injectites. Earth-Science Rev. 106, 215–246. https://doi.org/10.1016/j.earscirev.2011.02.004

Iglesia Llanos, M.P., Prezzi, C.B., 2013. The role of true polar wander on the Jurassic palaeoclimate. Int.

J. Earth Sci. 102, 745–759. https://doi.org/10.1007/s00531-012-0818-8

Iglesia Llanos, M.P., Riccardi, A.C., Singer, S.E., 2006. Palaeomagnetic study of Lower Jurassic marine strata from the Neuquén Basin, Argentina: A new Jurassic apparent polar wander path for South America. Earth Planet. Sci. Lett. 252, 379–397. https://doi.org/10.1016/j.epsl.2006.10.006

Ilgar, A., Nemec, W., 2005. Early Miocene lacustrine deposits and sequence stratigraphy of the Ermenek Basin, Central Taurides, Turkey. Sediment. Geol. 173, 233–275. https://doi.org/10.1016/j.sedgeo.2003.07.007

Ilyah, A.A., 2013. Comparing point counting & image analysis in sandstone North Carnarvon Basin, Australia, in: 2nd International Conference on Geological and Environmental Sciences. IPCBEE. pp. 20–24.

Ingersoll, R. V., Bullard, T.F., Ford, R.L., Grimm, J.P., Pickle, J.D., Sares, S.W., 1984. The Effect of Grain Size on Detrital Modes: A Test of the Gazzi-Dickinson Point-Counting Method. J. Sediment. Res. 54, 103–116. https://doi.org/10.1306/212F83B9-2B24-11D7-8648000102C1865D

Ingersoll, R. V., Cavazza, W., 1991. Reconstruction of Oligo-Miocene Volcaniclastic Dispersal Patterns in North-Central New Mexico using Sandstone Petrofacies, in: Fisher, R. V., Smith, G.A. (Eds.), Sedimentation in Volcanic Settings. SEPM Special Publications. SEPM (Society for Sedimentary Geology), pp. 227–236. https://doi.org/10.2110/pec.91.45.0227

Ireland, T.R., Williams, I.S., 2003. Considerations in Zircon Geochronology by SIMS, in: Hanchar, J.M., Hoskin, P.W.O. (Eds.), Zircon: Reviews in Mineralogy and Geochemistry. De Gruyter, Berlin, Boston, pp. 215–242. https://doi.org/10.1515/9781501509322-011

Ito, M., 2008. Downfan Transformation from Turbidity Currents to Debris Flows at a Channel-to-Lobe Transitional Zone: The Lower Pleistocene Otadai Formation, Boso Peninsula, Japan. J. Sediment. Res. 78, 668–682. https://doi.org/10.2110/jsr.2008.076

Jackson, C.A.L., Barber, G.P., Martinsen, O.J., 2008. Submarine slope morphology as a control on the development of sand-rich turbidite depositional systems: 3D seismic analysis of the Kyrre Fm (Upper Cretaceous), Måløy Slope, offshore Norway. Mar. Pet. Geol. 25, 663–680. https://doi.org/10.1016/j.marpetgeo.2007.12.007

Jackson, Christopher A.L., Bell, R.E., Rotevatn, A., Tvedt, A.B.M., 2017. Techniques to determine the kinematics of synsedimentary normal faults and implications for fault growth models, in: Childs, C., Holdsworth, R.E., Jackson, C.A.L., Manzocchi, T., Walsh, J.J., Yielding, G. (Eds.), The Geometry and Growth OfNormal Faults. Geological Society, London, Special Publications. pp. 187–217. https://doi.org/10.1144/SP439.22

Jackson, C.A.L., Gawthorpe, R.L., Carr, I.D., Sharp, I.R., 2005. Normal faulting as a control on the stratigraphic development of shallow marine syn-rift sequences: the Nukhul and Lower Rudeis Formations, Hammam Faraun fault block, Suez Rift, Egypt. Sedimentology 52, 313–338. https://doi.org/10.1111/j.1365-3091.2005.00699.x

Jackson, C.A.L., Gawthorpe, R.L., Sharp, I.R., 2002. Growth and linkage of the East Tanka fault zone, Suez rift: structural style and syn-rift stratigraphic response. J. Geol. Soc. London. 159, 175–187. https://doi.org/10.1144/0016-764901-100

Jackson, C.A.L., Larsen, E., Hanslien, S., Tjemsland, A.-E., 2011. Controls on synrift turbidite deposition on the hanging wall of the South Viking Graben, North Sea rift system, offshore Norway. Am. Assoc. Pet. Geol. Bull. 95, 1557–1587. https://doi.org/10.1306/01031110037

Japsen, P., Chalmers, J.A., Green, P.F., Bonow, J.M., 2012. Elevated, passive continental margins: Not rift shoulders, but expressions of episodic, post-rift burial and exhumation. Glob. Planet. Change 90–91, 73–86. https://doi.org/10.1016/j.gloplacha.2011.05.004

Jarsve, E.M., Faleide, J.I., Gabrielsen, R.H., Nystuen, J.P., 2014. Mesozoic and cenozoic basin configurations in the North Sea, in: Martinius, A.W., Ravnås, R., Howell, J.A., Steel, R.J., Wonham, J.P. (Eds.), From Depositional Systems to Sedimentary Successions on the Norwegian Continental Margin. John Wiley & Sons, Ltd, Chichester, UK, pp. 417–452. https://doi.org/10.1002/9781118920435.ch15

Jegou, I., Savoye, B., Pirmez, C., Droz, L., 2008. Channel-mouth lobe complex of the recent Amazon Fan: The missing piece. Mar. Geol. 252, 62–77. https://doi.org/10.1016/j.margeo.2008.03.004

Jobe, Z.R., Lowe, D.R., Morris, W.R., 2012. Climbing-ripple successions in turbidite systems: depositional environments, sedimentation rates and accumulation times. Sedimentology 59, 867–898. https://doi.org/10.1111/j.1365-3091.2011.01283.x

Jobe, Z.R., Sylvester, Z., Howes, N., Pirmez, C., Parker, A., Cantelli, A., Smith, R., Wolinsky, M.A., O'Byrne, C., Slowey, N., Prather, B., 2017. High-resolution, millennial-scale patterns of bed compensation on a sand-rich intraslope submarine fan, western Niger Delta slope. Geol. Soc. Am. Bull. 129, 23–37. https://doi.org/10.1130/B31440.1

Kane, I.A., 2010. Development and flow structures of sand injectites: The Hind Sandstone Member injectite complex, Carboniferous, UK. Mar. Pet. Geol. 27, 1200–1215. https://doi.org/10.1016/j.marpetgeo.2010.02.009

Kane, I.A., Catterall, V., McCaffrey, W.D., Martinsen, O.J., 2010. Submarine channel response to intrabasinal tectonics: The influence of lateral tilt. Am. Assoc. Pet. Geol. Bull. 94, 189–219. https://doi.org/10.1306/08180909059

Kane, I.A., Ponten, A.S.M., 2012. Submarine transitional flow deposits in the Paleogene Gulf of Mexico. Geology 40, 1119–1122. https://doi.org/10.1130/G33410.1

Kane, I.A., Pontén, A.S.M., Vangdal, B., Eggenhuisen, J.T., Hodgson, D.M., Spychala, Y.T., 2017. The stratigraphic record and processes of turbidity current transformation across deep-marine lobes. Sedimentology 64, 1236–1273. https://doi.org/10.1111/sed.12346

Kapp, P., Taylor, M., Stockli, D., Ding, L., 2008. Development of active low-angle normal fault systems during orogenic collapse: Insight from Tibet. Geology 36, 7–10. https://doi.org/10.1130/G24054A.1

Karner, G.D., 1991. Sediment blanketing and the flexural strength of extended continental lithosphere. Basin Res. 3, 177–185. https://doi.org/10.1111/j.1365-2117.1991.tb00127.x

Karner, G.D., Driscoll, N.W., 1999. Style, timing and distribution of tectonic deformation across the Exmouth Plateau, northwest Australia, determined from stratal architecture and quantitative basin modelling, in: Mac Niocaill, C., Ryan, P.D. (Eds.), Continental Tectonics. Geological Society, London, Special Publications. pp. 271–311. https://doi.org/10.1144/GSL.SP.1999.164.01.14

Karner, G.D., Egan, S.S., Weissel, J.K., 1992. Modeling the tectonic development of the Tucano and Sergipe-Alagoas rift basins, Brazil. Tectonophysics 215, 133–160. https://doi.org/10.1016/0040-1951(92)90078-K

Kay, S.M., Ramos, V.A., Mpodozis, C., Sruoga, P., 1989. Late Paleozoic to Jurassic silicic magmatism at the Gondwana margin: Analogy to the Middle Proterozoic in North America? Geology 17, 324–328. https://doi.org/10.1130/0091-7613(1989)017<0324:LPTJSM>2.3.CO;2

Kenter, J.A.M., 1990. Carbonate platform flanks: slope angle and sediment fabric. Sedimentology 37, 777–794. https://doi.org/10.1111/j.1365-3091.1990.tb01825.x

Khalil, S.M., McClay, Ken R., 2018. Extensional fault-related folding in the northwestern Red Sea, Egypt: segmented fault growth, fault linkages, corner folds and basin evolution, in: McClay, K. R., Hammerstein, J.A. (Eds.), Passive Margins: Tectonics, Sedimentation and Magmatism. Geological

Society, London, Special Publications. https://doi.org/10.1144/SP476.12

Kjennerud, T., Faleide, J.I., Gabrielsen, R.H., Gillmore, G.K., Kyrkjebø, R., Lippard, S.J., Løseth, H., 2001. Structural restoration of Cretaceous-Cenozoic (post-rift) palaeobathymetry in the northern North Sea, in: Martinsen, O.J., Dreyer, T. (Eds.), Sedimentary Environments Offshore Norway - Palaeozoic to Recent. NPF Special Publication 10. pp. 347–364. https://doi.org/10.1016/S0928-8937(01)80021-7

Klaucke, I., Masson, D.G., Kenyon, N.H., Gardner, J. V., 2004. Sedimentary processes of the lower Monterey Fan channel and channel-mouth lobe. Mar. Geol. 206, 181–198. https://doi.org/10.1016/j.margeo.2004.02.006

Kneller, B., Edwards, D., McCaffrey, W., Moore, R., 1991. Oblique reflection of turbidity currents. Geology 19, 250–252. https://doi.org/10.1130/0091-7613(1991)019<0250:OROTC>2.3.CO;2

Kneller, B.C., Bennett, S.J., McCaffrey, W.D., 1999. Velocity structure, turbulence and fluid stresses in experimental gravity currents. J. Geophys. Res. Ocean. 104, 5381–5391. https://doi.org/10.1029/1998JC900077

Kneller, B.C., Branney, M.J., 1995. Sustained high-density turbidity currents and the deposition of thick massive sands. Sedimentology 42, 607–616. https://doi.org/10.1111/j.1365-3091.1995.tb00395.x

Kochhann, K.G.D., Baecker-Fauth, S., Pujana, I., Santos da Silveira, A., Fauth, G., 2011. Toarcian–Aalenian (Early–Middle Jurassic) radiolarian fauna from the Los Molles Formation, Neuqu{é}n Basin, Argentina: Taxonomy and paleobiogeographic affinities. J. South Am. Earth Sci. 31, 253–261. https://doi.org/10.1016/j.jsames.2011.01.001

Komar, P.D., 1971. Hydraulic Jumps in Turbidity Currents and Their Deposits. GSA Bull. 82, 1477–1488. https://doi.org/10.1130/0016-7606(1971)82[1477:HJITC]2.0.CO;2

Kondo, Y., Abbott, S.T., Kitamura, A., Kamp, P.J.J., Naish, T.R., Kamataki, T., Saul, G.S., 1998. The relationship between shellbed type and sequence architecture: examples from Japan and New Zealand. Sediment. Geol. 122, 109–127. https://doi.org/10.1016/S0037-0738(98)00101-8

Kusznir, N.J., Karner, G.D., 2007. Continental lithospheric thinning and breakup in response to upwelling divergent mantle flow: application to the Woodlark, Newfoundland and Iberia margins, in: Karner, G.D., Manatschal, G., Pinheiro, L.M. (Eds.), Imaging, Mapping and Modelling Continental Lithosphere Extension and Breakup. Geological Society, London, Special Publications. pp. 389–419. https://doi.org/10.1144/SP282.16

Kusznir, N.J., Park, R.G., 1987. The extensional strength of the continental lithosphere: its dependence on geothermal gradient, and crustal composition and thickness, in: Coward, M.P., Dewey, J.F., Hancock, P.L. (Eds.), Continental Extensional Tectonics. Geological Society, London, Special Publications. pp. 35–52. https://doi.org/10.1144/GSL.SP.1987.028.01.04

Kyrkjebø, R., Gabrielsen, R.H., Faleide, J.I., 2004. Unconformities related to the Jurassic-Cretaceous synrift-post-rift transition of the northern North Sea. J. Geol. Soc. London 161, 1–17. https://doi.org/10.1144/0016-764903-051

Lachkar, N., Guiraud, M., El Harfi, A., Dommergues, J.L., Dera, G., Durlet, C., 2009. Early Jurassic normal faulting in a carbonate extensional basin: characterization of tectonically driven platform drowning (High Atlas rift, Morocco). J. Geol. Soc. London 166, 413–430. https://doi.org/10.1144/0016-76492008-084

Lambiase, J.J., Bosworth, W., 1995. Structural controls on sedimentation in continental rifts, in: Liambase, J.J. (Ed.), Hydrocarbon Habitat in Rift Basins. Geological Society, London, Special Publications. pp. 117–144. https://doi.org/10.1144/GSL.SP.1995.080.01.06

Lanés, S., Giambiagi, L., Bechis, F., Tunik, M., 2008. Late triassic - Early Jurassic successions of the Atuel Depocenter: Sequence stratigraphy and tectonic controls. Rev. la Asoc. Geológica Argentina 63, 534–548.

Larsen, M., Nedkvitne, T., Olaussen, S., 2001. Lower cretaceous (Barremian-Albian) deltaic and shallow marine sandstones in north-east greenland — sedimentology, sequence stratigraphy and regional implications, in: Sedimentary Environments Offshore Norway - Palaeozoic to Recent. NPF Special Publication. pp. 259–278. https://doi.org/10.1016/S0928-8937(01)80017-5

Leanza, H.A., 1993. Estratigrafia del Mesozoico posterior a los Movimientos intermálmicos en la comarca del Cerro Chachil, provincia del Neuquén. Rev. Asoc. Geológica Argentina 48, 71–83.

Leanza, H.A., 1990. Estratigrafía del Paleozoico y Mesozoico anterior a los movimientos intermalmicos en la comarca del cerro Chachil, provincia del Neuquén. Rev. la Asoc. Geológica Argentina 45, 272–299.

Leanza, H.A., Blasco, G., 1990. Estratigrafía y ammonites pliensbachianos del área del Arroyo Ñireco, Neuquén, Argentina, con la descripción de Austromorphites gen. nov. Rev. la Asoc. Geológica Argentina 45, 159–174.

Leanza, H.A., Mazzini, A., Corfu, F., Llambías, E.J., Svensen, H., Planke, S., Galland, O., 2013. The Chachil Limestone (Pliensbachian–earliest Toarcian) Neuquén Basin, Argentina: U–Pb age calibration and its significance on the Early Jurassic evolution of southwestern Gondwana. J. South Am. Earth Sci. 42, 171–185. https://doi.org/10.1016/j.jsames.2012.07.012

Leclair, S.F., Arnott, R.W.C., 2005. Parallel Lamination Formed by High-Density Turbidity Currents. J. Sediment. Res. 75, 1–5. https://doi.org/10.2110/jsr.2005.001

Ledesma-Vázquez, J., Johnson, M.E., 2001. Miocene–Pleistocene tectono-sedimentary evolution of Bahía Concepción region, Baja California Sur (México). Sediment. Geol. 144, 83–96. https://doi.org/10.1016/S0037-0738(01)00136-1

Leeder, M.R., Collier, R.E.L., Abdul Aziz, L.H., Trout, M., Ferentinos, G., Papatheodorou, G., Lyberis, E., 2002. Tectono-sedimentary processes along an active marine/lacustrine half-graben margin: Alkyonides Gulf, E. Gulf of Corinth, Greece. Basin Res. 14, 25–41. https://doi.org/10.1046/j.1365-2117.2002.00164.x

Leeder, M.R., Gawthorpe, R.L., 1987. Sedimentary models for extensional tilt-block/half-graben basins. Cont. Extensional Tectonics. Geol. Soc. London, Spec. Publ. 28, 139–152. https://doi.org/10.1144/GSL.SP.1987.028.01.11

Leeder, M.R., Harris, T., Kirkby, M.J., 1998. Sediment supply and climate change: implications for basin stratigraphy. Basin Res. 10, 7–18. https://doi.org/10.1046/j.1365-2117.1998.00054.x

Legarreta, L., Gulisano, C., 1989. Análisis estratigráfico secuencial de la cuenca Neuquina (Triásico superior - Terciario inferior), Argentina, in: Chebli, G.A., Spalletti, L.A. (Eds.), Cuencas Sedimentarias Argentinas. Serie Correlación Geológica. pp. 221–243.

Legarreta, L., Uliana, M.A., 1996. The Jurassic succession in west-central Argentina: stratal patterns, sequences and paleogeographic evolution. Palaeogeogr. Palaeoclimatol. Palaeoecol. 120, 303–330. https://doi.org/10.1016/0031-0182(95)00042-9

Legarreta, L., Uliana, M.A., 1991. Jurassic/Cretaceous marine oscillations and geometry of a back-arc basin fill, central Argentine Andes, in: Mc Donald, D.I.M. (Ed.), Sedimentation, Tectonics and Eustacy. I.A.S. Special Publication. pp. 429–450.

Leinfelder, R.R., Wilson, R., Chris, L., 1998. Third-Order Sequences in an Upper Jurassic Rift-Related Second-Order Sequence, Central Lusitanian Basin, Portugal, in: Graciansky, P.C., Hardenbol, J., Jacquin, T., Vail, P.R. (Eds.), Mesozoic and Cenozoic Sequence Stratigraphy of European Basins.

SEPM (Society for Sedimentary Geology), Tulsa, pp. 507–525. https://doi.org/10.2110/pec.98.02.0507

Leppard, C.W., Gawthorpe, R.L., 2006. Sedimentology of rift climax deep water systems; Lower Rudeis Formation, Hammam Faraun Fault Block, Suez Rift, Egypt. Sediment. Geol. 191, 67–87. https://doi.org/10.1016/j.sedgeo.2006.01.006

Lewis, M.M., Jackson, C.A.L., Gawthorpe, R.L., Whipp, P.S., 2015. Early synrift reservoir development on the flanks of extensional forced folds: A seismic-scale outcrop analog from the Hadahid fault system, Suez rift, Egypt. Am. Assoc. Pet. Geol. Bull. 99, 985–1012. https://doi.org/10.1306/12011414036

Li, J., Ma, Z., Zhang, Y., Dong, S., Li, Y., Lu, M., Tan, J., 2014. Tectonic evolution of Cretaceous extensional basins in Zhejiang Province, eastern South China: structural and geochronological constraints. Int. Geol. Rev. 56, 1602–1629. https://doi.org/10.1080/00206814.2014.951978

Lien, T., 2005. From rifting to drifting: Effects on the development of deep-water hydrocarbon reservoirs in a passive margin setting, Norwegian Sea. Nor. J. Geol. 85, 319–332.

Lien, T., Midtbø, R.E., Martinsen, O.J., 2006. Depositional facies and reservoir quality of deep-marine sandstones in the Norwegian Sea. Nor. J. Geol. 86, 71–92.

Liu, M., Shen, Y., 1998. Crustal collapse, mantle upwelling, and Cenozoic extension in the North American Cordillera. Tectonics 17, 311–321. https://doi.org/10.1029/98TC00313

Lizarralde, D., Axen, G.J., Brown, H.E., Fletcher, J.M., González-Fernández, A., Harding, A.J., Holbrook, W.S., Kent, G.M., Paramo, P., Sutherland, F., Umhoefer, P.J., 2007. Variation in styles of rifting in the Gulf of California. Nature 448, 466–469. https://doi.org/10.1038/nature06035

Llambías, E.J., Leanza, H.A., Carbone, O., 2007. Evolución Tectono-magmática durante el pérmico al Jurásico temprano en la Cordillera del Viento (37°05'S - 37°15'S): Nuevas evidencias geológicas y geoquímicas Del Inicio de la Cuencas Neuquina. Rev. la Asoc. Geológica Argentina 62, 217–235.

Llambías, E.J., Sato, A.M., 2011. Ciclo Gondwánico : La Provincia Magmática Choiyoi En Neuquén. Relat. del XVIII Congr. Geológico Argentino, Neuquén 53–62.

Llambías, E.J., Sato, A.M., Castro, C.E., 1990. Relaciones entre el Grupo Choiyoi y el batolito de Colangüil. XI Congr. Geológico Argentino, San Juan Actas 1, 99–108.

Llambías, E.J., Quenardelle, S., Montenegro, T., 2003. The Choiyoi Group from central Argentina: a subalkaline transitional to alkaline association in the craton adjacent to the active margin of the Gondwana continent. J. South Am. Earth Sci. 16, 243–257. https://doi.org/10.1016/S0895-9811(03)00070-1

Lohr, T., Underhill, J.R., 2015. Role of rift transection and punctuated subsidence in the development of the North Falkland Basin. Pet. Geosci. 21, 85–110. https://doi.org/10.1144/petgeo2014-050

López-Gamundi, O., Barragan, R., 2012. Structural Framework of Lower Cretaceous Half Grabens in the Presalt Section of the Southeastern Continental Margin of Brazil, in: Gao, D. (Ed.), Tectonics and Sedimentation: Implications for Petroleum Systems. AAPG Memoir, 100. American Association of Petroleum Geologists, Tulsa, Oklahoma, pp. 143–158. https://doi.org/10.1306/13351551M1003531

Loss, M.L., Brinkworth, W., Vocaturo, G., Sánchez, D., Mortaloni, E.M., Olariu, C., Steel, R., 2018. Frentes deltaicos, cañones y turbiditas en el Grupo Cuyo. Definición de plays a partir de un modelo sismoestratigráfico regional y afloramientos análogos, in: 10º Congreso de Exploración y Desarrollo de Hidrocarburos. pp. 647–668.

Lowe, L.R., 1982. Sediment Gravity Flows: II Depositional Models with Special Reference to the Deposits of High-Density Turbidity Currents. J. Sediment. Petrol. 52.

https://doi.org/10.1306/212F7F31-2B24-11D7-8648000102C1865D

Ludwig, K.R., 2001a. User's Manual for Isoplot/Ex rev. 2.49: A Geochronological Toolkit for Microsoft Excel. Berkeley Geochronol. Cent. Spec. Publ. 1a, 1–55.

Ludwig, K.R., 2001b. SQUID 1.02, A User Manual, a Geochronological Toolkit for Microsoft Excel. Berkeley Geochronol. Cent. Spec. Publ. 2, 1–19.

Lykousis, V., Sakellariou, D., Moretti, I., Kaberi, H., 2007. Late Quaternary basin evolution of the Gulf of Corinth: Sequence stratigraphy, sedimentation, fault–slip and subsidence rates. Tectonophysics 440, 29–51. https://doi.org/10.1016/j.tecto.2006.11.007

Macdonald, H.A., Peakall, J., Wignall, P.B., Best, J., 2011. Sedimentation in deep-sea lobe-elements: implications for the origin of thickening-upward sequences. J. Geol. Soc. London. 168, 319–332. https://doi.org/10.1144/0016-76492010-036

MacEachern, J.A., Bann, K.L., Bhattacharya, J.P., Howell, C.D., 2005. Ichnology of Deltas: Organism Responses to the Dynamic Interplay of Rivers, Waves, Storms, and Tides. River Deltas-Concepts, Model. Examples. SEPM Spec. Publ. 83, 49–85. https://doi.org/10.2110/pec.05.83.0049

MacEachern, J.A., Bann, K.L., Pemberton, S.G., Gingras, M.K., 2007. The ichnofacies paradigm: High-resolution paleoenvironmental interpretation of the rock record, in: MacEachern, J.A., Bann, K.L., Gingras, M.K., Pemberton, S.G. (Eds.), Applied Ichnology. SEPM Short Course Notes. pp. 27–64. https://doi.org/10.2110/pec.07.52.0027

Manceñido, M.O., 2002. Paleobiogeography of Mesozoic brachiopod faunas from Andean–Patagonian areas in a global context. Geobios Mem. spécial 24, 176–192. https://doi.org/10.1016/S0016-6995(02)00058-X

Manville, V., Németh, K., Kano, K., 2009. Source to sink: A review of three decades of progress in the understanding of volcaniclastic processes, deposits, and hazards. Sediment. Geol. 220, 136–161. https://doi.org/10.1016/j.sedgeo.2009.04.022

Marin, D., Escalona, A., Śliwińska, K.K., Nøhr-Hansen, H., Mordasova, A., 2017. Sequence stratigraphy and lateral variability of Lower Cretaceous clinoforms in the southwestern Barents Sea. Am. Assoc. Pet. Geol. Bull. 101, 1487–1517. https://doi.org/10.1306/10241616010

Marini, M., Milli, S., Ravnås, R., Moscatelli, M., 2015. A comparative study of confined vs. semi-confined turbidite lobes from the Lower Messinian Laga Basin (Central Apennines, Italy): Implications for assessment of reservoir architecture. Mar. Pet. Geol. 63, 142–165. https://doi.org/10.1016/j.marpetgeo.2015.02.015

Marr, J.G., Harff, P.A., Shanmugam, G., Parker, G., 2001. Experiments on subaqueous sandy gravity flows: The role of clay and water content in flow dynamics and depositional structures. Geol. Soc. Am. Bull. 113, 1377–1386. https://doi.org/10.1130/0016-7606(2001)113<1377:EOSSGF>2.0.CO;2

Marsaglia, K., Ingersoll, R. V., 1992. Compositional trends in arc-related, deep-marine sand and sandstone: A reassessment of magmatic-arc provenance. Geol. Soc. Am. Bull. 104, 1637–1649. https://doi.org/10.1130/0016-7606(1992)104<1637:CTIARD>2.3.CO;2

Marsaglia, K.M., 1991. Provenance of Sands and Sandstones from a Rifted Continental Arc, Gulf of California, Mexico, in: Fisher, R. V., Smith, G.A. (Eds.), Sedimentation in Volcanic Settings. SEPM Special Publication. SEPM (Society for Sedimentary Geology), pp. 237–248. https://doi.org/10.2110/pec.91.45.0237

Marsaglia, K.M., Barone, M., Critelli, S., Busby, C., Fackler-Adams, B., 2016. Petrography of volcaniclastic rocks in intra-arc volcano-bounded to fault-bounded basins of the Rosario segment of the Lower Cretaceous Alisitos oceanic arc, Baja California, Mexico. Sediment. Geol. 336, 138–

146. https://doi.org/10.1016/j.sedgeo.2015.11.008

Marsaglia, K.M., Boggs, S., Clift, P., Seyedolali, A., Smith, R., 1995. Sedimentation in western Pacific backarc basins: New insights from recent ODP drilling, in: Taylor, B., Natland, J. (Eds.), Active Margins and Marginal Basins of the Western Pacific. Geophysical Monograph Series. pp. 291–314. https://doi.org/10.1029/GM088p0291

Martínez, M.A., Prámparo, M.B., Quattrocchio, M.E., Zavala, C.A., 2008. Depositional environments and hydrocarbon potential of the Middle Jurassic Los Molles Formation, Neuquén Basin, Argentina: palynofacies and organic geochemical data. Rev. geológica Chile 35, 279–305. https://doi.org/10.4067/S0716-02082008000200005

Martini, M., Ortega-Gutiérrez, F., 2016. Tectono-stratigraphic evolution of eastern Mexico during the break-up of Pangea: A review. Earth-Science Rev. https://doi.org/10.1016/j.earscirev.2016.06.013

Martins-Neto, M.A., 2000. Tectonics and sedimentation in a paleo/mesoproterozoic rift-sag basin (Espinhaço basin, southeastern Brazil). Precambrian Res. 103, 147–173. https://doi.org/10.1016/S0301-9268(00)00080-2

Martins-Neto, M.A., Catuneanu, O., 2010. Rift sequence stratigraphy. Mar. Pet. Geol. 27, 247–253. https://doi.org/10.1016/j.marpetgeo.2009.08.001

Martinsen, O.J., Helland-Hansen, W., 1995. Strike variability of clastic depositional systems: Does it matter for sequence-stratigraphic analysis? Geology 23, 439–442. https://doi.org/10.1130/0091-7613(1995)023<0439:SVOCDS>2.3.CO;2

Martinsen, O.J., Lien, T., Jackson, C., 2005. Cretaceous and Palaeogene turbidite systems in the North Sea and Norwegian Sea Basins: source, staging area and basin physiography controls on reservoir development, in: Doré, A.G., Vining, B.A. (Eds.), Petroleum Geology: North-West Europe and Global Perspectives – Proceedings of the 6th Petroleum Geology Conference, Geological Society, London. Geological Society of London, pp. 1147–1164. https://doi.org/10.1144/0061147

Mattern, F., 2005. Ancient sand-rich submarine fans: depositional systems, models, identification, and analysis. Earth-Science Rev. 70, 167–202. https://doi.org/10.1016/j.earscirev.2004.12.001

McArthur, A.D., Hartley, A.J., Archer, S.G., Jolley, D.W., Lawrence, H.M., 2016. Spatiotemporal relationships of deep-marine, axial, and transverse depositional systems from the synrift Upper Jurassic of the central North Sea. Am. Assoc. Pet. Geol. Bull. 100, 1469–1500. https://doi.org/10.1306/04041615125

McArthur, A.D., Hartley, A.J., Jolley, D.W., 2013. Stratigraphic development of an Upper Jurassic deep marine syn-rift succession, Inner Moray Firth Basin, Scotland. Basin Res. 25, 285–309. https://doi.org/10.1111/j.1365-2117.2012.00557.x

McCaffrey, W., Kneller, B., 2001. Process controls on the development of stratigraphic trap potential on the margins of confined turbidite systems and aids to reservoir evaluation. Am. Assoc. Pet. Geol. Bull. 85, 971–988. https://doi.org/10.1306/8626CA41-173B-11D7-8645000102C1865D

McCave, I.N., 1984. Size spectra and aggregation of suspended particles in the deep ocean. Deep Sea Res. Part A. Oceanogr. Res. Pap. 31, 329–352. https://doi.org/10.1016/0198-0149(84)90088-8

McKenzie, D., Nimmo, F., Jackson, J.A., 2000. Characteristics and consequences of flow in the lower crust. J. Geophys. Res. 105, 11029–11046.

McKenzie, D.P., 1978. Some remarks on the development of sedimentary basins. Earth Planet. Sci. Lett. 40, 25–32.

Migeon, S., Ducassou, E., Le Gonidec, Y., Rouillard, P., Mascle, J., Revel-Rolland, M., 2010. Lobe construction and sand/mud segregation by turbidity currents and debris flows on the western

Nile deep-sea fan (Eastern Mediterranean). Sediment. Geol. 229, 124–143. https://doi.org/10.1016/j.sedgeo.2010.02.011

Mignard, S., Mulder, T., Martinez, P., Garlan, T., 2019. The Ogooue Fan (offshore Gabon): a modern example of deep-sea fan on a complex slope profile. Solid Earth 10, 851–869. https://doi.org/10.5194/se-10-851-2019

Milliman, J.D., Syvitski, J.P.M., 1992. Geomorphic/Tectonic Control of Sediment Discharge to the Ocean: The Importance of Small Mountainous Rivers. J. Geol. 100, 525–544. https://doi.org/10.1086/629606

Milton-Worssell, R.J., Stoker, S.J., Cavill, J.E., 2006. Lower Cretaceous deep-water sandstone plays in the UK Central Graben. Geol. Soc. London, Spec. Publ. 254, 169–186. https://doi.org/10.1144/GSL.SP.2006.254.01.09

Modica, C.J., Brush, E.R., 2004. Postrift sequence stratigraphy, paleogeography, and fill history of the deep-water Santos Basin, offshore southeast Brazil. Am. Assoc. Pet. Geol. Bull. 88, 923–945. https://doi.org/10.1306/01220403043

Mohrig, D., Marr, J.G., 2003. Constraining the efficiency of turbidity current generation from submarine debris flows and slides using laboratory experiments. Mar. Pet. Geol. 20, 883–899. https://doi.org/10.1016/j.marpetgeo.2003.03.002

Monaldi, C.R., Salfity, J.A., Kley, J., 2008. Preserved extensional structures in an inverted Cretaceous rift basin, northwestern Argentina: Outcrop examples and implications for fault reactivation. Tectonics 27. https://doi.org/10.1029/2006TC001993

Montenat, C., D'Estevou, P.O., Jarrige, J.J., Richert, J.P., 1998. Rift development in the Gulf of Suez and the north-western Red Sea: structural aspects and related sedimentary processes, in: Purser, B.H., Bosence, D.W.J. (Eds.), Sedimentation and Tectonics in Rift Basins Red Sea-Gulf of Aden. Springer Netherlands, Dordrecht, pp. 97–116. https://doi.org/10.1007/978-94-011-4930-3_7

Moore, J.G., 1992. A syn-rift to post-rift transition sequence in the Main Porcupine Basin, offshore western Ireland. Geol. Soc. London, Spec. Publ. 62, 333–349. https://doi.org/10.1144/GSL.SP.1992.062.01.26

Morad, S., Al-Ramadan, K., Ketzer, J.M., De Ros, L.F., 2010. The impact of diagenesis on the heterogeneity of sandstone reservoirs: A review of the role of depositional facies and sequence stratigraphy. Am. Assoc. Pet. Geol. Bull. 94, 1267–1309. https://doi.org/10.1306/04211009178

Moretti, I., Colletta, B., 1987. Spatial and temporal evolution of the Suez rift subsidence. J. Geodyn. 7, 151–168. https://doi.org/10.1016/0264-3707(87)90069-X

Moretti, I., Lykousis, V., Sakellariou, D., Reynaud, J.-Y., Benziane, B., Prinzhoffer, A., 2004. Sedimentation and subsidence rate in the Gulf of Corinth: what we learn from the Marion Dufresne's long-piston coring. Comptes Rendus Géoscience 336, 291–299. https://doi.org/10.1016/j.crte.2003.11.011

Morley, C.K., 2015. Five anomalous structural aspects of rift basins in Thailand and their impact on petroleum systems, in: Richards, F.L., Richardson, N.J., Rippington, S.J., Wilson, R.W., Bond, C.E. (Eds.), Industrial Structural Geology: Principles, Techniques and Integration. Geological Society, London, Special Publications. pp. 143–168. https://doi.org/10.1144/SP421.2

Morley, C.K., 2001. Combined escape tectonics and subduction rollback–back arc extension: a model for the evolution of Tertiary rift basins in Thailand, Malaysia and Laos. J. Geol. Soc. London. 158, 461–474. https://doi.org/10.1144/jgs.158.3.461

Morley, C.K., 1999. Patterns of Displacement Along Large Normal Faults: Implications for Basin Evolution and Fault Propagation, Based on Examples from East Africa. Am. Assoc. Pet. Geol. Bull.

83, 613–634. https://doi.org/10.1306/00AA9C0A-1730-11D7-8645000102C1865D

Morley, C.K., Haranya, C., Phoosongsee, W., Pongwapee, S., Kornsawan, A., Wonganan, N., 2004. Activation of rift oblique and rift parallel pre-existing fabrics during extension and their effect on deformation style: examples from the rifts of Thailand. J. Struct. Geol. 26, 1803–1829. https://doi.org/10.1016/j.jsg.2004.02.014

Morley, C.K., King, R., Hillis, R., Tingay, M., Backe, G., 2011. Deepwater fold and thrust belt classification, tectonics, structure and hydrocarbon prospectivity: A review. Earth-Science Rev. 104, 41–91. https://doi.org/10.1016/j.earscirev.2010.09.010

Morley, C.K., Nelson, R.A., Patton, T.L., Munn, S.G., 1990. Transfer Zones in the East African Rift System and Their Relevance to Hydrocarbon Exploration in Rifts. Am. Assoc. Pet. Geol. Bull. 74, 1234–1253.

Morley, C.K., Nixon, C.W., 2016. Topological characteristics of simple and complex normal fault networks. J. Struct. Geol. 84, 68–84. https://doi.org/10.1016/j.jsg.2016.01.005

Morley, C.K., Westaway, R., 2006. Subsidence in the super-deep Pattani and Malay basins of Southeast Asia: a coupled model incorporating lower-crustal flow in response to post-rift sediment loading. Basin Res. 18, 51–84. https://doi.org/10.1111/j.1365-2117.2006.00285.x

Mortimer, E.J., Paton, D.A., Scholz, C.A., Strecker, M.R., 2016. Implications of structural inheritance in oblique rift zones for basin compartmentalization: Nkhata Basin, Malawi Rift (EARS). Mar. Pet. Geol. 72, 110–121. https://doi.org/10.1016/j.marpetgeo.2015.12.018

Moscardelli, L., Ramnarine, S.K., Wood, L., Dunlap, D.B., 2013. Seismic geomorphological analysis and hydrocarbon potential of the Lower Cretaceous Cromer Knoll Group, Heidrun field, Norway. Am. Assoc. Pet. Geol. Bull. 97, 1227–1248. https://doi.org/10.1306/02081312155

Mosquera, A., 2002. Inversión tectónica jurásica inferior en el sector central de la Dorsal de Huincul, área Los Bastos. 5° Congr. Explor. y Desarro. Hidrocarburos (Mar del Plata) Actas en C, 11.

Mosquera, A., Ramos, V.A., 2006. Intraplate deformation in the Neuquén Embayment, in: Kay, S.M., Ramos, V.A. (Eds.), Evolution of an Andean Margin: A Tectonic and Magmatic View from the Andes to the Neuquén Basin (35°-39°S Lat). GSA Special Paper. Geological Society of America, pp. 97–123. https://doi.org/10.1130/2006.2407(05)

Mosquera, A., Silvestro, J., Ramos, V.A., Alarcón, M., Zubiri, M., 2011. La estructura de la dorsal de huincul, in: Relatorio Del XVIII Congreso Geológico Argentino, Neuquén. pp. 385–398.

Moustafa, A.R., Khalil, S.M., 2017. Control of compressional transfer zones on syntectonic and post-tectonic sedimentation: implications for hydrocarbon exploration. J. Geol. Soc. London. 174, 336–352. https://doi.org/10.1144/jgs2016-030

Mpodozis, C., Kay, S.M., 1992. Late Paleozoic to Triassic evolution of the Gondwana margin: Evidence from Chilean Frontal Cordilleran batholiths (28°S to 31°S). Geol. Soc. Am. Bull. 104, 999–1014. https://doi.org/10.1130/0016-7606(1992)104<0999:LPTTEO>2.3.CO;2

Mpodozis, C., Ramos, V., 2008. Tectonica Jurásica En Argentina y Chile: extension, Subduccion Oblicua, Rifting, Deriva y Colisiones? Rev. la Asoc. Geológica Argentina 63, 481–497.

Mpodozis, C., Ramos, V.A., 1990. The Andes of Chile and Argentina, in: Geology of the Andes and Its Relation to Hydrocarbon and Mineral Resources. Circum-Pacific Council for Energy and Mineral Resources, Earth Science Series. pp. 59–90.

Mulder, T., Alexander, J., 2001. The physical character of subaqueous sedimentary density flows and their deposits. Sedimentology 48, 269–299. https://doi.org/10.1046/j.1365-3091.2001.00360.x

Mulder, T., Syvitski, J.P.M., Migeon, S., Faugères, J.-C., Savoye, B., 2003. Marine hyperpycnal flows:

initiation, behavior and related deposits. A review. Mar. Pet. Geol. 20, 861–882. https://doi.org/10.1016/j.marpetgeo.2003.01.003

Muravchik, M., 2008. Controles estructurales sobre la depositación de la base del ciclo Cuyano en depocentros del Suroeste de la Cuenca Neuquina, in: Actas Del XVII Congreso Geológico Argentino, Jujuy. pp. 781–782.

Muravchik, M., Bilmes, A., D'Elia, L., Franzese, J.R., 2014. Alluvial fan deposition along a rift depocentre border from the Neuquén Basin, Argentina. Sediment. Geol. 301, 70–89. https://doi.org/10.1016/j.sedgeo.2013.12.007

Muravchik, M., D'Elia, L., Bilmes, A., Franzese, J.R., 2011. Syn-eruptive/inter-eruptive relations in the syn-rift deposits of the Precuyano Cycle, Sierra de Chacaico, Neuquén Basin, Argentina. Sediment. Geol. 238, 132–144. https://doi.org/10.1016/j.sedgeo.2011.04.008

Mutti, E., 1992. Turbidite sandstones. AGIP Istituto di Geologia, Universita di Parma, Milan.

Mutti, E., 1977. Distinctive thin-bedded turbidite facies and related depositional environments in the Eocene Hecho Group (South-central Pyrenees, Spain). Sedimentology 24, 107–131. https://doi.org/10.1111/j.1365-3091.1977.tb00122.x

Mutti, E., Tinterri, R., Benevelli, G., di Biase, D., Cavanna, G., 2003. Deltaic, mixed and turbidite sedimentation of ancient foreland basins. Mar. Pet. Geol. 20, 733–755. https://doi.org/10.1016/j.marpetgeo.2003.09.001

Muzzi Magalhaes, P., Tinterri, R., 2010. Stratigraphy and depositional setting of slurry and contained (reflected) beds in the Marnoso-arenacea Formation (Langhian-Serravallian) Northern Apennines, Italy. Sedimentology 57, 1685–1720. https://doi.org/10.1111/j.1365-3091.2010.01160.x

Naipauer, M., García Morabito, E., Marques, J.C., Tunik, M., Rojas Vera, E.A., Vujovich, G.I., Pimentel, M.P., Ramos, V.A., 2012. Intraplate Late Jurassic deformation and exhumation in western central Argentina: Constraints from surface data and U-Pb detrital zircon ages. Tectonophysics 524–525, 59–75. https://doi.org/10.1016/j.tecto.2011.12.017

Naipauer, M., Morabito, E.G., Manassero, M., Valenica, V. V., Ramos, V.A., 2018a. A Provenance Analysis from the Lower Jurassic Units of the Neuquén Basin. Volcanic Arc or Intraplate Magmatic Input?, in: Folguera, A., Contreras-Reyes, E., Heredia, N., Encinas, A., B. Iannelli, S., Oliveros, V., M. Dávila, F., Collo, G., Giambiagi, L., Maksymowicz, A., Iglesia Llanos, M.P., Turienzo, M., Naipauer, M., Orts, D., D. Litvak, V., Alvarez, O., Arriagada, C. (Eds.), The Evolution of the Chilean-Argentinean Andes, Springer Earth System Sciences. Springer International Publishing, pp. 191–222. https://doi.org/10.1007/978-3-319-67774-3

Naipauer, M., Morabito, E.G., Ramos, V.A., 2018b. The Evolution of the Chilean-Argentinean Andes, Springer Earth System Sciences. Springer International Publishing, Cham. https://doi.org/10.1007/978-3-319-67774-3

Navarro, V., Ruiz-Ortiz, P.A., Molina, J.M., 2012. Birth and demise of a Middle Jurassic isolated shallow-marine carbonate platform on a tilted fault block: Example from the Southern Iberian continental palaeomargin. Sediment. Geol. 269–270, 37–57. https://doi.org/10.1016/j.sedgeo.2012.05.017

Nemec, W., Steel, R. j., 1988. What is a fan delta and how do we recognize it?, in: Nemec, W., Steel, R.J. (Eds.), Fan Deltas: Sedimentology and Tectonic Settings. pp. 3–13.

Nielsen, M.T., Weibel, R., Friis, H., 2015. Provenance of gravity-flow sandstones from the Upper Jurassic–Lower Cretaceous Farsund Formation, Danish Central Graben, North Sea. Mar. Pet. Geol. 59, 371–389. https://doi.org/10.1016/j.marpetgeo.2014.09.016

Noda, A., Tuzino, T., 2007. Characteristics of sediments and their dispersal systems along the shelf and

slope of an active forearc margin, eastern Hokkaido, northern Japan. Sediment. Geol. 201, 341–364. https://doi.org/10.1016/j.sedgeo.2007.07.002

Normark, W.R., 1970. Growth patterns of deep-sea fans. Am. Assoc. Pet. Geol. Bull. 54, 2170–2195.

Nøttvedt, A., Gabrielsen, R.H., Steel, R.J., 1995. Tectonostratigraphy and sedimentary architecture of rift basins, with reference to the northern North Sea. Mar. Pet. Geol. 12, 881–901. https://doi.org/10.1016/0264-8172(95)98853-W

Ogg, J.G., Hinnov, L.A., Huang, C., 2012. Jurassic, in: Gradstein, F.M., Ogg, James G., Schmitz, M.D., Ogg, G.M. (Eds.), The Geologic Time Scale. Elsevier, pp. 731–791. https://doi.org/10.1016/B978-0-444-59425-9.00026-3

Ogston, A.S., Cacchione, D.A., Sternberg, R.W., Kineke, G.C., 2000. Observations of storm and river flood-driven sediment transport on the northern California continental shelf. Cont. Shelf Res. 20, 2141–2162. https://doi.org/10.1016/S0278-4343(00)00065-0

Olive, J.-A., Behn, M.D., Malatesta, L.C., 2014. Modes of extensional faulting controlled by surface processes. Geophys. Res. Lett. 41, 6725–6733. https://doi.org/10.1002/2014GL061507

Ostera, H.A., García, R., Malizia, D., Kokot, P., Wainstein, L., Ricciutti, M., 2016. Shale gas plays, Neuquén Basin, Argentina: chemostratigraphy and mud gas carbon isotopes insights. Brazilian J. Geol. 46, 181–196. https://doi.org/10.1590/2317-4889201620150001

Paim, P.S.G., Lavina, E.L.C., Faccini, U.F., da Silveira, A.S., Leanza, H., D'Avila, R.S.F., 2011. Fluvial-derived turbidites in the Los Molles Formation (Jurassic of the Neuquén Basin): Initiation, transport, and deposition, in: Slatt, R.M., Zavala, C. (Eds.), Sediment Transfer from Shelf to Deep Water—Revisiting the Delivery System: AAPG Studies in Geology. pp. 95–116. https://doi.org/10.1306/13271352St613437

Paim, P.S.G., Silveira, A.S., Lavina, E.L.C., Faccini, U.F., Leanza, H.A., Teixeira De Oliveira, J.M.., D'Avila, R.S.F., 2008. High resolution stratigraphy and gravity flow deposits in the Los Molles formation (Cuyo Group - Jurassic) at La Jardinera region, Neuquén Basin. Rev. la Asoc. Geológica Argentina 63, 728–753.

Palmer, B.A., Purves, A.M., Donoghue, S.L., 1993. Controls on accumulation of a volcaniclastic fan, Ruapehu composite volcano, New Zealand. Bull. Volcanol. 55, 176–189. https://doi.org/10.1007/BF00301515

Pángaro, F., Melli, A.T., Malone, P., Cevallos, M., Soraci, A., Mosquera, A., Kim, J.H., 2006a. Modelos de entrampamiento de la dorsal de Huincul, Cuenca Neuquina, Argentina. VI Congr. Explor. y Desarro. Hidrocarburos 48–88.

Pángaro, F., Pereira, D.M., Micucci, E., 2009. El sinrift de la dorsal de Huincul, Cuenca Neuquina: Evolución y control sobre la estratigrafía y estructura del área. Rev. la Asoc. Geológica Argentina 65, 265–277.

Pángaro, F., Pereira, M., Giorgetti, M., 2006b. Volcanic reservoirs of the Precuyano, Neuquen Basin, Argentina: Extrapolation of Surface Analogs to Seismic and Log Interpretation. 9° Simp. Boliv. Pet. en las Cuencas Subandinas.

Pángaro, F., Pereira, M., Raggio, F., Pioli, O., Silvestro, J.L., Zubiri, M., Gozalvez, G., 2006c. Tectonic Inversion of the Huincul High, Neuquen Basin, Argentina: An Endangered Species. Stratigraphic evidences of It's Disappearance. 9° Simp. Boliv. Explor. Subandean Basins.

Pángaro, F., Veiga, R., Vergani, G., 2002. Evolución tecto-sedimentaria del área de Cerra Bandera, Cuenca Neuquina, Argentina, in: 5° Congreso de Exploración y Desarrollo de Hidrocarburos (Mar Del Plata). p. 16.

Pankhurst, R.J., Rapela, C.W., Fanning, C.M., Márquez, M., 2006. Gondwanide continental collision and

the origin of Patagonia. Earth-Science Rev. 76, 235–257. https://doi.org/10.1016/j.earscirev.2006.02.001

Pankhurst, R.J., Rapela, C.W., López De Luchi, M.G., Rapalini, A.E., Fanning, C.M., Galindo, C., 2014. The Gondwana connections of northern Patagonia. J. Geol. Soc. London. 171, 313–328. https://doi.org/10.1144/jgs2013-081

Parsons, J.D., Bush, J.W.M., Syvitski, J.P.M., 2001. Hyperpycnal plume formation from riverine outflows with small sediment concentrations. Sedimentology 48, 465–478. https://doi.org/10.1046/j.1365-3091.2001.00384.x

Patacci, M., Haughton, P.D.W., Mccaffrey, W.D., 2015. Flow Behavior of Ponded Turbidity Currents. J. Sediment. Res. 85, 885–902. https://doi.org/10.2110/jsr.2015.59

Patacci, M., Haughton, P.D.W., McCaffrey, W.D., 2014. Rheological Complexity In Sediment Gravity Flows Forced To Decelerate Against A Confining Slope, Braux, SE France. J. Sediment. Res. 84, 270–277. https://doi.org/10.2110/jsr.2014.26

Patton, T.L., Moustafa, A.R., Nelson, R.A., Abdine, S.A., 1994. Tectonic evolution and structural setting of the Suez Rift, in: Landon, S.M., Coury, A.B. (Eds.), Interior Rift Basins. AAPG Memoir. pp. 9–55. https://doi.org/10.1306/M59582C2

Payros, A., Pujalte, V., 2008. Calciclastic submarine fans: An integrated overview. Earth-Science Rev. 86, 203–246. https://doi.org/10.1016/j.earscirev.2007.09.001

Pelletier, B., 2006. Geology of the New Caledonia region and its implications for the study of the New Caledonian biodiversity, in: Payri, C.E., Richer de Forges, B. (Eds.), Compendium of Marine Species of New Caledonia. Doc. Sci. Tech. II7, IRD Nouméa. pp. 19–32.

Pinter, P.R., Butler, R.W.H., Hartley, A.J., Maniscalco, R., Baldassini, N., Di Stefano, A., 2017. Tracking sand-fairways through a deformed turbidite system: the Numidian (Miocene) of Central Sicily, Italy. Basin Res. 0–2. https://doi.org/10.1111/bre.12261

Porten, K.W., Kane, I.A., Warchoł, M., Southern, S.J., 2016. A Sedimentological Process-Based Approach To Depositional Reservoir Quality of Deep-Marine Sandstones: An Example From the Springar Formation, Northwestern Vøring Basin, Norwegian Sea. J. Sediment. Res. 86, 1269–1286. https://doi.org/10.2110/jsr.2016.74

Postma, G., 1990. Depositional Architecture and Facies of River and Fan Deltas: A Synthesis, in: Colella, A., Prior, D.B. (Eds.), Coarse-Grained Deltas. Special Publications of the International Association of Sedimentologists. Blackwell Publishing Ltd., Oxford, UK, pp. 13–27. https://doi.org/10.1002/9781444303858.ch2

Postma, G., Drinia, H., 1993. Architecture and sedimentary facies evolution of a marine, expanding outer-arc half-graben (Crete, late Miocene). Basin Res. 5, 103–124. https://doi.org/10.1111/j.1365-2117.1993.tb00060.x

Prather, B.E., 2003. Controls on reservoir distribution, architecture and stratigraphic trapping in slope settings. Mar. Pet. Geol. 20, 529–545. https://doi.org/10.1016/j.marpetgeo.2003.03.009

Prather, B.E., Booth, J.R., Steffens, G.S., Craig, P.A., 1998. Classification, Lithologic Calibration, and Stratigraphic Succession of Seismic Facies of Intraslope Basins, Deep-Water Gulf of Mexico. Am. Assoc. Pet. Geol. Bull. 82, 701–728. https://doi.org/10.1306/1D9BC5D9-172D-11D7-8645000102C1865D

Prather, B.E., O'Byrne, C., Pirmez, C., Sylvester, Z., 2017. Sediment partitioning , continental slopes and base-of-slope systems. Basin Res. 29, 394–416. https://doi.org/10.1111/bre.12190

Prélat, A., Hodgson, D.M., 2013. The full range of turbidite bed thickness patterns in submarine lobes: controls and implications. J. Geol. Soc. London 170, 209–214. https://doi.org/10.1144/jgs2012-

056

Prélat, A., Hodgson, D.M., Flint, S.S., 2009. Evolution, architecture and hierarchy of distributary deep-water deposits: a high-resolution outcrop investigation from the Permian Karoo Basin, South Africa. Sedimentology 56, 2132–2154. https://doi.org/10.1111/j.1365-3091.2009.01073.x

Prélat, A., Pankhania, S.S., Jackson, C.A.L., Hodgson, D.M., 2015. Slope gradient and lithology as controls on the initiation of submarine slope gullies; Insights from the North Carnarvon Basin, Offshore NW Australia. Sediment. Geol. 329, 12–17. https://doi.org/10.1016/j.sedgeo.2015.08.009

Privat, A.M.L., Hodgson, D.M., Jackson, C.A.L., Schwarz, E., Peakall, J., n.d. Evolution from syn-rift carbonates to early post-rift deep-marine intraslope lobes: the role of rift basin physiography on sedimentation patterns.

Prosser, S., 1993. Rift-related linked depositional systems and their seismic expression, in: Tectonics and Seismic Sequence Stratigraphy. Geological Society, London, Special Publications. pp. 35–66. https://doi.org/10.1144/GSL.SP.1993.071.01.03

Pujols, E.J., Leva López, J., Stockli, D.F., Rossi, V.M., Steel, R.J., 2018. New insights into the stratigraphic and structural evolution of the middle Jurassic S. Neuquén Basin from Detrital Zircon (U-Th)/(He-Pb) and Apatite (U-Th)/He ages. Basin Res. 30, 1280–1297. https://doi.org/10.1111/bre.12304

Purkis, S.J., Harris, P.M., Ellis, J., 2012. Patterns of Sedimentation In the Contemporary Red Sea As An Analog for Ancient Carbonates In Rift Settings. J. Sediment. Res. 82, 859–870. https://doi.org/10.2110/jsr.2012.77

Pyles, D.R., 2008. Multiscale stratigraphic analysis of a structurally confined submarine fan: Carboniferous Ross Sandstone, Ireland. Am. Assoc. Pet. Geol. Bull. 92, 557–587. https://doi.org/10.1306/01110807042

Pyles, D.R., Jennette, D.C., 2009. Geometry and architectural associations of co-genetic debrite–turbidite beds in basin-margin strata, Carboniferous Ross Sandstone (Ireland): Applications to reservoirs located on the margins of structurally confined submarine fans. Mar. Pet. Geol. 26, 1974–1996. https://doi.org/10.1016/j.marpetgeo.2009.02.018

Quattrocchio, M.E., Martinez, M.A., Volkheimer, W., 2007. Las floras jurásicas de la Argentina. Asoc. Paleontológica Argentina. Publicación Espec. 11, 87–100.

Rahl, J.M., McGrew, A.J., Foland, K.A., 2002. Transition from Contraction to Extension in the Northeastern Basin and Range: New Evidence from the Copper Mountains, Nevada. J. Geol. 110, 179–194. https://doi.org/10.1086/338413

Ramos, V.A., 2010. The tectonic regime along the Andes: Present-day and Mesozoic regimes. Geol. J. 45, 2–25. https://doi.org/10.1002/gj.1193

Ramos, V.A., 2008. Patagonia: A paleozoic continent adrift? J. South Am. Earth Sci. 26, 235–251. https://doi.org/10.1016/j.jsames.2008.06.002

Ramos, V.A., 1999. Plate tectonic setting of the Andean Cordillera. Episodes 22, 183–190.

Ramos, V.A., Folguera, A., 2005. Tectonic evolution of the Andes of Neuquén: constraints derived from the magmatic arc and foreland deformation, in: Veiga, G.D., Spalletti, L.A., Howell, J.A., Schwartz, E. (Eds.), The Neuquén Basin, Argentina: A Case Study in Sequence Stratigraphy and Basin Dynamics. Geological Society, London, Special Publications. pp. 15–35. https://doi.org/10.1144/GSL.SP.2005.252.01.02

Ramos, V.A., Kay, S.M., 1991. Triassic rifting and associated basalts in the Cuyo basin, central Argentina, in: Harmon, R.S., Rapela, C.W. (Eds.), Andean Magmatism and Its Tectonic Setting. GSA Special Papers. pp. 79–92. https://doi.org/10.1130/SPE265-p79

Ramos, V.A., Litvak, V.D., Folguera, A., Spagnuolo, M., 2014. An Andean tectonic cycle: From crustal thickening to extension in a thin crust (34°–37°SL). Geosci. Front. 5, 351–367. https://doi.org/10.1016/j.gsf.2013.12.009

Ramos, V.A., Mosquera, A., Folguera, A., García Morabito, E., 2011. Evolución Tectónica De Los Andes Y Del Engolfamiento Neuquino Adyacente, in: Leanza, H.A., Arregui, C., Carbone, O., Danielli, J.C., Vallés, J.M. (Eds.), Geología y Recursos Naturales de La Provincia Del Neuquén: Relatorio Del XVIII Congreso Geológico Argentino, Neuquén. Asociación Geológica Argentina, Buenos Aires, pp. 335–348.

Rapalini, A.E., 2005. The accretionary history of southern South America from the latest Proterozoic to the Late Palaeozoic: some palaeomagnetic constraints, in: Vaughan, A.P.M., Leat, P.T., Pankhurst, R.J. (Eds.), Terrane Processes at the Margins of Gondwana. Geological Society, London, Special Publications. pp. 305–328. https://doi.org/10.1144/GSL.SP.2005.246.01.12

Rapela, C. W., Pankhurst, R. J., Casquet, C., Baldo, E., Saavedra, J., Galindo, C., Fanning, C.M., 1998. The Pampean Orogeny of the southern proto-Andes: Cambrian continental collision in the Sierras de Córdoba, in: Pankhurst, Robert J., Rapela, Carlos W. (Eds.), The Proto-Andean Margin of Gondwana. Geological Society, London, Special Publications. pp. 181–217. https://doi.org/10.1144/GSL.SP.1998.142.01.10

Rapela, C.W., Pankhurst, R.J., Fanning, C.M., Hervé, F., 2005. Pacific subduction coeval with the Karoo mantle plume: the Early Jurasssic Subcordilleran belt of northwestern Patagonia, in: Vaughan, A.P.M., Leat, P.T., Pankhurst, R.J. (Eds.), Terrane Processes at the Margins of Gondwana. Geological Society, London, Special Publications. pp. 217–239. https://doi.org/10.1144/GSL.SP.2005.246.01.07

Rapela, C.W., Verdecchia, S.O., Casquet, C., Pankhurst, R.J., Baldo, E.G., Galindo, C., Murra, J.A., Dahlquist, J.A., Fanning, C.M., 2016. Identifying Laurentian and SW Gondwana sources in the Neoproterozoic to Early Paleozoic metasedimentary rocks of the Sierras Pampeanas: Paleogeographic and tectonic implications. Gondwana Res. 32, 193–212. https://doi.org/10.1016/j.gr.2015.02.010

Ravnås, R., Bondevik, K., 1997. Architecture and controls on Bathonian-Kimmeridgian shallow-marine synrift wedges of the Oseberg-Brage area, northern North Sea. Basin Res. 9, 197–226. https://doi.org/10.1046/j.1365-2117.1997.00041.x

Ravnås, R., Steel, R.J., 1998. Architecture of Marine Rift-Basin Successions. Am. Assoc. Pet. Geol. Bull. 82, 110–146. https://doi.org/10.1306/1D9BC3A9-172D-11D7-8645000102C1865D

Ravnås, R., Steel, R.J., 1997. Contrasting styles of Late Jurassic syn-rift turbidite sedimentation: a comparative study of the Magnus and Oseberg areas, northern North Sea. Mar. Pet. Geol. 14, 417–449. https://doi.org/10.1016/S0264-8172(97)00010-X

Reading, H.G., Richards, M., 1994. Turbidite systems in deep-water basin margins classified by grain size and feeder system. Am. Assoc. Pet. Geol. Bull. 78, 792–822.

Renaut, R.W., Jones, B., Tiercelin, J.., Tarits, C., 2002. Sublacustrine precipitation of hydrothermal silica in rift lakes: evidence from Lake Baringo, central Kenya Rift Valley. Sediment. Geol. 148, 235–257. https://doi.org/10.1016/S0037-0738(01)00220-2

Reynolds, D.J., Steckler, M.S., Coakley, B.J., 1991. The role of the sediment load in sequence stratigraphy: The influence of flexural isostasy and compaction. J. Geophys. Res. Solid Earth 96, 6931–6949. https://doi.org/10.1029/90JB01914

Riccardi, A., Kamo, S., 2014. Biostratigraphy and Geochronology of the Pliensbachian-Toarcian Boundary in Argentina, in: XIX Congreso Geológico Argentino, Junio 2014, Córdoba.

Riccardi, A.C., 2008. El Jurasico de la Argentina y sus amonites. Rev. la Asoc. Geológica Argentina 63,

625–643.

Riccardi, A.C., 1991. Jurassic and cretaceous marine connections between the Southeast Pacific and Tethys. Palaeogeogr. Palaeoclimatol. Palaeoecol. 87, 155–189. https://doi.org/10.1016/0031-0182(91)90134-D

Riccardi, A.C., Damborenea, S.E., Manceñido, M.O., Leanza, H.A., 2011. Megainvertebrados del jurásico y su importancia geobiológica, in: Geología y Recursos Naturales de La Provincia Del Neuquén: 18º Congreso Geológico Argentino. pp. 441–464.

Riccardi, A.C., Westermann, G.E.G., Elmi, S., 1991. Biostratigraphy of the upper Bajocian-middle Callovian (Middle Jurassic), South America. J. South Am. Earth Sci. 4, 149–157. https://doi.org/10.1016/0895-9811(91)90027-I

Ring, U., 2014. The East African rift system. Austrian J. Earth Sci. 107, 132–146.

Roberts, Alan M., Yielding, Graham, 1991. Deformation around basin-margin faults in the North Sea/mid-Norway rift, in: Roberts, A.M., Yielding, G., Freeman, B. (Eds.), The Geometry of Normal Faults. Geological Society, London, Special Publications. pp. 61–78. https://doi.org/10.1144/GSL.SP.1991.056.01.05

Roduit, N., 2007. JMicroVision : un logiciel d'analyse d'images pétrographiques polyvalent. PhD thesis, Université de Genève, Geneva, Suiss.

Rohais, S., Barrois, A., Colletta, B., Moretti, I., 2016. Pre-salt to salt stratigraphic architecture in a rift basin: insights from a basin-scale study of the Gulf of Suez (Egypt). Arab. J. Geosci. 9. https://doi.org/10.1007/s12517-016-2327-8

Romans, B.W., Normark, W.R., McGann, M.M., Covault, J.A., Graham, S.A., 2009. Coarse-grained sediment delivery and distribution in the Holocene Santa Monica Basin, California: Implications for evaluating source-to-sink flux at millennial time scales. Geol. Soc. Am. Bull. 121, 1394–1408. https://doi.org/10.1130/B26393.1

Rosas, S., Fontboté, L., Tankard, A., 2007. Tectonic evolution and paleogeography of the Mesozoic Pucará Basin, central Peru. J. South Am. Earth Sci. 24, 1–24. https://doi.org/10.1016/j.jsames.2007.03.002

Rosenfeld, U., Eppinger, K.-J., 1993. The western margin of the Neuquen basin (Argentina) in the upper Jurassic and lower Cretaceous, in: Second ISAG, Oxford (UK), 21-23 September, 1993. pp. 313–315.

Ross, J.A., Peakall, J., Keevil, G.M., 2011. An integrated model of extrusive sand injectites in cohesionless sediments. Sedimentology 58, 1693–1715. https://doi.org/10.1111/j.1365-3091.2011.01230.x

Rossi, A., Moussaoui, S. El, 2014. Sedimentary evolution of the siliciclastic Aptian-Albian Massylian flysch of the Chouamat Nappe (central Rif , Morocco). J. African Earth Sci. https://doi.org/10.1016/j.jafrearsci.2014.08.004

Rotevatn, A., Kristensen, T.B., Ksienzyk, A.K., Wemmer, K., Henstra, G.A., Midtkandal, I., Grundvåg, S.A., Andresen, A., 2018. Structural Inheritance and Rapid Rift-Length Establishment in a Multiphase Rift: The East Greenland Rift System and its Caledonian Orogenic Ancestry. Tectonics 37, 1858–1875. https://doi.org/10.1029/2018TC005018

Rouillard, P., Collot, J., Sutherland, R., Bache, F., Patriat, M., Etienne, S., Maurizot, P., 2017. Seismic stratigraphy and paleogeographic evolution of Fairway Basin, Northern Zealandia, Southwest Pacific: from Cretaceous Gondwana breakup to Cenozoic Tonga-Kermadec subduction. Basin Res. 29, 189–212. https://doi.org/10.1111/bre.12144

Rowland, J. V., Wilson, C.J.N., Gravley, D.M., 2010. Spatial and temporal variations in magma-assisted

rifting, Taupo Volcanic Zone, New Zealand. J. Volcanol. Geotherm. Res. 190, 89–108. https://doi.org/10.1016/j.jvolgeores.2009.05.004

Royden, L., Keen, C.E., 1980. Rifting process and thermal evolution of the continental margin of Eastern Canada determined from subsidence curves. Earth Planet. Sci. Lett. 51, 343–361. https://doi.org/10.1016/0012-821X(80)90216-2

Ruiz-Ortiz, P.A., Bosence, D.W.J., Rey, J., Nieto, L.M., Castro, J.M., Molina, J.M., 2004. Tectonic control of facies architecture, sequence stratigraphy and drowning of a Liassic carbonate platform (Betic Cordillera, Southern Spain). Basin Res. 16, 235–257. https://doi.org/10.1111/j.1365-2117.2004.00231.x

Ruppel, C., 1995. Extensional processes in continental lithosphere. J. Geophys. Res. Solid Earth 100, 24187–24215. https://doi.org/10.1029/95JB02955

Sanchez, C.M., Fulthorpe, C.S., Steel, R.J., 2012. Miocene shelf-edge deltas and their impact on deepwater slope progradation and morphology, Northwest Shelf of Australia. Basin Res. 24, 683–698. https://doi.org/10.1111/j.1365-2117.2012.00545.x

Santantonio, M., 1994. Pelagic Carbonate Platforms in the Geologic Record: Their Classification, and Sedimentary and Paleotectonic Evolution. Am. Assoc. Pet. Geol. Bull. 78, 122–141. https://doi.org/10.1306/BDFF9032-1718-11D7-8645000102C1865D

Sattar, N., Juhlin, C., Koyi, H., Ahmad, N., 2017. Seismic stratigraphy and hydrocarbon prospectivity of the Lower Cretaceous Knurr Sandstone lobes along the southern margin of Loppa High, Hammerfest Basin, Barents Sea. Mar. Pet. Geol. 85, 54–69. https://doi.org/10.1016/j.marpetgeo.2017.04.008

Satur, N., Hurst, A., Cronin, B.., Kelling, G., Gürbüz, K., 2000. Sand body geometry in a sand-rich, deep-water clastic system, Miocene Cingöz Formation of southern Turkey. Mar. Pet. Geol. 17, 239–252. https://doi.org/10.1016/S0264-8172(99)00005-7

Schellart, W.P., Lister, G.S., Toy, V.G., 2006. A Late Cretaceous and Cenozoic reconstruction of the Southwest Pacific region: Tectonics controlled by subduction and slab rollback processes. Earth-Science Rev. 76, 191–233. https://doi.org/10.1016/j.earscirev.2006.01.002

Schieber, J., 2016. Mud re-distribution in epicontinental basins – Exploring likely processes. Mar. Pet. Geol. 71, 119–133. https://doi.org/10.1016/j.marpetgeo.2015.12.014

Schiuma, M., Llambías, E.J., 2008. New ages and chemical analysis on lower jurassic volcanism close to the dorsal de Huincul, Neuquén. Rev. la Asoc. Geológica Argentina 63, 644–652.

Schiuma, M., Rodriguez, E., Tortora, L., Llambías, R., 2011. Depósitos de origen volcánico en el yacimiento Cupen Mahuida, Cuenca Neuquina. VII Congr. Explor. y Desarro. Hidrocarburos 147–167.

Schlische, R.W., 1995. Geometry and Origin of Fault-Related Folds in Extensional Settings. Am. Assoc. Pet. Geol. Bull. 79, 1661–1678. https://doi.org/10.1306/7834DE4A-1721-11D7-8645000102C1865D

Schlische, R.W., 1993. Anatomy and evolution of the Triassic-Jurassic Continental Rift System, eastern North America. Tectonics 12, 1026–1042. https://doi.org/10.1029/93TC01062

Schlische, R.W., Anders, M.H., 1996. Stratigraphic effects and tectonic implications of the growth of normal faults and extensional basins, in: Reconstructing the History of Basin and Range Extension Using Sedimentology and Stratigraphy, Geological Society of America, Special Paper. Geological Society of America, pp. 183–203. https://doi.org/10.1130/0-8137-2303-5.183

Schmid, M., Tietze, K., Halbwachs, M., Lorke, A., McGinnis, D., Wüest, A., 2003. How hazardous is the gas accumulation in Lake Kivu? Arguments for a risk assessment in light of the Nyiragongo

Volcano eruption of 2002. Acta Vulcanol. 14–15, 115–121. https://doi.org/10.1400/19084

Schneider, J.-L., 2000. Volcaniclastic sedimentation in submarine settings: products and processes, in: Leurit, H., Montenat, C. (Eds.), Volcaniclastic Rocks, from Magmas to Sediments. Gordon & Breach Science Publishers, Amsterdam, pp. 175–192.

Schneider, S., Hornung, J., Hinderer, M., 2016. Evolution of the western East African Rift System reflected in provenance changes of Miocene to Pleistocene synrift sediments (Albertine Rift, Uganda). Sediment. Geol. 343, 190–205. https://doi.org/10.1016/j.sedgeo.2016.07.013

Scholz, C.H., Campos, J., 1995. On the mechanism of seismic decoupling and back arc spreading at subduction zones. J. Geophys. Res. Solid Earth 100, 22103–22115. https://doi.org/10.1029/95JB01869

Sdrolias, M., Müller, R.D., 2006. Controls on back-arc basin formation. Geochemistry, Geophys. Geosystems 7. https://doi.org/10.1029/2005GC001090

Seidler, L., Steel, R.J., Stemmerik, L., Surlyk, F., 2004. North Atlantic marine rifting in the Early Triassic: new evidence from East Greenland. J. Geol. Soc. London 161, 583–592. https://doi.org/10.1144/0016-764903-063

Sengör, A.M.C., Burke, K., 1978. Relative timing of rifting and volcanism on Earth and its tectonic implications. Geophys. Res. Lett. 5, 419–421. https://doi.org/10.1029/GL005i006p00419

Sharp, I.R., Gawthorpe, R.L., Underhill, J.R., Gupta, S., 2000. Fault-propagation folding in extensional settings: Examples of structural style and synrift sedimentary response from the Suez rift, Sinai, Egypt. Geol. Soc. Am. Bull. 112, 1877–1899. https://doi.org/10.1130/0016-7606(2000)112<1877:FPFIES>2.0.CO;2

Shumaker, L.E., Sharman, G.R., King, P.R., Graham, S.A., 2018. The source is in the sink: Deep-water deposition by a submarine volcanic arc, Taranaki Basin, New Zealand. Sedimentology 65, 2506–2530. https://doi.org/10.1111/sed.12475

Sigismondi, M.E., Ramos, V.A., 2011. El Basamento de la Cuenca Neuquina. Relat. del XVIII Congr. Geológico Argentino, Neuquén 327–333.

Silvestro, J., Zubiri, M., 2008. Convergencia oblica: Modelo estructural alternativo para la dorsal Neuquina (39°S) - Neuquén. Rev. la Asoc. Geológica Argentina 63, 49–64. https://doi.org/10.1016/j.chemgeo.2013.04.007

Sinclair, H.D., Tomasso, M., 2002. Depositional Evolution of Confined Turbidite Basins. J. Sediment. Res. 72, 451–456. https://doi.org/10.1306/111501720451

Skuce, A.G., 1996. Forward modelling of compaction above normal faults: an example from the Sirte Basin, Libya, in: Buchanan, P.G., Nieuwland, D.A. (Eds.), Modern Developments in Structural Interpretation, Validation and Modelling, Geological Society, London, Special Publications. pp. 135–146. https://doi.org/10.1144/GSL.SP.1996.099.01.11

Smith, G.A., 1986. Coarse-grained nonmarine volcaniclastic sediment: Terminology and depositional process. Geol. Soc. Am. Bull. 97, 1–10. https://doi.org/10.1130/0016-7606(1986)97<1:CNVSTA>2.0.CO;2

Smith, R., 2004. Turbidite systems influenced by structurally induced topography in the multi-sourced Welsh Basin. Geol. Soc. London, Spec. Publ. 222, 209–228. https://doi.org/10.1144/GSL.SP.2004.222.01.11

Soares, D.M., Alves, T.M., Terrinha, P., 2012. The breakup sequence and associated lithospheric breakup surface: Their significance in the context of rifted continental margins (West Iberia and Newfoundland margins, North Atlantic). Earth Planet. Sci. Lett. 355–356, 311–326. https://doi.org/10.1016/j.epsl.2012.08.036

Sohn, Y.K., Rhee, C.W., Kim, B.C., 1999. Debris Flow and Hyperconcentrated Flood-Flow Deposits in an Alluvial Fan, Northwestern Part of the Cretaceous Yongdong Basin, Central Korea. J. Geol. 107, 111–132. https://doi.org/10.1086/314334

Southern, S.J., Kane, I.A., Warchoł, M., Porten, K.W., McCaffrey, W.D., 2017. Hybrid event beds dominated by transitional-flow facies: character, distribution and significance in the Maastrichtian Springar Formation, north-west Vøring Basin, Norwegian Sea. Sedimentology 64, 747–776. https://doi.org/10.1111/sed.12323

Southern, S.J., Patacci, M., Felletti, F., McCaffrey, W.D., 2015. Influence of flow containment and substrate entrainment upon sandy hybrid event beds containing a co-genetic mud-clast-rich division. Sediment. Geol. 321, 105–122. https://doi.org/10.1016/j.sedgeo.2015.03.006

Spalletti, L., Franzese, J., Morel, E., D'Elia, L., Zúñiga, A., Fanning, C.M., 2010. Consideraciones acerca de la sedimentología, paleobotánica y geocronología de la Formación Piedra del Águila (Jurásico Inferior, Neuquén). Rev. la Asoc. Geológica Argentina 66, 305–313.

Spalletti, L.A., Arrondo, O.G., Morel, E.M., Ganuza, D.G., 1991. Evidencias sobre la edad triásica de la Formación Lapa en la región de Chacaico, Provincia del Neuquén. Rev. la Asoc. Geológica Argentina 46, 167–172.

Spychala, Y.T., Hodgson, D.M., Flint, S.S., Mountney, N.P., 2015. Constraining the sedimentology and stratigraphy of submarine intraslope lobe deposits using exhumed examples from the Karoo Basin, South Africa. Sediment. Geol. 322, 67–81. https://doi.org/10.1016/j.sedgeo.2015.03.013

Spychala, Y.T., Hodgson, D.M., Prélat, A., Kane, I.A., Flint, S.S., Mountney, N.P., 2017. Frontal and Lateral Submarine Lobe Fringes: Comparing Sedimentary Facies, Architecture and Flow Processes. J. Sediment. Res. 87, 75–96. https://doi.org/10.2110/jsr.2017.2

Stanton, P.T., Wilson, M.D., 1994. Measurement of Independent Variables – Composition, in: Wilson, M.D. (Ed.), Reservoir Quality Assessment and Prediction in Clastic Rocks. SEPM Short Course Notes. SEPM (Society for Sedimentary Geology), pp. 277–291. https://doi.org/10.2110/scn.94.30.0277

Stevenson, C.J., Jackson, C.A.L., Hodgson, D.M., Hubbard, S.M., Eggenhuisen, J.T., 2015. Deep-Water Sediment Bypass. J. Sediment. Res. 85, 1058–1081. https://doi.org/10.2110/jsr.2015.63

Stewart, A.L., McPhie, J., 2004. An Upper Pliocene coarse pumice breccia generated by a shallow submarine explosive eruption, Milos, Greece. Bull. Volcanol. 66, 15–28. https://doi.org/10.1007/s00445-003-0292-z

Stinco, L.P., Mosquera, A., 2005. Estimación del contenido total de carbono orgánico a partir de registros de pozo para las formaciones Vaca Muerta y los Molles, Cuenca Neuquina, Argentina, in: II Congreso de Hidrocarburos, Buenos Aires, Actas. pp. 18–30.

Stow, D.A.V., Bowen, A.J., 1980. A Physical Model for the Transport and Sorting of Fine-Grained Sediment by Turbidity Currents, in: Stow, D.A.V. (Ed.), Deep-Water Turbidite Systems. Blackwell Publishing Ltd., Oxford, UK, pp. 25–40. https://doi.org/10.1002/9781444304473.ch2

Strachan, L.J., Rarity, F., Gawthorpe, R.L., Wilson, P., Sharp, I., Hodgetts, D., 2013. Submarine slope processes in rift-margin basins, Miocene Suez Rift, Egypt. Geol. Soc. Am. Bull. 125, 109–127. https://doi.org/10.1130/B30665.1

Strogen, D.P., Bland, K.J., Nicol, A., King, P.R., 2014. Paleogeography of the Taranaki Basin region during the latest Eocene–Early Miocene and implications for the 'total drowning' of Zealandia. New Zeal. J. Geol. Geophys. 57, 110–127. https://doi.org/10.1080/00288306.2014.901231

Suárez, M., Márquez, M., 2007. A Toarcian retro-arc basin of Central Patagonia (Chubut), Argentina: Middle Jurassic closure, arc migration and tectonic setting. Rev. Geológica Chile 34, 63–79.

https://doi.org/10.4067/S0716-02082007000100004

Suárez, R.J., González, P.D., 2018. Caracterización geológica del metamorfismo diastatermal mesozoico en la Cuenca Neuquina y su relación con la anomalía térmica en el sinrift. Rev. la Asoc. Geológica Argentina 75, 457–472.

Sumner, E.J., Amy, L.A., Talling, P.J., 2008. Deposit Structure and Processes of Sand Deposition from Decelerating Sediment Suspensions. J. Sediment. Res. 78, 529–547. https://doi.org/10.2110/jsr.2008.062

Surlyk, F., Korstgård, J., 2013. Crestal unconformities on an exposed Jurassic tilted fault block, Wollaston Forland, East Greenland as an analogue for buried hydrocarbon traps. Mar. Pet. Geol. 44, 82–95. https://doi.org/10.1016/j.marpetgeo.2013.03.009

Surlyk, F., Noe-Nygaard, N., 2001. Sand remobilisation and intrusion in the Upper Jurassic Hareelv Formation of East Greenland Sedimentary facies The primary sedimentary facies of the Katedralen. Bull. Geol. Soc. Denmark 48, 169–188.

Takano, O., 2002. Changes in depositional systems and sequences in response to basin evolution in a rifted and inverted basin: An example from the Neogene Niigata-Shin'etsu basin, Northern Fossa Magna, central Japan. Sediment. Geol. 152, 79–97. https://doi.org/10.1016/S0037-0738(01)00286-X

Talling, P.J., 2013. Hybrid submarine flows comprising turbidity current and cohesive debris flow: Deposits, theoretical and experimental analyses, and generalized models. Geosphere 9, 460–488. https://doi.org/10.1130/GES00793.1

Talling, P.J., Amy, L.A., Wynn, R.B., Peakall, J., Robinson, M., 2004. Beds comprising debrite sandwiched within co-genetic turbidite: Origin and widespread occurrence in distal depositional environments. Sedimentology 51, 163–194. https://doi.org/10.1111/j.1365-3091.2004.00617.x

Talling, P.J., Malgesini, G., Felletti, F., 2013. Can liquefied debris flows deposit clean sand over large areas of sea floor? Field evidence from the Marnoso-arenacea Formation, Italian Apennines. Sedimentology 60, 720–762. https://doi.org/10.1111/j.1365-3091.2012.01358.x

Talling, P.J., Masson, D.G., Sumner, E.J., Malgesini, G., 2012. Subaqueous sediment density flows: Depositional processes and deposit types. Sedimentology 59, 1937–2003. https://doi.org/10.1111/j.1365-3091.2012.01353.x

Talling, P.J., Wynn, R.B., Schmmidt, D.N., Rixon, R., Sumner, E., Amy, L., 2010. How Did Thin Submarine Debris Flows Carry Boulder-Sized Intraclasts for Remarkable Distances Across Low Gradients to the Far Reaches of the Mississippi Fan? J. Sediment. Res. 80, 829–851. https://doi.org/10.2110/jsr.2010.076

Tankard, A.J., Uliana, M.A., Welsink, H.J., Ramos, V.A., Turic, M., França, A.B., Milani, E.J., de Brito Neves, B.B., Eyles, N., Skarmeta, J., Santa Ana, H., Wiens, F., Cirbián, M., López Paulsen, O., Germs, G.J.B., De Wit, M.J., Machacha, T., Miller, R.M., 1995. Structural and Tectonic Controls of Basin Evolution in Southwestern Gondwana During the Phanerozoic, in: Tankard, A.J., Suárez Soruco, R., Welsink, H.J. (Eds.), Petroleum Basins of South America. AAPG Memoir. pp. 5–52. https://doi.org/10.1306/M62593C1

Taylor, A.M., Goldring, R., 1993. Description and analysis of bioturbation and ichnofabric. J. Geol. Soc. London. 150, 141–148. https://doi.org/10.1144/gsjgs.150.1.0141

Taylor, K.G., Gawthorpe, R.L., Van Wagoner, J.C., 1995. Stratigraphic control on laterally persistent cementation, Book Cliffs, Utah. J. Geol. Soc. London. 152, 225–228. https://doi.org/10.1144/gsjgs.152.2.0225

Taylor, S.K., Bull, J.M., Lamarche, G., Barnes, P.M., 2004. Normal fault growth and linkage in the

Whakatane Graben, New Zealand, during the last 1.3 Myr. J. Geophys. Res. Solid Earth 109. https://doi.org/10.1029/2003JB002412

Taylor, T.R., Giles, M.R., Hathon, L.A., Diggs, T.N., Braunsdorf, N.R., Birbiglia, G. V., Kittridge, M.G., Macaulay, C.I., Espejo, I.S., 2010. Sandstone diagenesis and reservoir quality prediction: Models, myths, and reality. Am. Assoc. Pet. Geol. Bull. 94, 1093–1132. https://doi.org/10.1306/04211009123

Tentori, D., Marsaglia, K.M., Milli, S., 2016. Sand Compositional Changes As A Support For Sequence-Stratigraphic Interpretation: The Middle Upper Pleistocene To Holocene Deposits of the Roman Basin (Rome, Italy). J. Sediment. Res. 86, 1208–1227. https://doi.org/10.2110/jsr.2016.75

Tinterri, R., 2011. Combined flow sedimentary structures and the genetic link between sigmoidal- and hummocky-cross stratification. GeoActa 10, 43–85. https://doi.org/-

Tinterri, R., Muzzi Magalhaes, P., Tagliaferri, A., Cunha, R.S., 2016. Convolute laminations and load structures in turbidites as indicators of flow reflections and decelerations against bounding slopes. Examples from the Marnoso-arenacea Formation (northern Italy) and Annot Sandstones (south eastern France). Sediment. Geol. 344, 382–407. https://doi.org/10.1016/j.sedgeo.2016.01.023

Traykovski, P., Wiberg, P.L., Geyer, W.R., 2007. Observations and modeling of wave-supported sediment gravity flows on the Po prodelta and comparison to prior observations from the Eel shelf. Cont. Shelf Res. 27, 375–399. https://doi.org/10.1016/j.csr.2005.07.008

Trugdill, B., Cartwright, J., 1994. Relay-ramp forms and normal-fault linkages, Canyonlands National Park, Utah. Geol. Soc. Am. Bull. 106, 1143–1157. https://doi.org/10.1130/0016-7606(1994)106<1143:RRFANF>2.3.CO;2

Tudor, E., 2014. Facies Variability in Deep Water Channel-to Lobe Transition Zone: Jurassic Los Molles Formation, Neuquen Basin, Argentina. Master Degree Thesis, University of Texas, Austin, USA.

Twichell, D.C., Schwab, W.C., Nelson, C.H., Kenyon, N.H., Lee, H.J., 1992. Characteristics of a sandy depositional lobe on the outer Mississippi fan from SeaMARC IA sidescan sonar images. Geology 20, 689–692. https://doi.org/10.1130/0091-7613(1992)020<0689:COASDL>2.3.CO;2

Tyson, R. V., 1995. Sedimentary Organic Matter: Organic facies and palynofacies. Springer Netherlands, Dordrecht. https://doi.org/10.1007/978-94-011-0739-6

Tyson, R. V., 1993. Palynofacies Analysis, in: Jenkins, D.G. (Ed.), Applied Micropalaeontology. Kluwer Academic Publishers, The Netherlands, Amsterdam, Dordrecht, pp. 153–191. https://doi.org/10.1007/978-94-017-0763-3_5

Uchman, A., Wetzel, A., 2011. Deep-Sea Ichnology: The Relationships Between Depositional Environment and Endobenthic Organisms, in: Hüneke, H., Mulder, T. (Eds.), Developments in Sedimentology. Elsevier B.V., pp. 517–556. https://doi.org/10.1016/B978-0-444-53000-4.00008-1

Uliana, M.A., Biddle, K.T., Cerdan, J., 1989. Mesozoic Extension and the Formation of Argentine Sedimentary Basins, in: Tankard, A.J., Balkwill, H.R. (Eds.), Extensional Tectonics and Stratigraphy of the North Atlantic Margins. American Association of Petroleum Geologists, Tulsa, pp. 599–614. https://doi.org/10.1306/M46497C39

Uliana, M.A., Legarreta, L., 1993. Hydrocarbons Habitat in a Triassic-To-Cretaceous Sub-Andean Setting: Neuquén Basin, Argentina Introduction and Regional Setting. J. Pet. Geol. 16, 397–420. https://doi.org/10.1111/j.1747-5457.1993.tb00350.x

van der Plas, L., Tobi, A.C., 1965. A chart for judging the reliability of point counting results. Am. J. Sci. 263, 87–90. https://doi.org/10.2475/ajs.263.1.87

Vann, N.K., 2013. Slope to basin floor evolution of channels to lobes, Jurassic Los Molles Formation, Neuquen Basin, Argentina. Master Degree Thesis, University of Texas, Austin, USA.

Veiga, G.D., Schwarz, E., Spalletti, L.A., Massaferro, J.L., 2013. Anatomy And Sequence Architecture of the Early Post-Rift In the Neuquen Basin (Argentina): A Response To Physiography and Relative Sea-Level Changes. J. Sediment. Res. 83, 746–765. https://doi.org/10.2110/jsr.2013.56

Veiga, R., Pángaro, F., Fernández, M., 2002. Modelado bidimensional y migración de hidrocarburos en el ámbito occidental de la Dorsal de Huincul, Cuenca Neuquina–Argentina, in: V Congreso de Exploración y Desarrollo de Hidrocarburos.

Vergani, G.D., 2005. Control estructural de la sedimentación jurásica (Grupo Cuyo) en la Dorsal de Huincul, Cuenca Neuquina, Argentina. Modella de falla lístrica rampa-plano, invertida. Boletín Inf. Pet. 1, 32–42.

Vergani, G.D., Tankard, A.J., Belotti, H.J., Welsink, H.J., 1995. Tectonic Evolution and Paleogeography of the Neuquén Basin, Argentina, in: Tankard, A.J., Suárez, R., Welsink, H.J. (Eds.), Petroleum Basins of South America, AAPG Memoir. pp. 383–402. https://doi.org/10.1306/7834F6E1-1721-11D7-8645000102C1865D

Verzi, H., Raggio, M.F., Suarez, M., 2005. Volume interpretation of a turbidite system, Los Molles Formation, Neuqu{é}n Basin, Argentina, in: Soubies, D., Arteaga, M., Fant$\$'$\$in, F. (Eds.), Simposio La S{$\$'{$\$i}}smica de Reflexi{ó}n, M{á}s All{á} de La Imagen Estructural. VI Congreso de Exploraci{ó}n y Desarolla de Hidracarburos, Mar Del Plata. pp. 219–226.

Vicente, J.C., 2005. Dynamic paleogeography of the Jurassic Andean Basin: pattern of transgression and localisation of main straits through the magmatic arc. Rev. la Asoc. Geológica Argentina 60, 221–250.

Villar, H.J., Legarreta, L., Cruz, C.E., Laffite, G.A., Vergani, G., 2005. Los Cinco Sistemas Petroleros Coexistentes En El Sector Sudeste De La Cuenca Neuquina: Definición Geoquímica Y Comparación a Lo Largo De Una Transecta De 150 Km. 6° Congr. Explor. y Desarro. Hidrocarburos (Mar del Plata) 50–67.

Volkheimer, W., 1973. Palinología estratigráfica del Jurásico de la Sierra de Chacai Co y adyacencias (Cuenca Neuquina, República Argentina). I. Estratigrafía de las formaciones Sierra Chacai Co (Pliensbachiano), de Los Molles (Toarciano, Aaleniano), Cura Niyeu (Bayociano) y L. Ameghiniana - Rev. la Asoc. Paleontológica Argentina 10, 105–129.

Volkheimer, W., Rauhut, O.W.M., Quattrocchio, M.E., Martinez, M.A., 2008. Jurassic paleoclimates in Argentina, a review. Rev. la Asoc. Geológica Argentina 63, 549–556.

Walderhaug, O., 1994. Precipitation rates for quartz cement in sandstones determined by fluid-inclusion microthermometry and temperature-history modeling. J. Sediment. Res. 64, 324–333. https://doi.org/10.2110/jsr.64.324

Walsh, J.J., Bailey, W.R., Childs, C., Nicol, A., Bonson, C.G., 2003. Formation of segmented normal faults: a 3-D perspective. J. Struct. Geol. 25, 1251–1262. https://doi.org/10.1016/S0191-8141(02)00161-X

Watt, S., Talling, P., Hunt, J., 2014. New Insights into the Emplacement Dynamics of Volcanic Island Landslides. Oceanography 27, 46–57. https://doi.org/10.5670/oceanog.2014.39

Watton, T.J., Jerram, D.A., Thordarson, T., Davies, R.J., 2013. Three-dimensional lithofacies variations in hyaloclastite deposits. J. Volcanol. Geotherm. Res. 250, 19–33. https://doi.org/10.1016/j.jvolgeores.2012.10.011

Weaver, C., 1942. A general summary of the Mesozoic of South and Central America, in: 8° American Science Congress, Proceeding (1940) 4. Geology, pp. 149–193.

Weaver, C., 1931. Paleontology of the Jurassic and Cretaceous of west central Argentina. Memoir University of Washington 1. Seattle, pp. 1–469.

Weiß, B.J., Hübscher, C., Lüdmann, T., Serra, N., 2016. Submarine sedimentation processes in the southeastern Terceira Rift/São Miguel region (Azores). Mar. Geol. 374, 42–58. https://doi.org/10.1016/j.margeo.2016.02.004

Weltje, G.J., 2006. Ternary sandstone composition and provenance: an evaluation of the 'Dickinson model,' in: Buccianti, A., Mateu-Figueras, G., Pawlowsky-Glahn, V. (Eds.), Compositionall Data Analysis in the Geosciences: From Theory to Practice. Geological Society, London, Special Publications. pp. 79–99. https://doi.org/10.1144/GSL.SP.2006.264.01.07

Wernicke, B., 1985. Uniform-sense normal simple shear of the continental lithosphere. Can. J. Earth Sci. 22, 108–125. https://doi.org/10.1139/e85-009

Westaway, R., 2002. The Quaternary evolution of the Gulf of Corinth, central Greece: Coupling between surface processes and flow in the lower continental crust. Tectonophysics 348, 269–318. https://doi.org/10.1016/S0040-1951(02)00032-X

Westaway, R., 1998. Dependence of active normal fault dips on lower-crustal flow regimes. J. Geol. Soc. London. 155, 233–253. https://doi.org/10.1144/gsjgs.155.2.0233

Wheatley, D.F., Chan, M.A., 2017. Clastic Pipe Diagenesis of the Jurassic Carmel Formation , Southern Utah. AAPG Search Discov. Artic. #51352.

Whipp, P.S., Jackson, C.A.L., Gawthorpe, R.L., Dreyer, T., Quinn, D., 2014. Normal fault array evolution above a reactivated rift fabric; a subsurface example from the northern Horda Platform, Norwegian North Sea. Basin Res. 26, 523–549. https://doi.org/10.1111/bre.12050

White, J.D.L., Houghton, B.F., 2006. Primary volcaniclastic rocks. Geology 34, 677–680. https://doi.org/10.1130/G22346.1

White, N., McKenzie, D., 1988. Formation of the "steer's head" geometry of sedimentary basins by differential stretching of the crust and mantle. Geology 16, 250–253. https://doi.org/10.1130/0091-7613(1988)016<0250:FOTSSH>2.3.CO;2

Whittaker, A., Bott, M.H.P., Waghorn, G.D., 1992. Stresses and plate boundary forces associated with subduction plate margins. J. Geophys. Res. 97, 11933–11944. https://doi.org/10.1029/91JB00148

Williams, G.D., 1993. Tectonics and seismic sequence stratigraphy: an introduction, in: Williams, G.D., Dobb, A. (Eds.), Tectonics and Seismic Sequence Stratigraphy. Geological Society, London, Special Publications. pp. 1–13. https://doi.org/10.1144/GSL.SP.1993.071.01.01

Williams, I.S., 1998. U-Th-Pb Geochronology by Ion Microprobe, in: Applications of Microanalytical Techniques to Understanding Mineralizing Processes. https://doi.org/10.5382/Rev.07.01

Withjack, M.O., Schlische, R.W., Malinconico, M.L., Olsen, P.E., 2013. Rift-basin development: lessons from the Triassic–Jurassic Newark Basin of eastern North America. Geol. Soc. London, Spec. Publ. 369, 301–321. https://doi.org/10.1144/SP369.13

Withjack, M.O., Schlische, R.W., Olsen, P.E., 2002. Rift-Basin Structure and Its Influence on Sedimentary Systems, in: Sedimentation in Continental Rifts, SEPM Special Publication. SEPM (Society for Sedimentary Geology), pp. 57–81. https://doi.org/10.2110/pec.02.73.0057

Woodcock, N.H., 2004. Life span and fate of basins. Geology 32, 685–688. https://doi.org/10.1130/G20598.1

Wooller, L., van Wyk de Vries, B., Cecchi, E., Rymer, H., 2009. Analogue models of the effect of long-term basement fault movement on volcanic edifices. Bull. Volcanol. 71, 1111–1131.

https://doi.org/10.1007/s00445-009-0289-3

Wright, V.P., 2012. Lacustrine carbonates in rift settings: the interaction of volcanic and microbial processes on carbonate deposition, in: Garland, J., Neilson, J.E., Laubach, S.E., Whidden, K.J. (Eds.), Advances in Carbonate Exploration and Reservoir Analysis. Geological Society, London, Special Publications. pp. 39–47. https://doi.org/10.1144/SP370.2

Xie, X., Heller, P., 2009. Plate tectonics and basin subsidence history. Geol. Soc. Am. Bull. 121, 55–64. https://doi.org/10.1130/B26398.1

Yagupsky, D.L., 2009. Metodología para el estudio de sistemas compresivos y de sus controles estructurales. PhD thesis, Universidad de Buenos Aires, Facultad de Ciencias Exactas y Naturales.

Yagupsky, D.L., Cristallini, E.O., Fantín, J., Valcarce, G.Z., Bottesi, G., Varadé, R., 2008. Oblique half-graben inversion of the Mesozoic Neuquén Rift in the Malargüe Fold and Thrust Belt, Mendoza, Argentina: New insights from analogue models. J. Struct. Geol. 30, 839–853. https://doi.org/10.1016/j.jsg.2008.03.007

Young, M.J., Gawthorpe, R.L., Sharp, I.R., 2003. Normal fault growth and early syn-rift sedimentology and sequence stratigraphy: Thal Fault, Suez Rift, Egypt. Basin Res. 15, 479–502. https://doi.org/10.1046/j.1365-2117.2003.00216.x

Young, M.J., Gawthorpe, R.L., Sharp, I.R., 2002. Architecture and evolution of syn-rift clastic depositional systems towards the tip of a major fault segment, Suez Rift, Egypt. Basin Res. 14, 1–23. https://doi.org/10.1046/j.1365-2117.2002.00162.x

Yu, N.-T., Teng, L.S., Chen, W.-S., Yue, L.-F., Chen, M.-M., 2013. Early post-rift sequence stratigraphy of a Mid-Tertiary rift basin in Taiwan: Insights into a siliciclastic fill-up wedge. Sediment. Geol. 286–287, 39–57. https://doi.org/10.1016/j.sedgeo.2012.12.009

Zachariah, A.-J., Gawthorpe, R., Dreyer, T., 2009a. Evolution and strike variability of early post-rift deep-marine depositional systems: Lower to Mid-Cretaceous, North Viking Graben, Norwegian North Sea. Sediment. Geol. 220, 60–76. https://doi.org/10.1016/j.sedgeo.2009.06.006

Zachariah, A.-J., Gawthorpe, R., Dreyer, T., Corfield, S., 2009b. Controls on early post-rift physiography and stratigraphy, lower to mid-Cretaceous, North Viking Graben, Norwegian North Sea. Basin Res. 21, 189–208. https://doi.org/10.1111/j.1365-2117.2008.00371.x

Zappettini, E.O., Dalponte, M., Segal, S., 2012. Mineralogía Y Aspectos Genéticos Del Depósito Volcanogénico Submarino De Manganeso “La Casualidad”, Cerro Atravesada, Neuquén. Rev. la Asoc. Geológica Argentina 69.

Zavala, C., 1996. High resolution sequence stratigraphy in the Middle Jurassic Cuyo Group, South neuquén Basin, Argentina. GeoResearch Forum, Adv. Jurassic Res. 1–2, 295–304.

Zelilidis, A., 2003. The geometry of fan-deltas and related turbidites in narrow linear basins. Geol. J. 38, 31–46. https://doi.org/10.1002/gj.925

Ziegler, P.A., Cloetingh, S., 2004. Dynamic processes controlling evolution of rifted basins. Earth-Science Rev. 64, 1–50. https://doi.org/10.1016/S0012-8252(03)00041-2

Zuffa, Gian Gaspare, 1985. Optical Analyses of Arenites: Influence of Methodology on Compositional Results, in: Zuffa, G.G. (Ed.), Provenance of Arenites. NATO ASI Series. Springer Netherlands, Dordrecht, pp. 165–189. https://doi.org/10.1007/978-94-017-2809-6_8

Appendices

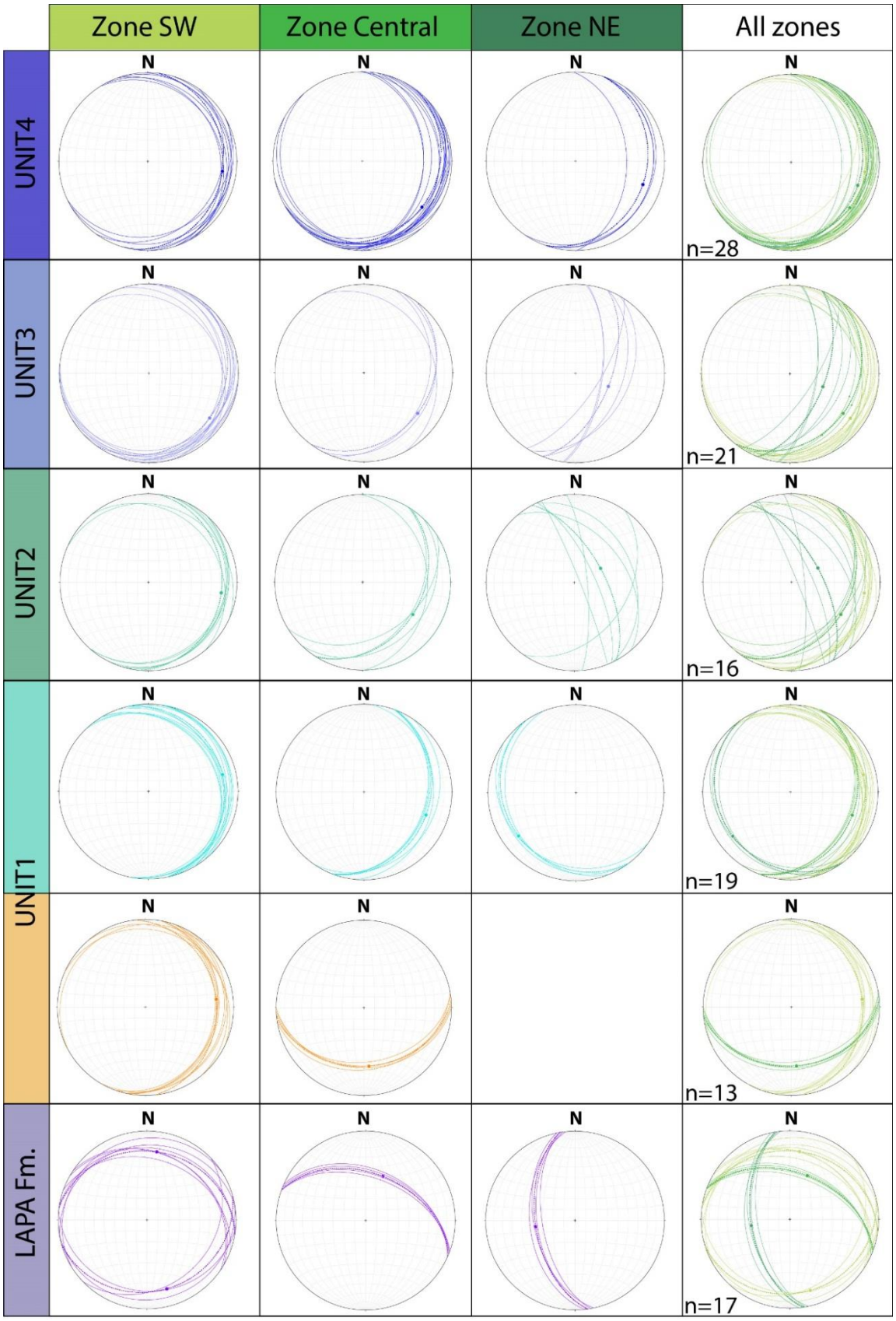

Appendix 1: Stereonets of strike-dips measurements for each tectono-sedimentary unit and separated by zones (zone numbers refer to the location of sections with same numbers). The "all zones" stereonets represent all the measured strike-dip planes for a unit with colours corresponding to zone colour.

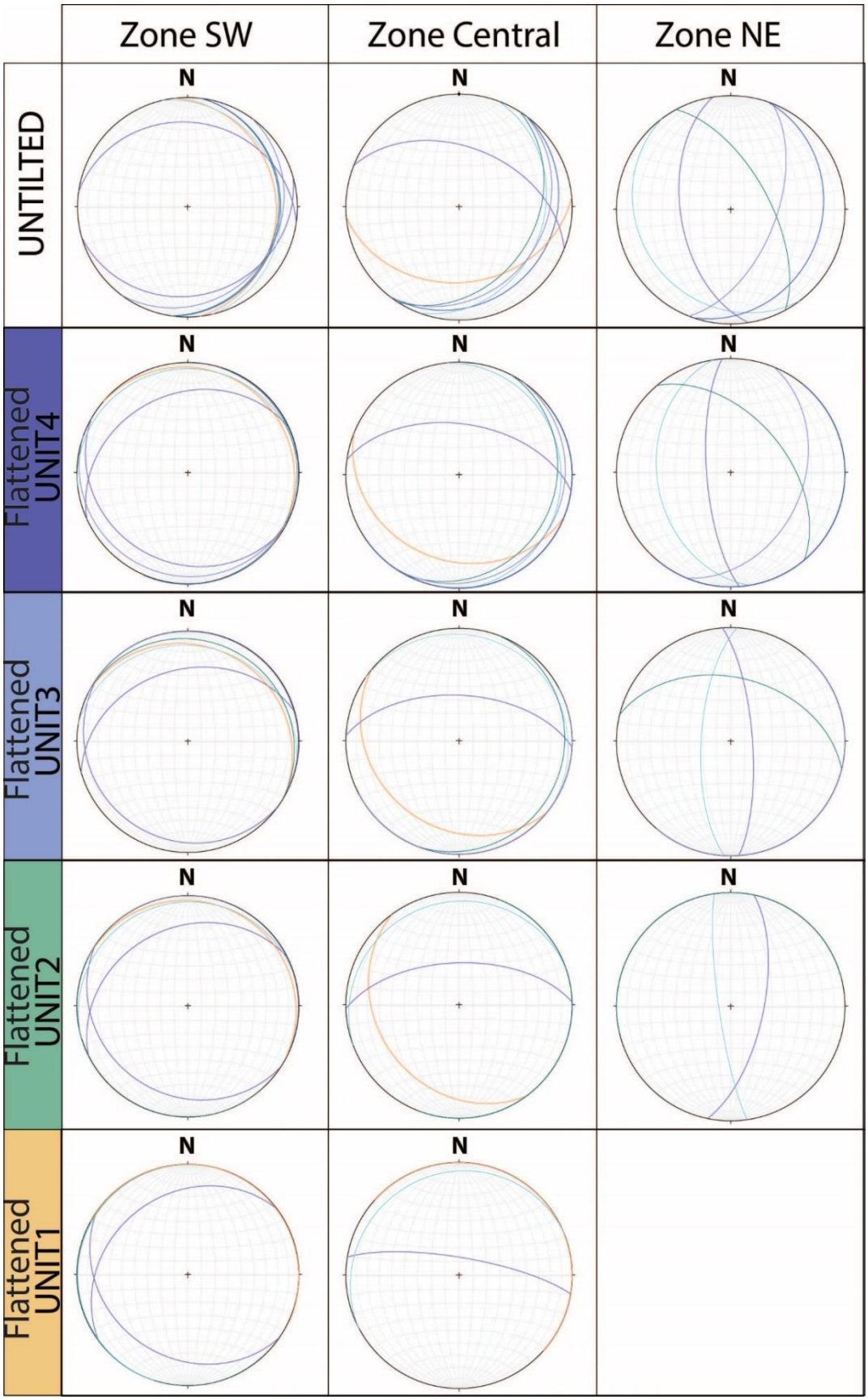

Appendix 2: Stereonets of restored mean structural bedding planes (see Fig. 4) for each tectono-sedimentary units and in each zones.

Section number in figures	Section name notebook	Stratigaphic elements orientations			
		Ripple cross-laminations	Sole marks	Cross-stratification	Strike-dip of units for palaeocurrent measures
1	Road46	42	106		**N10 19E**
		40	104		
			60		
			50		
2	Mirador	110			**N148 14NE**
		320			
		128			
		122			
		134			
		132			
		130			
		335			
		301			
		290			
		305			
		292			
		290			
		294			
5b	ChaS5bisC	40	100		**N35 20E**
			80		
			20		
5	ChaS5bisAB-SonadaS2	20	25	**98**	**N05 20E**
		22	88	**12**	
		100	50	**176**	
		115	38	**54**	
		105	40		
		110	150		
		102	162		
		98	30		
		38	15		
		40	20		
		42	142		
		44	28		
		58			
		40			
		38			
		240	90	50	
		65	160		
		55	200		
		50			
		210			
		230			
		40			
		30			
		50			
		12			
		15			
		42			
6	SonadaS1	185		28	**N60 17SE**
		178			
		162			
		132			
		150			
		162			
		30			
		15			
		20			
		142			
		138			
		140			

Appendix 3: Table of palaeocurrent measurements with bedding strike and dip indicated, section number in figures and section names.

Section number in figures	Section name notebook	Stratigaphic elements orientations			
		Ripple cross-laminations	Sole marks	Cross-stratification	Strike-dip of units for palaeocurrent measures
7	Picun Leufu	50	143	1	**N78 9S**
		20	80	238	
		50	132	200	
		10	128		
		348	138		
			122		
			78		
			134		
			192		
		10		210	
				20	
8	ChaS8-8bis	160	340		**N79 15SE**
		158	335		
		200	310		
		30			
		220			
		220			
		320			
		20			
		40			
		20			
		18			
		10			
9	ChaS16	200			
		210			
		240			
		205			
		211			
10	El Luchador S1	276	130		**N24 20E**
			132		
			162		
			178		
			148		
		332		324	
		148			
11	ChaS11	10	10	**20**	**N1 45SE**
		20	18	**210**	
		40	20		
		25			
		30			
12bis	ChaS12	20	330	**30**	**N60 17SE**
		50	350	**50**	
		230		**30**	
		31		**210**	
				30	
				30	
				5	
				200	
				250	
				240	
				100	
				60	
				120	
				130	
				160	
				140	
West Catan-Lil		160			**N110 8NE**
		150			
		280			
		282			
		270			
		260			
		264			
		282			
		128			
		320			
		322			
		328			
		321			

Appendix 3 (continue)

Section number in figures	Section name notebook	Stratigaphic elements orientations			
		Ripple cross-laminations	Sole marks	Cross-stratification	Strike-dip of units for palaeocurrent measures
1	Cha-S1	10	140	72	**N29 22E**
		12	138	254	
		11	108	234	
		15	120	52	
		13	60	60	
		30	72	88	
		40	80	22	
		52	58	40	
		58	302	40	
		46	139	30	
		8	160	30	
		10	46	40	
		12	120	58	
		15	288	58	
		13	300	72	
			127	230	
			160	60	
			139	38	
			38	40	
			120	240	
			60	60	
			72	58	
			80	72	
			58		
			302		
			282		
			299		
			295		
			307		
2	Cha-S2	260	30	65	
		320		240	
		310		80	
		60		320	
		90		80	
		100		320	
		240		160	
		80			
		101			
3	Cha-S3	310		10	
				160	
				30	

Appendix 3 (continue)

Section number in figures	Section name notebook	Stratigaphic elements orientations			
		Ripple cross-laminations	Sole marks	Cross-stratification	Strike-dip of units for palaeocurrent measures
4	Ma-S1	235	280		
		200	240		
		2	230		
		210	250		
			260		
			210		
			270		
			20		
			260		
5	Ma-S2	300	290	310	
		310	300	310	
		290	280	320	
		300	260	340	
		340	280	20	
		350	340	30	
		340	320		
		342	322		
		290	270		
		352	340		
		290	320		
		288	280		
		290	275		
		300	100		
		330	100		
		350	320		
		352	290		
		190	300		
		180	340		
		290	220		
		300			
		340			
		350			
		345			
		292			
		352			
		290			
		288			
		15			
		290			
		350			
		352			
		272			
6	Ma-S3	310	130		
		290	60		
		300	270		
		292			

Appendix 3 (continue)

Section number in figures	Section name notebook	Stratigaphic elements orientations			
		Ripple cross-laminations	Sole marks	Cross-stratification	Strike-dip of units for palaeocurrent measures
7	Espinazo del Zorro S2	110			
		150			
		160			
		168			
		108			
		94			
		100			
		290			
		330			
		340			
		348			
		288			
		274			
		220			
		280			
		288			
		110			
		222			
		300			
		320			
8	Tut-S1	160	100		
		178	94		
		175	98		
		180	96		
		182	97		
			84		
			98		
			96		
			97		
			84		
			80		
			85		
			92		
			100		
			98		
			101		
			102		
9	Tut-S2	40	290		**N17 15E**
		10	295		
		20	10		
		2	200		
			260		
			270		
			280		
			265		

Appendix 3 (continue)

Depocentre	Section number in figures	Section name in stratigraphic chart	Section name notebook	Base		Middle top		Middle base		Top		Thickness (m)
Chacaico	1	E	Cha-S1	377549.61 m E	5639052.30 m S					378189.90 m E	5638529.03 m S	310
	2		Cha-S2	373574.00 m E	5637670.00 m S					373938.00 m E	5638144.00 m S	300.8
	3		Cha-S3	370617.00 m E	5638765.00 m S	370719.00 m E	5638905.00 m S	370088.00 m E	5639593.00 m S	371090.00 m E	5639991.00 m S	205
East Catan-Lil	4	B base	Ma-S1	364879.00 m E	5645889.00 m S					365993.00 m E	5645935.00 m S	326.4
	5		Ma-S2	364786.00 m E	5649496.00 m S	364917.00 m E	5649647.00 m S	365192.00 m E	5649232.00 m S	365608.00 m E	5649414.00 m S	314
	6		Ma-S3a A/Espinazo del Zorro S1	363727.00 m E	5649997.00 m S	363977.00 m E	5650228.00 m S					120
			Ma-S3a B					364719.00 m E	5650034.00 m S	364994.00 m E	5650057.00 m S	97
	7		Espinazo del Zorro S2	363254.00 m E	5649844.00 m S	363229.00 m E	5651098.00 m S			363550.20 m E	5651219.32 m S	495
	8		Tut-S1	362491.81 m E	5653064.08 m S					363381.14 m E	5652796.07 m S	442
	9		TutS2-a	363187.00 m E	5654016.00 m S	363547.00 m E	5653239.00 m S					192
			TutS2-b					363547.00 m E	5653239.00 m S	363991.00 m E	5652929.00 m S	160
	10	B top	Ps1a	363671.26 m E	5654407.76 m S	363956.01 m E	5654207.00 m S					200
			Ps1b					363891.00 m E	5654005.00 m S	364530.00 m E	5654150.00 m S	100
West Catan-Lil		D	Death valley S1	358121.84 m E	5651450.20 m S					358625.13 m E	5651983.60 m S	323
Jardinera		C	Jardinera S1	346520.29 m E	5637286.24 m S					347137.00 m E	5637311.00 m S	255
Chachil	1	A base	Road46	366655.58 m E	5658853.71 m S					367059.96 m E	5659057.95 m S	130
	2		MiradorS1	365989.00 m E	5660559.00 m S					366788.51 m E	5660064.81 m S	201
	3		MiradorS2	365921.55 m E	5661089.24 m S					366022.71 m E	5660927.53 m S	80
	4		Morro del Aguila	367089.28 m E	5661994.18 m S					367025.97 m E	5661764.91 m S	85
			Sonada S2	367658.29 m E	5662246.19 m S	368231.00 m E	5661851.00 m S					
	5		ChaS5bisA			368084.00 m E	5661785.00 m S	368117.00 m E	5661784.00 m S			270
			ChaS5bisB					368121.00 m E	5661792.00 m S	368231.00 m E	5661851.00 m S	
	5a		ChaS5bis	368266.00 m E	5661868.00 m S					368343.00 m E	5661837.00 m S	18
	5b		ChaS5bisC	368330.00 m E	5661899.00 m S	368408.00 m E	5661924.00 m S			368408.00 m E	5661924.00 m S	56
			ChaS5bisD					368528.00 m E	5662039.00 m S	368556.00 m E	5661923.00 m S	
	6		Sonada S1	368332.80 m E	5662690.52 m S					368737.64 m E	5662121.89 m S	315
	7		Picun Leufu	368473.79 m E	5663013.60 m S	369037.62 m E	5662597.49 m S					232
			ChaS7					369014.00 m E	5662617.00 m S	368890.00 m E	5662392.00 m S	
	8		ChaS8	369160.00 m E	5662937.00 m S					370108.00 m E	5662799.00 m S	86
	9		ChaS16	370192.00 m E	5663121.00 m S					370108.00 m E	5662799.00 m S	120
	10		El LuchadorS1	368495.91 m E	5663411.77 m S					368947.17 m E	5663413.16 m S	111
	11		ChaS11	370296.00 m E	5663952.00 m S					370782.00 m E	5664060.00 m S	120
	12		Paine Milla	370459.00 m E	5664718.00 m S					370608.00 m E	5664643.00 m S	22
	12bis	A top	ChaS12	370426.00 m E	5662423.00 m S					370930.00 m E	5662369.00 m S	141
	15		CP13	370650.00 m E	5662156.00 m S					370814.00 m E	5662153.00 m S	80
	14		CP14	370678.00 m E	5662220.00 m S					370691.00 m E	5662218.00 m S	10
	13		CP15	370702.00 m E	5662255.00 m S					370708.00 m E	5662255.00 m S	10

Appendix 4: Table of log coordinates with indicated section number in figures of the thesis and section names.

Sample name	GPS location		Section name notebook	Section number in figures	Depocentre
MAS1 1	39°19'28.45"S	70°33'43.93"W	MaS1	4	East Catan-Lil
MAS1 2	39°19'27.93"S	70°33'42.04"W			
MAS1 3	39°19'29.27"S	70°33'31.67"W			
MAS1 4	39°19'35.78"S	70°33'27.30"W			
MAS1 5	39°19'32.96"S	70°33'22.44"W			
MAS2 1	39°17'43.57"S	70°33'47.57"W	MaS2	5	
MAS2 2	39°17'42.12"S	70°33'41.86"W			
MAS2 3	39°17'41.07"S	70°33'40.29"W			
MAS3 1	39°17'18.37"S	70°34'04.25"W	MaS3	6	
MAS3 2	39°17'17.47"S	70°34'03.47"W			
MAS3 3	39°17'17.75"S	70°34'01.69"W			
PS1B-1	39°15'12.15"S	70°34'26.38"W	PS1b	10	
PS1B-2	39°15'05.15"S	70°34'13.71"W			
TUTS2A 1	39°15'30.02"S	70°34'55.53"W	TutS2-a	9	
TUTS2A 2	39°15'31.59"S	70°34'53.98"W			
CHAS2-1	39°24'00.15"S	70°27'59.72"W	ChaS2	2	Chacaico
CHAS2-2	39°23'54.06"S	70°27'56.37"W			
CHAS3-1	39°22'55.44"S	70°30'03.97"W	ChaS3	3	
CHAS3-2	39°22'48.97"S	70°29'49.95"W			
LJS2-1	39°23'58.41"S	70°46'31.13"W	LJS1		La Jardinera
LJS2-2	39°24'00.32"S	70°46'31.09"W			
S5 BIS A 1	39°10'59.43"S	70°31'38.40"W	ChaS5bisA	5	Chachil
S5 BIS B 2	39°10'56.84"S	70°31'30.76"W	ChaS5bisB		
S5 BIS B 3	39°10'57.04"S	70°31'30.35"W			
S5 BIS B 4	39°10'57.38"S	70°31'28.52"W			
S8-1	39°10'24.60"S	70°30'53.14"W	ChaS8	8	
S8-2	39°10'33.48"S	70°30'53.41"W			
SI2 1	39°10'31.37"S	70°29'40.98"W	ChaS12	12bis	
SI2 2	39°10'31.93"S	70°29'40.12"W			

Appendix 5: Table of sample coordinates indicating the corresponding logs and their numbers in figures of the thesis.

				J1.1									
				Cha52-1				Cha52-2					
Class	Code	Lithoclast		Points	%	Class %		Points	%	Class %			
	Qspherulitic	Monocrystalline quartz with vesicles		0	0,00			2	0,32				
	Qmnu	Monocrystalline quartz non undulose		114	19,22			120	19,20				
Qm	QmU <5	Monocrystalline quartz undulose (extinction angle <5°)		58	9,78	29,0		38	6,08	25,6			
	Qpc <2-3	Polycrystalline quartz, with 2-3 grains		13	2,19			5	0,80				
Qp	Qpf >3	Polycrystalline quartz, with >3 grains		10	1,69	3,9		19	3,04	3,8			
	P polys twin	Plagioclase feldspar with polysynthetic twinning		28	4,72			52	8,32				
	P simple twin	Plagioclase feldspar with simple twinning		1	0,17			5	0,80				
	P perth	Plagioclase feldspar with perthite		0	0,00			0	0,00				
P	P Sericitized	Plagioclase feldspar with sericite		0	0,00	4,9		0	0,00	9,1			
	K O	Potassium feldspar orthose		11	1,85			9	1,44				
	K O perth	Potassium feldspar orthose with perthite		2	0,34			9	1,44				
	K Myrmekite	Potassium feldspar with myrmekite		0	0,00			0	0,00				
	K Microcline	Potassium feldspar microcline		0	0,00			0	0,00				
K	K Microcline perth	Potassium feldspar microcline with perthite		1	0,17	2,4		0	0,00	2,9			
	Lvf se	Volcanic lithic felsitic with seriate texture		1	0,17			10	1,60				
	Lvm pi/tra	Volcanic lithic microlitic with pilotaxitic or trachytic texture		32	5,40			33	5,28				
	Lvv gl	Volcanic lithic vitric with glassy or devitrified texture		0	0,00			0	0,00				
	Lvm lat/hya	Volcanic lithic microlitic with lathwork or or hyalopilitic texture			0,00			7	1,12				
	Lvv pu	Volcanic lithic pumice			0,00			0	0,00				
Lv	Lvf gr	Volcanic lithic felsitic with granular to microcrystalline texture		105	17,71	23,3		95	15,20	23,2			
	Ls Sh	Sedimentary lithic shale		37	6,24			36	5,76				
Ls	Ls Si	Sedimentary lithic siltstone		2	0,34	6,6		7	1,12	6,9			
	Lm Slate	Metamorphic lithic slate			0,00			1	0,16				
	Lm Phyllite	Metamorphic lithic phyllite			0,00			0	0,00				
	Lm Schist	Metamorphic lithic schist			0,00			1	0,16				
Lm	Lm Gneiss	Metamorphic lithic gneiss		1	0,17	0,2			0,00	0,3			
	Qm (Lm)	Monocrystalline quartz in metamorphic lithics			0,00				0,00				
	Qm (Ls)	Monocrystalline quartz in sedimentary lithics			0,00				0,00				
	Qm (Lv)	Monocrystalline quartz in volcanic lithics			0,00				0,00				
	K (Lm)	Potassium feldspar orthose in metamorphic lithics			0,00				0,00				
	K O (Ls)	Potassium feldspar orthose in sedimentary lithics			0,00				0,00				
	K O (Lp)	Potassium feldspar orthose in plutonic lithics			0,00				0,00				
	K O (Lv)	Potassium feldspar orthose in volcanic lithics			0,00				0,00				
	K Microcline (Lm)	Potassium feldspar microcline in metamorphic lithics			0,00				0,00				
	K Microcline (Lp)	Potassium feldspar microcline in plutonic lithics			0,00				0,00				
	P (Lm)	Plagioclase feldspar in metamorphic lithics			0,00				0,00				
	P (Ls)	Plagioclase feldspar in sedimentary lithics			0,00				0,00				
	P (Lp)	Plagioclase feldspar in plutonic lithics			0,00				0,00				
	P (Lv)	Plagioclase feldspar in volcanic lithics			0,00				0,00				
	Mi (Lm)	Mica in metamorphic lithics			0,00				0,00				
	Phyllosil Chlo	Chlorite		1	0,17				0,00				
	Phyllosil Ms	Muscovite		3	0,51			4	0,64				
Phyl	Phyllosil Bt	Biotite		0	0,00	0,7		1	0,16	0,8			
	CaMicri	Calcilith Micrite			0,00			0	0,00				
	CaMicro	Calcilith Microspar			0,00				0,00				
	CaSp	Calcilith Sparry			0,00				0,00				
	CaC	Calcilith Large crystal			0,00				0,00				
CE	CaBio	Calcilith Bioclast (fibrous)		6	1,01	1,0		1	0,16	0,2			
	Ox	Iron Oxydes			0,00			0	0,00				
	Gc	Glauconite			0,00				0,00				
Accessory	Zr	Zircons			0,00	0,0			0,00	0,0			
	CeSi	Cement Siliceous		50	8,43			57	9,12				
	CeSil	Cement Silica			0,00				0,00				
NCI	CeFe	Cement Ferruginous			0,00	8,4			0,00	9,1			
	Ps	Pseudomatrix (intergranular mudstone)		113	19,06			11	1,76				
Matrix	Ep	Epimatrix (silica, zeolite, clay)			0,00	19,1			0,00	1,8			
	CeCasp	Cement calcite sparite			0,00				0,00				
CI	CeCamic	Cement calcite microspar (Pseudomatrix)			0,00	0,0		92	14,72	14,7			
	Mostru	Phyto Flaky structured			0,00				0,00				
		Phyto Massive no to weak structures			0,00				0,00				
	Moma	Phyto Blade opaque			0,00			7	1,12				
		Amorphous MO Spongy membraneous		1	0,17				0,00				
MO	Moam	Amorphous MO granular with Py diffuse edges		3	0,51	0,7		3	0,48	1,6			
					0,00				0,00				
				593		100,0		625		100,0			

Appendix 6: Table of point counting showing the main classes of grains, types of grains and their representation percentage for J 1.1 samples.

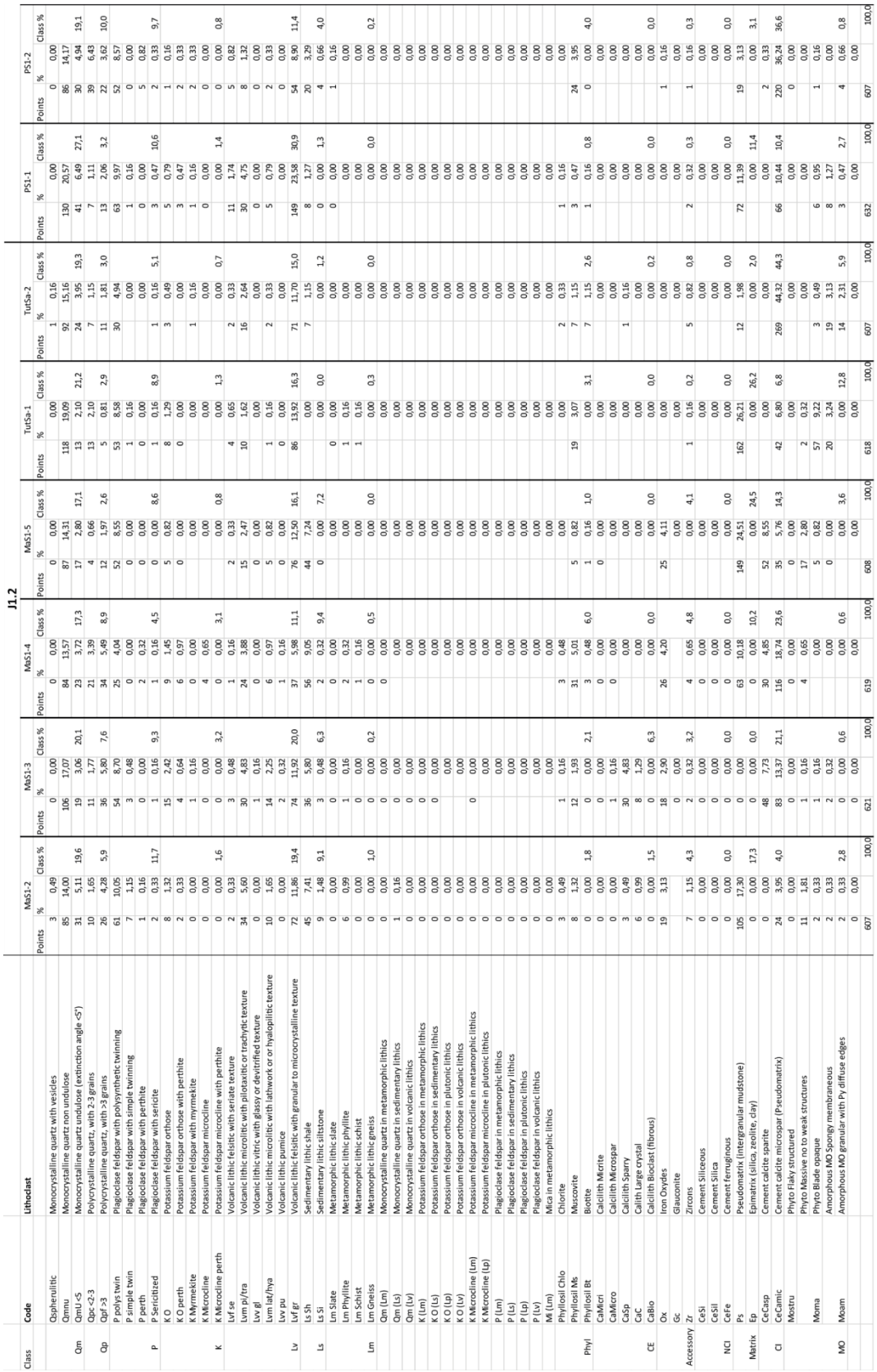

J1.2

Class	Code	Lithodast	MaS1-2			MaS1-3			MaS1-4			MaS1-5			TutSa-1			TutSa-2			PS1-1			PS1-2		
			Points	%	Class %	Points	%	Class %	Points	%	Class %	Points	%	Class %	Points	%	Class %	Points	%	Class %	Points	%	Class %	Points	%	Class %
	Spherulitic	Monocrystalline quartz with vesicles	3	0,49		0	0,00		0	0,00		0	0,00					1	0,16					0	0,00	
	Qmnu	Monocrystalline quartz non undulose	85	14,00		106	17,07		84	13,57		87	14,31		118	19,09		92	15,16		130	20,57		86	14,17	
Qm	QmU<5	Monocrystalline quartz undulose (extinction angle <5°)	31	5,11	19,6	19	3,06	20,1	23	3,72	17,3	17	2,80	17,1	13	2,10	21,2	24	3,95	19,3	41	6,49	27,1	30	4,94	19,1
	Qpc <2-3	Polycrystalline quartz, with 2-3 grains	10	1,65		11	1,77		21	3,39		4	0,66		13	2,10		7	1,15		7	1,11		39	6,43	
Qp	Qpf >3	Polycrystalline quartz, with >3 grains	26	4,28	5,9	36	5,80	7,6	34	5,49	8,9	12	1,97	2,6	5	0,81	2,9	11	1,81	3,0	13	2,06	3,2	22	3,62	10,0
	P polys twin	Plagioclase feldspar with polysynthetic twinning	61	10,05		54	8,70		25	4,04		52	8,55		53	8,58		30	4,94		63	9,97		52	8,57	
	P simple twin	Plagioclase feldspar with simple twinning	7	1,15		3	0,48		0	0,00		0	0,00		1	0,16			0,00		1	0,16		0	0,00	
	P perth	Plagioclase feldspar with perthite	1	0,16		0	0,00		2	0,32		0	0,00		0	0,00			0,00		0	0,00		5	0,82	
P	P Sericitized	Plagioclase feldspar with sericite	2	0,33	11,7	1	0,16	9,3	1	0,16	4,5	0	0,00	8,6	1	0,16	8,9	1	0,16	5,1	3	0,47	10,6	2	0,33	9,7
	K O	Potassium feldspar orthose	8	1,32		15	2,42		9	1,45		5	0,82		8	1,29		3	0,49		5	0,79		1	0,16	
	K O perth	Potassium feldspar orthose with perthite	2	0,33		4	0,64		6	0,97		0	0,00		0	0,00					3	0,47		2	0,33	
	K Myrmekite	Potassium feldspar with myrmekite	0	0,00		1	0,16		0	0,00			0,00			0,00		1	0,16		1	0,16		2	0,33	
	K Microcline	Potassium feldspar microcline	0	0,00		0	0,00		4	0,65			0,00						0,00		0	0,00		0	0,00	
K	K Microcline perth	Potassium feldspar microcline with perthite	0	0,00	1,6	0	0,00	3,2	0	0,00	3,1		0,00	0,8		0,00	1,3		0,00	0,7		0,00	1,4	0	0,00	0,8
	Lvf se	Volcanic lithic felsitic with seriate texture	2	0,33		3	0,48		1	0,16		2	0,33		4	0,65		2	0,33		11	1,74		5	0,82	
	Lvm p/tra	Volcanic lithic microlitic with pilotaxitic or trachytic texture	34	5,60		30	4,83		24	3,88		15	2,47		10	1,62		16	2,64		30	4,75		8	1,32	
	Lvv gl	Volcanic lithic vitric with glassy or devitrified texture	0	0,00		1	0,16		0	0,00		0	0,00			0,00			0,00		0	0,00		0	0,00	
	Lvm lat/hya	Volcanic lithic microlitic with lathwork or or hyalopilitic texture	10	1,65		14	2,25		6	0,97		5	0,82		1	0,16		2	0,33		5	0,79		2	0,33	
	Lvv pu	Volcanic lithic pumice	0	0,00		2	0,32		1	0,16		0	0,00		0	0,00			0,00			0,00		0	0,00	
Lv	Lvf gr	Volcanic lithic felsitic with granular to microcrystalline texture	72	11,86	19,4	74	11,92	20,0	37	5,98	11,1	76	12,50	16,1	86	13,92	16,3	71	11,70	15,0	149	23,38	30,9	54	8,90	11,4
	Ls Sh	Sedimentary lithic shale	45	7,41		36	5,80		56	9,05		44	7,24			0,00		7	1,15		8	1,27		20	3,29	
Ls	Ls Si	Sedimentary lithic siltstone	9	1,48	9,1	3	0,48	6,3	2	0,32	9,4	0	0,00	7,2		0,00	1,2		0,00	1,2	0	0,00	1,3	4	0,66	4,0
	Lm Slate	Metamorphic lithic slate	0	0,00		0	0,00		0	0,00			0,00		0	0,00			0,00		0	0,00		1	0,16	
	Lm Phyllite	Metamorphic lithic phyllite	6	0,99		1	0,16		2	0,32			0,00		1	0,16			0,00			0,00			0,00	
	Lm Schist	Metamorphic lithic schist	0	0,00		0	0,00		1	0,16			0,00		1	0,16			0,00			0,00			0,00	
Lm	Lm Gneiss	Metamorphic lithic gneiss	0	0,00	1,0	0	0,00	0,2	0	0,00	0,5		0,00	0,0		0,00	0,3		0,00	0,0		0,00	0,0		0,00	0,2
	Qm (Lm)	Monocrystalline quartz in metamorphic lithics	0	0,00		0	0,00		0	0,00			0,00			0,00			0,00			0,00			0,00	
	Qm (Ls)	Monocrystalline quartz in sedimentary lithics	1	0,16		0	0,00			0,00			0,00			0,00			0,00			0,00			0,00	
	Qm (Lv)	Monocrystalline quartz in volcanic lithics	0	0,00		0	0,00			0,00			0,00			0,00			0,00			0,00			0,00	
	K (Lm)	Potassium feldspar orthose in metamorphic lithics	0	0,00		0	0,00			0,00			0,00			0,00			0,00			0,00			0,00	
	K O (Ls)	Potassium feldspar orthose in sedimentary lithics	0	0,00		0	0,00			0,00			0,00			0,00			0,00			0,00			0,00	
	K O (Lp)	Potassium feldspar orthose in plutonic lithics	0	0,00			0,00			0,00			0,00			0,00			0,00			0,00			0,00	
	K O (Lv)	Potassium feldspar orthose in volcanic lithics	0	0,00			0,00			0,00			0,00			0,00			0,00			0,00			0,00	
	K Microcline (Lm)	Potassium feldspar microcline in metamorphic lithics	0	0,00		0	0,00			0,00			0,00			0,00			0,00			0,00			0,00	
	K Microcline (Lp)	Potassium feldspar microcline in plutonic lithics	0	0,00			0,00			0,00			0,00			0,00			0,00			0,00			0,00	
	P (Lm)	Plagioclase feldspar in metamorphic lithics	0	0,00			0,00			0,00			0,00			0,00			0,00			0,00			0,00	
	P (Ls)	Plagioclase feldspar in sedimentary lithics	0	0,00			0,00			0,00			0,00			0,00			0,00			0,00			0,00	
	P (Lp)	Plagioclase feldspar in plutonic lithics	0	0,00			0,00			0,00			0,00			0,00			0,00			0,00			0,00	
	P (Lv)	Plagioclase feldspar in volcanic lithics	0	0,00			0,00			0,00			0,00			0,00			0,00			0,00			0,00	
	Mi (Lm)	Mica in metamorphic lithics	0	0,00			0,00			0,00			0,00			0,00			0,00			0,00			0,00	
	Phyllosil Chlo	Chlorite	3	0,49		1	0,16		3	0,48			0,00			0,00		2	0,33		1	0,16			0,00	
	Phyllosil Ms	Muscovite	8	1,32		12	1,93		31	5,01		5	0,82		19	3,07		7	1,15		3	0,47		24	3,95	
Phyl	Phyllosil Bt	Biotite	0	0,00	1,8	0	0,00	2,1	3	0,48	6,0	1	0,16	1,0		0,00	3,1	7	1,15	2,6	1	0,16	0,8	0	0,00	4,0
	CaMicri	Calcilith Micrite	0	0,00		0	0,00		0	0,00		0	0,00			0,00			0,00			0,00			0,00	
	CaMicro	Calcilith Microspar	0	0,00		1	0,16		0	0,00			0,00			0,00			0,00			0,00			0,00	
	CaSp	Calcilith Sparry	3	0,49		30	4,83			0,00			0,00			0,00		1	0,16			0,00			0,00	
	CaC	Calcite Large crystal	6	0,99		8	1,29			0,00			0,00			0,00			0,00			0,00			0,00	
CE	CaBio	Calcilith Bioclast (fibrous)	0	0,00	1,5	0	0,00	6,3		0,00	0,0		0,00	0,0		0,00	0,0		0,00	0,2		0,00	0,0		0,00	0,0
	Ox	Iron Oxydes	19	3,13		18	2,90		26	4,20		25	4,11			0,00			0,00			0,00		1	0,16	
	Gc	Glauconite				0	0,00						0,00			0,00			0,00			0,00			0,00	
Accessory	Zr	Zircons	7	1,15	4,3	2	0,32	3,2	4	0,65	4,8		0,00	4,1	1	0,16	0,2	5	0,82	0,8	2	0,32	0,3	1	0,16	0,3
	CeSi	Cement Siliceous	0	0,00		0	0,00		0	0,00			0,00			0,00			0,00			0,00			0,00	
	CeSil	Cement Silica	0	0,00		0	0,00		0	0,00			0,00			0,00			0,00			0,00			0,00	
NCI	CeFe	Cement ferruginous	0	0,00	0,0	0	0,00	0,0	0	0,00	0,0		0,00	0,0		0,00	0,0		0,00	0,0		0,00	0,0		0,00	0,0
	Ps	Pseudomatrix (intergranular mudstone)	105	17,30		0	0,00		63	10,18		149	24,51		162	26,21		12	1,98		72	11,39		19	3,13	
Matrix	Ep	Epimatrix (silica, zeolite, clay)	0	0,00	17,3	0	0,00	0,0	26	4,20	10,2		0,00	24,5		0,00	26,2		0,00	2,0		0,00	11,4		0,00	3,1
	CeCasp	Cement Calcite sparite	0	0,00		48	7,73		30	4,85		52	8,55			0,00			0,00			0,00		2	0,33	
CI	CeCamic	Cement calcite microspar (Pseudomatrix)	24	3,95	4,0	83	13,37	21,1	116	18,74	23,6	35	5,76	14,3	42	6,80	6,8	269	44,32	44,3	66	10,44	10,4	220	36,24	36,6
	Mostru	Phyto Flaky structured	0	0,00		0	0,00		0	0,00		0	0,00			0,00			0,00			0,00		0	0,00	
		Phyto Massive no to weak structures	11	1,81		1	0,16		4	0,65		17	2,80		2	0,32			0,00			0,00			0,00	
	Moma	Phyto Blade opaque	2	0,33		1	0,16			0,00		5	0,82		57	9,22		3	0,49		6	0,95		1	0,16	
		Amorphous MO Spongy membraneous	2	0,33		2	0,32			0,00		0	0,00		20	3,24		19	3,13		8	1,27			0,00	
MO	Moam	Amorphous MO granular with Py diffuse edges	2	0,33	2,8	0	0,00	0,6		0,00	0,6		0,00	3,6		0,00	12,8	14	2,31	5,9	3	0,47	2,7	4	0,66	0,8
			0	0,00		0	0,00			0,00			0,00			0,00			0,00			0,00			0,00	
			607		100,0	621		100,0	619		100,0	608		100,0	618		100,0	607		100,0	632		100,0	607		100,0

Appendix 7: Table of point counting showing the main classes of grains, types of grains and their representation percentage for J 1.2 samples.

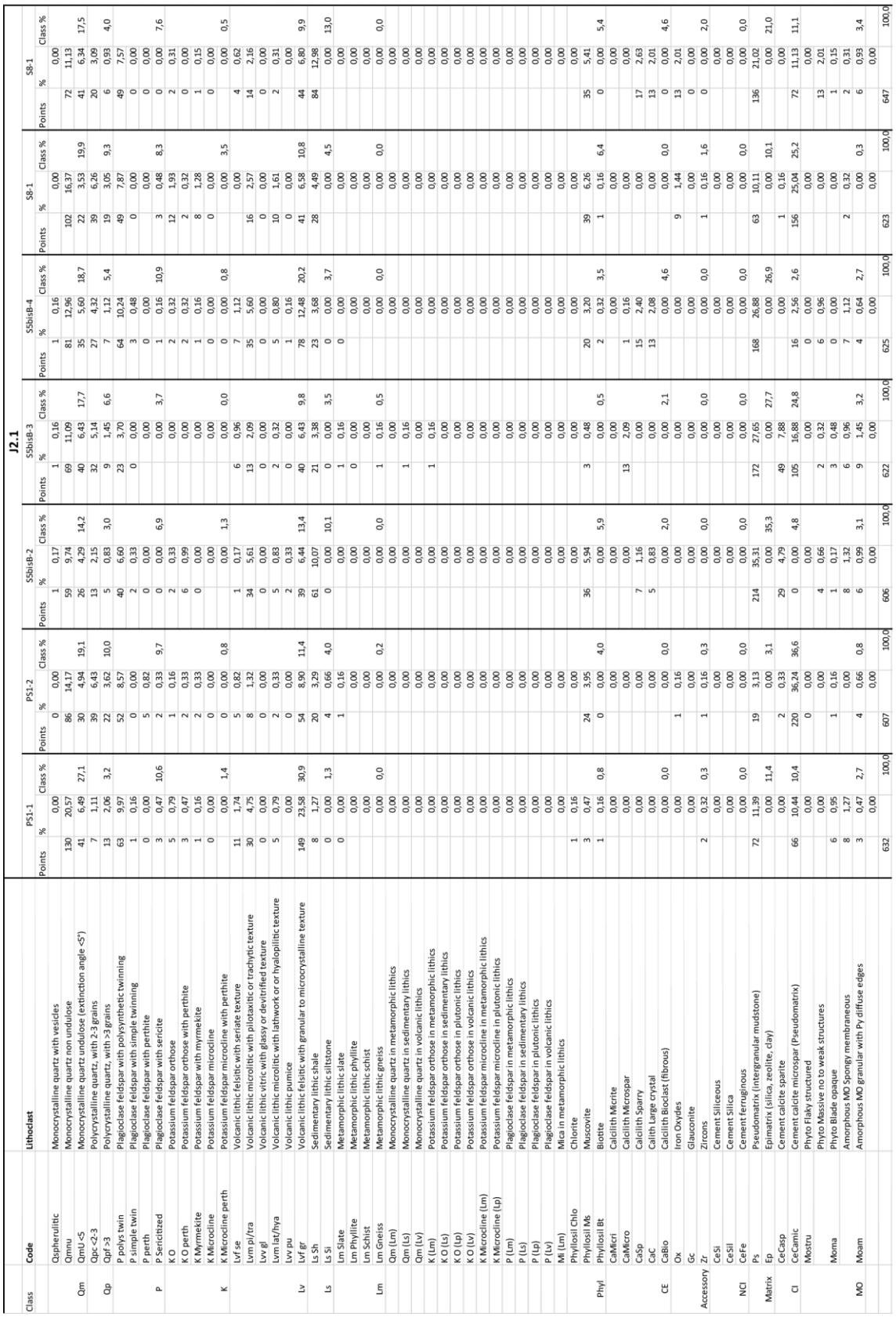

Class	Code	Lithoclast	J2.1 PS1-1 Points	PS1-1 %	PS1-1 Class %	PS1-2 Points	PS1-2 %	PS1-2 Class %	S5bisB-2 Points	S5bisB-2 %	S5bisB-2 Class %	S5bisB-3 Points	S5bisB-3 %	S5bisB-3 Class %	S5bisB-4 Points	S5bisB-4 %	S5bisB-4 Class %	S8-1 Points	S8-1 %	S8-1 Class %
	Qspherulitic	Monocrystalline quartz with vesicles		0,00		0	0,00		1	0,17		1	0,16		1	0,16			0,00	
	Qmnu	Monocrystalline quartz non undulose	130	20,57		86	14,17		59	9,74		69	11,09		81	12,96		102	16,37		72	11,13	
Qm	QmU <5	Monocrystalline quartz undulose (extinction angle <5°)	41	6,49	27,1	30	4,94	19,1	26	4,29	14,2	40	6,43	17,7	35	5,60	18,7	22	3,53	19,9	41	6,34	17,5
	Qpc <2-3	Polycrystalline quartz, with 2-3 grains	7	1,11		39	6,43		13	2,15		32	5,14		27	4,32		39	6,26		20	3,09	
Qp	Qpf >3	Polycrystalline quartz, with >3 grains	13	2,06	3,2	22	3,62	10,0	5	0,83	3,0	9	1,45	6,6	7	1,12	5,4	19	3,05	9,3	6	0,93	4,0
	P polys twin	Plagioclase feldspar with polysynthetic twinning	63	9,97		52	8,57		40	6,60		23	3,70		64	10,24		49	7,87		49	7,57	
	P simple twin	Plagioclase feldspar with simple twinning	1	0,16		0	0,00		2	0,33		0	0,00		3	0,48		0	0,00		0	0,00	
	P perth	Plagioclase feldspar with perthite	0	0,00		5	0,82		0	0,00			0,00		0	0,00		0	0,00		0	0,00	
P	P Sericitized	Plagioclase feldspar with sericite	3	0,47	10,6	2	0,33	9,7	0	0,00	6,9		0,00	3,7	1	0,16	10,9	3	0,48	8,3	0	0,00	7,6
	K O	Potassium feldspar orthose	5	0,79		1	0,16		2	0,33			0,00		2	0,32		12	1,93		2	0,31	
	K O perth	Potassium feldspar orthose with perthite	3	0,47		2	0,33		6	0,99			0,00		2	0,32		2	0,32		0	0,00	
	K Myrmekite	Potassium feldspar with myrmekite	1	0,16		2	0,33		0	0,00			0,00		1	0,16		8	1,28		1	0,15	
	K Microcline	Potassium feldspar microcline	0	0,00		0	0,00			0,00			0,00		0	0,00		0	0,00		0	0,00	
K	K Microcline perth	Potassium feldspar microcline with perthite		0,00	1,4	0	0,00	0,8		0,00	1,3		0,00	0,0	0	0,00	0,8		0,00	3,5		0,00	0,5
	Lvf se	Volcanic lithic felsitic with seriate texture	11	1,74		5	0,82		1	0,17		6	0,96		7	1,12			0,00		4	0,62	
	Lvm pi/tra	Volcanic lithic microlitic with pilotaxitic or trachytic texture	30	4,75		8	1,32		34	5,61		13	2,09		35	5,60		16	2,57		14	2,16	
	Lvv gl	Volcanic lithic vitric with glassy or devitrified texture	0	0,00		0	0,00		0	0,00		0	0,00		0	0,00		0	0,00		0	0,00	
	Lvm lat/hya	Volcanic lithic microlitic with lathwork or or hyalopilitic texture	5	0,79		2	0,33		5	0,83		2	0,32		5	0,80		10	1,61		2	0,31	
	Lvv pu	Volcanic lithic pumice		0,00		0	0,00		2	0,33		0	0,00		1	0,16		0	0,00			0,00	
Lv	Lvf gr	Volcanic lithic felsitic with granular to microcrystalline texture	149	23,58	30,9	54	8,90	11,4	39	6,44	13,4	40	6,43	9,8	78	12,48	20,2	41	6,58	10,8	44	6,80	9,9
	Ls Sh	Sedimentary lithic shale	8	1,27		20	3,29		61	10,07		21	3,38		23	3,68		28	4,49		84	12,98	
Ls	Ls Si	Sedimentary lithic siltstone	0	0,00	1,3	4	0,66	4,0	0	0,00	10,1	0	0,00	3,5	0	0,00	3,7		0,00	4,5		0,00	13,0
	Lm Slate	Metamorphic lithic slate	0	0,00		1	0,16		1	0,00		1	0,16		0	0,00			0,00			0,00	
	Lm Phyllite	Metamorphic lithic phyllite		0,00			0,00			0,00		0	0,00			0,00			0,00			0,00	
	Lm Schist	Metamorphic lithic schist		0,00			0,00			0,00		2	0,32		5	0,80		10	1,61		2	0,31	
Lm	Lm Gneiss	Metamorphic lithic gneiss		0,00	0,0		0,00	0,2		0,00	0,0	1	0,16	0,5		0,00	0,0		0,00	0,0		0,00	0,0
	Qm (Lm)	Monocrystalline quartz in metamorphic lithics		0,00			0,00			0,00			0,00			0,00			0,00			0,00	
	Qm (Ls)	Monocrystalline quartz in sedimentary lithics		0,00			0,00			0,00		1	0,16			0,00			0,00			0,00	
	Qm (Lv)	Monocrystalline quartz in volcanic lithics		0,00			0,00			0,00			0,00			0,00			0,00			0,00	
	K (Lm)	Potassium feldspar orthose in metamorphic lithics		0,00			0,00			0,00		1	0,16			0,00			0,00			0,00	
	K O (Ls)	Potassium feldspar orthose in sedimentary lithics		0,00			0,00			0,00			0,00			0,00			0,00			0,00	
	K O (Lp)	Potassium feldspar orthose in plutonic lithics		0,00			0,00			0,00			0,00			0,00			0,00			0,00	
	K O (Lv)	Potassium feldspar orthose in volcanic lithics		0,00			0,00			0,00			0,00			0,00			0,00			0,00	
	K Microcline (Lm)	Potassium feldspar microcline in metamorphic lithics		0,00			0,00			0,00			0,00			0,00			0,00			0,00	
	K Microcline (Lp)	Potassium feldspar microcline in plutonic lithics		0,00			0,00			0,00			0,00			0,00			0,00			0,00	
	P (Lm)	Plagioclase feldspar in metamorphic lithics		0,00			0,00			0,00			0,00			0,00			0,00			0,00	
	P (Ls)	Plagioclase feldspar in sedimentary lithics		0,00			0,00			0,00			0,00			0,00			0,00			0,00	
	P (Lp)	Plagioclase feldspar in plutonic lithics		0,00			0,00			0,00			0,00			0,00			0,00			0,00	
	P (Lv)	Plagioclase feldspar in volcanic lithics		0,00			0,00			0,00			0,00			0,00			0,00			0,00	
	Mi (Lm)	Mica in metamorphic lithics		0,00			0,00			0,00			0,00			0,00			0,00			0,00	
	Phyllosil Chlo	Chlorite	1	0,16			0,00			0,00			0,00			0,00			0,00			0,00	
	Phyllosil Ms	Muscovite	3	0,47		24	3,95		36	5,94		3	0,48		20	3,20		39	6,26		35	5,41	
Phyl	Phyllosil Bt	Biotite	1	0,16	0,8	0	0,00	4,0		0,00	5,9		0,00	0,5	2	0,32	3,5	1	0,16	6,4	0	0,00	5,4
	CaMicri	Calcilith Micrite		0,00			0,00			0,00		13	2,09		1	0,16			0,00			0,00	
	CaMicro	Calcilith Microspar		0,00			0,00			0,00			0,00		15	2,40			0,00		17	2,63	
	CaSp	Calcilith Sparry		0,00			0,00		7	1,16			0,00		13	2,08			0,00		13	2,01	
CE	CaBio	Calcilith Bioclast (fibrous)		0,00	0,0		0,00	0,0	5	0,83	2,0		0,00	2,1		0,00	4,6	9	1,44	0,0	0	0,00	4,6
	Ox	Iron Oxydes		0,00		1	0,16			0,00			0,00			0,00			0,00		13	2,01	
Accessory	Gc	Glauconite		0,00			0,00			0,00			0,00			0,00			0,00		0	0,00	
	Zr	Zircons	2	0,32	0,3	1	0,16	0,3		0,00	0,0		0,00	0,0	1	0,16	0,1	1	0,16	1,6	0	0,00	2,0
	CeSi	Cement Siliceous		0,00			0,00			0,00			0,00			0,00			0,00			0,00	
	CeSil	Cement Silica		0,00			0,00			0,00			0,00			0,00			0,00			0,00	
NCl	CeFe	Cement ferruginous		0,00	0,0		0,00	0,0		0,00	0,0		0,00	0,0		0,00	0,0		0,00	0,0		0,00	0,0
	Ps	Pseudomatrix (intergranular mudstone)	72	11,39		19	3,13		214	35,31		172	27,65		168	26,88		63	10,11		136	21,02	
Matrix	Ep	Epimatrix (silica, zeolite, clay)		0,00	11,4		0,00	3,1		0,00	35,3		0,00	27,7		0,00	26,9		0,00	10,1		0,00	21,0
	CeCasp	Cement calcite sparite		0,00		2	0,33		29	4,79		49	7,88			0,00		1	0,16			0,00	
Cl	CeCamic	Cement calcite microspar (Pseudomatrix)	66	10,44	10,4	220	36,24	36,6	0	0,00	4,8	105	16,88	24,8	16	2,56	2,6	156	25,04	25,2	72	11,13	11,1
	Mostru	Phyto Flaky structured		0,00		0	0,00			0,00			0,00		0	0,00			0,00			0,00	
		Phyto Massive no to weak structures		0,00			0,00		4	0,66		2	0,32		6	0,96			0,00		13	2,01	
	Moma	Phyto Blade opaque	6	0,95		1	0,16		1	0,17		3	0,48		0	0,00			0,00		1	0,15	
		Amorphous MO Spongy membraneous	8	1,27			0,00		8	1,32		6	0,96		7	1,12		2	0,32		2	0,31	
MO	Moam	Amorphous MO granular with Py diffuse edges	3	0,47	2,7	4	0,66	0,8	6	0,99	3,1	9	1,45	3,2	4	0,64	2,7		0,00	0,3	6	0,93	3,4
			632		100,0	607		100,0	606		100,0	622		100,0	625		100,0	623		100,0	647		100,0

Appendix 8: Table of point counting showing the main classes of grains, types of grains and their representation percentage for J2.1 samples.

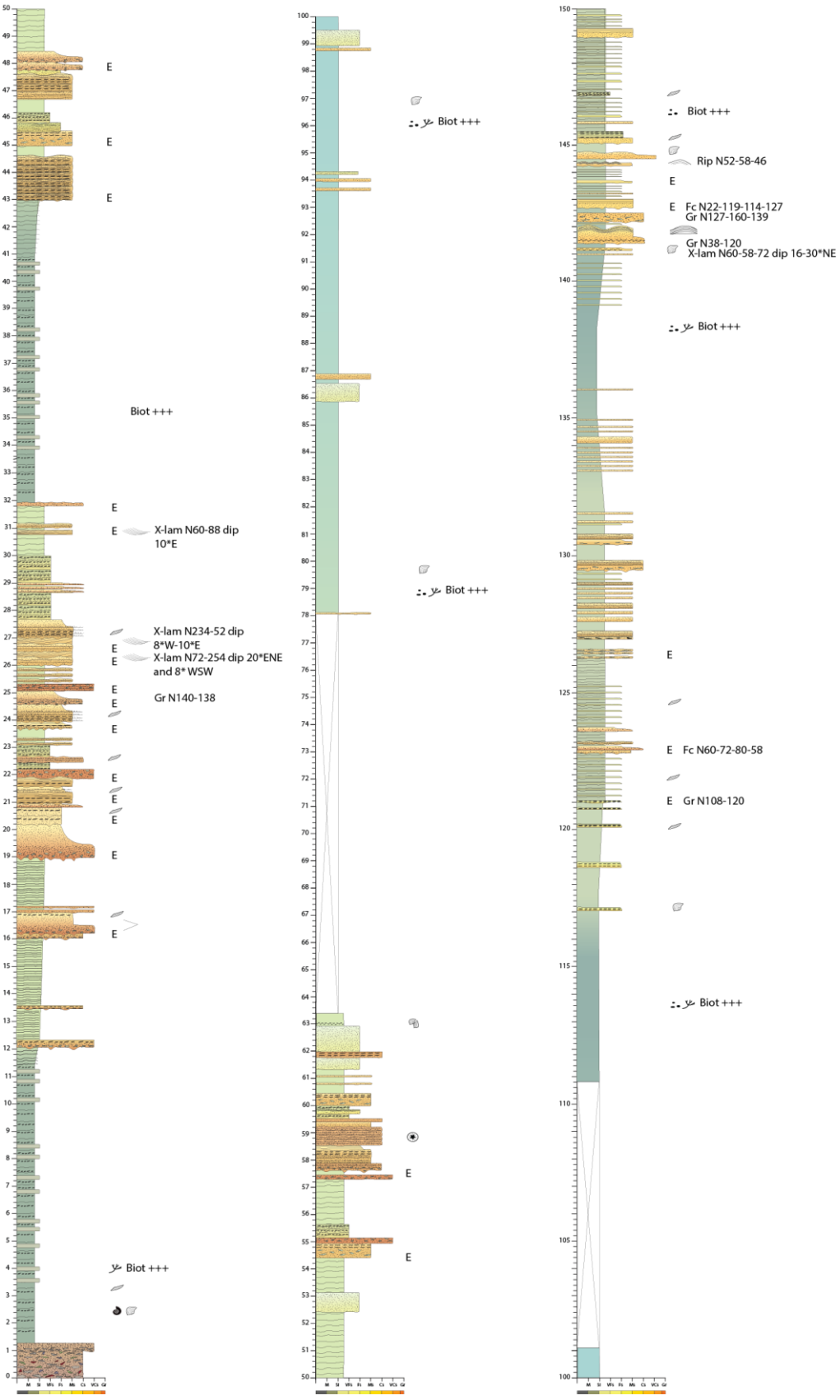

Appendix 9: Log number 1 (Cha-S1) part 1.

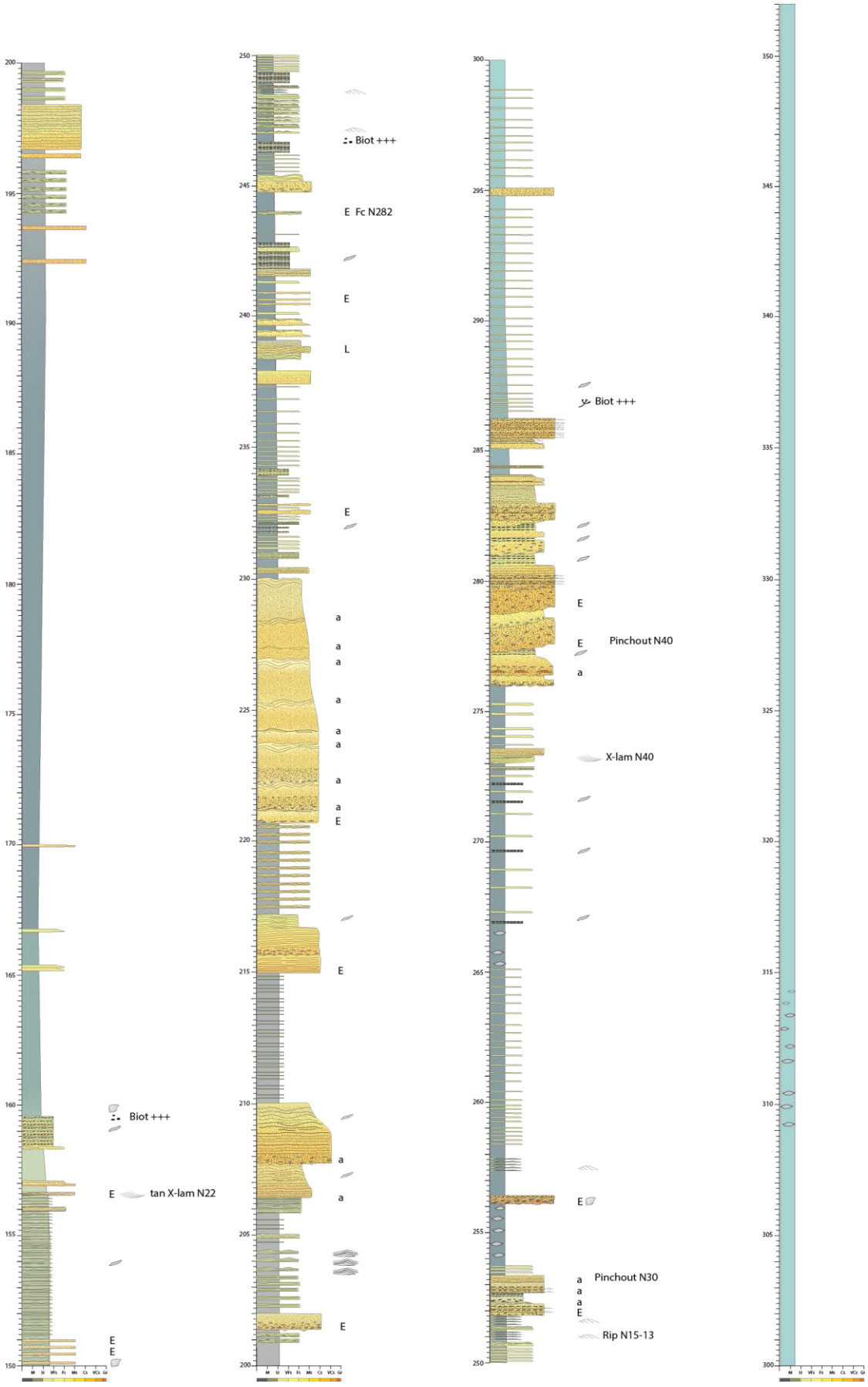

Appendix 10: Log number 1 (Cha-S1) part 2.

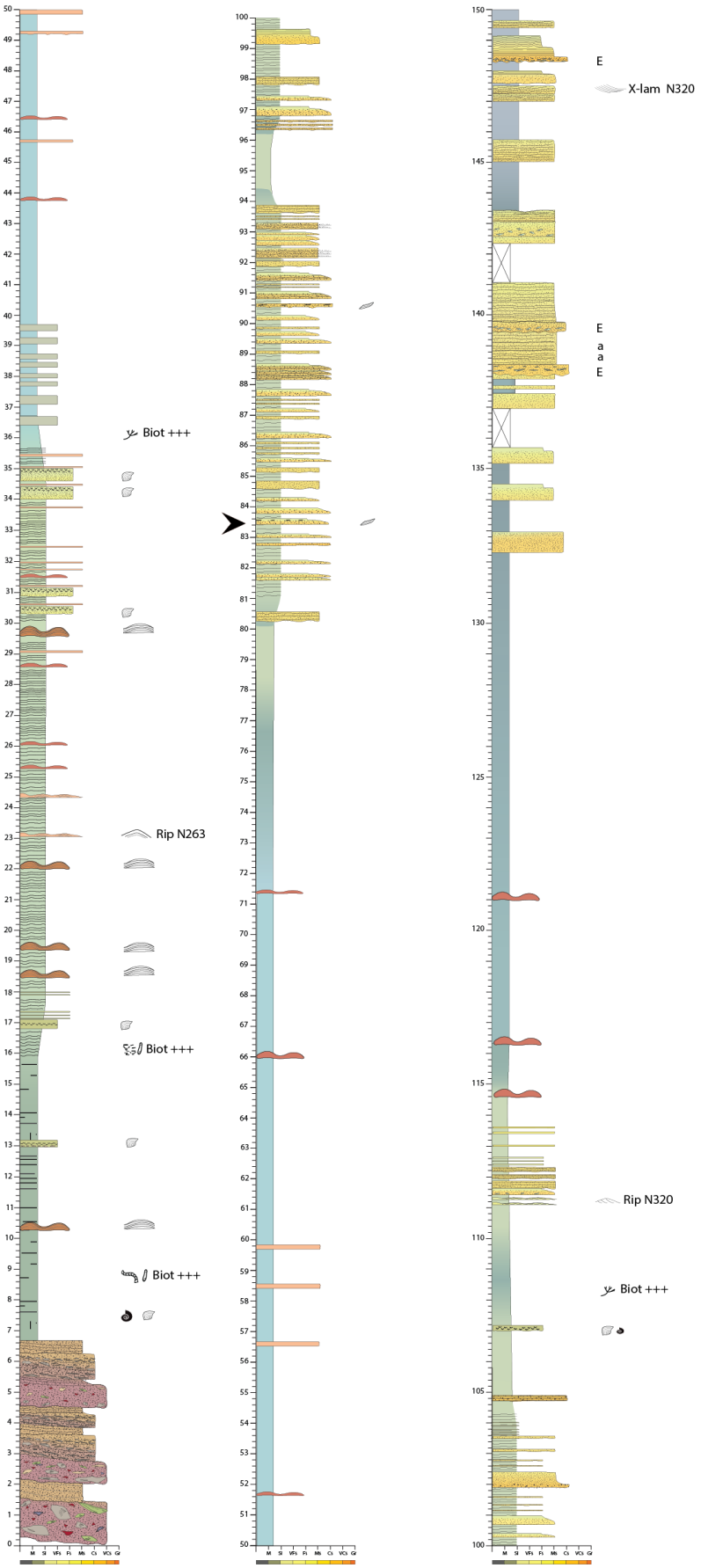

Appendix 11: Log number 2 (Cha-S2) part 1.

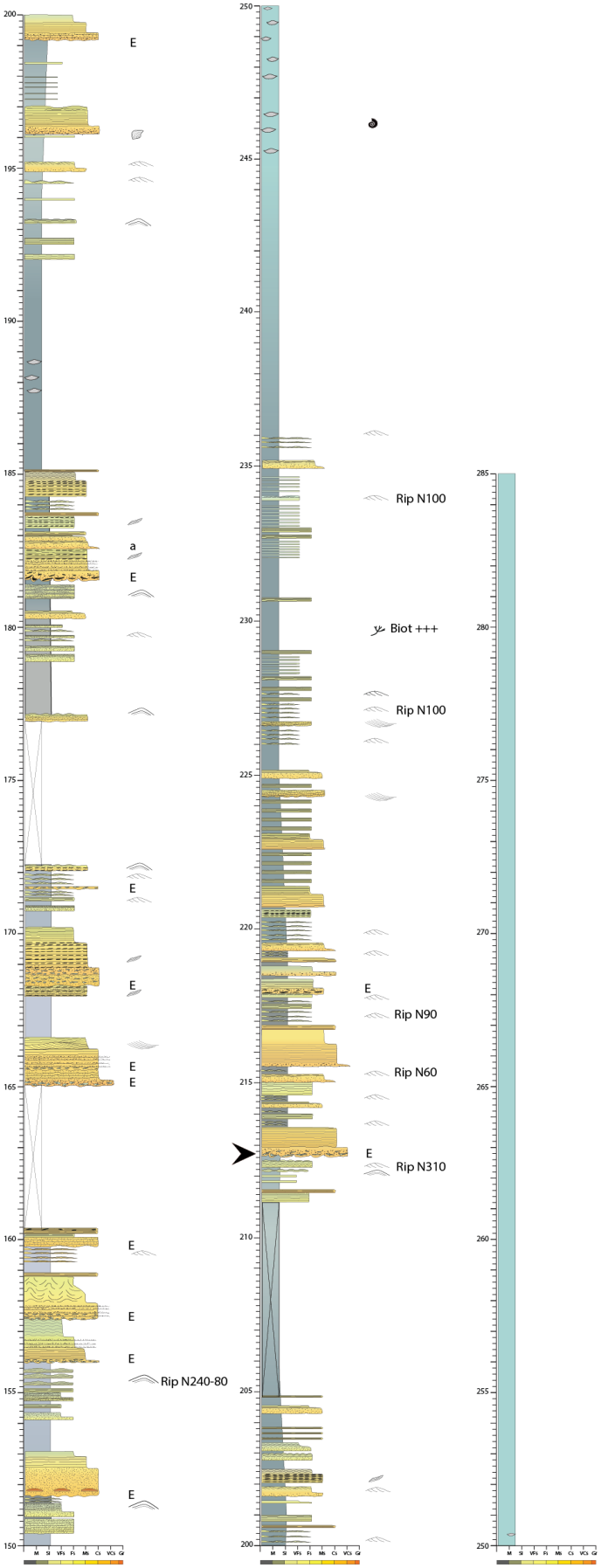

Appendix 12: Log number 2 (Cha-S2) part 2.

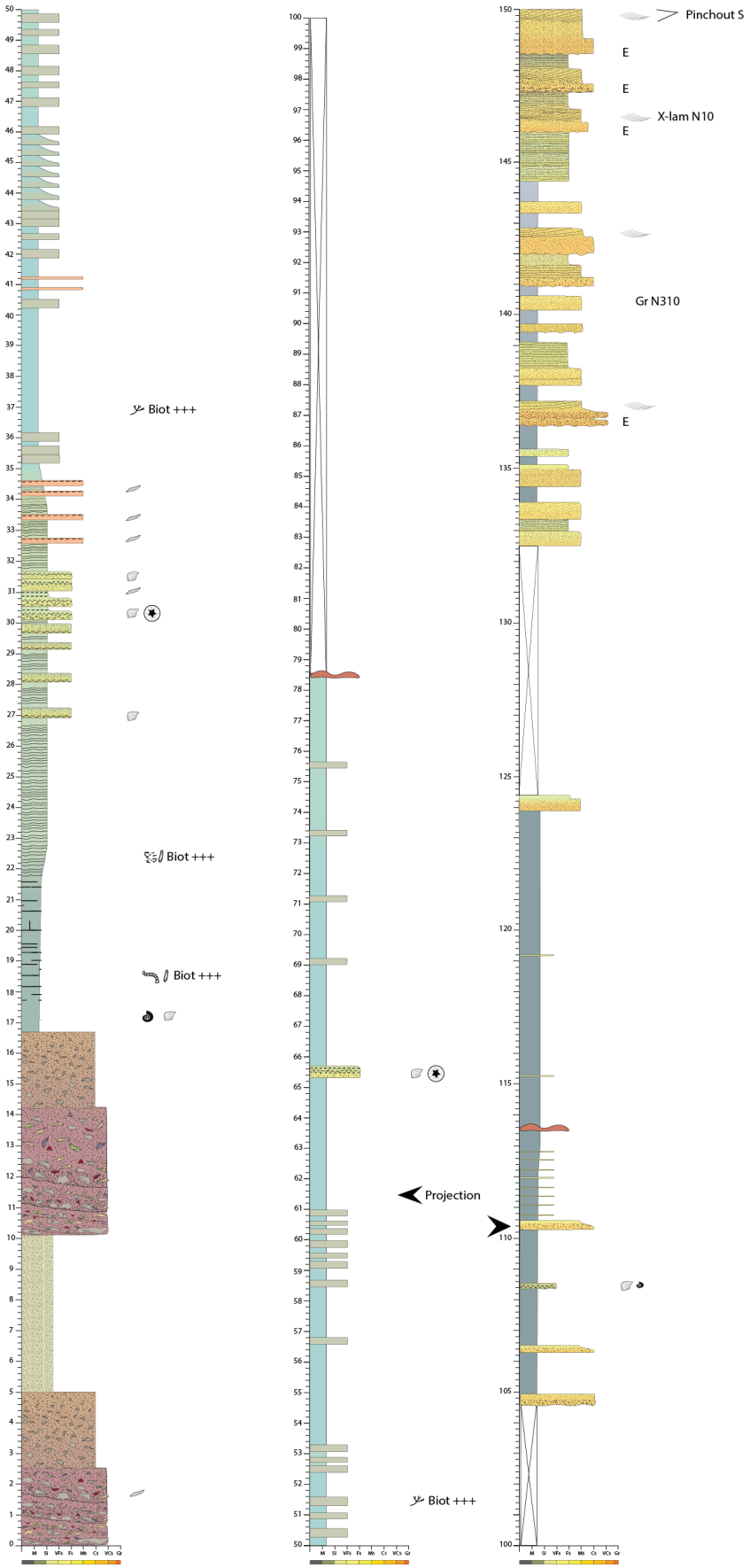

Appendix 13: Log number 3 (Cha-S3) part 1.

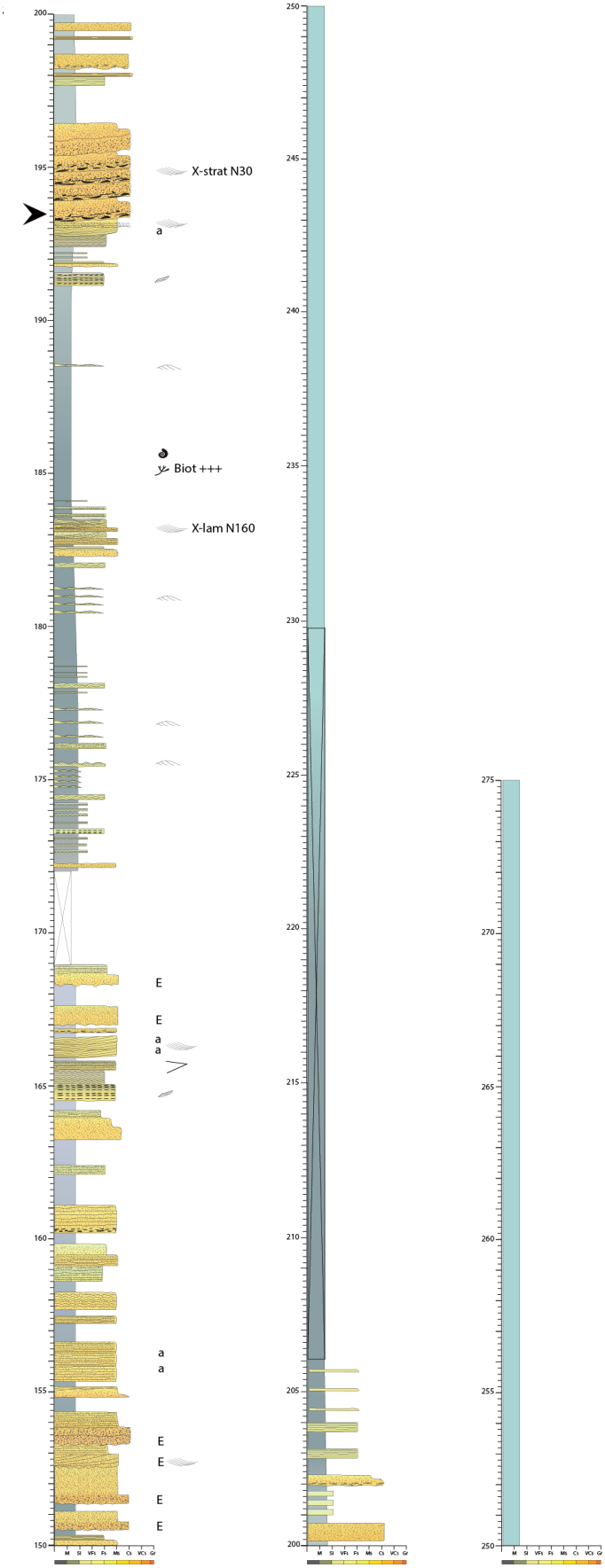

Appendix 14: Log 3 (Cha-S3) part 2.

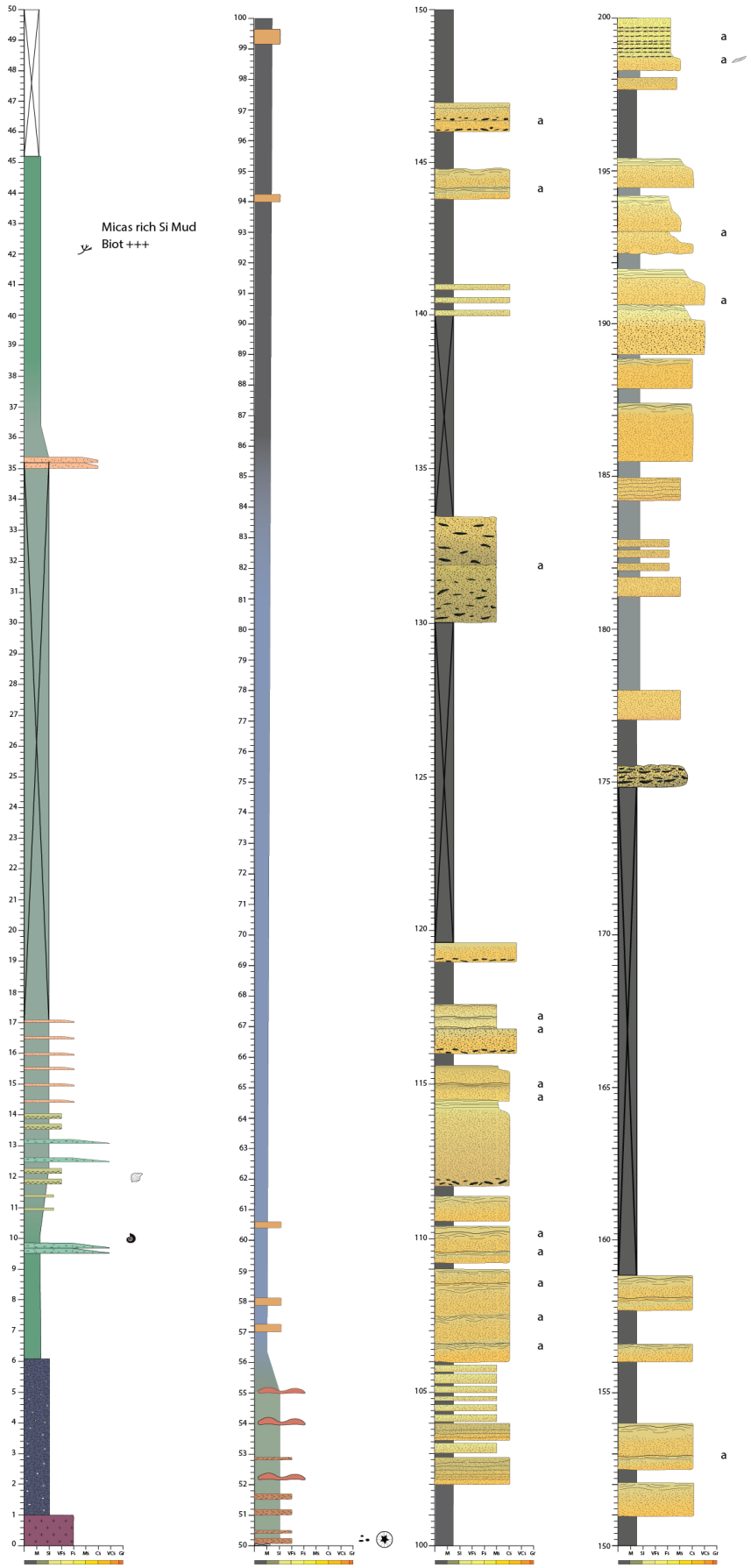

Appendix 15: Log number 4 (Ma-S1) part 1.

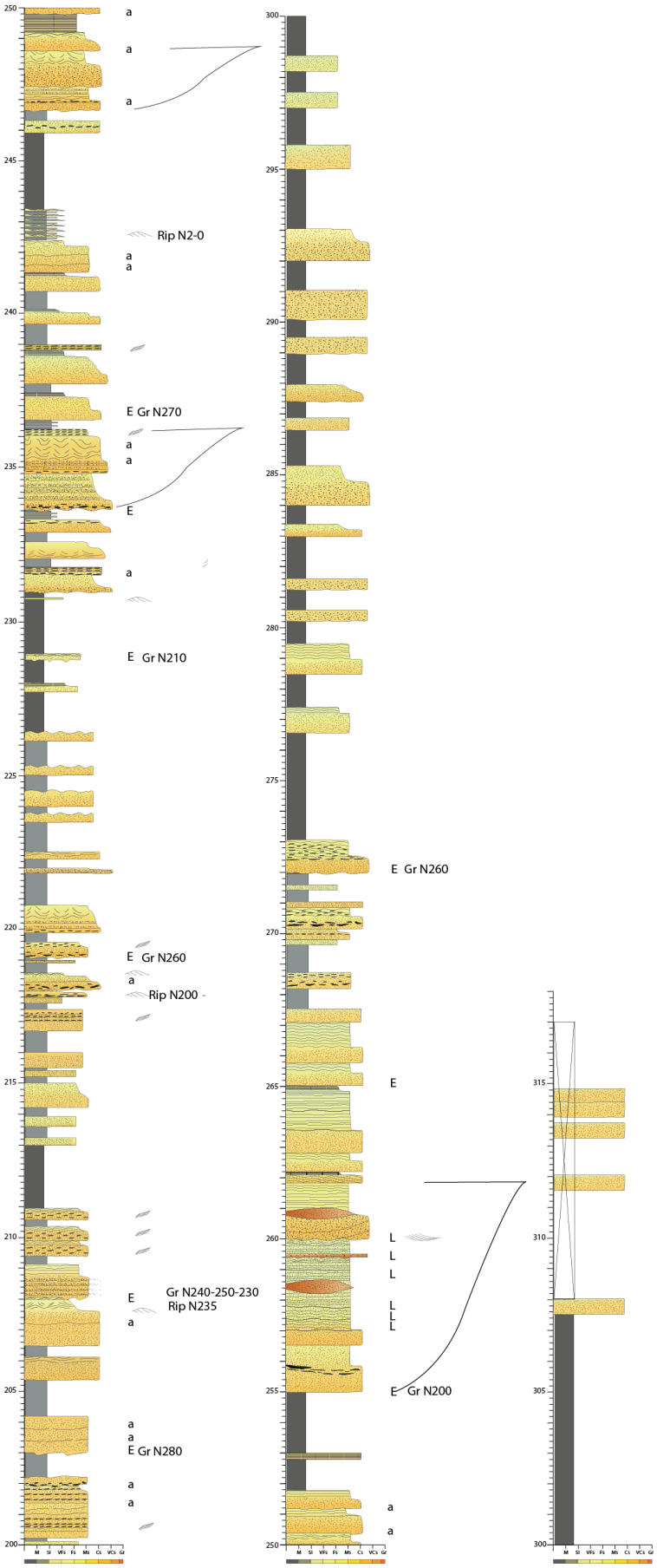

Appendix 16: Log number 4 (Ma-S1) part 2.

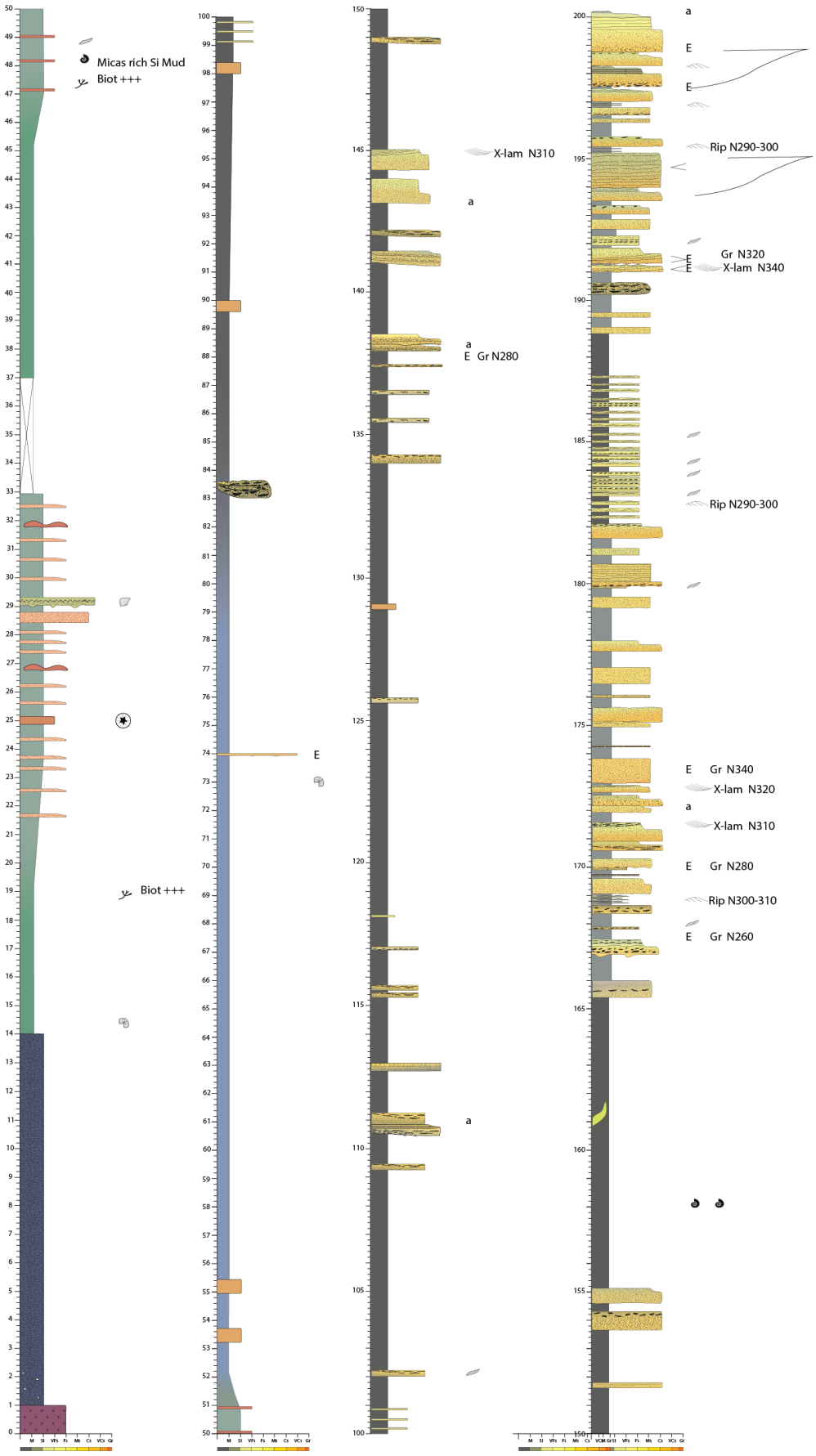

Appendix 17: Log number 5 (Ma-S2) part 1.

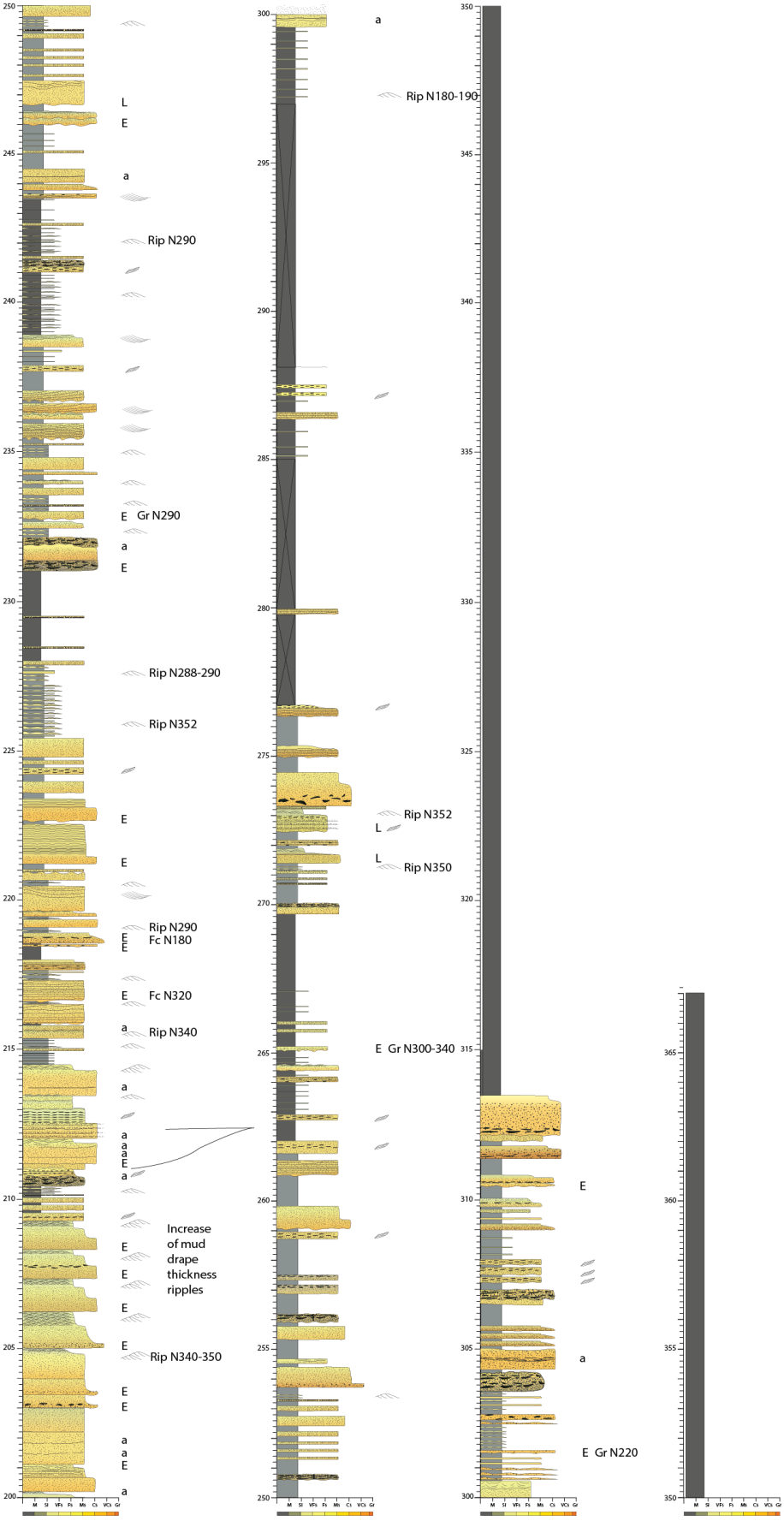

Appendix 18: Log number 5 (Ma-S2) part 2.

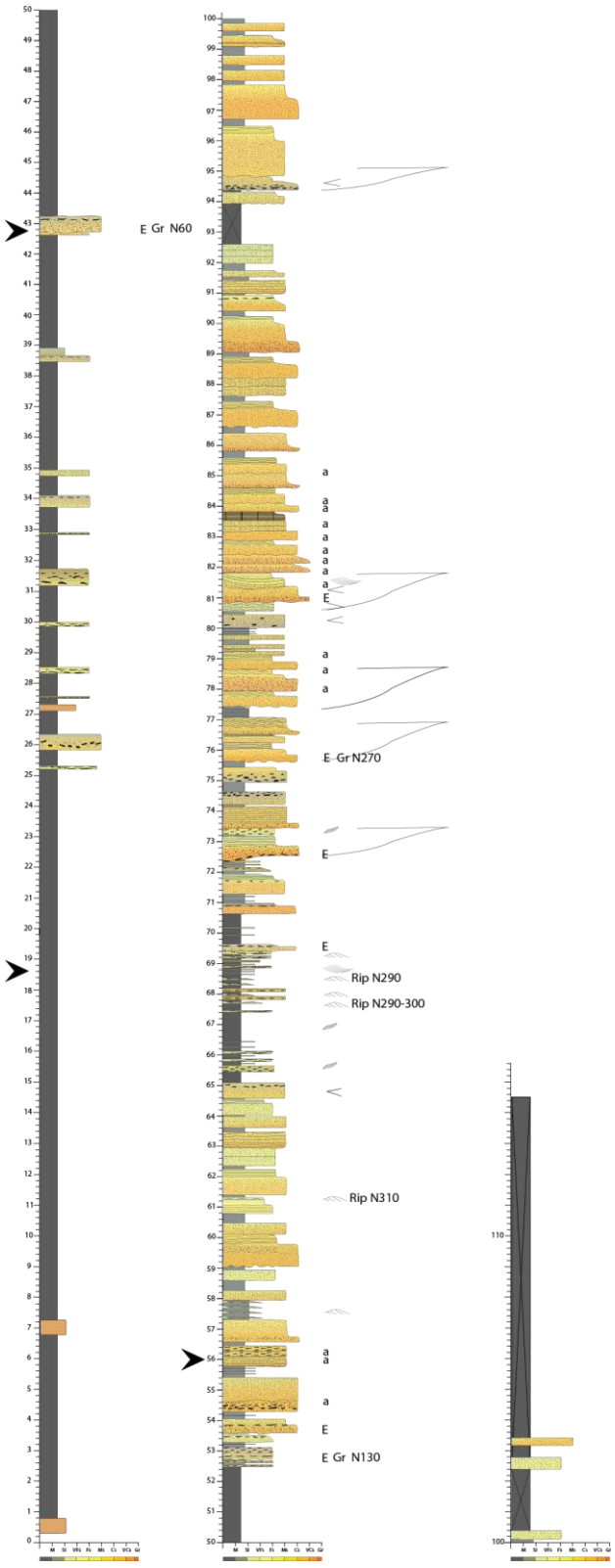

Appendix 19: Log number 6 (Ma-S3).

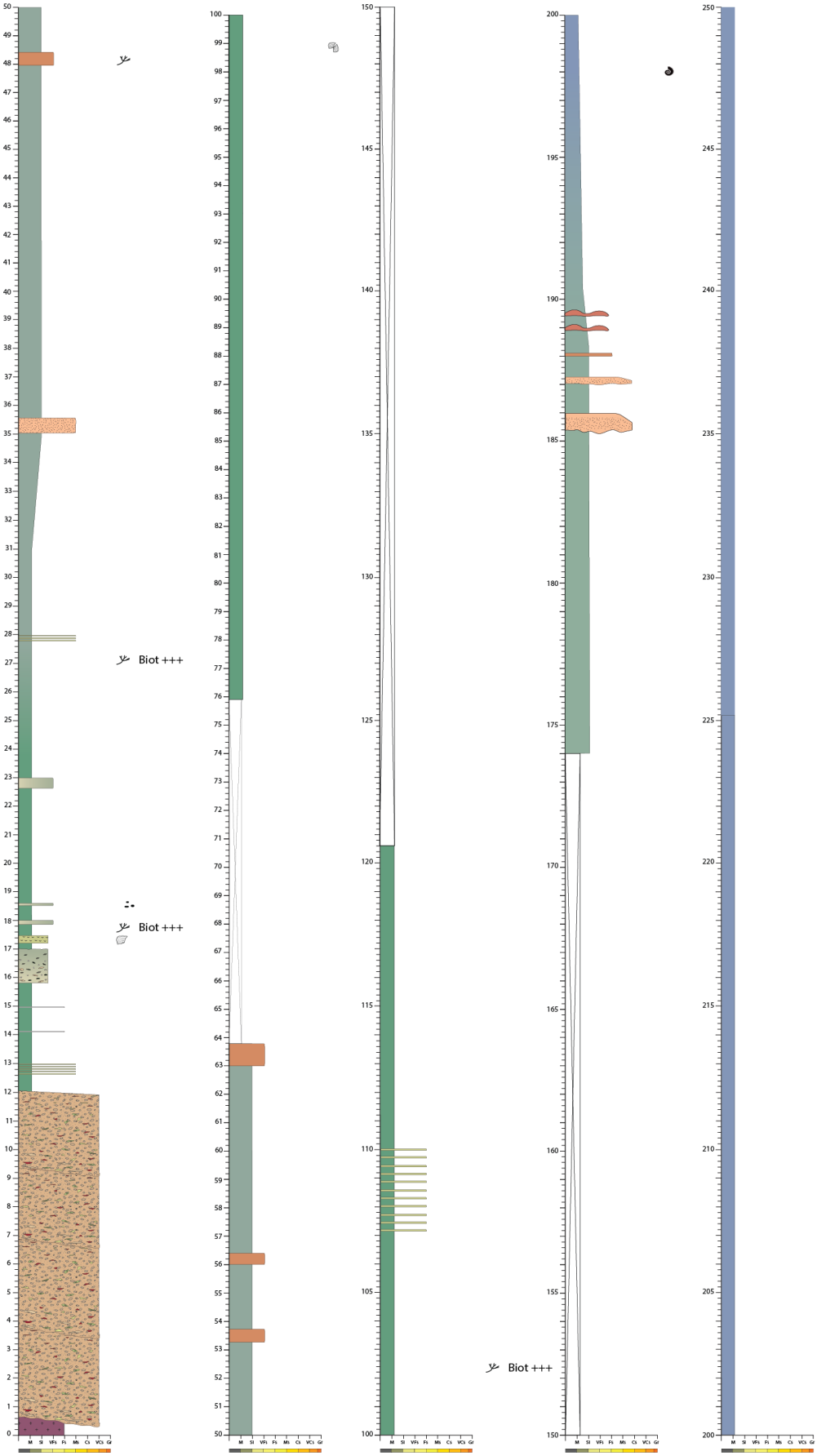

Appendix 20: Log number 7 (EZ-S2) part 1.

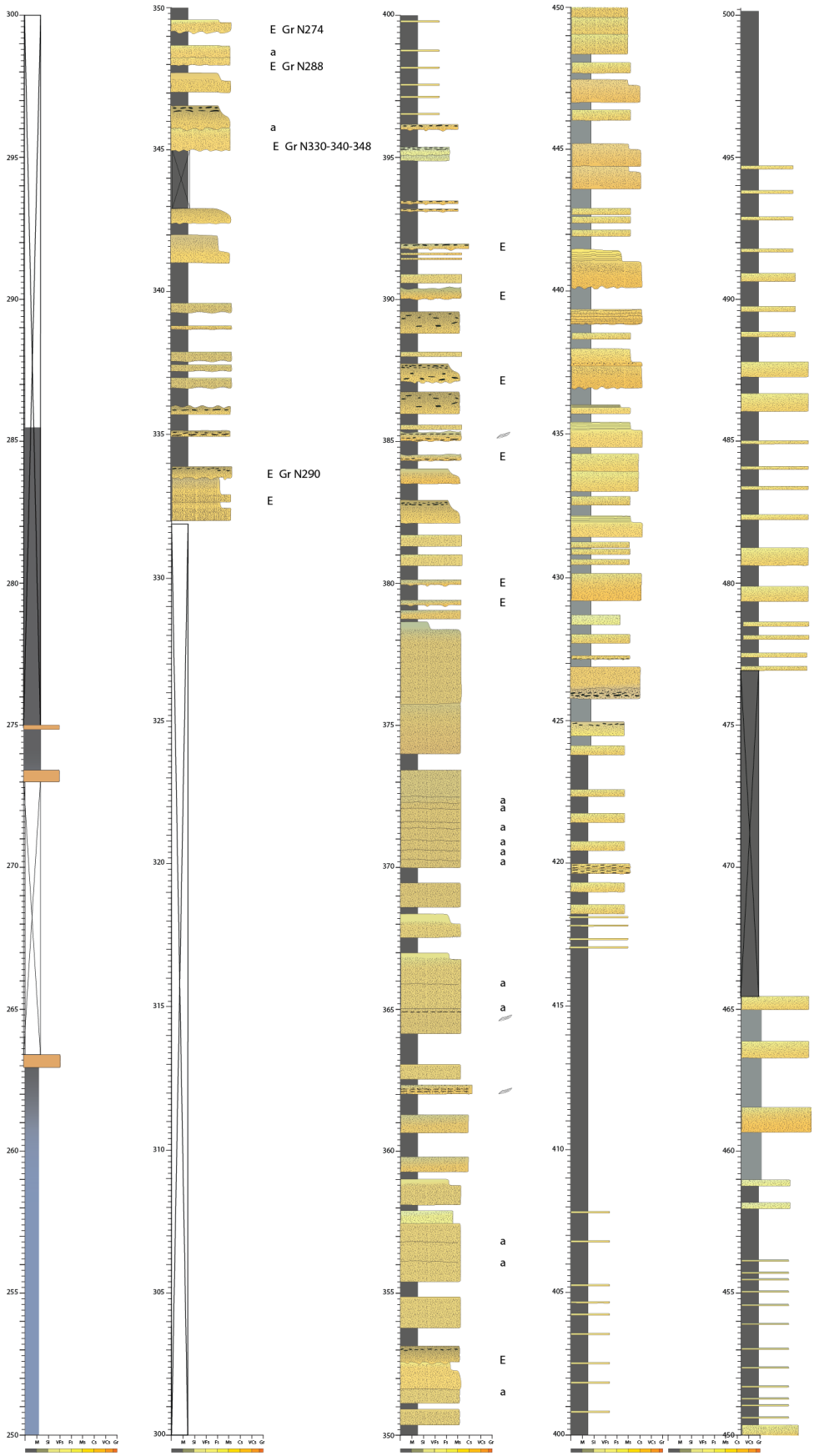

Appendix 21: Log number 7 (EZ-S2) part 2.

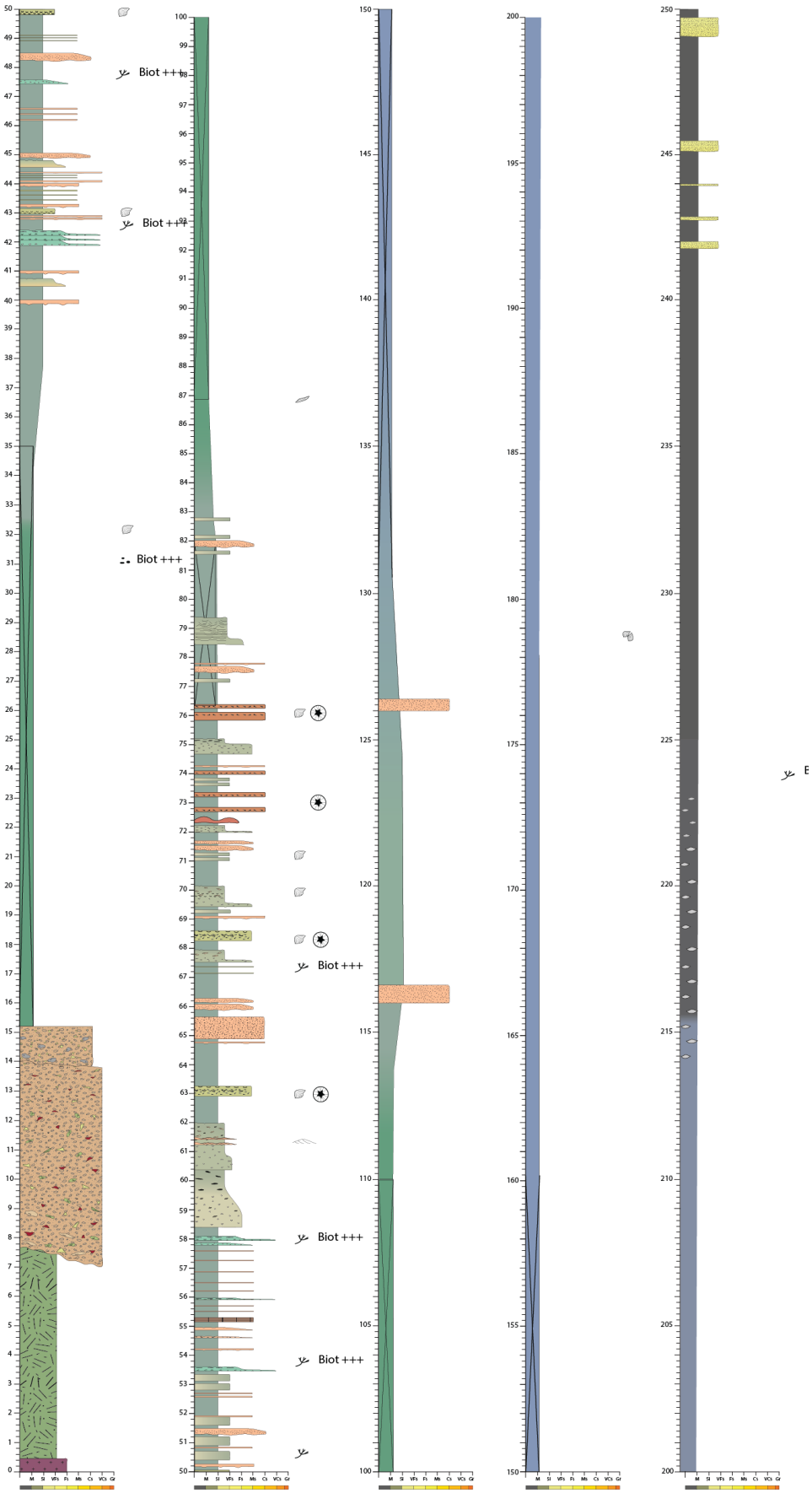

Appendix 22: Log number 8 (Tut-S1) part 1.

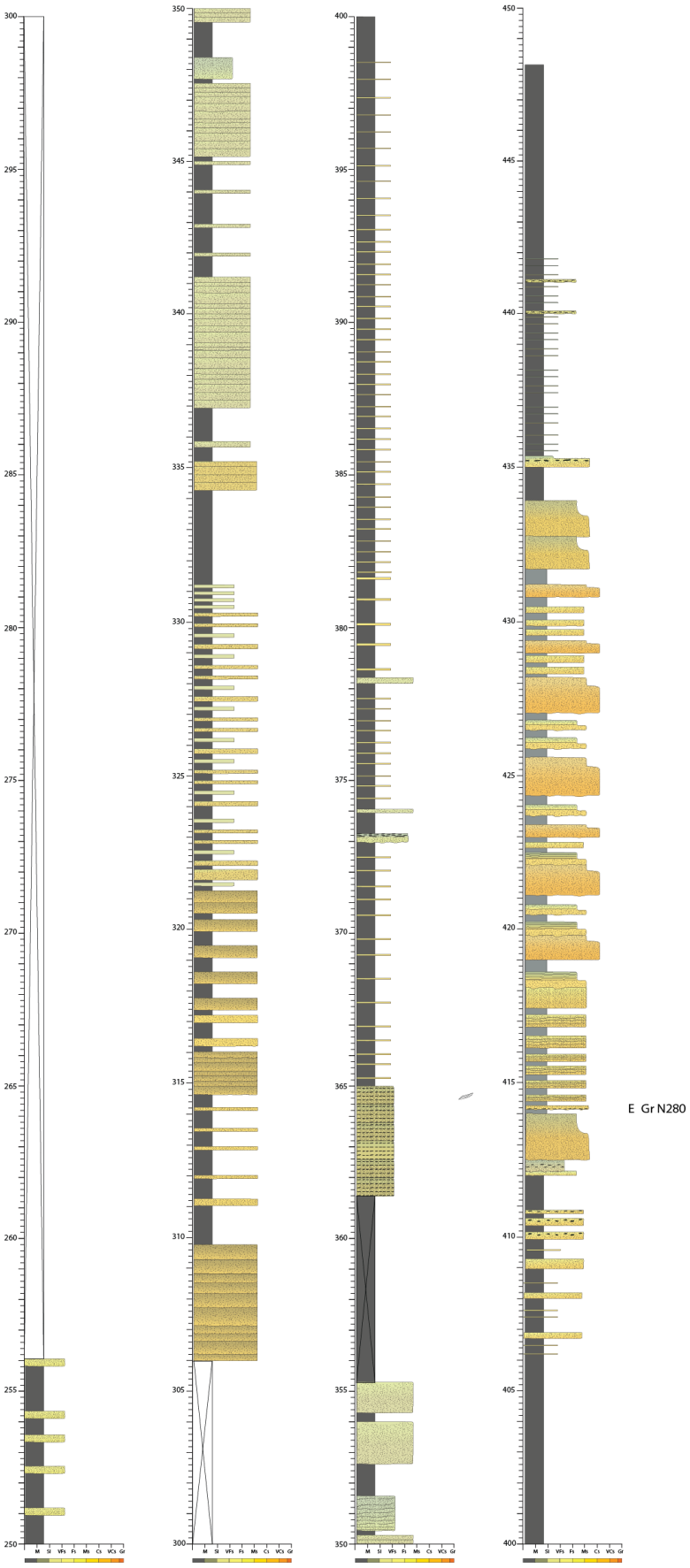

Appendix 23: Log number 8 (Tut-S1) part 2.

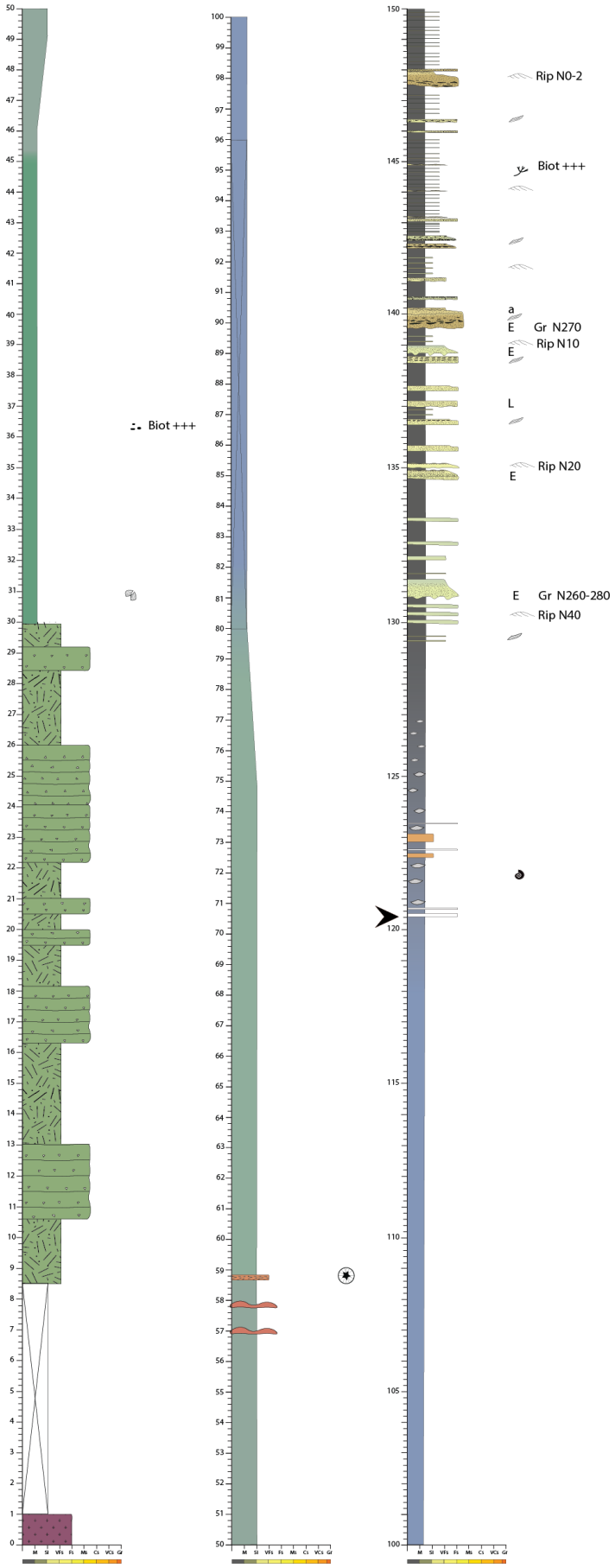

Appendix 24: Log number 9 (Tut-S2a) part 1.

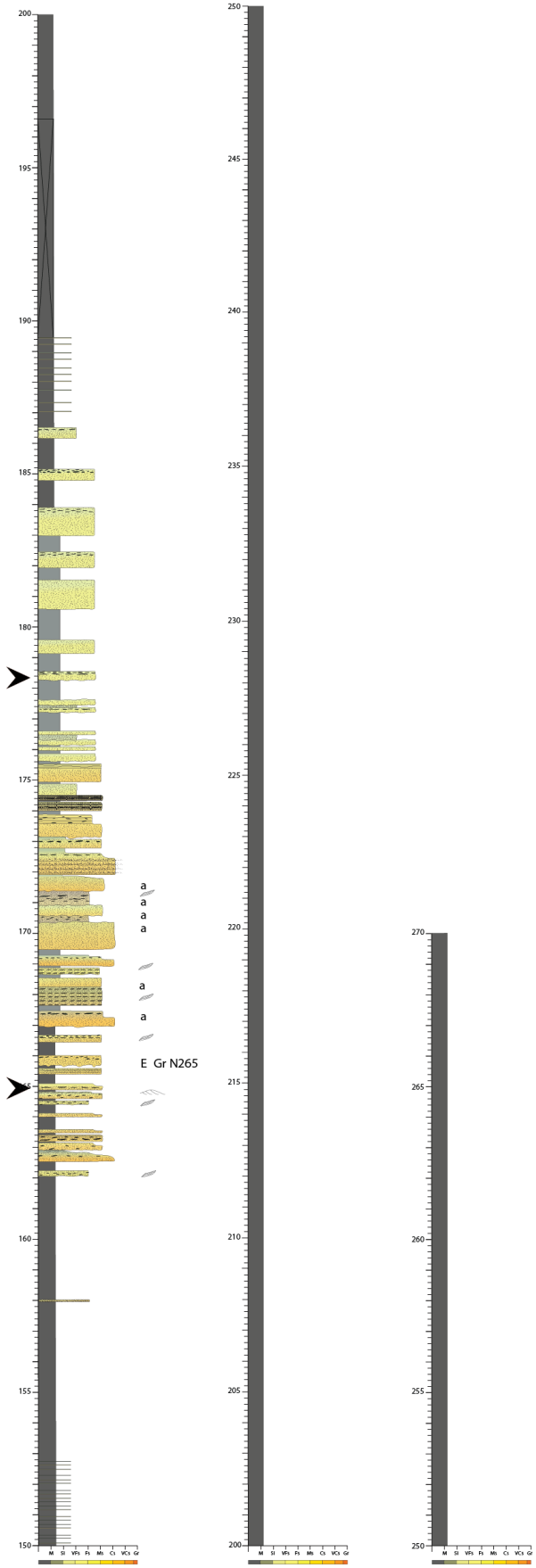

Appendix 25: Log number 9 (Tut-S2a) part 2.

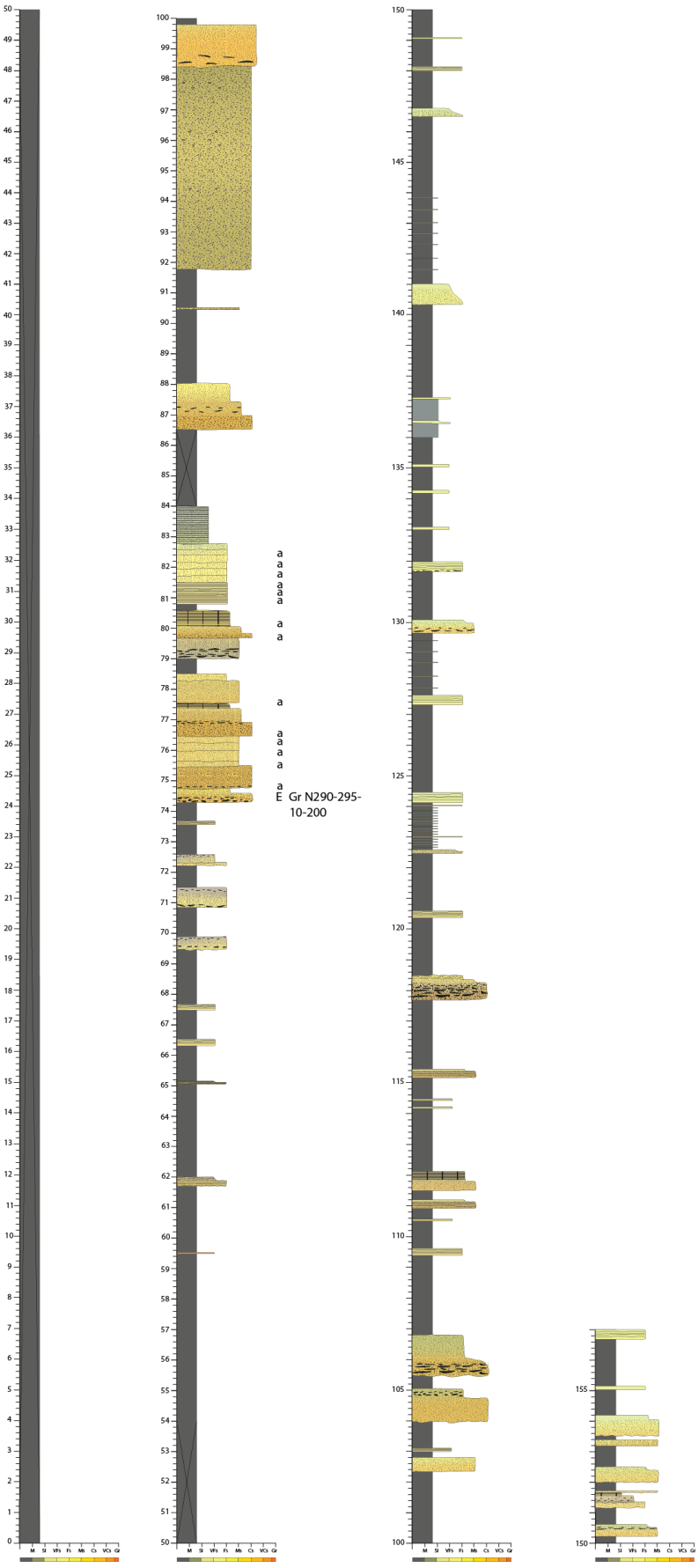

Appendix 26: Log number 9 (Tut-S2b).

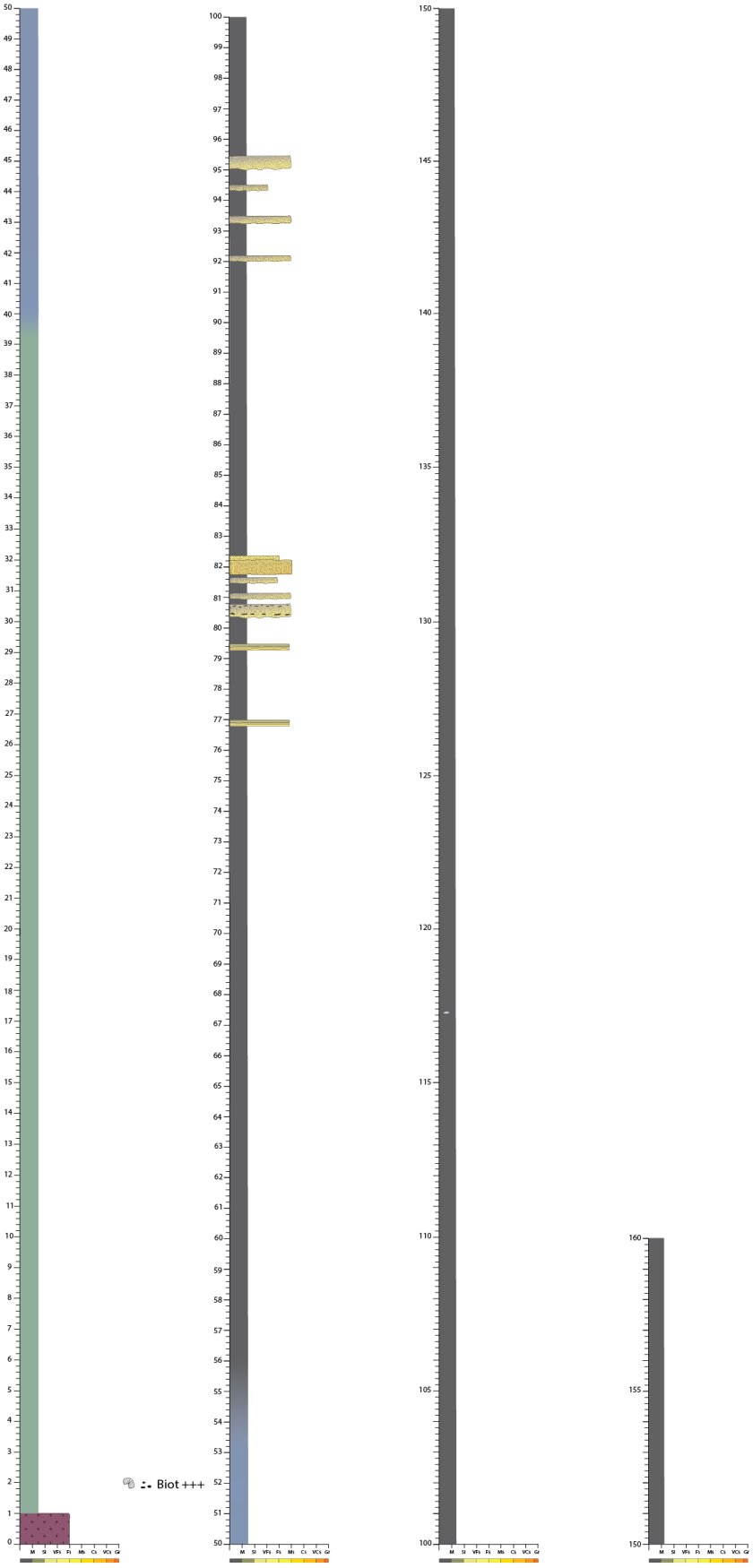

Appendix 27: Log number 10 (PS1-a).

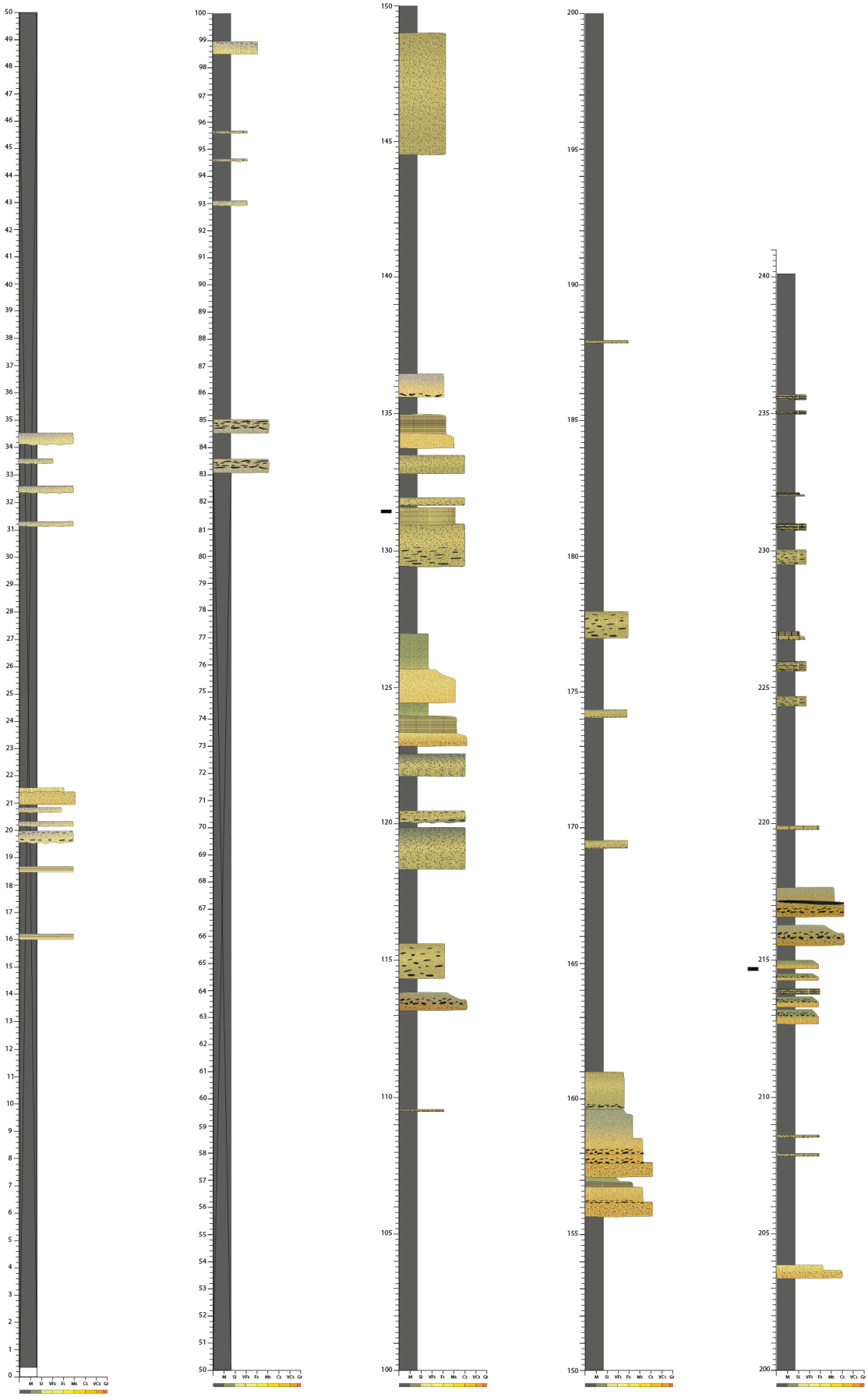

Appendix 28: Log number 10 (PS1-b).

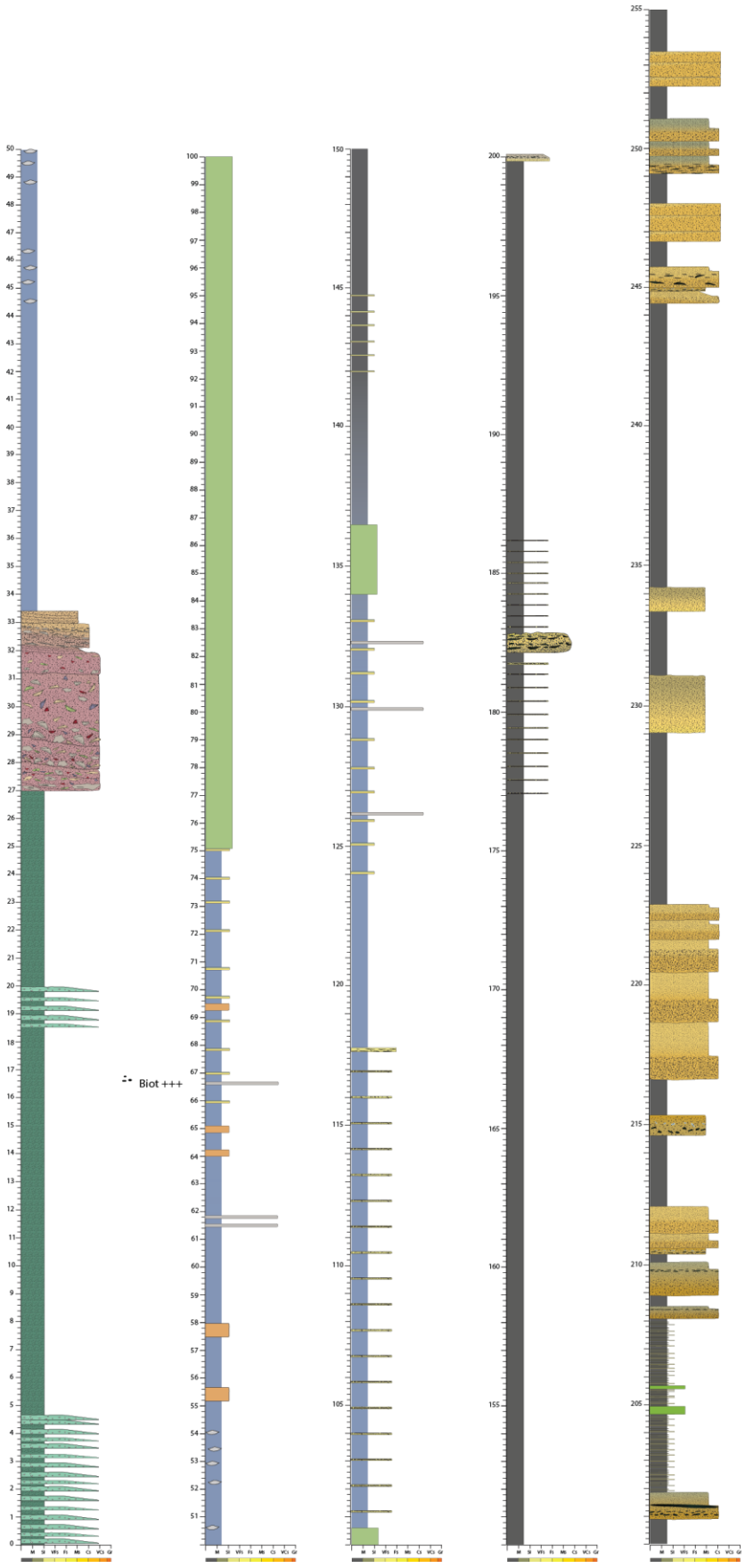

Appendix 29: Log C (La Jardinera).

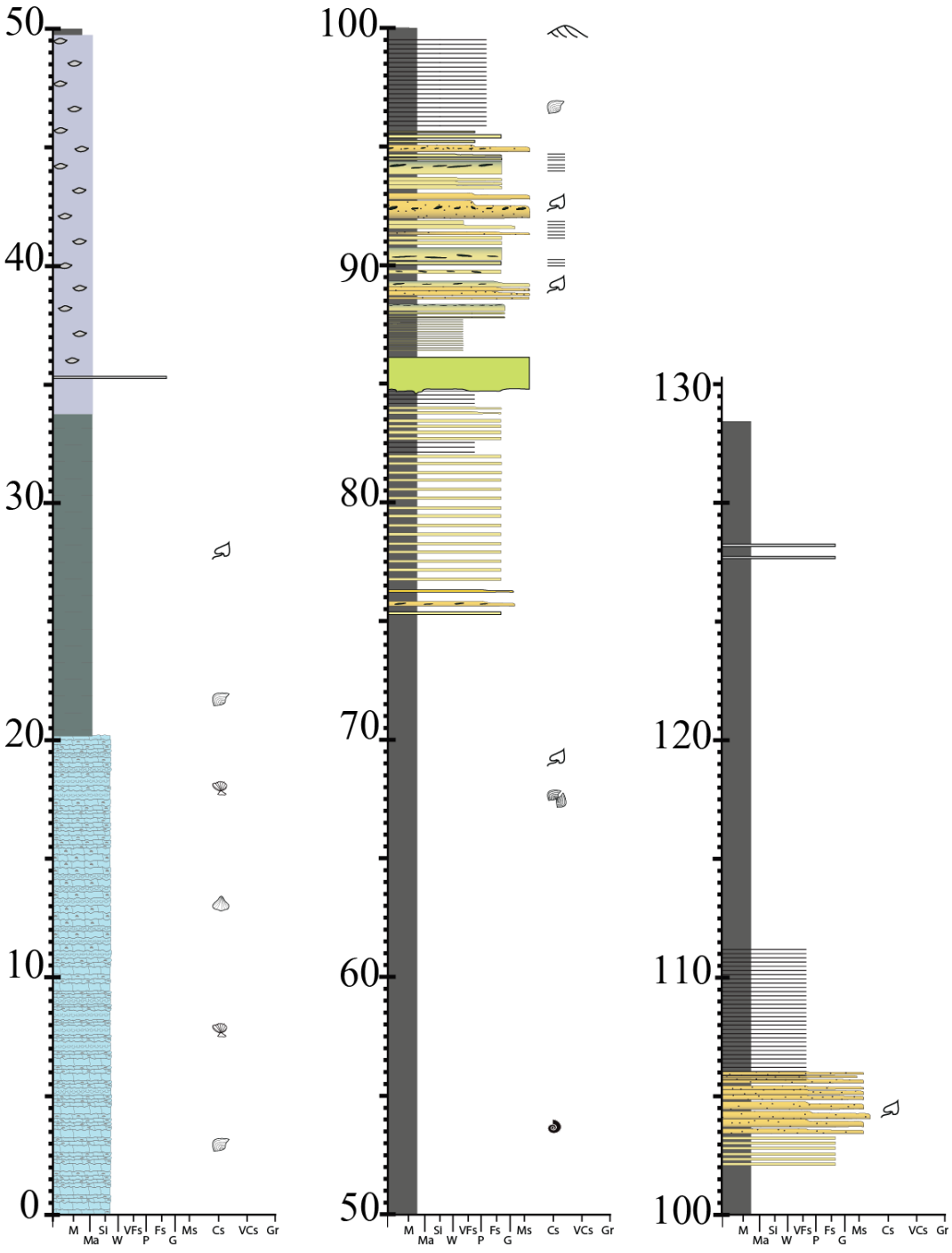

Appendix 30: Log number 1 (Road46).

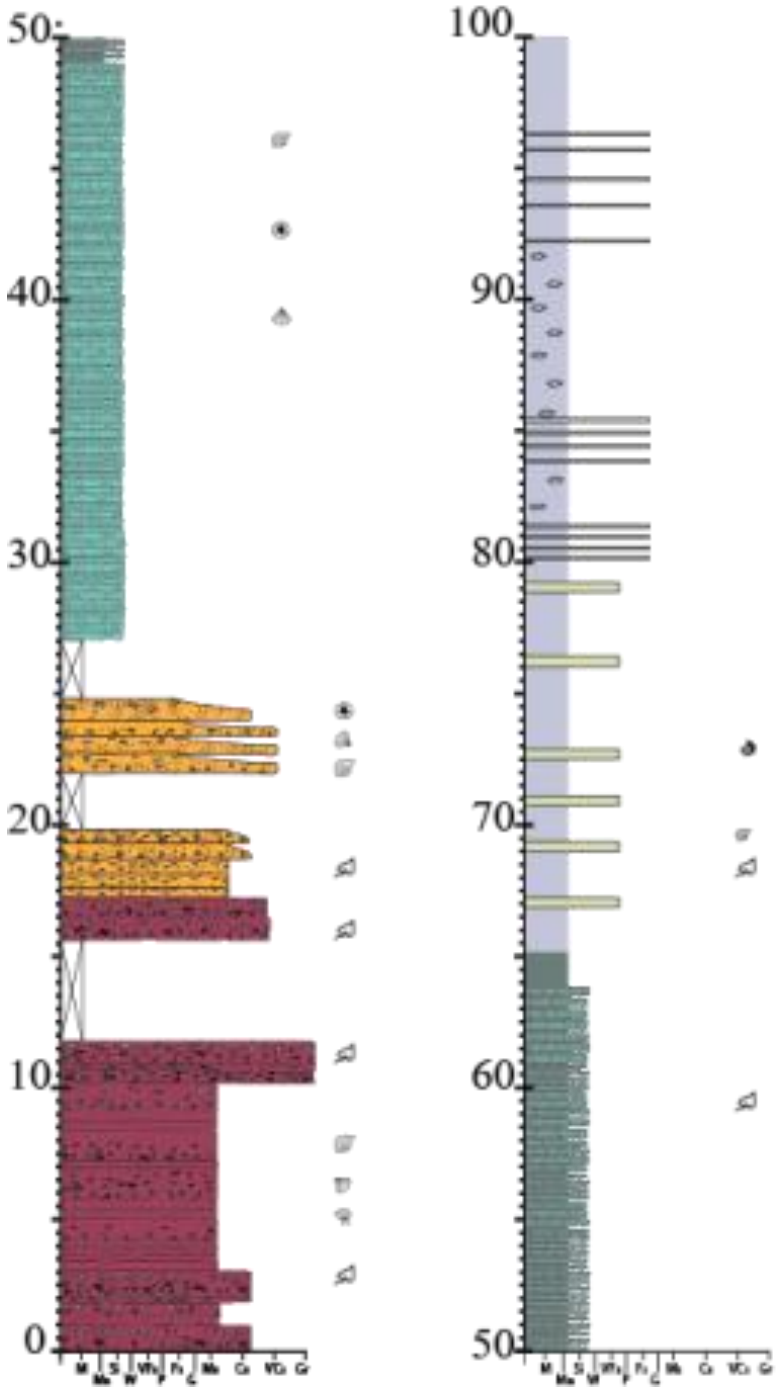

Appendix 31: Log number 2 (MiradorS1) part 1.

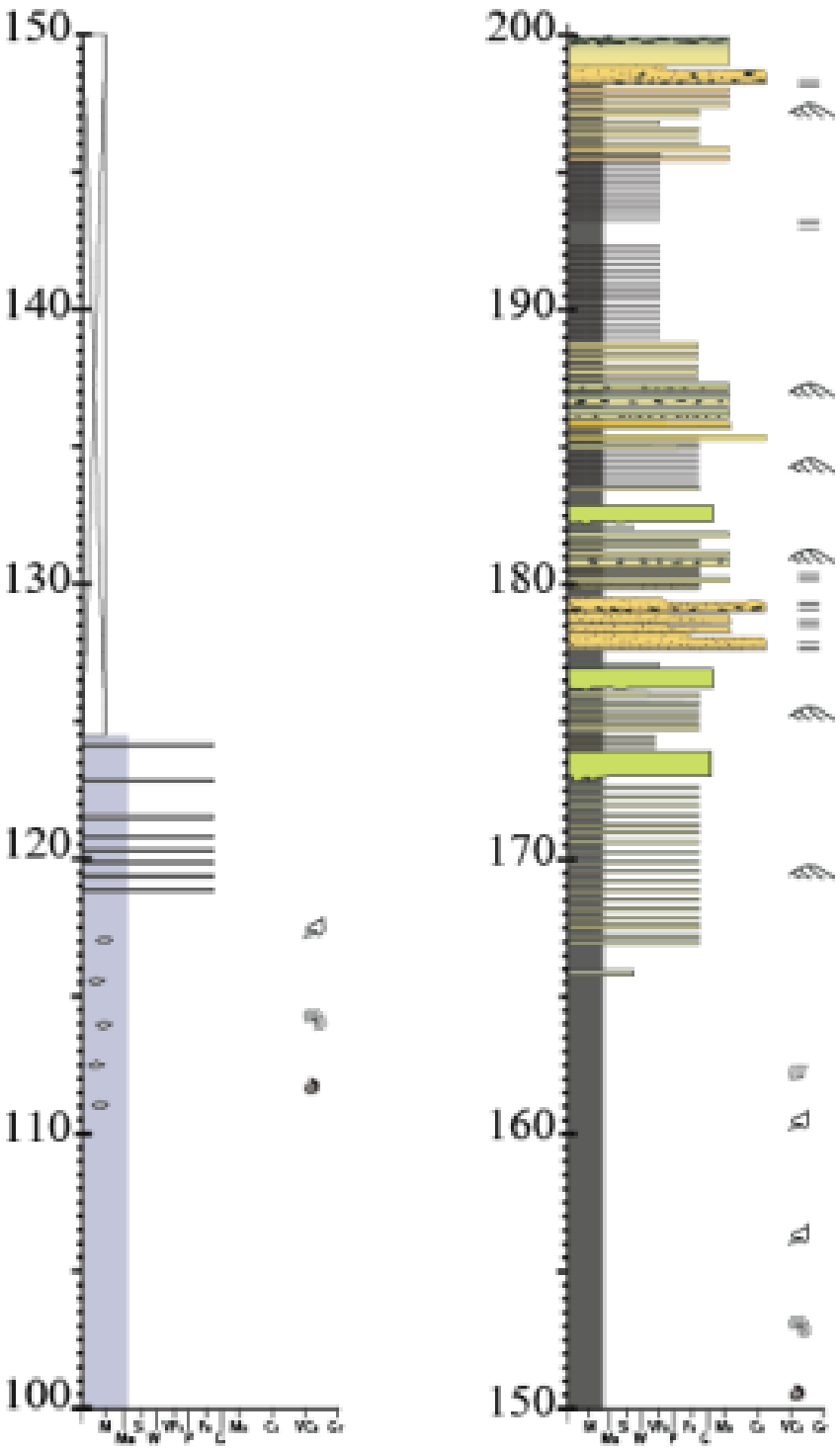

Appendix 32:Log number 2 (MiradorS1) part 2.

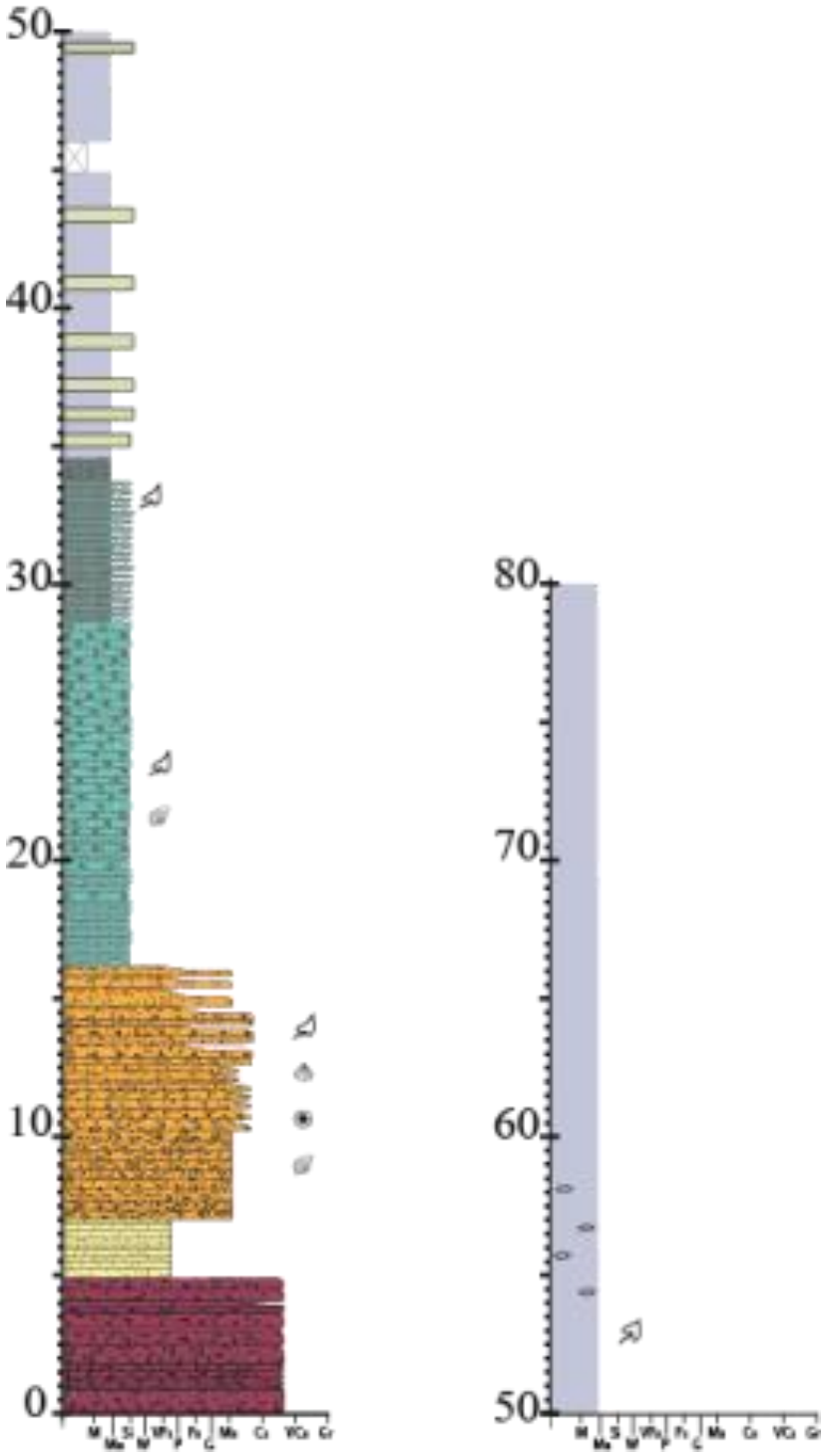

Appendix 33: Log number 3 (MiradorS2).

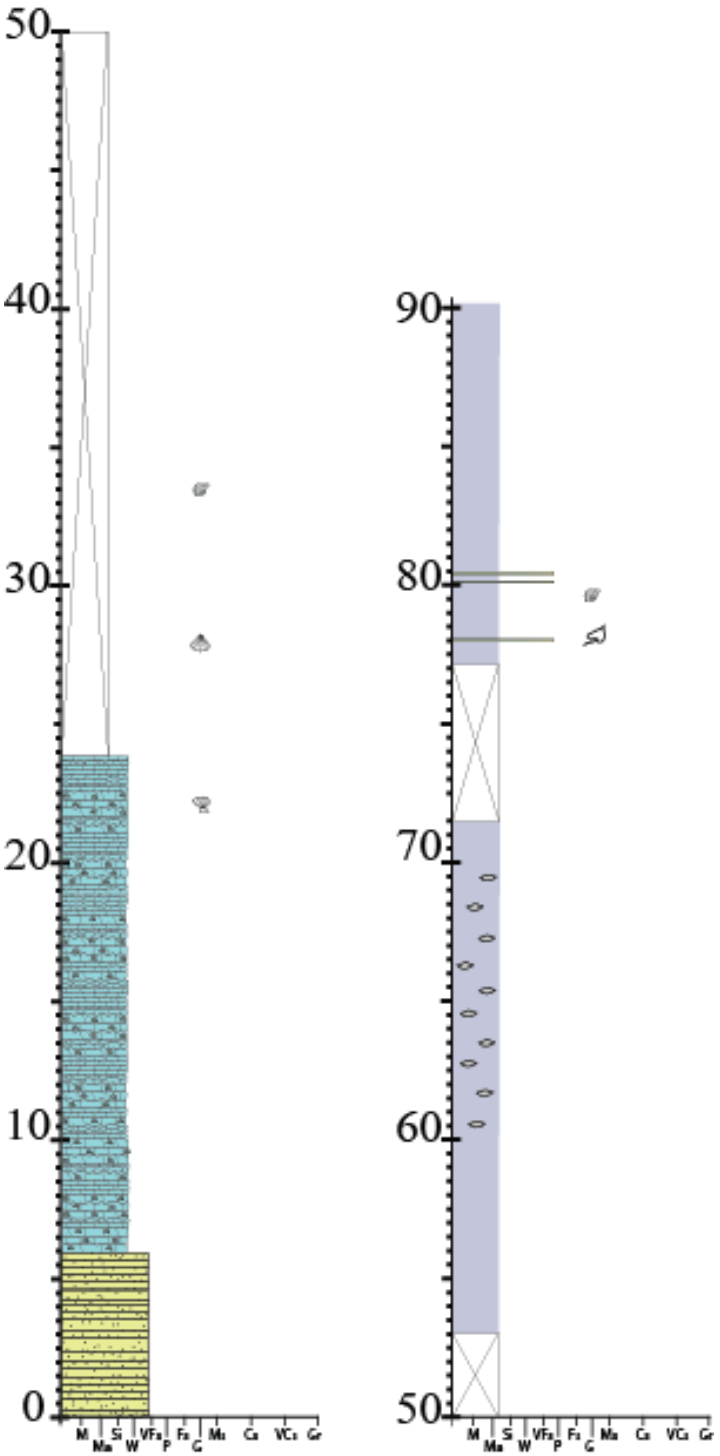

Appendix 34: Log number 4 (Morro del Aguila).

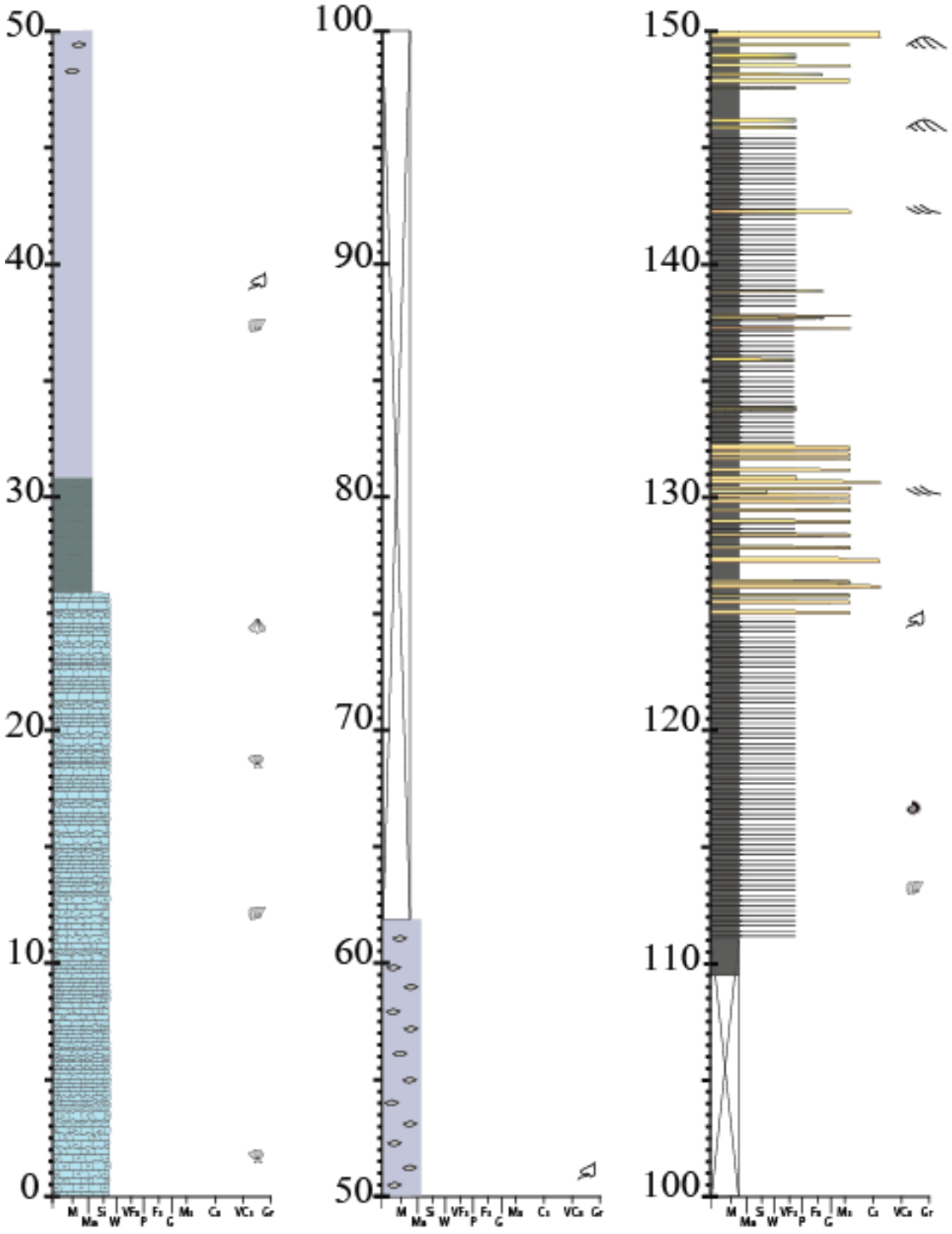

Appendix 35: Log number 5 (SonadaS2) part 1.

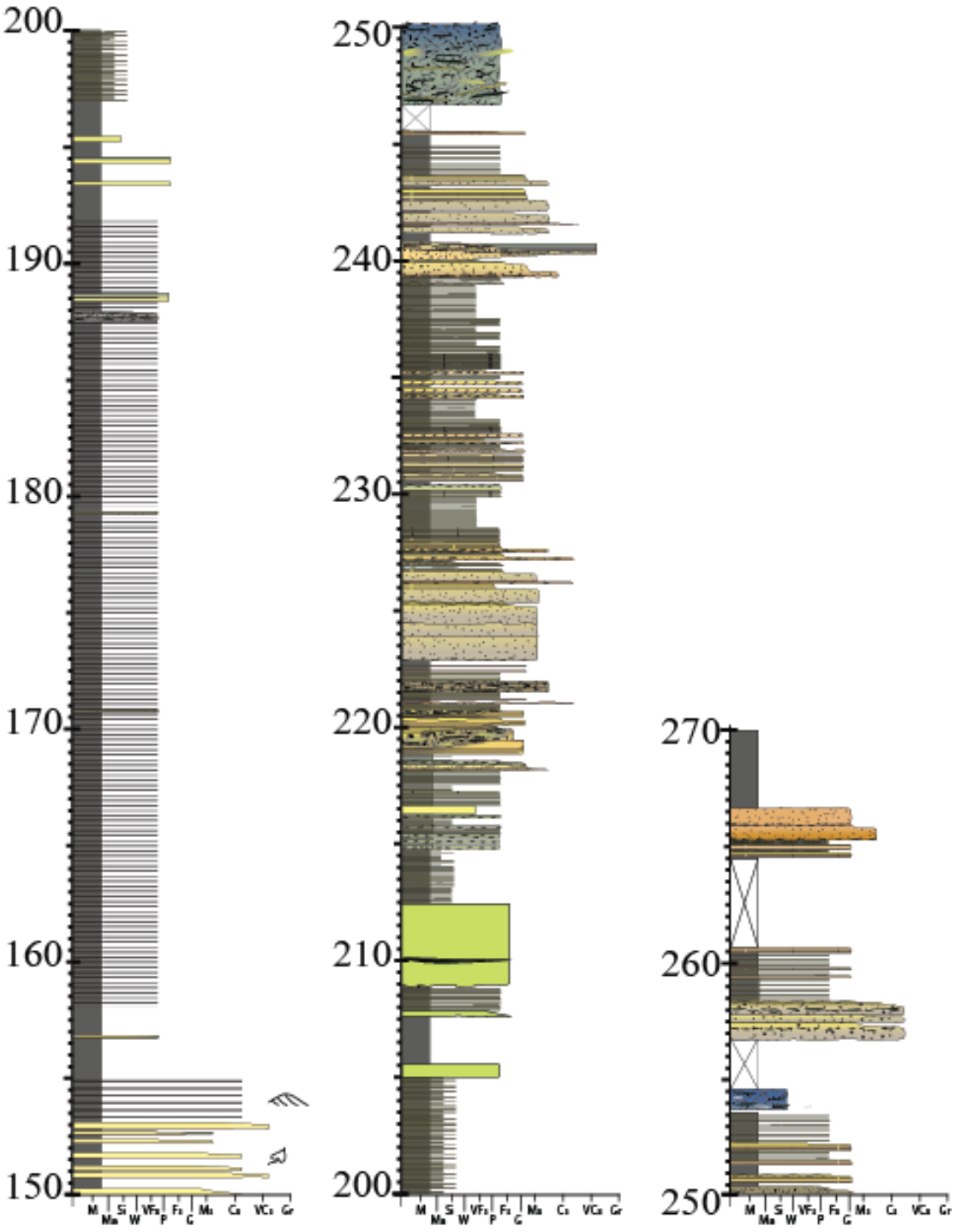

Appendix 36: Log number 5 (ChaS5bisAB) part 2.

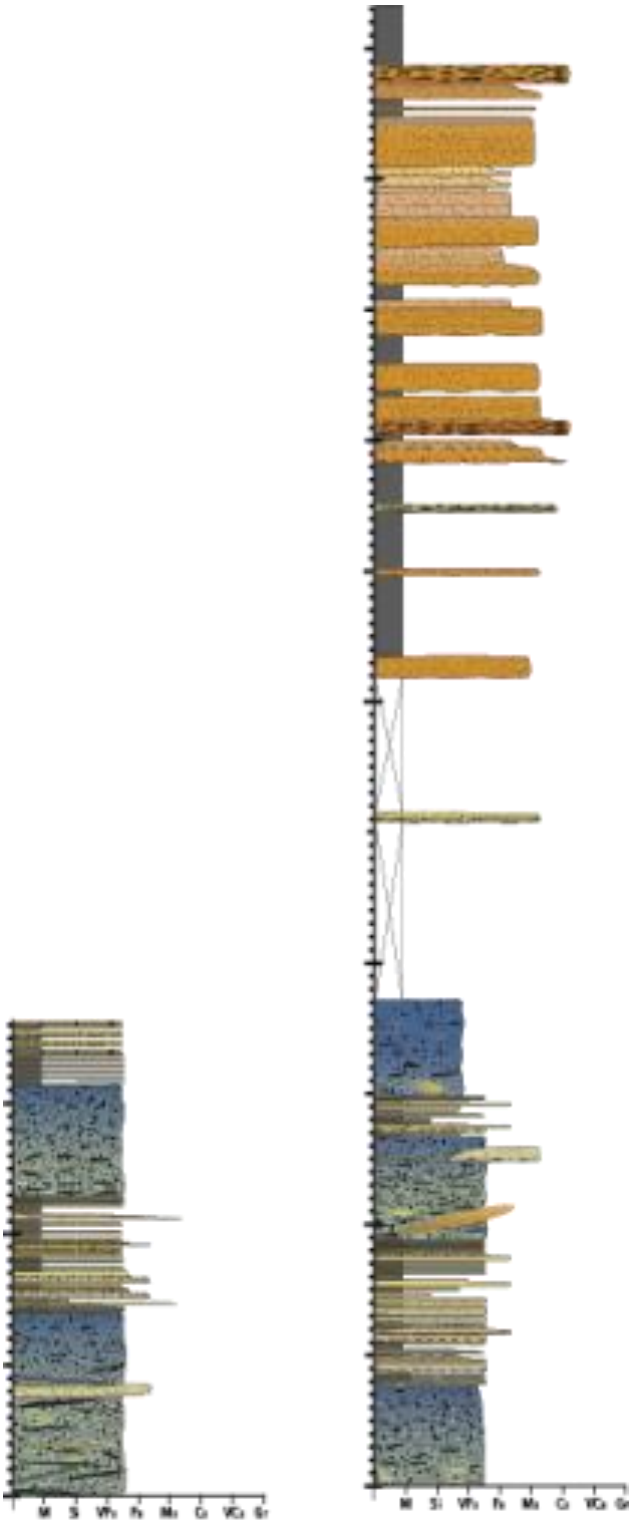

Appendix 37: Log number 5a (ChaS5bis) and b (ChaS5bis-CD).

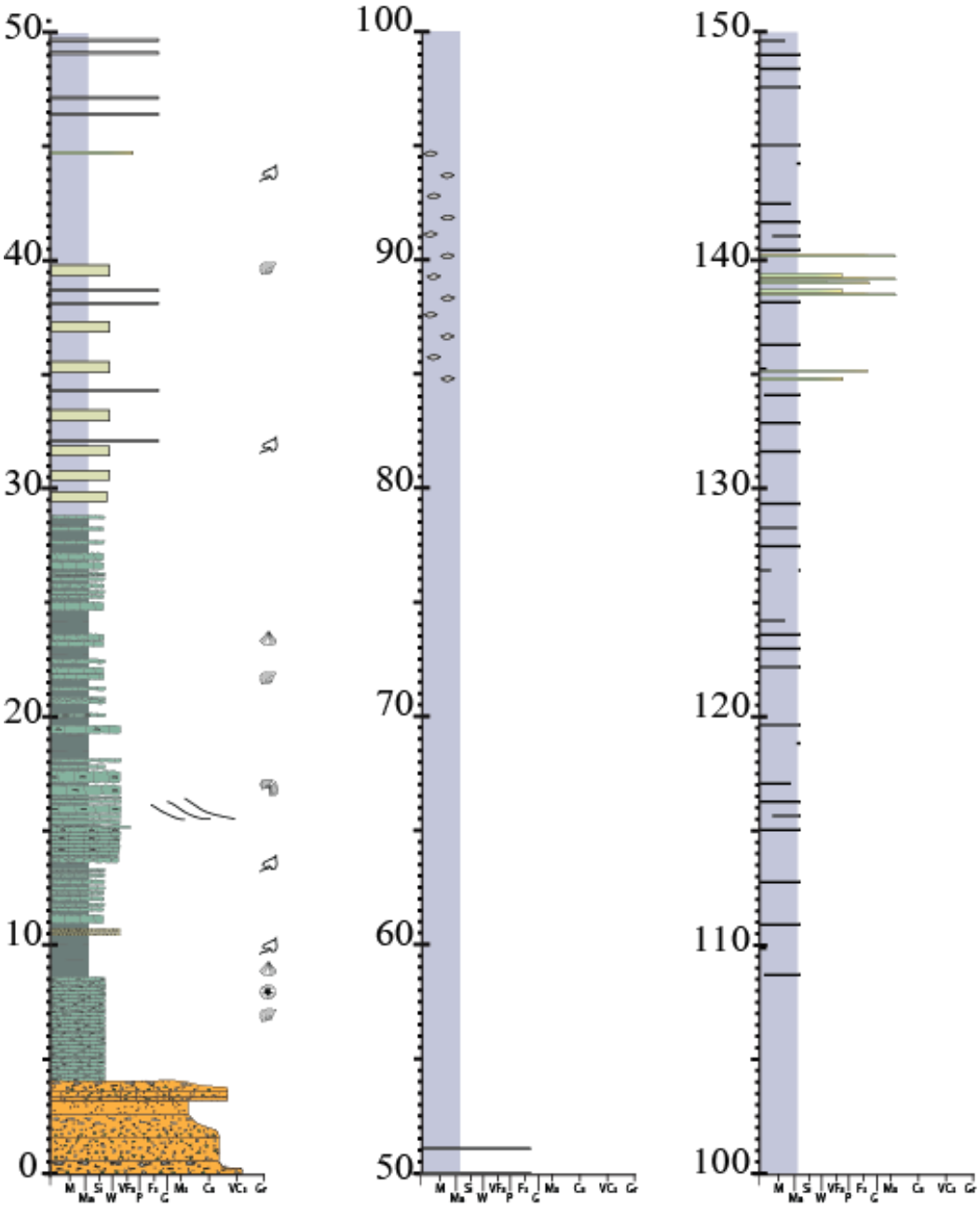

Appendix 38: Log number 6 (SonadaS1) part 1.

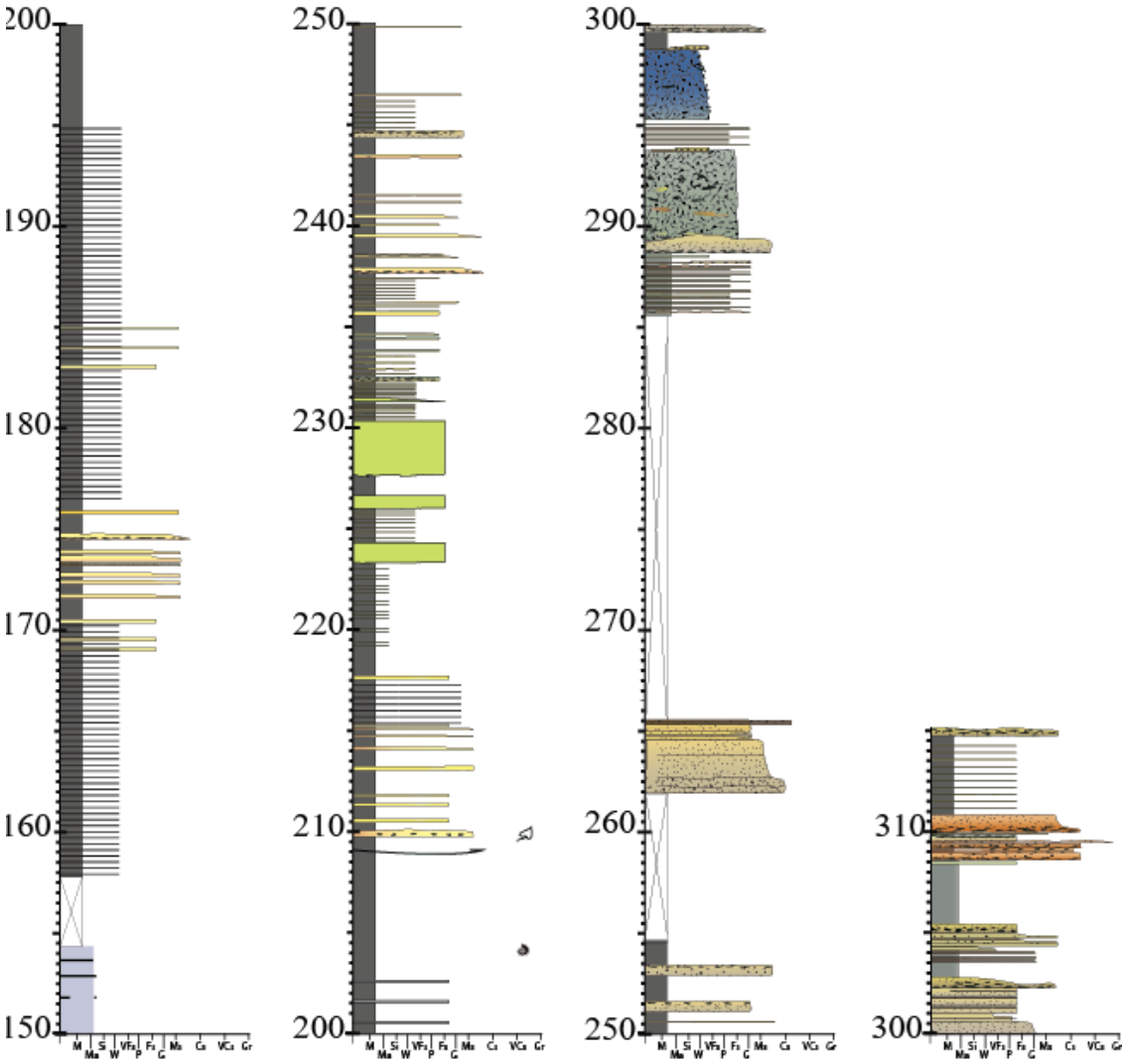

Appendix 39: Log number 6 (SonadaS1) part 2.

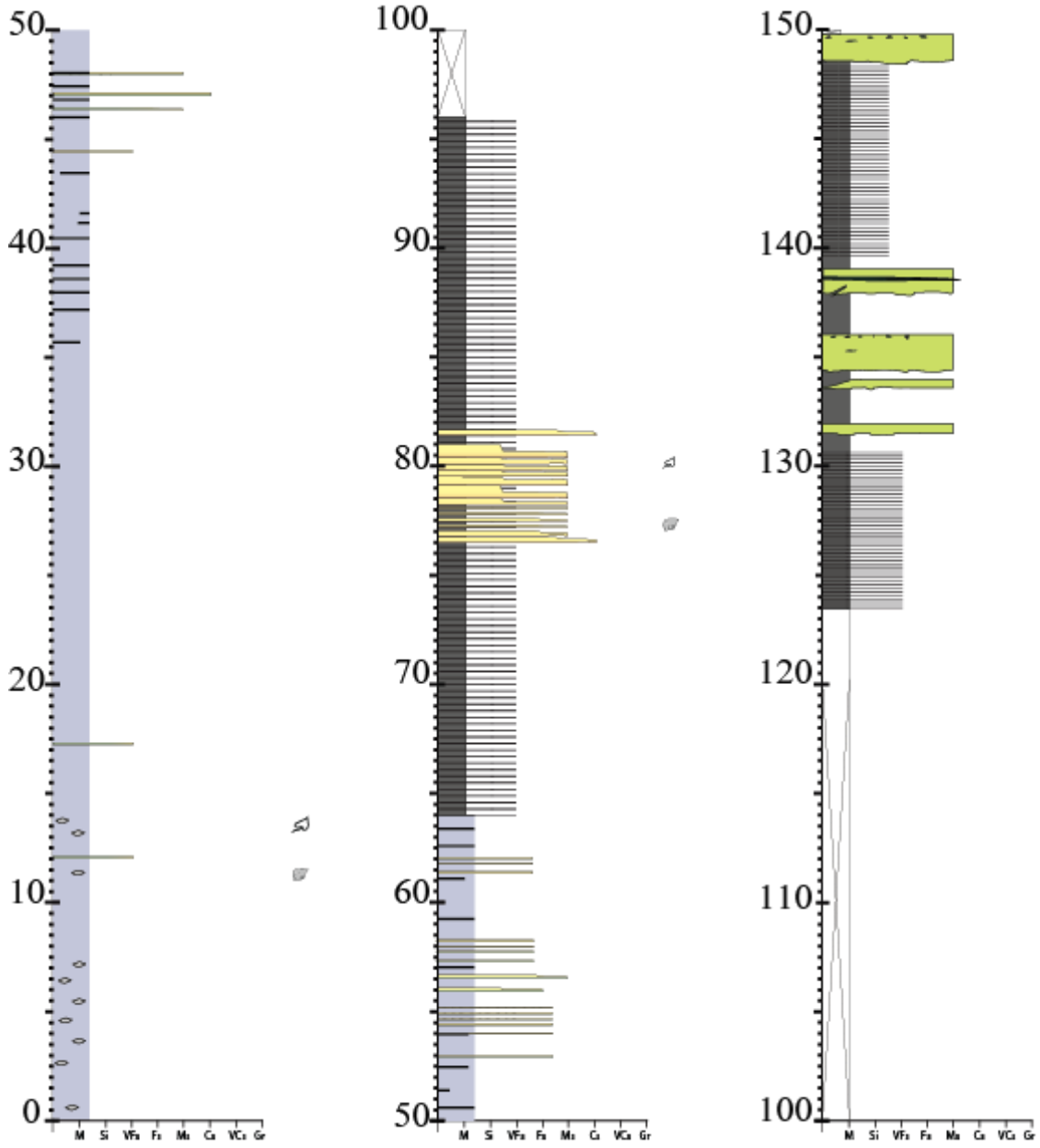

Appendix 40: Log number 7 (Picun Leufu) part 1.

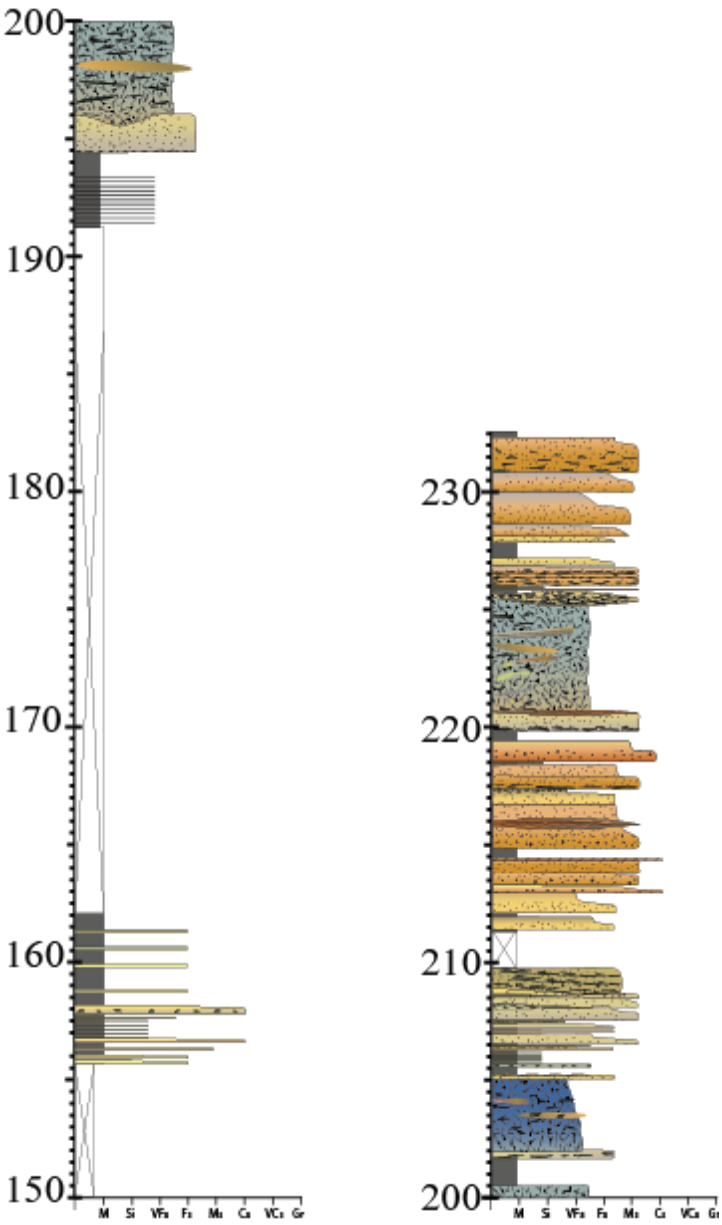

Appendix 41: Log number 7 (ChaS7) part 2.

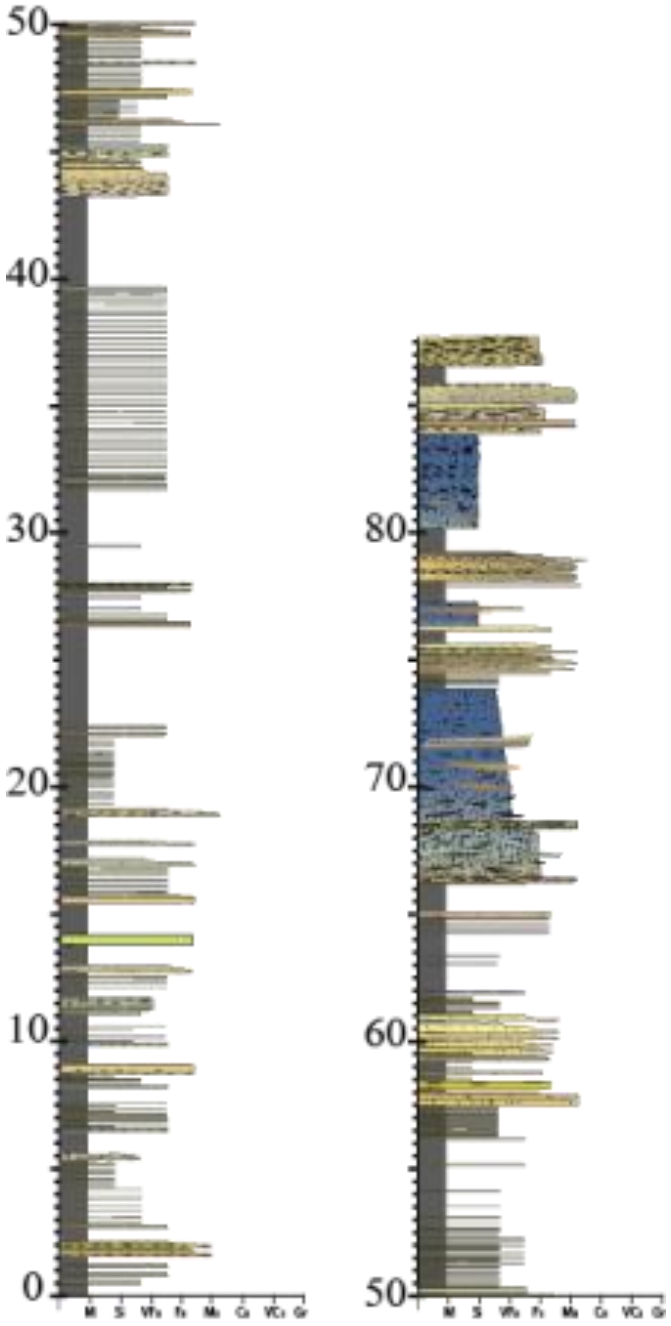

Appendix 42: Log number 8 (ChaS8).

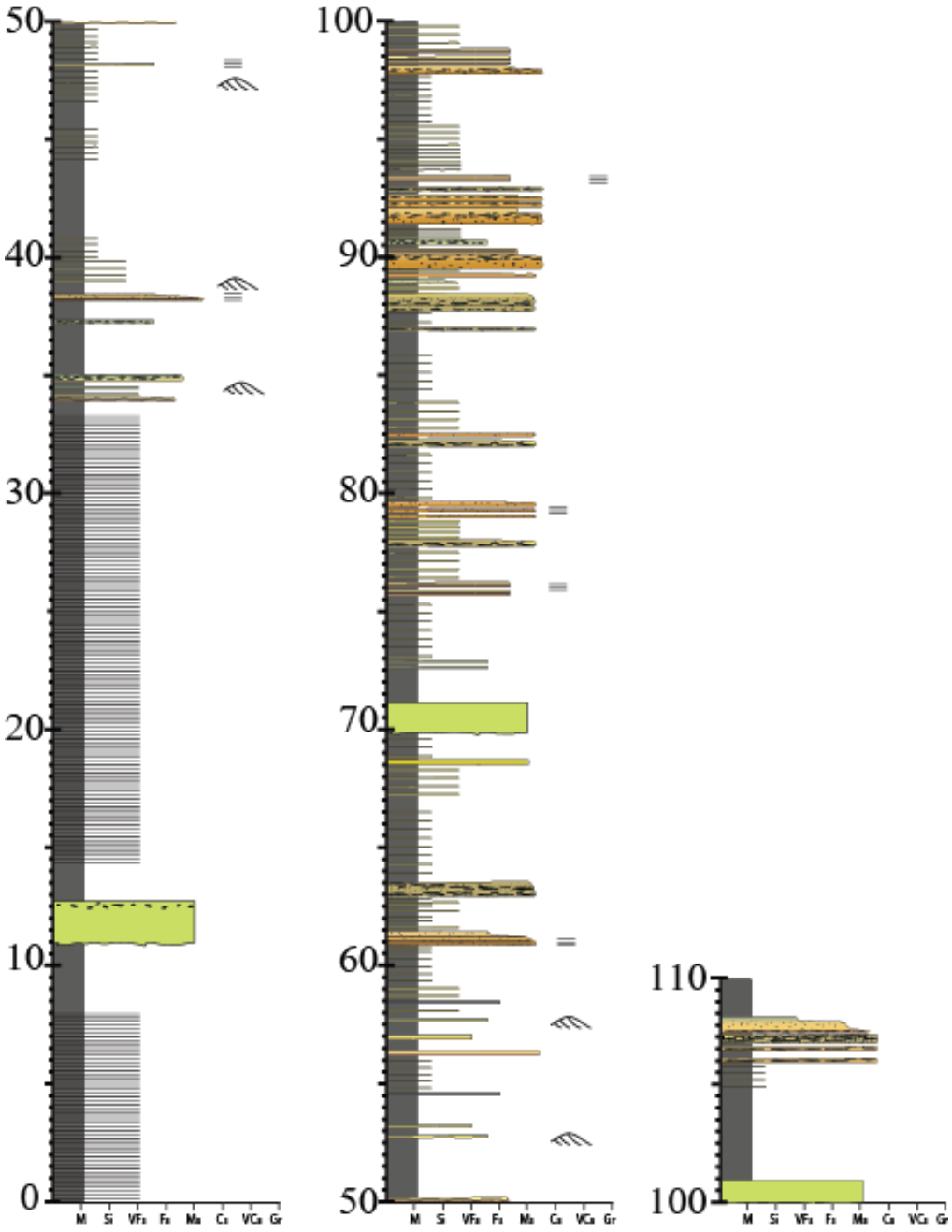

Appendix 43: Log number 9 (ChaS16).

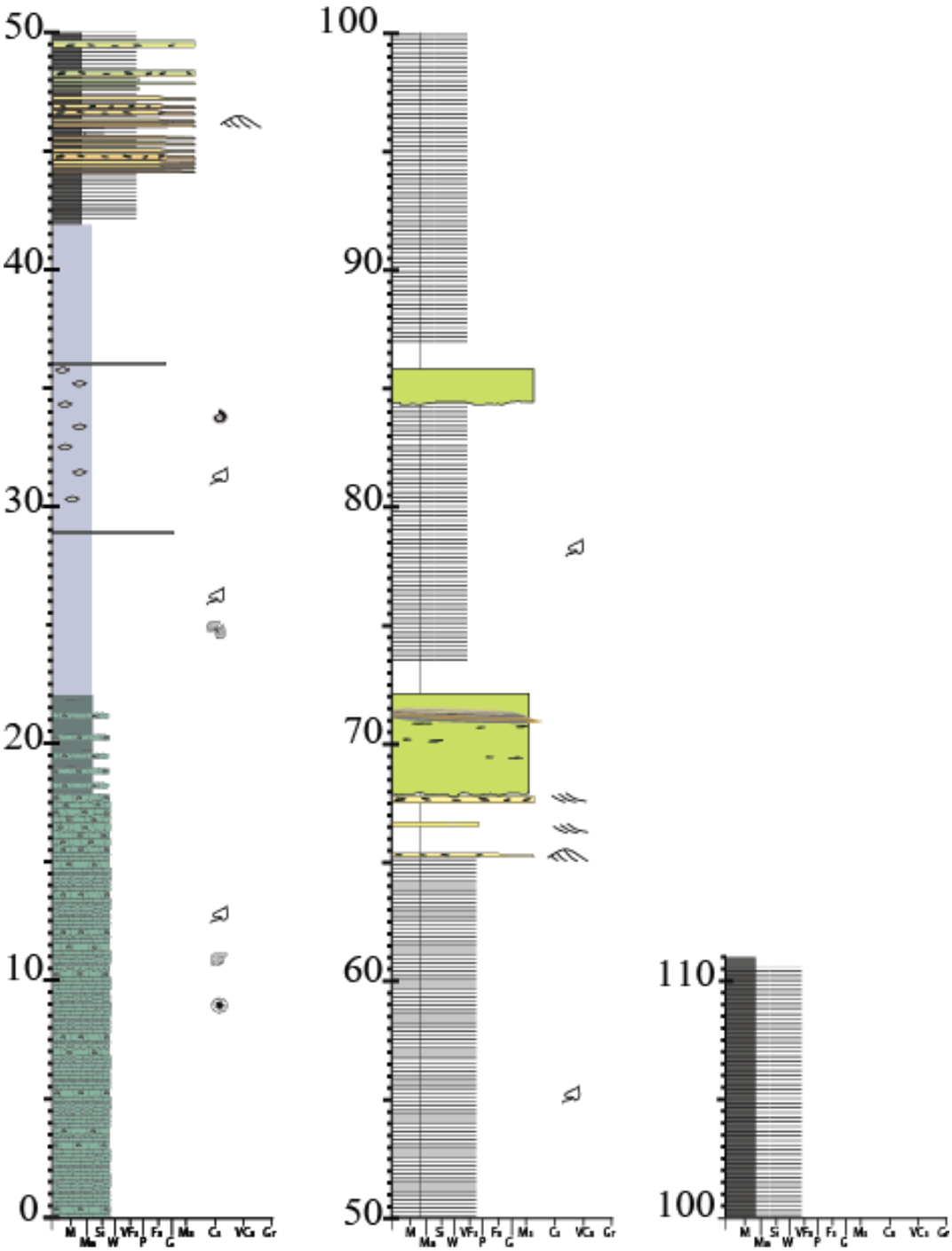

Appendix 44: Log number 10 (El Luchador S1).

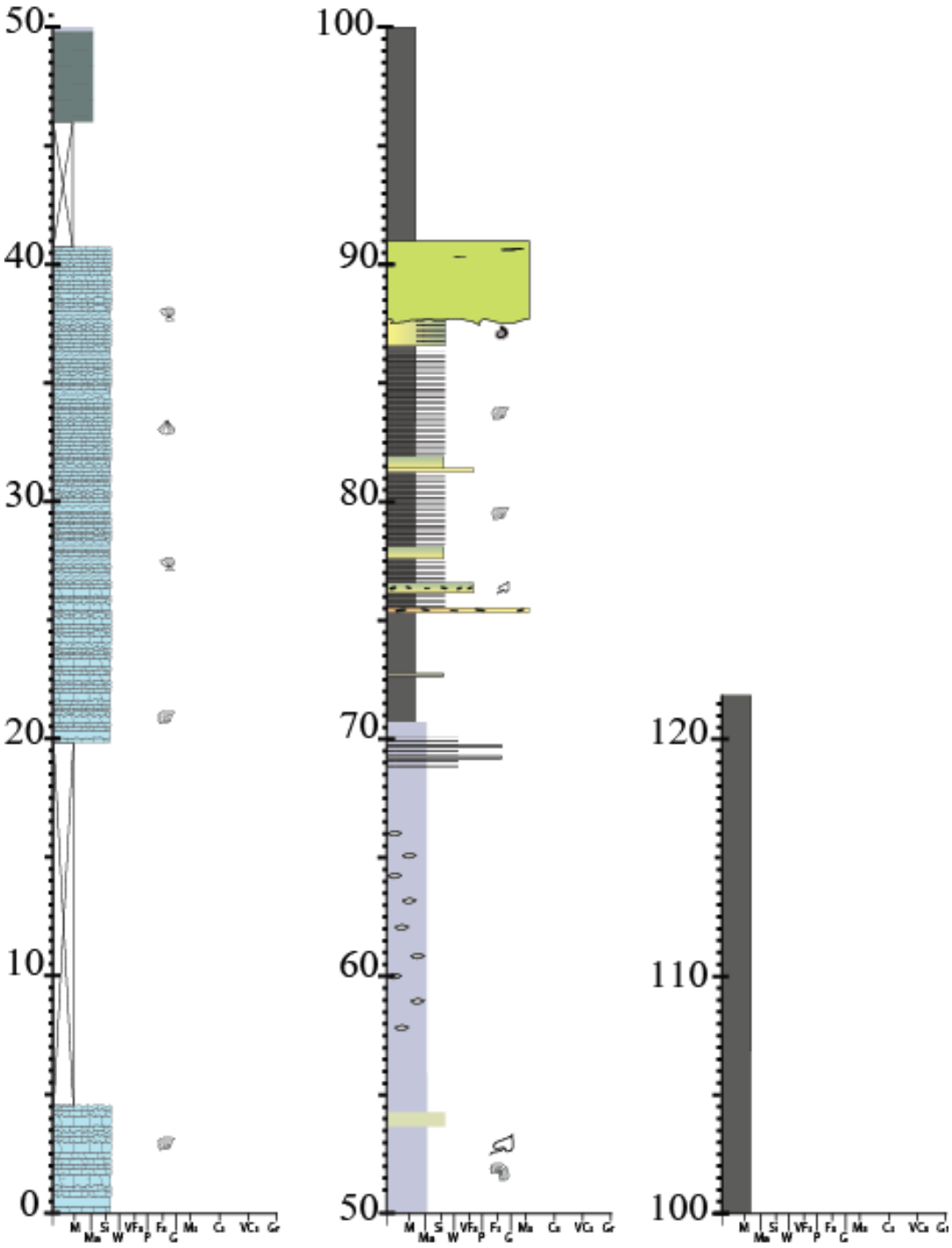

Appendix 45: Log number 12 (Paine Milla).

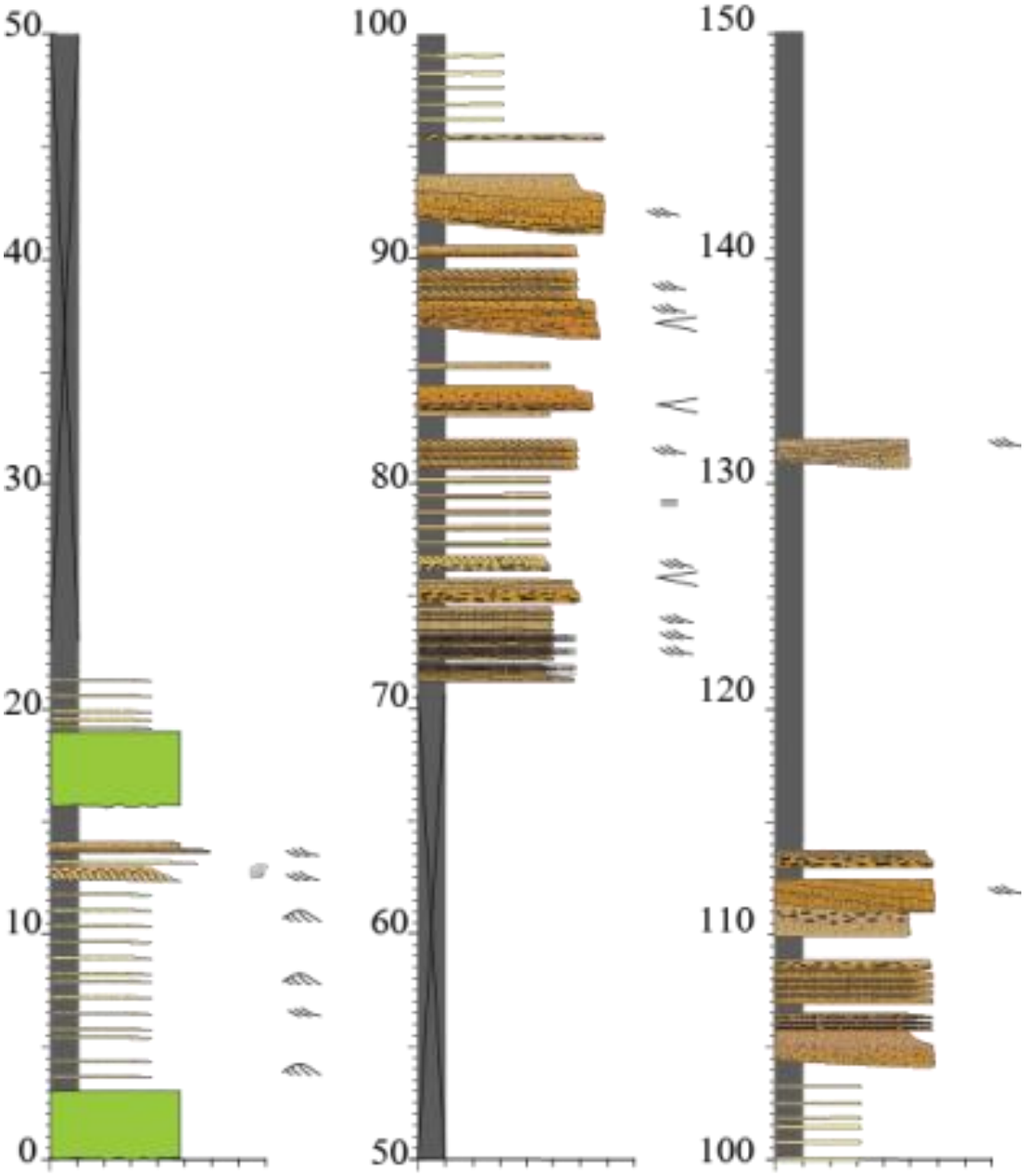

Appendix 46: Log number 12bis (ChaS12).

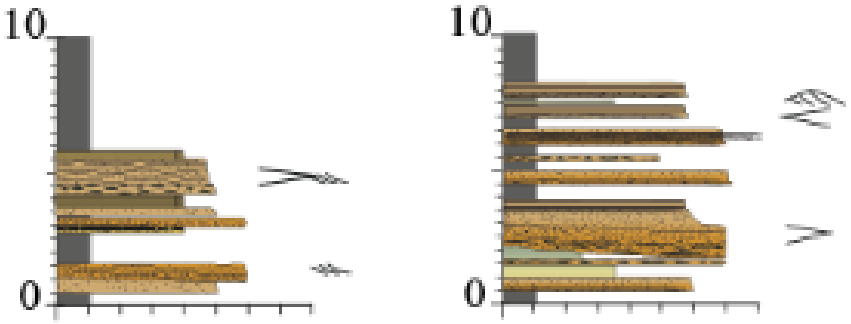

Appendix 47: Log number 13 (CP15) and 14 (CP14).

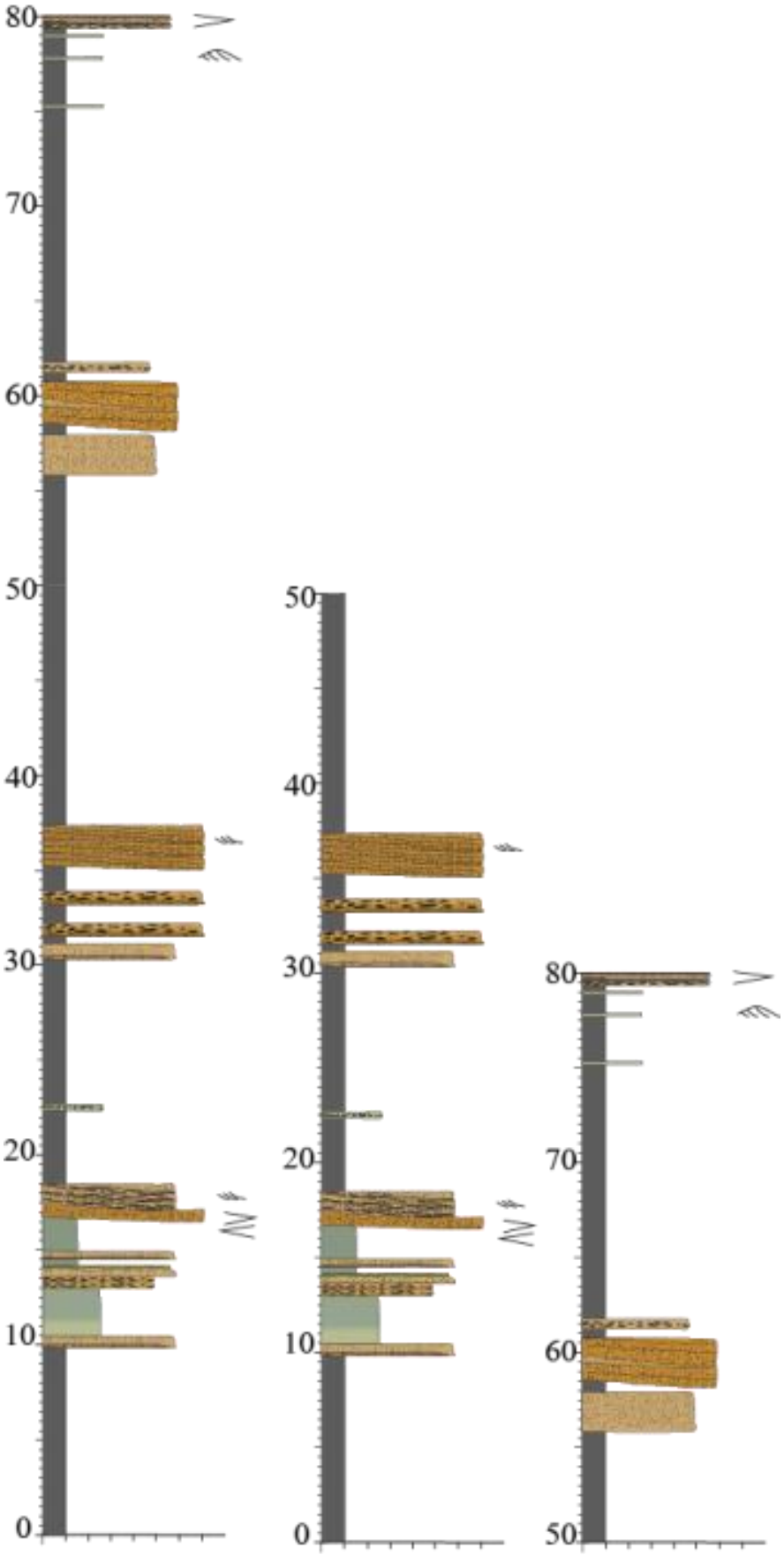

Appendix 48: Log number 15 (CP13).